AJNR

AMERICAN JOURNAL OF NEURORADIOLOGY

THE JOURNAL OF DIAGNOSTIC AND
INTERVENTIONAL NEURORADIOLOGY

Calcified cerebral emboli

Spine DWI of infection versus Modic changes

Vessel wall imaging differentiates vasculitis
from vasoconstriction syndrome

Official Journal ASNR • ASFNR • ASHNR • ASPNR • ASSR

ENHANCED CONTROL TO
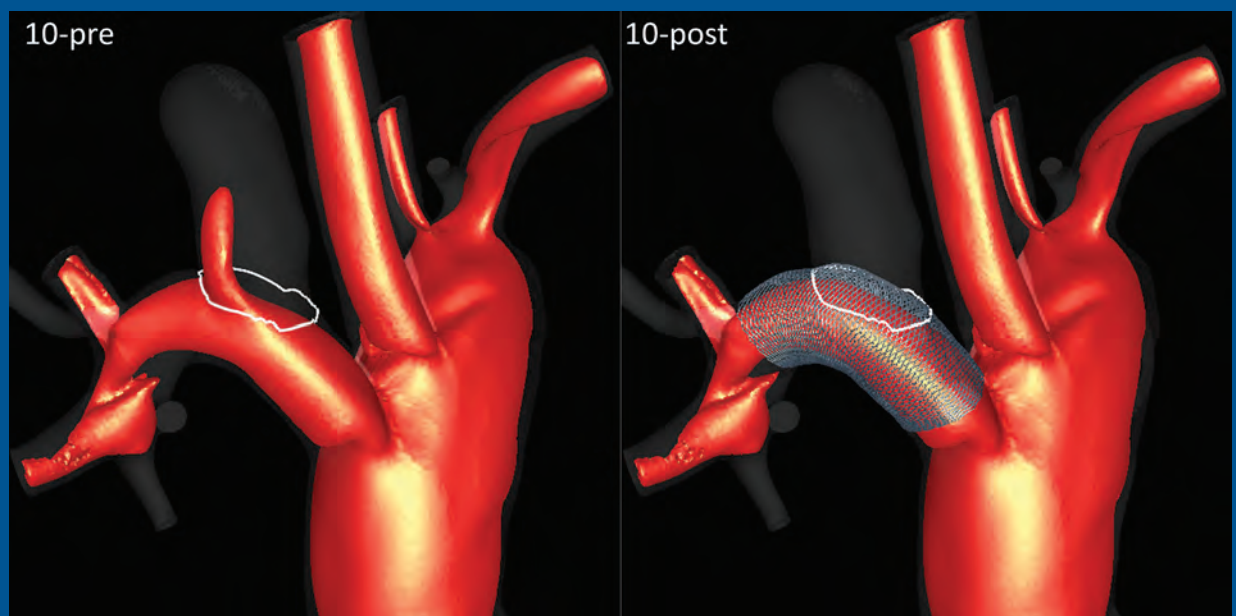
V-Trak® Advanced Coil System

Introducing the **V-Trak® Advanced Coil System**, the next generation to power the performance of our most technically advanced line of coils.

Excellent feel	– Balanced design provides enhanced feel during coil delivery
Reengineered, anatomically designed pusher wire	– Superior control and 1:1 coil responsiveness even in tortuous anatomy – Smooth trackability and efficient pushability – Distal softness for minimal microcatheter deflection and kick-out
Streamlined detachment mechanism	– Enhanced detachment reliability
Robust and tapered introducer sheath	– Smooth introduction of even the smallest coils – More secure seating inside microcatheter hub with smallest in-hub gap
Enhanced stretch resistance	– Precise coil repositioning and improved durability
Gapped coil hoop	– Easy flushing during coil preparation

Call your MicroVention representative to check availability and learn more about our new V-Trak® Advanced Coils including Cosmos®, HyperSoft®, HyperSoft® 3D, VFC®, HydroFrame®, HydroFill® and HydroSoft® coils.

microvention.com

MAXIMIZE COIL PERFORMANCE

OPTIMAL COMBINATION OF SUPPORT AND FLEXIBILITY

ROBUST RELIABILITY

- **Streamlined detachment mechanism has best-in-class detachment reliability in bench testing**

SOFTNESS ZONE

- **Ultra soft coiled pusher wire for:**
  - Controlled, safe tracking through distal vasculature
  - Minimal catheter deflection and kick-out
  - Consistent pushability

TRANSITION ZONE

- Tapered transition from hypotube to coiled pusher wire
- Engineered polymer jacket for stability
- Optimized combination of support and softness

SUPPORT ZONE

- **Stable hypotube for:**
  - Excellent and smooth pushability
  - 1 : 1 coil responsiveness
- **Fluoro safe markers for ease of use, visualization and reduced fluoroscopy time**

MicroVention®
TERUMO

BARRICADE™
COIL SYSTEM

BLOCKADE
M E D I C A L

18 TECHNOLOGY DRIVE #169, IRVINE CA 92618 | **P** 949.788.1443
WWW.BLOCKADEMEDICAL.COM

MADE IN AMERICA

CE
0297
MKTG-020   REV. B

AJNR

AMERICAN JOURNAL OF NEURORADIOLOGY

Publication Preview at www.ajnr.org features articles released in advance of print. Visit www.ajnrblog.org to comment on AJNR content and chat with colleagues and AJNR's News Digest at http://ajnrdigest.org to read the stories behind the latest research in neuroimaging.

Indicates Editor's Choices selection

Indicates Fellows' Journal Club selection

Indicates open access to non-subscribers at www.ajnr.org

Indicates article with supplemental on-line table

Indicates article with supplemental on-line photo

Indicates article with supplemental on-line video

EBM 1 Indicates Evidence-Based Medicine Level 1

EBM 2 Indicates Evidence-Based Medicine Level 2

Flow-diverting treatment shows complete aneurysm occlusion.

Trevo® XP

PROVUE RETRIEVER

Take Control. Capture More.

The newly designed Trevo® XP ProVue Retriever takes proven Trevo Retriever performance to new levels for **easy delivery, easy placement,** and **easy visualization.**

When you're in control, it's amazing what you can capture.

stryker®
Neurovascular

Stroke: *Our Only Focus. Our Ongoing Promise.*

ASNR 53rd Annual Meeting & The Foundation of the ASNR Symposium 2015

Getting Personal • Getting Personal • Getting Personal • Getting Personal

ASNR
CHICAGO ★ 2015
April 25-30, 2015
Sheraton Chicago Hotel & Towers

ASFNR ASHNR ASPNR ASSR SNIS

THE FOUNDATION OF THE ASNR

Abstract Deadline:
Friday, December 12, 2014
Please visit www.asnr.org/2015
for more information

**Request Programming and Registration Materials
for the ASNR 53rd Annual Meeting, Contact:**

ASNR 53rd Annual Meeting
c/o American Society of Neuroradiology
800 Enterprise Drive, Suite 205
Oak Brook, Illinois 60523-4216
Phone: 630-574-0220
Fax: 630-574-0661
Email: meetings@asnr.org
Website: www.asnr.org/2015

Scan now to visit our website

ONLINE FEATURES (www.ajnr.org)

BOOK REVIEWS *R.M. Quencer, Section Editor*
Please visit www.ajnrblog.org to read and comment on Book Reviews.

AJNR

AMERICAN JOURNAL OF NEURORADIOLOGY

Publication Preview at www.ajnr.org features articles released in advance of print.
Visit www.ajnrblog.org to comment on AJNR content and chat with colleagues and AJNR's News Digest at http://ajnrdigest.org to read the stories behind the latest research in neuroimaging.

AUGUST 2014 • VOLUME 35 • NUMBER 8 • WWW.AJNR.ORG

AJNR

Go Green!

AJNR urges American Society of Neuroradiology members to reduce their environmental footprint by voluntarily suspending their print subscription.

The savings in paper, printing, transportation, and postage not only help members cut down on clutter, but go to fund new electronic enhancements and expanded content.

The digital edition of *AJNR* presents the print version in its entirety, along with extra features including:

- Publication Preview
- Case of the Week
- Podcasts
- Special Collections
- The *AJNR* Blog
- Weekly Poll

It also **reaches subscribers much faster than print**. An **electronic table of contents** will be sent directly to your mailbox to notify you as soon as it publishes.

Readers can **search, reference, and bookmark** current and archived content 24 hours a day on www.ajnr.org, rather than thumb through stacks of accumulated paper issues for articles and images they need.

http://www.ajnr.org/cgi/feedback

ASNR members who wish to opt out of print can do so by using the Feedback form on the *AJNR* Website (**http://www.ajnr.org/cgi/feedback**). Just type "Go Green" in the subject line to stop print and spare our ecosystem.

A Call to Action: Maintain Your Happiness, Be Generous!

M. Castillo, *Editor-in-Chief*

Generosity comes in many flavors: the giving of time, resources, goods, and, of course, money. No matter what is given, Americans are considered to be most generous. With respect to donating money, in 2006 Americans donated over $295 billion, which, corrected for inflation and population changes, made for a 190% increase compared with 50 years previously. Americans donate more than the citizens of any other country, encouraged by a tax system of deductions.[1]

"Generosity" is defined as the habit of giving without expecting anything in return. The practical manifestations of generosity are donations. In basically all religions, generosity is rewarded, and in Buddhism, it is the opposite of greed. Americans who donate give one-third to religious institutions, the rest to secular causes, and it is known that "religious and conservative" individuals donate more than nonreligious liberal individuals.

The University of Notre Dame's initiative, the Science of Generosity, explores the relationship between philanthropy, volunteerism, and altruism. This initiative gives about $3 million annually for research, and in its first year, 2009, it received over 600 proposals, of which 9 were funded. A list of currently funded projects can be found at: http://generosityresearch.nd.edu/current-research-projects. An interesting project funded by this institution looked into the genetic origins of altruism in young children.[2] The authors found that the presence of the arginine vasopressin (AVP) receptor 1A leads to a lower altruistic proclivity. In short, AVP serves as a peripheral hormone that regulates water balance and has effects in the hippocampi and amygdalae. It is also thought that AVP plays some role in the brain's dopaminergic mechanisms because its sites of expression are somehow related to those of the dopamine reward-associated pathways. Oxytocin is also involved in mediating generosity. In one experiment, individuals injected with 40 IU of this hormone were found to be 80% more generous than those who received a placebo.[3] This last study comes from the Center of Neuroeconomics Studies headed by Dr Paul J. Zak, a mathematician and economist with postdoctoral training in neuroimaging at Harvard. Dr Zak believes that oxytocin is our "moral molecule," and he has written a popular book about it.[4] It seems that oxytocin is also associated with feelings of well-being, and that is why individuals who give feel pleasure at doing so.

fMRI shows activation of the precuneus and lingual gyri when generosity is called for, and greater lingual gyral activation is associated with an increased propensity to give.[5] The same brain regions are used when taking an outside perspective of one's self, thinking about the death of a loved one, and recalling vivid memories of one's life. These thoughts bring us closer to mortality, and the feeling presumably triggers a desire to leave a legacy and give. What is fascinating is that generosity is its own reward because it results in additional oxytocin release and increasing feelings of happiness (not a "vicious" but a "virtuous" cycle). Whether we are being generous for our own benefit or acting that way on behalf of others, the brain activates and produces identical feelings of reward.

Happiness leads to generosity, and this idea is explored in Richard Powers' wonderful book *Generosity: An Enhancement*.[6] In it, a young woman with excess happiness that leads to marked generosity is thought to harbor the gene for happiness/generosity and is exploited and, not surprisingly, abused by the media. Of course, such a condition does not exist, and in the book, it serves as a device to tackle the idea that some excessively generous individuals are viewed by society as anomalies. What is true is that some bipolar individuals express extreme happiness during their hypomanic periods, which disastrously leads to periods of mania and/or depression.[7] The "syndrome of excess happiness" may be a serious psychiatric condition.

Happiness is now more popular than ever. The Greater Good Web site (www.greatergood.com) contains more than 400 articles dealing with happiness and, specifically, how to bring up happy children. Extreme and constant happiness leads to decreased creativity.[8] Extreme happiness also leads to riskier behaviors, such as binge eating, sexual promiscuity, and drug abuse. Children who are considered very happy have higher mortality rates because they tend to engage in riskier behaviors. The problem is also that the term "happiness" is really an umbrella that encompasses different types of feelings and not just one. What is even worse, obsessively pursuing happiness makes you unhappy.

Does having money (lots of it) make us happier and more generous? The best rated jobs in the United States are dentists and physicians; and though they are not the best paid ones, no one in these professions lacks money.[9] Although among physicians, radiologists are number 3 on salary scales, they do not even rank in the top 10 when job happiness is evaluated.[10] If asked, only 50% of all physicians stated that they would study medicine again. Judging by donations, specifically those to the Foundation of the American Society of Neuroradiology (ASNR), I cannot say that neuroradiologists are very generous.* An informal poll, taken by myself, tells me that neuroradiologists are not happy with their salaries (think they should get more) and especially are not happy with the idea of lower ones in the next few years. How much money is needed to be happy?

Daniel Kahneman, a Princeton psychologist who won the Nobel Prize for economics in 2002, has explored the issue of money and happiness. He has concluded that happiness and a sense of

---

*Only 7% of ASNR members donated to our Foundation in 2012 (and most were members of the Executive Committee). The total donations for that year were slightly over $300,000, but this included 7 corporate donors and 1 practice group donor. Conversely, more than 60% of the ASNR staff, who get paid much less than physicians (average salary for radiologists in the United States: $349,000 per year in 2012), donated to the Foundation last year.

well-being increase with salary but just up to US $75,000 per year.[11] Above that amount, there are no more increases in happiness (however people making at least that amount are twice as happy as those making, on average, US $20,000 per year). He suggests that higher income buys satisfaction but not happiness. Moreover, individuals earning higher incomes tend to be tenser, lose their ability to savor small pleasures, and spend less time doing activities they enjoy. It is also clear that lower income correlates with unhappiness and that increases in salary lead to only transient happiness due to the phenomenon of "adaptation." Among other factors, even college education has little to do with happiness but clearly correlates with stress. Having children is the biggest contributor to unhappiness; they lead to constant feelings of stress, sadness, and worry.[12]

In one study, actors were asked to express feelings of happiness and sadness while examined with fMRI.[13] In both states, activation occurred in the frontal lobes, anterior temporal lobes, and the pons. Although the regions were similar for both emotional states, different subregions were activated for each. In a different fMRI study, the mode and tempo of music were manipulated to be perceived as either sad or happy and the former elicited responses in the left orbito- and mid-dorsolateral frontal cortices.[14] Happy voices elicit stronger and different fMRI responses than angry ones.[15] Body postures may also indicate happiness or other emotions. When observing human body postures, our brain always records 2 things: action and emotion. These states activate visual representation/motion processing and emotional interpretation areas. Both areas are activated simultaneously but differently in men than in women.[16] Men seem to show more reliable activation but in lesser amounts than women.

It seems to me that we neuroradiologists have every reason to be happy, and despite that, only a small group of us are generous with our money and time. Generosity is generally encouraged by the so-called "immediacy bias," better known as a "call to action." Crises and feelings of uncertainty and worry lead to greater donations. What better call to action than the lack of scientific evidence of what we do and the ever-decreasing government funding of research? If we do not support our Foundation, these issues will never be solved. If we continue to be as happy as we are now and do not increase our generosity by contributing to our Foundation, our jobs and other sources of happiness will soon disappear.

REFERENCES

1. Brooks AC. **A nation of givers.** *The American* 2008 http://www.american.com/archive/2008/march-april-magazine-contents/a-nation-of-givers. Accessed September 17, 2013
2. Avinun R, Israel S, Shalev I, et al. **AVPR1A variant associated with preschooler's lower altruistic expression.** *PloS One* 2011;6:e25274
3. Zak PJ, Stanton AA, Ahmado S. **Oxytocin increases generosity in humans.** *PloS One* 2007;2:e1128
4. Zak PJ. *The Moral Molecule: The Source of Love and Prosperity.* New York: Dutton Adult; 2012
5. James RN, O'Boyle MW. Charitable estate planning as visualized autobiography: an fMRI Study of its neural correlates. February 6, 2012. Social Science Research Network. http://papers.ssrn.com/sol3/papers.cfm?abstract_id=2000345. Accessed September 17, 2013
6. Powers R. *Generosity: An Enhancement.* New York: Farrar, Straus, and Giroux; 2009
7. Hibbing JR, Alford J, Lohrenz T, et al. **Generosity is its own reward: the neural basis of representation.** In: *Proceedings of the Annual Meeting of the American Political Science Association,* Toronto, Canada; September 3–6, 2009. http://ssrn.com/abstract=1451309 Accessed on September 17, 2013
8. Davis MA. **Understanding the relationship between mood and creativity: a meta-analysis.** *Organizational Behavior and Human Decision Processes* 2009;108:25–38
9. Graves JA. **The 25 best jobs of 2013.** *US News & World Report Money Careers.* http://money.usnews.com/money/careers/slideshows/the-25-best-jobs-of-2013. Accessed September 17, 2013
10. Physician Compensation Report 2013. Medscape Multispecialty. http://www.medscape.com/features/slideshow/compensation/2013/public. Accessed September 17, 2013
11. Kahneman D, Deaton A. **High income improves evaluation of life but not emotional well-being.** *Proc Natl Acad Sci U S A* 2010;107:16489–93. www.pnas.org/cgi/doi/10.1073/pnas.1011492107. Accessed September 17, 2013
12. Kahneman D, Krueger AB, Schkade D, et al. **Would you be happier if you were richer? A focusing illusion.** *Science* 2006;312:1908–10
13. Pelletier M, Bouthillier A, Lévesque J, et al. **Separate neural circuits for primary emotions? Brain activity during self-induced sadness and happiness in professional authors.** *Neuroreport* 2003;14:1111–16
14. Khalfa S, Schon D, Anton JL, et al. **Brain regions involved in the recognition of happiness and sadness in music.** *Neuroreport* 2005;16:1981–84
15. Johnstone T, van Reekum CM, Oakes TR, et al. **The voice of emotion: an fMRI study of neural responses to angry and happy vocal expressions.** *Soc Cogn Affect Neurosci* 2006;1:242–49
16. Kana RK, Travers BG. **Neural substrates of interpreting actions and emotions from body postures.** *Soc Cogn Affect Neurosci* 2012;7:446–56

EDITORIAL

Level 1 EBM Expedited Review

J.S. Ross

A recent poll of Canadian researchers identified the top 3 factors that influence where they send their own manuscripts: 1) ensuring methodologic soundness by peer review, 2) journal reputation, and 3) fast publication.[1] The *AJNR* (independent of this poll) has recognized these important factors, as well as the competitive nature of scientific publishing, by the introduction of a Level 1 Evidence-Based Medicine Expedited Program. The details of this significant program are defined on the *AJNR* Web site (see the "Author Info" section). Briefly, the program entails a very fast peer review time of 5–7 days, followed by an immediate editorial decision. The length of time from acceptance of the final revision to electronic publication would be 4 weeks. Other perks of this program include the waiving of various fees, such as the open access, color, and over-the-limit word count charges.

What is level 1 evidence? That depends. Levels of evidence were initially defined in 1979 by the Canadian Task Force on Periodic Health Examination.[2] Sackett[3] further defined this in 1989 in an article looking at the evidence for antithrombotic agents. This seminal paper was barely 2 pages in length. Since that time, interest in this subject has exploded, and there are now

multiple stakeholders eyeing evidence-based medicine ranging from individual patients to the Federal government. Multiple excellent reviews are available for the intrepid reader of this complex and controversial topic.[4,5]

For the purpose of classification for the *AJNR*, the Oxford Centre for Evidence-Based Medicine Levels of Evidence (2009) is used (also on the *AJNR* Web site).[6] For neuroradiologists, the questions to be answered primarily involve therapy and diagnosis. Therapy level 1 studies include systematic reviews of randomized controlled trials, and randomized controlled trials with narrow confidence limits. Diagnosis level 1 studies include systematic reviews of level 1 studies, a validating cohort study with good reference standards, or a clinical decision rule tested within 1 clinical center. For reference, a nonconsecutive study is level 3, a case series is level 4, and expert opinion is level 5 (ouch).

Evidence-based medicine defines a hierarchy of clinically relevant information; however, this information is by no means absolute.[7] Certain therapies and treatments may be so effective or dramatic that they will never experience a randomized controlled trial. The oft-cited tongue-in-cheek manuscript evaluating randomized controlled trials in parachute use is a case in point.[8] In our specialty, with its emphasis on technologic advancement, there will be seminal articles that advance the field and which provide important contributions to patient care, but do not achieve level 1–2 status (such as the initial diffusion imaging papers).

Despite its flaws and increasing complexity, the sorting and weighting of manuscripts that define high quality and minimal bias is an important foundation upon which evidence-based medicine is built. This journal will do its part to bring such manuscripts to readers.

REFERENCES

1. The Scholarly Kitchen. **What researchers value from publishers, Canadian survey.** http://scholarlykitchen.sspnet.org/2014/05/15/what-researchers-value-from-publishers-canadian-survey/. Accessed May 22, 2014
2. Canadian Task Force on the Periodic Health Examination. **The periodic health examination.** *Can Med Assoc J* 1979;121:1193–254
3. Sackett DL. **Rules of evidence and clinical recommendations on the use of antithrombotic agents.** *Chest* 1989;95(2 suppl):2S–4S.
4. Manchikanti L. **Evidence-based medicine, systematic reviews, and guidelines in interventional pain management, part I: introduction and general considerations.** *Pain Physician* 2008;11:161–86
5. Burns PB, Rohrich RJ, Chung KC. **The levels of evidence and their role in evidence-based medicine.** *Plast Reconstr Surg* 2011;128:305–10
6. OCEBM Levels of Evidence Working Group. **The Oxford levels of evidence 2.** Oxford Centre for Evidence-Based Medicine. http://www.cebm.net/index.aspx?o=5653. Accessed May 22, 2014
7. Glasziou P, Chalmers I, Rawlins M, et al. **When are randomised trials unnecessary? Picking signal from noise.** *BMJ* 2007;334:349–51
8. Smith GCS, Pell JP. **Parachute use to prevent death and major trauma related to gravitational challenge: systematic review of randomised controlled trials.** *Int J Prosthodont* 2003;19:126–28

Functional Anatomy of Essential Tremor: Lessons from Neuroimaging

R. Klaming and J. Annese

ABSTRACT

SUMMARY: The neuropathogenetic processes underlying essential tremor appear to cause subtle morphologic changes in neural networks that include multiple brain structures, primarily the cerebellum, brain stem, frontal lobes, and thalamus. One of the main challenges of neuroimaging in essential tremor is differentiating disease-specific markers from the spectrum of structural changes that occur due to aging. This review discusses recent neuroimaging studies in the light of current knowledge of the neuropsychology and pathology of the disease. We suggest that the application of multiple macroscopic and microscopic neuroimaging modalities, combined with personalized information relative to cognitive and behavioral symptoms, is the prerequisite for a comprehensive classification and correct diagnosis of essential tremor.

ABBREVIATIONS: ET = essential tremor

Essential tremor (ET) is one of the most common yet least understood movement disorders.[1] It is primarily characterized by a shaking of the hands and forearms that is evident during simple voluntary actions, such as drinking, pouring, eating, or writing.[2] For this reason, in addition to causing obvious disruption of daily activities, patients with ET often avoid social situations, even though they develop strategies to cope with the condition. Tremor is not limited to the upper limbs; the head, neck, voice, legs, or trunk may also be affected. Although ET is much more common in the elderly, the tremors can appear in children and young adults. Therefore, it cannot be considered purely an age-related disease, nor is it clearly sex-specific.

Despite the serious impairment that most patients experience, ET was, until recently, viewed merely as a benign, monosymptomatic (ie, motor) condition. Increased public awareness and new research have shifted the perception of ET to that of an actual neurodegenerative disease that is characterized by motor symptoms and cognitive

changes.[3] Nevertheless, unlike other neurologic conditions such as Alzheimer and Parkinson diseases, for which the dynamics and the topography of degeneration are reasonably well-mapped, the neuropathologic phenomena underlying ET seem to be much more subtle and their distribution, more elusive.

To date, specific noninvasive markers of ET have not been identified and localized. This may be because the pathology of ET is overshadowed by broad features of age-related neurologic degeneration. It is also possible that available tools do not afford the resolution (Fig 1) or scope of analysis to detect patterns of correlation that may constitute the neural architecture of the disease.

The Diagnosis of ET Is Not Definitive

Given that definitive radiologic and pathologic criteria do not exist,[2,4] the diagnosis of ET is based solely on behavioral symptoms. Relevant factors to establish a diagnosis and distinguish ET from other movement disorders include the age of onset, the evolution of clinical signs with time, which factors aggravate the symptoms, past or chronic exposure to toxic substances (heavy metals in particular), and family history.

In the case of other neurodegenerative disorders, the diagnosis of the disease can be validated at postmortem examination. For example, postmortem gross dissection of the brain of patients with Parkinson disease reveals lack of pigmentation in the substantia nigra. Cortical thinning and enlargement of the ventricles are macroscopic indicators of Alzheimer disease pathology, which is ultimately confirmed when plaques and tangles are present in silver-stained histologic preparations. The distribution of Alzheimer disease and Parkinson disease pathology follows a very con-

FIG 1. Comparison among images of the cerebellum obtained with different hardware and in different imaging conditions. In vivo 1.5T MR image (*A*) of a patient with ET, in vivo 3T MR image (*B*) of the same patient, postmortem high-resolution 1.5T MR image (*C*) acquired in situ, and 1.5T MR image (*D*) of formaldehyde-fixed specimen obtained ex situ. The direct comparison between the modalities shows the morphologic detail intrinsic to the cerebellar cortex and the potential of different scans (and different scanners) to reveal geometric complexity and contrast between the cerebellar cortex and WM. *A*, Sagittal T1 3D inversion recovery fast-spoiled gradient recalled (FSPGR); matrix size, 256 × 256; pixel spacing, 1/1 mm; section spacing, 1.2 mm; section thickness, 1.2 mm. *B*, T1 FSPGR; matrix size, 256 × 256; pixel spacing, isometric 1 mm; section spacing, 1 mm; section thickness, 1 mm. *C*, High-resolution inversion recovery T1 spoiled gradient recalled imaging; matrix size, 512 × 512; pixel spacing, 0.5273 × 0.5273 mm; section spacing, 0.7 mm; section thickness, 0.7 mm. *D*, High-resolution coronal T1 3D inversion recovery FSPGR; matrix size, 512 × 512; pixel spacing, 0.5 × 0.5 mm; section spacing, 1 mm; section thickness, 1 mm.

sistent pattern, as described by the staging of Braak and Braak[5] and Braak et al.[6]

For ET, there is no particular protocol for examination of the tissue at a microscopic level. Moreover, because ET seems to affect several structures in the brain, the typical sampling protocol (ie, the selection of only few small blocks of tissue) for institutional neuropathologic examination may not be adequate to map the distribution of cellular-level pathology.[7] It is conceivable, however, that ET-specific patterns of the distribution of susceptible cell types may emerge as more brain specimens are examined postmortem. Hence, it is important to invest in the curation and study of collections of brain specimens donated by patients who were thoroughly characterized.

Cognitive Deficits in ET

As mentioned above, ET is not a purely motor disorder but has instead been linked to additional mild cognitive deficits.[3] Despite an increasing body of neuropsychological studies of ET, the set of diagnostic criteria currently used does not include cognitive symptoms.[2,4] The affected functions are fairly heterogeneous, including impairments in attention, executive function, verbal fluency, visuospatial functioning, memory, and working memory.[3] A clear neuropsychological profile of ET is needed, and the pathophysiology of these behavioral symptoms remains to be established.

When patients with ET were asked to perform a task measuring selective attention and response inhibition[8] as well as a verbal working memory task known to involve cerebellar circuits,[9] their performance was comparable with that of controls. However, neural overactivation was detected, likely reflecting compensatory responses to subtle cognitive deficits.[8,9] The question of whether this compensation fails as the disease progresses, which would imply a degenerative component, needs to be explored with longitudinal studies.[9]

In the context of neuropsychological symptoms, cerebellar disease and damage have been associated with a pattern of cognitive deficits similar to that observed in ET.[10] The deficits seen in individuals with cerebellar lesions are believed to be produced by a disruption in the communication processes between the cerebellum and the prefrontal cortex via parietal, temporal, and limbic structures.[10]

Diverse Etiologic Factors in ET

As mentioned above, tremor onset and progression are important for diagnosing ET; however, its etiology has not been ascertained. The "usual suspects" in terms of risk factors are aging,[11] specific environmental agents,[12] and hereditary predisposition.[13] Discrepancies between multisite genetic studies and the expression of diverse phenotypes in the same family suggest genetic heterogeneity.[14] The logistics and the data to support large-scale neuroimaging studies combined with genetic studies to identify variants associated with putative noninvasive markers of ET are currently lacking. Therefore, the focus should be placed on developing accurate methodologies to identify neuroimaging markers and relate these to individual histories and etiologies.

Environmental factors discussed in the context of ET include increased blood levels of lead and beta-carboline alkaloids.[12] These neurotoxins cause damage to the cerebellum and the olivary-cerebellar tract.[15] Toxicologic research to evaluate accumulation of agents in the tissue from multiple brain structures could reveal buildup patterns in the brain of patients with ET. Whole-brain, noninvasive imaging techniques could also be used to relate neurodegeneration in the brain to other measures of toxin accumulation, such as lead poisoning.[16]

Options and Reticence in Treatment

The symptoms of ET are treated pharmacologically only when the tremor is severe enough to interfere significantly with the performance of daily activities. The 2 most commonly prescribed drugs are primidone, an anticonvulsant, and propranolol, a beta-adrenergic-blocking agent. Medication may be taken either on a daily basis or as needed, for instance, before a social event. Crucially, treatment is ineffective in >30% of the patient population.[17] These statistics are partly responsible for many patients not seeking or adhering to treatment unless the tremor is intolerable.

In the most severe and pharmacologically unresponsive cases, deep brain stimulation of the thalamus can be effective in subduing and even eliminating tremor. ET symptoms are reduced when the electrode is positioned within the ventral intermediate nucleus of the thalamus,[18] a region that receives input from the striatum (specifically, the globus pallidus) and the cerebellum and, in turn, projects to the motor cortex.[19] The fact that deep

brain stimulation works suggests not only that multiple connected brain regions are involved in the production of the tremors but also that ET shares common neurologic substrates with Parkinson disease, for which deep brain stimulation is an established palliative procedure.

Not surprisingly, alcohol relieves tremor symptoms in many patients with ET,[20] likely via the inhibition of glutamatergic pathways, but only temporarily. As the effects of ethanol wear off, the tremor symptoms actually worsen. Most interesting, transcranial magnetic stimulation, applied on the occipital area (in the region of the inion), has the same temporary mitigating effect as ethanol on tremor symptoms.[21] Given the shallow range of the magnetic pulses in transcranial magnetic stimulation, unless the visual cortex is inexplicably implicated in the disease, we conclude that the cerebellum is at least partially involved in tremor and that the body of research that focused on this structure is vindicated.

ET and the Aging Brain
It is difficult (if not impractical) to distinguish ET-related pathology from more general age-related structural changes that are detectable with MR imaging. ET is more prevalent among the elderly,[1] and neuroimaging must inevitably contend with this potential bias. If the onset of ET occurs later in life (ie, after 65 years of age), the progression of tremor symptoms is faster and more severe degenerative pathology in the cerebellum occurs.[22] This is puzzling because one would expect a greater accumulation of degeneration at the cellular level in longer-standing early-onset cases.

From a cognitive perspective, ET has also been linked to a faster decline compared with healthy age-matched subjects.[23] Furthermore, late-onset ET has been linked to an increased risk of dementia.[11] The relationship between cognitive decline and tremor symptoms is unclear. However, including well-defined cohorts with ET in the context of large-scale longitudinal neuroimaging studies that also track cognitive functioning could identify anomalous rates of cognitive decline and patterns of cerebral atrophy as valuable predictive indicators of ET. To be revealed, these effects may require specialized imaging and analysis methods. As a start, given that many individuals with ET do not tend to volunteer information about their condition unless a diagnosis is made and the personnel who perform the scans are not trained (or instructed) to pay attention to the signs of ET, it would be useful to screen for ET in participants of abundant ongoing imaging studies.[24]

The Lack of a Definitive Neuropathologic Signature for ET
At least 2 separate histopathologic features have been observed postmortem in samples of brains of patients with ET: loss of Purkinje cells in the cerebellum (in two-thirds of cases examined) and the presence of Lewy bodies in the brain stem (these features have never been found in the same brain).[25,26] One explanation for this scenario is that distinct abnormalities at the cellular level are markers of different subtypes of ET.[27]

Purkinje cells, which are motor in function, are inhibitory neurons; therefore, their loss could be linked to hyperactivity of the cerebellum and, consequently, to tremor symptoms.[26] Lewy bodies concentrate in the locus coeruleus,[25] which is the most

important source for norepinephrine in the brain and has major efferent connections to Purkinje cells in the cerebellum.[15] It has, therefore, been proposed that pathologic changes in the locus coeruleus may eventually lead to changes in Purkinje cells[26] (but then we should find both features in the same brain). Lewy bodies are prevalent in tissue from many elderly donors, including those without neurodegeneration or dementia in the last years of their lives; thus, it is unlikely that this pathology could ever become the hallmark for ET.[28]

"Torpedoes" are attenuated axonal swellings that are believed to be secondary markers related to the degeneration and death of Purkinje cells.[27] "Torpedo" sounds certainly more rare and exotic, but a review of the literature published on these peculiar silver-stained structures gives the disappointing result that they are indeed not characteristic of normal brain aging and they are not unique to brains of patients with ET either. Finally, 2 histologic studies reported abnormal attenuation of tangled basket cells surrounding the Purkinje cell bodies[29] and increased Bergman astrogliosis.[27] The cause and effects of these secondary pathologic changes remain unclear.

The findings reported in this section originate largely from studies that re-examined the same collection of brain specimens[28] (studies on the neuropathology of ET are still conducted by a handful of laboratories and on very few brains). Any apparent convergence of results could, therefore, be attributable, at least in part, to the paucity and redundancy of analyses. However, even within this small and contained research community, not everyone agrees with the idea that ET should be seen primarily as a cerebellar disease.[30,31] As mentioned earlier, there may very well be several subtypes of ET that display different (partly overlapping) pathology. It is possible that the samples studied so far only show a limited cross-section and incomplete picture of the disease. In either case, the logical solution is to increase collection and distribution of research samples for controlled (and reproducible) postmortem studies. Availability of biosamples for studies of the neuropathology of ET should improve both in terms of quantity but also in quality—that is, each sample should come fortified with clinical, neuropsychological, and even radiologic characterizations.[7]

The Need for Neuroimaging Markers as a Diagnostic Tool for ET
Histologic studies can give a definitive view of the tissue-level phenomena underlying observed signs of neurologic disease, but unfortunately, they cannot assist directly with the premorbid detection of pathologic changes. MR imaging, on the contrary, has promise in terms of predicting and tracking clinical outcomes. Several MR imaging studies, published in the past decade, sought to detect ET-specific morphologic abnormalities. Most studies highlighted atrophic changes in different lobules of the cerebellum[32,33] (but also in other brain regions[34,35]).

Patients with both head and hand tremor showed reduced GM volume in the vermis of the cerebellum, compared with patients with only hand tremor.[32] Increased GM and WM atrophy (relative to analogous measures in control subjects) was also detected in the frontal, occipital, parietal, and temporal lobes and the medulla and insula.[34,35] Taken at face value, these reports suggest a

generalized effect of ET on the cerebellothalamocortical network,[34,35] but these positive results are not ubiquitous in the literature.[36] The lack of definitive macroscopic markers for cerebellar atrophy[36] and ET-specific morphologic changes reflect the ambiguous picture that currently describes pathology at the microscopic level.

Some questions regarding ET pathology could be explored with existing tools. For example, it should be possible to determine whether ET affects the entire cerebellum or whether it selectively affects specific lobules or nuclei of the cerebellum.[37] This distinction may be of particular interest because the anterior lobule of the cerebellum is associated with motor function while the posterior regions are involved in cognition.[37] In particular, neural activation patterns among the frontal regions and the cerebellar hemispheres and the dentate nucleus are involved in executive functioning and verbal working memory.[38] Perhaps ET affects the anterior regions of the cerebellum first, leading to motor symptoms, and then spreads to the posterior regions as the disease progresses, leading to cognitive impairments.

Do patients with ET with more severe cognitive impairments also show more severe atrophy in the posterior lobules of the cerebellum? Remarkably, none of the structural MR imaging studies discussed in this review evaluated the level of cognitive impairment in their study participants. In addition to mapping the topography of structural abnormalities, defining the relative changes in different tissue compartments by using specialized imaging sequences and morphometric analyses could lead to identifying specific degeneration patterns in ET, distinguishable from those occurring due to aging.

Preliminary findings from a small ET pilot study have revealed selective atrophy in the cerebellar cortex in the absence of overall cortical atrophy.[39] In particular, the sulci of the cerebellum were found to be deeper and wider, likely indicating selective deterioration of cerebellar GM. Most interesting, the patients showed no overall volume loss in the cerebellum and minimal cerebral cortical atrophy. In addition to neuroimaging, subjects also underwent detailed neuropsychological assessment and tremor quantification, which revealed different cognitive profiles and tremor characteristics. These preliminary findings suggest that cerebellar cortical atrophy may serve as a potential selective neuroimaging marker for ET, separate from the other effects of age-related degeneration.[39]

Evaluating Neural Networks Rather than Localized Brain Regions

Undoubtedly, evidence from most published neuroimaging studies suggests that the cerebellum or neural networks involving the cerebellum play a key role in the pathophysiology of ET.[32-35,40-42] The unresolved question is whether the tremors originate in the cerebellum and are subsequently mediated by other structures within that network or whether a concerted disruption in connectivity between several brain structures causes ET-related symptoms.

MR-based diffusion imaging measures water diffusion and diffusion directionality along axons as an indicator of axonal injury. In ET research, diffusion imaging studies focus on fiber tracts projecting to and from the cerebellum. The first study to explore functional connectivity in patients with ET compared with healthy controls used DWI.[43] No major structural abnormalities were detected in the pons, middle cerebellar peduncles, cerebellar WM, dentate nucleus, red nucleus, thalamus, caudate, putamen, pallidum, and frontal WM.[43] Yet, DWI may not be sufficiently sensitive because it measures diffusion in only 1 direction as opposed to DTI, which measures diffusion in multiple directions.[44] If that were the case in this study, more subtle WM abnormalities may have been overlooked in the ET cohort.[43]

Subsequent DTI studies explored WM fiber integrity and directionality in patients with ET. DTI measures mean diffusivity and ADC, as markers of the magnitude of water diffusion along fiber tracts, and fractional anisotropy, as a marker of the directionality of water diffusion.[45] Decreased fractional anisotropy and increased mean diffusivity/ADC indicate WM damage.[45] Increased ADC values of the red nucleus, indicative of neuronal loss or injury in this region, have been reported in patients with ET compared with healthy controls.[44]

Because it is possible that pathologic changes in ET may spread with time, affecting various brain regions, the red nucleus may be a structure affected earlier than others.[44] However, this explanation is unlikely because abnormal DTI values in the red nucleus are not a consistent finding in patients with ET.[40] Likewise, while longer disease duration did correlate with lower fractional anisotropy values in the dentate nucleus in 1 study,[40] a relationship between disease duration or tremor severity and DTI measures was not confirmed by others.[41,42] This discrepancy shows that the question of whether ET is progressive warrants further study.

That the tremor origin has not been localized in ET thus far suggests that an abnormal communication between several brain regions causes motor symptoms. Several neural loops have been proposed to be affected. For instance, DTI values of the superior cerebellar peduncle fiber tracts, which receive input from the dentate nucleus and send output to the red nucleus, indicated damaged WM in a study by Nicoletti et al.[40] Based on these findings, a disturbance in the dentatorubro-olivary tract (ie, neural fibers connecting the dentate nucleus via the superior cerebellar peduncles with the red nucleus and inferior olive) may underlie tremor genesis in ET.[40]

A later study, however, failed to find WM abnormalities in the middle and superior cerebellar peduncles.[41] Instead, compromised fiber integrity was found in the inferior cerebellar peduncles, suggesting a disturbance in tracts projecting through the cerebellum via the inferior cerebellar peduncles.[41] Based on reduced fractional anisotropy in the pons, cerebellum, and midbrain and extensive WM damage in the frontal cortex and temporoparietal regions in patients with ET, others proposed that an abnormality in the cerebellothalamocorticocerebellar loop is responsible for the tremor.[46] Similarly, compromised WM has been reported in frontoparietal regions, cerebral hemispheres, the thalamus, and brain stem.[42]

In summary, with the exception of 1 study,[43] most DTI research in ET demonstrated that widespread disintegrity of cerebral and cerebellar fiber tracts is common and likely underlies tremor generation.[40-42,46] Although it is known that DTI measures are indicators for WM integrity, the exact nature underlying these pathologic processes is unknown. Whether demyelination,

myelin injury, neuronal loss, or other processes underlie abnormal DTI values in patients with ET remains to be ascertained.

Potential Bias in ET Neuroimaging Studies

The obvious discrepancy between the results of different studies may be due to a number of methodologic inconsistencies. For example, while some studies used region-of-interest–based analysis methods,[44] others used whole-brain analysis approaches[46] or both.[41] Region-of-interest–based analysis is more biased, and overall abnormalities may be overlooked. Whole-brain analysis, on the other hand, allows exploration of widespread networks but may not be specific enough, with the risk of ignoring smaller regions and nuclei.[41]

The data that make up all of the neuroimaging descriptions of ET were acquired at different magnet field strengths (most at 1.5T[32,33,36,40,46] and 3T[34,35,41,42,44]). Accordingly, contrast and resolution, the parameters that, for the most part, guide the interpretation and analysis of the images, cannot be assumed constant. The cerebellum is a very complex structure in terms of geometry, and the scale of morphologic features (and their aberrations) is much smaller than that in the cerebral hemispheres. The fractal gyrification of the cerebellar cortex is an exquisite example of this principle. Cerebellar anatomy is extremely difficult to visualize at the relatively low resolutions afforded by clinical scans[34] (Fig 1). The need for validation studies across scanners of different manufacturers and with different field strengths is even more crucial for ET than for other areas of investigation using MR imaging to model cerebral structures.

Other factors that varied considerably among studies are subject and tremor characteristics. Because it is likely that ET is a heterogeneous disease with different phenotypes, the general ET diagnosis could be inadequate to define cohorts undergoing imaging studies. It may be necessary to screen for more subtle differences between patients, such as the pattern of tremor manifestation (circadian fluctuations, effect of medication, and so forth), the history and severity of the disease (these could be documented via personalized medical history and could be measured quantitatively with commercially available tremormeters, respectively), and simple genetics (discriminating between familial-versus-nonfamilial ET).

While some patient cohorts were limited to subjects with a family history of ET,[32,40] others included patients with and without familial ET[41-43,46] or did not control for this variable.[44] While a positive family history is not the only factor proposed to play a role in the etiology of ET, this factor should be controlled for, because it could be a possible confounder. That ET often goes undiagnosed for many decades and subjects may not know about the medical history of estranged or deceased relatives should also be taken into consideration.

Finally, only 3 of the neuroimaging studies reviewed included young adults.[35,42,46] The age bias toward elderly subjects, not only dictated by the prevalence of the disease among older men and women but also by the predominance of subjects who are retired and amenable to participate and adhere to the research, could overlook crucial clues deposited by ET in otherwise young and "clean" brains. Last, neuroimaging studies might be looking too selectively at structures that are known to be "motor," such as the cerebellum; the effect is made obvious in Fig 2.

The Dysfunctional Correlates of ET

Using PET, researchers have looked for metabolic abnormalities that may trigger the tremor, such as increased blood flow in the cerebellum of patients with ET (compared with control subjects).[47,48] Patients with ET who underwent PET showed increased blood flow in the striatum, thalamus, and sensorimotor cortex[47] and in the region of the red nucleus.[48] These pontine structures were also implicated by measures of blood flow with fMRI.[49] Bilateral activation of the red nucleus, along with the dentate nuclei and both cerebellar hemispheres, was observed in patients with ET, while control subjects only showed unilateral activation of these regions when they affected tremor with the opposite limb.

PET research has also provided a neurologic explanation for the above-mentioned fact that consumption of ethanol modulates ET. This effect was mirrored by decreased metabolic rates in the cerebellum and increased activation in the inferior olivary nuclei.[47,20] Magnetoencephalography, which is characterized by a high temporal resolution, demonstrated coherent activation patterns between the arm muscle and motor cortices, thalamus, brain stem, and cerebellum, suggesting that this network of structures plays a role in ET-related tremor.[50] However, such coherent activation patterns were not confirmed by others questioning the temporal dynamics of the disease.[51]

By measuring the level of various cellular metabolites, in particular NAA and total creatine, MR spectroscopy can localize neuronal injury or loss in the brain. Patients with ET showed reduced NAA/total creatine in the cerebellum, and these values correlated with both age and tremor severity, suggesting the degenerative nature of this disease.[52] The readers of this review will be used to cautionary tales by now; therefore, they will understand that other studies could not confirm the above-stated relationship between metabolic abnormality, age, and tremor.[53]

Due to the poor spatial resolution afforded by MR spectroscopy in most typical clinical and research settings, it was possible to neither measure metabolic levels selectively in smaller nuclei nor distinguish between WM and GM within the cerebellum.[52,53] In addition, longitudinal measurements in the same subject would also be required to link metabolic changes to the progression of tremor symptoms.[52]

CONCLUSIONS

Neuroimaging research in the field of ET has demonstrated that widespread structural changes in cortical and subcortical brain regions and metabolic abnormalities are common in symptomatic patients. Clearly, detecting structural and functional changes in the cerebellum is essential in understanding the neurologic basis of motor and behavioral manifestations of ET. Nevertheless, the detailed characterization of cerebellar abnormalities that can be obtained by applying multiple, noninvasive, and postmortem neuroimaging modalities (at macroscopic and microscopic resolution, respectively) needs to be integrated with a temporal and spatial network-based approach to trace the origin and progression of the symptoms.
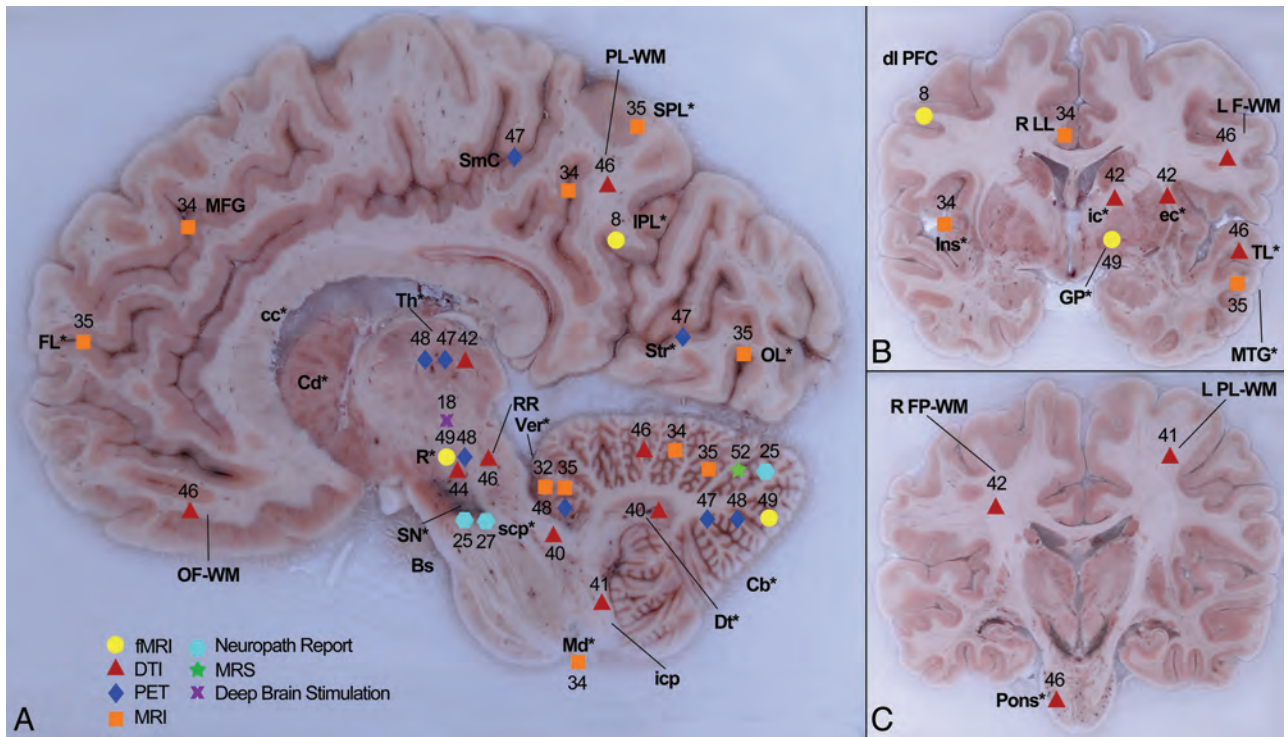
FIG 2. Summary of observed or measured phenomena derived from multiple neuroimaging modalities, neuropsychological testing, and postmortem examination (indicated by differently colored symbols). The location of neuroimaging results was projected onto tomographic anatomic images of the brain acquired during the sectioning process[7]: Purkinje cell loss,[25] presence of Lewy bodies,[25,27] reduced fractional anisotropy,[40,41,46] placing of deep brain stimulation electrode,[18] GM loss,[32,34,35] increased blood flow,[8,47,48,49] WM loss,[34] increased ADC,[44] increased mean diffusivity,[40,41,42] increased axial diffusivity,[42] reduced NAA/total creatine.[52] Bs indicates brain stem; Cd*, caudate; Cb*, cerebellum; cc*, corpus callosum; dl PFC, dorsolateral prefrontal cortex; Dt*, dentate nucleus; ec*, external capsule; FL*, frontal lobes; GP*, globus pallidus; icp*, inferior cerebellar peduncle; Ins*, insula; ic*, internal capsule; IPL*, inferior parietal cortex; LF-WM, lateral frontal WM; (L) PL-WM, (left) parietal WM; Md*, medulla; MFG, medial frontal gyrus; MTG*, middle temporal gyrus; OL*, occipital lobes; OF-WM, orbitofrontal WM; PL-WM, parietal WM; Pons*, pons; R*, red nucleus; R FP-WM, right frontoparietal WM; RLL, right limbic lobe; RR, retrorubal area of midbrain; SmC, sensorimotor cortex; scp*, superior cerebellar peduncle; SN*, substantia nigra; SPL*, superior parietal lobule; Str*, striatum; TL*, temporal WM; Th*, thalamus; VIM, ventral intermediate nucleus of the thalamus; Ver*, vermis. The asterisks denote anatomic abbreviations from Mai et al.[54]

Tangible inconsistencies between different ET neuroimaging studies emerge from the review of existing literature. These need to be addressed to resolve potential neuroimaging markers for this condition. Discrepancies could be due to methodologic differences; but different subjects examined may embody different subtypes of ET. The establishment of neuroimaging consortia in the context of which sequences and hardware could be evaluated and calibrated, as well as effective data-sharing mechanisms, could effectively eliminate site-dependent technical idiosyncrasies. Achieving shared neuroimaging resources based on well-defined (and transparent) protocols has proved very successful,[24] and it would be especially effective in the case of ET, for which the neuropathogenesis is so elusive.

The confederation of existing and emerging brain banks that share an interest in ET would create the basis for large-scale histologic studies, thereby gradually assembling the complete cellular-level landscape of the disease from thousands of cases as has been done for Alzheimer and Parkinson diseases. This approach would require not only new investments in resources (brain banks are expensive both in terms of operation and real estate) but also active engagement of the public via "citizen science" and partnerships with advocacy groups, the latter often being tremendously successful in educating and mobilizing patient populations (http://www.essentialtremor.org).

Most important, we believe that it is crucial for future research to aim at the correlation of longitudinal neuroimaging data with neuropsychologic testing, quantitative measurements of tremor characteristics (such as frequency and amplitude), and detailed personal medical and biographic information. Our close interactions with (still) few but exceptionally engaged research participants have demonstrated how varied the symptoms can be and the differences in the history of and attitude toward the condition. Quantitative and qualitative differences among patients with ET are often reflected in the results of the complete spectrum of their tests; further studies will determine whether these personal differences are also traceable to distinct patterns in their individual MR imaging.[39]

REFERENCES
1. Louis ED, Ottmann R, Hauser WA. **How common is the most common adult movement disorder? Estimates of the prevalence of essential tremor throughout the world.** *Mov Disord* 1998;13:5–10
2. Deuschl G, Bain P, Brin M. **Consensus statement of the movement**

disorder society on tremor: Ad Hoc Scientific Committee. *Mov Disord* 1998;13(suppl 3):2–23

3. Bermejo-Pareja F, Puertas-Martin V. **Cognitive features of essential tremor: a review of the clinical aspects and possible mechanistic underpinnings.** *Tremor Other Hyperkinet Mov (NY)* 2012;2 [Epub 2012 Sep 14]

4. Louis ED, Ottman R, Ford B. **The Washington Heights-Inwood genetic study of essential tremor: methodological issues in essential tremor research.** *Neuroepidemiology* 1997;16:124–33

5. Braak H, Braak E. **Neuropathological staging of Alzheimer-related changes.** *Acta Neuropathol* 1991;82:239–59

6. Braak H, Del Tredici K, Rueb U, et al. **Staging of brain pathology related to sporadic Parkinson's disease.** *Neurobiol Aging* 2003;24:197–211

7. Annese J. **The importance of combining MRI and large-scale digital histology in neuroimaging studies of brain connectivity and disease.** *Front Neuroinform* 2012;6:13

8. Cerasa A, Passamonti L, Novellino F, et al. **Fronto-parietal overactivation in patients with essential tremor during stroop task.** *Neuroreport* 2010;21:148–51

9. Passamonti L, Novellino F, Cerasa A, et al. **Altered cortical-cerebellar circuits during verbal working memory in essential tremor.** *Brain* 2011;134:2274–86

10. Schmahmann JD, Sherman JC. **The cerebellar cognitive affective syndrome.** *Brain* 1998;121:561–79

11. Benito-Leon J, Louis ED, Bermejo-Pareja F. **Elderly-onset essential tremor is associated with dementia.** *Neurology* 2006;66:1500–05

12. Louis ED, Zheng W, Jurewicz EC, et al. **Elevation of blood β-carboline alkaloids in essential tremor.** *Neurology* 2002;59:1940–44

13. Higgins JJ, Jankovic J, Patel PI. **Evidence that a gene for essential tremor maps to chromosome 2p in four families.** *Mov Disord* 1998;13:972–77

14. Lorenz D, Deuschl G. **Update on pathogenesis and treatment of essential tremor.** *Curr Opin Neurol* 2007;20:447–52

15. Louis ED, Vonsattel JP. **The emerging neuropathology of essential tremor.** *Mov Disord* 2008;23:174–82

16. Stewart WF, Schwartz BS, Davatzikos C, et al. **Past adult lead exposure is linked to neurodegeneration measured by brain MRI.** *Neurology* 2006;66:1476–84

17. Louis ED. **Essential tremor.** *N Engl J Med* 2001;345:887–91

18. Lyons KE, Pahwa R. **Thalamic deep brain stimulation and essential tremor.** In: Tarsy D, Vitek JL, Star PA, et al, eds. *Deep Brain Stimulation in Neurological and Psychiatric Disorders.* New York: Humana Press; 2008:205–14

19. Perlmutter JS, Mink JW. **Deep brain stimulation.** *Annu Rev Neurosci* 2006;29:229–57

20. Boecker H, Wills AJ, Ceballos-Baumann A, et al. **The effect of ethanol on alcohol-responsive essential tremor: a positron emission tomography study.** *Ann Neurol* 1996;39:650–58

21. Gironell A, Kulisevsky J, Lorenzo J, et al. **Transcranial magnetic stimulation of the cerebellum in essential tremor.** *Arch Neurol* 2002;59:413–17

22. Louis ED, Faust P, Vonsattel JP, et al. **Older onset essential tremor: more rapid progression and more degenerative pathology.** *Mov Disord* 2009;24:1606–12

23. Louis ED, Benito-Leon J, Vega-Quiroga S, et al. **Faster rate of cognitive decline in essential tremor cases than controls: a prospective study.** *Eur J Neurol* 2010;17:1291–97

24. Mueller SG, Weiner MW, Thal LJ, et al. **The Alzheimer's disease neuroimaging initiative.** *Neuroimaging Clin N Am* 2005;15:869–77, xi-xii

25. Louis ED, Faust PL, Vonsattel JPG, et al. **Neuropathological changes in essential tremor: 33 cases compared with 21 controls.** *Brain* 2007;130:3297–307

26. Louis ED. **Essential tremor: evolving clinicopathological concepts in an era of intensive post-mortem enquiry.** *Lancet Neurol* 2010;9:613–22

27. Louis ED, Vonsattel JPG, Honig LS, et al. **Neuropathologic findings in essential tremor.** *Neurology* 2006;66:1756–59

28. Deuschl G, Elble R. **Essential tremor: neurodegenerative or nondegenerative disease towards a working definition of ET.** *Mov Disord* 2009;24:2033–41

29. Erickson-Davis C, Faust PL, Vonsattel J-PG, et al. **"Hairy baskets" associated with degenerative Purkinje cell changes in essential tremor.** *J Neuropathol Exp Neurol* 2010;69:262–71

30. Rajput AH, Robinson CA, Rajput ML, et al. **Essential tremor is not dependent upon cerebellar Purkinje cell loss.** *Parkinsonism Relat Disord* 2012;18:626–28

31. Shill HA, Adler CH, Sabbagh MN, et al. **Pathologic findings in prospectively ascertained essential tremor subjects.** *Neurology* 2008;70:1452–55

32. Quattrone A, Cerasa A, Messina D, et al. **Essential head tremor is associated with cerebellar vermis atrophy: a volumetric and voxel-based morphometric MR imaging study.** *AJNR Am J Neuroradiol* 2008;29:1692–97

33. Cerasa A, Messina D, Nicoletti G, et al. **Cerebellar atrophy in essential tremor using an automated segmentation method.** *AJNR Am J Neuroradiol* 2009;30:1240–43

34. Benito-León J, Alvarez-Linera J, Hernandez-Tamames JA, et al. **Brain structural changes in essential tremor: voxel-based morphometry at 3-Tesla.** *J Neurol Sci* 2009;287:138–42

35. Bagepally BS, Bhatt MD, Chandran V, et al. **Decrease in cerebral and cerebellar gray matter in essential tremor: a voxel-based morphometric analysis under 3T MRI.** *J Neuroimaging* 2012;22:275–78

36. Daniels D, Peller M, Wolff S, et al. **Voxel-based morphometry shows no decreases in cerebellar gray matter volume in essential tremor.** *Neurology* 2006;24:1452–56

37. Passamonti L, Cerasa A, Quattrone A. **Neuroimaging of essential tremor: what is the evidence for cerebellar involvement?** *Tremor Other Hyperkinet Mov (N Y)* 2012;2 [Epub 2012 Sep 17]

38. Marvel CL, Desmond JE. **The contributions of cerebro-cerebellar circuitry to executive verbal working memory.** *Cortex* 2010;46:880–95

39. Klaming R, Kayano J, Bartsch H, et al. **Multimodal longitudinal imaging and close monitoring of single-case studies may demonstrate the relationship between structural and behavioral markers of essential tremor.** In: *Proceedings of the Annual Meeting of the Society for Neuroscience*, Washington, DC; November 12–16, 2011

40. Nicoletti G, Manners D, Novellino F, et al. **Diffusion tensor MRI changes in cerebellar structures of patients with familial essential tremor.** *Neurology* 2010;74:988–94

41. Klein JC, Lorenz B, Kang JS, et al. **Diffusion tensor imaging of white matter involvement in essential tremor.** *Hum Brain Mapp* 2011;32:896–904

42. Saini J, Bagepally BS, Bhatt MD, et al. **Diffusion tensor imaging: tract based spatial statistics study in essential tremor.** *Parkinsonism Relat Disord* 2012;18:477–82

43. Martinelli P, Giovanni R, Manners D, et al. **Diffusion-weighted imaging study of patients with essential tremor.** *Mov Disord* 2007;22:1182–85

44. Jia L, Jia-Lin S, Qin D, et al. **A diffusion tensor imaging study in essential tremor.** *J Neuroimaging* 2011;21:370–74

45. Mori S, Zhang J. **Principles of diffusion tensor imaging and its applications to basic neuroscience research.** *Neuron* 2006;51:527–39

46. Shin DH, Han BS, Kim HS, et al. **Diffusion tensor imaging in patients with essential tremor.** *AJNR Am J Neuroradiol* 2008;29:151–53

47. Jenkins IH, Bain PG, Colebatch JG, et al. **A positron emission tomography study for essential tremor: evidence for overactivity of cerebellar connections.** *Ann Neurol* 1993;34:82–90

48. Wills AJ, Jenkins IH, Thompson PD, et al. **Red nuclear and cerebellar but not olivary activation associated with essential tremor: a positron emission tomographic study.** *Ann Neurol* 1994;36:636–42

49. Bucher SF, Seelos K, Dodel RC, et al. **Activation mapping in essential tremor with functional magnetic resonance imaging.** *Ann Neurol* 1997;41:32–40

50. Schnitzler A, Muenks C, Butz M, et al. **Synchronized brain network associated with essential tremor as revealed by magnetoencephalography.** *Mov Disord* 2009;24:1629–35

51. Halliday DM, Conway BA, Farmer SF, et al. **Coherence between low-frequency activation of the motor cortex and tremor in patients with essential tremor.** *Lancet* 2000;355:1149–53

52. Louis ED, Shungu DC, Chan S, et al. **Metabolic abnormality in the cerebellum in patients with essential tremor: a proton magnetic resonance spectroscopy imaging study.** *Neurosci Lett* 2002;333: 17–20

53. Pagan F, Butman JA, Dambrosia JM, et al. **Evaluation of essential tremor with multi-voxel magnetic resonance spectroscopy.** *Neurology* 2003;60:1344–47

54. Mai J, Paxinos G, Voss T. *Atlas of the Human Brain.* 3rd ed. New York: Elsevier; 2008

Conventional and Advanced Imaging in Neuromyelitis Optica

Y. Barnett, I.J. Sutton, M. Ghadiri, L. Masters, R. Zivadinov, and M.H. Barnett

ABSTRACT

SUMMARY: Myelitis and optic neuritis are prototypic clinical presentations of both multiple sclerosis and neuromyelitis optica. Once considered a subtype of multiple sclerosis, neuromyelitis optica, is now known to have a discrete pathogenesis in which antibodies to the water channel, aquaporin 4, play a critical role. Timely differentiation of neuromyelitis optica from MS is imperative, determining both prognosis and treatment strategy. Early, aggressive immunosuppression is required to prevent the accrual of severe disability in neuromyelitis optica; conversely, MS-specific therapies may exacerbate the disease. The diagnosis of neuromyelitis optica requires the integration of clinical, MR imaging, and laboratory data, but current criteria are insensitive and exclude patients with limited clinical syndromes. Failure to recognize the expanding spectrum of cerebral MR imaging patterns associated with aquaporin 4 antibody seropositivity adds to diagnostic uncertainty in some patients. We present the state of the art in conventional and nonconventional MR imaging in neuromyelitis optica and review the place of neuroimaging in the diagnosis, management, and research of the condition.

ABBREVIATIONS: AQP4 = aquaporin 4; LESCL = longitudinally extensive spinal cord lesion; MT = magnetization transfer; NMO = neuromyelitis optica

Neuromyelitis optica (NMO) is a severe inflammatory demyelinating disorder of the CNS that is distinct from multiple sclerosis. Once considered to be a monophasic illness defined by the co-occurrence of acute bilateral visual loss and longitudinally extensive myelitis,[1] NMO is now recognized as a predominantly relapsing condition in which these index events may be separated by years and, in some cases, decades.[2] The past 10 years have seen dramatic advances in the understanding of NMO pathogenesis, heralded by the discovery of the "NMO-Immunoglobulin G" antibody in the serum of approximately 70% of patients with the condition[3] and the subsequent identification of the target antigen,

aquaporin 4 (AQP4),[4] a cell membrane water channel concentrated on astrocyte foot processes at the glial limiting membrane surrounding blood vessels and in association with the pia mater. In keeping with the notion that NMO is an "autoimmune astrocytopathy" and in contradistinction to MS, biopsy studies of evolving lesions show fragmentation and loss of astrocytes that precede demyelination[5] and the immunopathologic signature of granulocyte infiltration with perivascular immunoglobulin and complement deposition.[6]

The identification of AQP4 antibodies in patients with only a single index event, in some patients with relapsing optic neuropathy,[7] and in patients with more recently recognized patterns of cerebral disease[8] predicts progression to NMO[9-11] and has led to the introduction of the term "NMO spectrum disorder. " However, false-positive AQP4 antibody results have been reported in patients with definite MS, and the classification and pathogenesis of clinical and radiologic syndromes consistent with classic relapsing NMO, but without serum AQP4 antibodies, remain uncertain.

Current diagnostic criteria (Table 1) still mandate the occurrence of both optic neuritis and myelitis and at least 2 of 3 supportive criteria, including longitudinally extensive spinal cord lesion (LESCL), seropositivity for immunoglobulin G antibodies that bind AQP4 on astrocytes, and brain MR imaging nondiagnostic for MS.[12] While the presence of LESCLs is the radiologic signature of NMO, the spectrum of MR imaging changes associated with the condition has been significantly expanded by the

Table 1: Diagnostic criteria for the diagnosis of NMO

Criteria
Optic neuritis
Acute myelitis
At least 2 of the following 3 supportive criteria:
Contiguous spinal cord MRI lesion extending over at least 3 vertebral segments
Onset brain MRI not meeting the diagnostic criteria for MS
NMO-IgG seropositivity status

Note:—IgG indicates immunoglobulin G.

recognition of an array of characteristic brain lesion patterns[8] and the introduction of multiparametric and advanced MR imaging techniques in the assessment of the disease.

Neuroimaging has an increasingly important role in both the diagnosis and management of this potentially devastating condition. First, timely differentiation of NMO from MS is critical and the motivator for this review: Early and aggressive immunosuppression is required to prevent or reduce potentially severe disability in NMO, whereas the application of MS-specific therapies can exacerbate the disease[13,14] or even precipitate severe atypical relapses.[5,15] Second, serial imaging has an important role in disease monitoring and informs understanding of the temporal aspects of NMO pathophysiology. Third, routine imaging surveillance is necessary to monitor for complications of immunosuppressive therapy. In this review, we summarize state-of-the-art conventional and nonconventional MR imaging in NMO and its place in the clinical management and research of the disease.

CONVENTIONAL SPINE MR IMAGING
Typical Spinal Cord Imaging Features

The presence of LESCLs ($\geq$3 vertebral segments) that preferentially involve spinal central gray matter is characteristic of NMO.[12,16] LESCLs in NMO are T2 hyperintense and frequently T1 hypointense. They may acutely expand the cord and patchily enhance throughout their length (Fig 1*A–C*). T1 hypointensity[16-18] and cord atrophy (Fig 1*D*)[19] are prominent findings in established NMO, reflecting the severity of tissue injury and a propensity for recurrent bouts of inflammatory activity to occur in old lesions. In such cases, we have observed short segments of gadolinium enhancement within pre-existing T2 LESCLs during acute spinal relapse (Fig 1*A*, -*B*). Additionally, short-segment T2-hyperintense lesions are described in NMO[20] and should not necessarily deter one from the diagnosis, particularly in the presence of other typical neuroimaging findings. While cord pathology in NMO is traditionally associated with a severe clinical phenotype, including the need for ventilatory support in association with high cervical lesions, excellent clinical and radiologic recovery may be seen in some patients. This observation implicates reversible vasogenic edema, a phenomenon described in cerebral NMO lesions[8] and attributed to transient functional impairment of water transport mediated by AQP4 antibodies,[21,22] in the pathogenesis of some NMO cord syndromes.

Differential Diagnosis of the LESCL

Although a confluence of multiple short-segment MS lesions may occasionally mimic the MR imaging features of spinal NMO, contiguous T2 hyperintensity of central gray matter over many segments is rarely observed in MS.[12,16] Differentiation of spinal
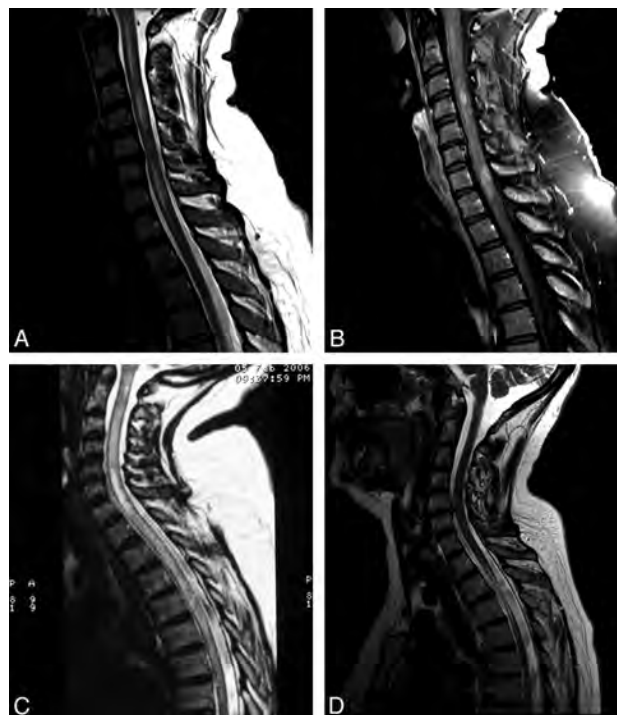
FIG 1. *A*, T2WI shows extensive patchy pericentral signal change extending from the cervicomedullary junction to the T1 vertebral level in acute symptomatic spinal AQP4-positive NMO. *B*, Contrast-enhanced T1WI shows that short-segment gadolinium enhancement is present within the cord at the C4 and C7/8 vertebral levels. *C*, T2WI shows prototypic longitudinally extensive holocord inflammation in acute symptomatic AQP4-positive NMO relapse. *D*, T2WI shows severe atrophy in a chronic thoracic spinal cord NMO lesion spanning 3 vertebral segments (T2–T4).

Table 2: Differential diagnosis of LESCLs[a]

Diagnosis
NMO/NMO spectrum disorder
Idiopathic isolated or relapsing (AQP4 negative) transverse myelitis
Myelitis associated with systemic autoimmunity (Sjögren/systemic lupus erythematosus)
Postinfectious myelitis
MS: confluent multiple short-segment lesions
Neurosarcoidosis
Behçet disease
Paraneoplastic myelitis
Vascular causes (spinal cord infarction, dural arteriovenous fistula)

[a] Excludes infective/metabolic myelitides and spinal cord tumors.

NMO and other immune-mediated myelitides, such as those associated with Sjögren disease or systemic lupus erythematosus, is more difficult; long cord lesions with a severe clinical phenotype are well-described in the context of systemic autoimmunity (Table 2).[23,24] However, autoantibodies directed to antigens other than AQP4 are often also detectable in NMO sera,[25,26] and a proportion of patients have clinical features of systemic autoimmunity. Of 8 patients with Sjögren syndrome–associated myelopathy identified by Kim et al,[27] 7 met the diagnostic criteria for NMO, and AQP4 antibodies were present in 4/5 patients whose serum was available for testing. It is, therefore, likely that many of the Sjögren syndrome–associated myelopathy cases described before the advent of AQP4 antibody testing had coexistent NMO. Other inflammatory disorders that should be considered in patients
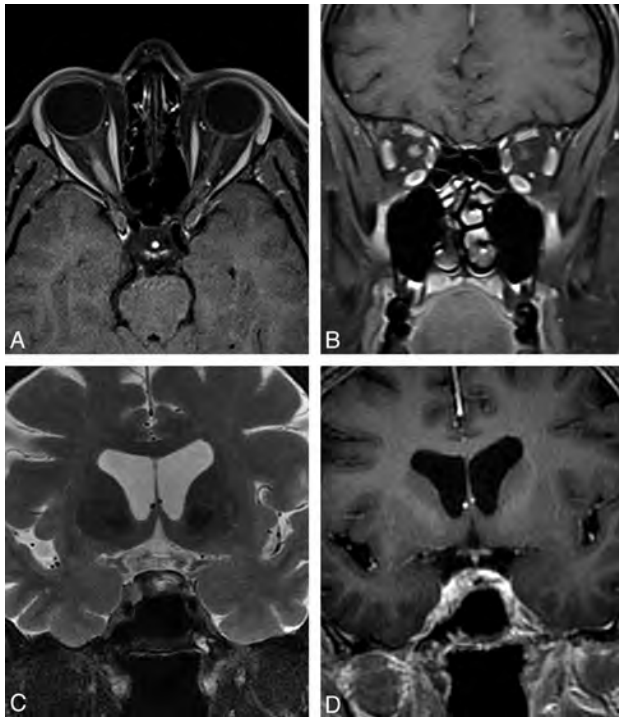
FIG 2. *A* and *B*, Contrast-enhanced fat-suppressed T1WI shows acute swelling and enhancement of the right optic nerve during symptomatic AQP4-positive NMO relapse with severe right-eye visual loss. *C*, Fat-suppressed T2WI. *D*, Contrast-enhanced fat-suppressed T1WI shows chiasmatic hyperintensity and enhancement during symptomatic AQP4-positive NMO relapse with severe visual impairment affecting the entire field of vision in the left eye and the temporal hemifield of the right eye.

FIG 3. Typical periependymal lesions following the known distribution of AQP4. *A* and *B*, FLAIR MR imaging shows hypothalamic and medullary lesions in symptomatic AQP4-positive NMO spectrum disorder presenting with diplopia, dysarthria, dysphagia, and a right-sided sensorimotor syndrome. *C* and *D*, FLAIR MR imaging shows midbrain tegmentum lesions in the same patient during a second symptomatic attack, presenting with diplopia and clinical evidence of bilateral internuclear ophthalmoplegia. (Images courtesy of Prof. Junichi Kira and Dr. Koji Shinoda, Kyushi University, Kyushi, Japan.)

with LESCLs include neurosarcoidosis and postinfectious myelitis; while surface enhancement due to meningeal involvement is more common in these conditions, they may be indistinguishable from spinal NMO on radiologic grounds. While rare, paraneoplastic myelitis merits consideration in patients with an isolated LESCL, and testing for serum antibodies to onconeural antigens, including collapsing response mediator protein 5, amphiphysin, or glutamic acid decarboxylase, is advisable in such cases.[28] Infective and metabolic myelitides are rarely confused with NMO on clinical grounds and are beyond the scope of this review. Of the noninflammatory causes of LESCL, spinal dural arteriovenous fistula is perhaps the most important treatable differential diagnosis.

CONVENTIONAL OPTIC NERVE MR IMAGING

Long-segment involvement of the optic nerve associated with acute swelling and enhancement (Fig 2*A*, -*B*), particularly when bilateral or extending posteriorly into the optic chiasm (Fig 2*C*, -*D*), should raise the suspicion of NMO in the appropriate clinical context.[29-31]

CONVENTIONAL BRAIN MR IMAGING

Cerebral involvement in NMO has traditionally been considered exceptional; indeed, lack of brain involvement was one of the major supportive diagnostic criteria published by Wingerchuk et al in 1999.[2] However, in 2006, the same group observed brain abnormalities, predominantly asymptomatic, in up to 60% of a cohort of patients with clinically defined NMO.[32] A series of independent reports has subsequently expanded on these findings and defined a spectrum of brain lesion types in up to 93% of patients with NMO and AQP4 antibody–positive NMO spectrum disorder.[8,9,19,30,33,34] While "typical" NMO lesions (Fig 3) mirror the distribution of AQP4,[35,36] a number of less specific brain MR imaging changes are increasingly recognized.[8] Individual brain lesions in NMO have a variable appearance but are often of heterogeneous signal intensity with blurred margins.[34] The mechanisms and extent of injury also vary from lesion to lesion. Reflecting the now well-described pathology of NMO,[5,37] extensive cavitation may follow bouts of brain inflammation and result in permanent and severe cognitive dysfunction (Fig 4*E*, -*F*). Conversely, astrocyte destruction is an unlikely pathologic substrate for clinically silent and evanescent hemispheric lesions observed in some patients with NMO.[8]

MR Imaging Lesion Distribution

Nonspecific punctate or small (<3 mm) lesions in the deep or, less commonly, subcortical white matter are frequent[8,9,32,33] and usually asymptomatic. Such lesions may appear MS-like in 10%–12.5% of cases,[12,19,32,38] and in most series, only occasionally fulfill the Barkhof criteria[39] for the diagnosis of MS in patients who are seropositive for AQP4 antibodies.[20] To the authors' knowledge, the Magnetic Resonance in Multiple Sclerosis (MAGNIMS) criteria for dissemination in space, which have been incorporated into the most recent iteration of the McDonald criteria for the diagnosis of MS,[40] have not been formally evaluated in patients with NMO.
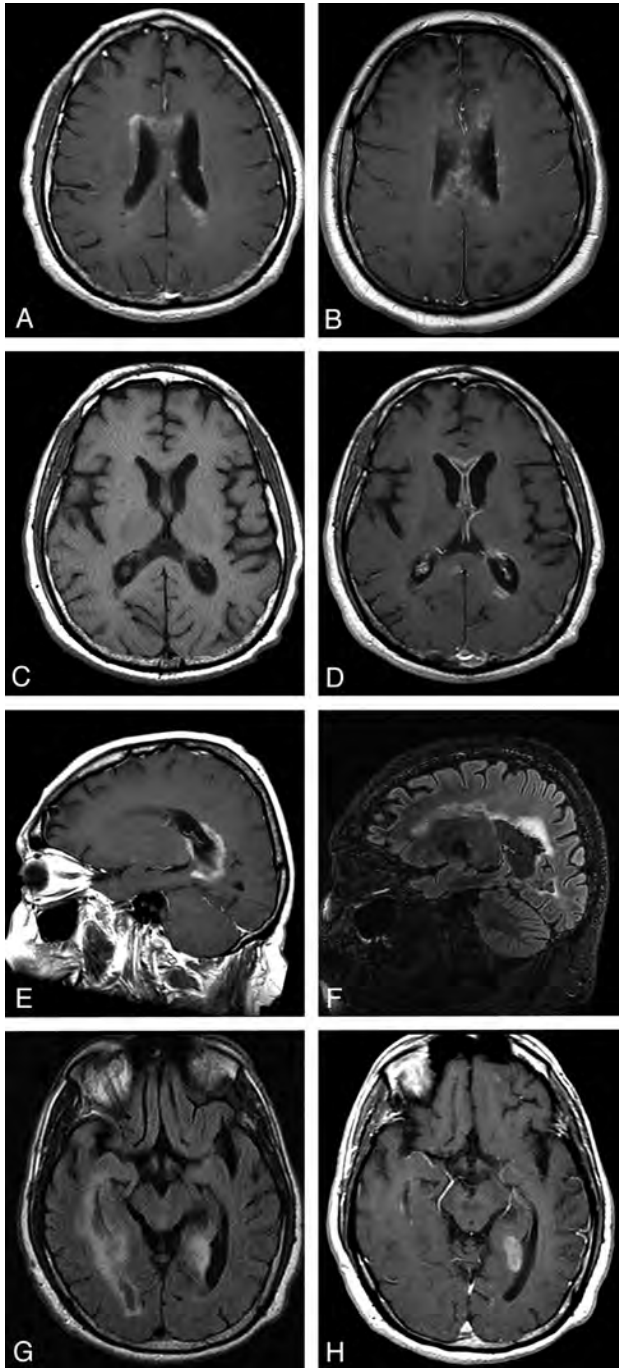
FIG 4. Periependymal/periventricular lesions in acute AQP4-positive NMO. *A*, Contrast-enhanced T1WI shows ill-defined periventricular cloudlike enhancement. While relatively specific for NMO, similar patterns can be observed in other inflammatory CNS diseases, such as active neurosarcoidosis (*B*, Contrast-enhanced T1WI). *C* and *D*, T1WI and contrast-enhanced T1WI demonstrate pencil-thin ependymal enhancement involving the anterior horns of the lateral ventricles in AQP4-positive NMO. *E*, Contrast-enhanced T1WI shows thick periependymal enhancement around the posterior horn of the lateral ventricle in acute symptomatic cerebral AQP4-positive NMO relapse. *F*, 3T follow-up FLAIR MR imaging shows ventriculomegaly and periventricular encephalomalacia and gliosis. *G* and *H*, FLAIR MR imaging and contrast-enhanced T1WI shows extensive periependymal disease involving the right lateral ventricle and a discrete, well-demarcated enhancing lesion abutting the posterior horn of the left lateral ventricle.

A number of relatively specific lesion types are helpful in the radiologic diagnosis of NMO:

1) Typical lesions, which follow the distribution of AQP4, are found in the periependymal regions surrounding the third ventricle, cerebral aqueduct, and fourth ventricle (Fig 3).[35,36,38,41] Lesions within the thalamus and hypothalamus are usually of this type and may be extensive.[36,42] While often asymptomatic, hypothalamic lesions have been described in patients with NMO with the syndrome of inappropriate antidiuretic hormone secretion[43]; narcolepsy[44]; behavioral change[42]; and hypothermia, hypotension, hypersomnia, and obesity.[45] Dorsal brain stem lesions adjacent to the fourth ventricle, which may be contiguous with cervical spinal cord lesions, can result in a variety of bulbar symptoms, among which intractable hiccups, nausea, and vomiting are relatively specific for NMO and attributable to involvement of the area postrema and the nucleus tractus solitarius. Additionally, linear medullary lesions have been reported in 48% of Chinese patients with NMO and discriminated NMO from MS with a high predictive value.[46]

2) Periependymal/periventricular and corpus callosum lesions situated in proximity to the lateral ventricles are common to both MS and NMO. However, the radially oriented, well-demarcated perivenular lesions (Dawson fingers) that characterize MS are absent in most (but not all) cases of NMO; rather, NMO lesions tend to extend along the walls of the lateral ventricles in close association with the ependymal lining (Fig 4). Extension into the white matter of the hemispheres may form large, confluent lesions. Multiple, edematous lesions with heterogeneous signal intensity (higher in the rim and lower in the core of the lesions) in the body of the corpus callosum ("marbled pattern"),[47] and diffuse involvement and swelling of the splenium may be notable in the acute phase of the disease (Fig 5A–C). Such lesions may diminish in size and intensity or even disappear on follow-up imaging[47]; however, chronic cystic changes have been described in the genu and splenium of corpus callosum,[34] and we documented severe atrophy of the callosum at 2.5-year follow-up in 1 case (Fig 5D).

3) Large, confluent, and heterogeneous lesions occur in the cerebral hemispheric white matter in some cases of NMO (Fig 5E), possibly with a predilection for patients from the Far East and Africa and among children.[48] These lesions do not exert mass effect[9] and often vanish following steroid therapy or, in some cases, spontaneously. The pathology of these lesions, which may be contiguous with periependymal lesions or have a "spilled ink" appearance along white matter tracts,[8] is uncertain, though nondestructive intramyelinic edema has been described in some pathologic studies.[21] The evanescent nature and presence of facilitated diffusion (Fig 5F)[49] within lesions also implicates vasogenic edema, potentially due to a reversible or limited astrocytopathy, as the underlying pathology.[21,22,50] Hemispheric lesions may be clinically silent or result in focal neurologic deficits.

4) Unilateral or bilateral, longitudinally extensive lesions involving the corticospinal tract occur commonly in Korean patients[8,9] and have occasionally been reported in other co-
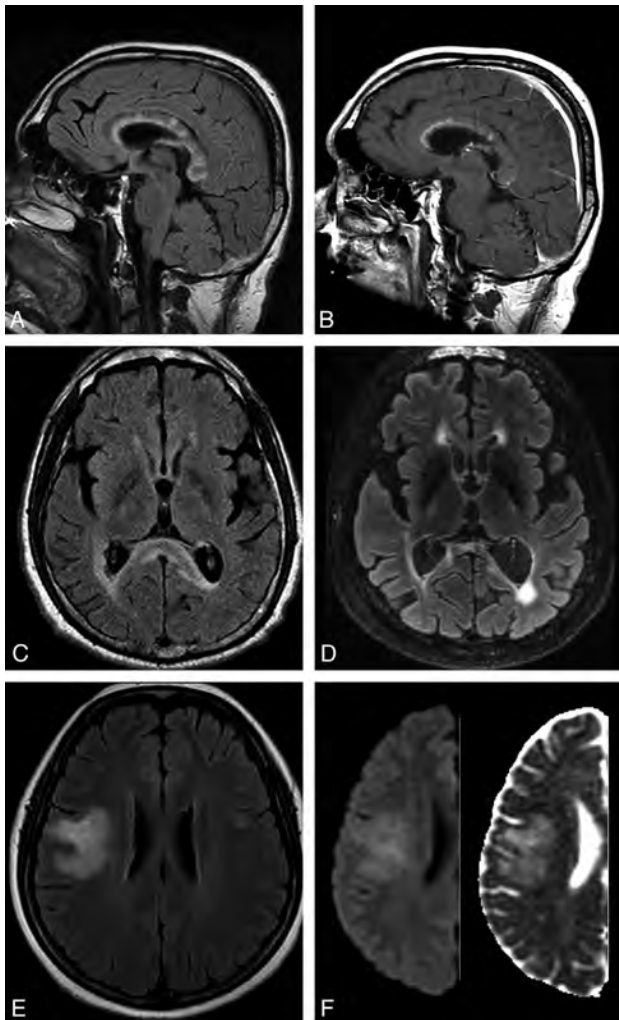
FIG 5. *A* and *C*, FLAIR MR imaging shows acute, heterogeneous, "fluffy," corpus callosum lesions, with prominent splenial hyperintensity and swelling, during symptomatic cerebral AQP4-positive NMO relapse. *B*, Contrast-enhanced T1WI shows linear enhancement involving the undersurface of the corpus callosum in its anterior third and more focal enhancement within lesions in the body of the corpus callosum. *D*, 3T follow-up FLAIR MR imaging at 2.5 years shows severe splenial (and global cerebral) atrophy. *E*, FLAIR MR imaging shows a large, evanescent lesion in the right hemisphere in AQP4-negative NMO spectrum disorder. *F*, DWI (left) and ADC map (right) confirm facilitated diffusion in the lesion.

horts.[32,51] Such lesions may be associated with severe contralateral motor deficits.

MR Imaging Enhancement Patterns

While most reported NMO brain lesions do not show gadolinium enhancement, the frequency of acute lesional enhancement is unknown. Patchy enhancement with blurred margins ("cloudlike enhancement") in cerebral lesions has been reported as relatively specific for NMO (Fig 4*A*),[8,52] and the presence of asymptomatic "pencil-thin ependymal enhancement" (similar to that observed in infectious ependymitis) may serve to further differentiate the condition from MS (Fig 4*C*, -*D*).[53,54] Rarely, NMO lesions exhibit a solid enhancement pattern that is indistinguishable from acute MS (Fig 4*G*, -*H*). Incomplete ring enhancement, a common feature in larger, acute MS lesions, has not, to the authors' knowledge, been described in NMO.

ADVANCED MR IMAGING

The recent application of advanced imaging techniques to NMO, including ultra-high-field MR imaging (7T),[55] magnetization transfer (MT) imaging,[56,57] double inversion recovery imaging,[58] DTI,[56,59-61] MR spectroscopy,[57,62,63] iron-deposition imaging,[64] and MR volumetric/morphometric assessments,[56,58,65] is beginning to yield important insights into disease pathogenesis and to build on the MR imaging signature of the disease that has emerged from conventional imaging studies during the last 15 years. In addition, multiparametric approaches may provide complementary information in establishing nonconventional MR imaging patterns unique to patients with NMO (On-line Table).

Cortical and Deep Gray Matter Pathology

The presence of cortical lesions is almost universal in longstanding MS, and recent pathologic and imaging studies show that cortical pathology is common, even at first presentation.[66] Cortical pathology correlates better with cognitive and motor parameters than white matter T2 lesion burden in MS,[67] and gray matter atrophy has gained acceptance as an outcome measure in therapeutic clinical trials. In NMO, neuropathologic studies have thus far failed to demonstrate cortical pathology,[68] though patient numbers studied are relatively low. Calabrese[58] recently used double inversion recovery imaging, a technique that can reveal up to 18% (37% with retrospective scoring) of the histopathologically confirmed cortical lesion load in MS,[69] to study 30 patients with NMO, 30 with relapsing MS, and 30 healthy controls. While more than two-thirds of the patients with relapsing MS had cortical lesions, none were demonstrable in either patients with NMO or healthy controls. Mild regional reductions in cortical thickness, determined by using FreeSurfer (http://surfer.nmr.mgh.harvard.edu/) in the precentral, postcentral, and calcarine gyri, and a mild reduction in thalamic volume were observed in patients with NMO versus healthy controls. The authors attributed these changes to secondary axonal degeneration following severe spinal cord and anterior optic pathway inflammation. Using an alternative approach, Kister et al[55] found no cortical lesions in 10 patients with NMO spectrum disorder studied with ultra-high-field (7T); of 92 white matter lesions studied, only 8 were traversed by a central venule, a further distinction from MS that indicates a fundamental dichotomy in the pathogenesis of the 2 conditions.

Voxel-based morphometry has been used to compare gray matter structures in NMO, MS, and healthy controls.[56,65,70] Duan et al[65] documented regional gray matter atrophy in the frontal cortex, temporal cortex, right inferior parietal lobule, and right insula of patients with NMO (*n* = 26) versus controls, but these differences lost statistical significance when a family-wise error correction for multiple comparisons at the voxel level was applied. Conversely, marked atrophy of cortical and deep gray structures was present in patients with relapsing MS, and compared with NMO, significant gray matter volume loss was present in the thalami, caudate, mammillary body, parahippocampal gyrus, right hippocampus, and right insula. Chanson et al[70] observed volume loss in the thalamus in patients with NMO (*n* = 30) versus healthy controls (*n* = 30), and Pichiecchio et al[56] found a reduction in the attenuation
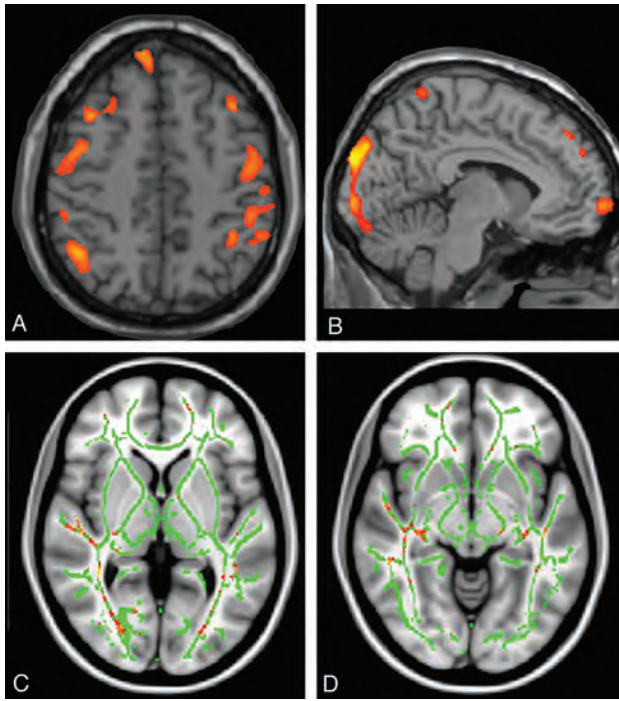
FIG 6. Voxel-based morphometry analysis shows a reduction in the attenuation and volume of gray matter in the motor (*A*) and visual (*B*) cortices in patients with NMO compared with the healthy controls. Voxel-based morphometry output is overlaid on the standard CH2 template. Voxelwise DTI analysis shows a significantly lowered fractional anisotropy along the pathway of the optic radiation bilaterally (*C*) and involvement of both lateral geniculate nuclei (*D*). Pichiecchio A, Tavazzi E, Poloni G, et al. **Advanced magnetic resonance imaging of neuromyelitis optica: a multiparametric approach.** *Mult Scler* 18(6):817–24, copyright © 2012. Reprinted by Permission of SAGE.

and volume of gray matter in the motor and visual cortices and regions associated with executive and language functions in patients with NMO (*n* = 8) versus healthy controls (*n* = 7) by using a similar voxel-based morphometry method (Fig 6*A*, -*B*). MT imaging has been explored in NMO, thus far with discrepant results: Rocca et al[57] observed a reduced MT ratio in normal-appearing gray matter in 10 patients with NMO, suggesting occult gray matter damage, while Pichiecchio et al[56] observed no differences in either the cortical or deep gray matter MT ratio between patients (*n* = 8) and healthy controls (*n* = 7). Finally, while iron deposition in the deep gray matter structures is described in MS[71] and may contribute to disease progression,[72] Chen et al[64] found no evidence of abnormal iron deposition in the putamen, globus pallidus, caudate nucleus, thalamus, substantia nigra, red nucleus, or dentate nucleus by using quantitative 3D-enhanced susceptibility-weighted angiography in 42 patients with NMO compared with healthy controls.

In summary, nonconventional imaging data, while limited by small patient numbers and a variety of technical issues, indicate that the gray matter structures are less affected by NMO than by MS and, in particular, suggest that an absence of focal cortical lesions in NMO may differentiate the 2 conditions. In contradistinction to MS, the relative sparing of gray matter structures in NMO may explain the lack of a progressive phenotype in the condition.

Normal-Appearing White Matter

In patients with NMO and normal structural brain MR imaging findings, DTI has identified increased mean diffusivity and transverse ($\lambda2,3$) eigenvalues (reflecting the average diffusion coefficient perpendicular to the direction of maximal diffusivity) in the corticospinal tract and optic radiation, but not the cingulum or corpus callosum,[60] implicating axonal degeneration secondary to spinal cord and anterior optic pathway lesions. Liu et al[59] inferred the presence of subtle, widespread pathology in NMO normal-appearing white matter from an analysis of white matter connectivity matrices derived from deterministic tractography performed in 26 patients with NMO. In a more recent DTI study, Zhao et al[61] confirmed the presence of occult damage to normal-appearing white matter in relapsing NMO but found that while mean diffusivity was increased in regions of interest in the optic radiation (and genu of the corpus callosum) versus controls, reduced values were observed in the internal capsule, thalamus, and medulla oblongata. Furthermore, Pichiecchio et al[56] examined mean diffusivity histogram-derived metrics of normal-appearing white matter in NMO and healthy controls and found no significant differences, while tract-based spatial statistics in the same cohort identified lowered fractional anisotropy in the optic radiation bilaterally (Fig 6*C*, -*D*).

Quantitative structural brain assessment using SIENAX software (http://fsl.fmrib.ox.ac.uk/fsl/fslwiki/SIENA) has demonstrated a significant reduction in total white matter volume in patients with NMO (*n* = 30), even in the absence of T2 hyperintensities, versus healthy controls (*n* = 30).[70] Regional voxel-based morphometry analysis in the same cohort identified possible volume loss clustered in the optic radiations and corpus callosum.

Finally, the metabolic pattern of normal-appearing white matter in NMO/NMO spectrum disorder, as assessed by multivoxel chemical shift imaging at 1.5T[56,63] and 3T[62] with ^{1}H-MR spectroscopy, is identical to that in controls.

Taken together, these studies indicate subtle and, with the possible exception of the corpus callosum, selective structural alterations in the optic and motor pathways in the brain, implicating trans-synaptic axonal degeneration secondary to destructive lesions in the optic nerves and spinal cord, respectively. The normal spectroscopy data suggest that the diffuse degenerative process that affects the white matter in MS is lacking in NMO. However, variability in the severity of the disease and the exclusion of cases with brain abnormalities may have confounded the results of these studies, and larger multiparametric studies of well-phenotyped patients are required.

Spinal Cord

Few studies have assessed the application of nonconventional MR imaging techniques to the spinal cord in NMO. Filippi et al[17] were unable to demonstrate a difference in cervical cord MT ratio histogram metrics in clinically defined NMO (*n* = 8) versus MS (*n* = 10), despite cord T1 hypointensity and atrophy being restricted to the NMO cases. Two studies have used DTI in the assessment of cervical spinal cord damage in NMO. In the first, Qian et al[73] showed abnormal DTI-derived metrics (especially fractional anisotropy) in the cervical spinal cord of patients with NMO (*n* =

10), even in the absence of signal alteration on conventional T2WI. Similarly, there was no correlation between diffusivity alterations and the number or extent of focal T2 hyperintensities in the cervical cord of patients with MS.[74] In the second, Klawiter et al[75] demonstrated higher radial diffusivity within damaged (as assessed by T2WI) white matter tracts in NMO ($n = 10$) versus MS ($n = 10$), consistent with the more destructive nature of the former condition. DTI metrics of damaged gray matter regions did not differentiate NMO and MS. These studies indicate that DTI may inform the pathology of spinal cord disease in NMO. Specific measures such as fractional anisotropy may provide quantitative biomarkers of white matter damage not readily identified by conventional MR imaging techniques.

CONCLUSIONS

The seminal discovery of serum AQP4 antibodies in patients with NMO has validated earlier clinical and radiologic observations that separated the condition from conventional MS. While the presence of LESCLs suggests NMO and expedites referral for appropriate serologic testing, the absence of serum AQP4 antibodies in patients with classic clinical and radiologic features and their presence in patients with a spectrum of brain lesions have recently led to a re-appraisal of current diagnostic criteria for the disease. Recommendations by an international task force[76] to include newly recognized imaging features of NMO, such as periependymal brain lesions, emphasize the importance of MR imaging in the diagnostic work-up of patients with CNS inflammatory disease.

Greater scrutiny of brain MR imaging in patients with NMO has revealed an expanding array of lesion subtypes with which the neuroradiologist must become familiar. The integration of imaging with clinical and laboratory data in individual patients facilitates rapid differentiation of NMO/NMO spectrum disorder from MS. This distinction has critical therapeutic implications: NMO does not respond to traditional MS immunomodulatory therapy with β-interferon, which in some patients may even be deleterious.[13,14] Similarly, severe exacerbations of NMO have been reported in patients treated with natalizumab,[5] an efficacious monoclonal antibody therapy for MS. Case series do suggest that NMO responds to immunosuppressive therapy and, in particular, to the B-cell-depleting anti-CD20 monoclonal antibody, rituximab.[77] Of relevance to the neuroradiologist, rituximab has been associated with progressive multifocal leukoencephalopathy in patients with systemic autoimmune disease,[78] and heightened vigilance for this complication in patients with NMO is paramount.

Nonconventional brain imaging is beginning to offer new insights into the pathophysiology of NMO and further differentiates the condition from MS. The lack of focal cortical lesions as assessed by ultra-high-field MR imaging and double inversion recovery imaging is of particular interest; if confirmed, double inversion recovery sequences may be helpful in distinguishing NMO from MS in difficult clinical cases. Early DTI, MT imaging, and MR spectroscopy data indicate an absence of diffuse "degenerative" disease in the normal-appearing white and gray matter in NMO, consistent with the lack of a progressive phenotype in this condition, an important distinction from MS that may also have therapeutic repercussions.

Conventional and nonconventional neuroimaging investigations in NMO have accelerated in tandem with rapid developments in the understanding of NMO pathobiology during the past 5–10 years. These studies underscore the importance of neuroimaging in the diagnosis and monitoring of NMO and emphasize its role in directing the early commencement of targeted immunotherapy.

ACKNOWLEDGMENTS

REFERENCES

1. Devic E. **Myélite subaiguë compliquée de névrite optique.** *Bull Med (Paris)* 1894;8:1033–34
2. Wingerchuk DM, Hogancamp WF, O'Brien PC, et al. **The clinical course of neuromyelitis optica (Devic's syndrome).** *Neurology* 1999;53:1107–14
3. Lennon VA, Wingerchuk DM, Kryzer TJ, et al. **A serum autoantibody marker of neuromyelitis optica: distinction from multiple sclerosis.** *Lancet* 2004;364:2106–12
4. Lennon VA, Kryzer TJ, Pittock SJ, et al. **IgG marker of optic-spinal multiple sclerosis binds to the aquaporin-4 water channel.** *J Exp Med* 2005;202:473–77
5. Barnett MH, Prineas JW, Buckland ME, et al. **Massive astrocyte destruction in neuromyelitis optica despite natalizumab therapy.** *Mult Scler* 2012;18:108–12
6. Lucchinetti CF, Mandler RN, McGavern D, et al. **A role for humoral mechanisms in the pathogenesis of Devic's neuromyelitis optica.** *Brain* 2002;125:1450–61
7. Giovannoni G. **To test or not to test: NMO-IgG and optic neuritis.** *Neurology* 2008;70:2192–93
8. Kim W, Park MS, Lee SH, et al. **Characteristic brain magnetic resonance imaging abnormalities in central nervous system aquaporin-4 autoimmunity.** *Mult Scler* 2010;16:1229–36
9. Kim W, Kim SH, Huh SY, et al. **Brain abnormalities in neuromyelitis optica spectrum disorder.** *Mult Scler Int* 2012;2012:735486
10. Matiello M, Lennon VA, Jacob A, et al. **NMO-IgG predicts the outcome of recurrent optic neuritis.** *Neurology* 2008;70:2197–200
11. Weinshenker BG, Wingerchuk DM, Vukusic S, et al. **Neuromyelitis optica IgG predicts relapse after longitudinally extensive transverse myelitis.** *Ann Neurol* 2006;59:566–69
12. Wingerchuk DM, Lennon VA, Pittock SJ, et al. **Revised diagnostic criteria for neuromyelitis optica.** *Neurology* 2006;66:1485–89
13. Palace J, Leite MI, Nairne A, et al. **Interferon beta treatment in neuromyelitis optica: increase in relapses and aquaporin 4 antibody titers.** *Arch Neurol* 2010;67:1016–17
14. Shimizu J, Hatanaka Y, Hasegawa M, et al. **IFNβ-1b may severely

exacerbate Japanese optic-spinal MS in neuromyelitis optica spectrum. *Neurology* 2010;75:1423–27

15. Min JH, Kim BJ, Lee KH. **Development of extensive brain lesions following fingolimod (FTY720) treatment in a patient with neuromyelitis optica spectrum disorder.** *Mult Scler* 2012;18:113–15

16. Nakamura M, Miyazawa I, Fujihara K, et al. **Preferential spinal central gray matter involvement in neuromyelitis optica: an MRI study.** *J Neurol* 2008;255:163–70

17. Filippi M, Rocca MA, Moiola L, et al. **MRI and magnetization transfer imaging changes in the brain and cervical cord of patients with Devic's neuromyelitis optica.** *Neurology* 1999;53:1705–10

18. Filippi M, Rocca MA. **MR imaging of Devic's neuromyelitis optica.** *Neurol Sci* 2004;25(suppl 4):S371–73

19. Pires CE, Silva CM, Lopes FC, et al. **Brain MRI abnormalities in Brazilian patients with neuromyelitis optica.** *J Clin Neurosci* 2012;19:969–74

20. Downer JJ, Leite MI, Carter R, et al. **Diagnosis of neuromyelitis optica (NMO) spectrum disorders: is MRI obsolete?** *Neuroradiology* 2012;54:279–85

21. Hinson SR, Romero MF, Popescu BF, et al. **Molecular outcomes of neuromyelitis optica (NMO)-IgG binding to aquaporin-4 in astrocytes.** *Proc Natl Acad Sci U S A* 2012;109:1245–50

22. Magaña SM, Matiello M, Pittock SJ, et al. **Posterior reversible encephalopathy syndrome in neuromyelitis optica spectrum disorders.** *Neurology* 2009;72:712–17

23. Delalande S, de Seze J, Fauchais AL, et al. **Neurologic manifestations in primary Sjögren syndrome: a study of 82 patients.** *Medicine (Baltimore)* 2004;83:280–91

24. Schulz SW, Shenin M, Mehta A, et al. **Initial presentation of acute transverse myelitis in systemic lupus erythematosus: demographics, diagnosis, management and comparison to idiopathic cases.** *Rheumatol Int* 2012;32:2623–27

25. McKeon A, Lennon VA, Jacob A, et al. **Coexistence of myasthenia gravis and serological markers of neurological autoimmunity in neuromyelitis optica.** *Muscle Nerve* 2009;39:87–90

26. Pittock SJ, Lennon VA, de SJ, et al. **Neuromyelitis optica and non organ-specific autoimmunity.** *Arch Neurol* 2008;65:78–83

27. Kim SM, Waters P, Vincent A, et al. **Sjögren's syndrome myelopathy: spinal cord involvement in Sjögren's syndrome might be a manifestation of neuromyelitis optica.** *Mult Scler* 2009;15:1062–68

28. Trebst C, Raab P, Voss EV, et al. **Longitudinal extensive transverse myelitis: it's not all neuromyelitis optica.** *Nat Rev Neurol* 2011;7:688–98

29. Khanna S, Sharma A, Huecker J, et al. **Magnetic resonance imaging of optic neuritis in patients with neuromyelitis optica versus multiple sclerosis.** *J Neuroophthalmol* 2012;32:216–20

30. Li Y, Xie P, Lv F, et al. **Brain magnetic resonance imaging abnormalities in neuromyelitis optica.** *Acta Neurol Scand* 2008;118:218–25

31. McKeon A, Lennon VA, Lotze T, et al. **CNS aquaporin-4 autoimmunity in children.** *Neurology* 2008;71:93–100

32. Pittock SJ, Lennon VA, Krecke K, et al. **Brain abnormalities in neuromyelitis optica.** *Arch Neurol* 2006;63:390–96

33. Cabrera-Gómez JA, Quevedo-Sotolongo L, Gonzalez-Quevedo A, et al. **Brain magnetic resonance imaging findings in relapsing neuromyelitis optica.** *Mult Scler* 2007;13:186–92

34. Makino T, Ito S, Mori M, et al. **Diffuse and heterogeneous T2-hyperintense lesions in the splenium are characteristic of neuromyelitis optica.** *Mult Scler* 2013;19:308–15

35. Pittock SJ, Weinshenker BG, Lucchinetti CF, et al. **Neuromyelitis optica brain lesions localized at sites of high aquaporin 4 expression.** *Arch Neurol* 2006;63:964–68

36. Poppe AY, Lapierre Y, Melancon D, et al. **Neuromyelitis optica with hypothalamic involvement.** *Mult Scler* 2005;11:617–21

37. Parratt JD, Prineas JW. **Neuromyelitis optica: a demyelinating disease characterized by acute destruction and regeneration of perivascular astrocytes.** *Mult Scler* 2010;16:1156–72

38. Wang F, Liu Y, Duan Y, et al. **Brain MRI abnormalities in neuromyelitis optica.** *Eur J Radiol* 2011;80:445–49

39. Barkhof F, Filippi M, Miller DH, et al. **Comparison of MRI criteria at first presentation to predict conversion to clinically definite multiple sclerosis.** *Brain* 1997;120(pt 11):2059–69

40. Polman CH, Reingold SC, Banwell B, et al. **Diagnostic criteria for multiple sclerosis: 2010 revisions to the McDonald criteria.** *Ann Neurol* 2011;69:292–302

41. Nakashima I, Fujihara K, Miyazawa I, et al. **Clinical and MRI features of Japanese patients with multiple sclerosis positive for NMO-IgG.** *J Neurol Neurosurg Psychiatry* 2006;77:1073–75

42. Viegas S, Weir A, Esiri M, et al. **Symptomatic, radiological and pathological involvement of the hypothalamus in neuromyelitis optica.** *J Neurol Neurosurg Psychiatry* 2009;80:679–82

43. Nakajima H, Fujiki Y, Ito T, et al. **Anti-aquaporin-4 antibody-positive neuromyelitis optica presenting with syndrome of inappropriate antidiuretic hormone secretion as an initial manifestation.** *Case Rep Neurol* 2011;3:263–67

44. Baba T, Nakashima I, Kanbayashi T, et al. **Narcolepsy as an initial manifestation of neuromyelitis optica with anti-aquaporin-4 antibody.** *J Neurol* 2009;256:287–88

45. Suzuki K, Nakamura T, Hashimoto K, et al. **Hypothermia, hypotension, hypersomnia, and obesity associated with hypothalamic lesions in a patient positive for the anti-aquaporin 4 antibody: a case report and literature review.** *Arch Neurol* 2012;69:1355–59

46. Lu Z, Qiu W, Zou Y, et al. **Characteristic linear lesions and longitudinally extensive spinal cord lesions in Chinese patients with neuromyelitis optica.** *J Neurol Sci* 2010;293:92–96

47. Nakamura M, Misu T, Fujihara K, et al. **Occurrence of acute large and edematous callosal lesions in neuromyelitis optica.** *Mult Scler* 2009;15:695–700

48. Cabrera-Gomez JA, Kister I. **Conventional brain MRI in neuromyelitis optica.** *Eur J Neurol* 2012;19:812–19

49. Saiki S, Ueno Y, Moritani T, et al. **Extensive hemispheric lesions with radiological evidence of blood-brain barrier integrity in a patient with neuromyelitis optica.** *J Neurol Sci* 2009;284:217–19

50. Barnett MH, Sutton I. **Neuromyelitis optica: not a multiple sclerosis variant.** *Curr Opin Neurol* 2012;25:215–20

51. Bichuetti DB, Oliveira EM, Souza NA, et al. **Neuromyelitis optica in Brazil: a study on clinical and prognostic factors.** *Mult Scler* 2009;15:613–19

52. Ito S, Mori M, Makino T, et al. **"Cloud-like enhancement" is a magnetic resonance imaging abnormality specific to neuromyelitis optica.** *Ann Neurol* 2009;66:425–28

53. Banker P, Sonni S, Kister I, et al. **Pencil-thin ependymal enhancement in neuromyelitis optica spectrum disorders.** *Mult Scler* 2012;18:1050–53

54. McGraw CA, Swerdlow ML, Robbins MS. **Acute reversible periependymal ventricular enhancement in neuromyelitis optica.** *Eur J Neurol* 2012;19:e57–e58

55. Kister I, Herbert J, Zhou Y, et al. **Ultrahigh-field MR (7T) imaging of brain lesions in neuromyelitis optica.** *Mult Scler Int* 2013;2013:398259

56. Pichiecchio A, Tavazzi E, Poloni G, et al. **Advanced magnetic resonance imaging of neuromyelitis optica: a multiparametric approach.** *Mult Scler* 2012;18:817–24

57. Rocca MA, Agosta F, Mezzapesa DM, et al. **Magnetization transfer and diffusion tensor MRI show gray matter damage in neuromyelitis optica.** *Neurology* 2004;62:476–78

58. Calabrese M, Oh MS, Favaretto A, et al. **No MRI evidence of cortical lesions in neuromyelitis optica.** *Neurology* 2012;79:1671–76

59. Liu Y, Duan Y, He Y, et al. **Altered topological organization of white matter structural networks in patients with neuromyelitis optica.** *PLoS One* 2012;7:e48846

60. Yu C, Lin F, Li K, et al. **Pathogenesis of normal-appearing white matter damage in neuromyelitis optica: diffusion-tensor MR imaging.** *Radiology* 2008;246:222–28

61. Zhao DD, Zhou HY, Wu QZ, et al. **Diffusion tensor imaging char-**

acterization of occult brain damage in relapsing neuromyelitis optica using 3.0T magnetic resonance imaging techniques. *Neuroimage* 2012;59:3173–77

62. Aboul-Enein F, Krssak M, Hoftberger R, et al. **Diffuse white matter damage is absent in neuromyelitis optica.** *AJNR Am J Neuroradiol* 2010;31:76–79

63. de Seze J, Blanc F, Kremer S, et al. **Magnetic resonance spectroscopy evaluation in patients with neuromyelitis optica.** *J Neurol Neurosurg Psychiatry* 2010;81:409–11

64. Chen X, Zeng C, Luo T, et al. **Iron deposition of the deep grey matter in patients with multiple sclerosis and neuromyelitis optica: a control quantitative study by 3D-enhanced susceptibility-weighted angiography (ESWAN).** *Eur J Radiol* 2012;81:e633–e639

65. Duan Y, Liu Y, Liang P, et al. **Comparison of grey matter atrophy between patients with neuromyelitis optica and multiple sclerosis: a voxel-based morphometry study.** *Eur J Radiol* 2012;81:e110–e114

66. Lucchinetti CF, Popescu BF, Bunyan RF, et al. **Inflammatory cortical demyelination in early multiple sclerosis.** *N Engl J Med* 2011;365:2188–97

67. Calabrese M, Rinaldi F, Grossi P, et al. **Cortical pathology and cognitive impairment in multiple sclerosis.** *Expert Rev Neurother* 2011;11:425–32

68. Popescu BF, Parisi JE, Cabrera-Gomez JA, et al. **Absence of cortical demyelination in neuromyelitis optica.** *Neurology* 2010;75:2103–09

69. Seewann A, Kooi EJ, Roosendaal SD, et al. **Postmortem verification of MS cortical lesion detection with 3D DIR.** *Neurology* 2012; 78:302–08

70. Chanson JB, Lamy J, Rousseau F, et al. **White matter volume is de-creased in the brain of patients with neuromyelitis optica.** *Eur J Neurol* 2013;20:361–67

71. Habib CA, Liu M, Bawany N, et al. **Assessing abnormal iron content in the deep gray matter of patients with multiple sclerosis versus healthy controls.** *AJNR Am J Neuroradiol* 2012;33:252–58

72. Zivadinov R, Heininen-Brown M, Schirda CV, et al. **Abnormal sub-cortical deep-gray matter susceptibility-weighted imaging filtered phase measurements in patients with multiple sclerosis: a case-control study.** *Neuroimage* 2012;59:331–39

73. Qian W, Chan Q, Mak H, et al. **Quantitative assessment of the cervical spinal cord damage in neuromyelitis optica using diffusion tensor imaging at 3 Tesla.** *J Magn Reson Imaging* 2011;33:1312–20

74. Agosta F, Absinta M, Sormani MP, et al. **In vivo assessment of cervical cord damage in MS patients: a longitudinal diffusion tensor MRI study.** *Brain* 2007;130:2211–19

75. Klawiter EC, Xu J, Naismith RT, et al. **Increased radial diffusivity in spinal cord lesions in neuromyelitis optica compared with multiple sclerosis.** *Mult Scler* 2012;18:1259–68

76. Miller DH, Weinshenker BG, Filippi M, et al. **Differential diagnosis of suspected multiple sclerosis: a consensus approach.** *Mult Scler* 2008;14:1157–74

77. Bedi GS, Brown AD, Delgado SR, et al. **Impact of rituximab on relapse rate and disability in neuromyelitis optica.** *Mult Scler* 2011;17:1225–30

78. Carson KR, Evens AM, Richey EA, et al. **Progressive multifocal leukoencephalopathy after rituximab therapy in HIV-negative patients: a report of 57 cases from the Research on Adverse Drug Events and Reports project.** *Blood* 2009;113:4834–40

Transforaminal versus Intra-Articular Facet Corticosteroid Injections for the Treatment of Cervical Radiculopathy: A Randomized, Double-Blind, Controlled Study

N.J. Bureau, T. Moser, J.H. Dagher, D. Shedid, M. Li, P. Brassard, and B.E. Leduc

ABSTRACT

BACKGROUND AND PURPOSE: Transforaminal corticosteroid injections can be performed in the management of cervical radiculopathy but carry the risk of catastrophic complications. This study compares the efficacy of transforaminal and facet corticosteroid injections at 4 weeks' follow-up.

MATERIALS AND METHODS: We randomly assigned 56 subjects to receive CT-guided transforaminal (15 men, 13 women; mean age, 52 years; range, 28–72 years) or facet (8 men, 20 women; mean, 44 years; range, 26–60 years) injections. The primary outcome was pain severity rated on a Visual Analog Scale (0–100). Secondary outcomes were the Neck Disability Index and the Medication Quantitative Scale.

RESULTS: In the intention-to-treat and as-treated analyses, for a mean baseline score, facet injections demonstrated a significant pain score reduction of 45.3% (95% CI, 21.4–69.2) and 37.0% (95% CI, 9.2–64.7), while transforaminal injections showed a nonsignificant pain score reduction of 9.8% (95% CI, +11.5–31.2) and 17.8% (95% CI, +6.6–42.2). While facet injections demonstrated an improvement in the Neck Disability Index score of 24.3% (95% CI, +2.9–51.5) and 20.7% (95% CI, +6.2–47.6) as opposed to transforaminal injections of 9.6% (95% CI, +15.2–34.4) and 12.8% (95% CI, +11.2–36.7), the results were not statistically significant. Noninferiority of facet to transforaminal injections was demonstrated for baseline pain scores of ≤60, while noninferiority analysis was inconclusive for baseline pain scores of ≥80 and for the Neck Disability Index. Neither intervention showed a significant medication-intake score reduction with time.

CONCLUSIONS: Facet injections are effective for the treatment of cervical radiculopathy and represent a valid and safer alternative to transforaminal injections.

ABBREVIATIONS: IFSI = intra-articular facet corticosteroid injection; NDI = Neck Disability Index; MQS = Medication Quantitative Scale; TFSI = transforaminal corticosteroid injection; VAS = Visual Analog Scale

Cervical radiculopathy is a debilitating condition caused by the irritation of a cervical spinal nerve root. Patients typically present with pain radiating to the upper arm and a combination of sensory disorder, altered reflexes, or motor weakness.[1] It affects approximately 1 person per 1000 of population per year and is most often caused by degenerative spondylosis and/or a disk her-

niation.[2] Historically, approximately 30% of patients have required surgery.[3] Most patients will be treated medically, including rest, analgesics, nonsteroidal anti-inflammatory drugs, physical therapy, and corticosteroid injections.

Disk herniation and degenerative changes occurring at the intervertebral disk level, the uncovertebral joint, and/or the facet joint can potentially irritate the spinal nerve root by 2 major mechanisms: production of mediators of inflammation[4] and compression of the nerve. The presumed therapeutic effect of corticosteroid injections is the suppression of the inflammatory cascade. Transforaminal corticosteroid injections (TFSI) allow delivery of a high concentration of corticosteroids directly and

precisely at the site of the involved spinal nerve and are used to treat cervical radiculopathy.[5,6] In the past 15 years, a significant number of catastrophic neurologic complications after TFSI have been reported in the literature.[7] Although the exact prevalence of these devastating adverse events is unknown, some authors have questioned the continued use of TFSI,[8] while others advocate technical strategies to improve the safety of the procedure[9,10] or alternative approaches, which potentially carry fewer risks.[8,11]

Preliminary work by Kim et al in 2005[12] and by Richarme et al in 2008[11] suggested that intra-articular facet steroid injections (IFSIs) could be effective in patients with cervical radiculopathy secondary to disk herniation. Anatomically, the facet joint ventral recess is in close proximity to the spinal nerve root. Furthermore, Richarme et al[11] suggested that leakage of contrast into the foramen could be a potential mechanism of action. Therefore, using a facet joint injection approach to deliver corticosteroids in the vicinity of the injured spinal nerve root appears to be a viable alternative to the riskier transforaminal approach.

We hypothesized that IFSI could be at least as effective as TFSI for the treatment of cervical radiculopathy, and we devised this study to compare, at 4 weeks' follow-up, the efficacy of IFSI with TFSI in subjects with cervical radiculopathy of at least 1 month's duration due to degenerative spondylosis and/or a disk herniation.

MATERIALS AND METHODS
Subjects

Recruitment. The Research Ethics Committee of our institution approved this study. All subjects received written and verbal information and gave their written consent. The study was performed according to the Declaration of Helsinki, was approved by the scientific committee of the Research Funding Agency of the Quebec Government (grant 21230–2), and was registered at the University of Montreal as part of a master's thesis in biomedical science.

Prospectively, 56 adults with cervical radiculopathy, capable of giving written consent, were enrolled in the study. The subjects were recruited from the hospital community. One of 2 physiatrists or 1 of 2 neurosurgeons performed a clinical evaluation of the subjects to confirm the diagnosis of cervical radiculopathy according to eligibility criteria, similar to criteria used in previous studies,[5,9] and to identify the presence of exclusion criteria.

The eligibility criteria were the following: evidence of a cervical radiculopathy involving 1 spinal nerve of at least 1 month's duration refractory to medical treatment; symptoms of cervical pain radiating to the upper limb; and signs of altered sensations, abnormal reflexes, or motor weakness caused by degenerative spondylosis and/or disk herniation as documented at CT or MR imaging and a current mean pain score of ≥ 6 on a Verbal Analog Scale of 0 (no pain) to 10 (worse pain imaginable). The exclusion criteria were the following: evidence of vertebral fracture, tumor, or infection of the cervical spine; treatment with cervical corticosteroid injections within the past 3 months; coagulopathy; and allergy to iodinated contrast media. One of 2 radiologists reviewed the imaging studies to confirm the presence of degenerative spondylosis and/or a disk herniation at the level of the involved spinal nerve and to exclude other pathology.

Enrollment in the Study. The research assistant performed a telephone interview with the subjects who agreed to participate in the study, to discuss the research protocol in detail, to collect medical and demographic data, and to schedule an appointment for the intervention within 2 weeks of their clinical evaluation. The subjects were informed of the risk of minor adverse effects and of major complications after the procedure. On request, the subjects could meet with one of the researchers for any inquiry concerning their participation in the study.

Randomization. Patients were randomized to 1 of 2 groups: treatment with TFSI at the level of the involved spinal nerve root or treatment with IFSI of the facet joint adjacent to the involved spinal nerve root. The randomization sequence with block sizes of 8 was computer-generated by a person not otherwise directly involved with the subjects. The envelopes were sealed and sequentially numbered from 1 to 56. The randomization was done without stratification to allow evaluating the demographic and clinical aspects of interest. On the day of the procedure, the research assistant gave the sealed envelope matching the sequential number of the subject to the radiologist in charge of performing the intervention. The radiologist checked the content of the envelope and resealed the envelope before returning it to the assistant. Hence, the assistant remained blinded to the type of injection for the duration of the study.

Interventions
One of 2 musculoskeletal radiologists with 10 and 18 years of experience in interventional spine procedures performed the injections. The TFSIs were performed according to a standard technique,[9] and the IFSIs were performed by using a lateral approach. The setup of the patient, the sequential steps of the technique, and the material used were identical, with the exception of the targeted site of injection, which was the posterior and lateral aspects of the neural foramen for the TFSI (Fig 1A) and the facet joint space for the IFSI (Fig 1B). This method ensured that the subjects remained blinded to the type of injection they received.

The subject was placed in the supine position, with his or her head turned 45° to the side contralateral to the injection. Scout images of the targeted neural foramen were obtained. The appropriate entry site was marked on the skin. Then, the skin was prepped and draped in the usual fashion. The skin and subcutaneous tissue were anesthetized with lidocaine 1%. Then, a 22-ga, 2.5-inch spinal needle was advanced by using intermittent CT fluoroscopy (Brilliance-64; Philips Healthcare, Best, the Netherlands) with a collimation of 2.5 mm × 4 images set. Once the needle was in the appropriate location, 0.5–1.0 mL of contrast material (iohexol, Omnipaque 240; GE Healthcare Canada, Mississauga, Canada) was injected by using minibore tubing connected to a 3-mL syringe; and at the end of the injection, CT fluoroscopy images were acquired by the radiologist to exclude an intravascular position of the needle and to confirm adequate distribution of the contrast material. Then, 1 mL of dexamethasone sodium phosphate, 10 mg/mL was injected by using a 1-mL syringe. Then, the needle was withdrawn and the subject was observed for 30 minutes.
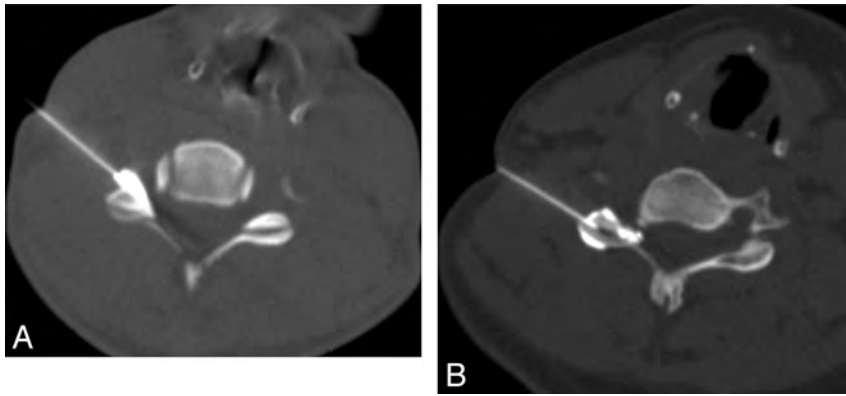
FIG 1. *A*, CT-guided transforaminal corticosteroid injection. The needle is positioned in the posterolateral aspect of the foramen with contrast media flowing in the foramen. *B*, CT-guided intra-articular facet corticosteroids injection. The needle is positioned in the facet joint. Contrast media injection confirms an intracapsular distribution.
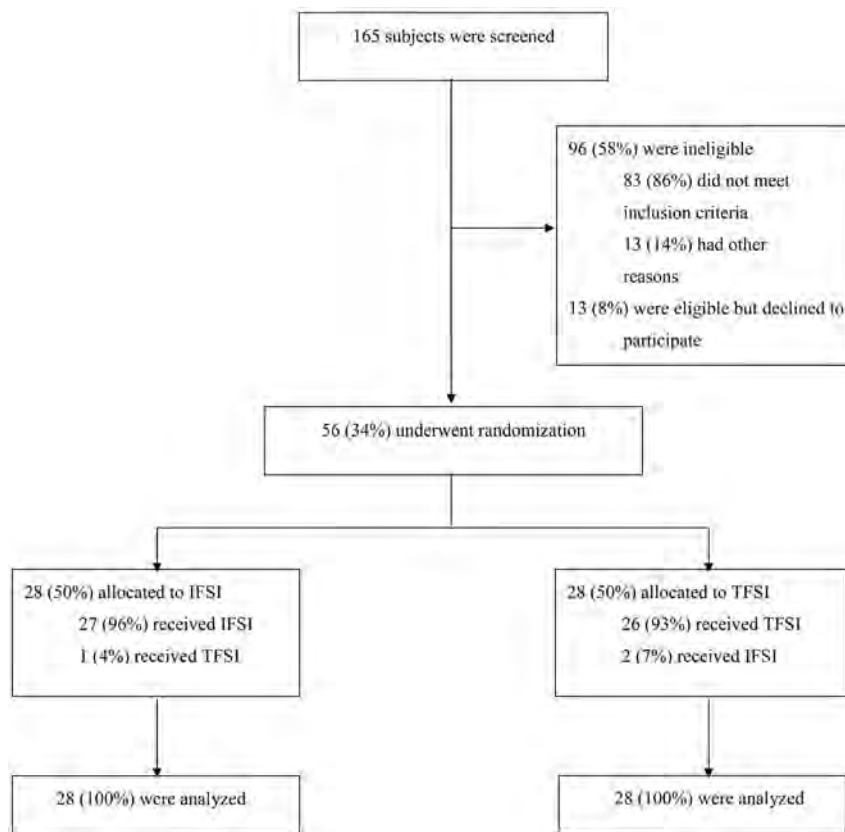
FIG 2. Flow diagram of the progress of subjects through the phases of the study.

Outcome Measures

The primary outcome was pain severity rated on a Visual Analog Scale (VAS) measured 4 weeks after the intervention. Subjects were asked to indicate the mean pain level experienced during the past few days on a VAS consisting of a straight line extending from 0 (no pain) to 100 mm (worse pain imaginable). Secondary outcome measures were the Neck Disability Index (NDI)[13] and the Medication Quantitative Scale (MQS).[14] The NDI is a valid questionnaire, which measures the impact of neck pain on everyday life activities related mainly to personal care, work, sleeping, driving, reading, and recreation. It comprises 10 items, each scored from 0 (no disability) to 5 (total disability). The minimal clinically

important difference is 5 (10%). We used the MQS to quantify medication use on a weekly basis after the intervention. Scores were calculated for each pain-related medication based on weights assigned by pharmacologic class and dosage level and were summed to yield the total MQS score. Although the lowest possible MQS score is 0, there is no definite upper limit. The minimal clinically significant reduction in MQS score is 4. At baseline, subjects were instructed to continue taking their usual medication after the procedure and to keep a written daily record of the type and dose of their medication intake during the next 4 weeks.

Follow-Up Time Points

On the day of the intervention, before randomization, the subjects met with the research assistant at the university hospital to sign the consent form and to complete the baseline VAS and the NDI questionnaire. Thirty minutes after the intervention, the assistant met with the subjects to assess any immediate adverse reactions. The subjects were asked to rate the worst pain experienced during the intervention and their level of pain at the current time on a Verbal Analog Scale (0–10). The assistant met again with the subjects 4 weeks after their procedure to complete the postintervention VAS and the NDI questionnaire. The subjects were questioned about any delayed adverse effects following the procedure. The medication record notebooks were also collected.

Statistical Analysis

It was determined that a sample size of 56 subjects, divided equally into the 2 groups, would be required to detect an efficacy in VAS pain score reduction of at least 30% in both groups, with a power of 80% and a type I error of 5% in 2 paired Student *t* tests. Descriptive statistics were used to characterize the 2 subject groups at baseline, and the Student *t* and χ^2 tests with a 2-sided α level of .05 were used to compare the characteristics between the 2 groups.

The main analyses followed the intention-to-treat principle, analyzing all patients according to randomization. In addition, an as-treated analysis was performed according to the type of injection the subjects received. Relative differences between postintervention and baseline scores were calculated for the VAS pain score and the NDI. The clinical efficacy of the IFSI and TFSI, in terms of VAS pain score reduction and NDI improvement, was defined as

Table 1: Baseline characteristics of subjects (per randomization) treated with either transforaminal or intra-articular facet corticosteroid injections

Variables	Groups		P Value
	IFSI	TFSI	
Subjects (No.)	28	28	
Sex (No.) (%)			.059
Male	8 (29)	15 (54)	
Female	20 (71)	13 (46)	
Age (yr) (mean) (range)	44 ± 8.3 (26–60)	52 ± 11.1 (29–72)	.007
Duration of pain (mo) (mean) (range)	14 ± 20 (1–84)	17 ± 21 (1–84)	.649
Imaging findings (No.) (%)			.357
Disk herniation	12 (43)	7 (25)	
Spondylosis	14 (50)	20 (71)	
Spondylosis/disk herniation	2 (7)	1 (4)	
Level of injection (No.) (%)			.566
C3–C4	1 (4)	0 (0)	
C4–C5	1 (4)	3 (11)	
C5–C6	16 (57)	15 (53)	
C6–C7	10 (35)	10 (36)	
Side of injection (No.) (%)			.284
Right	13 (46)	17 (61)	
Left	15 (54)	11 (39)	
VAS (0–100) (mean) (range)	61 ± 17 (23–95)	63 ± 18 (17–85)	.691
NDI (0–50) (mean) (range)	21 ± 8 (10–44)	19 ± 7 (5–30)	.301
Employment status (No.) (%)			.030
Working	12 (42.9)	16 (57.1)	
Retired	1 (3.6)	4 (14.3)	
Not working	15 (53.5)	8 (28.6)	
On sick leave with insurance	10 (35.71)	4 (14.29)	
On sick leave without insurance	0 (0.00)	2 (7.14)	
Workers' compensation	4 (14.29)	0 (0.00)	
On welfare	1 (3.57)	2 (7.14)	

Table 2: Pain severity and Neck Disability Index scores for intra-articular facet and transforaminal corticosteroid injections

Variable	Groups	
	IFSI	TFSI
Subjects (No.)		
It	28	28
At	29	27
VAS% (mean) (95% CI)		
It	45.3 (21.4–69.2)	9.8 (+11.5–31.2)
At	37.0 (9.2–64.7)	17.8 (+6.6–42.2)
NDI% (mean) (95% CI)		
It	24.3 (+2.9–51.5)	9.6 (+15.2–34.4)
At	20.7 (+6.2–47.6)	12.8 (+11.2–36.7)

Note:—VAS% indicates the relative difference between postintervention and baseline VAS pain scores; NDI%, the relative difference between postintervention and baseline Neck Disability Index scores; It, intention-to-treat analysis; At, as-treated analysis.

means of at least 30% and 10%, respectively. For the MQS, a mean reduction of at least 4 in the crude score was considered a significant reduction.

The group differences in the VAS pain score and NDI were analyzed by using an ANCOVA adjusted for baseline values, age, sex, and employment status. Noninferiority of the IFSI to the TFSI was claimed when the mean and 95% CI of the outcome variables of the IFSI were at least equivalent to or worse by <15% than the outcome variables of TFSI.[15] The efficacy of IFSI and TFSI was also compared in terms of the MQS with a repeated measures ANOVA adjusted for age, sex, and employment status. Contrasts were used to test the presence of a linear tendency with time in each group. Statistical software used for analyses was SAS, Version 9.3 (SAS Institute, Cary, North Carolina).

RESULTS

Of 165 subjects who were screened, 56 were enrolled in the study from December 1, 2010, through September 30, 2013. The study flow chart is shown in Fig 2.

Among the eligible subjects at screening ($n = 69$), 81% ($n = 56$) agreed to participate in the study. No subjects were lost to follow-up. Among the subjects randomized to receive an IFSI, 1 subject received a TFSI by a mistake of the radiologist. Among the subjects randomized to receive a TFSI, 2 subjects received an IFSI. In 1 case, the anterior recess of the articular facet was entered inadvertently. In the other case, the radiologist tried unsuccessfully to perform a TFSI at the C6–C7 level and finally opted to perform an IFSI instead.

Subject characteristics at baseline are presented in Table 1. The baseline characteristics of the 2 groups were similar except for age, sex, and employment status variables, for which a significant or almost-significant difference was found. In addition, those receiving TFSI had an apparent higher percentage with spondylosis (71%) compared with disk herniation (25%), while the subjects receiving IFSI had a more even distribution with spondylosis at 50% compared with disk herniation at 43%.

The mean level of worst pain felt during the intervention was similar in both the intention-to-treat and as-treated analyses respectively, at 7.1 and 7.3 for the TFSI group and 6.2 and 6.0 for the IFSI group. Similarly, the mean level of cervical pain reported at 30 minutes after the intervention was equivalent in both groups, at 3.1 in the intention-to-treat analysis and 3.2 in the as-treated analysis. No adverse events occurred following the interventions. At the 4-week follow-up, in the intention-to-treat analysis, 1 subject of the TFSI group reported having tinnitus and vertigo since the intervention and 1 subject in each group reported having headaches during the 2 days following the intervention. In the as-treated analysis, all the delayed adverse effects were reported in the TFSI group.

Clinical Efficacy of IFSI and TFSI

The clinical efficacy of IFSI and TFSI, in terms of VAS pain score reduction for a mean baseline VAS pain score of 62.4 and of NDI improvement, is presented in Table 2. Regarding the MQS outcome, neither type of intervention demonstrated a significant reduction in the medication-intake score for all time measurements.

We also performed a subgroup analysis of the etiologic imaging findings for IFSI and TFSI in terms of VAS pain score reduction to discern any difference between apparently more acute

Table 3: Pain severity subgroup analysis of the etiologic imaging findings for intra-articular facet and transforaminal corticosteroid injections

| | Subgroups | | | |
| | Disk Herniation ± Spondylosis | | Spondylosis | |
Variable	IFSI	TFSI	IFSI	TFSI
Subjects (No.)				
It	14	8	14	20
At	13	9	16	18
VAS% (mean) (95% CI)				
It	65.0 (31.2–98.9)	8.0 (+20.2–36.2)	30.1 (0.4–59.7)	+1.6 (+33.7–30.4)
At	46.5 (9.4–83.6)	22.7 (+6.6–51.9)	23.6 (+6.7–53.9)	5.6 (+27.1–38.2)

Note:—VAS% indicates the relative difference between postintervention and baseline VAS pain scores; It, intention-to-treat analysis; At, as-treated analysis.

Table 4: Pain severity scores for intra-articular facet and transforaminal corticosteroid injections according to the baseline score

| Variable and Baseline VAS Pain Score (0–100) | Groups | |
	IFSI	TFSI
Subjects (No.)		
It	28	28
At	29	27
VAS% (mean) (95% CI)		
20		
It	53.3 (4.0–102.7)	+83.4 (+132.8 to +34.0)
At	41.6 (17.1–100.3)	+70.6 (+128.5 to +12.7)
40		
It	49.5 (16.7–82.4)	+39.4 (+72.1 to +6.6)
At	39.4 (0.6–78.2)	+28.9 (+66.9–9.2)
60		
It	45.8 (21.8–69.8)	4.6 (+17.2–26.5)
At	37.2 (9.4–65.0)	12.9 (+12.0–37.8)
80		
It	42.0 (11.6–72.4)	48.7 (23.3–74.0)
At	35.0 (+0.3–70.4)	54.6 (25.2–84.0)
95		
It	39.1 (2.7–80.9)	81.7 (46.0–117.3)
At	33.4 (15.6–82.3)	86.0 (44.1–127.8)

Note:—VAS% indicates the relative difference between postintervention and baseline VAS pain scores; It, intention-to-treat analysis; At, as-treated analysis.

(disk herniation) and more chronic (spondylosis) causal factors. These results are presented in Table 3.

Analysis of Group Differences in Efficacy

An interaction term was found between the randomized groups and the baseline VAS pain score ($P = .001$). Hence, the efficacy of the interventions was linked to the level of the baseline VAS pain score (Table 4). The noninferiority analysis results for VAS pain scores are presented in Fig 3.

Regarding the NDI outcome, the difference in efficacy between IFSI and TFSI was 14.6% (95% CI, +18.4–47.7) in the intention-to-treat analysis and 7.9% (95% CI, +22.9–38.8) in the as-treated analysis. Although IFSI appeared to be more effective than TFSI at reducing the level of disability, this difference was not statistically significant and the result regarding noninferiority was inconclusive.

The difference in efficacy between the 2 groups in terms of the MQS score with time is presented in Fig 4. Although the visual perception would suggest a linear tendency for medication-intake reduction during the time in the IFSI group, this trend was not statistically significant both in the intention-to-treat analysis ($P =$

.654) and in the as-treated analysis ($P = .441$). The hypothesis of a linear tendency for medication-intake reduction with time was also rejected for the TFSI group in both analyses ($P = .902$, $P = .675$).

DISCUSSION

In 1997, Persson et al,[16] in a randomized study, demonstrated that surgery, a custom physical therapy treatment, or the use of a cervical collar were equally effective at treating cervical radiculopathy. Because an inflammatory reaction is recognized as at least partly responsible for the irritation of the spinal nerve, corticosteroids should logically be part of the armamentarium used to treat this entity. Furthermore, to obtain optimal results, corticosteroids should be delivered at a high concentration as close as technically feasible to the site of the lesion. These principles provide the basis for the use of TFSI in the treatment of cervical radiculopathy. Notwithstanding that controlled studies demonstrating the efficacy of TFSI are lacking, the primary reason limiting the use of TFSI is the risk of serious complications. In an effort to determine the prevalence of severe complications, Scanlon et al[7] performed a survey among the members of the American Spine Society. Among 1340 members, the response rate was 21.4% (287). In all, 78 complications were reported, including vertebrobasilar brain infarcts, cervical spinal cord infarcts, and 13 deaths. Arterial embolism of particulate corticosteroids is the most frequently cited presumptive cause of brain and spinal cord infarcts.[17] While performing a TFSI, despite using a careful and precise technique, one can possibly cause inadvertent injection of material into radicular arteries that feed the spinal cord.[18]

The intention of this randomized controlled study was to test the hypothesis that IFSIs are at least as effective as TFSIs for the treatment of cervical radiculopathy. Both interventions were equally well tolerated by the subjects, and no major adverse events occurred with either type of intervention. For a mean baseline pain severity score, IFSI provided a clinically and statistically significant reduction in pain at 4 weeks' follow-up, while the improvement provided by TFSI was clinically and statistically nonsignificant. Furthermore, the subgroup analyses suggested that IFSIs were effective in subjects with cervical radiculopathy secondary to a disk herniation and maybe to a lesser degree in subjects with degenerative spondylosis, while TFSIs did not appear to provide significant relief in both subgroups. When we compared the efficacy of both interventions, an interaction with the baseline pain severity score was found. On the basis of these analyses, IFSIs were more effective or at least as effective as TFSIs for baseline pain severity scores of ≤60, while whether TFSIs were more effective than IFSIs for baseline pain severity scores of ≥80 could not be determined. Most interesting, for overall baseline pain severity scores between 20 and 95, IFSI provided significant relief for cervical radiculopathy. Conversely, TFSI appeared to be effective only in subjects presenting with baseline pain severity scores of >80. These last findings remain unclear. There was no relationship between the imaging findings and the baseline pain severity score, thus refuting the hypothesis that disk herniations could be

associated with greater baseline pain severity than degenerative spondylosis and would respond better to TFSI.

Regarding the NDI outcome, while IFSI appeared to ease the performance of specific daily activities on a clinical basis, the results did not reach statistical significance. When we compared the 2 interventions, IFSI appeared to be more effective than TFSI, but the difference was not statistically significant. Neither intervention was associated with a clinically significant pain medication–intake reduction with time.

An observational study by Kim et al in 2005[12] suggested that IFSI could be effective in patients with cervical disk herniation. Unfortunately, the study group appeared to be inhomogeneous and the methodology was incompletely described for drawing any sound conclusions from that study. In 2007, Richarme et al[19] presented preliminary results on contrast distribution following CT-guided intra-articular facet injections in 31 patients. Using this alternative approach, they obtained foraminal opacification in 21/31 (68%) patients and epidural opacification in 19/31 (63%). The following year, the same investigators presented their preliminary results on the efficacy of CT-guided IFSI in 17 patients with cervical radiculopathy secondary to a disk herniation.[11] They obtained pain relief of >50% on a visual analog pain scale in 7/17 (41%) patients and reported extension of contrast in the foraminal space in 5/7 patients with >50% pain relief.

The exact mechanism of the apparent beneficial effect of IFSI for the treatment of cervical radiculopathy remains uncertain and unclear. As these studies suggest, 1 potential explanation is the proximity of the facet joint ventral capsular recess to the intervertebral foramen and/or leakage of the medication from the facet joint into the epidural and/or foraminal spaces. If this hypothetic mechanism of indirect delivery of corticosteroids to the site of pa-
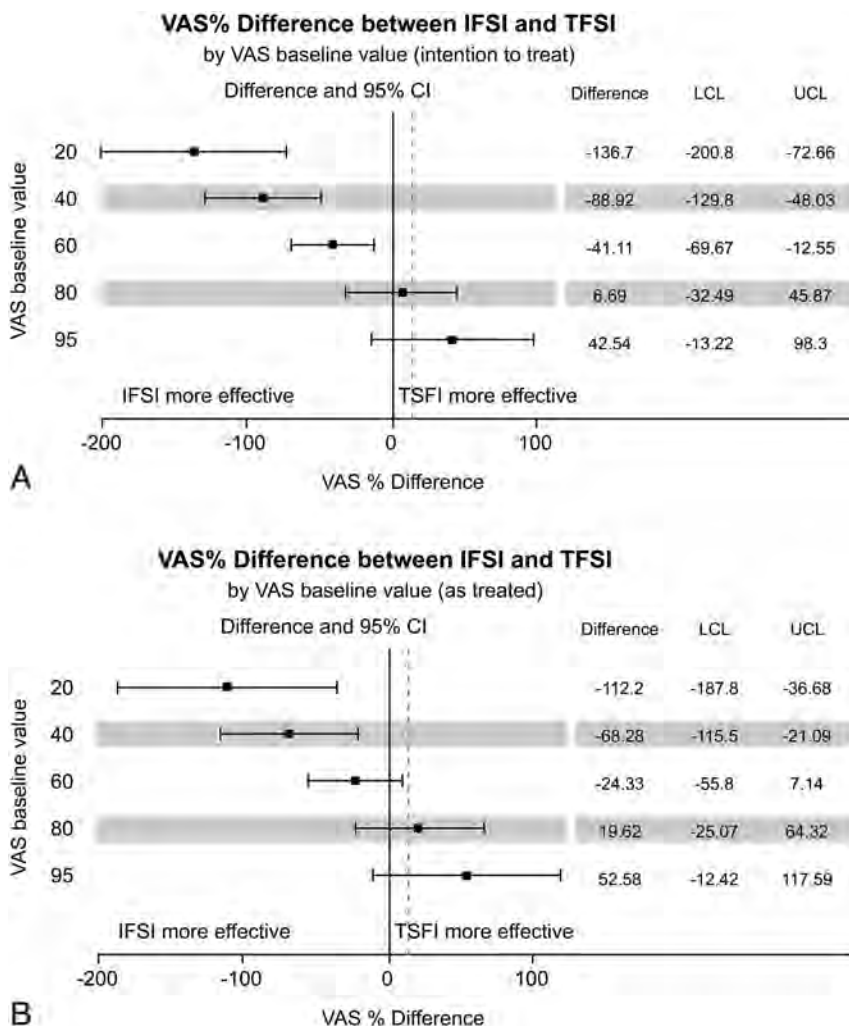
FIG 3. Relative Visual Analog Scale pain score differences between intra-articular facet and transforaminal corticosteroid injections, according to the VAS baseline value with adjustments for age, sex, and employment status. The intention-to-treat (A) and as-treated (B) analyses are presented. Error bars indicate 2-sided 95% CIs. Squares indicate mean differences. The dotted vertical line marks the 15% margin of noninferiority. LCL indicates lower confidence limit; UCL, upper confidence limit.
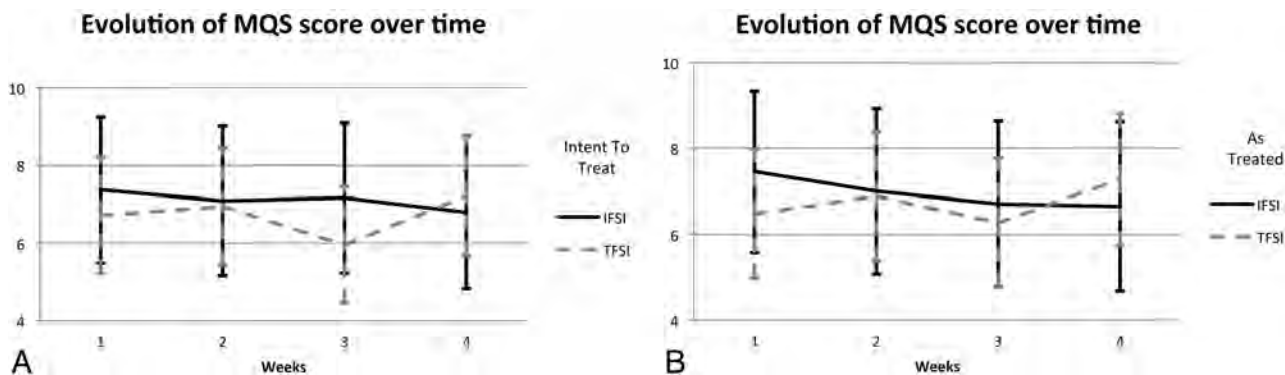
FIG 4. Medication Quantitative Scale scores with time adjusted for age, sex, and employment status, for the intra-articular facet and transforaminal corticosteroid injections groups. The intention-to-treat (A) and as-treated (B) analyses are presented. Error bars indicate 2-sided 95% CIs.

thology were the explanation for the efficacy of IFSI, then one would expect TFSI to provide at least equivalent results. In that regard, our results appear to be discordant with those of several noncontrolled, observational studies, which reported good-to-excellent results in anywhere from 24% to 76% of cases,[5,6,20,21] including a more recent prospective case series study of 140 patients with chronic cervical radiculopathy due to degenerative spondylosis who received 3 consecutive TFSIs at 3-week intervals.[22] These authors reported a significant pain reduction in 49% (69/140) of their patients at 12–14 weeks' follow-up.

Conversely, our results are in agreement with a randomized controlled study by Anderberg et al.[23] These authors assigned 40 patients presenting with chronic cervical radiculopathy from degenerative spondylosis, with a mean duration of symptoms of 31 months, to receive 1 fluoroscopically guided TFSI. The treatment group received an injection of mepivacaine and methylprednisolone, while the control group received an injection of mepivacaine and saline. There was a positive response in only 30% (6/20) of the patients in the treatment group at 3 weeks' follow-up. There were no significant differences in treatment results between the 2 groups.

The results of this study must be interpreted in light of some limitations. Facet joint syndrome may cause neck pain, which may radiate to the shoulders and can mimic cervical radiculopathy.[24] We are confident that the randomized study design and the diagnosis of cervical radiculopathy made by specialists based on strict inclusion criteria with correlative imaging findings guarantee that the subjects in our study had cervical radiculopathy and that our results cannot be explained on the basis of a positive effect of IFSI on facet joint syndrome. While this randomized study allows evaluating the efficacy of IFSI and TFSI with a power of 80%, our sample size is small for a study design of noninferiority comparing both interventions, to prove, without a doubt, that IFSIs are not less effective than TFSIs in treating cervical radiculopathy. This would require a prohibitively greater number of subjects. Nevertheless, this study is one of the few randomized controlled trials examining the efficacy of TFSI for the treatment of cervical radiculopathy and provides specialists who treat these patients and who perform these interventions with data to consider an alternative technique.

Although including 2 different etiologic causes for radiculopathy could be perceived as a limitation of this study, this is more representative of common clinical practice. According to Radhakrishnan et al,[2] disk herniation is responsible for cervical radiculopathy in 20%–25% of cases, and spondylosis with or without disk herniation, in 70%–75% of the cases. Furthermore, regardless of the current etiology of cervical radiculopathy, the inclusion and exclusion criteria, the outcome measures, and the clinical question that we were addressing remained the same. Finally, although in our study we did not attempt to rupture the joint capsule while performing IFSI, we will address the issue of the potential interaction between contrast distribution and the efficacy of cervical corticosteroid injections in a future retrospective analysis of our data base.

CONCLUSIONS
IFSIs are effective for the treatment of cervical radiculopathy due to spondylosis and/or disk herniation. IFSIs were more or at least

as effective as TFSIs in providing pain relief when the baseline pain severity score was low-to-moderate, while the comparison between the 2 interventions remained inconclusive for severe baseline pain level. IFSI can represent a valid and safer alternative to TFSI because no serious complications have been reported to date with this approach, to our knowledge. Consequently, we suggest that within an optimized medical treatment management, corticosteroid injections should initially be performed by using an intra-articular facet approach instead of a transforaminal approach.

REFERENCES
1. Carette S, Fehlings MG. **Clinical practice: cervical radiculopathy.** *N Engl J Med* 2005;353:392–99
2. Radhakrishnan K, Litchy WJ, O'Fallon WM, et al. **Epidemiology of cervical radiculopathy: a population-based study from Rochester, Minnesota, 1976 through 1990.** *Brain* 1994;117(pt 2):325–35
3. Sampath P, Bendebba M, Davis JD, et al. **Outcome in patients with cervical radiculopathy: prospective, multicenter study with independent clinical review.** *Spine* 1999;24:591–97
4. Kang JD, Stefanovic-Racic M, McIntyre LA, et al. **Toward a biochemical understanding of human intervertebral disc degeneration and herniation: contributions of nitric oxide, interleukins, prostaglandin E2, and matrix metalloproteinases.** *Spine* 1997;22:1065–73
5. Cyteval C, Thomas E, Decoux E, et al. **Cervical radiculopathy: open study on percutaneous periradicular foraminal steroid infiltration performed under CT control in 30 patients.** *AJNR Am J Neuroradiol* 2004;25:441–45
6. Vallée JN, Feydy A, Carlier RY, et al. **Chronic cervical radiculopathy: lateral-approach periradicular corticosteroid injection.** *Radiology* 2001;218:886–92
7. Scanlon GC, Moeller-Bertram T, Romanowsky SM, et al. **Cervical transforaminal epidural steroid injections: more dangerous than we think?** *Spine* 2007;32:1249–56
8. Provenzano DA, Fanciullo G. **Cervical transforaminal epidural steroid injections: should we be performing them?** *Reg Anesth Pain Med* 2007;32:168, author reply 169–170
9. Wagner AL. **CT fluoroscopic-guided cervical nerve root blocks.** *AJNR Am J Neuroradiol* 2005;26:43–44
10. Hoang JK, Apostol MA, Kranz PG, et al. **CT fluoroscopy-assisted cervical transforaminal steroid injection: tips, traps, and use of contrast material.** *AJR Am J Roentgenol* 2010;195:888–94
11. Richarme D, Thevenin FS, Chevrot A, et al. **Cervical radiculopathy: efficiency of CT-guided cervical facet joint corticosteroid injection.** In: *Proceedings of the 94th Annual Meeting of the Radiological Society of North America Annual Meeting.* Chicago, Illinois; November 30–December 5, 2008
12. Kim KH, Choi SH, Kim TK, et al. **Cervical facet joint injections in the neck and shoulder pain.** *J Korean Med Sci* 2005;20:659–62
13. Wlodyka-Demaille S, Poiraudeau S, Catanzariti JF, et al. **French translation and validation of 3 functional disability scales for neck pain.** *Arch Phys Med Rehabil* 2002;83:376–82
14. Harden RN, Weinland SR, Remble TA, et al. **Medication Quantification Scale Version III: update in medication classes and revised detriment weights by survey of American Pain Society Physicians.** *J Pain* 2005;6:364–71
15. Piaggio G, Elbourne DR, Altman DG, et al. **Reporting of noninferi-**

ority and equivalence randomized trials: an extension of the CONSORT statement. *JAMA* 2006;295:1152–60

16. Persson LC, Carlsson CA, Carlsson JY. **Long-lasting cervical radicular pain managed with surgery, physiotherapy, or a cervical collar: a prospective, randomized study.** *Spine* 1997;22:751–58

17. Malhotra G, Abbasi A, Rhee M. **Complications of transforaminal cervical epidural steroid injections.** *Spine (Phila Pa 1976)* 2009; 34:731–39

18. Baker R, Dreyfuss P, Mercer S, et al. **Cervical transforaminal injection of corticosteroids into a radicular artery: a possible mechanism for spinal cord injury.** *Pain* 2003;103:211–15

19. Richarme D, Thevenin FS, Campagna R, et al. **CT-guided cervical foraminal injection: is a direct foraminal approach still necessary?** In: *Proceedings of the 93rd Annual Meeting of the Radiological Society of North America.* Chicago, Illinois; November 25–30, 2007

20. Bush K, Hillier S. **Outcome of cervical radiculopathy treated with periradicular/epidural corticosteroid injections: a prospective study with independent clinical review.** *Eur Spine J* 1996;5:319–25

21. Lasbleiz J, Siegfried D, Chales G, et al. **Evaluation of CT guided cervical epidural injections in patients with mechanical cervicobrachial neuralgia [in French].** *J Radiol* 2008;89(3 Pt 1):317–23

22. Persson L, Anderberg L. **Repetitive transforaminal steroid injections in cervical radiculopathy: a prospective outcome study including 140 patients.** *Evid Based Spine Care J* 2012;3:13–20

23. Anderberg L, Annertz M, Persson L, et al. **Transforaminal steroid injections for the treatment of cervical radiculopathy: a prospective and randomised study.** *Eur Spine J* 2007;16:321–28

24. Kirpalani D, Mitra R. **Cervical facet joint dysfunction: a review.** *Arch Phys Med Rehabil* 2008;89:770–74

Fluoroscopic-Guided Lumbar Puncture: Fluoroscopic Time and Implications of Body Mass Index—A Baseline Study

S.R. Boddu, A. Corey, R. Peterson, A.M. Saindane, P.A. Hudgins, Z. Chen, X. Wang, and K.E. Applegate

ABSTRACT

BACKGROUND AND PURPOSE: Fluoroscopic-guided lumbar puncture is an effective alternative to bedside lumbar puncture in challenging patients. However, no published guidelines are available for an acceptable range of fluoroscopic time for this procedure. The purpose of this study was to set department benchmark fluoroscopic times for lumbar puncture, accounting for body mass index in our patient population.

MATERIALS AND METHODS: We identified and reviewed all patients who underwent fluoroscopic-guided lumbar puncture at 4 hospitals during a 2-year period (July 2011 to June 2013). Data collection included patient information (demographics, body mass index, history of prior lumbar surgery and/or lumbar hardware, scoliosis); procedure details (fluoroscopic time, level of access, approach, needle gauge and length); level of operator experience; and hospital site. A generalized linear model was used to test whether body mass index influenced fluoroscopic time while controlling other factors.

RESULTS: Five hundred eighty-four patients (mean age, 47.8 ± 16.2 years; range, 16–92 years; 33% male) had successful fluoroscopic-guided lumbar puncture s. Mean body mass index and fluoroscopic time were higher in female patients (34.4 ± 9.9 kg/m^2 and 1.07 minutes; 95% CI, 0.95–1.20) than in male patients (29.2 ± 7.3 kg/m^2 and 0.91 minutes; 95% CI, 0.79–1.03). Body mass index ($P = .001$), hospital site ($P < .001$), and level of experience ($P = .03$) were factors significantly affecting fluoroscopic time on multivariate analysis. Benchmark fluoroscopic times in minutes were the following: 0.48 (95% CI, 0.40–0.56) for normal, 0.61 for overweight (95% CI, 0.52–0.71), 0.63 (95% CI, 0.58–0.73) for obese, and 0.86 (95% CI, 0.74–1.01) in extremely obese body mass index categories.

CONCLUSIONS: In patients undergoing fluoroscopic-guided lumbar punctures, fluoroscopy time increased with body mass index We established benchmark fluoroscopic-guided lumbar puncture time ranges as related to body mass index in our patient population.

ABBREVIATIONS: ACR = American College of Radiology; BMI = body mass index; FGLP = fluoroscopic-guided lumbar puncture; IIH = idiopathic intracranial hypertension; LP = lumbar puncture

L umbar puncture (LP) is an invasive technique that accesses the restricted compartment of the subarachnoid space to sample CSF. This procedure involves the percutaneous introduction of a needle below the termination level of the spinal cord, passing through the dura mater of the spinal canal and entering the sub-

arachnoid space. The diagnostic LP is typically performed at the bedside by using surface landmark guidance, as first described by Quincke in 1891.[1] However, surface landmark identification of underlying structures has been shown to be accurate only 30% of the time and can be difficult in the obese patient.[2]

CSF analysis is a valuable diagnostic tool. The American College of Radiology (ACR) Appropriateness Criteria include LP as a recommended procedure in the setting of negative findings on CT head in the clinical scenario of thunderclap headache when subarachnoid hemorrhage is suspected.[3] Valid indications for CSF sampling also include suspected CNS infection, demyelinating disease, and CNS malignancy. The LP technique is also used to access the CSF space to allow instillation of chemotherapeutic agents, antispasmodics, and contrast media.[4]

Fluoroscopic-guided lumbar puncture (FGLP) is an effective alternative to bedside LP in patients with challenging body habitus. LP performed under fluoroscopic guidance can be less trau-

FIG 1. The distribution of log-transformed fluoroscopic time versus patient population. Normal distribution of the fluoroscopic time following log transformation of the skewed raw data of the fluoroscopic time.
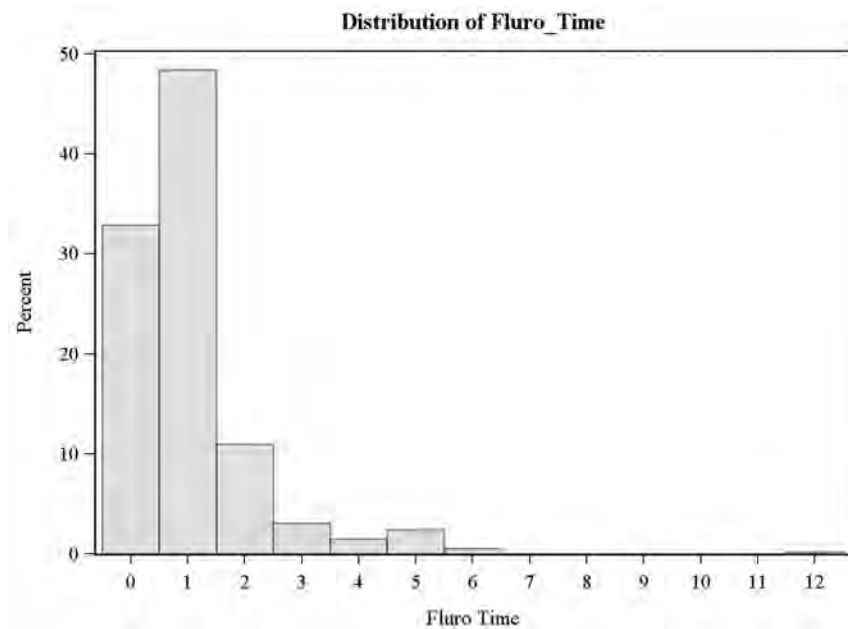
FIG 2. The distribution of fluoroscopic time versus patient population. Because the distribution of the fluoroscopic time is highly skewed, log transformation is applied to the fluoroscopic time to fit the model better.

matic, therefore having a decreased likelihood of spurious false-positive results of hemorrhage and hence avoiding subsequent investigations such as CTA and conventional angiography.[5] However patients are exposed to ionizing radiation during the procedure and obesity by itself is a predisposing factor for an increased procedure-associated radiation dose, as proved with interventional cardiology.[6] Obesity is a growing epidemic with a specific increase in the obese and extremely obese body mass index (BMI) categories during the past 50 years.[7,8] Increasing reliance by the clinicians on radiology to perform FGLPs may be a reflection of this epidemic. Both the

American Board of Radiology and the Accreditation Council for Graduate Medical Education have recognized FGLP as a core competency in radiology residency and neuroradiology fellowship training.[9-11]

In 2011, The Joint Commission released a sentinel alert expressing concern about the American population exposure to ionizing radiation and significant increase in the contribution of medical imaging to overall ionizing radiation. Medical radiation constitutes almost half (3.0 mSv) of the US population average annual radiation exposure (6.1 mSv) and 5 times the per capita effective dose of the global population from medical exposure (0.64 mSv).[12] The Joint Commission advised physicians to review their practices to reduce radiation exposure to as low as reasonably achievable without compromising patient care.[13]

The ACR recommends documentation of actual fluoroscopy time for all procedures in the patient medical record.[14,15] In addition, the ACR also recommends that the documented fluoroscopic times for various procedures should then be compared with benchmark figures.[14] However, a thorough literature search revealed a lack of guideline or benchmark data for the FGLP procedure.

The purpose of this study was to establish baseline fluoroscopic time ranges for FGLP and to evaluate the variability of fluoroscopic time ranges relative to national BMI categories in our patient population. We tested the hypothesis that the fluoroscopic times for the LP increase with increases in BMI.

MATERIALS AND METHODS
Patient Population
All patients who had FGLP at any of the 4 hospitals in our health care system (University Hospital, University Hospital Midtown, Orthopedic and Spine Center, and Memorial Hospital) during 24 consecutive months (July 1, 2011 to June 30, 2013) were identified for review. The radiology information system at these 4 hospitals was searched by using the department procedure codes "XR Spine LP" and "Fluoroscopic-guided spinal tap" to identify subjects. All successful FGLPs performed on a standard fluoroscopic table for which the fluoroscopic time and BMI were known were included in this study. On the basis of the standard policy for requesting FGLP by the radiology department, most of these patients had at least 2 failed attempts at bedside LP. Direct FGLP was available to patients with pre-existing challenging conditions such as marked obesity, severe scoliosis, and/or

prior lumbar surgery with underlying scar tissue and/or spinal-fixation hardware. This study was reviewed and granted institutional review board exemption.

Procedure Technique

Following informed consent, all patients underwent the FGLP procedure in the prone or prone oblique position by using a standard fluoroscopic table in the radiology department. The procedure is performed by using sterile technique.[4] The Centers for Disease Control and Prevention recommendations of using a facemask, aseptic technique, and following other safe injection practices for performing a spinal injection procedure to prevent the risk of bacterial meningitis[16] are routinely applied.

Routine access was at the L3/4 level with few variations involving the L2/3, L4/5, and L5/S1 levels. Twenty-two-gauge needles were most commonly used and occasionally lower (14 ga, 16 ga, 18 ga, and 20 ga) or higher (23 ga and 25 ga) gauge needles were used. Intermittent-pulse fluoroscopy was used to identify the appropriate site for the LP and to monitor the course of the advancing needle during the procedure until the subarachnoid space was entered, confirmed by the reflux of clear CSF, marking the end point of the fluoroscope use. The radiology report routinely included the fluoroscopy time and any known immediate complications from the procedure. Board-certified, subspecialty-trained neuroradiologists and trainees (diagnostic radiology residents and neuroradiology fellows) performed the FGLPs during the study period. Faculty directly or indirectly supervised trainees. The level of experience of the operator was recorded.

Data Collection

The radiology information at the 4 hospitals was searched by using the department procedure codes "XR Spine LP" and "Fluoroscopic-guided spinal tap." The procedure report and the stored images were reviewed (A.C., S.R.B., R.P.) by using electronic medical records and PACS, respectively. Age, sex, BMI, and hospital site parameters were obtained from the electronic medical records. The BMI was obtained from the electronic medical records directly or calculated on the basis of the height and weight documented in the records by using the formula: Weight (kg) / [Height (m)]^2. Fluoroscopic screening time, clinical indication, approach, side, level of procedure, needle size and length, and experience of the operator were documented from the radiology report. A history of prior lumbar surgery, scoliosis, and spinal hardware were identified on image review and review of patient clinical notes.

Categorization of BMI, Clinical Indication, and Other Variables

Patients were grouped on the basis of their body mass index according to obesity guidelines of the National Heart, Lung, and Blood Institute[17]: underweight (BMI < 18.5), normal (BMI = 18.5–24.9), overweight (BMI = 25–29.9), obese (BMI = 30–39.9), and extremely obese (BMI ≥ 40). Patients were also categorized on the basis of the clinical indications provided by the referring clinicians, including the following: altered mental status, infection, inflammation, neoplasm, cognitive decline, CSF leak, intrathecal chemotherapy or baclofen, idiopathic intracranial hypertension (IIH), and suspected hemorrhage.

Patients were dichotomized for the presence or absence of

Table 1: Exclusion criteria

Criteria	No. of Procedures Excluded
Procedure performed using C-arm	1
Cervical puncture	2
Lumbar drain insertion	11
No documentation of fluoroscopic time	6
No documentation of BMI	16
Unsuccessful procedure (dry tap)	21
Unsuccessful procedure (abandoned due to patient discomfort)	12
Total procedures excluded	69

lumbar surgery, scoliosis, and lumbar orthopedic hardware as noted from radiograph and chart review. The variable "approach" was categorized into "Media/Interspinal" and "Paramedian/Paraspinal" needle approach. Variable "Side" was documented for patients with "Paramedian/Paraspinal" approach as "Right" or "Left." "Needle length" was categorized as "Standard (3.5 inches)" or "Longer" (5 or 7 inches)" as related to the spinal needle length used. "Level of procedure" was categorized as "Upper" (L2/3 and L3/4) and "Lower" (L4/5 and L5/S1) to describe the level at which access to the subarachnoid space was achieved. "Needle size" was divided into 3 groups: "22 ga," "<22 ga," and ">22 ga." Operator experience was grouped as "Junior Resident (R1/R2)," "Senior Resident (R3/R4)," "Fellow," and "Attending." Sixteen attending neuroradiologists and 32 trainees (radiology residents and neuroradiology fellows) performed the procedures. Trainees performed 94% of the procedures under the direct or indirect supervision of the attending physicians.

Statistical Analysis

The outcome variable, fluoroscopic time, was considered as the continuous variable. BMI, sex, age, prior lumbar surgery, scoliosis, lumbar spine hardware, approach, indication, level, side, needle size, needle length, operator experience, and hospital site were all considered potential factors affecting the fluoroscopic time. The mean, median, SD, and 95% CI of the mean were calculated for the continuous variables. One-way ANOVA was used to test for any difference of BMI across the groups of the characteristics of patients. The Fisher exact test was used to test for any association between the characteristics of patients and categorized BMI. Generalized linear model regression was used for univariate and multivariate analyses on fluoroscopic time. Log transformation was applied for fluoroscopic time (Fig 1), to fit the model better because the distribution was highly skewed (Fig 2). The Akaike information criterion was used for model selection. The significance level for the analyses was .05. SAS 9.3 (SAS Institute, Cary, North Carolina) was used for data management and analyses.

RESULTS

Patient Population

A total of 653 procedures were found in the radiology information system search. Following the exclusion criteria (Table 1), we excluded 69 patients. Five hundred eighty-four patients (389 men and 195 women) constituted the study population. The mean age was 47.8 ± 16.2 years, and the mean BMI of study population was 31.8 ± 8.6 kg/m^2. The age of the obese (46.8 ± 14.9 years) and extremely

Table 2: The association between categorized BMI and clinical indication of patients

Variable	<18.5 (n = 12)	18.5–24.9 (n = 120)	25–29.9 (n = 142)	30–39.9 (n = 175)	≥40 (n = 135)	P Value
Indication						<.0001
AMS	0	20	6	6	3	
Baclofen/chemotherapy	3	13	21	5	0	
CSF leak	0	4	6	5	1	
Cognitive decline	0	10	14	8	3	
Hemorrhage	0	3	2	4	5	
IIH[a]	0	4	17	48	80	
Infection	5	36	37	44	20	
Inflammation	1	12	20	38	19	
Malignancy	3	16	17	12	2	

Note:—AMS indicates altered mental status.
[a] The overall BMI of patients in the IIH category is significantly higher than any other clinical indication.

Table 3: Fluoroscopic time in minutes based on the clinical indication of the patients

Variable	No.	Mean	Standard Error	95% CI of Mean
AMS	35	0.43	0.17	0.30–0.63
Baclofen/chemotherapy	42	0.67	0.17	0.49–0.91
CSF leak	16	0.73	0.37	0.43–1.24
Cognitive decline	35	0.57	0.11	0.43–0.76
Hemorrhage	14	0.41	0.21	0.22–0.74
IIH[a]	149	0.81	0.09	0.70–0.93
Infection	142	0.61	0.09	0.53–0.74
Inflammation	90	0.58	0.16	0.46–0.74
Malignancy	50	0.53	0.1	0.42–0.69

Note:—AMS indicates altered mental status.
[a] IIH is the clinical indication with maximum fluoroscopic time compared with all other clinical indications. However, there is no significant variation in fluoroscopic time based on the clinical indication.

Table 4: Benchmark fluoroscopic time in minutes based on BMI categories[17]

Variable	No.	Mean[a]	Standard Error	95% CI of Mean
BMI				
<18.5	12	0.77	0.39	0.35–1.67
18.5–24.9	120	0.48	0.03	0.40–0.56
25–29.9	142	0.61	0.01	0.52–0.71
30–39.9	175	0.63	0.01	0.58–0.73
≥40	135	0.86	0.02	0.74–1.01

[a] The mean fluoroscopic times of the obese and extremely obese patients are significantly higher compared with those of patients with normal BMI.

obese (40 ± 12.8 years) patients was significantly lower ($P < .001$) than that in the patients with normal BMI (51.1 ± 16.7 years).

Patient Characteristics Based on BMI and Clinical Indication

The mean BMI of the female patients (34.4 ± 9.9) was significantly higher ($P < .001$) than that of the male patients (29.2 ± 7.3). The mean BMI of the patients with prior lumbar spine surgery (30.4 ± 6.7) and scoliosis (25.8 ± 6.4) was significantly lower than that in patients without surgery (32.9 ± 9.6, $P < .01$) and without scoliosis (33.1 ± 9.4, $P < .001$).

The most common reasons for referral for FGLP were IIH closely followed by infection and inflammation (Table 2). The mean BMI of patients with IIH (40.5 ± 8.6) was significantly higher than any other clinical indications ($P < .001$). The mean BMI of patients who required a longer LP needle (5 or 7 inches) was 39.2 ± 7.7 and 46.9 ± 7.5, respectively, significantly higher ($P < .001$) than that in patients (27.6 ± 6.0) who had the procedure with a standard needle (3.5 inches). No significant variation in the patient BMI was noted between different operator levels of experience or different health care sites.

Fluoroscopic Time Based on Clinical Indication

Patients with IIH had the maximum mean fluoroscopic time of 0.81 minutes (95% CI, 0.70–0.93 minutes) compared with all other clinical indications. Patients with suspected subarachnoid hemorrhage evaluation had the least fluoroscopic time of 0.41 minutes (95% CI, 0.22–0.74 minutes). The fluoroscopic time distribution based on the clinical indication is summarized in Table 3.

Fluoroscopic Time: Univariate Analysis

Approach ($P = .01$), clinical indication ($P = .01$), BMI ($P < .001$), level ($P = .005$), needle length ($P < .001$), operator experience ($P < .001$), and hospital site ($P < .001$) significantly affected the fluoroscopic time. Sex ($P = .66$), surgery ($P = .88$), scoliosis ($P = .22$), hardware ($P = .61$), side ($P = .15$) and needle size ($P = .3$) had no significant effect on fluoroscopic time. The fluoroscopic time of patients with normal BMI was significantly shorter than that of the patients in overweight ($P < .05$), obese ($P = .02$), and extremely obese ($P < .001$) BMI weight categories.

Fluoroscopic Time: Multivariate Analysis

BMI ($P = .001$), hospital site ($P < .001$), and experience of the operator ($P = .03$) were factors significantly affecting the fluoroscopic time. On the basis of operator experience, fluoroscopic time for the LPs performed by the "Fellows" was significantly lower ($P = .03$) compared with "Residents" and "Attendings." Note that the "Attending" cases may have been completed after failed resident or fellow attempts. Approach and level variables had a marginally significant effect on fluoroscopic time. FGLP performed by using a paramedian approach had a shorter fluoroscopic time compared with a midline approach ($P = .08$). Fluoroscopic time for FGLP performed at lower levels (L4/5 and L5/S1) was marginally longer than procedures performed at higher levels (L2/3 and L3/4) ($P = .07$). BMI affected the fluoroscopic time significantly after controlling for approach, hospital site, level, and experience variables.

Fluoroscopic Time according to the BMI

The benchmark fluoroscopic times for the LP based on the BMI are summarized in Table 4. The mean fluoroscopic time for LP increased with an increase in the BMI compared with patients with normal BMI on both pre- and postlogarithmic conversion of the data. The fluoroscopic time of the patients with normal BMI was

Table 5: Comparison of the percentage of overweight, obese, and extreme obesity distribution of patient population from the current study versus age-adjusted prevalence among US adults 20 years of age and older

Category	NHANES[a] 2009–2010	Study Population	P Value
Sample size	5926	584	
Total (%)			
Overweight	33.0%	24.3%	.56
Obese	35.7%	29.9%	.8
Extremely obese	6.3%	23.1%	.008
Men (%)			
Overweight	38.4%	36.9%	.5
Obese	35.5%	26.1%	.1
Extremely obese	4.4%	9.2%	.5
Women (%)			
Overweight	27.9%	17.9%	.8
Obese	35.8%	31.8%	.5
Extremely obese	8.1%	30.0%	.0008

Note:—NHANES indicates National Health and Nutrition Examination Survey.
[a] The percentage of the extremely obese female patients is significantly higher in our study population compared with the age-adjusted prevalence in US population.

significantly shorter than that of the patients who are obese ($P = .02$) or extremely obese ($P < .001$), while controlling for other variables. The significantly shorter fluoroscopic time of the normal BMI compared with overweight BMI noted on univariate analysis ($P < .05$) was not confirmed in the multivariate analysis ($P = .09$).

DISCUSSION

Our study demonstrated a longer fluoroscopic time with increasing BMI. Table 5 summarizes the differences in the patient distribution based on the BMI categories between the study population and age-adjusted American adults 20 years or older, based on the National Health and Nutrition Examination Survey 2009–2010 data.[8] The percentage of the extremely obese patients in our study population was almost 4 times higher than the national average. The percentage of the extremely obese female patients was significantly higher ($P < .001$) in our study population compared with the age-adjusted prevalence in the US population. The normal BMI patient subgroup constituted only 21% of the study population, whereas the obese and extremely obese patients together constituted more than half (53%) of the study population. The prevalence of the obese and extremely obese BMI distribution in our study population was significantly higher ($P < .001$) in the female population (62%) compared with males (39%) and higher in the younger age group. This pattern of BMI distribution with obese and extremely obese patients among the young female patients was well above the national average. The authors hypothesize that this finding can be related to the number of patients with IIH in our study and note the correlation of that diagnosis and both female sex and obesity. In our study population, IIH was the single largest clinical indication, with 149 patients (26%), closely followed by infection. The mean BMI of the IIH group was significantly higher ($P < .001$) than the mean BMI of any other clinical indication.

There were 12 underweight (BMI < 18.5 kg/m^2) patients in our study. Despite low BMI, these patients had paradoxically higher mean fluoroscopic time than any other BMI groups. The authors propose that this group, more so than the others, had very challenging patients, including individuals with cerebral palsy ($n = 3$), HIV encephalopathy ($n = 5$), terminally ill malignancy ($n = 3$), and CNS vaculities ($n = 1$). Many of these patients were poorly oriented and

had difficulty maintaining position and following the instructions. In addition, the small number of patients in this category contributing only 2% of the study population could explain the paradoxical trend in this group. This theory was substantiated by the wide confidence intervals and higher SD and standard error of this group compared with the other BMI groups.

Understandably, patients with IIH present a greater challenge to successful bedside LP due to associated high BMI and difficulty in palpating the bony landmarks. Laxity of adipose tissues and long needle lengths necessary in the obese patients can complicate the procedure and potentially increase the amount of fluoroscopic time. In our study group, patients in the IIH subgroup had the highest mean fluoroscopic time of 0.81 minutes (95% CI, 0.70–0.93 minutes) as well as a maximum mean BMI of 40.5 ± 8.8 kg/m^2. Although clinical indication was a statistically significant variable on the univariate analysis, this variable was not chosen by the multivariate analysis.

The referrals of patients in the infection subgroup were not related to their BMI; mean BMI in this subgroup was 30.5 ± 8.6 kg/m^2. These patients pose a challenge for the bedside LP related to increased agitation and inability to stay still for longer times, which was usually documented on clinical request or progress notes accessed from the electronic medical records. Increased referrals for FGLP in this subgroup were likely related to the potential of more rapid access to the subarachnoid space with fluoroscopic guidance, as reflected in our study with a mean fluoroscopic time of 0.61 minutes (95% CI, 0.53–0.74 minutes).

The health care facility is a significant variable affecting the fluoroscopic time. There is no significant variation in the BMI categories between the health care facilities to explain this variation. The authors hypothesize that this variation is related to the work flow variations such as technicians obtaining a localizer image before the start of a procedure by a radiologist and variability in the duration of hands-on for the trainees before faculty take-over for difficult cases. Also, IIH, the clinical indication with the maximum mean fluoroscopic time, constitutes 29% of Memorial Hospital study population. IIH represents 24% at University and 21% at University Midtown hospital site study population.

The level of operator experience is another significant variable affecting the fluoroscopic time. Fluoroscopic time for the LPs performed by "Fellows" is significantly lower ($P = .03$), compared with "Residents" and "Attendings." The variation between "Resident" and "Fellow" fluoroscopic times is probably related to increased operator experience by/during fellowship. The variation between "Fellow" and "Attending" fluoroscopic times might reflect the fact that at our teaching institution, trainees typically perform the procedures (under supervision) to the point of completion or until the attending takes over in cases of difficulty. In rare instances of no resident or fellow on service or by patient request, the attending is the sole operator. In either of these instances, the cumulative fluoroscopic time is credited to the attending.

The authors realize that target time values are needed to assess the quality and safety of the current practice of FGLP at their institutions. The authors searched the current literature and were unable to identify targeted fluoroscopic time values for this procedure or for variation in the fluoroscopic time of LP as related to BMI.

Brook et al[18] showed that both the CT and fluoroscopic-guided LP are a useful alternatives with low procedure times and radiation dose in obese patients with prior failed unguided attempts. However, the authors in that study measured the total procedure time but not the actual radiation screening time. While CT guidance is a viable alternative to FGLP, at our facilities, the greater availability of the fluoroscopy slots, workflow considerations, rapid room turnaround time, and patient physical characteristics as related to the geometry of the tube size and table limit are some of the reasons we do not routinely use CT for subarachnoid space access. Recently the Stanford Orthopedic Group published their experience of a 30% increase in the fluoroscopic time in overweight patients undergoing spine interventions. However subcategorization of the overweight BMI (>25 kg/m^2) was not considered, and none of the patients had FGLP in this study.[19]

Given the lack of published guidelines, this study contributes to the literature by providing the baseline fluoroscopic time based on the BMI categories. We plan to use these data as a benchmark in the evaluation of the individual and department performance with an aim to keep the fluoroscopic time as low as reasonably achievable and specifically within the 2 SD range. Furthermore, these data can be used to identify the individual trends in the fluoroscopic times, provide feedback to operators about their performance, identify the outliers, and prompt targeted education and/or intervention for the outliers. Overall, these data can be a great resource toward improvement of patient care, radiation safety, and training.

Limitations
We acknowledge the limitations of the study, including but not limited to its retrospective nature and the regionally specific patient population of this single institution. This study was performed at an academic center and has inevitable patient-selection bias. Because most of the procedures are performed by the trainees, variable trainee confidence levels and the point of takeover by the attending in difficult cases were not documented; this lack of documentation can be an area of potential bias. In addition, we could not control for certain patient factors including anxiety, ability/willingness to cooperate, individual pain threshold, pre-existing degenerative changes or spinal stenosis, and postsurgical scar tissue or hardware. Those variables could certainly impact the time it takes to do the procedure.

CONCLUSIONS
BMI affects the fluoroscopic time significantly after controlling for other variables (approach, hospital site, level of access, and operator experience). The fluoroscopic time increases with increasing BMI. We were able to establish benchmark fluoroscopic time ranges for our patient population in relation to their BMI. Tracking fluoroscopy time and an ongoing quality assurance program with operators are essential to minimize radiation exposure for both patients and radiation heath workers.

REFERENCES

1. Dugacki V. **A hundred years of lumbar puncture.** [Article in English, Croatian] Neurol Croat 1992;41:241–45
2. Stiffler KA, Jwayyed S, Wilber ST, et al. **The use of ultrasound to identify pertinent landmarks for lumbar puncture.** Am J Emerg Med 2007;25:331–34
3. Jordan J, Wippold II F, Cornelius R. ACR Appropriateness Criteria. American College of Radiology. 2009. http://www.acr.org/~/media/ACR/Documents/AppCriteria/Diagnostic/Headache.pdf. Accessed September 14, 2013
4. Kieffer S, Mukundan S, Rollins N. **ACR–ASNR–SPR Practice Guideline for the Performance of Myelography and Cisternography.** 2013. http://www.acr.org/~/media/f4c49aa1834d46a081f5f0ff20e1e26b.pdf. Accessed September 12, 2013
5. Eskey CJ, Ogilvy CS. **Fluoroscopy-guided lumbar puncture: decreased frequency of traumatic tap and implications for the assessment of CT-negative acute subarachnoid hemorrhage.** AJNR Am J Neuroradiol 2001;22:571–76
6. Ector J, Dragusin O, Adriaenssens B, et al. **Obesity is a major determinant of radiation dose in patients undergoing pulmonary vein isolation for atrial fibrillation.** J Am Coll Cardiol 2007;50:234–42
7. Wang Y, Beydoun MA. **The obesity epidemic in the United States: gender, age, socioeconomic, racial/ethnic, and geographic characteristics—a systematic review and meta-regression analysis.** Epidemiol Rev 2007;29:6–28
8. Fryar C, Carroll M, Ogden C. Prevalence of Overweight, Obesity, and Extreme Obesity Among Adults: United States, Trends 1960–62 Through 2009–2010. 2012. http://www.cdc.gov/nchs/data/hestat/obesity_adult_09_10/obesity_adult_09_10.htm. Accessed August 18, 2013
9. Accreditation Council for Graduate Medical Education. ACGME Program Requirements for Graduate Medical Education in Diagnostic Radiology. 2007. http://www.acgme.org/acgmeweb/Portals/0/PFAssets/2013-PR-FAQ-PIF/420_diagnostic_radiology_07012013.pdf. Accessed September 14, 2013
10. Accreditation Council for Graduate Medical Education. ACGME Program Requirements for Graduate Medical Education in Neuroradiology. 2007. http://www.acgme.org/acgmeweb/Portals/0/PFAssets/2013-PR-FAQ-PIF/423_neuroradiology_diag_rad_07012013_1-YR.pdf. Accessed September 14, 2013
11. The Diagnostic Radiology Milestone Project. 2012. https://www.acgme.org/acgmeweb/Portals/0/PDFs/Milestones/DiagnosticRadiologyMilestones.pdf. Accessed September 12, 2013
12. Schauer DA, Linton OW. **NCRP Report No. 160, Ionizing radiation exposure of the population of the United States, medical exposure: are we doing less with more, and is there a role for health physicists?** Health Phys 2009;97:1–5
13. The Joint Commission: Sentinel Event Alert. Radiation risks of diagnostic imaging. 2011. https://www.wvdhhr.org/rtia/pdf/SEA_47[1].pdf. Accessed September 14, 2013
14. Amis ES Jr, Butler PF, Applegate KE, et al. **American College of Radiology white paper on radiation dose in medicine.** J Am Coll Radiol 2007;4:272–84
15. Amis ES Jr, Butler PF, **American College of Radiology: ACR white paper on radiation dose in medicine—three years later.** J Am Coll Radiol 2010;7:865–70
16. Centers for Disease Control and Prevention. CDC Clinical Reminder: Spinal Injection Procedures Performed without a Facemask Pose Risk for Bacterial Meningitis. http://www.cdc.gov/injectionsafety/SpinalInjection-Meningitis.html. Accessed September 12, 2013
17. National Heart, Lung, and Blood Institute. How Are Overweight and Obesity Diagnosed? http://www.nhlbi.nih.gov/health/health-topics/topics/obe/diagnosis.html. Accessed September 27, 2013
18. Brook AD, Burns J, Dauer E, et al. **Comparison of CT and fluoroscopic guidance for lumbar puncture in an obese population with prior failed unguided attempt.** J Neurointerv Surg 2014;6:324–28
19. Smuck M, Zheng P, Chong T, et al. **Duration of fluoroscopic-guided spine interventions and radiation exposure is increased in overweight patients.** PM R 2013;5:291–96, quiz 296

Effect of Direct Neuroradiologist Participation in Physician Marketing on Imaging Volumes in Outpatient Radiology

L. Grignon, M. Keiper, J. Vavricek, W. Horsley, R. Murphy, A. Grignon, and F. Yu

ABSTRACT

BACKGROUND AND PURPOSE: Over the past several years, decreased demand for and increased supply of imaging services has increased competition among outpatient imaging centers in the United States. This study hypothesizes that using a radiology sales representative and neuroradiologist as a team in marketing and sales will increase imaging referrals in outpatient imaging.

MATERIALS AND METHODS: From January to December 2009, baseline monthly physician referral data of CT and MR scans of 19 referring clinicians (neurologists, neurosurgeons, and anesthesiologists) to an outpatient radiology group were collected. During that time, a nonphysician radiology sales representative visited the referring clinicians' offices every 2 weeks. From January to June 2010, the same radiology sales representative visited the referring clinicians' offices every 2 weeks but was accompanied by a neuroradiologist once a month. From July 2010 to June 2011, the same radiology sales representative visited the referring clinicians' offices twice a month without a neuroradiologist.

RESULTS: Cross-sectional imaging referral volumes were approximately 2.5 times greater during the 6-month period using the neuroradiologist for direct physician-to-physician marketing when compared with the volumes achieved with the sales representative alone, and continued neuroradiologist involvement in marketing and sales is required to maintain referral volumes over time.

CONCLUSIONS: The impact on imaging referral volumes during the 6-month use of the neuroradiologist for direct physician-to-physician marketing in this study supports the assertion that neuroradiologist visits are an important element in establishing and maintaining a relationship with the referring clinician's office and thereby maximizing imaging referrals.

The imaging growth rate in outpatient radiology has slowed significantly during the past several years. Medicare data show that the annual growth rate for CT scans fell to just 1.4% in 2006–2009 from 14.3% annual growth in 2000–2005, and the annual growth rate for MR imaging fell to 2.6% in 2006–2009 from 14% annual growth in 2000–2005.[1] Similarly, data from private insurers found that the annual growth rate for CT scans fell to 3.1% in 2006–2009 from 20.4% annual growth in 2002–2006, and the annual growth rate for MR imaging fell to 1.1% in 2006–2009 from 16.6% annual growth in 2002–2006.[1] Compounding the

decrease in growth rate and demand, the number of imaging centers and supply of imaging services in the United States has progressively increased. The number of imaging centers has grown nationally from 6383 in 2011 to 6514 sites in 2012, increasing the percentage of single-site operations from 29% to 34% in 1 year.[2] The evolution of radiology supply and demand has created increased competition among outpatient imaging centers in the United States.

Radiology services have also increasingly become a commodity during the past decade. This may, in large part, be due to the previously described rapid increase in the supply of imaging services, the advancement and ubiquity of teleradiology, and the progressive lack of direct interaction between radiologists and referring clinicians in modern outpatient medicine. Radiologists are becoming increasingly removed from direct interaction with referring clinicians due to teleradiology, advances in PACS access for referring clinicians, and the increasing use of hospitalists, among other factors. In addition, the prevailing use of hospitalists has removed most referring clinicians from the hospital setting, eliminating substantive interactions with radiologists in outpatient imaging.

To combat commoditization and to distinguish itself from the vast array of competitors, an imaging provider can use innovative marketing and sales efforts that target the primary customer and re-establish the relationships with referring clinicians. This study hypothesizes that the use of the radiology sales representative and neuroradiologist as a team in marketing and sales visits to referring providers is an effective method by which to increase imaging referrals in outpatient radiology.

MATERIALS AND METHODS

All potential referring clinicians to a busy outpatient imaging provider located in a single geographic locale were chosen on the basis of their referral volumes. Referring providers were categorized into A, B, C, and D categories. These categories were established through evaluation of Medicare and private insurer radiology referral data for individual referring providers and through personal knowledge of referring clinicians' practices. Category A clinicians referred most of their patients to the imaging provider for radiologic examinations. Category B and C clinicians referred approximately 25%–75% of their patients to the imaging provider. The B and C providers were categorized as opportunity accounts. Category D clinicians referred few or no patients to the imaging provider due to geographic constraints or self-referral barriers. Nineteen category B and C referring clinicians (neurologists, neurosurgeons, and anesthesiologists) in both solo and group practices were selected, and baseline monthly referral data of CT and MR scans to an outpatient radiology practice were collected during a 12-month period from January to December 2009.

During that time, a senior and experienced nonphysician radiology representative with a successful track record in radiology sales and marketing made personal visits to the referring physicians' offices every two weeks, providing office staff and clinicians with technical support, substantive educational material, collateral marketing material from the radiology practice, and personal encounters to gather feedback regarding the imaging provider's service to the referring clinician's office. The representative did not provide meals or any other material that may be considered an inducement. From

Mean scan volumes for an outpatient radiology group during control and test periods

	Sales Representative (2009)	Sales Representative + Neuroradiologist (2010)	Sales Representative (2010)	P Value (Compared with 2009)
January	8.5	19.2	–	<.0001
February	8.3	20.0	–	<.0001
March	8.4	20.9	–	<.0001
April	7.8	20.1	–	<.0001
May	7.6	18.5	–	<.0001
June	5.7	15.8	–	<.0001
July	5.5	–	14.9	<.0001
August	5.4	–	13.1	<.0001
September	4.1	–	11.4	<.0001
October	3.9	–	8.9	<.0001
November	6	–	6.1	.49
December	7.6	–	7.6	1

■ Sales Representative (2009)   ■ Sales Representative + Neuroradiologist (2010)   ■ Sales Representative (2010)

✳ Time point at which the neuroradiologist stopped accompanying the sales representative in 2010

✳ *P* value no longer statistically significant
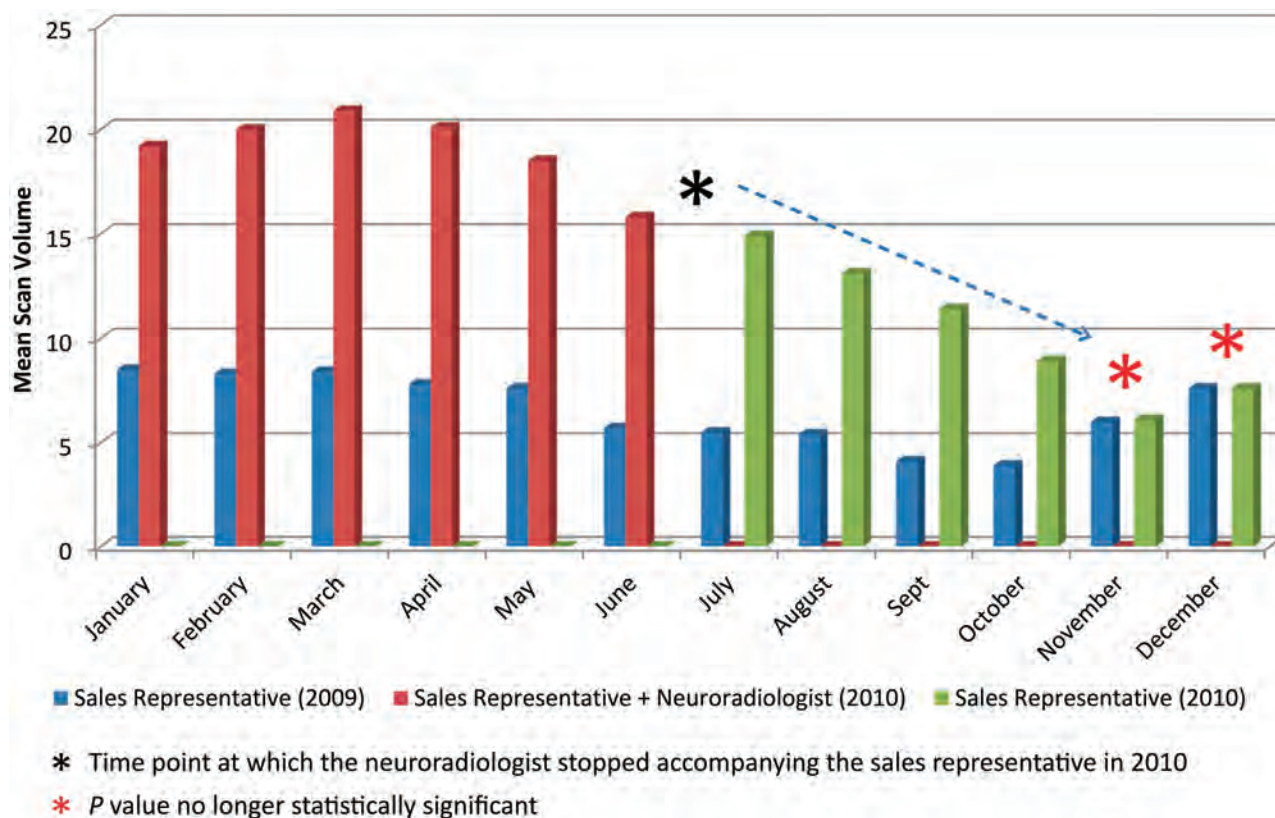
FIG 1. Duration of effect of the neuroradiologist's participation in outpatient radiology marketing.
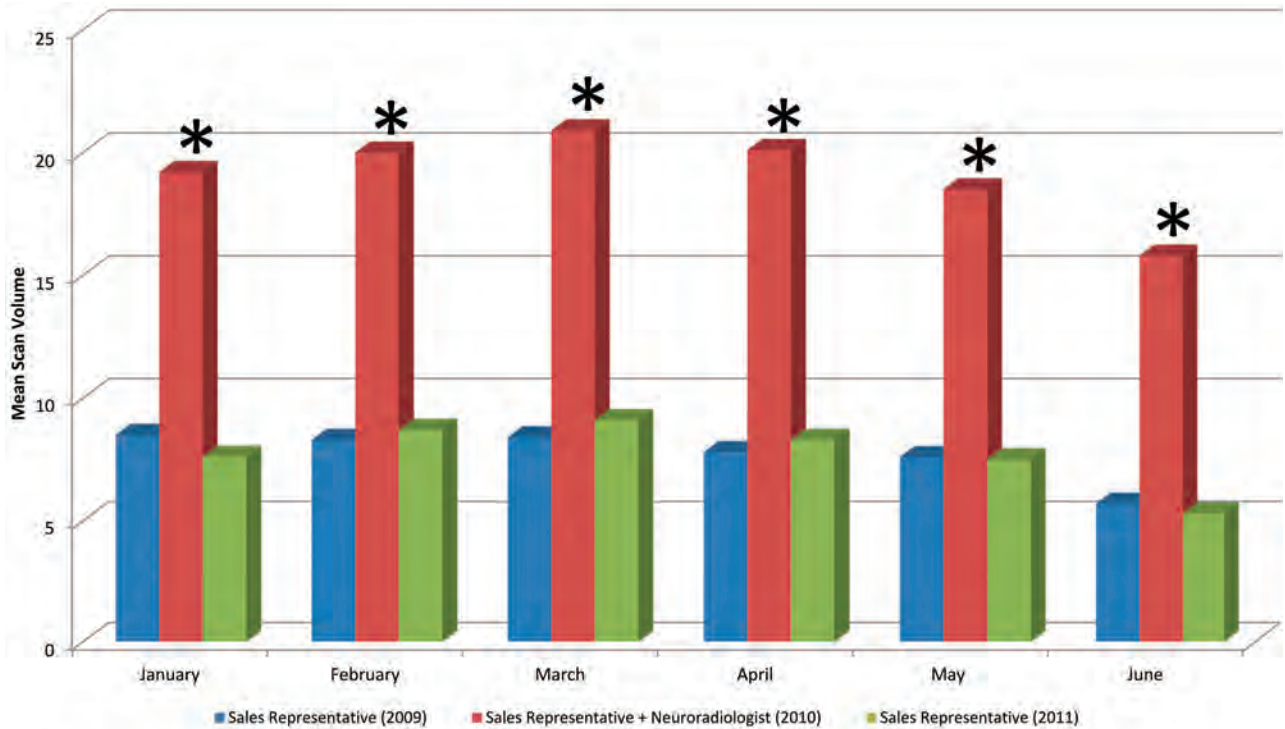
* Mean scan volume with sales representative + neuroradiologist (2010) is significantly greater than with the sales representative alone in 2009 or 2011 ($p < 0.0001$)

FIG 2. Effect of joint sales representative and neuroradiologist participation in outpatient radiology marketing.

January to June 2010, the same radiology sales representative visited the same referring clinician offices every 2 weeks but was accompanied by a neuroradiologist once a month. The neuroradiologist provided educational lectures, imaging advice, and additional substantive personal interaction with referring clinicians during the visits. In July 2010, the neuroradiologist stopped accompanying the sales representative. From July 2010 to June 2011, the same radiology sales representative visited the referring clinicians' offices twice a month without the neuroradiologist.

Monthly CT and MR imaging referral volumes were collected during the same time periods as well. The time periods were separated by a year to control for typical seasonal variations of referral patterns due to marked increases in patient population during the winter months in this market. Comparisons were made between identical months of successive years because inherent variations of patient population and imaging volumes occurred not only on a seasonal basis, but also varied monthly during any given season due to the rapid flux in the patient population. No notable changes or improvements occurred in the service parameters of the radiology group, such as in the telecommunications equipment, scheduling or authorization personnel, or quantity of scanners or imaging centers available for scheduling. In addition, no change in the individual referring clinicians' practices occurred between the time periods.

The generalized estimating equation model for negative binomial data with a log link was used to fit the scan data to adjust for correlation among the repeated interventions on a single referring clinician. The monthly referral volumes of CT and MR imaging examinations collected for both time periods were compared for the years 2009–2011 on a month-by-month basis to control for additional potential monthly variations in referral volume.

RESULTS

The results demonstrate the relatively dramatic effect of the use of a neuroradiologist in garnering increases in imaging referral volumes. Cross-sectional imaging volumes were approximately 2.25–2.75 times ($P < .0001$) greater during the 6-month period using the neuroradiologist for direct physician-to-physician marketing when compared with the volumes achieved for the identical month of the corresponding time period with the sales representative alone. Additionally, the referral volumes began to decrease for all providers approximately 1.5 months after the neuroradiologist stopped visiting the clinicians. The referral volumes returned to baseline levels approximately 5 months after the neuroradiologist terminated visits ($P > .05$) (Table and Fig 1). Moreover, the referral volumes remained at baseline values for the entire following 6-month period when the sales representative continued to visit the referring clinicians' offices alone (Fig 2).

DISCUSSION

Radiology sales representatives and neuroradiologists are both important in maximizing clinician referrals and subsequent imaging growth. However, they face individual limitations in developing a relationship with the referring provider's office. Maximizing the unique positive attributes and skills of both the sales representative and the neuroradiologist is crucial to achieving the most successful outcomes.

Radiology sales representatives are an important link between outpatient radiology centers and referring providers by serving as a vital source of information through educational and service visits and by providing a support structure for the referring provider's office. A survey of physicians in private practice found that they were more likely than those in university hospitals to interact with, value, and rely on sales representatives, with 76% perceiving sales representatives as valuable.[3] Therefore, the sales professional is an established, respected source for the referring clinician, particularly in the outpatient setting.

However, radiologists are perhaps the most important element in establishing and maintaining a relationship with the referring clinician's office. Radiologists are perceived as the leaders of the radiology entity and provide instant credibility as experts in the field. Because they have an extensive fund of radiologic and medical expertise, they can more precisely educate clinicians on the advantages of referring to their outpatient center. A study of factors affecting the choice of specialist by primary care physicians found that 59.2% of respondents chose "previous experience with specialist" and 53% chose "quality of specialist communication to the primary care physician" as major factors in choosing a specialist.[4] An effective direct interaction with the referring clinician, therefore, likely creates a bond through which a meaningful referral source may develop.

A team consisting of both the sales representative and neuroradiologist ideally incorporates both the medical expertise and clout of the neuroradiologist and the sales expertise and greater availability of the sales representative. Radiology sales representatives are limited in their medical knowledge and also lack radiologic expertise, thereby potentially encountering a lack of appreciation and respect because they are not considered medical peers. However, neuroradiologists are limited in their marketing and sales abilities and are not traditionally sales-oriented, so they may be unwilling to make a sales visit to a referring clinician's office or may be less effective during the visit. By combining the marketing and sales ability of the radiology sales representative with the medical expertise and leadership of the neuroradiologist, the outpatient center may overcome the practical limitations each may individually face and achieve the most successful outcomes.

The results of this study support the hypothesis that using the neuroradiologist and sales representative as a team during sales visits provides added value to the referring clinicians and consequently increases imaging center referral volumes. The data suggest that a sales team approach for developing a relationship with referring providers garners a statistically significant increase in referral scan volumes over traditional strategies that use a sales representative alone, even when the neuroradiologist has previously established a relationship with the provider. The sales team approach may justify the opportunity cost in lost clinical revenue value units incurred by the neuroradiologist on sales visits because the decrease in clinical productivity may be outweighed by the marked increase in referral volumes engendered during the sales visits. The use of the neuroradiologist during sales visits also improves the effectiveness of a sales representative working alone because the representative's credibility and value as a team member is enhanced by joint office visits.

Further study is needed to more precisely determine the optimal frequency and duration of sales visits and to determine the long-term effect of neuroradiologist involvement in sales. In addition, further study is warranted to determine the long-term outcomes for the sales representative working alone because the agent may ultimately be seen as an extension or valuable substitute for the neuroradiologist after repeated joint visits. This may increase the representative's value and allow for more substantive interactions with referring clinicians' offices without the need for frequent involvement in marketing and sales by the neuroradiologist.

CONCLUSIONS

The dramatic impact on imaging referral volumes during the time of neuroradiologist involvement in marketing and sales supports the hypothesis that neuroradiologists are an important element in establishing and maintaining a relationship with the referring clinician's office. The change in imaging volumes also supports the hypothesis that a neuroradiologist's direct interaction with the referring clinician through personal visits re-establishes a bond through which a meaningful referral source may develop. By combining the marketing and sales ability of the radiology sales representative with the medical expertise and leadership of the neuroradiologist, the outpatient center may be able to achieve improved market share.

REFERENCES

1. Lee DW, Levy F. **The sharp slowdown in growth of medical imaging: an early analysis suggests combination of policies was the cause.** *Health Aff (Millwood)* 2012;31:1876–84
2. Proval C. **2012's Top 20 imaging-center chains: third annual report.** *Radiology Business Journal.* September 4, 2012. http://www.radiologybusiness.com/topics/business/2012%E2%80%99s-top-20-imaging-center-chains-third-annual-report. Accessed March 8, 2014
3. Anderson B, Silverman G, Loewenstein G, et al. **Factors associated with physicians' reliance on pharmaceutical sales representatives.** *Acad Med* 2009;84:994–1002
4. Kinchen KS, Cooper LA, Levine D, et al. **Referral of patients to specialists: factors affecting choice of specialist by primary care physician.** *Ann Fam Med* 2004;2:245–52

Critical Findings: Timing of Notification in Neuroradiology

S.E. Honig, E.L. Honig, L.B. Babiarz, J.S. Lewin, B. Berlanstein, and D.M. Yousem

ABSTRACT

BACKGROUND AND PURPOSE: Timely reporting of critical findings in radiology has been identified by The Joint Commission as one of the National Patient Safety Goals. Our aim was to determine the magnitude of delays between identifying a neuroradiologic critical finding and verbally notifying the caregiver in an effort to improve clinical outcomes.

MATERIALS AND METHODS: We surveyed the time of critical finding discovery, attempted notification, and direct communication between neuroradiologists and caregivers for weekday, evening, overnight, and weekend shifts during an 8-week period. The data were collected by trained observers and/or trainees and included 13 neuroradiology attendings plus fellows and residents. Critical findings were based on a previously approved 17-item list. Summary and comparative t test statistics were calculated, and sources of delays were identified.

RESULTS: Ninety-one critical findings were recorded. The mean time from study acquisition to critical finding discovery was 62.2 minutes, from critical finding discovery to call made 3.7 minutes, and from call made to direct communication, 5.2 minutes. The overall time from critical finding discovery to caregiver notification was within 10 minutes in 72.5% (66/91) and 15 minutes in 93.4% (85/91) of cases. There were no significant differences across shifts except for daytime versus overnight and weekend shifts, when means were 2.4, 5.6, and 8.7 minutes, respectively ($P < .01$). If >1 physician was called, the mean notification time increased from 3.5 to 10.1 minutes ($P < .01$). Sources of delays included inaccurate contact information, physician unavailability (shift change/office closed), patient transfer to a different service, or lack of responsiveness from caregivers.

CONCLUSIONS: Direct communication with the responsible referring physician occurred consistently within 10–15 minutes after observation of a critical finding. These delays are less than the average interval from study acquisition to critical finding discovery (mean, 62.2 minutes).

ABBREVIATIONS: CF = critical finding; ED = emergency department; TJC = The Joint Commission

The eradication of preventable medical errors is of paramount importance in the field of health care. In July 2011, The Joint Commission (TJC) released a National Patient Safety Goal that mandated that healthcare providers "report critical results of tests and diagnostic procedures on a timely basis."[1] There have subsequently been protocols created to reach this goal, including those for the following: 1) defining a critical finding (CF), 2) communicating the critical finding to the physician, and 3) indicating what makes a report "timely."[2-6]

TJC has never defined a CF, stating only "each organization can define for itself the circumstances under which a test result is considered 'critical.'"[1] The American College of Radiology identifies findings that require nonroutine communication as those "that suggest a need for immediate or urgent intervention."[2] Likewise, TJC has never defined what "timely" means. Once again it has suggested that institutions define for themselves what is timely for a given laboratory or imaging finding. However TJC demands that institutions monitor compliance with the communication of CFs (Appendix).

At our institution, we have created, in neuroradiology, a list of critical findings that neuroradiology, neurosurgery, neurology, and otorhinolaryngology departments have agreed is acceptable to all services. It has been reviewed at 5-year intervals. As to CF notification times, the only mandate has come from our Brain Attack team for being a Stroke Center of Excellence, which requires 20 minute Team turnaround times for

reports after scans. There have been no guidelines set for other CFs.

Recent studies involving the determination and communication of critical findings in neuroradiology have analyzed such compliance with the National Patient Safety Goals of the TJC by conducting surveys of academic radiology departments for the presence of a critical finding list and the method of disseminating and implementing the information.[3,7] Another publication studied the existing list of critical findings in neuroradiology and revised that list to include frequent findings that were not previously identified in an effort to be more inclusive of lesions that warrant immediate communication.[4] Others have suggested that careful review of performance on an ongoing basis with regard to communication of radiologic critical findings can result in significant improvement in adherence to institutional guidelines.[5]

Because TJC has been ambiguous about what constitutes appropriate timing for communicating CFs in radiology and no one has established baseline data with which to assess interval improvements, we sought to address this knowledge gap. The purpose of this study was to assess the extent of delays occurring between identification of a critical finding and communication to the referring physician. We focused only on this communication process (rather than delays from study ordered to study completion) to address TJC concerns about physician-physician communication delays. A broad interpretation of the mandate of TJC might suggest that radiologists must record when they see a CF, when they attempt to notify a caregiver, and when they actually communicate with the caregiver about that CF, as part of the monitoring function for critical results. For that reason, we investigated each of these intervals to assess their magnitude. We hypothesized that the time between the discovery of a critical finding and the attempt to contact the referring physician would be short and consistent across all timeframes of daily practice. However, the time between attempted notification of the referring physician and communication with the clinician would vary widely depending on the time of day the CF was discovered, the service being notified, and weekday or weekend shift. We also sought to determine the nature of such communication delays. This is the first step in improving patient care. By identifying sources of delays, addressing the sources of these delays, remediating them, and then reassessing notification times after corrections are made, we believe that patient care can be enhanced. Patients with critical health care needs can be treated earlier; hopefully, this change will positively impact outcomes.

MATERIALS AND METHODS
This study of critical findings notification timing was reviewed and approved by our institutional review board. Due to the quality assurance nature of the study, informed consent by patients and providers was not required and the study was Health Insurance Portability and Accountability–compliant.

The time of completion of the critical finding discovery, the time of attempted notification of the referring physician, and the time of direct communication between the radiologist and referring physician were recorded for 4 different time periods ("shifts") in the division of neuroradiology between June 15 and August 16, 2013. The time periods were defined as the following:

weekday (8 AM to 4 PM); weekday evening (4 PM to 11 PM), weekday overnight (11 PM to 8 AM), and weekend (8 AM to 4 PM). One of 2 trained volunteer observers independently recorded these times sitting in the radiology reading room for all critical findings during the weekday, weekday evening, and weekend periods for 20 days of the 8 weeks. These 20 days were randomly selected on the basis of the availability of the volunteers who were participating in research activities elsewhere in the institution on the other days. The volunteer observers were trained to record the times by using the stop watch function of their cell phones on 2 separate days, with verification that the methodology was accurate by the senior author (D.M.Y.). Because of the off-hours and the infrequent occurrences of neuroradiology CFs, instead of these volunteers, the neuroradiology on-call fellow and/or resident recorded the times in the same exact manner during the weekday (11 PM to 8 AM) and weekend overnight shifts (4 PM to 8 AM) for 4 weeks of nights. The same methodology was used. The trained observers sat in the central neuroradiology reading area, and as a reader identified a CF, that reader notified the observer and the trained observer recorded the time the CF was identified, the time a call was made to contact a referrer, and the time the referring physician responded and was told the finding. The same process was used for on-call trainees for overnight shifts, who recorded the same data points and provided the data to the trained observer the next day in the morning. The participants all were aware that the data were being collected to assess delays in notification times.

Although the first attempted call was to the responsible licensed caregiver "of record" who ordered the imaging test, we, as a policy, allow "substituted" caregivers of record, which include physicians, nurse practitioners, and physician assistants associated with the caregiver of record in our institution for a "completed" communication. All of these health care providers can write orders to address critical findings in our institution (thus secretaries or floor nurses or clerks are not legitimate substitutions for CF notifications). This directive was used for this project. Trainees are instructed at our institution to make CF calls on their own, before a faculty attending has finalized the reading, unless the trainee is unsure of the finding, at which time the trainee reviews the case with the attending beforehand. Only radiologists (trainees and attendings) made calls to clinicians. There were no surrogates. The study included all patients evaluated in our institution, including inpatients, emergency department (ED) patients, research patients, and outpatients who had CFs. All data were anonymized with respect to trainees and patients.

To put these times in perspective, the radiology information system was queried for all CF cases identified to determine the time the study was ordered and the time the study was completed. These data were not the focus of the study (which evaluated the notification cycle) but were used to provide background for the magnitude of time intervals.

An approved list of these critical findings is found in Table 1.[4]

The mean, median, and mode for the following time intervals were calculated for each of the 4 shifts: 1) elapsed time between the completion of the radiologic study and identification of a critical finding, 2) elapsed time between identification of a critical finding and attempted notification of referring physician, 3) elapsed time between attempted notification and direct communication with

the referring physician, and 4) the total elapsed communication time from critical finding discovery to direct communication with the referring physician.

Table 1: Approved list of neuroradiologic critical findings[4]

Findings
1) New hemorrhage (epidural, subdural, intraparenchymal, subarachnoid, intraventricular, intramedullary)
2) New stroke
3) New mass, markedly enlarging mass
4) New herniation
5) Increased intracranial pressure, brain edema
6) New or worsening hydrocephalus
7) Misplaced surgical drainage catheter
8) Misplaced surgical hardware
9) Findings suggestive of meningitis or abscess
10) Incompletely clipped aneurysm
11) Clipped normal vessel
12) Findings suggestive of child abuse
13) New or enlarging aneurysm or AVM
14) Cord compression
15) New or enlarging cord mass
16) Suspected cord infarction
17) Spinal ligamentous injury in a trauma patient
18) Findings of spinal instability in a trauma patient
19) Congenital variations that may alter a surgical approach
20) New aneurysm, AVM, or vascular malformation

Reprinted from the Journal of the American College of Radiology, Volume 10/Issue 1, Stacey A. Trotter, Lukasz S. Babiarz, Valentina G. Viertel, Paul Nagy, Jonathan S. Lewin, David M. Yousem, Determination and Communication of Critical Findings in Neuroradiology, pages 45–50, 2013, with permission from Elsevier.

Paired t tests were performed between each of the 4 work shifts, looking at the time intervals of the following: 1) the time the study was completed to the time of notification of the referring physician; 2) the time the study was completed to the time the CF was identified by the neuroradiologist; 3) the time the CF was identified to the time of an attempt to reach the referring physician; 4) the time between an attempt to reach the referring physician; and 5) the actual time of communication between the radiologist and referring physician, and the time the CF was identified to the time the referring physician was notified. Paired t tests were also evaluated in the same manner for the services that had ≥9 CFs (Internal Medicine, Emergency Department, Neurosurgery, and Intensive Care Unit).

RESULTS

There were 6566 neuroradiologic studies performed between June 15 and August 16, 2013. Ninety-one neuroradiology critical findings were recorded during the 8-week period (Table 2). Thirty-seven critical findings were recorded during the weekday shifts, 24 critical findings were recorded during the weekday evening (4–11 PM) shifts, 24 critical findings were identified during the overnight shifts (11 PM to 8 AM), and 6 were recorded during the weekend shifts. Thirty-one of the 91 critical findings resulted from emergency department cases, 18 resulted from neurosurgery cases, 10 resulted from internal medicine cases, 9 resulted from neurology cases, and 9, from intensive care unit cases. These data are listed in Table 3. Seventy-two and one-half percent (66/

Table 2: Total time from CF discovery to referring physician notified by shift

Shift	Total No. of CFs	Time from CF Discovery to Call Made to Physician (Notification Time) (min)	Time from CF Discovery to Referring Physician Notified (Total Communication Time) (min)	Time from Study Completed to CF Identified (min)
8 AM to 4 PM (weekday)	37			
Mean/SD		2.4/2.8	7.4/3.9	94.7/87.4
Mode		0	10	81
Median		1	7	72
4 PM to 11 PM (night)	24			
Mean/SD		2.5/2.9	7.8/6.9	49.8/45.7
Mode		0	5	11
Median		2	5	44
11 PM to 8 AM (overnight)	24			
Mean/SD		5.6/3.6	10.1/7.6	31.6/37.8
Mode		3	15	9
Median		5	9	18
8 AM to 4 PM (weekend)	6			
Mean/SD		8.7/9.0	16.8/13.1	33.5/23.9
Mode		3	None	None
Median		4.5	11.5	22
All shifts	91			
Mean/SD		3.7/4.1	8.8/6.9	62.2/69.0
Mode		0	5	16
Median		3	8	43

Table 3: Elapsed times for top 5 services

Service	Total No. of CFs	Mean Response Time (min)	Range (min)	SD	Mode (min)	Median (min)	Mean Notific. Time (min)	SD	Mean Total Comm. Time (min)	SD
Emergency	31	3.4	21	4.3	1	2	5.3	7.9	8.7	8.5
Neurosurgery	18	6.5	33	7.7	5	5	2.7	3.3	9.2	8.1
Medicine	10	5.6	13	4.7	1	4.5	2.8	3.7	8.4	4.9
Neurology	9	7.2	23	7.8	2	5	3	2.1	10.2	8.7
Intensive care	9	2.8	7	2.4	2	3	4.7	3.3	7.4	4.3

Note:—Notific indicates Notification; Comm., communication.

Distribution of Total Communication Time
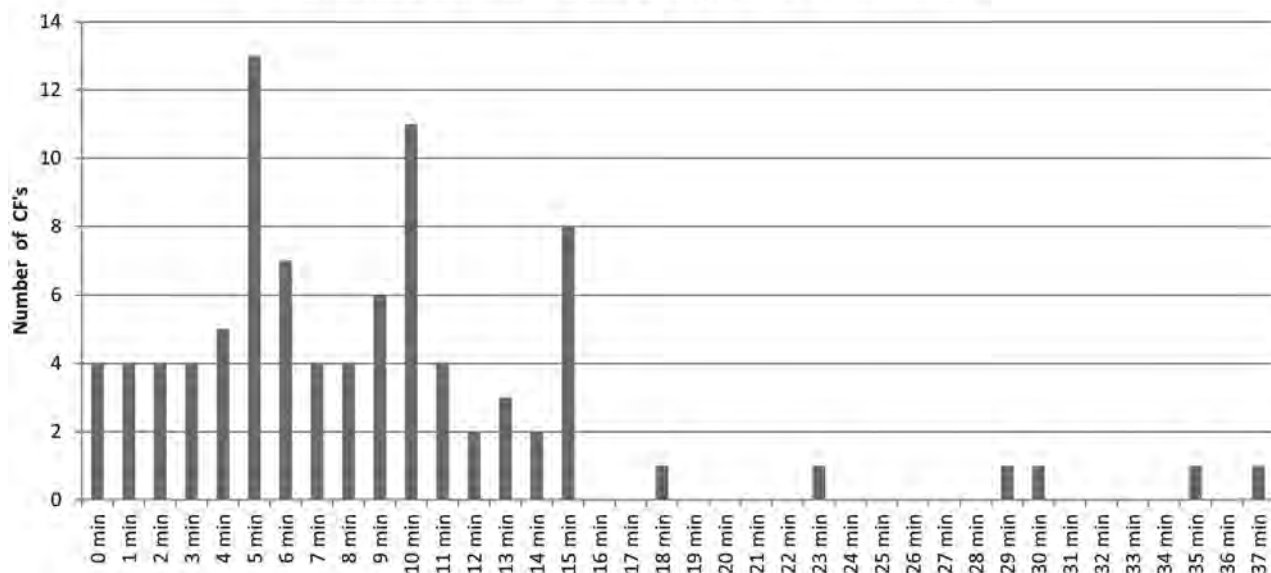
FIG 1. Distribution of total notification times of all CFs.

91) of the critical findings were directly communicated by the radiologist to 1 health care professional, 20.9% (19/91) required calls to 2 health care professionals, and 3.3% (3/91) required calls to 3 health care professionals. Data were incomplete in 3 cases. The missing data were the times from CF discovered to the call made in all 3 cases.

Although the denominator of the total number of cases read during the various shifts on the 20 data-collection days was not recorded, the mean percentage of cases read by neuroradiologists that were deemed critical was 9.0% (7591/84,348) for the calendar year 2013. Assuming this was consistent during the data-collection period, it would suggest that 1011 studies were reviewed during the study period.

The mean time from the completion of the neuroradiologic study by the technologist to the CF discovery by the radiologist was 62.2 ± 69 minutes (median, 43 minutes; mode, 16 minutes) (Table 2). The time from CF discovery to attempted call ("attempted notification time") was a mean of 3.7 ± 4.1 minutes (Table 2). The mean time from call/page made to actual communication with the requesting physician ("response time") was 5.2 minutes. This meant that the mean time from CF discovery to referring physician notification ("Total Communication Time") was 8.8 ± 6.9 minutes with 72.5% (66/91) of these CFs communicated within 10 minutes and 93.4% (85/91) communicated within 15 minutes from the time of discovery (Table 2 and Fig 1).

There was little difference in the time between the discovery of a critical finding and the attempt to contact the referring physician ("attempted notification time") between the day and evening shifts (2.4 versus 2.5 minutes), with a slight delay (5.6 minutes) noted during the overnight period and an even greater delay on the weekend (8.7 minutes). The time between attempted notification of the referring physician and communication with the referring physician ("response time") was similar for the weekday (5.0 minutes), evening (5.3 minutes), and overnight shifts (4.5 minutes) but slightly delayed during the weekend shifts (8.2 min-

utes). The total communication time was similar for the weekday shift (7.4 minutes) and evening shift (7.8 minutes; $P =$ not significant) but was moderately delayed during the overnight shift (10.1 minute; $P =$ not significant) and was most delayed during the weekend (16.8 minutes; $P = .0006$ for weekday-versus-weekend shifts). The statistical tests of the intervals between CF observed and referring physician called did not detect any differences across shifts except for daytime versus overnight and weekend shifts in which the means were 2.4, 5.6, and 8.7 minutes, respectively ($P <$ .01 for difference between daytime and overnight and daytime and weekend). Similarly, we did not detect any differences between the work shifts for physician call-back times from referring physician called to referring physician directly informed. However, if >1 physician had to be called, the mean time from referring physician called to referring physician notified increased from 3.5 minutes to 10.1 ($P < .01$).

The attempted notification time ranged from 0 to 6 minutes and was similar for all clinical services. Of the top 5 services in terms of CFs notified (emergency department, internal medicine, neurosurgery, intensive care unit, and neurology), the greatest variability in mean response time was between the intensive care unit and neurology, but the difference was between 2.8 and 7.2 minutes, just 4.4 minutes. With respect to the services that had the most CFs reported, the only time interval that was statistically significant for notifications was a shorter time of referring physician paged to referring physician called back for the ED service (3.4 minutes) versus the neurology service (7.2 minutes) (Table 3).

In 13 cases, the radiologists recorded the reasons for delays in communication, which included the following: 1) inaccurate contact information for the ordering physician in the information system (5.5%, 5/91), 2) the physician being unavailable (change of shift or outpatient office closed) (4.4%, 4/91), 3) the physician did not respond in a timely fashion (3.3%, 3/91), and 4) the patient

was transferred to the neonatal intensive care unit (so previous floor contact information was incorrect) (1.1%, 1/91).

When multiple paired t tests were applied to the mean times between study ordered versus referring physician notified, there were statistically significantly differences between the day shift (8 AM to 4 PM) and each of the other shifts, with the exception of the weekend shift, the latter likely because of the small number of CFs reported during the weekend shift, causing loss of statistical power ($n = 7$). These findings were also true for day shift versus other shifts for the time interval from study completed to CF observed. The mean value of the day shift for study completed to physician notified/CF observed (102.1 minutes; SD = 87.6/94.7 minutes; SD = 87.4) varied from the means of the evening (57.6 minutes; SD = 45.9/49.8 minutes; SD = 45.7), overnight (41.5 minutes; SD = 37.7/31.6 minutes; SD = 37.8), and weekend (50.3 minutes; SD = 34.1/33.5 minutes; SD = 23.9) by the widest margins of all intervals.

The mean and median time intervals from physician placing the order to the study begun were 2 hours 50 minutes (range = 1 minute to 17 hours 49 minutes ± 6 hours 53 minutes) and 44 minutes (median) for CT (eliminating 1 case with a delay of 7 days scheduled as an outpatient), respectively, and 13 hours 59 minutes (range = 20 minutes to 19 hours 6 minutes ± 21 hours 49 minutes) and 7 hours 24 minutes (median) for MR imaging (eliminating 2 cases with delays of 7 and 8 days scheduled as outpatients), respectively. For the combined CT and MR imaging studies, the mean and median values were 6 hours 43 minutes (range = 1 minute to 19 hours 51 minutes ± 14 hours 54 minutes) and 1 hour 10 minutes.

The time interval for study completion averaged 4 ± 6 minutes for CT and 47 ± 24 minutes for MR imaging, with an average for both modalities of 21 ± 33 minutes (median, 7 minutes). The delays from study ordered to preliminary report generated for CT were a mean of 2 hours 54 minutes ± 6 hours 53 minutes with a median of 45 minutes. For MR imaging, the same intervals showed a mean of 14 hours 46 minutes ± 21 hours 43 minutes from order to completion and a median value of 8 hours 51 minutes. If one combined MR imaging and CT, the mean was 7 hours 3 minutes ± 14 hours 58 minutes and the median was 1 hour 41 minutes.

DISCUSSION

The Joint Commission encourages timely recording and communication of a critical finding to facilitate accurate diagnosis and appropriate treatment of urgent medical conditions, which in turn improves patient care and reduces unfavorable outcomes. Delays in the communication of critical findings could lead to greater morbidity or even death of patients with serious illnesses. TJC requires that radiologists take measures to ensure that critical findings are communicated expeditiously and accurately.[8] However they are not proscriptive about what constitutes a critical finding or what timeframe is considered "expeditious." Expeditious may vary from one setting to another. In the treatment of acute cerebrovascular accidents, benefits may accrue with interventions that may be minutes earlier in their onset. Similarly, early communication of critical findings has been shown to result in improved clinical outcomes in areas such as the treatment of

acute pulmonary embolism.[9] The Brigham and Women's Radiology Department has created the red, orange, and yellow alert system, by which caregivers are supposed to be notified for critical findings in <60 minutes, <3 hours, or <15 days, respectively.[5] They include tension pneumothorax, ischemic bowel, and intracerebral hemorrhage as red alerts, intra-abdominal abscess and impending pathologic hip fracture as orange alerts, and lung nodules and solid renal masses as yellow alerts. Face-to-face or telephone communication, as described herein, is required for red and orange alert items.[5]

Although there is universal agreement among health care providers that rapid and accurate communication of critical radiologic findings is imperative, there are few data in neuroradiology to prove that these practices are being fully implemented and that critical findings are being notified in a timely manner.

Our data reveal that the mean time from CF discovery to physician notification was 8.8 minutes with 72.5% (66/91) of these findings communicated within 10 minutes and 93% (85/91) communicated within 15 minutes. The most common notification time (ie, the mode) was 5 minutes. These data suggest that notifications are being done within a short timeframe at our institution to ensure urgent medical attention and promote positive patient outcomes. The mean time elapsed between when the study was completed and the CF was discovered (62.2 minutes) dwarfs any part of the total notification time components. Furthermore, we found that the time interval for all CFs from study ordered to study completed constituted a mean of 7 hours 3 minutes and median of 1 hour 41 minutes. Compared to the values above, the mean time from CF discovery to physician notification of 8.8 minutes is a relatively insignificant portion of time in the overall process of obtaining and reporting the CF results of a neuroradiology imaging study.

The notifications we describe include those patients evaluated as ED patients and inpatients but also those who are outpatients for whom ready access to physicians of record may be less forthcoming, especially if cases are read after hours.

The presence of outlier notification times of >10 minutes (especially those notification times at 23, 29, 30, 35, and 37 minutes) also implies that certain modifications could be made to reduce the variability in our notification protocol for patient care. The causes of delays in communication that were identified included inaccurate contact information for the ordering physician, physician unavailable (change of shift or outpatient office closed, physician did not respond in a timely fashion, or patient transferred to another floor so that previous floor contact information was incorrect). In 1 instance, the PACS system crashed, and the delay on reboot created the delay. When only the ordering physician's name appears in our radiology information system and/or PACS, not the covering physician, our service is predisposed to errors related to "change of shift" ordering doctor versus covering doctor miscommunication.

Although it was not the focus of this article, which investigated the delays between identification of the CF and speaking to a responsible caregiver, the data regarding the interval between study completed to CF discovered had some peculiarities. Daytime cases had a longer mean delay between study completed and CF discovered (94.7 minutes) compared with evenings (49.8 min-

utes), nights (31.6 minutes), and weekends (33.5 minutes). The reason is not clear from the data. Various factors, including the volume of cases versus the physician staffing full time equivalents (one would expect that with fewer physicians in-house over the weekend and night shifts that the delays would be longer during these shifts), inpatient and outpatient ratios in the various shifts, the ratio of ED cases to inpatient to outpatient studies among the various shifts, and the number of on-call medical personnel, could influence these values. Overnight shifts and weekend shifts have far fewer magnets ($n = 1–2$) operating to manage the work lists, as opposed to the full complement of clinical magnets operating during the day shifts (10 magnets for all MR imaging clinical services). We have noted that the backup of cases in the work queue is less troublesome on the "off-shifts" than on the day shifts at our institution.

Our data compare favorably with systems reported elsewhere. Using internally developed software (later sold as a PACS plug-in called RadStream; Amicas/Merge Healthcare; http://www.beverlyhospital.org/media/483167/amicasradstream.pdf) radiologists at the Cincinnati Children's Medical Center were able to achieve an average critical result reporting time of 10.8 minutes with 53% communicated in <10 minutes and approximately 75% communicated within 20 minutes.[6] Using a commercially available system (PowerScribe 360/Critical Results; Nuance Health Care/Communications; http://www.nuance.com/products/powerscribe-360-critical-results/index.htm), the Virginia Commonwealth University Health System radiology department was able to achieve an average turnaround time of 18 minutes to communicate a critical finding.[10] PowerScribe 360/Critical Results software is currently in use in >300 hospitals nationally, and another system from Amcom software called Critical Test Results Management (CTRM) for Radiology is also available (Amcomsoftware.com/CTRM-Radiology).[11] Our results, without using purchased software programs, are in the same range as the results provided in these reports using software solutions, albeit performed by our radiologists using their own manual effort.

The medicolegal ramifications of improved communication of critical findings between radiologists and referring physicians are obvious. Malpractice cases are often filed because of poor communication between radiologists and clinicians.[12,13] Improved communication (as measured by decreased communication delay times) may lead to fewer malpractice cases brought against radiologists or medical institutions. However, the absence of communication (rather than the speed of communication) often is the more hazardous misstep in medicolegal cases.

Prior publications on critical findings have focused on determination and standardization of critical findings in neuroradiology. Some studies analyzed neuroradiologists' compliance with the National Patient Safety Goals of The Joint Commission by conducting surveys asking whether each radiology department had a critical finding list.[7] As part of a practice quality-improvement initiative, another study analyzed the existing lists of critical findings and revised these lists to include frequent findings that were not already included—all in an effort to increase efficiency.[4]

In our neuroradiology division, we do not treat every study in the same way because stat cases and emergency department cases (eg, brain attack cases) are moved to the top of the work list.

Additionally, our technologists do notify our service when they see a significant finding on a study or if they have a stat case on the technique. This practice could influence the time from acquisition to observation of a CF, the single longest time interval. However, this would not influence the communication times from time observed, to the time the call was attempted, or to the time the communication was completed, which was the emphasis of this article. What starts the clock on the communication issue is the observation of a critical finding. In other words, there is no pretest probability/suspicion of a CF mentioned. Our emphasis in this article was gaps in notification times from time observed to time communicated.

The Joint Commission mandate does not specify which times must be recorded when documenting communication of a critical finding in a patient's imaging report. However, in our institution, more detail is being sought to make sure we can meet any TJC inspections. Thus, it was proposed that radiologists should record all 3 time points (CF seen, call made, caregiver spoken to). This study has shown that in our practice, there is limited value in consistently documenting the time between initial discovery to attempted notification (mean, 3.7 minutes) and the time from attempted call to communication with the referring physician (mean, 5.2 minutes) because the overall time intervals for these steps (mean, 8.8 minutes) are so small compared with the times between completion of the studies and initially looking at the studies (62.2 minutes) and from physician ordering the study and study completion (mean 7 hours 3 minutes). Reporting the time of referring physician notification alone would seem to be sufficient because from the information system, one can readily provide the times from study completion to notification; the time of notification starts the clock for any delays in treating the critical finding by the clinical service. The delays in subsequent treatment have been shown to dwarf the communication delays provided herein as well.[14] Radiologists may, in limited instances in which there is a response time delay that may impact patient care, document the delay, but this should not be perceived as a means of relieving the radiologists of a responsibility for the prompt care of the patient. Calling the patient directly is an option that the American College of Radiology guidelines mention as one possibility.[2] The value in noting the time of discovery and time of contact may be to investigate any systemic sources of the breakdown of communication. Efficient communication of CFs may avert a potentially poor outcome and have a positive effect on the health of our patients.

Current protocols for notifying physicians in our neuroradiology division have led to prompt notification of neuroradiologic critical findings. The outliers for notification largely revolve around shift changes that may be mitigated by universal sign out protocols or electronic solutions in which paged physicians no longer on call provide automated feedback to other physicians informing the callers that they are off service. The hospital information system ideally should provide covering-physician contact information for all patients at all times. In addition, the use of cell phones may be a more efficient mode of communication than contact via calling a medical floor or pagers. Problems with calling a floor include residents changing shifts and services and the limited hours of duty of present-day interns and residents.

How do our results compare with another subspecialty service that frequently must notify caregivers about critical findings? In 2008, Valenstein et al[14] assessed the CF notification times of 3545 specimens across 121 institutions in the College of American Pathologists Q-Probes program. The authors found that the median time from identifying the critical finding to communication of that finding was 4–5 minutes, whereas the median time from specimen collection to notification was 56–57 minutes.[14] These numbers are remarkably similar to our median values of 8 minutes and 43 minutes, respectively. Valenstein et al did not record the times from lab test ordered to lab test completed. They did note that the median notification times for rural/suburban facilities (median 3 minutes) was shorter than that for a city location (median, 7 minutes—our facility is in a city environment) and was shorter in smaller hospitals (ours is a 930-bed hospital). The authors stated, "Given the amount of time that typically elapsed between specimen collection and notification, in even the speediest facilities, it is doubtful that…institution variation in calling speed makes much clinical difference."[14] They noted that the time it takes for caregivers to act on critical laboratory values ranged from 2 to 5 hours, making 5-minute notification times a very tiny proportion of the patient care process.[14]

Although this study presents much useful data regarding the reporting of CFs, it has some obvious limitations. We recognize that this was a random sample of cases, and in some instances, each shift or service did not have large numbers of CFs. There may be a bias because physicians were aware that this was an ongoing study; therefore, they may have been more compliant and more compulsive about pursuing the communication, knowing that data were being recorded. This could have caused artificially shortened notification times. Because there was a preponderance of inpatient/ED cases, there could be additional bias in that these services are generally more easily located and the physicians are more easily notified because of "on-call" services. Three cases had incomplete data. Outpatient studies, particularly after hours and on weekends from private physician offices, usually incur greater delays because weekend/nighttime office hours are limited. Finally, because we have some services that respond to a single phone number (ie, the neurosurgical resident on call or the emergency department main number), there may be some inherent favorable bias to the system at our institution.

This was a pilot study designed to detect general trends in the sources of communication delays. We acknowledge that using ANOVA with a Bonferroni correction rather than paired *t* tests would have been a more rigorous approach. At this stage, we wanted to cast a wider net, and we were willing to accept a higher cumulative false-positive rate for all of our analyses taken together. In follow-up studies, however, we plan to focus on a smaller number of the most promising factors to explore the observed relationships further and to verify our preliminary results.

CONCLUSIONS

Given the results of this study with 93.4% (85/91) of notification times in <15 minutes, there may be more merit focusing on reducing the time from study completed to study interpreted (mean in this study of 62.2 minutes) and study ordered to study completed (mean, 7 hours 3 minutes) to advance patient safety and health care quality. We agree with the conclusion of Valenstein et al[14] in their article on the pathology CFs: The notification interval "represents one of the least important vulnerabilities in the process that leads to timely correction of a critical…result." However, any effort to provide caregivers more accurate and more timely data with which to diagnose and treat their patients is a worthy endeavor. This may lead to improved outcomes, and we encourage such quality improvement projects to optimize the provision of care of radiology departments.

APPENDIX

The Joint Commission's Patient Safety Goal 02.03.01

NPSG.02.03.01: Report critical results of tests and diagnostic procedures on a timely basis. Get important test results to the right staff person on time.

Rationale for NPSG.02.03.01

Critical results of tests and diagnostic procedures fall significantly outside the normal range and may indicate a life-threatening situation. The objective is to provide the responsible licensed caregiver these results within an established timeframe so that the patient can be promptly treated.

Elements of Performance for NPSG.02.03.01

1) Develop written procedures for managing the critical results of tests and diagnostic procedures that address the following:

A) The definition of critical results of tests and diagnostic procedures
B) By whom and to whom critical results of tests and diagnostic procedures are reported
C) The acceptable length of time between the availability and reporting of critical results of tests and diagnostic procedures

2) Implement the procedures for managing the critical results of tests and diagnostic procedures.

3) Evaluate the timeliness of reporting the critical results of tests and diagnostic procedures.

REFERENCES

1. The Joint Commission. **National Patient Safety Goals.** http://www.jointcommission.org/standards_information/npsgs.aspx. Accessed July 10, 2013
2. American College of Radiology. **ACR practice guidelines for communication of diagnostic imaging findings 2013.** http://www.acr.org/~/media/ACR/Documents/PGTS/guidelines/Comm_Diag_Imaging.pdf. Accessed August 15, 2013
3. Viertel VG, Trotter SA, Babiarz LS, et al. **Reporting of critical findings in neuroradiology.** *AJR Am J Roentgenol* 2013;200:1132–37
4. Trotter SA, Babiarz LS, Viertel VG, et al. **Determination and communication of critical findings in neuroradiology.** *J Am Coll Radiol* 2013;10:45–50
5. Anthony SG, Prevedello LM, Damiano MM, et al. **Impact of a 4-year quality improvement initiative to improve communication of critical imaging test results.** *Radiology* 2011;259:802–07

6. Ridley EL. **Critical results notification system speeds timely results.** AuntMinnie.com. http://www.auntminnie.com/index.aspx?sec=ser&sub=def&pag=dis&ItemID=104083. Accessed July 31, 2013

7. Babiarz LS, Trotter S, Viertel VG, et al. **Neuroradiology critical findings lists: survey of neuroradiology training programs.** *AJNR Am J Neuroradiol* 2013;34:735–39

8. Yee, KM. **Critical test results: make every effort to communicate.** AuntMinnie.com. http://www.auntminnie.com/index.aspx?sec=ser&sub=def&pag=dis&ItemID=99363. Accessed July 31, 2013

9. Kumamaru KK, Hunsker AR, Kumamaru H, et al. **Correlation between early direct communication of positive CT pulmonary angiography findings and improved clinical outcomes.** *Chest* 2013;144:1546–54

10. VCU Medical Center. **Virginia Commonwealth University Health System significantly reduces CTR notification turnaround time.** http://www.nuance.com/ucmprod/groups/healthcare/@web-enus/documents/collateral/nd_003048.pdf. Accessed August 2, 2013

11. Amcom Software. **Improve communication of radiology test results.** http://www.amcomsoftware.com/solutions/clinical_alerting_and_notification/critical_test_results/. Accessed August 2, 2013

12. Whang JS, Baker SR, Patel R, et al. **The causes of medical malpractice suits against radiologists in the United States.** *Radiology* 2013;266:548–54

13. Gale BD, Bissett-Siegel DP, Davidson SJ, et al. **Failure to notify reportable test results: significance in medical malpractice.** *J Am Coll Radiol* 2011;8:776–79

14. Valenstein PN, Wagar EA, Stankovic AK, et al. **Notification of critical results: a College of American Pathologists Q-Probes study of 121 institutions.** *Arch Pathol Lab Med* 2008;132:1862–67

Accountable Care Organizations: What Radiologists Should Know

R.A. Charalel and P.C. Sanelli

ABBREVIATION: ACO = Accountable Care Organization

The landscape of health care is quickly changing, with new legislation and economic factors driving health care reform. Yet, fundamentally many health care delivery professionals, including physicians, remain unaware of the changing landscape and its implications for their practice. We seek to review Accountable Care Organizations (ACOs), a legal entity developed in November 2011, and their implications for radiologists.

WHY WERE ACCOUNTABLE CARE ORGANIZATIONS CREATED?

ACOs were created in an amendment to the Patient Protection and Affordable Care Act to foster shared savings between Medicare and health care providers. By eliminating unnecessary procedures and tests, ACOs strive to reduce overall health care expenditures, improve health care outcomes, and redistribute a portion of the shared savings between the provider and Medicare.

WHAT IS AN ACO?

ACOs are groups of physicians, hospitals, and other health care workers who come together by choice to provide high-quality health care to Medicare patients. Four main subtypes of ACOs exist, including the Medicare Shared Savings Program, the Advance Payment ACO Model, the Pioneer ACO Model, and ACO: Accelerated Development Learning Sessions. The Medicare Shared Savings Program is targeted toward providers who provide fee-for-service health care to Medicare patients or beneficiaries.[1] This program is incentivized to reduce health care costs by allowing ACO participants to split shared savings, which are determined by the annual decrease in health care costs compared with an individual ACO's calculated benchmark (on the basis of prior 3-year spending) and specific contract terms. The Advance

Payment ACO Model is a supplementary incentive program for eligible providers already participating in the Medicare Shared Savings Program. The Pioneer ACO Model is intended for health care organizations and providers already experienced in coordinating care for patients across care settings. For existing or emerging ACOs, there is also an opportunity to understand population health while reducing cost growth as well as how to establish and implement care delivery through the ACO: Accelerated Development Learning Sessions. For providers who are interested in newly joining an ACO, the Medicare Shared Savings Program is currently accepting applications.[1]

WHAT ARE THE REQUIREMENTS FOR ELIGIBILITY/PARTICIPATION?

To form an ACO, a provider must be Medicare-enrolled and bill for primary care services (as defined by Medicare billing codes). ACOs must have a group of Medicare patients (who are termed beneficiaries), for which the single ACO provides all primary care. Providers may join an ACO as an ACO participant or other entity. ACO participants must have a 3-year Medicare billing history, with a Medicare-enrolled taxpayer identification number, to calculate a benchmark and properly assign beneficiaries.[1] If a provider does meet ACO participant eligibility criteria or wishes to have more flexibility, they may join an ACO as another entity. Another entity is simply a Medicare-enrolled group that bills Medicare through a Medicare-enrolled taxpayer identification number. If provider(s) do not have a 3-year history of billing for primary care services, they may join with ACO participant(s) who have an eligible history and form an ACO together. Once an ACO is formed, the contract is valid for 3 years, though there is opportunity for addition or removal of ACO participants annually.[1]

HOW CAN A RADIOLOGIST PARTICIPATE?

In addition to providing image interpretation, radiologists may contribute to cost savings programs by guiding imaging examination choices[2] on the basis of evidence-based guidelines (such as the American College of Radiology appropriateness criteria) and

local practice patterns for standard of care. Radiologists are uniquely qualified to serve in such a role, given their imaging expertise, and would add value to the ACO system by decreasing the number of unnecessary imaging examinations and helping to provide the patient with the best possible examination.

As a specialist, a radiologist may become involved as an ACO participant or as another entity. However, shared savings are calculated through the use of only contributions from ACO participants and are thus only distributed among ACO participants. Groups that join an ACO as another entity are not eligible to profit from shared savings. In addition, ACO participants who are not billing for primary care services are eligible to be a participant in more than one ACO. As a result, for radiologists who are billing for specialized services (not primary care), they may be able to team up with a number of different ACOs and benefit from shared savings in multiple groups.

WHAT ARE THE CHALLENGES?

Even in an initially ideal scenario with increased shared savings, given reduced numbers of unnecessary imaging procedures, radiologists may face potentially negative downstream effects. Initially radiologists may expect decreased demand for imaging procedures and make up some of this reduced revenue with the shared savings that this cost reduction may create. However, as spending continues to decrease and the benchmark cost (on the basis of prior 3-year spending) also decreases, the practice may cease to be able to further reduce costs and thus be ineligible for future savings after the first few successful years.

Additionally, the logistics of providing a gateway for study approval are challenging and may have a number of new implications.[2] First, there is potential to be penalized for increased numbers of performed imaging examinations as compared with a national or local average, despite the reality that the decision to perform a study is joint between radiologist and clinician, and does not rest solely with the radiologist. Second, if a radiologist is not compliant with a study, the radiologist may be implicated in any potential downstream tort cases, despite an informed decision by both clinician and patient. In such a situation, formalizing the role of image selection consultation, by use of evidence-based criteria, may actually protect radiologists, given that it will provide the opportunity to document rationale.

Another challenge to ACO health care delivery is that effective teams, consisting of health care providers from different special-ties, are essential for synchronizing and coordinating care efficiently.[3] To be successful, health care providers in an ACO will need to utilize specific skills in the areas of collaboration, communication, and teamwork to coordinate care[4] that will not only reduce cost but also improve outcomes.

WHAT ARE THE FUTURE IMPLICATIONS?

Although initially, it may seem challenging to redistribute health care delivery systems to create an ACO, there are many incentives to do so. First, there is the promise of potential shared savings by reducing unnecessary imaging examinations and procedures while still delivering high-quality health care. Second, in their current stage, ACOs are entirely voluntary groups that come together to accomplish a shared goal. At this stage, the terms of an ACO are still malleable. In the future, such groups may have rigid structures with committees and chairs, which may be difficult for radiologists to join or have a significant voice within. As a result, it is advantageous to participate in ACOs and increase our bargaining power within them while the structure is not yet predetermined. Finally, there are a number of ramifications to being left behind, aside from losing shared savings. Groups who do not participate in ACOs may be viewed as non–resource conscious and penalized in future legislation. Additionally, they may lose opportunities to grow their practice referrals or gain leadership experience in imaging examination selection and ultimately may be viewed as less desirable ACO participants in the future if forced to participate. Thus, although there is considerable angst and reluctance to join ACOs, it may be beneficial to get involved early on, so that we can actively help shape the changing landscape of health care.

REFERENCES

1. Medicare Shared Savings Program. **Frequently asked questions.** http://www.cms.gov/Medicare/Medicare-Fee-for-Service-Payment/sharedsavingsprogram/Downloads/MSSP-FAQs.pdf. Accessed June 15, 2013
2. Breslau J, Lexa FJ. **A radiologist's primer on accountable care organizations.** *J Am Coll Radiol* 2011;8:164–68
3. McClellan M, McKethan AN, Lewis JL, et al. **A natural strategy to put accountable care into practice.** *Health Affairs* 2010;29:982–90
4. Press MJ, Michelow MD, MacPhail LH. **Care coordination in accountable care organizations: moving beyond structure and incentives.** *Am J Manag Care* 2012;18:778–80

Comparison of Perfusion, Diffusion, and MR Spectroscopy between Low-Grade Enhancing Pilocytic Astrocytomas and High-Grade Astrocytomas

M. de Fatima Vasco Aragao, M. Law, D. Batista de Almeida, G. Fatterpekar, B. Delman, A.S. Bader, M. Pelaez, M. Fowkes, R. Vieira de Mello, and M. Moraes Valenca

ABSTRACT

BACKGROUND AND PURPOSE: The differentiation of pilocytic astrocytomas and high-grade astrocytomas is sometimes difficult. There are limited comparisons in the literature of the advanced MR imaging findings of pilocytic astrocytomas versus high-grade astrocytomas. The purpose of this study was to assess the MR imaging, PWI, DWI, and MR spectroscopy characteristics of pilocytic astrocytomas compared with high-grade astrocytomas.

MATERIALS AND METHODS: Sixteen patients with pilocytic astrocytomas and 22 patients with high-grade astrocytomas (8–66 years of age; mean, 36 ± 17 years) were evaluated by using a 1.5T MR imaging unit. MR imaging, PWI, DWI, and MR spectroscopy were used to determine the differences between pilocytic astrocytomas and high-grade astrocytomas. The sensitivity, specificity, and the area under the receiver operating characteristic curve of all analyzed parameters at respective cutoff values were determined.

RESULTS: The relative cerebral blood volume values were significantly lower in pilocytic astrocytomas compared with the high-grade astrocytomas (1.4 ± 0.9 versus 3.3 ± 1.4; $P = .0008$). The ADC values were significantly higher in pilocytic astrocytomas compared with high-grade astrocytomas ($1.5 \times 10^{-3} \pm 0.4$ versus $1.2 \times 10^{-3} \pm 0.3$; $P = .01$). The lipid-lactate in tumor/creatine in tumor ratios were significantly lower in pilocytic astrocytomas compared with high-grade astrocytomas (8.3 ± 11.2 versus 43.3 ± 59.2; $P = .03$). The threshold values ≥ 1.33 for relative cerebral blood volume provide sensitivity, specificity, positive predictive values, and negative predictive values of 100%, 67%, 87%, and 100%, respectively, for differentiating high-grade astrocytomas from pilocytic astrocytomas. The optimal threshold values were ≤ 1.60 for ADC, ≥ 7.06 for lipid-lactate in tumor/creatine in tumor, and ≥ 2.11 for lipid-lactate in tumor/lipid-lactate in normal contralateral tissue.

CONCLUSIONS: Lower relative cerebral blood volume and higher ADC values favor a diagnosis of pilocytic astrocytoma, while higher lipid-lactate in tumor/creatine in tumor ratios plus necrosis favor a diagnosis of high-grade astrocytomas.

ABBREVIATIONS: GBM = glioblastoma multiforme; HGA = high-grade astrocytoma; HGG = high-grade glioma; LGG = low-grade glioma; Lip-Lac = lipid-lactate; n = normal contralateral; PA = pilocytic astrocytoma; rCBV = relative cerebral blood volume; ROC = receiver operating characteristic analysis curve; tu = tumor; WHO = World Health Organization

Pilocytic astrocytoma (PA) is the most common pediatric central nervous system glioma and one of the most common pediatric cerebellar tumors. This tumor occurs most frequently in the first 2 decades of life,[1] composing up to 25% of brain tumors in pediatric neurosurgical practices,[2] and it only rarely occurs in adults.[2] The incidence is approximately 4.8 cases per million people per year,[3] with 2.3%–6% of all brain tumors classified as PAs.[3,4] PAs are usually clinically benign and are classified as grade I by the World Health Organization (WHO).[4] They are potentially curable by surgery and are associated with a longer survival.[1,5] Very rarely, a PA may undergo spontaneous malignant transformation and become an anaplastic astrocytoma.[6]

A PA typically appears on MR imaging as a large cystic mass with a mural nodule[1,5]; however, this pattern can also occur in a hemangioblastoma of the posterior fossa.[7] MR imaging features of PAs can also be seen in high-grade gliomas (HGGs) and metastases,[7] particularly when a PA appears as a solidly enhancing mass. Moreover, despite their benign biologic behavior, PAs may be confused with malignant tumors and resemble high-grade astro-

cytomas (HGAs) on both histopathology and during a neuroimaging evaluation, making the diagnosis difficult.[1,4] This confusion can occur because PAs present a variety of histologic patterns and may have markedly hyalinized and glomeruloid vessels, accompanied by extensive nuclear pleomorphism, which can sometimes make classification a challenge.[1,4]

Given that differentiation of PAs and HGAs is sometimes challenging to both the neuroradiologist and the pathologist, advanced MR imaging techniques that add functional information to the anatomic MR imaging can be helpful in the characterization and grading of astrocytomas.[8] Although both PA and HGA belong to the same family of gliomas, a great amount of evidence suggests that PAs present histologic aspects (cellularity, vascularity, cystic formation, necrosis) very distinct from those found in HGAs. Thus, the use of these advanced MR imaging techniques may better evaluate and distinguish the anatomic and functional differences occurring between PAs and HGAs. These include the following: diffusion-weighted imaging (DWI), which evaluates the microstructure and cellularity of brain tissue by analyzing the motion of the water in the tissue[9]; perfusion-weighted imaging (PWI), which evaluates the microvasculature by using relative cerebral blood volume (rCBV)[9,10]; and MR spectroscopy, which provides metabolic and histologic marker information about the brain or neoplastic tissue.[9-11]

There are only a few small series assessing the advanced MR imaging features of PAs, particularly when evaluating neovascularity on PWI[7,12] and their differentiation from HGAs.[12]

Our hypothesis is that in comparison with HGAs, PAs present lower cellularity, less vascularity, and a lower metabolism, and each one of these characteristics may be detected with the use of DWI, PWI, and MR spectroscopy, respectively. Therefore, advanced MR imaging techniques should demonstrate findings that may help in the differentiation of PAs from HGAs. The purpose of this study was to assess MR imaging, DWI, PWI, and MR spectroscopy characteristics of PAs compared with HGAs.

MATERIALS AND METHODS
Patients and Histopathologic Analysis
MR imaging studies of 38 patients with astrocytomas were reviewed (16 patients with PAs and 22 patients with HGAs). MR imaging examinations were performed from April 2002 to April 2008. Patient ages ranged from 8 to 66 years, with a mean of 36.23 ± 16.95 years. There were 23 male and 15 female patients. In this retrospective study, primarily newly diagnosed, untreated astrocytomas (36/38) were included; only 2 PA cases were studied after biopsy.

Histopathologic evaluation was performed by 2 experienced neuropathologists and was based on the WHO classification of astrocytomas[13]: grade I, PA; grade II, diffuse astrocytoma; grade III, anaplastic astrocytoma; and grade IV, glioblastoma multiforme (GBM). Only grade I (PA) and grade III–IV (HGA) astrocytomas were included in this study. Grade III and IV astrocytomas were allocated in a single group because their aggressive biologic behavior is quite often similar, but this will depend on many factors including genetic profile. All patients had histopathologic confirmation of PAs and HGAs, with specimens obtained by open excisional biopsy or resection. Our institutional review board approved the study.

Imaging Protocol
Because this was a retrospective study, a full complement of imaging was not available for each patient. Based on the histopathologic criteria for seeking the signs of morphology that express the greatest aggressiveness, we selected the PWI, DWI, and MR spectroscopy measurements that best correlated with the grading of tumors.

Magnetic Resonance Imaging. Imaging was performed with a 1.5T unit (Signa Infinity; GE Healthcare, Milwaukee, Wisconsin). The MR imaging sequences were performed by using sagittal and axial T1-weighted imaging, axial T2, axial FLAIR, and axial T2*-weighted imaging. Contrast-enhanced axial reference T1-weighted imaging was performed after the perfusion MR imaging data had been obtained. An experienced neuroradiologist reviewed the conventional MR images and evaluated each lesion on the basis of location (supratentorial or infratentorial), tumor characteristics (solid, cystic, or necrotic), and type of enhancement (none, homogeneous, heterogeneous, or ring).

Dynamic Perfusion MR Imaging. PWI was performed in 9 patients with PA and 20 with HGA. Gadopentetate dimeglumine contrast medium (Magnevist; Bayer HealthCare Pharmaceuticals, Leverkusen, Germany) was intravenously administered, with a contrast dose of 0.1 mmol/Kg of body weight, by a power injector at a rate of approximately 4 mL/s, followed by a saline bolus (10–20 mL at approximately 4 mL/s). Nine to 10 sections were selected for PWI through the tumor, by using T2-weighted images as a guide. Spin-echo PWI was performed by using the following parameters: TR/TE, flip angle, FOV, matrix, section thickness, section gap: 1900/80 ms, 90°, 24 cm, 128 × 64 pixel, 7 mm, 1.5 mm. Preload contrast was administered before the PWI acquisition to correct T1-weighted leakage effects that might underestimate rCBV measurement. Data processing was performed by using an Advantage Windows 4.2 workstation with FuncTool as the analytic program (GE Healthcare). After the construction of an rCBV color map to target the regions of maximal abnormality, measurements at 4 regions of interest were obtained, and the maximum rCBV was recorded. A standardized region of interest measuring approximately 2–4 mm^2 was used. CBV measurements were made relative to the normal-appearing contralateral white matter.

Proton MR Spectroscopic Imaging. Multivoxel 2D MR spectroscopy was performed before the administration of gadopentetate dimeglumine in 5 patients with PAs and 21 with HGAs. Using the T2 sequence as reference for voxel placement, a 2D spectroscopy field was prescribed to contain tumor and contralateral supposedly normal brain parenchyma. A multivoxel MR spectroscopy was performed with the point-resolved spectroscopy technique: TR/TE, 1500/35 ms; VOI thickness, 16.5 mm; FOV, 18 cm; coding phase, 16 × 16; NEX, 1; direction of the frequency, anteroposterior. All spectra were processed by using an Advantage Windows 4.2 workstation with FuncTool as the analytic program. The metabolite peaks were assigned at the following frequencies: choline (Cho) at 3.22 ppm, creatine (Cr) at 3.02 ppm, N-acetylaspartate (NAA) at 2.02 ppm, lipid-lactate (Lip-Lac) at 0.5–1.5 ppm, and myo-inositol (mIns) at 3.56 ppm. The peak area measurements of metabolites were used to calculate the following ratios: minimal tumor Cr to contralateral normal Cr (Cr^{tu}/Cr^{n}), maximal tumor

Table 1: The characteristics of PA and HGA on conventional MR imaging

Tumor	Solid	Solid-Cystic	Necrotic	Enhancement	Type of Enhancement		
					Heterogeneous	Homogeneous	Ringlike
PA	8/16 (50%)	7/16 (44%)	1/16 (6%)	14/15 (93%)	8/14 (57%)	5/14 (36%)	1/14 (7%)
HGA	8/22 (36%)	0/22 (0%)	14/22 (64%)	20/22 (91%)	7/20 (35%)	1/20 (5%)	12/20 (60%)

Cho to contralateral Cho (Cho^{tu}/Cho^n), minimal mIns to contralateral mIns ($mIns^{tu}/mIns^n$), and maximal Lip-Lac to contralateral Lip-Lac ($Lip-Lac^{tu}/Lip-Lac^n$). In addition to ratios against normal tissue, the following intrinsic tumor metabolite ratios were also obtained: minimal NAA^{tu}/Cr^{tu}, minimal $mIns^{tu}/Cr^{tu}$, maximal Cho^{tu}/Cr^{tu}, maximal Cho^{tu}/NAA^{tu}, and maximal $Lip-Lac^{tu}/Cr^{tu}$. These MR spectroscopy criteria were selected to best correlate with the grading of the tumors on histopathology. In this way, among all the multivoxel spectroscopy graphs of the tumor, we chose the metabolite that presented the greatest alteration, independent of its position within the tumor (solid or necrotic). The smallest NAA of all the spectroscopy graphics and the greatest Cho were chosen. When the tumor had necrosis, the greatest Lip-Lac peak coincided with the necrotic area.

Diffusion-Weighted Imaging. DWI was performed in 13 patients with PAs and 12 with HGAs. DWI was performed in the transverse plane by using a spin-echo echo-planar imaging sequence with the following parameters: TR/TE, 5000/78.6 ms; diffusion gradient encoding in 3 orthogonal directions; b-value = 1000 s/mm²; FOV, 24 cm; matrix size, 96 × 192 pixels; section thickness, 5 mm; section gap, 1.5 mm; and NEX, 2. DWI scans were performed before PWI and contrast-enhanced T1-weighted imaging. The minimal apparent diffusion coefficient (ADC) value was chosen in solid and enhanced areas of the tumor to best characterize the maximal cellularity of the tumor.

Statistical Analysis

All parameters are reported as means ± SD. For a comparison of the quantitative variances between the PA and HGA groups, we applied the nonparametric Mann-Whitney statistical test because of the lack of normality of the data.

The sensitivity, specificity, positive predictive value, and negative predictive value of each advanced MR imaging technique used in this study were calculated to differentiate PAs from HGAs.

We used a receiver operating characteristic analysis curve (ROC) to decide the cutoff between PAs and HGAs. The cutoff values chosen were those that provided greater sensitivity and specificity jointly (ie, the best combination of the 2 measures).

The analyses were performed in the Statistical Package for the Social Sciences, Version 12.0 (IBM, Armonk, New York). A P value < .05 was statistically significant.

RESULTS

Within the PA group, 10/16 (62%) patients were younger than 21 years old at presentation. With regard to the location of the tumor, 9/16 (56%) cases were supratentorial and 7/16 (45%) were infratentorial. Among the supratentorial tumors, 6/9 (67%) were hypothalamic-chiasmatic.

Within the HGA group, most of the patients were adults (21/22, 95%) and most tumors were supratentorial (21/22, 95%). The

Table 2: Comparison of the PA and HGA groups with regard to the variables of interest (mean ± standard deviation)

	PA	HGA	P Value
rCBV	1.408 ± 0.870	3.322 ± 1.401	.0008
ADC	1.534 ± 0.382	1.193 ± 0.279	.0134
NAA^{tu}/Cr^{tu}	1.180 ± 0.708	1.247 ± 0.681	.8457
Cho^{tu}/NAA^{tu}	2.020 ± 1.090	1.417 ± 0.782	.1628
Cho^{tu}/Cr^{tu}	3.158 ± 2.651	2.838 ± 1.595	.6028
Cho^{tu}/Cho^n	1.390 ± 0.743	1.963 ± 2.275	.3958
$Lip-Lac^{tu}/Cr^{tu}$	8.326 ± 11.180	43.320 ± 59.240	.0273
Cr^{tu}/Cr^n	0.464 ± 0.234	0.495 ± 0.326	.8437
$Lip-Lac^{tu}/Lip-Lac^n$	1.746 ± 0.918	6.555 ± 7.480	.0618
$mIns^{tu}/mIns^n$	1.020 ± 0.419	0.749 ± 0.733	.0961
$mIns^{tu}/Cr^{tu}$	1.924 ± 0.468	1.607 ± 0.9953	.1264

Note:—ADC measurements are expressed in $\times 10^{-3}$ mm² per second.

main characteristics of PA and HGA on conventional MR imaging are shown in Table 1.

The rCBV values were significantly lower in the PA group compared with the HGA group (Table 2 and Fig 1). Only 3/9 (33%) PA cases showed elevated perfusion (rCBV > 1.75), while 17/20 of the HGA group (85%) showed markedly elevated perfusion.

In analyzing ADC values, there was a statistically significant difference between the PA group and the HGA group (Table 2 and Fig 2).

The $Lip-Lac^{tu}/Cr^{tu}$ values were significantly higher in the HGA group than in the PA group (Table 2 and Fig 3). There was a trend toward higher $Lip-Lac^{tu}/Lip-Lac^n$ ratios in the HGA group compared with the PA group (P = .06). There were no statistically significant differences between the PA and HGA groups in the remaining metabolite ratios (Table 2).

The sensitivity, specificity, positive predictive value, negative predictive value, and the area under the ROC curve of each of the MR imaging–analyzed parameters at respective cutoff values are shown respectively in Tables 3 and 4.

DISCUSSION

In an attempt to differentiate PA and HGA, our data showed that lower rCBV and higher ADC values favor a diagnosis of PA, while higher $Lip-Lac^{tu}/Cr^{tu}$ ratios plus necrosis favor a diagnosis of HGA.

Although PA is classified as grade I by the WHO because of its benign biologic behavior, this tumor can have contradictory findings on both neuroimaging and histopathology and may be confused with a malignant tumor.[1,4]

PA has been commonly described as a large cystic mass with a mural nodule that shows a marked enhancement.[1,5,7] Therefore, when a typical solid-cystic tumor is found on MR imaging in a patient younger than 20 years of age, the most probable diagnosis is PA,[1,5] particularly when it is located in the posterior fossa.
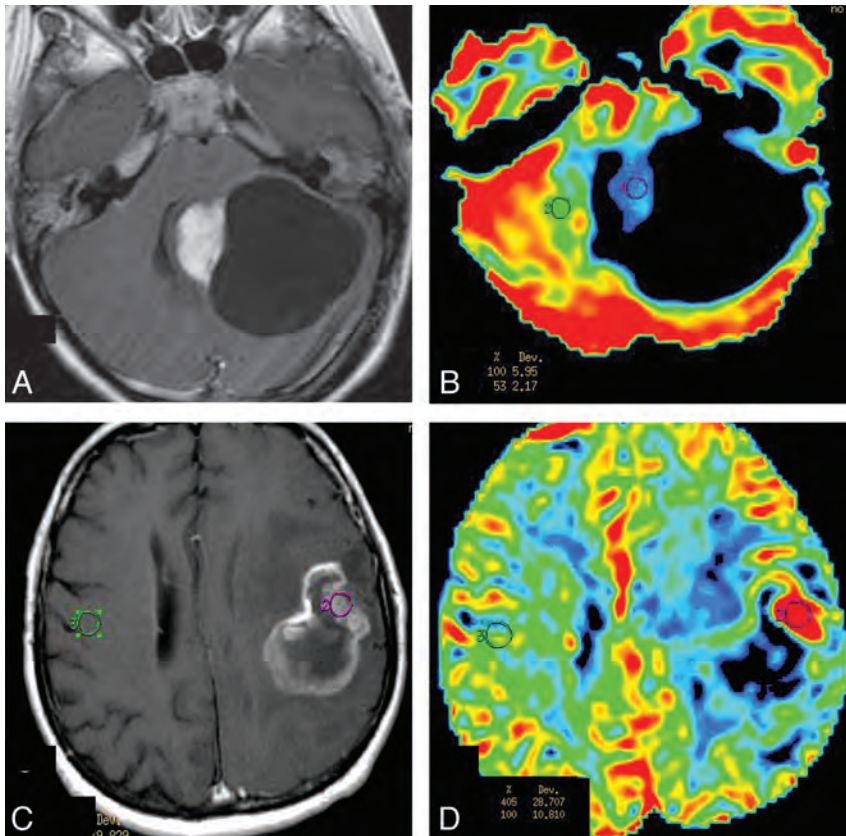
FIG 1. Comparison of rCBV between PA and HGA on PWI. *A* and *B*, Solid-cystic PA in the left cerebellar hemisphere. *A*, Contrast-enhanced axial T1-weighted imaging demonstrates intense homogeneous enhancement in the solid portion of the tumor and lack of enhancement of the walls of the cystic portion. *B*, PWI, with an rCBV color overlay map, shows low rCBV on the solid portion of PA. *C* and *D*, GBM in the left frontoparietal lobe. *C*, Contrast-enhanced axial T1-weighted imaging demonstrates ring and irregular peripheral enhancement with central necrosis. *D*, PWI with an rCBV color overlay map shows increased rCBV in the solid tumor area.

Conversely, when imaging reveals a single tumor with ring enhancement, suggesting central necrosis, the most probable diagnosis is HGA, specifically GBM.[14] These MR imaging features were found in 60% of the HGAs and in only 7% of the PAs in our series.

However, when the tumor is solid and seems to infiltrate adjacent brain tissue with intense enhancement, as it did in 50% of the PAs and 37% of the HGAs in our study, there is less certainty as to whether the tumor is a PA or HGA. This ambiguity can occur even in patients who are younger than 20 years of age, when age favors a diagnosis of PA,[1] as well as in adult patients, in whom PA is rare.[2]

Advanced MR imaging techniques can help distinguish these entities much better than conventional imaging alone.[8,14,15] Enhanced accuracy helps in treatment planning and prognostication before surgery.[8,14] This information is even more important when histopathologic diagnosis cannot be obtained due to contraindications to surgery, such as when there is tumor involvement of eloquent areas (motor, speech, or visual brain areas) or when the biopsy tissue collected is insufficient for diagnosis.[11] Advanced MR imaging techniques can also help overcome sampling errors in the histopathologic grading of tumor and can sample the entire lesion noninvasively in vivo.[10] Furthermore, there may be instances when a neuropathologist is unable to definitively differ-

entiate PA and HGA,[1,4] in which case advanced MR imaging could be crucial in the diagnosis of the lesion.

Several studies have demonstrated that rCBV has clinical utility in glioma grading. However, most of these studies only included WHO grade II tumors in the low-grade glioma (LGG) group and WHO grades III and IV in the HGG group.[10,16,17] Most of these studies failed to include PA in the LGG group or even to consider it as a separate cohort.[9,10,16,17] To our knowledge, there are only a few studies assessing PWI in PAs, all of which are case series or anecdotal case reports in review articles.[7,18-21]

Despite the usual avid enhancement on conventional MR imaging in both PAs and HGAs, the present study found significantly lower rCBV values in PAs compared with HGAs. Some small case series of PAs have also demonstrated low rCBV values (< 1.5) in PA,[7,12,19] while HGAs show high rCBV values in analytical studies (3.64–7.32).[9,10,16,17,22,23] To the best of our knowledge, there are only 2 case reports in review articles that have found high perfusion in PAs.[18,21]

Uematsu et al[12] demonstrated in a case series that the mean vascularity index of GBMs is higher than that of PAs, but the mean vascular leakage was lower in GBMs. This finding could be explained by the different features of PAs and GBMs on histopathology. In the present study, all patients had pathologic confirmation but no formal qualitative evaluation of the neoplasia vascularity was performed. Uematsu et al[12] reported that PAs have sparse vasculature in a wide interstitial space, while GBMs have abundant vascularity in a tight interstitial space.[12] According to some electron microscopy studies of the gap junctions of the endothelial cells, PAs and HGGs probably have similar blood-brain barrier integrity.[24,25] Taken together, we may postulate that the decreased rCBV observed in PA tumors strongly suggests a decreased vascularity in this low-grade astrocytoma compared with HGA.

Information on the metabolism of brain tissue may be obtained from proton MR spectroscopy.[11,26] The ability of MR spectroscopy to predict glioma grade is controversial.[11] The presence of lipids has been recognized as a marker of myelin breakdown, as well as a potential indicator of necrosis in malignant astrocytomas.[27] Lactate is considered an end product of the anaerobic glycolytic cycle, and its presence within a tumor often indicates tumor necrosis.[10,26] The prominent lipid peak, which resonates at 1.3 ppm observed in HGAs, corresponds, mainly, to the methylene group of lipid molecules, whereas in PA, it is mainly a lactate peak.
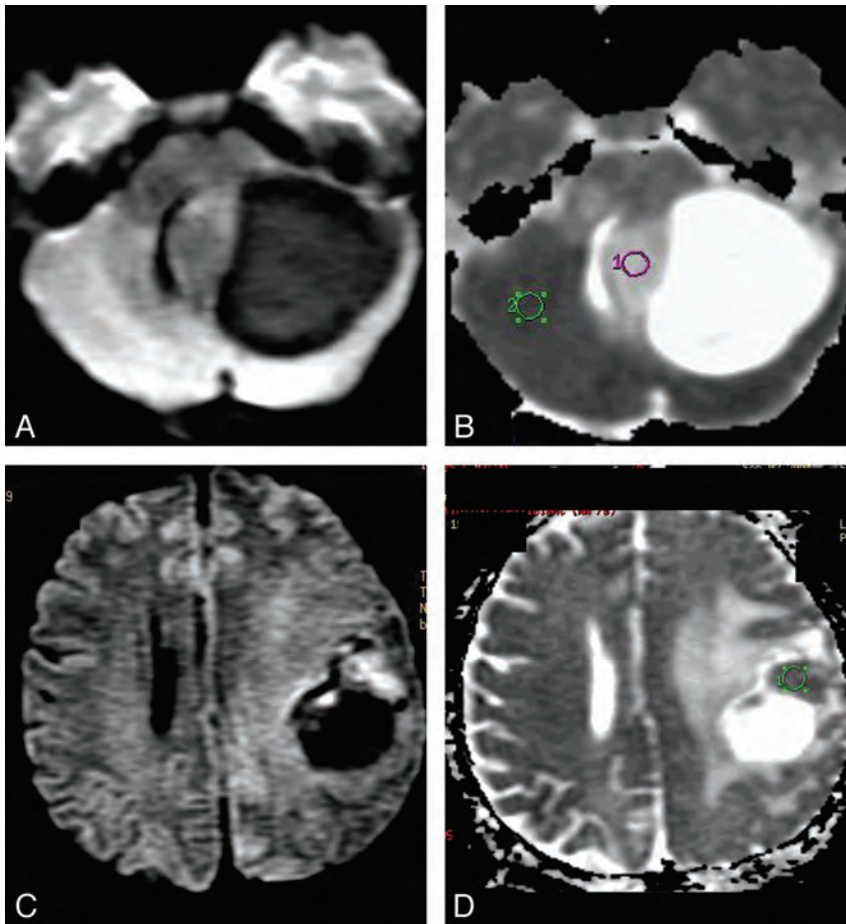
FIG 2. DWI in PA and HGA. *A* and *B*, Solid-cystic PA in the left cerebellar hemisphere. The solid part of this tumor is hypointense on DWI (*A*) and hyperintense on ADC map (*B*) in comparison with normal brain parenchyma. *C* and *D*, The frontoparietal HGA (GBM) shows decreased water diffusion (*C*) in the more hyperintense solid tumor area on DWI, which is more hypointense (*D*) on ADC than the normal brain parenchyma and indicates greater cellularity of this GBM than is observed in the PA shown (*A* and *B*).

HGGs than in non-PA LGGs,[9,10,36] very likely due to the greater cellularity of malignant tumors. However, our study found the opposite to be true in the comparison between PA, which is an LGG, and HGA, though the difference was not significant. Our finding may be explained by the presence of necrosis within the GBMs, which decreases the number of neoplastic cells and consequently lowers the Cho^{tu}/NAA^{tu} and Cho^{tu}/Cr^{tu} ratios[11] in the HGA group. This process does not occur with the PAs that showed higher values of these ratios.

It has been demonstrated that the MR spectroscopy pattern appears slightly different between PA in adults and in children, though no significant differences have been identified.[37] Only 5 PAs were investigated with MR spectroscopy in our study, in 4 children (8, 12, 12, 14 years of age) and 1 adult (20 years of age). Similar to the previous article,[37] our study also shows that the normalized Cr (Cr^{tu}/Cr^n) was reduced in all PAs. As in the previous article,[37] the reduced normalized mean Cr^{tu}/Cr^n ratio (0.52) in the PA pediatric group was higher compared with the PA of the adult patient ratio (0.26). All our cases in the PA pediatric group presented increased values of normalized Cho (Cho^{tu}/Cho^n) according to the previous study.[37] However, unlike the previous study,[37] in our study, the normalized Cho (Cho^{tu}/Cho^n) of our 1 adult patient was low (0.97) and lower than the mean of the 1.5 ratio in the pediatric group. It is always difficult to compare the results of studies because usually different equipment (eg, the prior study used 3T MR imaging), different technical parameters of MR spectroscopy (eg, the prior study used TE = 144 ms),[37] and different methodologies are used. The small number of cases of PA in the pediatric and adult groups was another major limitation in both studies.

Castillo et al[38] suggest that mIns levels could be a marker for astrocytoma grade, with a trend toward higher mIns levels in low-grade astrocytomas (including both WHO grade I and II tumors) compared with anaplastic astrocytomas and GBMs.[28,38] In our study, the means of the $mIns^{tu}/Cr^{tu}$ and $mIns^{tu}/mIns^n$ ratios were also higher in PAs than in HGAs, but the differences were not statistically significant. Schneider et al,[39] by using a different technique to normalize metabolites (water was used as an internal reference), found that grade II gliomas demonstrated significantly higher levels of mIns than PAs. However, contradictory reports have also demonstrated low mIns levels in PAs.[34,40]

Several studies have indicated that lactate is more likely to be present in HGGs than in LGGs,[9,28-31] but most of these studies did not include PAs among the LGGs. There have been a few studies assessing the $Lip-Lac^{tu}/Cr^{tu}$ ratio in PAs, but all used long-TE (270 ms) single-voxel spectroscopy.[26,32] Although necrosis is seldom found in PAs, Hwang et al[26] described the presence of lipids and lactate in PAs, despite their benign tumor histology.

In our study, among all metabolite ratios analyzed, only $Lip-Lac^{tu}/Cr^{tu}$ values were significantly higher in HGAs than in PAs. There was also a trend toward a higher $Lip-Lac^{tu}/Lip-Lac^n$ ratio in HGAs. The $Lip-Lac^{tu}/Cr^{tu}$ ratio was present and increased in both tumor types, but it was much higher in HGAs, probably due to the presence of tumoral necrosis. Although the presence of Lip-Lac in PAs in the absence of necrosis can be explained by several mechanisms, including mitochondrial dysfunction,[26] our hypothesis is that it may be attributed to the commonly occurring microscopic cysts on histopathology.

As in previous reports,[26,32-35] we also found increased Cho^{tu}/NAA^{tu} and Cho^{tu}/Cr^{tu} ratios in PAs, with values lower than those in some studies,[26,33] but higher than those of Sutton et al.[32] Some authors made the comparison between gliomas without including PAs and found higher Cho^{tu}/NAA^{tu} and Cho^{tu}/Cr^{tu} ratios in

FIG 3. Comparison of the Lip-Lac^{tu}/Cr^{tu} ratio on short-TE multivoxel MR spectroscopy in PA and HGA. *A* and *C*, Axial T2-weighted imaging was used for positioning of the regions of interest in the tumor. *A* and *B*, The solid homogeneous enhancing hypothalamic-chiasmatic PA has a Lip-Lac peak. The (*C* and *D*) necrotic ring-enhancing GBM located on the lateral wall of the left lateral ventricular trigone also has an elevated Lip-Lac peak (*D*), but the Lip-Lac^{tu}/Cr^{tu} ratio in this tumor is higher than that found in the PA (*B*). *A* and *B* reproduced with permission from Aragao et al.[47]

Table 3: Cutoff values, sensitivity, specificity, positive predictive value, negative predictive value, and accuracy of the different studied MRI parameters to identify high-grade (III/IV) astrocytomas (HGA)

Parameter	Cutoff Value[a]	Sensitivity	Specificity	PPV	NPV	Accuracy
rCBV	≥1.33	100%	67%	87%	100%	90%
ADC	≤1.60	100%	54%	63%	100%	72%
Lip-Lac^{tu}/Cr^{tu}	≥7.06	80%	80%	94%	50%	80%
Lip-Lac^{tu}/Lip-Lac^{n}	≥2.11	73%	80%	94%	44%	76%

Note:—PPV indicates positive predictive value; NPV, negative predictive value.
[a] HGA group.

Table 4: Areas under the receiver operating characteristic analysis curve for the variables of interest for distinguishing PA from HGA

Parameters	Area	95% CI	*P* Value
rCBV	0.906	0.790–1.000	.001
ADC	0.795	0.610–0.980	.012
Lip-Lac^{tu}/Cr^{tu}	0.830	0.626–1.000	.025
Lip-Lac^{tu}/Lip-Lac^{n}	0.780	0.585–0.975	.047

The diffusion of water in brain tissue may vary in magnitude and direction, depending on several factors; ADC measurements can offer quantitative information regarding the restriction of movement of water molecules.[9,41] In our series, HGAs demonstrated significantly lower minimum ADC values than PAs (*P* =

.01). The difference may be related to the increased cellularity of higher grade tumors,[42,43] with resultant restriction of water movement in the interstitial space.[43,44] Although measurements of necrosis could potentially elevate ADC values,[9,43] we analyzed the minimum ADC of the solid enhancing portion of the lesion, taking care to exclude the necrotic areas frequently seen in high-grade tumors. Other studies, by using a technique similar to ours, have shown similar results[9,43,45] when comparing HGGs and LGGs. However, these studies did not include PA cases. Most of the reports that have assessed ADC in PAs have compared them with medulloblastomas, ependymomas, or other LGGs.[39,46]

As far as we know, this is the first time that PAs are compared with HGAs by using the described advanced MR imaging techniques together. The methodology used sought to follow that used in histopathology: to seek brain tumor markers that represent the criteria of greater malignancy. The sensitivity, specificity, predictive values, and accuracy for rCBV, ADC, Lip-Lac^{tu}/Cr^{tu}, and Lip-Lac^{tu}/Lip-Lac^{n} thresholds were determined as the optimal cutoff value in differentiating PAs from HGAs.

This study has some limitations. First, because it is a retrospective study, a full complement of imaging was not available for each patient. Therefore, we have a small population of cases, mainly of pilocytic astrocytomas, with advanced MR imaging techniques. Second, we used a short TE of 35 ms. Even though short-TE MR spectroscopy has the advantage of showing the mIns peak and has better sensitivity to the presence of lipids, its disadvantage is that one cannot separate the lipid peak from the lactate peak because both appear at 1.33 ppm above the baseline. Additionally, there is more noise at the baseline in short-TE than in long-TE MR spectroscopy; and because the glutamine-glutamate peak is close to the NAA peak, it is difficult to properly measure the NAA peak when it is low. Finally, choosing a region of interest to evaluate the rCBV leads to another difficulty in cases in which the tumor is in the gray matter because it is unclear whether the high perfusion value is due to the properties of the gray matter or to the tumor itself. Another limitation of our study is the lack of a multiparametric analysis, which would demon-

strate the relative contribution of all the clinical, conventional MR imaging and advanced findings to the diagnosis of PA versus HGA. We hope that further investigation will be made by prospective studies with a greater number of cases and multiparametric analysis, by using advanced MR imaging techniques to confirm our findings.

CONCLUSIONS

We have demonstrated that PWI (rCBV) is one of the best MR imaging techniques in differentiating PA from HGA. Lower rCBV and higher ADC values favor a diagnosis of PA, while higher rCBV values, lower ADC values, and higher Lip-Lac^{tu}/Cr^{tu} ratios plus necrosis favor a diagnosis of HGA. Even though the histopathologic and conventional MR imaging features of PA may occasionally suggest a more malignant tumor, patient age and advanced MR imaging findings should be considered together with the pathologic characteristics to establish the final diagnosis in difficult cases. In this way, the findings of our study may contribute to a change in the current clinical approach, especially in difficult cases encountered by radiologists as well as pathologists in differentiating these 2 types of tumors.

REFERENCES

1. Koeller KK, Rushing EJ. **From the archives of the AFIP: pilocytic astrocytoma: radiologic-pathologic correlation.** *Radiographics* 2004;24:1693–708

2. Stuer C, Vilz B, Majores M, et al. **Frequent recurrence and progression in pilocytic astrocytoma in adults.** *Cancer* 2007;110:2799–808

3. Burkhard C, Di Patre PL, Schuler D, et al. **A population-based study of the incidence and survival rates in patients with pilocytic astrocytoma.** *J Neurosurg* 2003;98:1170–74

4. Scheithauer BW, Hawkins C, Tihan T, et al. **Pilocytic astrocytoma.** In: Louis DN, Ohgaki H, Wiestler OD, et al, eds. *WHO Classification of Tumours of Central Nervous System.* Lyon, France: IARC; 2007:14–21

5. Lee YY, Van Tassel P, Bruner JM, et al. **Juvenile pilocytic astrocytomas: CT and MR characteristics.** *AJR Am J Roentgenol* 1989;152:1263–70

6. Kuroiwa T, Ohta T, Tsutsumi A. **Malignant pilocytic astrocytoma in the medulla oblongata: case report.** *Brain Tumor Pathol* 1999;16:81–85

7. Grand SD, Kremer S, Tropres IM, et al. **Perfusion-sensitive MRI of pilocytic astrocytomas: initial results.** *Neuroradiology* 2007;49:545–50

8. Cha S, Knopp EA, Johnson G, et al. **Intracranial mass lesions: dynamic contrast-enhanced susceptibility-weighted echo-planar perfusion MR imaging.** *Radiology* 2002;223:11–29

9. Yang D, Korogi Y, Sugahara T, et al. **Cerebral gliomas: prospective comparison of multivoxel 2D chemical-shift imaging proton MR spectroscopy, echoplanar perfusion and diffusion-weighted MRI.** *Neuroradiology* 2002;44:656–66

10. Law M, Yang S, Wang H, et al. **Glioma grading: sensitivity, specificity, and predictive values of perfusion MR imaging and proton MR spectroscopic imaging compared with conventional MR imaging.** *AJNR Am J Neuroradiol* 2003;24:1989–98

11. Aragão Mde F, Otaduy MC, Melo RV, et al. **Multivoxel spectroscopy with short echo time: choline/N-acetyl-aspartate ratio and the grading of cerebral astrocytomas** [in Portuguese]. *Arq Neuropsiquiatr* 2007;65:286–94

12. Uematsu H, Maeda M, Sadato N, et al. **Measurement of the vascularity and vascular leakage of gliomas by double-echo dynamic magnetic resonance imaging: a preliminary study.** *Invest Radiol* 2002;37:571–76

13. Louis DN, Reifenberg G, Brat DJ, Ellison DW. **Tumours: introduction and neuroepithelial tumors.** In Love S, Louis DN, Ellison DW, eds. *Greenfield's Neuropathology.* London, UK: Edward Arnold Publishers; 2008:1821–2000

14. Nelson SJ, Cha S. **Imaging glioblastoma multiforme.** *Cancer J* 2003;9:134–45

15. Martin AJ, Liu H, Hall WA, et al. **Preliminary assessment of turbo spectroscopic imaging for targeting in brain biopsy.** *AJNR Am J Neuroradiol* 2001;22:959–68

16. Sugahara T, Korogi Y, Kochi M, et al. **Correlation of MR imaging-determined cerebral blood volume maps with histologic and angiographic determination of vascularity of gliomas.** *AJR Am J Roentgenol* 1998;171:1479–86

17. Aronen HJ, Gazit IE, Louis DN, et al. **Cerebral blood volume maps of gliomas: comparison with tumor grade and histologic findings.** *Radiology* 1994;191:41–51

18. Ball WS Jr, Holland SK. **Perfusion imaging in the pediatric patient.** *Magn Reson Imaging Clin N Am* 2001;9:207–30, ix

19. Maeda M, Itoh S, Kimura H, et al. **Tumor vascularity in the brain: evaluation with dynamic susceptibility-contrast MR imaging.** *Radiology* 1993;189:233–38

20. Uematsu H, Maeda M. **Double-echo perfusion-weighted MR imaging: basic concepts and application in brain tumors for the assessment of tumor blood volume and vascular permeability.** *Eur Radiol* 2006;16:180–86

21. Cha S. **Dynamic susceptibility-weighted contrast-enhanced perfusion MR imaging in pediatric patients.** *Neuroimaging Clin N Am* 2006;16:137–47, ix

22. Shin JH, Lee HK, Kwun BD, et al. **Using relative cerebral blood flow and volume to evaluate the histopathologic grade of cerebral gliomas: preliminary results.** *AJR Am J Roentgenol* 2002;179:783–89

23. Knopp EA, Cha S, Johnson G, et al. **Glial neoplasms: dynamic contrast-enhanced T2*-weighted MR imaging.** *Radiology* 1999;211:791–98

24. Nir I, Levanon D, Iosilevsky G. **Permeability of blood vessels in experimental gliomas: uptake of 99mTc-glucoheptonate and alteration in blood-brain barrier as determined by cytochemistry and electron microscopy.** *Neurosurgery* 1989;25:523–31

25. Long DM. **Capillary ultrastructure and the blood-brain barrier in human malignant brain tumors.** *J Neurosurg* 1970;32:127–44

26. Hwang JH, Egnaczyk GF, Ballard E, et al. **Proton MR spectroscopic characteristics of pediatric pilocytic astrocytomas.** *AJNR Am J Neuroradiol* 1998;19:535–40

27. Kuesel AC, Briere KM, Halliday WC, et al. **Mobile lipid accumulation in necrotic tissue of high grade astrocytomas.** *Anticancer Res* 1996;16:1485–89

28. Howe FA, Barton SJ, Cudlip SA, et al. **Metabolic profiles of human brain tumors using quantitative in vivo 1H magnetic resonance spectroscopy.** *Magn Reson Med* 2003;49:223–32

29. Di Costanzo A, Scarabino T, Trojsi F, et al. **Multiparametric 3T MR approach to the assessment of cerebral gliomas: tumor extent and malignancy.** *Neuroradiology* 2006;48:622–31

30. Kaminogo M, Ishimaru H, Morikawa M, et al. **Diagnostic potential of short echo time MR spectroscopy of gliomas with single-voxel and point-resolved spatially localised proton spectroscopy of brain.** *Neuroradiology* 2001;43:353–63

31. Tzika AA, Zarifi MK, Goumnerova L, et al. **Neuroimaging in pediatric brain tumors: Gd-DTPA-enhanced, hemodynamic, and diffusion MR imaging compared with MR spectroscopic imaging.** *AJNR Am J Neuroradiol* 2002;23:322–33

32. Sutton LN, Wang Z, Gusnard D, et al. **Proton magnetic resonance spectroscopy of pediatric brain tumors.** *Neurosurgery* 1992;31:195–202

33. Sutton LN, Wehrli SL, Gennarelli L, et al. **High-resolution 1H-mag-**

netic resonance spectroscopy of pediatric posterior fossa tumors in vitro. *J Neurosurg* 1994;81:443–48

34. Panigrahy A, Krieger MD, Gonzalez-Gomez I, et al. **Quantitative short echo time 1H-MR spectroscopy of untreated pediatric brain tumors: preoperative diagnosis and characterization.** *AJNR Am J Neuroradiol* 2006;27:560–72

35. Lazareff JA, Olmstead C, Bockhorst KH, et al. **Proton magnetic resonance spectroscopic imaging of pediatric low-grade astrocytomas.** *Childs Nerv Syst* 1996;12:130–35

36. Fulham MJ, Bizzi A, Dietz MJ, et al. **Mapping of brain tumor metabolites with proton MR spectroscopic imaging: clinical relevance.** *Radiology* 1992;185:675–86

37. Porto L, Kieslich M, Franz K, et al. **Spectroscopy of untreated pilocytic astrocytomas: do children and adults share some metabolic features in addition to their morphologic similarities?** *Childs Nerv Syst* 2010;26:801–06

38. Castillo M, Smith JK, Kwock L. **Correlation of myo-inositol levels and grading of cerebral astrocytomas.** *AJNR Am J Neuroradiol* 2000;21:1645–49

39. Schneider JF, Confort-Gouny S, Viola A, et al. **Multiparametric differentiation of posterior fossa tumors in children using diffusion-weighted imaging and short echo-time 1H-MR spectroscopy.** *J Magn Reson Imaging* 2007;26:1390–98

40. Schneider JF, Viola A, Confort-Gouny S, et al. **Infratentorial pediatric brain tumors: the value of new imaging modalities.** *J Neuroradiol* 2007;34:49–58

41. Tanner JE. **Intracellular diffusion of water.** *Arch Biochem Biophys* 1983;224:416–28

42. Cha S. **Update on brain tumor imaging: from anatomy to physiology.** *AJNR Am J Neuroradiol* 2006;27:475–87

43. Sugahara T, Korogi Y, Kochi M, et al. **Usefulness of diffusion-weighted MRI with echo-planar technique in the evaluation of cellularity in gliomas.** *J Magn Reson Imaging* 1999;9:53–60

44. Le Bihan D, Breton E, Lallemand D, et al. **MR imaging of intravoxel incoherent motions: application to diffusion and perfusion in neurologic disorders.** *Radiology* 1986;161:401–07

45. Murakami R, Hirait T, Kitajima M, et al. **Magnetic resonance imaging of pilocytic astrocytomas: usefulness of the minimum apparent diffusion coefficient (ADC) value for differentiation from high-grade gliomas.** *Acta Radiol* 2008;49:462–67

46. Yamasaki F, Kurisu K, Satoh K, et al. **Apparent diffusion coefficient of human brain tumors at MR imaging.** *Radiology* 2005;235:985–91

47. Aragao MF, Soares ML, Holanda GR. **Tumores supratentoriais.** In: Silva CI, D'Ippolito G, Rocha AJ, et al, eds. *Série Colégio Brasileiro de Radiologia e Diagnóstico por Imagem- Encéfalo.* Rio de Janeiro, Brazil: Elsevier; 2012:292

Evaluation of Microvascular Permeability with Dynamic Contrast-Enhanced MRI for the Differentiation of Primary CNS Lymphoma and Glioblastoma: Radiologic-Pathologic Correlation

P. Kickingereder, F. Sahm, B. Wiestler, M. Roethke, S. Heiland, H.-P. Schlemmer, W. Wick, A. von Deimling, M. Bendszus, and A. Radbruch

ABSTRACT

BACKGROUND AND PURPOSE: Dynamic contrast-enhanced MR imaging can provide in vivo assessment of the microvasculature in intracranial tumors. The aim of the present study was to evaluate the diagnostic performance of dynamic contrast-enhanced MR imaging derived vascular permeability parameters, including the volume transfer constant, the volume of extravascular extracellular space, and the flux rate constant between the extravascular extracellular space and plasma, for the differentiation of primary CNS lymphoma and glioblastoma.

MATERIALS AND METHODS: Sixty glioblastomas and 11 primary central nervous system lymphomas were included. Pretreatment T1-weighted dynamic contrast-enhanced MR imaging with a 3D T1-weighted spoiled gradient-echo sequence was performed on a 3T MR imaging scanner. Perfusion parameters (volume transfer constant, the volume of extravascular extracellular space, and the flux rate constant) were measured on the basis of the Tofts-Kernmode model. The Mann-Whitney U test and receiver operating characteristic analysis were used to compare those parameters between primary central nervous system lymphoma and glioblastoma. Histopathologic correlation of dynamic contrast-enhanced MR imaging findings was performed by using reticulin staining and CD31 immunohistochemistry.

RESULTS: Median volume transfer constant and flux rate constant values were significantly higher in primary central nervous system lymphoma (0.145 ± 0.057 and 0.396 ± 0.088) than in glioblastoma (0.064 ± 0.021 and 0.230 ± 0.058) ($P < .001$, respectively). Median volume of extravascular extracellular space values did not differ significantly between primary central nervous system lymphoma (0.434 ± 0.165) and glioblastoma (0.319 ± 0.107). On receiver operating characteristic analysis, volume transfer constant had the best discriminative value for differentiating primary central nervous system lymphoma and glioblastoma (threshold, 0.093; sensitivity, 90.9%; specificity, 95.0%). Histopathologic evaluation revealed intact vascular integrity in glioblastoma despite endothelial proliferation, whereas primary central nervous system lymphoma demonstrated destroyed vessel architecture, thereby promoting vascular disintegrity.

CONCLUSIONS: Primary central nervous system lymphoma demonstrated significantly higher volume transfer constant and flux rate constant values compared with glioblastoma, implying a higher vascular permeability in primary central nervous system lymphoma. These findings confirm initial observations from perfusion CT and dynamic contrast-enhanced MR imaging studies, correlating with underlying histopathologic features, and may be useful in distinguishing primary central nervous system lymphoma from glioblastoma.

ABBREVIATIONS: DCE-MRI = dynamic contrast-enhanced MRI; GB = glioblastoma; HE = hematoxylin-eosin; K_{ep} = flux rate constant; K^{trans} = volume transfer constant; PCNSL = primary central nervous system lymphoma; V_e = volume of extravascular extracellular space

Preoperative differentiation of primary central nervous system lymphomas (PCNSLs) and glioblastomas (GBs) is of high clinical relevance because neurosurgical strategies for PCNSL and GB favor a biopsy-only versus a maximal safe resection.[1,2] Dynamic contrast-enhanced (DCE) MR imaging allows characterization of the vascular microenvironment in brain tumors by measurement of a range of parameters that reflect specific physiologic characteristics.[3] Several recent studies have successfully applied DCE-MR imaging for quantitative estimates of vascular permeability parameters, essentially for glioma grading[4-6] and response assessment to antiangiogenic therapies.[7,8] The most widely applied and accepted MR imaging standard to measure microvascular permeability is the DCE steady-state T1-weighted method, which is based on the 2-compartment pharmacokinetic model of Tofts and Kermode.[9,10] Thereby the diffusive transport of low-molecular-weight contrast agent across the capillary endothelium from the blood plasma to the ex-

travascular extracellular space is represented by the volume transfer constant (K^{trans}, minute^{-1}). Further parameters considered in this model are the flux rate constant (K_{ep}, minute^{-1}) between the extravascular extracellular space and the blood plasma and the volume (V_e) of the extravascular extracellular space per volume unit of tissue.[3,9]

Distinct structural and ultrastructural differences in the microenvironment of the tumor vasculature on histologic assessment have been reported for PCNSL and GB, suggesting increased vascular permeability for PCNSL.[11] However, radiologic comparison of vascular permeability in PCNSL and GB has as yet only been performed with perfusion CT[12,13] or with DSC-PWI processed with a mathematic leakage-correction model,[14] which, in part, confirmed the increased vascular permeability for PCNSL. The aim of our study was to evaluate the diagnostic performance of DCE-MR imaging–derived vascular permeability parameters, including K^{trans}, K_{ep}, and V_e for the preoperative differentiation of PCNSL and GB. Furthermore, histopathologic correlation of DCE-MR imaging findings was performed for all patients by using reticulin and CD31 immunohistochemistry.

MATERIALS AND METHODS

Patient Selection

Our institutional review board approved this retrospective study, and the requirement for patient informed consent was waived. Potentially eligible patients from October 2009 to June 2013 were identified on the basis of the diagnosis of PCNSL or GB. Next, for the selection of appropriate patients with PCNSL, only previously untreated, immunocompetent candidates were included. Thereby, 11 patients with PCNSLs with available DCE-MR imaging data on pretreatment MR imaging were available for inclusion in the present study. For selection of appropriate patients with GB, similar inclusion criteria were used. In detail, only previously untreated patients with the availability of pretreatment DCE-MR imaging data were included. Thereby, a control sample of 60 patients with GB was selected for inclusion in the present study.

MR Imaging

Images were acquired in the routine clinical work-up by using a 3T MR imaging system (Magnetom Verio/Trio Tim; Siemens, Erlangen, Germany) with a 12-channel head-matrix coil. Axial DCE-MR imaging was performed with a 3D spoiled gradient-echo sequence providing coverage of the entire brain by using the following parameters: matrix size, 128×128; FOV, 172×230 mm; TR, 5.28 ms; TE, 2.45 ms; flip angle, 10°; section thickness, 5 mm. Thereby, 22 dynamic acquisitions, each including 26 sections, were obtained every 13.34 seconds, resulting in a total measurement time of 4:53 minutes. After the third dynamic acquisition, a standard dose (0.1 mmol/kg body weight) of gadoterate meglumine (Dotarem; Guerbet, Aulnay-sous-Bois, France) was injected as a bolus through a pneumatically driven injection pump at an injection rate of 5 mL/s. After completion of the DCE-MR imaging sequence, standard postcontrast MPRAGE data were acquired with TI = 1100 ms, TE = 4 ms, TR = 1710 ms, and flip angle = 15°.
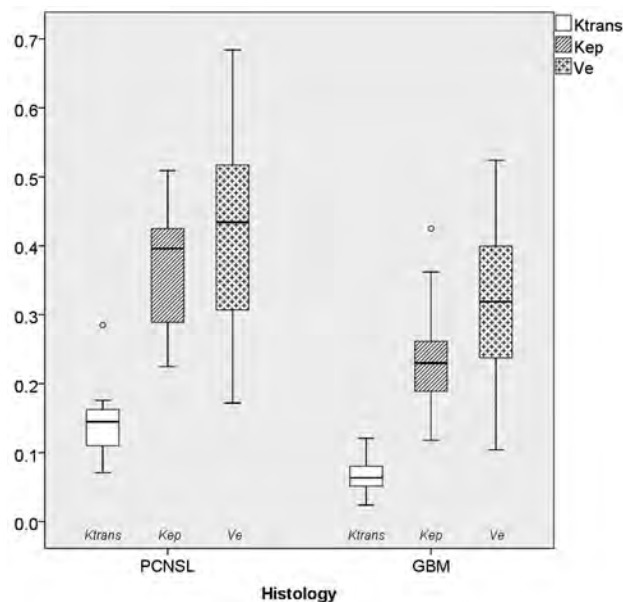
FIG 1. Boxplots of microvascular permeability parameters in primary CNS lymphoma and glioblastoma, including the volume transfer constant (minute^{-1}), the volume of extravascular extracellular space per volume unit of tissue, and the flux rate constant between extravascular extracellular space and plasma (minute^{-1}). The solid line inside the box represents the median value, while the edges represent the 25th and 75th percentiles. The straight line (bar) on each box indicates the range of data distribution. Circles represent outliers (values >1.5 box length from the 75th and 25th percentile).

Image Postprocessing and Analysis

Postprocessing of DCE-MR imaging data was performed with dedicated postprocessing software (Tissue 4D; Siemens) based on the Tofts-Kermode model.[9] First, motion correction was performed on the dynamic images on the basis of an elastic 3D registration technique. Signal intensity was then converted to gadoterate meglumine concentration, and the time–signal intensity curve was calculated. A value for the arterial input function was determined automatically on the basis of a mathematic simulation as described by Orton et al.[15] After obtaining a kinetic modeling parameter map, a radiologist who was blinded to the patient's histology placed freehand ROIs within the entire contrast-enhancing tumor on each section of the DCE-MR images. Cystic or necrotic regions and normal vessels were avoided during region-of-interest placement. Following delineation of the entire contrast-enhancing tumor, vascular permeability parameters (K^{trans}, K_{ep}, and V_e) were automatically generated on the basis of the pixel information from all placed freehand ROIs.

Histopathologic Correlation

To assess whether DCE-MR imaging–derived vascular permeability parameters correlate with vascular integrity on histopathology, we performed reticulin (Tibor-Pap) and hematoxylin-eosin (HE) staining of formalin-fixed paraffin-embedded tumor tissue for all patients. Thereby, both HE and Tibor-Pap stains were used to illustrate the architecture of the tumor and vessels, whereas Tibor-Pap highlights the reticulin fibers in the outer border of the vessel wall, which may be destroyed and detached from the inner endothelium membrane in case of decreased vascular integrity.[16]
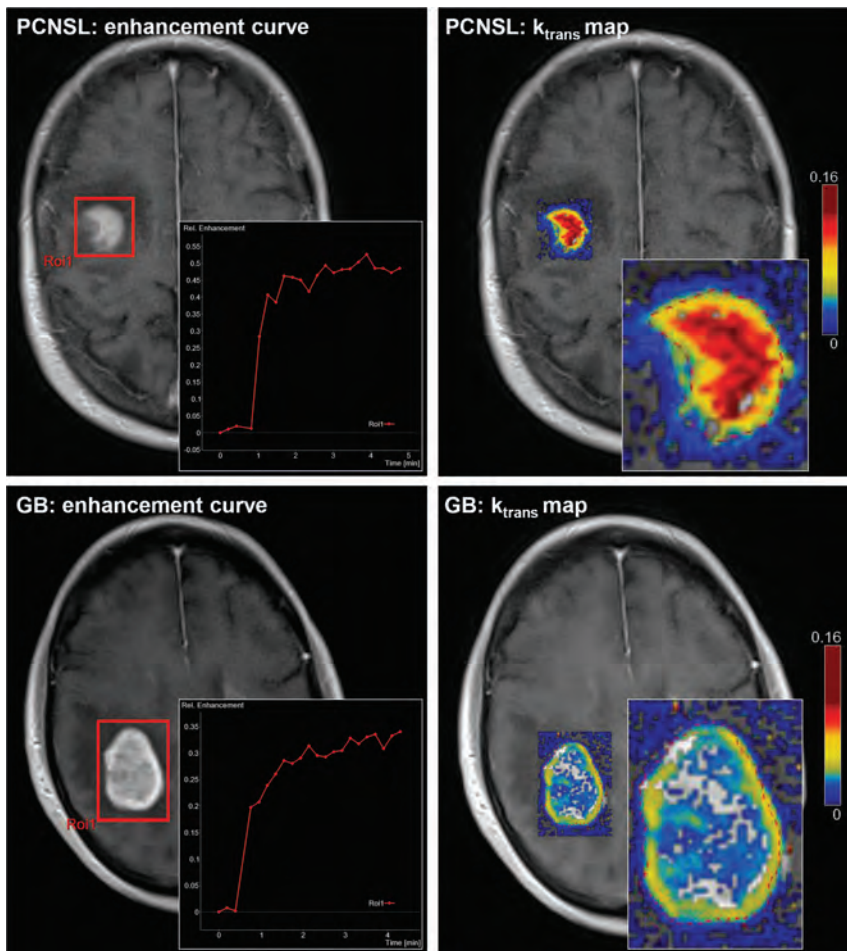
FIG 2. Tissue concentration of contrast agent after bolus injection of 0.1 mmol/g of gadoterate meglumine (left column) in primary CNS lymphoma (upper row) and glioblastoma (lower row). Note the differences in the relative enhancement curve within the region of interest, encompassing the tumor (red square), which peaks at 0.53 in PCNSL and at 0.34 in GB. Perfusion parameters from kinetic modeling parameter maps (right column) were measured by using freehand region-of-interest placement within the solid part of the entire contrast-enhancing tumor (dashed red line within the zoomed kinetic maps; only 1 section is shown here). In these samples, median K^{trans} values were 0.147 ± 0.031 for PCNSL and 0.045 ± 0.014 for GB.

Statistical analysis was performed by using the Statistical Package for the Social Sciences Statistics, Version 20.0 (IBM, Armonk, New York). A Mann-Whitney U test was used to compare vascular permeability parameters (K^{trans}, K_{ep}, and V_e) between PCNSL and GB. Receiver operating characteristic analysis was performed to determine the optimum thresholds for discrimination of PCNSL and GB. P values < .05 were considered significant.

RESULTS

Figure 1 shows a boxplot of DCE-MR imaging–derived vascular permeability parameters, including K^{trans}, K_{ep}, and V_e. Median K^{trans} values were higher in PCNSL (0.145 ± 0.057; 95% CI, 0.106–0.183; range, 0.071–0.285) than in GB (0.064 ± 0.021; 95% CI, 0.060–0.071; range, 0.024–0.121) (P < .001). Similarly, median K_{ep} values were higher in PCNSL (0.396 ± 0.088; 95% CI, 0.305–0.423; range, 0.225–0.509) than in GB (0.230 ± 0.058; 95% CI, 0.215–0.245; range, 0.118–0.425) (P < .001). Median V_e values did not differ significantly between PCNSL (0.434 ± 0.165; 95% CI, 0.311–0.534; range, 0.172–0.684) and GB (0.319 ± 0.107; 95% CI, 0.292–0.347; range, 0.104–0.524). On receiver operating characteristic analysis, K^{trans} had the best discriminative value for differentiating PCNSL and GB (area under the curve, 95.6%; threshold, 0.093; sensitivity, 90.9%; specificity, 95.0%) compared with K_{ep} (area under the curve, 89.1%; threshold, 0.272; sensitivity, 90.9%; specificity; 78.3%) or V_e (area under the curve, 68.6%; threshold, 0.410; sensitivity, 63.6%; specificity, 76.7%). The workflow of postprocessing DCE-MR imaging data of 2 representative patients with PCNSL and GB is shown in Fig 2.

On histopathologic assessment of vascular integrity, tissue samples from PCNSL demonstrated destroyed vessel architecture in each case. Thereby, the outer border of the vessel wall was infiltrated by tumor cells (ie, angiocentric growth pattern), destroyed, and detached from the inner endothelial membrane, thereby contributing to vascular disintegrity (Fig 3, left column). In contrast, vascular integrity was rated as intact for all GBs (Fig 3, right column).

DISCUSSION

The present study evaluated the diagnostic performance of DCE-MR imaging–derived vascular permeability parameters to facilitate the preoperative differentiation of PCNSL and GB. As a principal finding, our study shows that PCNSL demonstrates significantly higher K^{trans} and K_{ep} values on DCE-MR imaging com-

Additionally, in cases in which the endothelial architecture was not evident from HE and reticulin staining, CD31 immunohistochemistry, highlighting endothelial cells, was performed. Tissue was provided by the Department of Neuropathology, Institute of Pathology, University of Heidelberg Medical Center, Germany, in accordance with local ethics approval. Sections cut to 3 μm were processed by using a BenchMark XT immunostainer (Ventana Medical Systems, Tucson, Arizona). Reticulin and HE staining was performed by applying standard protocols. Pretreatment for antigen retrieval was followed by incubation with antihuman CD31 antibody (Dako, Glostrup, Denmark). Incubation was followed by Ventana standard signal amplification, UltraWash, counter-staining with 1 drop of hematoxylin for 4 minutes and 1 drop of bluing reagent for 4 minutes. For visualization, the Ultra-View Universal DAB Detection Kit (Ventana Medical Systems) was used. Reticulin, HE, and CD31 stains were analyzed by a neuropathologist by using a Olympus BX-50 microscope (Olympus America, Lake Success, New York), and vascular integrity was rated as intact or decreased.

FIG 3. Histopathologic assessment of vascular integrity from those patients shown in Fig 2 (original magnification ×200 for all stains): Immunohistochemistry for CD31 (left column) highlights endothelium in primary CNS lymphoma (PCNSL) (upper row) and glioblastoma (GB) tissue (lower row). Black arrows point to the endothelium and indicate the actual lumen of the vessel in PCNSL tissue. In contrast, white arrows in the reticulin staining of the PCNSL tissue (upper row, right) illustrate the outer border of the vessel wall, which is infiltrated by tumor cells, destroyed, and detached from the inner endothelial membrane and thus contributing to decreased vascular integrity. White arrows in the reticulin staining of the GB tissue (lower row, right) underline the integer basal membrane of vessels despite endothelial proliferation.

pared with GB, thereby implying a greater degree of BBB disruption and thus higher vascular permeability in PCNSL, ultimately confirming initial observations from perfusion CT and DSC-MR imaging studies.[13,14] Furthermore, we could demonstrate that these findings correlate with underlying histopathologic features, with intact vascular integrity for GB and destroyed vessel architecture in PCNSL, thereby promoting vascular disintegrity in the latter group.

Radiologic comparison of vascular permeability patterns between PCNSL and GB was initially performed by Warnke et al,[13] who demonstrated significantly higher K^{trans} values on CT perfusion imaging for PCNSL compared with GB. These results were in contrast to a subsequent study by Schramm et al,[12] who performed CT perfusion imaging in a series of 31 high-grade gliomas and 8 PCNSLs, reporting no significant difference in K^{trans} values on Patlak analysis. This pharmacokinetic model assumes that the transfer of the contrast agent across the BBB is unidirectional from the blood plasma to the extravascular extracellular space throughout the entire measurement.[17] In contrast, the equation of Tofts and Kermode[9] also considers the backflow of contrast agent from the extravascular extracellular space to the blood plasma. However, neglecting the backflow of the contrast agent in the Patlak model essentially underestimates K^{trans} in brain tumors[18-20] and may explain the nonsignificant differences in the study of Schramm et al.[12]

Recently, Toh et al[14] performed a study on 15 patients with PCNSL and 20 with GB, evaluating the pseudoleakage parameter K_2 derived from DSC-PWI with a mathematic leakage-correction model, reporting significant higher K_2 values in PCNSL compared with GB. This model is based on the assumption that in brain tumors with substantial BBB breakdown, contrast agent extravasates into the extravascular extracellular space, thereby reducing the T2* DSC-PWI signal-intensity loss by signal-intensity increase in regions where T1 effects are significant.[21,22] In such instances, CBV will be underestimated. Therefore Boxerman et al[21,22] and Weisskoff et al[23] proposed a mathematic leakage-correction model in which linear fitting is used to determine the voxelwise deviation from nonleaky reference tissue and, by removing the leakage term, allowing generation of both corrected CBV maps and first-order estimates of vascular permeability. Although direct comparison is limited by differences in study populations and methodology, the diagnostic performance of DCE-derived K^{trans} in the present study was superior compared with the mathematic leakage-corrected DSC-derived K_2 in the study of Toh et al[14] (area under the curve on receiver operating characteristic analysis, 95.6% versus 77.1%). Due to the complex relationship between contrast agent concentration in tissue and the measured change in signal intensity on DSC-PWI, a positive relationship between DSC-PWI and DCE-MR imaging– derived vascular permeability parameters (ie, K_2 and K^{trans}) may only exist with high flip angles on DSC-PWI (90°).[24]

Furthermore, the DSC-PWI leakage-correction model assumes that the contrast agent arrives at the same time in the tumor and unaffected normal brain tissue and that tumor and nontumor tissue have equal MTT.[25,26] However, tumor vasculature is extremely variable and heterogeneous,[27] and elevated tumor MTT may cause overestimation of CBV and underestimation of K_2.[22,26] Therefore, Bjornerud et al[26] recently described a novel leakage-correction algorithm for evaluating microvascular permeability on DSC-PWI that is insensitive to MTT. However, the clinical value of such mathematically leakage-corrected DSC-PWI permeability parameters has to be determined in future studies and correlated with those from DCE-MR imaging.

Previous studies have demonstrated that CBV values significantly differ between PCNSL and GB, with only modest increased values in the former and markedly increased values in the latter group.[14,28-30] These results may be explained by the differences in neovascularization, which is a hallmark in GB,[31] however, an unusual feature in (non-AIDS-related) PCNSL.[32] Thus, the microvascular blood flow to the tumor tissue in GB is often hampered by an abnormal tumor vasculature due to neovascularization comprising immature or defective endothelium, tortuosity, and thrombosis. Hence, the uptake of contrast agent by the GB tissue is likely limited by blood flow.[10] In contrast, the absence of neovascularization and the substantial disruption of the BBB in

PCNSL is related to the clustering of tumor cells within and around pre-existing brain vessels (ie, angiocentric growth pattern).[33] These distinct morphologic differences may make the uptake of contrast agent in PCNSL less flow-limited compared with GB, which may serve as an explanation for the significantly higher K^{trans} and K_{ep} values in PCNSL in the present study.

A potential limitation of the present study is that due to the given section thickness of the DCE-MR imaging sequence, volume-averaging effects may have limited exact region-of-interest placement for precise delineation of the contrast-enhancing tumor. Another limitation is that DCE-MR imaging–derived vascular permeability parameters may be affected by several factors, including blood flow; blood volume; endothelial permeability; endothelial permeability surface area; and hydrostatic, interstitial, and osmotic gradients across the endothelium.[10] Thus, we could not definitely state whether changes in K^{trans} and K_{ep} were solely due to changes in vascular permeability or to what extent other factors may have contributed.

CONCLUSIONS

PCNSL demonstrated significantly higher K^{trans} and K_{ep} values compared with GB, thereby implying a higher vascular permeability in PCNSL. These findings correlate with underlying histopathologic features, with intact vascular integrity for GB and destroyed vessel architecture in PCNSL, thereby promoting vascular disintegrity in the latter group, and they may improve the preoperative differentiation of PCNSL and GB.

REFERENCES

1. Stupp R, Mason WP, van den Bent MJ, et al. **Radiotherapy plus concomitant and adjuvant temozolomide for glioblastoma.** *N Engl J Med* 2005;352:987–96
2. Schlegel U. **Primary CNS lymphoma.** *Ther Adv Neurol Disord* 2009;2:93–104
3. Tofts PS. **T1-weighted DCE imaging concepts: modelling, acquisition and analysis.** *MAGNETOM Flash* 2010;30–39
4. Nguyen TB, Cron GO, Mercier JF, et al. **Diagnostic accuracy of dynamic contrast-enhanced MR imaging using a phase-derived vascular input function in the preoperative grading of gliomas.** *AJNR Am J Neuroradiol* 2012;33:1539–45
5. Cha S, Yang L, Johnson G, et al. **Comparison of microvascular permeability measurements, K$^{\text{trans}}$, determined with conventional steady-state T1-weighted and first-pass T2*-weighted MR imaging methods in gliomas and meningiomas.** *AJNR Am J Neuroradiol* 2006;27:409–17
6. Mills SJ, Patankar TA, Haroon HA, et al. **Do cerebral blood volume and contrast transfer coefficient predict prognosis in human glioma?** *AJNR Am J Neuroradiol* 2006;27:853–58
7. Sorensen AG, Batchelor TT, Zhang WT, et al. **A "vascular normalization index" as potential mechanistic biomarker to predict survival after a single dose of cediranib in recurrent glioblastoma patients.** *Cancer Res* 2009;69:5296–300
8. Zhang W, Kreisl T, Solomon J, et al. **Acute effects of bevacizumab on glioblastoma vascularity assessed with DCE-MRI and relation to patient survival.** In: *Proceedings of the 17th Scientific Meeting and Exhibition of the International Society for Magnetic Resonance in Medicine,* Honolulu, Hawaii; April 18–24, 2009:282
9. Tofts PS, Kermode AG. **Measurement of the blood-brain barrier permeability and leakage space using dynamic MR imaging. 1. Fundamental concepts.** *Magn Reson Med* 1991;17:357–67
10. Cha S. **Update on brain tumor imaging: from anatomy to physiology.** *AJNR Am J Neuroradiol* 2006;27:475–87
11. Molnár PP, O'Neill BP, Scheithauer BW, et al. **The blood-brain barrier in primary CNS lymphomas: ultrastructural evidence of endothelial cell death.** *Neuro Oncol* 1999;1:89–100
12. Schramm P, Xyda A, Klotz E, et al. **Dynamic CT perfusion imaging of intra-axial brain tumours: differentiation of high-grade gliomas from primary CNS lymphomas.** *Eur Radiol* 2010;20:2482–90
13. Warnke PC, Timmer J, Ostertag CB, et al. **Capillary physiology and drug delivery in central nervous system lymphomas.** *Ann Neurol* 2005;57:136–39
14. Toh CH, Wei KC, Chang CN, et al. **Differentiation of primary central nervous system lymphomas and glioblastomas: comparisons of diagnostic performance of dynamic susceptibility contrast-enhanced perfusion MR imaging without and with contrast-leakage correction.** *AJNR Am J Neuroradiol* 2013;34:1145–49
15. Orton MR, d'Arcy JA, Walker-Samuel S, et al. **Computationally efficient vascular input function models for quantitative kinetic modelling using DCE-MRI.** *Phys Med Biol* 2008;53:1225–39
16. Louis DN, Ohgaki H, Wiestler OD, et al. **The 2007 WHO classification of tumours of the central nervous system.** *Acta Neuropathol* 2007;114:97–109
17. Patlak CS, Blasberg RG, Fenstermacher JD. **Graphical evaluation of blood-to-brain transfer constants from multiple-time uptake data.** *J Cereb Blood Flow Metab* 1983;3:1–7
18. Bagher-Ebadian H, Jain R, Nejad-Davarani SP, et al. **Model selection for DCE-T1 studies in glioblastoma.** *Magn Reson Med* 2012;68:241–51
19. Bergamino M, Saitta L, Barletta L, et al. **Measurement of blood-brain barrier permeability with T1-weighted dynamic contrast-enhanced MRI in brain tumors: a comparative study with two different algorithms.** *ISRN Neurosci* 2013;2013:6
20. Jain R, Bagher-Ebadian H, Narang J, et al. **Optimal period of linearity using Patlak analysis in brain tumors.** In: *Proceedings of the 18th Scientific Meeting and Exhibition of the International Society for Magnetic Resonance in Medicine,* Stockholm, Sweden; May 1–7, 2010:4090
21. Boxerman J, Schmainda K, Weisskoff R. **Relative cerebral blood volume maps corrected for contrast agent extravasation significantly correlate with glioma tumor grade, whereas uncorrected maps do not.** *AJNR Am J Neuroradiol* 2006;27:859–67
22. Boxerman JL, Prah DE, Paulson ES, et al. **The role of preload and leakage correction in gadolinium-based cerebral blood volume estimation determined by comparison with MION as a criterion standard.** *AJNR Am J Neuroradiol* 2012;33:1081–87
23. Weisskoff RM, Boxerman JL, Sorensen AG, et al. **Simultaneous blood volume and permeability mapping using a single Gd-based contrast injection.** In: *Proceedings of the 2nd Scientific Meeting and Exhibition of the International Society for Magnetic Resonance in Medicine,* San Francisco, California; August 6–12, 1994
24. Emblem K, Mouridsen K, Borra R, et al. **Does DSC-derived CA extravasation correlate with DCE Ktrans?** In: *Proceedings of the 19th International Society of Magnetic Resonance in Medicine,* Montreal, Quebec, Canada; May 6–13, 2011
25. Emblem KE, Bjornerud A, Mouridsen K, et al. **T(1)- and T(2)(*)-dominant extravasation correction in DSC-MRI. Part II. Predicting patient outcome after a single dose of cediranib in recurrent glioblastoma patients.** *J Cereb Blood Flow Metab* 2011;31:2054–64
26. Bjornerud A, Sorensen AG, Mouridsen K, et al. **T1- and T2*-dominant extravasation correction in DSC-MRI: part I–theoretical considerations and implications for assessment of tumor hemodynamic properties.** *J Cereb Blood Flow Metab* 2011;31:2041–53

27. McDonald DM, Choyke PL. **Imaging of angiogenesis: from microscope to clinic.** *Nat Med* 2003;9:713–25

28. Hartmann M, Heiland S, Harting I, et al. **Distinguishing of primary cerebral lymphoma from high-grade glioma with perfusion-weighted magnetic resonance imaging.** *Neurosci Lett* 2003;338:119–22

29. Wang S, Kim S, Chawla S, et al. **Differentiation between glioblastomas, solitary brain metastases, and primary cerebral lymphomas using diffusion tensor and dynamic susceptibility contrast-enhanced MR imaging.** *AJNR Am J Neuroradiol* 2011;32:507–14

30. Liao W, Liu Y, Wang X, et al. **Differentiation of primary central nervous system lymphoma and high-grade glioma with dynamic susceptibility contrast-enhanced perfusion magnetic resonance imaging.** *Acta Radiol* 2009;50:217–25

31. Wong ET, Brem S. **Antiangiogenesis treatment for glioblastoma multiforme: challenges and opportunities.** *J Natl Compr Canc Netw* 2008;6:515–22

32. Lister A, Abrey LE, Sandlund JT. **Central nervous system lymphoma.** *Hematology Am Soc Hematol Educ Program* 2002:283–96

33. Schlegel U, Hochberg F. **Primary CNS lymphoma.** In: Tonn JC, Westphal M, Rutka JT, et al, eds. *Neuro-Oncology of CNS Tumors.* Heidelberg, Germany: Springer-Verlag; 2006:292–302

Time Course of Axial and Radial Diffusion Kurtosis of White Matter Infarctions: Period of Pseudonormalization

T. Taoka, M. Fujioka, M. Sakamoto, T. Miyasaka, T. Akashi, T. Ochi, S. Hori, M. Uchikoshi, J. Xu, and K. Kichikawa

ABSTRACT

BACKGROUND AND PURPOSE: Diffusion kurtosis is a statistical measure for quantifying the deviation of the water diffusion profile from a Gaussian distribution. The current study evaluated the time course of diffusion kurtosis in patients with cerebral infarctions, including perforator, white matter, cortical, and watershed infarctions.

MATERIALS AND METHODS: Subjects were 31 patients, representing 52 observations of lesions. The duration between the onset and imaging ranged from 3 hours to 122 days. Lesions were categorized into 4 groups listed above. Diffusion kurtosis images were acquired with b-values of 0, 1000, and 2000 s/mm^2 applied in 30 directions; variables including DWI signal, ADC, fractional anisotropy, radial diffusivity, axial diffusivity, radial kurtosis, and axial kurtosis, were obtained. The time courses of the relative values (lesion versus contralateral) for these variables were evaluated, and the pseudonormalization period was calculated.

RESULTS: Diffusion kurtosis was highest immediately after the onset of infarction. Trend curves showed that kurtosis decreased with time after onset. Pseudonormalization for radial/axial kurtosis occurred at 13.2/59.9 days for perforator infarctions, 33.1/40.6 days for white matter infarctions, 34.8/35.9 days for cortical infarctions, and 34.1/28.2 days after watershed infarctions. For perforator infarctions, pseudonormalization occurred in the following order: radial kurtosis, ADC, axial kurtosis, and DWI.

CONCLUSIONS: Diffusion kurtosis variables in lesions increased early after infarction and decreased with time. Information provided by diffusion kurtosis imaging, including axial and radial kurtosis, seems helpful in conducting a detailed evaluation of the age of infarction, in combination with T2WI, DWI, and ADC.

ABBREVIATIONS: Dax = axial diffusivity; Drad = radial diffusivity; DKI = diffusion kurtosis imaging; FA = fractional anisotropy; Kax = axial kurtosis; Krad = radial kurtosis

Kurtosis is a descriptor of the "peakedness" of a variable relative to a Gaussian probability distribution. Higher kurtosis means that the distribution has a distinct peak near the mean and has heavy distribution tails, which are closely associated with diffusional heterogeneity.[1,2] Diffusion kurtosis can be calculated by a combination of >3 different strengths (b-values) of motion-probing gradients, by using cumulate expansion within a clinically feasible imaging time.[2] Diffusion kurtosis imaging (DKI) is reported to provide better characterization of normal and pathologic tissue, and it is less susceptible to free fluid contamination compared with mean diffusivity or fractional anisotropy (FA) provided by the diffusion tensor method.

DKI has recently been applied clinically for patients with ischemic stroke.[1,3] Hui et al reported that diffusion kurtosis increased in the acute-to-subacute phase after stroke onset.[4] They found that for lesions with strongly oriented axon bundles, the change in kurtosis along the direction of the fibers was greater than that occurring perpendicular to the direction of the fibers, and they speculated that this was due to a large decrease in the intra-axonal diffusivity.[3] However, to the best of our knowledge, the time course of diffusion kurtosis in humans has not been reported. The purpose of the current study was to evaluate the time course of diffusion kurtosis in patients with 4 types of infarctions, including perforator, white matter, cortical, and watershed infarctions, and to evaluate the period for pseudonormalization in the variables, including diffusion kurtosis. To evaluate the relationship between fiber bundle direction and changes in diffusion kurtosis, we attempted to evaluate diffusion kurtosis measured along the principal kurtosis eigenvector (axial kurtosis [Kax]) and that mea-

sured perpendicular to the principal kurtosis eigenvector (radial kurtosis [Krad]).

MATERIALS AND METHODS

Subjects of this prospective study comprised patients with cerebral infarction who underwent DKI between January and December 2012. Fifty-three patients were initially enrolled, but 22 were excluded due to the following criteria: 1) inability to determine the time of infarction onset, 2) treatment with thrombolytic agents, and 3) hemorrhage within the region of the infarction. Thirty-one patients (10 women and 21 men; 51–87 years of age) were therefore included in the analysis. Among these patients, 6 had >1 study for follow-up (5 patients had 2 studies and 1 had 4). Six patients had 2 lesions, 2 patients had 4, and we undertook 2 observations of 9 lesions and 4 of 1 lesion. Thus, 31 patients, representing 40 lesions and 52 observations with a known onset time, were included in the current analysis. The duration between infarction onset and imaging ranged from 3 hours to 122 days.

Imaging was performed with a 3T clinical scanner (Magnetom Verio; Siemens, Erlangen, Germany). The images obtained included T2WI (turbo spin-echo: TR = 4500 ms, TE = 90 ms, flip angle = 145°, FOV = 230 × 230 mm, matrix = 512 × 512, section thickness = 4.5 mm) and DKI (echo-planar: TR = 6600 ms, TE = 89 ms, b=0, 1000, 2000 s/mm^2, motion-probing gradient = 30 directions, FOV = 230 mm, matrix = 94 × 94, section thickness = 3 mm, acquisition time = 7.02 minutes [prototype product, provided by Siemens]). Motion correction by using rigid-body transformation was applied to the sequence. Output images from the diffusion kurtosis sequence included DWI, ADC, and fractional anisotropy, radial diffusivity (Drad, the diffusion coefficient perpendicular to the principal diffusion tensor eigenvector), axial diffusivity (Dax, the diffusion coefficient along the principal diffusion tensor eigenvector), Krad (diffusion kurtosis perpendicular to the principal diffusion tensor eigenvector), and Kax (diffusion kurtosis along the principal diffusion tensor eigenvector). Computation was performed automatically on the console workstation of the scanner immediately after scan completion. DWI, ADC, Drad, and Dax were calculated from the data by using b=1000 s/mm^2.

We categorized the lesions into 4 groups according to DWI: perforator infarctions, white matter territorial infarctions, cortical infarctions, and watershed infarctions. "Perforator infarctions" were defined as lesions smaller than 2 cm in diameter that were located in the perforator territory of the middle cerebral, basilar, or vertebral arteries. Thus, perforator infarctions included those in the basal ganglia, thalami, internal capsule, corona radiata, and brain stem. Territorial infarctions were defined as ischemic lesions that involved both the cortical and subcortical areas corresponding to an arterial territory. The term "white matter territorial infarction" was used for a lesion within the subcortical white matter of a territorial infarction. "Cortical infarction" signified a large cortical lesion that was part of a territorial infarction or a small lesion limited to the cortex. "Watershed infarctions" were defined as lesions occurring in the supraganglionic periventricular white matter within the borderzones of territories of >1 major artery. We diagnosed watershed infarctions by using DWI according to the templates of Bogousslavsky and Regli.[5]

Region-of-interest analysis was performed for lesions identified on DWI for each of the 4 groups. ROIs included the infarction lesion and consisted of areas with pixel values larger than 2 SDs of the contralateral side; ambiguous pixels were not included. The ROIs were selected by consensus among 3 neuroradiologists with 24, 17, and 8 years' experience. For all variables (T2WI signal, DWI signal, ADC, FA, Drad, Dax, Krad, and Kax), measurements were performed by averaging all pixels within the ROIs. For each variable, the ratio of the mean measurement in the region of interest in the ischemic tissue to that in the corresponding region of interest in the contralateral hemisphere was then calculated. The latter region of interest was set as an ellipsoid of the same size with an area corresponding to that of the lesion. In this way, T2WI signal ratio, DWI signal ratio, ADC ratio, FA ratio, Drad ratio, Dax ratio, Krad ratio, and Kax ratio were determined.

To evaluate gross changes in DKI with time in acute infarctions, we evaluated ratios of T2WI signal, DWI signal, ADC, FA, Drad, Dax, Krad, and Kax for the lesions at 2 time points: 1) within 10 days after infarction onset (early group, 31 observations) and 2) ≥11 days from the onset of infarction (late group, 21 observations), regardless of the type and location of infarctions. T tests were used to determine differences in these ratios between the early and late groups. Probability values < .05 were considered statistically significant.

To evaluate changes with time, we plotted the ratios of the above variables against duration (days) after infarction onset for the 4 infarction groups. To capture the period of pseudonormalization, we fitted the trend in each variable ratio to a line, by using the linear least-squares method, and we evaluated the time (days) for pseudonormalization of these variables by calculating when each ratio crossed the value of 1. We compared this pseudonormalization time for each variable and used t tests to determine whether the time points were statistically significantly different. We also calculated the absolute values of Krad and Kax.

RESULTS

Gross changes in DKI variables with time in acute infarctions between the early group and late group, regardless of the type and location of infarctions, are expressed as means as follows. Ratios of T2WI signal, ADC, Drad, and Dax were significantly greater in the late group than in the early group (T2WI signal— early versus late: 1.71 ± 0.39 versus 2.00 ± 0.47, P < .05; ADC: 1.39 ± 0.80 versus 0.63 ± 0.14, P < .001; Drad: 1.40 ± 0.65 versus 0.72 ± 0.21, P < .001; Dax: 1.12 ± 0.52 versus 0.68 ± 0.18, P < .01). Ratios of DWI signal, FA, Krad, and Kax were significantly greater in the early group than the late group (DWI signal— early versus late: 2.49 ± 0.67 versus 1.42 ± 0.99, P < .001; FA: 0.77 ± 0.41 versus 0.53 ± 0.31, P < .05; Krad: 1.45 ± 0.70 versus 0.79 ± 0.31, P < .001; and Kax: 1.88 ± 0.74 versus 1.07 ± 0.41, P < .001).

The breakdown of infarction type in the current study was as follows—perforator infarction: 18 patients, 19 lesions (corona radiata, 12; internal capsule, 3; caudate, 1; thalamus, 1; brain stem, 2) and 25 observations; white matter territorial infarction: 6 patients, 6 lesions (frontal, 3; parietal, 2; occipital, 1) and 8 observations; cortical infarction: 11 patients, 11 lesions (frontal, 6; parietal, 2; temporal, 1; and occipital, 2) and 15 observations; and watershed infarction: 3 patients, 4 lesions (corona radiata, 4) and
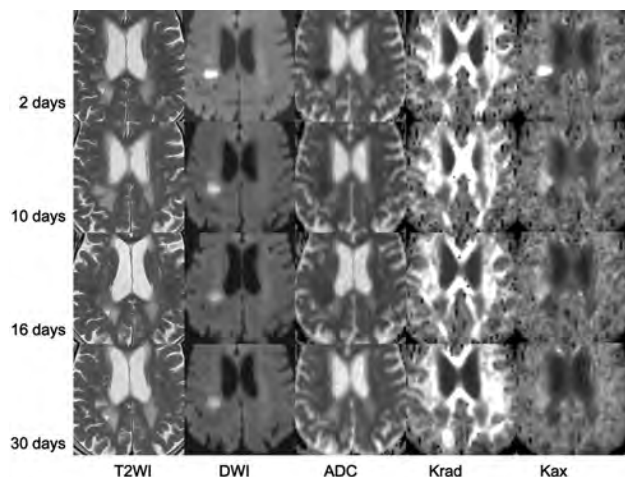
FIG 1. MR images from a 76-year-old woman with a right corona radiata infarction. Images (T2WI, DWI, ADC, Krad, Kax) were acquired on days 2, 10, 16, and 30 after onset of infarction. On T2WI, the lesion showed uniform high signal intensity. DWI demonstrated a prominent high-signal-intensity area, particularly on the image from day 2. The signal retained its high intensity even on the image from day 30. ADC was low immediately after infarction, and this became less obvious on the images from days 16 and 30. The white matter exhibited high Krad; in this case, the infarction showed higher values compared with the contralateral normal region. This elevation in Krad decreased soon after the infarction, and on the image from day 16, Krad was lower than that in the normal region. Kax values were similar in both white and gray matter, and Kax images appeared homogeneous. The infarction lesion showed a very high Kax value compared with the normal region immediately after the onset of infarction, but this soon diminished to the negative value shown in the later images.

4 observations. Figure 1 shows a representative patient for whom serial images could be obtained 4 times (a 76-year-old woman with a perforator infarction).

The time courses of the ratios of variables in the 4 groups are compared in Fig 2, in which a logarithmic scale was used for the time axis. Figure 3 shows the absolute values of Krad and Kax, with a logarithmic scale for the time axis. The plot for the T2WI signal ratio shows increased signal intensity with time after infarction onset in the perforator infarction, white matter territorial infarction, and cortical infarction groups. In these 3 groups, we noted the following patterns: DWI signal ratio was higher immediately after infarction onset and thereafter decreased with time. The ADC ratio tended to be lowest immediately after onset and increased with time, with faster pseudonormalization than in DWI signal ratio. Although the FA ratio tended to diminish with time, the trend was less obvious than for other variables. Drad and Dax ratios were lowest immediately after onset and increased with time, with a faster increase in Drad than in Dax. Krad and Kax ratios were highest immediately after onset and decreased with time, with a faster decrease in Krad than in Kax. The watershed infarction group, which had only 4 data points, did not show an obvious trend according to duration after infarction for DWI, ADC, T2WI, and FA ratios, with a low coefficient of determinations (R^2). On the other hand, Krad and Kax ratios in this group were higher immediately after onset and decreased with time. There was also an increasing trend in the Drad ratio of the watershed infarction group.

For all variables other than T2WI signal and FA ratio, which

did not show pseudonormalization, we evaluated the time for pseudonormalization by finding the point at which the fitted line crossed the line representing a ratio of 1.0. For perforator infarctions, pseudonormalization occurred at 67.2 days for DWI signal ratio, 22.9 days for ADC ratio, 15.9 days for Drad ratio, 37.3 days for Dax ratio, 13.2 days for Krad ratio, and 59.9 days for Kax ratio. For white matter territorial infarction, pseudonormalization occurred at 40.4 days for DWI signal ratio, 16.5 days for ADC ratio, 25.3 days for Drad ratio, 25.2 days for Dax ratio, 33.1 days for Krad ratio, and 40.6 days for Kax ratio. For cortical infarction, pseudonormalization occurred at 33.2 days for DWI signal ratio, 14.3 days for ADC ratio, 13.8 days for Drad ratio, 13.6 days for Dax ratio, 34.8 days for Krad ratio, and 35.9 days for Kax ratio. Although it consisted of only 4 time points, for watershed infarction, pseudonormalization was calculated to occur at 84.0 days for DWI signal ratio, 64.2 days for ADC ratio, 28.1 days for Drad ratio, 76.1 days for Dax ratio, 34.1 days for Krad ratio, and 28.2 days for Kax ratio. The pseudonormalization periods in all 4 groups are indicated by the numbers and arrows in Fig 2; Fig 4 shows the pseudonormalization periods with their SDs and the statistical difference ($P < .01$) between the variables.

DISCUSSION

The major hypothesis underlying the conventional diffusion imaging method is that diffusion shows a Gaussian distribution.[6,7] Although this hypothesis generally reflects tissue characteristics for clinical requirements, this conventional model cannot be used for complex microstructures within the tissue, including multiple barrier structures that lead to diffusion deviating from the Gaussian distribution. Acquiring the probability distribution of the water molecule can provide information about a complex barrier structure and help overcome this limitation of Gaussian modeling for diffusion imaging. Dedicated model-free methods for quantifying diffusion have been introduced, including q-space imaging, Q-ball imaging, and diffusion spectrum imaging, all of which place high demands on scanner hardware and require long acquisition periods.[8] Diffusion kurtosis is one way to analyze non-Gaussian distribution of the water molecule within tissues[2,9] and can be regarded as a biomarker of tissue heterogeneity.[2] Jensen and Helpern[1] and Jensen et al[2] reported that increased kurtosis in an ischemic lesion indicates an increase in the complexity or heterogeneity of the water microenvironment in the tissue. On the other hand, in an experimental model study exploring the time course of traumatic brain injury lesions, diffusion kurtosis was reported to increase in the subacute period, and this was shown to be associated with greater reactive astrogliosis.[10]

In the current study, the time course of T2WI and DWI signal and ADC showed a similar tendency to previous reports, in which the T2WI shows continuous high signal, while DWI shows high signal and ADC shows lower values in the early stage followed by pseudonormalization.[11-13] FA showed lower values and did not show pseudonormalization as reported in previous studies.[14,15] The plots in the current study suggested that the white matter infarctions generally showed higher ratios of diffusion kurtosis values soon after infarction onset, with the values falling to a level lower than those in normal tissue. These findings were similar to tendencies shown in an experimental study of infarctions in rats,
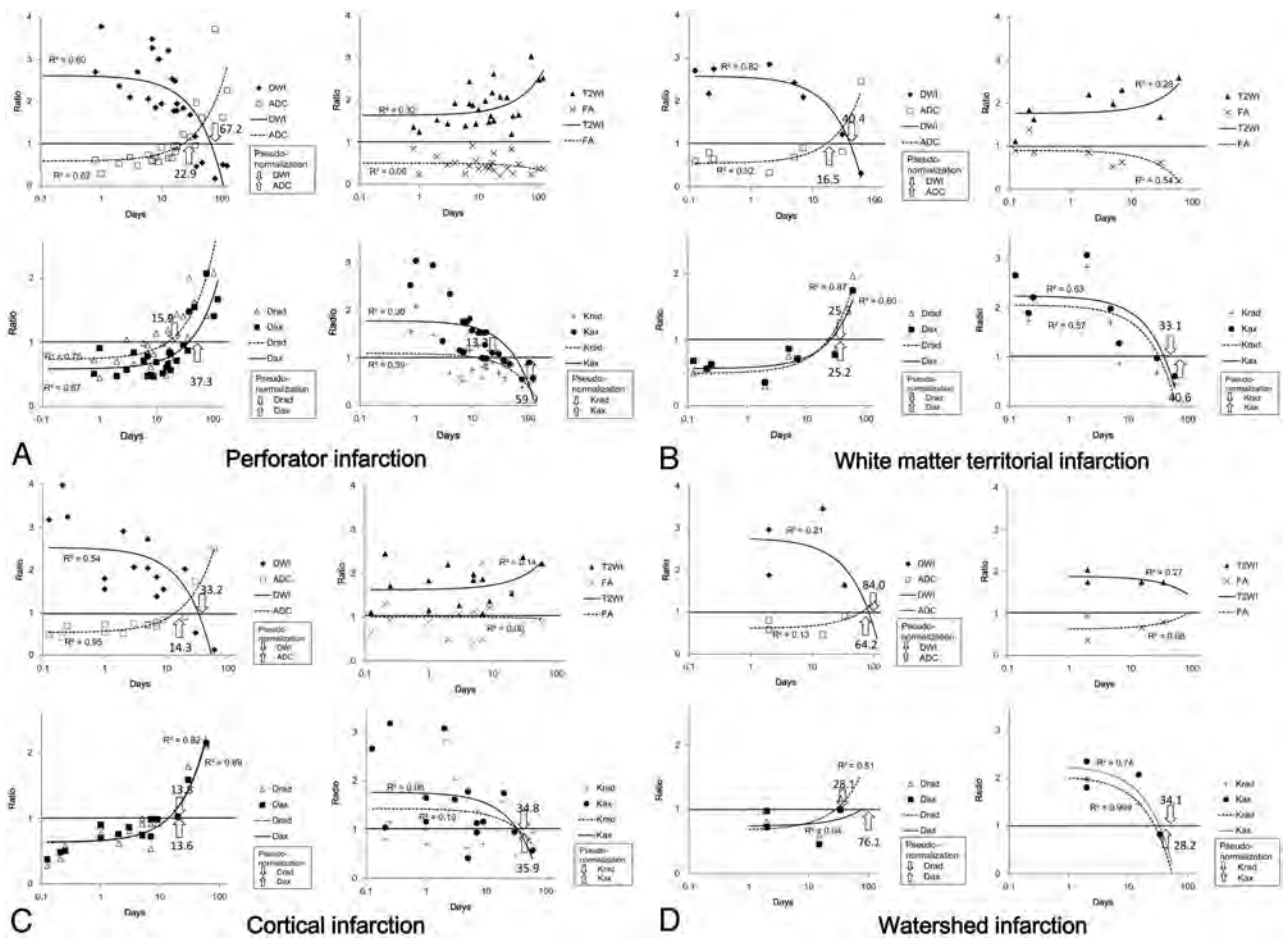
FIG 2. Plot of ratios (lesion versus normal tissue) of each variable and duration after onset of infarction. Linear regression lines are provided with their coefficient of determination (R^2). Because a logarithmic scale was used for the time axis, the first-order linear regression lines are drawn as exponential curves. *A*, Perforator infarction group. *B*, White matter territorial infarction group. *C*, Cortical infarction group. *D*, Watershed infarction group. For each variable (T2WI signal, DWI signal, ADC, FA, Drad, Dax, Krad, and Kax), the ratio of the value in the lesion compared with that in the contralateral normal tissue was plotted against time after infarction (days). The times at which pseudonormalization occurred are indicated by arrows. In general, T2WI showed increased signal intensity with time after infarction onset. DWI signal tended to be higher immediately after onset and decreased with time after infarction onset. ADC was lowest soon after onset and increased with time. Fractional anisotropy diminished throughout the observation period. Drad and Dax were lowest immediately after onset and increased with time; this increase was faster in Drad. Krad and Kax were highest immediately after onset and decreased with time.

in which diffusion kurtosis showed a higher value until 7 days after occlusion, whereas mean diffusivity showed pseudonormalization at days 1–2.[8] Specifically, when lesions in the current study were observed within a week after onset, the relative value of Kax, which represents diffusion kurtosis values along the principal diffusion kurtosis eigenvector, was higher than that of Krad. This observation suggests that the diffusive inhomogeneity of the axon direction increases in the early stage after infarction and exceeds that of diffusion kurtosis perpendicular to the fiber. In a preliminary human study, Jensen et al[3] reported that white matter infarction showed increased diffusion kurtosis with strong dependence on fiber tract orientation. They showed large increases in Kax in conjunction with small increases in Krad and speculated that these findings were due to large changes in intra-axonal diffusivity, which might have been related to either axonal varicosities or alterations associated with the endoplasmic reticulum. As shown in their report, the observed change in diffusion kurtosis was likely the result of the difference in membrane permeability at different time points after infarction onset.

We have observed the time courses for 4 different groups, including perforator, white matter, cortical, and watershed infarctions. For the perforator infarction group, in which most of the lesions (17 of 19) were located in the white matter, the time to pseudonormalization shown by lines fitted by using the linear least-squares method was the shortest for Krad, followed by Drad, ADC, Dax, Kax, and DWI signal, in increasing order. As shown in Fig 2*A*, ratios of Kax in this group tended to be larger than those of Krad in the early stage. Because the lesions in this group were small and most of the lesions in this group were located in the white matter, the lesion may be regarded as white matter infarction consisting of uniform fiber direction. In that sense, larger Kax can be explained by focal enlargement of axons as a result of osmotic imbalance, known as axonal swelling or "beading," which reduces the overall diffusivity along the fiber.[4,16] For both diffusivity and diffusion kurtosis, the values perpendicular to the nerve fiber (Drad, Krad) showed pseudonormalization earlier than those along the nerve fibers (Dax, Kax) in the perforator infarction group. This agreement may occur because the changes
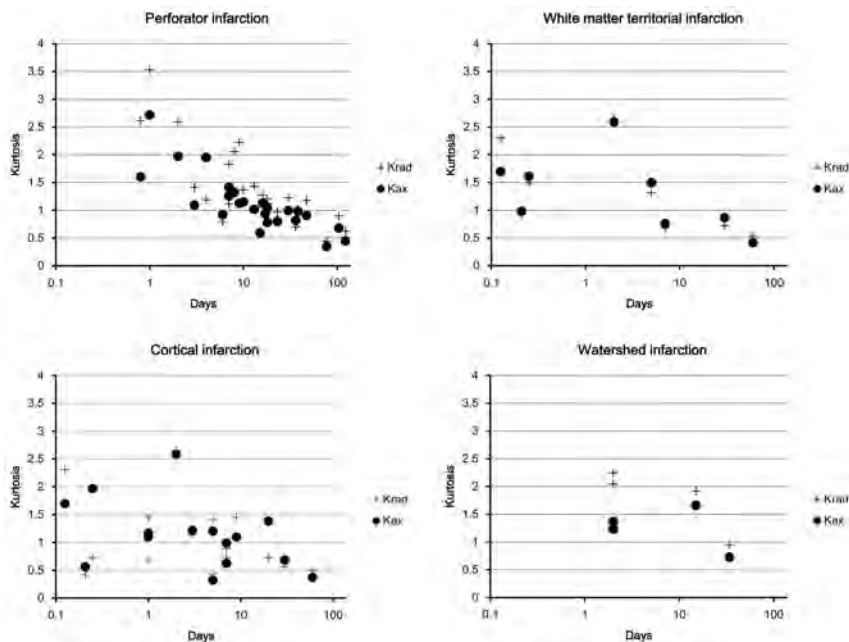
FIG 3. The absolute values of Krad and Kax (a logarithmic scale was used for the time axis). As was the case for the ratios, absolute values of these diffusion kurtosis variables were highest in the acute-to-subacute period and decreased until pseudonormalization, after which they fell further in the chronic period.

in the diffusivity observed in infarcted white matter may be dominated by the changes in diffusion kurtosis, and the alteration of water diffusivity may be mainly due to a drop in the intra-axonal diffusivity. Thus, infarction may have a greater effect on the interior of the axon than on its exterior.[4] In contrast, in the other groups including white matter, cortical, and watershed infarctions, earlier pseudonormalization in Drad or Krad compared with Dax or Kax was not clearly apparent. For cortical infarctions, this was probably due to the tissue structure, which lacks a uniform nerve fiber direction. In white matter infarctions including white matter territorial infarctions and watershed infarctions, the area of infarction contained a larger area with a variety of directions of fibers, which might have led to a difference in pseudonormalization between Drad/Krad and Dax/Kax.

The time course of diffusivity in infarcted tissue has previously been reported. One study found that signal intensity on DWI normalized approximately 14 days after symptom onset,[12] while another concluded that this variable normalized at 57 days and that the T2 shinethrough effect had a large contribution to the total infarct signal intensity— that is, the signal intensity of infarctions on DWI is mainly influenced by T2 relaxation and ADC.[17] ADC values decrease immediately after the onset of infarction, which is followed by pseudonormalization.[11,13,18-20] The reported period for ADC pseudonormalization varies among the types of infarction. Warach et al[19] reported pseudonormalization of ADC 5–10 days following an ischemic stroke. Huang et al[13] reported that ADC pseudonormalization following thromboembolic infarction began about 10 days after symptom onset but that this did not occur until about 1 month after symptom onset in watershed infarction. Due to the predictable time course of ADC after infarction, the age of an infarction can be estimated by using ADC.[21]

Similarly, in the present study, pseudonormalization for ADC oc-

curred later in watershed infarctions than in territorial or other types of infarctions. Pseudonormalization of diffusion kurtosis in experimental infarctions in rats has been demonstrated by Hui et al.[8] Although the progression of events after an ischemic insult in small animals such as rats is faster than that in humans and this model is, therefore, not directly comparable with the clinical situation, they reported that pseudonormalization of mean diffusion kurtosis occurred on day 7 after infarction onset, while that of mean diffusivity occurred on days 1–2. It was reported that the pseudonormalization of mean diffusivity could simply be due to vasogenic edema rather than to microstructural alterations and that this type of pseudonormalization was subject to error due to contamination from cerebral spinal fluid, whereas diffusion kurtosis might be a measure of specific structural changes during the degeneration process.[8] In clinical practice, the information obtained from diffusion kurtosis measurement seems to be especially useful in cases with small white matter infarctions as shown in the perforator group in the "Results" of the current study. The earlier pseudonormalization can help in detailed evaluation of the age of the infarction, in combination with T2WI, DWI, and ADC.

The current study has several limitations. The major limitation is the small number of cases. In particular, the number of lesions examined within 1 day after infarction onset was low; therefore, we could not evaluate the hyperacute phase in which increasing signal intensity on DWI and decreasing ADC are reported.[22] Although diffusion kurtosis has also shown a tendency to increase immediately after infarction in an experimental study of rats,[8] we could not show clear data to support this phenomenon in this series of patients. The number of patients with watershed infarction was also low, so the plots of ratios or pseudonormalization periods of variables might be less reliable than those for the other lesion types. Another limitation is that the characteristics of the lesions were rather heterogeneous. Although we categorized the lesions into 4 groups (perforator infarction, white matter territorial infarction, cortical infarction, and watershed infarction), we did not evaluate lesions separately according to their size or precise location. Regarding technical matters, the imaging sequence we used contained no eddy-current correction; however, because a twice-refocused sequence was used, eddy-current distortion was considered negligible. We used single b-value (1000 s/mm^2) for calculation of DWI, ADC, Drad, and Dax, instead of using DKI-derived diffusion metrics because of the limitation of our software. Therefore, we could not report on the differences between DTI-derived and DKI-derived diffusion metrics.

CONCLUSIONS
Diffusion kurtosis variables in lesions increased early after infarction and decreased earlier than DWI variables did. Krad showed
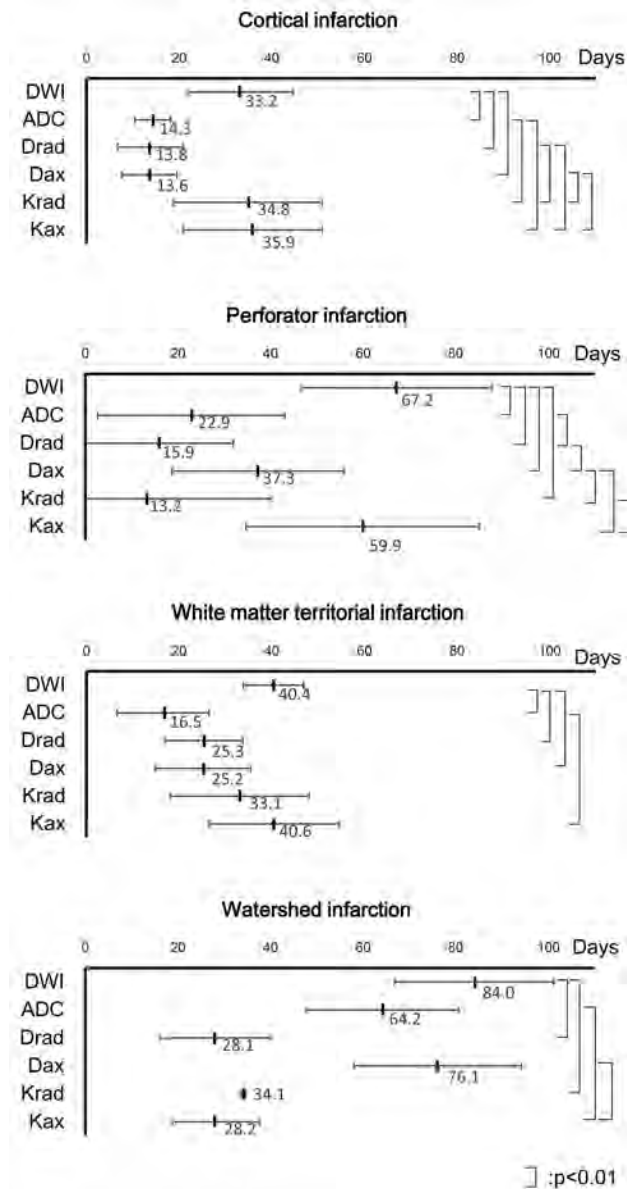
FIG 4. Pseudonormalization periods and their statistically significant differences between variables. Pseudonormalization periods of the 4 groups are shown with their SDs. A linear scale is used for the time axis. Statistical differences ($P < .01$) between the variables are shown.

pseudonormalization earlier than ADC did, and the pseudonormalization of Kax occurred a little later than that of ADC. Because DKI can have a different time course after the onset of infarction compared with DWI or ADC, additional information on white matter tissue infarction can be provided by using this imaging technique. Specifically, information provided by DKI, including Kax and Krad, appears helpful in conducting a detailed evaluation of the age of the infarction, in combination with T2WI, DWI, and ADC.

REFERENCES

1. Jensen JH, Helpern JA. **MRI quantification of non-gaussian water diffusion by kurtosis analysis.** *NMR Biomed* 2010;23:698–710
2. Jensen JH, Helpern JA, Ramani A, et al. **Diffusional kurtosis imaging: the quantification of non-Gaussian water diffusion by means of magnetic resonance imaging.** *Magn Reson Med* 2005;53:1432–40
3. Jensen JH, Falangola MF, Hu C, et al. **Preliminary observations of increased diffusional kurtosis in human brain following recent cerebral infarction.** *NMR Biomed* 2011;24:452–57
4. Hui ES, Fieremans E, Jensen JH, et al. **Stroke assessment with diffusional kurtosis imaging.** *Stroke* 2012;43:2968–73
5. Bogousslavsky J, Regli F. **Unilateral watershed cerebral infarcts.** *Neurology* 1986;36:373–77
6. Le Bihan D. **Looking into the functional architecture of the brain with diffusion MRI.** *Nat Rev Neurosci* 2003;4:469–80
7. Le Bihan D, Mangin JF, Poupon C, et al. **Diffusion tensor imaging: concepts and applications.** *J Magn Reson Imaging* 2001;13:534–46
8. Hui ES, Du F, Huang S, et al. **Spatiotemporal dynamics of diffusional kurtosis, mean diffusivity and perfusion changes in experimental stroke.** *Brain Res* 2012;1451:100–09
9. Hori M, Fukunaga I, Masutani Y, et al. **Visualizing non-Gaussian diffusion: clinical application of q-space imaging and diffusional kurtosis imaging of the brain and spine.** *Magn Reson Med Sci* 2012;11:221–33
10. Zhuo J, Xu S, Proctor JL, et al. **Diffusion kurtosis as an in vivo imaging marker for reactive astrogliosis in traumatic brain injury.** *Neuroimage* 2012;59:467–77
11. Schlaug G, Siewert B, Benfield A, et al. **Time course of the apparent diffusion coefficient (ADC) abnormality in human stroke.** *Neurology* 1997;49:113–19
12. Burdette JH, Ricci PE, Petitti N, et al. **Cerebral infarction: time course of signal intensity changes on diffusion-weighted MR images.** *AJR Am J Roentgenol* 1998;171:791–95
13. Huang IJ, Chen CY, Chung HW, et al. **Time course of cerebral infarction in the middle cerebral arterial territory: deep watershed versus territorial subtypes on diffusion-weighted MR images.** *Radiology* 2001;221:35–42
14. Axer H, Grassel D, Bramer D, et al. **Time course of diffusion imaging in acute brainstem infarcts.** *J Magn Reson Imaging* 2007;26:905–12
15. Harris AD, Pereira RS, Mitchell JR, et al. **A comparison of images generated from diffusion-weighted and diffusion-tensor imaging data in hyper-acute stroke.** *J Magn Reson Imaging* 2004;20:193–200
16. Murphy TH, Li P, Betts K, et al. **Two-photon imaging of stroke onset in vivo reveals that NMDA-receptor independent ischemic depolarization is the major cause of rapid reversible damage to dendrites and spines.** *J Neurosci* 2008;28:1756–72
17. Eastwood JD, Engelter ST, MacFall JF, et al. **Quantitative assessment of the time course of infarct signal intensity on diffusion-weighted images.** *AJNR Am J Neuroradiol* 2003;24:680–87
18. Warach S, Chien D, Li W, et al. **Fast magnetic resonance diffusion-weighted imaging of acute human stroke.** *Neurology* 1992;42:1717–23
19. Warach S, Gaa J, Siewert B, et al. **Acute human stroke studied by whole brain echo planar diffusion-weighted magnetic resonance imaging.** *Ann Neurol* 1995;37:231–41
20. Schwamm LH, Koroshetz WJ, Sorensen AG, et al. **Time course of lesion development in patients with acute stroke: serial diffusion- and hemodynamic-weighted magnetic resonance imaging.** *Stroke* 1998;29:2268–76
21. Lansberg MG, Thijs VN, O'Brien MW, et al. **Evolution of apparent diffusion coefficient, diffusion-weighted, and T2-weighted signal intensity of acute stroke.** *AJNR Am J Neuroradiol* 2001;22:637–44
22. Fiebach JB, Jansen O, Schellinger PD, et al. **Serial analysis of the apparent diffusion coefficient time course in human stroke.** *Neuroradiology* 2002;44:294–98

Calcified Cerebral Emboli, A "Do Not Miss" Imaging Diagnosis: 22 New Cases and Review of the Literature

B.S. Walker, L.M. Shah, and A.G. Osborn

ABSTRACT

BACKGROUND AND PURPOSE: Calcified cerebral emboli are a rarely reported but devastating cause of stroke and may be the first manifestation of vascular or cardiac disease. Our aim was to evaluate the diagnosis, prevalence, imaging appearance, presumed embolic source, treatment, and outcome of patients with calcified cerebral emboli.

MATERIALS AND METHODS: Our radiology information system was searched for all CT scans by using keywords "calcified," "emboli," and their permutations. The radiology information system was also searched to identify all "stroke" CT reports to calculate the prevalence of calcified cerebral emboli. We also performed a MEDLINE search to identify all published case reports.

RESULTS: Twenty-two cases were identified from our database, and 48 were cases reported from the literature. The middle cerebral artery was the site of 83% of calcified emboli. Presumed sources were calcific aortic stenosis (36%), carotid atherosclerotic plaque (30%), and mitral annular calcification (11%). Spontaneous embolism occurred in 86%. Surgical treatment was performed in 34% of patients. Sixty-four percent of the patients with calcified aortic stenosis underwent aortic valve replacement. Among those with identifiable arterial disease, 53% underwent endarterectomy. Forty-one percent of patients experienced at least 1 recurrent stroke. The prevalence of calcified cerebral emboli identified on stroke CT scans at our institution was 2.7%. Seventy-three percent of cases were correctly identified. Twenty-seven percent were misdiagnosed on initial interpretation, while 9% were overlooked on preliminary interpretation.

CONCLUSIONS: Calcified cerebral emboli are more common than previously assumed, are frequently overlooked or misinterpreted, affect clinical course when diagnosed, and carry substantial risk for recurrent stroke.

Calcified cerebral emboli are a rarely reported but potentially devastating cause of stroke and may be the first manifestation of vascular or cardiac disease. Proper identification can guide treatment toward preventing future embolic events, neurologic impairment, and death. Noncontrast CT of the head is the most common imaging procedure used as the initial assessment of suspected stroke. The first imaging report of calcified cerebral emboli was published in 1981.[1] Since then, there have been only 48 cases reported in the literature.[1-38]

The purpose of this study was to evaluate the diagnosis, prevalence, imaging appearance, presumed embolic source, treatment,

and outcome of patients with calcified cerebral emboli. We report the first comprehensive review of the literature and present the largest imaging series to date, to our knowledge. We demonstrate that these emboli are more common than previously assumed, are frequently overlooked, and carry substantial risk for recurrent stroke.

MATERIALS AND METHODS

In this institutional review board–approved study, our institutional radiology information system was searched for all noncontrast head CT scans obtained between 2001 and 2013 by using keywords "calcified," "emboli," and their permutations. Cases were identified and then reviewed by 2 board-certified neuroradiologists.

The radiology information system was also searched retrospectively for 12 consecutive months to identify all CT scan reports that contained the word "stroke" within the indication or body of the report. We reviewed all "stroke" NCCT scans and identified all cases with calcified cerebral emboli to calculate the prevalence among all patients obtaining a NCCT scan for stroke in the index period.
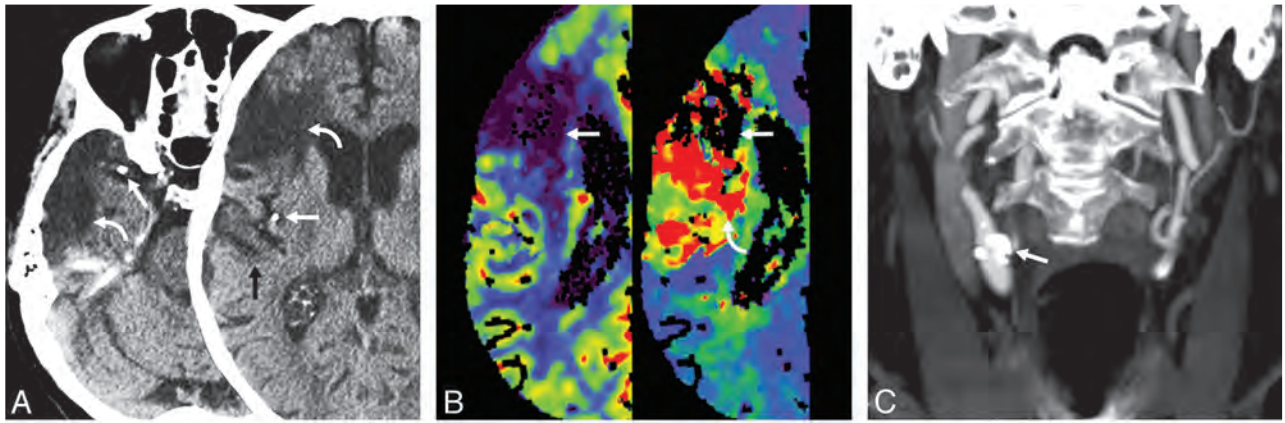
FIG 1. Case 1. An 84-year-old man with a known remote right MCA infarct had sudden onset of new strokelike symptoms. The noncontrast CT scan (*A*) shows calcified emboli (*straight arrows*) in the horizontal MCA segment and posterior division of the MCA with adjacent encephalomalacia (*curved arrows*). Subtle hypoattenuation of the adjacent gyrus is also present (*black arrow*). CT perfusion (*B*) shows the old infarction (*white arrows*) as a focal area of decreased cerebral blood volume (left). The new ischemic injury (*curved arrow, right*) is shown just posterior to the old infarction. Coronal MIP image (*C*) shows the calcific distal common proximal internal carotid artery plaque (*arrow*), which was identified as the probable source of emboli. NCCT (*D*) with initial scan (left) and follow-up scan (right) 1 day later shows interval migration of calcified embolus (*arrows*) within the right MCA. The patient underwent right carotid endarterectomy. Pathologic examination of the endarterectomy specimen revealed intimal proliferative material consisting of thrombotic debris, cholesterol clefts, dystrophic calcifications, and myxoid degeneration.
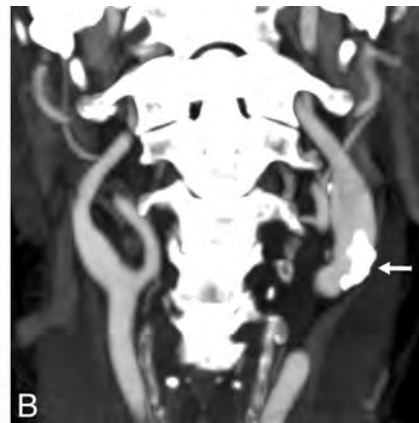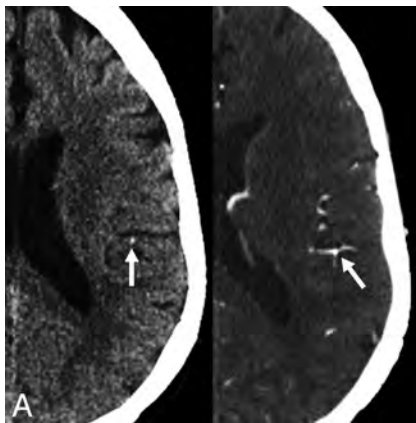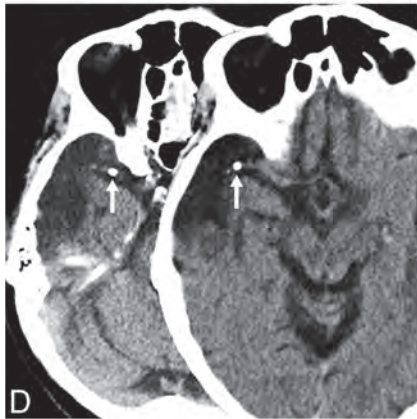
FIG 2. Case 2. Axial nonenhanced CT of the head (*A*, left) in a 59-year-old woman with acute-onset right hemiparesis shows a small hyperattenuated focus (*arrow*) that measured 101 HU, consistent with a calcific embolus within the posterior left frontal lobe. Axial CTA (*A*, right) confirms the intravascular location of the embolus. Coronal MIP CT angiogram of the neck (*B*) shows irregular calcified atherosclerotic plaque (*arrow*) within a dilated left carotid bulb and proximal internal carotid artery. The patient had surgical resection of the left carotid fusiform aneurysm and repair with a graft. Pathologic examination of the specimen disclosed a calcified and thickened wall with approximately 30% narrowing.

We also performed a MEDLINE search for "calcified" AND "emboli" AND "stroke" to identify all published case reports of calcified cerebral emboli diagnosed on imaging.

RESULTS

Twenty-two cases were identified from our institutional database, and 48 cases were identified in the literature. Seventy cases were used in our statistical analysis.

Demographics

Of the 70 cases, 61% were men and 39% women. The mean patient age was 66 years (range, 20–91 years). Sixty-eight (97%) of the 70 patients presented with neurologic symptoms concerning for stroke, while 2 patients (3%) had incidental findings of calcified emboli without acute symptoms. All 70 had noncontrast head CT scans (Fig 1). Twenty-one patients were further evaluated with CT angiography (Fig 2), and 27 patients, by MR imaging (Fig 3).

During the 12-month index period, 452 stroke head CT scans were obtained in our institution. Twelve of the 22 cases of calcified cerebral emboli occurred during this time. The prevalence of calcified cerebral emboli identified on stroke CT scans at our institution during the index period was 2.7%.

Location

The middle cerebral artery was the most common site with 83% of all calcified emboli located as follows: M1 (26%), M2 (24%), M3 (11%), and M4 (22%). The anterior (8%) and posterior (8%) cerebral arteries were the next most common sites. One calcified embolus (1%) lodged within the supraclinoid internal carotid artery.

Multiple calcified emboli were observed in 37% of patients (Fig 1). Bilateral emboli were observed in 13% of patients and were
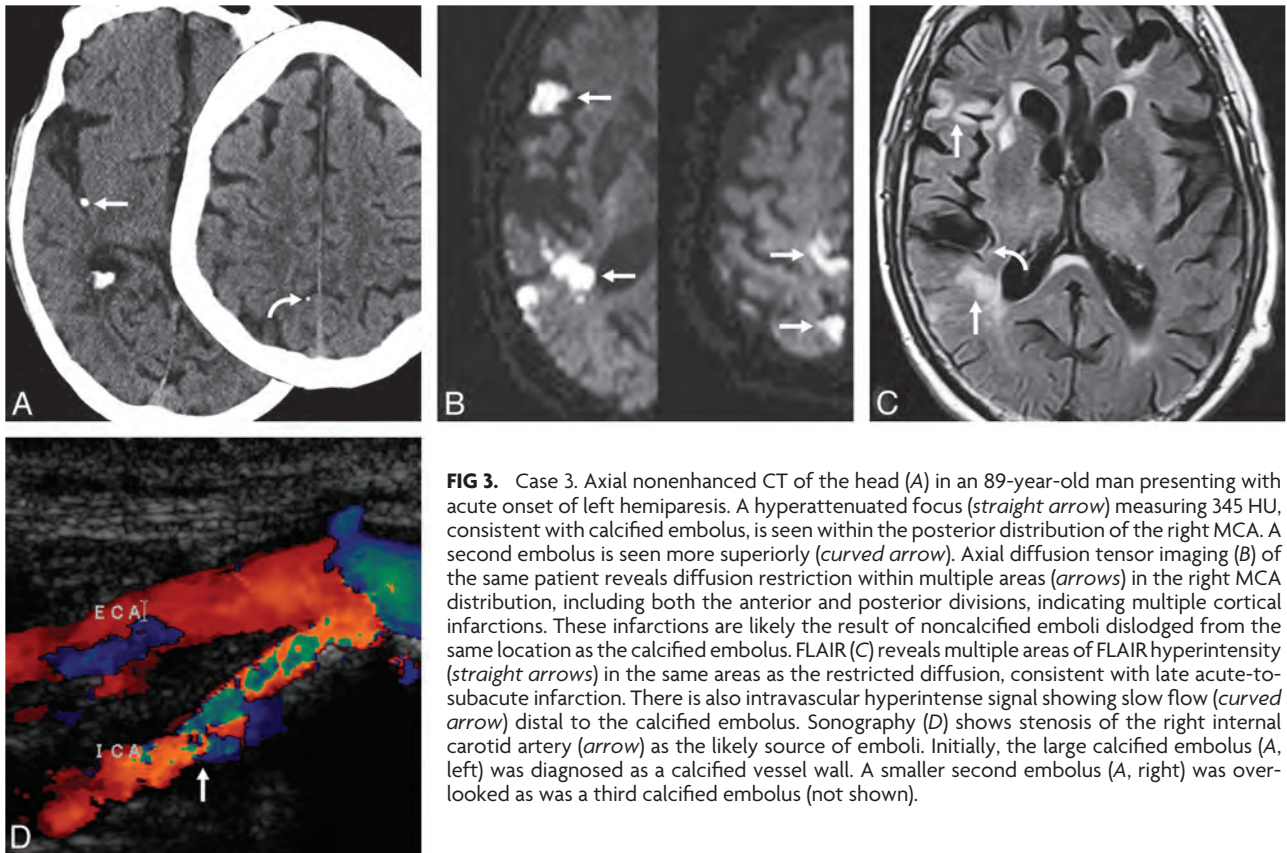
FIG 3. Case 3. Axial nonenhanced CT of the head (*A*) in an 89-year-old man presenting with acute onset of left hemiparesis. A hyperattenuated focus (*straight arrow*) measuring 345 HU, consistent with calcified embolus, is seen within the posterior distribution of the right MCA. A second embolus is seen more superiorly (*curved arrow*). Axial diffusion tensor imaging (*B*) of the same patient reveals diffusion restriction within multiple areas (*arrows*) in the right MCA distribution, including both the anterior and posterior divisions, indicating multiple cortical infarctions. These infarctions are likely the result of noncalcified emboli dislodged from the same location as the calcified embolus. FLAIR (*C*) reveals multiple areas of FLAIR hyperintensity (*straight arrows*) in the same areas as the restricted diffusion, consistent with late acute-to-subacute infarction. There is also intravascular hyperintense signal showing slow flow (*curved arrow*) distal to the calcified embolus. Sonography (*D*) shows stenosis of the right internal carotid artery (*arrow*) as the likely source of emboli. Initially, the large calcified embolus (*A*, left) was diagnosed as a calcified vessel wall. A smaller second embolus (*A*, right) was overlooked as was a third calcified embolus (not shown).

equally distributed between hemispheres. The maximum number of calcified cerebral emboli was 6, with an average of 1.7. Repeat imaging, when available, demonstrated distal migration of calcified emboli in 14% of cases. Following intravenous thrombolytic administration, 4 patients had lysis of a calcified embolus with distal migration of multiple calcified fragments that were identified on repeat scan.

Size, Density, and Configuration
The average diameter of emboli was 2.5 mm with a range of 1.0–5.5 mm. Mean embolus attenuation was 162 HU, with a range from 79 to 435 HU. All emboli were either round (82%) or ovoid (18%).

Source
Potential embolic sources were identified by using echocardiography, sonography, and CT angiography. Presumed sources were calcified aortic stenosis (36%), carotid atherosclerotic plaque (30%), mitral annular calcification (11%), aortic arch atherosclerotic plaque (4%), brachiocephalic artery atherosclerotic plaque (3%), and vertebral atherosclerotic plaque (1%). An embolic source was not reported in 14% of patients.

Eighty-six percent of calcified emboli were spontaneous, while 14% were identified as nonspontaneous events: 9% following left heart catheterization, 3% following carotid artery manipulation, and 3% following cardiopulmonary resuscitation.

Treatment
Heparin therapy was administered in 24% of all patients. Thrombolytic therapy was administered to 9 patients (13%). Postembolic surgical treatment was performed in 24 (34%) patients. Sixty-four per-

cent of surviving patients with calcified aortic stenosis underwent successful aortic valve replacement. Among those with identifiable arterial disease, 53% underwent successful endarterectomy.

Outcome
Data from the 22 cases at our institution showed that 43% of patients with initial CT evidence of calcified cerebral emboli subsequently experienced recurrent stroke, defined as >1 hospital presentation for stroke symptoms or imaging evidence of prior infarct on the initial study.

Nine patients received intravenous thrombolytic therapy with symptom improvement in 4 (44%) of 9. Residual neurologic impairment from calcified emboli occurred in 33% of cases. Complete neurologic recovery was seen in 29%. Sixteen percent of patients died during the initial hospitalization. In 23% of cases, there was no record or follow-up of neurologic outcome.

Diagnosis
Of the 22 cases at our institution, 73% were correctly identified as having calcified emboli on NCCT. Twenty-seven percent were misdiagnosed on initial NCCT interpretation as having hemorrhage, infectious, traumatic, or vascular calcification (Fig 3). These were only correctly diagnosed on the review for this study. Nine percent were overlooked on preliminary interpretation by the on-call radiology resident.

DISCUSSION
Noncontrast CT is the most frequently used technique to screen patients with a clinical diagnosis of acute "stroke." Initial NCCT

scan findings— even those obtained in the first 6 hours following ictus—are abnormal in most patients with acute ischemic stroke. Positive imaging findings include a hyperattenuating vessel with intraluminal thrombus (eg, the "attenuated MCA" sign and "dot" sign), cortical and/or basal ganglia edema with blurring of gray-white matter interfaces (eg, the "insular ribbon" and "disappearing basal ganglia" signs), and early mass effect with sulcal effacement.[39] To these widely recognized signs, we add a frequently overlooked but very important finding, calcified cerebral emboli.

Calcified emboli as a specific cause of stroke have been considered rare, with just 48 cases reported in the literature since the first description in 1981.[1] In a single calendar year, we identified ≥1 calcified emboli in 2.7% of all patients undergoing NCCT with the clinical indication of stroke. We also found that patients with documented calcified emboli are at significant risk for recurrent embolic infarcts, with nearly half (43%) experiencing at least 1 repeat stroke.

While previous reports have suggested that calcified cerebral emboli most commonly occur following manual dislodgement (eg, left heart catheterization, valve surgery, carotid artery manipulation), our data suggest that most of such strokes (86%) are spontaneous and occur in the absence of such provoking events.[4]

A putative embolic source could be identified in 86% of all reported cases. Cardiac valvular disease was more common than carotid atheromatous disease, with calcific aortic stenosis 3 times as common as mitral valve disease as the embolic source. More than one-third (34%) of patients with calcified emboli subsequently underwent a surgical intervention. Valve replacement was performed in nearly two-thirds of those with calcific aortic stenosis, and endarterectomy was performed in 53% of those with arterial disease.

Calcified cerebral emboli are often small (2–3 mm in diameter) and can be easily overlooked or mistaken for other diseases. More than one-quarter of cases at our institution were initially missed entirely or misinterpreted on initial evaluation. Common misdiagnoses included hemorrhage, vessel wall calcification, or infectious residua. All calcified emboli were significantly more attenuated (162 HU) than intraluminal thrombi (typically 50–70 HU) and were round or ovoid (not tubular or linear like vascular wall calcification). In no cases were parenchymal calcifications suggestive of neurocysticercosis or other infections identified.

Cardioembolic stroke is considered the most severe ischemic stroke subtype, with a high risk of recurrence and high mortality.[40] Patients with calcified cerebral emboli identified on NCCT should undergo further imaging to determine an embolic source because timely surgical intervention may prevent repeat ischemic episodes.

The retrospective nature of our radiology information system search may have led to bias because there is an increased sensitivity to identification of calcified emboli in our review of cases for this project. The residents and faculty at our institution have been educated on these findings and, therefore, have an increased awareness of identifying calcified emboli. This is evidenced by the fact that our index year accounts for more than half of all institutional cases in a 13-year period. Because we identified cases on the basis of search terms alone, it is assumed that a large number of cases were not identified that would otherwise have been included

had we visually searched through the thousands of NCCT scans obtained for stroke during the 13-year study period. This limitation suggests that reported calcified emboli in our radiology information system are probably a gross underestimation of the real disease prevalence.

CONCLUSIONS

Calcified cerebral emboli are more common than previously assumed and occur in nearly 3% of patients obtaining a head CT scan for stroke. They are also frequently misinterpreted or overlooked. Calcified cerebral emboli carry a substantial risk for recurrent stroke with almost half of all patients experiencing a subsequent event. When properly diagnosed, patients with calcified cerebral emboli may be able to undergo surgical correction of underlying cardiac or vascular disease to prevent recurrence. These findings support the need for increased recognition of calcified cerebral emboli and further imaging to establish a presumed source of emboli.

REFERENCES

1. Yock DH Jr. **CT demonstration of cerebral emboli.** *J Comput Assist Tomogr* 1981;5:190–96
2. Kapila A, Hart R. **Calcific cerebral emboli and aortic stenosis: detection of computed tomography.** *Stroke* 1986;17:619–21
3. Rancurel G, Marelle L, Vincent D, et al. **Spontaneous calcific cerebral embolus from a calcific aortic stenosis in a middle cerebral artery infarct.** *Stroke* 1989;20:691–93
4. Vernhet H, Torres GF, Laharotte JC, et al. **Spontaneous calcific cerebral emboli from calcified aortic valve stenosis.** *J Neuroradiol* 1993;20:19–23
5. O'Donoghue ME, Dangond F, Burger AJ, et al. **Spontaneous calcific embolization to the supraclinoid internal carotid artery from a regurgitant bicuspid aortic valve.** *Neurology* 1993;43:2715–17
6. Kirk GR, Johnson JK. **Computed tomography detection of a cerebral calcific embolus following coronary catheterization.** *J Neuroimaging* 1994;4:241–42
7. Doiron A, Blais C, Bonneau D. **Spontaneous cerebral embolus from a calcified aortic valve.** *AJR Am J Roentgenol* 1996;167:955–56
8. Shanmugam V, Chhablani R, Gorelick PB. **Spontaneous calcific cerebral embolus.** *Neurology* 1997;48:538–39
9. Mouton P, Biousse V, Crassard I, et al. **Ischemic stroke due to calcific emboli from mitral valve annulus calcification.** *Stroke* 1997;28:2325–26
10. Katsamakis G, Lukovits TG, Gorelick PB. **Calcific cerebral embolism in systemic calciphylaxis.** *Neurology* 1998;51:295–97
11. Mohammadkhani M, Schaefer P, Koroshetz W, et al. **Mitral annulus calcareous brain emboli.** *Neurology* 2000;54:817
12. Khaw N, Gailloud P. **CT of calcific cerebral emboli after carotid manipulation.** *AJR Am J Roentgenol* 2000;174:1467
13. Oliveira-Filho J, Massaro AR, Yamamoto F, et al. **Stroke as the first manifestation of calcific aortic stenosis.** *Cerebrovasc Dis* 2000;10:413–16
14. Kissela BM, Kothari RU, Tomsick TA, et al. **Embolization of calcific

thrombi after tissue plasminogen activator treatment. *J Stroke Cerebrovasc Dis* 2001;10:135–38

15. Martínez-Fernández E, Gil-Néciga E, Mir P, et al. **Spontaneous cerebral calcium embolism** [in Spanish]. *Rev Neurol* 2002;34:354–57

16. Lahey T, Horton S. **Massive left atrial calcification and devastating systemic emboli in a patient with chronic renal failure.** *Am J Kidney Dis* 2002;40:416–19

17. Debruxelles S, Sibon I, Rouanet F, et al. **Cerebral infraction by calcified embolism: a spontaneous complication of calcified aortic stenosis** [in French]. *Rev Neurol (Paris)* 2004;160(5 pt 1):582–84

18. Halloran JI, Bekavac I. **Unsuccessful tissue plasminogen activator treatment of acute stroke caused by a calcific embolus.** *J Neuroimaging* 2004;14:385–87

19. Gearry RB, Sharr JP, Avery SF. **Spontaneous calcific cerebral embolus.** *Australas Radiol* 2005;49:154–56

20. Moustafa RR, Antoun NM, Coulden RA, et al. **Stroke attributable to a calcific embolus from the brachiocephalic trunk.** *Stroke* 2006;37:e6–8

21. Kavanagh EC, Fenton DM, Heran MK, et al. **Calcified cerebral emboli.** *AJNR Am J Neuroradiol* 2006;27:1996–99

22. Sylaja PN, Hill MD. **Stroke due to calcific embolus following coronary angiography.** *Neurology* 2006;67:E16

23. Aoyama T, Ohtaki M, Nomura T, et al. **Artery-to-artery embolism due to ruptured calcified carotid plaque** [in Japanese]. *No Shinkei Geka* 2007;35:283–88

24. Bugnicourt JM, Bonnaire B, Lepage L, et al. **Stroke due to spontaneous calcified cerebral embolus as presenting feature of calcified aortic stenosis** [in French]. *J Mal Vasc* 2008;33:106–09

25. Schirmer CM, Thaler DE, Malek AM. **Stent-mediated wedging of a calcific embolus to recanalize an occluded middle cerebral artery: technical case report.** *Neurosurgery* 2008;63:E180–81, discussion E181

26. Mori M, Wakugawa Y, Yasaka M, et al. **Case with multiple brain infarcts due to calcified emboli from a calcified atheroma of the innominate artery** [in Japanese]. *Brain Nerv* 2008;60:955–61

27. Tardy J, Da Silva N, Glock Y, et al. **Neurological pictures. Stroke with calcium emboli related to a calcified stenosis of internal carotid artery.** *J Neurol Neurosurg Psychiatry* 2008;79:1273–74

28. Christian BA, Kirzeder DJ, Boyd J, et al. **Showered calcific emboli to the brain, the 'salted pretzel' sign, originating from the ipsilateral internal carotid artery causing acute cerebral infarction.** *Stroke* 2009;40:e319–21

29. Okazaki S, Sakaguchi M, Sugiyama Y, et al. **Ineffective thrombolytic therapy for calcified cerebral emboli originated from calcified internal carotid artery stenosis** [in Japanese]. *Rinsho Shinkeigaku* 2009;49:281–84

30. Roifman I, Glikstein RS, Rudski L. **Spontaneous cerebral embolism in a forty year old man: case report and review of the literature.** *J Am Soc Echocardiogr* 2009;22:1197.e1–3

31. Acha O, Novo F, Espina B, et al. **Spontaneous cerebral calcific embolus from the aortic arch.** *Clin Neurol Neurosurg* 2009;111:862–63

32. Yong SW, Lim TS, Hong JM, et al. **Migrating calcification on CT angiography: another sign of an embolic stroke.** *Eur Neurol* 2010;63:126

33. Konishi-Yakushiji M, Yakushiji Y, Kotooka N, et al. **Sonographic confirmation of the association between calcified cerebral emboli and mitral annular calcification.** *J Ultrasound Med* 2010;29:1507–10

34. Herskovitz M, Telman G, Carasso S, et al. **Ischemic stroke due to a calcified embolus from the mitral annular valve.** *Neurology* 2012;78:931

35. Gschwind M, Binaghi S, Zekeridou A, et al. **Neurological picture. Dispersion and 'salted pretzel sign' from thrombolysis of a spontaneous calcified embolus in an acute stroke.** *J Neurol Neurosurg Psychiatry* 2013;84:111–12

36. Chandran V, Pai A, Rao S. **Calcified embolism: a rare cause of cerebral infarction.** *BMJ Case Rep* 2013;2013:pii: bcr2013009509

37. Gokhale S, Lahoti S, Rojas R, et al. **Tissue plasminogen activator and calcific emboli.** *JAMA Neurol* 2013;70:642–43

38. Dandamudi VS, Thaler DE, Malek AM. **Cerebral embolus following chiropractic manipulation in a patient with a calcified carotid artery.** *J Neuroimaging* 2013;23:429–30

39. Osborn AG. **Acute cerebral ischemia—infarction.** *Osborn's Brain: Imaging, Pathology, and Anatomy.* Salt Lake City, Utah: Amirsys; 2013:180–91

40. Arboix A, Alió J. **Cardioembolic stroke: clinical features, specific cardiac disorders and prognosis.** *Curr Cardiol Rev* 2010;6:150–61

Hyperintense Basilar Artery on FLAIR MR Imaging: Diagnostic Accuracy and Clinical Impact in Patients with Acute Brain Stem Stroke

M. Gawlitza, U. Quäschling, C. Hobohm, J. Otto, P. Voigt, K.-T. Hoffmann, and D. Lobsien

ABSTRACT

BACKGROUND AND PURPOSE: FLAIR-hyperintense vessels are known to be a sign of sluggish collateral blood flow in hemispheric vessel occlusion. Additionally, they seem to have a prognostic implication. The aim of the current study was to evaluate the hyperintense configuration of the basilar artery (FLAIR-hyperintense basilar artery) as a marker of basilar artery occlusion and as a predictor of patient outcome.

MATERIALS AND METHODS: We retrospectively identified 20 patients with basilar artery occlusion who initially underwent MR imaging with subsequent DSA. The diagnostic accuracy of the FLAIR-hyperintense basilar artery sign was tested by 4 independent readers in a case-control design, and the relation among FLAIR-hyperintense basilar artery and DWI posterior circulation–ASPECTS, patient outcome, and patient survival was evaluated. To grade the extent of the FLAIR-hyperintense basilar artery sign, we generated a score by counting the number of sections from the basilar tip to the foramen magnum in which a hyperintense signal in the vessel lumen was present multiplied by the section thickness.

RESULTS: The FLAIR-hyperintense basilar artery sign showed moderate sensitivity (65%–95%) but very good specificity (95%–100%) and accuracy (85%–93%) for the detection of basilar artery occlusion. Substantial or excellent inter-reader agreement was observed (Cohen κ, 0.64−0.85). The FLAIR-hyperintense basilar artery inversely correlated with the posterior circulation–ASPECTS ($r = -0.67, P = .01$). Higher FLAIR-hyperintense basilar artery scores were associated with patient death (28.3 ± 13.7 versus 13.4 ± 11.1, $P < .05$).

CONCLUSIONS: The FLAIR-hyperintense basilar artery sign proved to be a valuable marker of vessel occlusion and may substantially support the diagnosis of basilar artery occlusion. The established FLAIR-hyperintense basilar artery score may be helpful for the prediction of individual patient survival.

ABBREVIATIONS: BAO = basilar artery occlusion; FHBA = FLAIR-hyperintense basilar artery; FHV = FLAIR-hyperintense vessel; pc-ASPECTS = posterior circulation–ASPECTS

FLAIR-hyperintense vessels (FHVs) are frequently observed in the M2-to-M4 segments of patients with acute ischemic stroke of the anterior circulation. They can be an indicator of occlusion,[1,2] reversible constriction,[3] or stenosis[4-6] of intra- and extracranial arteries, and they are identified as the absence of the typical "flow void" in the tortuous sulcal arteries on the cerebral surface.[2,7] It is hypothesized that the FHV sign is caused mainly by sluggish, slow blood flow and also by clot signal intensity, the latter as an effect of oxyhemoglobin.[8,9]

At the beginning, the FHV sign was mainly proposed as a very sensitive marker of vessel occlusion and of flow impairment in MCA stroke.[8,10-14] Publications dealing with its prognostic significance were rare[8,15] until Lee et al,[1] in 2009, observed a relation between the extent of the FHV and the amount of diffusion-perfusion mismatch in patients with MCA occlusions. They suggested that the FHV is an indicator of collateral flow besides its proved sensitivity for mere blood flow alterations. Since then, there have been several original studies[3,5,7,16-22] and 1 review[2] addressing the potential role of the FHV sign as an imaging biomarker of collateral circulation and as a predictor of patient outcome. Although some patients with basilar artery occlusion (BAO) in the low single-digit range were included in a few studies dealing with the diagnostic significance of the FHV sign,[10,12,14] the focus of these investigations has been on patients with MCA stroke. To date, neither the diagnostic nor the prognostic value of the FLAIR-hyperintense basilar artery (FHBA) sign has been investigated in a dedicated study, to our knowledge.

MATERIALS AND METHODS

Subjects

In a retrospective analysis, all patients with the diagnosis of an acute basilar artery occlusion in our department from January 2003 to January 2013 were identified. We included only patients with the following: proved occlusion of the basilar artery by DSA and/or contrast-enhanced MRA; DSA, at most, 12 hours from diagnosis; and MR imaging, including axial FLAIR and DWI sequences before DSA. Information about patient survival was gathered; if available, the modified Rankin Scale scores at discharge were assessed to evaluate patient outcome. mRS 0–2 was defined as favorable, and mRS 3–6, as unfavorable outcome. Detailed patient characteristics can be found in On-line Table 1. The diagnostic performance of the FHBA was tested by defining a control group: One control patient without BAO who had undergone MR imaging for suspected stroke, matched for age, sex, and MR imaging scanner type used, was randomly selected for each patient with proved BAO from the PACS, to reduce the pretest probability of the FHBA and to simulate a more realistic condition with patients examined for stroke without confirmation of BAO.[23] In 1 patient of the control group, an occlusion of the internal carotid artery with acute infarction in the MCA territory was present. The other patients in the control group showed no ischemia or acute infarction.

MR Imaging Protocol

Imaging was performed on either a 3T scanner (Trio; Siemens, Erlangen, Germany) or on a 1.5T MR imaging scanner (Gyroscan Intera; Philips Healthcare, Best, the Netherlands; and Magnetom Trio Symphony; Siemens) in a clinical setup with commercially available software and hardware. In most cases, a standardized stroke protocol consisting of axial DWI, axial FLAIR, axial gradient recalled-echo (T2* or SWI), DSC perfusion imaging, intracranial time-of-flight-angiography, and intra-/extracranial contrast-enhanced MRA was used. For DWI, echo-planar diffusion-weighted sequences with 2 b-values (0 s/mm^2 and 1000 s/mm^2) in 3 different directions were used (TR/TE = 2900–6000/74–113 ms; section thickness = 3-mm; in-plane resolution = 1.4×1.4–2.0×2.6 mm). FLAIR was performed with the following parameters: TR/TE = 8000–10,000/92–125 ms; section thickness = 3–5 mm; in-plane resolution = 0.9×0.9–1.0×1.5 mm.

Digital Subtraction Angiography

DSA studies were performed, in most cases, with a biplane (Axiom Artis BA; Siemens) and, in 1 case, a monoplane angiography unit (Innova 4100 flat panel; GE Healthcare, Milwaukee, Wisconsin). A diagnostic angiography of at least 1 vertebral artery was performed, followed by different therapeutic endovascular interventions for recanalization of the occluded vessel (On-line Table 1).

Image Analysis

For the analysis of the FHBA sign, only the FLAIR images of patients with BAO and their randomly selected control group without BAO were independently read the by 4 readers: 2 board-certified, subspecialized neuroradiologists with 13 (U.Q., reader 1) and 8 years (D.L., reader 2) and 2 radiologists-in-training (J.O.,

reader 3, and P.V., reader 4) with 3 years of experience in stroke imaging, respectively. Images were reviewed on a commercially available desktop computer with Mac OS X (Apple, Cupertino, California) and an open-source freeware 4D DICOM viewer (OsiriX; http://www.osirix-viewer.com).[24] Readers were fully blinded regarding patient information or MR imaging scanner. Visual hyperintensity of the basilar artery was graded on a 5-point Likert scale (1 = no, 2 = little, 3 = equivocal, 4 = distinct, 5 = sure). Scores of 4 and 5 were defined as positive FHBA signs.[23]

To grade the extent of the FHBA sign in patients with BAO, we generated a score (called the "FHBA score" in this article) by counting the number of sections from the basilar tip down to the foramen magnum, including the dominant vertebral artery, in which a hyperintense signal in the vessel lumen was present multiplied by the section thickness (eg, 3 sections with the FHBA at a section thickness of 5 mm would result in a score of 15). A possible elongation of the basilar artery, resulting in a diagonal cut of the vessel by the plane of the FLAIR sequence, was not taken into account. These measurements were performed in consensus by 2 readers with 8 (D.L.) and 4 years' (M.G.) experience in neuroradiologic imaging. The same readers calculated the posterior circulation–ASPECTS (pc-ASPECTS) on DWI sequences as published by Puetz et al[25] and Tei et al.[26] We subdivided the site of the BAO into proximal, middle, or distal, taking into account all available diagnostic modalities (ie, DSA, MR imaging, and, in several cases, CT).[27] We evaluated DSA datasets, grading the extent of vessel occlusion and subsequent revascularization by the TICI scale with TICI 2b and TICI 3 being defined as a successful reperfusion result.[28]

Statistical Analysis

Statistical analysis and graphics creation were performed with the Statistical Package for the Social Sciences, Version 20 (IBM, Armonk, New York) and GraphPad Prism 5 software (GraphPad Software, San Diego, California). The χ^2 test was used to compare categoric or nominal data, whereas continuous data were compared by using a Student unpaired t test and 1-way ANOVA. Pearson r was calculated for correlation analysis, in which 0–0.2 was defined as poor; 0.2–0.4, as weak; 0.4–0.6, as moderate; 0.6–0.8, as strong; and 0.8–1.0, as a very strong correlation. Inter-reader agreements were evaluated by using Cohen's κ; values of <0.00 indicated poor; 0.00–0.20, slight; 0.21–0.40, fair; 0.41–0.60, moderate; 0.61–0.80, substantial; and 0.81–1.00, excellent and/or almost perfect agreement. All continuous values are presented as mean ± SD. Receiver operating characteristic analysis was performed with the FHBA score as a test variable for the prediction of patient death and unfavorable outcome. For all tests, $P < .05$ was statistically significant.

RESULTS

Patient Characteristics

In total, 20 patients (7 men, 13 women) with proved BAO were included. The mean age was 65.5 ± 17.1 years (median, 69.0 years; range, 18–86 years). Four occlusions were localized at the basilar apex (20%); 12, in the middle (60%); and 4, at the proximal segment (20%). The mean time from MR imaging to DSA was 121.0 ± 105.1 minutes (median, 99.0 minutes; range, 50–541

Cross table with interobserver agreements (Cohen κ) among 4 readers[a]

	Reader 1	Reader 2	Reader 3	Reader 4
Reader 1	–	0.72	0.74	0.70
Reader 2	0.72	–	0.69	0.64
Reader 3	0.74	0.69	–	0.85
Reader 4	0.70	0.64	0.85	–

Note:— indicates not applicable.

[a] The FHBA sign was classified using the coding "positive FHBA sign" versus "equivocal" and "negative FHBA sign."

minutes). The mean time from symptom onset to MR imaging was 264.3 ± 263.9 minutes (median, 182 minutes; range, 20–923 minutes; 4 patients with unknown time of symptom onset). On initial DSA, 16 patients presented with TICI 0 (80%); 2 patients, with TICI 1 (10%); 1, with TICI 2a; and 1, with TICI 3 (patient 3, in whom vessel occlusion was already recanalized after IV thrombolysis). After DSA and intra-arterial recanalization procedures, respectively, 13 patients (65%) showed successful recanalization (6 patients with TICI 3, seven patients with TICI 2b), but in 7 patients (35%), only incomplete (2 patients with TICI 2a, two patients with TICI 1) or no reperfusion (3 patients with TICI 0) was achieved. Two complications related to DSA occurred (1 vessel perforation at the basilar apex, 1 complete in-stent thrombosis shortly after angiography), both fatal. Detailed patient records allowed retrospective mRS score calculation at discharge in 18 patients; 7 (38.9%) had a favorable outcome (1 patient with mRS 0, five patients with mRS 1, one patient with mRS 2) and 11 (61.1%) had an unfavorable outcome (2 patients with mRS 3, three patients with mRS 5, six patients with mRS 6). Information about patient survival was available in 19 of 20 patients; 13 patients survived and 6 died.

Diagnostic Value of FHBA Sign

Assigning visual hyperintensity ratings of 4 and 5 to a "positive FHBA sign" and 1, 2, and 3 to a "negative FHBA sign," we achieved the following sensitivity, specificity, and accuracy values for BAO: 70%, 100%, and 85% for reader 1; 65%, 95%, and 80% for reader 2; 85%, 95%, and 90% for reader 3; and 90%, 95%, and 93% for reader 4. Substantial-to-excellent interreader agreement measures (by using Cohen κ, 0.64–0.85; Table) were observed.

FHBA Sign, pc-ASPECTS, and Interacting Factors

If we took into account all available imaging studies of the 20 patients with proved BAO, the FHBA sign was unequivocally present in 17 (85%). The mean FHBA score was 18.5 ± 13.3 (median, 15.0; range, 0–45). Regarding the FHBA score and the BAO occlusion site, no significant relationship was evident. We did not observe a relationship between the preinterventional TICI grade and the FHBA; likewise, the FHBA score had no effect on the extent of vessel recanalization. Eighteen patients (90%) had DWI lesions on the initial MR imaging with a mean pc-ASPECTS of 6.2 ± 2.9 (median, 7.5; range, 0–10). The FHBA and pc-ASPECTS showed a highly significant negative correlation ($r = -0.67$; $P = .01$; Figs 1A, 2, and 3). All 3 patients without definitive FHBA signs showed a pc-ASPECTS of 8, each with a DWI lesion only in the pons.

Patient Outcome and Survival

There was a tendency toward a moderate correlation between the FHBA and mRS scores at discharge ($r = 0.41$; $P = .09$; Fig 1B), yet if one compared patients with favorable and unfavorable outcomes, no significant difference regarding mean FHBA scores between the groups was detected (Fig 1C). However, patient survival was associated with significantly lower FHBA values (13.4 ± 11.1 versus 28.3 ± 13.7; $P < .05$; Fig 1D). Whereas receiver operating characteristic analysis for patient outcome prediction revealed no statistically significant result (area under the curve, 0.71; $P = .15$), an area under the curve of 0.81 ($P < .05$) for the prediction of patient death was calculated. An optimal discrimination threshold for the FHBA score of ≥ 17.5 was determined, which yielded a sensitivity of 83% and a specificity of 77%. The odds ratio for patient death above the mentioned threshold value was 16.7.

pc-ASPECTS inversely correlated with mRS at discharge ($r = -0.45$; $P < .05$), and patients with favorable outcomes had significantly higher pc-ASPECTS than those with unfavorable outcomes (7.86 ± 1.87 versus 5.36 ± 3.01; $P < .05$; Fig 1D); also patient survival was associated with higher pc-ASPECTS (7.54 ± 1.66 versus 4.00 ± 3.34; $P < .01$).

No significant difference regarding the postinterventional TICI grade was observed between patients with favorable and unfavorable functionality outcomes or between patients who died or survived. Likewise, the time from symptom onset to MR imaging and from MR imaging to DSA showed no statistical disparity between those groups. Although not related to patient outcome, the site of the BAO had a significant effect on patient survival; 4 patients (100%) with proximal BAO died compared with 2 deaths if the occlusion was located in the midbasilar section (18%) and no deaths with an occlusion at the basilar apex ($P < .01$).

DISCUSSION

In our study population, the FHBA sign proved to be a reliable marker of BAO with moderate sensitivity (65%–95%) and with very good specificity (95%–100%) and accuracy (85%–93%), which could also be correctly identified by readers with lower experience levels. Concerning the FHBA sign in BAO, the available literature is scarce and only a few publications provide information about this specific condition. In a series of 74 patients with acute stroke, the FHBA sign was negative in 3 of 5 cases with vertebrobasilar ischemia.[7] In the same way, Maeda et al[12] and Toyoda et al[14] reported 3 cases of BAO, again, in patients with mainly MCA occlusions, with a negative FHBA sign, which they attributed to CSF pulsation artifacts in the prepontine cistern.[14] However, all these studies focused on patients with occlusion of the MCA. In the anterior circulation, the sensitivity of FHV for major vascular abnormalities—with reported values as high as 94%,[7] 96.7%,[14] or 100%[11]—is known to be comparable with that of 3D time-of-flight MRA,[10,29] but with a better accuracy and often shorter acquisition times. Cosnard et al,[10] therefore, even recommended the omission of time-of-flight MRA from the routine MR imaging diagnostics of stroke. As in our dedicated study, 3 patients (15%) with proved BAO did not show an unequivocally positive FHBA; therefore, we would not recommend that the diagnosis should be based solely on this sign.

When in doubt, additional MR angiography sequences are
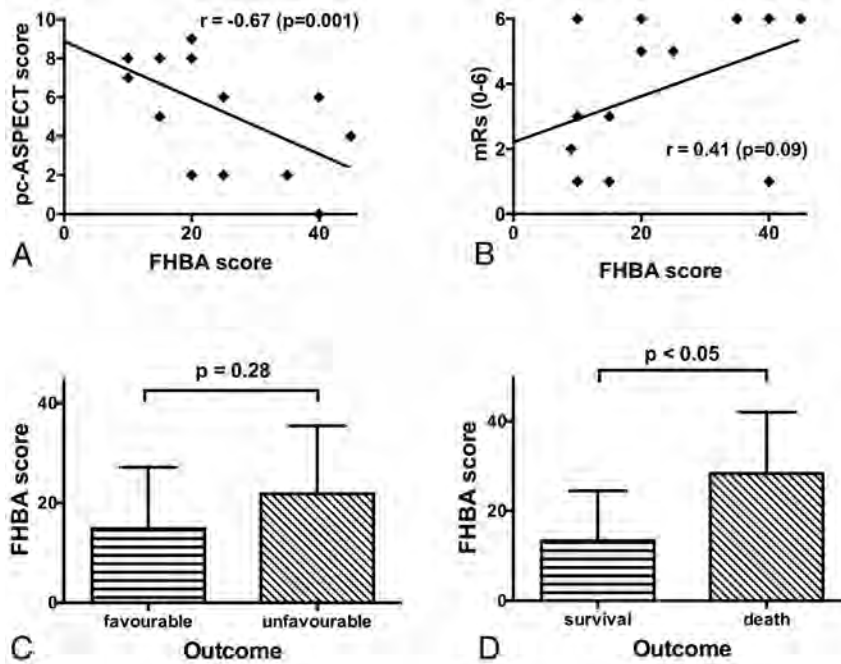
FIG 1. The FHBA score and its correlations with pc-ASPECTS (*A*) and mRS scores (*B*). *A*, A significant negative correlation between pc-ASPECTS and FHBA scores can be seen. *B*, Note a tendency for a correlation between FHBA and mRS; however, this was not significant at $P < .05$. In a comparison of FHBA between patients with favorable and unfavorable outcomes, a tendency toward higher scores with unfavorable outcomes was detected (*C*), yet there was no significant difference. *D*, Comparison between survival and patient death. Higher FHBA scores are significantly associated with death from BAO.
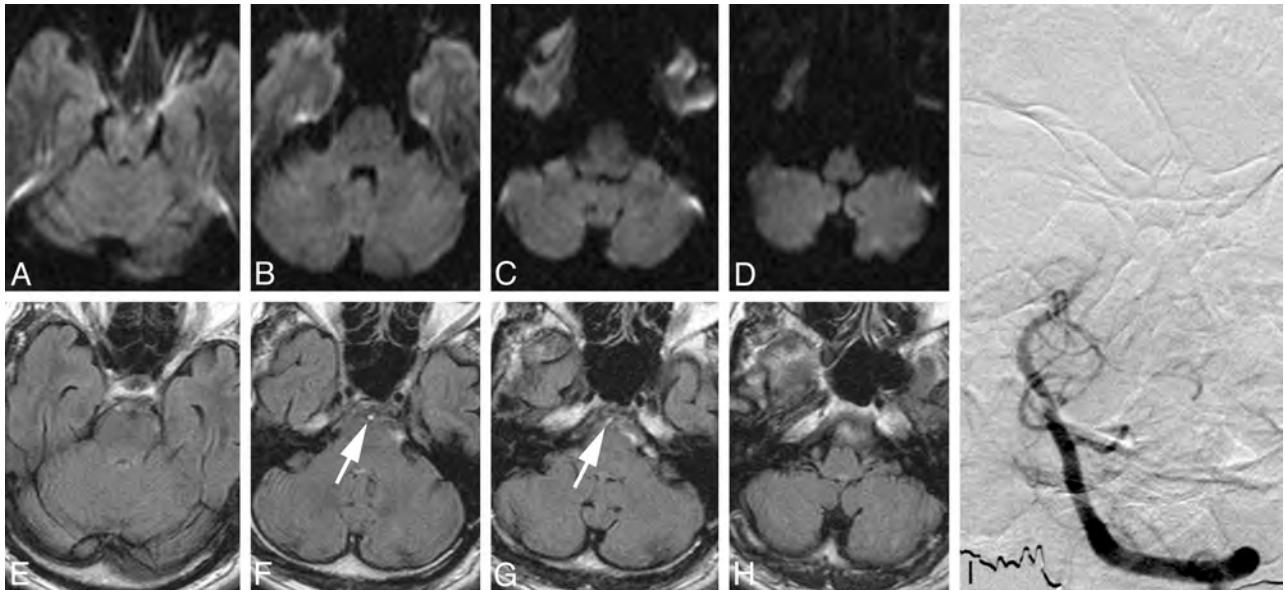
FIG 2. MR imaging and DSA of a patient with acute postural vertigo, double vision, and downbeat nystagmus. *A–D*, On axial DWI sections, no sign of acute infarction can be seen. *A–D*, Axial FLAIR images. *F* and *G*, A hyperintense basilar artery can be identified (*arrows*) and was graded with an FHBA score of ten. *I*, Anteroposterior left vertebral artery angiogram. Occlusion of the middle-to-superior segment of the basilar artery is shown. After intra-arterial administration of 30-mg rtPA, the patient recovered almost completely from his initial symptoms and left the hospital with slight residual gait ataxia (mRS 1).

necessary.[30,31] Nevertheless, we think that the FHBA sign is a valuable imaging characteristic that, if present and correctly identified, may support a fast diagnosis and avoid delay of a potentially lifesaving treatment.[32] The FHBA sign might be of particular importance if MR angiography is degraded by artifacts or if MR angiography is initially not scheduled, for example, in patients with atypical neurologic symptoms not suggestive of acute stroke.

Besides its diagnostic capabilities, the FHBA sign might also have prognostic relevance because high FHBA scores were associated with more extensive ischemic lesion patterns. This finding is in accordance with those in other publications that described the close relation between hyperintense vessels and larger DWI lesions in patients with stroke of the MCA territory. Also, a relation between the FHV and perfusion MR imaging was described,
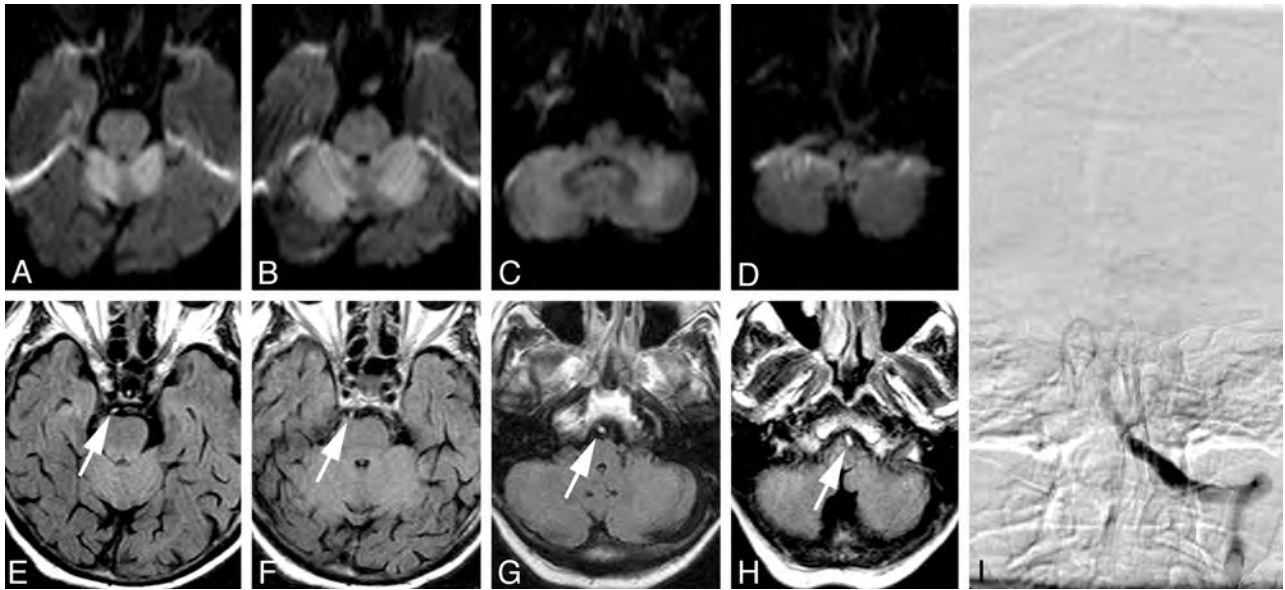
FIG 3. MR imaging and DSA of a patient who was found in a soporous state with anisocoria and fixed pupils. *A–D*, In axial DWI, extensive diffusion restriction (ADC maps not shown) can be identified in both cerebellar hemispheres (*A–C*), indicating acute cerebellar infarction. *E–H*, In axial FLAIR images, a hyperintense basilar artery can be identified throughout the course of the vessel, seen as a "bright dot" anterior to the brain stem, and was graded with an FHBA score of thirty-five. *I,* Anteroposterior left vertebral artery angiogram. Occlusion of the proximal-to-middle segment of the basilar artery is shown. The basilar artery could not be recanalized, and the patient died on the same day.

with a more pronounced FHV sign being associated with larger DSC perfusion imaging and mismatch volume[33]; FHV sign is, therefore, thought to be a marker of the amount of brain parenchyma with blood flow alteration and of potential salvageable tissue in MCA stroke.[1,2,7,11,13] Analogous to this, the extent of the FHBA sign might also be a marker of impaired hemodynamics in BAO with pronounced FHBA, meaning larger brain areas being hypoperfused; this more pronounced hypoperfusion could also explain larger DWI lesions, measured by the low pc-ASPECTS in our patient group. Unfortunately, because they were not performed in all of our patients and were several times distorted by motion artifacts, we had too few reliable perfusion studies available to directly address the connection among the FHBA sign, perfusion lesion size, and mismatch volumes; and it was beyond the scope of this article to investigate the meaning of the FHBA sign as an indicator of slow flow, collateral circulation, and tissue-at-risk. Furthermore, it was not the intention of the present study to relate the FHBA to the occlusion site (ie, whether it occurred proximal or distal or also at the level of the thrombus).[34] By analogy with hemispheric stroke,[7] the FHBA proximal to the occlusion site might be an expression of slow flow, whereas the FHBA distal to a thrombosis could be caused by retrograde perfusion of the basilar artery, for example, via the posterior communicating arteries. On the other hand, thrombus material can also be hyperintense on FLAIR images.[35] Concerning this topic, research projects comparing FLAIR images with perfusion MR imaging studies and DSA are necessary. In addition, follow-up MR imaging after thrombolysis might be interesting for further studies investigating whether wall abnormalities might play a role in the etiology of FHBA.

FHBA scores between patients with poor and good functional outcomes did not differ significantly, though there was a tendency toward good functional outcomes being associated with lower

FHBA scores (Fig 1*C*). The small patient sample might, at least partially, explain the lack of statistical significance. However, the FHBA score was significantly higher in deceased patients than in those who survived, a result also underpinned by the receiver operating characteristic analysis. To date, the prognostic role of the FHV sign in stroke (all published literature studied these hypotheses in patients with MCA stroke) is still under discussion. Whereas Lee et al[1] observed better outcomes in patients with distal FHV, several studies observed worse functional outcomes in patients with positive FHV signs.[11,15,17,33] These in part conflicting findings may result from different methodologic approaches. For example, Lee et al or Haussen et al[21] evaluated the significance of hyperintense vessels distal to the clot in occlusion of the MCA; Schellinger et al[8] published a study on several MR imaging vessel signs; and other investigators focused the prognostic value of the FHV sign, depending more on its presence or absence than on quantitative criteria.[11,17]

The baseline DWI pc-ASPECTS as a formerly described reliable and easy-to-apply scoring system for the prediction of patient outcome and survival[26,36] is confirmed by our data. Significantly higher pc-ASPECTSs were observed in patients with a good functional outcome and in patients who survived. Other DWI lesion scoring systems for BAO were not considered in our study, either because they do not account for supratentorial ischemic lesions[37] or because their increased complexity was considered to be a potential source of error in the image analysis.[38,39]

Also, the occlusion site was confirmed to be a predictor of patient outcome. Whereas all patients with an occlusion of the proximal basilar artery died, survival rates of 82% with an occlusion in the midbasilar section and 100% with a thrombus at the basilar tip were observed, which supports the results of previous studies, for example, by Cross et al[27] or Levy et al,[40] in which occlusions of the proximal basilar artery were considered to be

associated with patient death (eg, a survival rate of 71% in patients with distal versus 15% in patients with proximal and midbasilar clots reported by Cross et al). The postinterventional TICI score, time from symptom onset to imaging, and time from imaging to DSA were not related to patient outcome in our study in contrast to the reported data in earlier publications.[27,40,41]

Limitations of our study are the small patient number and its retrospective design. In addition, the lack of uniformity in the treatment regimens, ranging from intra-arterial rtPA with or without thrombus fragmentation to thrombus aspiration to stent retrievers, is a potential source of error. Furthermore, MR images were acquired on 3 different scanner types (including 1.5T and 3T). To date, no literature has been published concerning possible differences in the occurrence of the FHV sign at different field strengths. These issues should be evaluated in further studies on larger patient collectives and retrospective analyses of standardized stroke registries with a long-term recording of patient outcome.

CONCLUSIONS

The FHBA sign proved to be a reliable, moderately sensitive, but specific and robust sign of basilar artery occlusion that may have significant implications for the correct diagnosis of this potentially fatal condition. It is associated with more extensive DWI lesion patterns and may be helpful in the prediction of patient survival. However, larger patient studies are necessary to address these hypotheses.

REFERENCES

1. Lee KY, Latour LL, Luby M, et al. **Distal hyperintense vessels on FLAIR.** *Neurology* 2009;72:1134–39
2. Azizyan A, Sanossian N, Mogensen MA, et al. **Fluid-attenuated inversion recovery vascular hyperintensities: an important imaging marker for cerebrovascular disease.** *AJNR Am J Neuroradiol* 2011;32:1771–75
3. Chen SP, Fuh JL, Lirng JF, et al. **Hyperintense vessels on FLAIR imaging in reversible cerebral vasoconstriction syndrome.** *Cephalalgia* 2012;32:271–78
4. Iancu-Gontard D, Oppenheim C, Touzé E, et al. **Evaluation of hyperintense vessels on FLAIR MRI for the diagnosis of multiple intracerebral arterial stenoses.** *Stroke* 2003;34:1886–91
5. Liu W, Xu G, Yue X, et al. **Hyperintense vessels on FLAIR: a useful non-invasive method for assessing intracerebral collaterals.** *Eur J Radiol* 2011;80:786–91
6. Kawashima M, Noguchi T, Takase Y, et al. **Unilateral hemispheric proliferation of ivy sign on fluid-attenuated inversion recovery images in Moyamoya disease correlates highly with ipsilateral hemispheric decrease of cerebrovascular reserve.** *AJNR Am J Neuroradiol* 2009;30:1709–16
7. Sanossian N, Saver JL, Alger JR, et al. **Angiography reveals that fluid-attenuated inversion recovery vascular hyperintensities are due to slow flow, not thrombus.** *AJNR Am J Neuroradiol* 2009;30:564–68
8. Schellinger PD, Chalela JA, Kang D-W, et al. **Diagnostic and prognostic value of early MR imaging vessel signs in hyperacute stroke patients imaged <3 hours and treated with recombinant tissue plasminogen activator.** *AJNR Am J Neuroradiol* 2005;26:618–24
9. Wolf RL. **Intraarterial signal on fluid-attenuated inversion recovery images: a measure of hemodynamic stress?** *AJNR Am J Neuroradiol* 2001;22:1015–17
10. Cosnard G, Duprez T, Grandin C, et al. **Fast FLAIR sequence for detecting major vascular abnormalities during the hyperacute phase of stroke: a comparison with MR angiography.** *Neuroradiology* 1999;41:342–46
11. Kamran S, Bates V, Bakshi R, et al. **Significance of hyperintense vessels on FLAIR MRI in acute stroke.** *Neurology* 2000;55:265–69
12. Maeda M, Yamamoto T, Daimon S, et al. **Arterial hyperintensity on fast fluid-attenuated inversion recovery images: a subtle finding for hyperacute stroke undetected by diffusion-weighted MR imaging.** *AJNR Am J Neuroradiol* 2001;22:632–36
13. Tsushima Y, Endo K. **Significance of hyperintense vessels on FLAIR MRI in acute stroke.** *Neurology* 2001;56:1248–49
14. Toyoda K, Ida M, Fukuda K. **Fluid-attenuated inversion recovery intraarterial signal: an early sign of hyperacute cerebral ischemia.** *AJNR Am J Neuroradiol* 2001;22:1021–29
15. Girot M, Gauvrit JY, Cordonnier C, et al. **Prognostic value of hyperintense vessel signals on fluid-attenuated inversion recovery sequences in acute cerebral ischemia.** *Eur Neurol* 2007;57:75–79
16. Liu W, Yin Q, Yao L, et al. **Decreased hyperintense vessels on FLAIR images after endovascular recanalization of symptomatic internal carotid artery occlusion.** *Eur J Radiol* 2012;81:1595–600
17. Cheng B, Ebinger M, Kufner A, et al. **Hyperintense vessels on acute stroke fluid-attenuated inversion recovery imaging associations with clinical and other MRI findings.** *Stroke* 2012;43:2957–61
18. Pérez de la Ossa N, Hernández-Pérez M, Domènech S, et al. **Hyperintensity of distal vessels on FLAIR is associated with slow progression of the infarction in acute ischemic stroke.** *Cerebrovasc Dis* 2012;34:376–84
19. Huang X, Liu W, Zhu W, et al. **Distal hyperintense vessels on FLAIR: a prognostic indicator of acute ischemic stroke.** *Eur Neurol* 2012;68:214–20
20. Yoshioka K, Ishibashi S, Shiraishi A, et al. **Distal hyperintense vessels on FLAIR images predict large-artery stenosis in patients with transient ischemic attack.** *Neuroradiology* 2013;55:165–69
21. Haussen DC, Koch S, Saraf-Lavi E, et al. **FLAIR distal hyperintense vessels as a marker of perfusion-diffusion mismatch in acute stroke.** *J Neuroimaging* 2013;23:397–400
22. Olindo S, Chausson N, Joux J, et al. **Fluid-attenuated inversion recovery vascular hyperintensity: an early predictor of clinical outcome in proximal middle cerebral artery occlusion.** *Arch Neurol* 2012;69:1462–68
23. Connell L, Koerte IK, Laubender RP, et al. **Hyperdense basilar artery sign: a reliable sign of basilar artery occlusion.** *Neuroradiology* 2012;54:321–27
24. Rosset A, Spadola L, Ratib O. **OsiriX: an open-source software for navigating in multidimensional DICOM images.** *J Digit Imaging* 2004;17:205–16
25. Puetz V, Sylaja PN, Coutts SB, et al. **Extent of hypoattenuation on CT angiography source images predicts functional outcome in patients with basilar artery occlusion.** *Stroke* 2008;39:2485–90
26. Tei H, Uchiyama S, Usui T, et al. **Posterior circulation ASPECTS on diffusion-weighted MRI can be a powerful marker for predicting functional outcome.** *J Neurol* 2010;257:767–73
27. Cross DT, Moran CJ, Akins PT, et al. **Relationship between clot location and outcome after basilar artery thrombolysis.** *AJNR Am J Neuroradiol* 1997;18:1221–28
28. Higashida RT, Furlan AJ. **Trial design and reporting standards for intra-arterial cerebral thrombolysis for acute ischemic stroke.** *Stroke* 2003;34:e109–37
29. Gauvrit, Leclerc X, Girot M, et al. **Fluid–attenuated inversion recovery (FLAIR) sequences for the assessment of acute stroke.** *J Neurol* 2006;253:631–35
30. Mortimer AM, Saunders T, Cook J-L. **Cross-sectional imaging for diagnosis and clinical outcome prediction of acute basilar artery thrombosis.** *Clin Radiol* 2011;66:551–58

31. Röther J, Wentz KU, Rautenberg W, et al. **Magnetic resonance angiography in vertebrobasilar ischemia.** *Stroke* 1993;24:1310–15

32. Vergouwen MD, Algra A, Pfefferkorn T, et al. **Time is brain(stem) in basilar artery occlusion.** *Stroke* 2012;43:3003–06

33. Ebinger M, Kufner A, Galinovic I, et al. **Fluid-attenuated inversion recovery images and stroke outcome after thrombolysis.** *Stroke* 2012;43:539–42

34. Sanossian N, Hao Q, Liebeskind DS. **The thrombus and discontinuity of FLAIR vascular hyperintensity.** *Arch Neurol* 2011;68:950–51

35. Hu XY, Ge ZF, Zee CS, et al. **Differentiation of white and red thrombus with magnetic resonance imaging: a phantom study.** *Chin Med J (Engl)*. 2012;125:1889–92

36. Nagel S, Herweh C, Köhrmann M, et al. **MRI in patients with acute basilar artery occlusion: DWI lesion scoring is an independent predictor of outcome.** *Int J Stroke* 2012;7:282–88

37. Cho TH, Nighoghossian N, Tahon F, et al. **Brain stem diffusion-weighted imaging lesion score: a potential marker of outcome in acute basilar artery occlusion.** *AJNR Am J Neuroradiol* 2009;30:194–98

38. Renard D, Landragin N, Robinson A, et al. **MRI-based score for acute basilar artery thrombosis.** *Cerebrovasc Dis* 2008;25:511–16

39. Karameshev A, Arnold M, Schroth G, et al. **Diffusion-weighted MRI helps predict outcome in basilar artery occlusion patients treated with intra-arterial thrombolysis.** *Cerebrovasc Dis* 2011;32:393–400

40. Levy EI, Firlik AD, Wisniewski S, et al. **Factors affecting survival rates for acute vertebrobasilar artery occlusions treated with intra-arterial thrombolytic therapy: a meta-analytical approach.** *Neurosurgery* 1999;45:539–45

41. Brandt T, Kummer R von, Müller-Küppers M, et al. **Thrombolytic therapy of acute basilar artery occlusion variables affecting recanalization and outcome.** *Stroke* 1996;27:875–81

High-Resolution MRI Vessel Wall Imaging: Spatial and Temporal Patterns of Reversible Cerebral Vasoconstriction Syndrome and Central Nervous System Vasculitis

E.C. Obusez, F. Hui, R.A. Hajj-ali, R. Cerejo, L.H. Calabrese, T. Hammad, and S.E. Jones

ABSTRACT

BACKGROUND AND PURPOSE: High-resolution MR imaging is an emerging tool for evaluating intracranial artery disease. It has an advantage of defining vessel wall characteristics of intracranial vascular diseases. We investigated high-resolution MR imaging arterial wall characteristics of CNS vasculitis and reversible cerebral vasoconstriction syndrome to determine wall pattern changes during a follow-up period.

MATERIALS AND METHODS: We retrospectively reviewed 3T-high-resolution MR imaging vessel wall studies performed on 26 patients with a confirmed diagnosis of CNS vasculitis and reversible cerebral vasoconstriction syndrome during a follow-up period. Vessel wall imaging protocol included black-blood contrast-enhanced T1-weighted sequences with fat suppression and a saturation band, and time-of-flight MRA of the circle of Willis. Vessel wall characteristics including enhancement, wall thickening, and lumen narrowing were collected.

RESULTS: Thirteen patients with CNS vasculitis and 13 patients with reversible cerebral vasoconstriction syndrome were included. In the CNS vasculitis group, 9 patients showed smooth, concentric wall enhancement and thickening; 3 patients had smooth, eccentric wall enhancement and thickening; and 1 patient was without wall enhancement and thickening. Six of 13 patients had follow-up imaging; 4 patients showed stable smooth, concentric enhancement and thickening; and 2 patients had resoluton of initial imaging findings. In the reversible cerebral vasoconstriction syndrome group, 10 patients showed diffuse, uniform wall thickening with negligible-to-mild enhancement. Nine patients had follow-up imaging, with 8 patients showing complete resolution of the initial findings.

CONCLUSIONS: Postgadolinium 3T-high-resolution MR imaging appears to be a feasible tool in differentiating vessel wall patterns of CNS vasculitis and reversible cerebral vasoconstriction syndrome changes during a follow-up period.

ABBREVIATIONS: HRMRI = high-resolution MR imaging; RCVS = reversible cerebral vasoconstriction syndrome

Reversible cerebral vasoconstriction syndrome (RCVS) and CNS vasculitis are 2 distinct cerebrovascular disease entities with overlapping presenting symptoms of headache and, not uncommonly, neurologic deficits, which may be secondary to ischemic and/or hemorrhagic stroke.[1-4] Expeditious diagnosis is critical to discriminate the 2 disease entities to initiate appropriate and timely treatment.[4] In addition to clinical and laboratory work-up, DSA, MRA, and CTA are the preferred imaging modalities, essential to diagnosis and disease management. However, current vascular imaging fails to distinguish both entities, often due to shared nonspecific luminal findings on DSA, MRA, and CTA.[1,5]

Radiographic discrimination using current vascular imaging is difficult due to the relative thinness of intracranial vessel walls, at most, 1–2 mm thick in the largest intracranial vessels. The size scale is near the resolution limit of present imaging technology. While DSA provides superior resolution, it only images the vessel lumen. CTA and MR imaging, on the other hand, can image extraluminal tissue; however, the resolution is near the limit for imaging the vessel wall. Of these methods, MR imaging tends to be the technique of choice due to its superior soft-tissue contrast compared with CTA. Thus, the successful application of MR imaging to scan the vessel wall would require using a higher resolution than is routinely used in clinical practice while using standard clinical imaging hardware. This is accomplished by extending the technical parameters of a clinical MR imaging scanner as much as possible within the limits of the scan time and signal and is termed "high-resolution MR imaging" (HRMRI).

The utility of HRMRI in characterizing vessel wall patterns of

intracranial artery diseases has been investigated.[6-9] Recent studies have identified distinct characteristics of arterial wall thickening and wall enhancement in RCVS and CNS vasculitis.[6,7] While these studies have described spatial patterns on HRMRI, they have not described the temporal evolution of these diseases; this information could further aid diagnosis and management. The aim of this study was to describe the spatial patterns and temporal evolution of RCVS and CNS vasculitis by examining vessel wall characteristics during a follow-up period by using 3T-HRMRI and thereby assess the potential of HRMRI to serve as a surveillance technique to identify changes in wall morphology with disease progression or remission. We hypothesized that 3T-HRMRI vessel wall imaging may differentiate the spatial and temporal patterns of RCVS and CNS vasculitis.

MATERIALS AND METHODS
Patients
This single tertiary center study was approved by the institutional review board at our institution. Patients were identified from an electronic medical data base of 48 patients with intracranial vessel disease who underwent an HRMRI vessel wall imaging protocol between July 2009 and June 2012. Twenty-six patients with a known diagnosis of CNS vasculitis and RCVS were included in the study. Inclusion criteria comprised only patients with an established clinical diagnosis of RCVS and CNS vasculitis who underwent an HRMRI protocol. All diagnoses of RCVS and CNS vasculitis were confirmed to have met established RCVS experience-based guidelines and CNS vasculitis criteria,[1,11,12] by an expert rheumatologist (R.A.H.) and neuroradiologists (F.H., S.E.J.). A retrospective chart and imaging review was then conducted.

The experience-based guidelines used as criteria for RCVS were first proposed by Calabrese et al[1] and were subsequently adopted in the "International Classification of Headache Disorders: 2nd ed."[10] They include the following: 1) angiography, MRA, or CTA documenting multifocal segmental cerebral artery vasoconstriction; 2) no evidence of aneurysmal subarachnoid hemorrhage; 3) normal or near-normal CSF analysis; 4) severe, acute headaches, with or without additional neurologic signs or symptoms; and 5) reversibility of angiographic abnormality within 12 weeks after onset or postmortem examination to rule out vasculitis, intracranial atherosclerosis, and aneurysmal subarachnoid hemorrhage. Four patients had biopsy-proved CNS vasculitis; the remaining 9 patients met established criteria by Calabrese and Mallek[11] for CNS vasculitis. The criteria include the following: 1) the presence of an acquired, or otherwise unexplained, neurologic deficit after thorough clinical and laboratory evaluation; 2) documentation by cerebral angiography and/or histopathologic features of angiitis within the CNS; and 3) no evidence of systemic vasculitis or any condition with similar angiographic or pathologic features.

Intracranial Vessel Wall Protocol, Sequence, and Acquisition
All scans were obtained on 3T whole-body scanners (Skyra or Trio; Siemens, Erlangen, Germany) with a 20-channel coil. The protocol started with a standard multislab 3D TOF-MRA sequence centered in the circle of Willis for lumenographic identi-

fication of any stenosis. High-resolution imaging used 4 T1-weighted spin-echo sequences in the coronal, axial, and sagittal planes. The first was without contrast, followed by 3 with contrast (gadobutrol, Gadovist; Bayer Schering Pharma, Berlin, Germany): 1) a noncontrast T1 coronal 2-mm section with no gap (TR/TE = 11/544 ms), matrix = 256 × 256, and FOV = 130 × 130 mm; 2) a postgadolinium T1 coronal 2-mm section with no gap and fat suppression and a saturation band (TR/TE = 11/544 ms), matrix = 256 × 256, and FOV = 130 × 130 mm; 3) a postgadolinium T1 axial 2-mm section with no gap and fat suppression and a saturation band (TR/TE = 11/750 ms), matrix = 256 × 256, and FOV = 130 × 130 mm; and 4) a postgadolinium sagittal 2-mm section with a 0.4-mm gap and no fat suppression and a saturation band (TR/TE = 10/600 ms), matrix = 256 × 256, and FOV = 130 × 130 mm.

The resultant voxel size from the parameters was 0.51 × 0.51 × 0.2. The TR/TE parameters provided a black-blood technique for large-to-medium vessels. The protocol was designed for large-vessel evaluation (the middle cerebral arteries, basilar artery, and internal carotid arteries); however, smaller vessels were often interrogated. Due to the small size of each section, it was not practical to cover the entire brain in a clinically acceptable time; therefore, an imaging slab about 2 cm thick was selected to focus on only the large proximal vessels, with each major vessel viewed in both a longitudinal and transverse direction. If the TOF-MRA showed stenosis outside this default region, the imaging volume was adjusted accordingly or extra slabs were included. The TOF-MRA scan parameters were the following: matrix of 384 × 70, FOV of 200 × 150 mm, and section thickness of 0.50 (reconstructed). The resultant voxel sizes from the parameters were 0.74 × 0.52 × 0.80 (acquired) and 0.52 × 0.52 × 0.50 (reconstructed).

Image Analysis
Images were analyzed and interpreted on an Impax 6.0 PACS. A qualitative examination was initially performed by 2 experienced neuroradiologists (F.H., S.E.J.) blinded to clinical data, who rereviewed stenosis on TOF-MRA and then vessel wall pathology on HRMRI vessel wall images individually and then with consensus reading on the same workstation. They recorded the following properties: the location of pathology, the presence and character of wall thickening (including length and shape, either concentric or eccentric), and the presence and character of wall enhancement. The presence or absence of enhancement was determined by comparing pregadolinium and postgadolinium vessel wall imaging. The strength and pattern of enhancement on the postgadolinium images was considered unequivocal when found in >1 imaging plane. If enhancement was present, the strength of the enhancement was classified qualitatively on a 2-point scale as mild or strong and the pattern of enhancement, as concentric or eccentric. We subjectively determined the following on postgadolinium MR imaging; no enhancement if enhancement was absent, mild enhancement if there was thin-wall artery hyperintensity, and strong enhancement if there was thick-wall artery hyperintensity. Concentric enhancement was defined when the artery wall pattern was uniform and circumferential and distributed evenly along entire circumference of the wall. Eccentric enhance-

ment was defined as clearly nonuniform and noncircumferential, on 1 side of the vessel and not involving the entire circumference. The length of enhancement was measured in millimeters for each lesion by using the utility tool. MRA findings were compared with the HRMRI findings for concordance of abnormalities. The degree of stenosis expressed as a percentage was determined by using North American Symptomatic Carotid Endarterectomy Trial criteria[12] calculation [(Da-Db) / Da], where Da is the lumen diameter of a normal vessel and Db is the diameter of stenosed vessel to the normal vessel. It was determined to be mild if the stenosis was < 10%–29%, moderate if between 30% and 69%, severe if greater than 70%–99%, and occluded when a long flow void was seen in the vessel.

Demographic and Clinical Variables

The collected clinical and demographic data included age, sex, race, date of symptom onset, diagnosis, date of diagnosis, and medications.

RESULTS

Clinical and Demographic Data

Twenty-nine patients had an established clinical diagnosis of intracranial disease. Of these, 13 patients were diagnosed with RCVS; and 13 patients, with CNS vasculitis. The median age in the RCVS group was 52 years (range, 15–61 years) with 85% female, and 9 (69%) patients had follow-up imaging during a median period of 3 months. The median time from presentation to vessel wall imaging for RCVS was 0.5 months (range, 0.2–2.6 months) (On-line Table 1). The median age in the CNS vasculitis group was 42 years (range, 18–69 years) with 23% female, and 6 (46%) patients had follow-up imaging during a median time of 11.5 months. The median time from presentation to vessel wall imaging for CNS vasculitis was 9 months (range, 1.5–171 months).

Disease management in the RCVS group included all patients receiving oral verapamil as treatment until resolution of symptoms or as long-term maintenance therapy (On-line Table 2). In the CNS vasculitis group, initial treatment included an immunosuppressant at diagnosis and maintenance immunosuppressant therapy. Initially, glucocorticoids were used intravenously (high-dose methylprednisolone) in 39% (n = 5) of patients, and high-dose prednisone was used in 46% (n = 6) of patients. Each patient then received ≥1 dose of other immunosuppressants, which included azathioprine, mycophenolate mofetil, and cyclophosphamide. Seventy-seven percent (n = 10) of the patients received steroids for a median of 27 months (range, 5–156 months), 23% of patients (n = 3) received mycophenolate for a median of 10 months (range, 9–96 months), 62% of patients (n = 8) received cyclophosphamide for a median of 5.5 months (range, 1–12 months), and 54% of patients (n = 7) received azathioprine for a median period of 22 months (range, 1–78 months).

HRMRI Vessel Imaging and TOF-MRA Findings

Intracranial Vasculitis. In ≥1 artery, 9 patients had predominantly smooth, concentric wall enhancement and thickening; 3 patients had smooth, eccentric wall enhancement and thickening; and 1 patient had no wall enhancement or thickening. The diagnosis of CNS vasculitis was confirmed according to the proposed criteria by Calabrese and Mallek.[11] Sample images of smooth concentric wall enhancement and thickening pregadolinium and postgadolinium are shown in On-line Fig 1. Two of the 9 patients with concentric enhancement had multivessel enhancement. On MRA, these 9 patients revealed varying lumen characteristics of mild-to-severe focal stenosis, diffuse irregular narrowing, and occlusion. Each of these areas of narrowing, stenosis, and occlusion on MRA corresponded to the areas of thickening and enhancement on HRMRI.

A sample HRMRI showing wall enhancement and thickening in >1 imaging plane with corresponding MRA stenosis is shown in On-line Fig 2. MRA of 2 of the 3 patients with eccentric enhancement showed no luminal vessel abnormality, while 1 patient had narrowing and stenosis. The 1 patient without arterial wall thickening and enhancement on HRMRI had no luminal abnormality on corresponding MRA. For all 13 patients, the median length of enhancement was 6.1 mm (range, 3–14 mm). These enhancing segments were mostly unilateral and localized to the anterior cerebral artery, middle cerebral artery, supraclinoid ICA, and terminal ICA. These findings were less frequent in the posterior cerebral artery, basilar artery, and the vertebral artery.

Six patients had follow-up HRMRI, as summarized in On-line Table 2. The median length of enhancement for these 6 patients was 10.8 mm (range, 2.4–13 mm). Of these, 2 patients showed resolution of enhancement, while the remaining 4 patients showed stable but persistent smooth, concentric wall enhancement and thickening during a median follow-up period of 13.5 months (range, 11–16 months). MRA of these 4 patients showed 1 patient with resolution of the initial stenosis and 3 patients with stable narrowing and stenosis. The 2 patients with resolution of smooth, concentric wall enhancement and thickening were re-imaged at 7 months and 7.5 months (Fig 1). On MRA, one patient had complete resolution while the other patient had near resolution of initial stenosis.

Reversible Cerebral Vasoconstriction Syndrome

Thirteen patients were diagnosed with RCVS by using RCVS criteria.[1,10] The arterial wall findings on initial high-resolution imaging included 10 patients with diffuse, uniform wall thickening, of which 4 showed mild enhancement. Three patients had no arterial wall abnormality. These patterns were found mostly in a bilateral multivessel distribution (Fig 2 A, -B and On-line Fig 3A). All 10 patients with diffuse uniform wall thickening, with or without enhancement, had corresponding areas of diffuse irregular narrowing and/or stenosis on MRA (Fig 2E and On-line Fig 3C), except 1 patient with normal vessel findings. The 2 patients with no vessel wall abnormality had no abnormal MRA luminal findings.

Nine of the 13 patients had follow-up imaging, of these, 8 showed resolution of wall thickening and enhancement after 3.5 months, with 1 patient with near-complete resolution with minimal residual wall thickening (Fig 2D, -E and On-line Fig 3B). One patient remained with diffuse uniform wall thickening and mild concentric enhancement in 1 of the 3 vessels with narrowing on initial imaging. On MRA, 7 of the 9 patients with follow-up had resolution of luminal narrowing (Fig 2F and On-line Fig 3D), 1
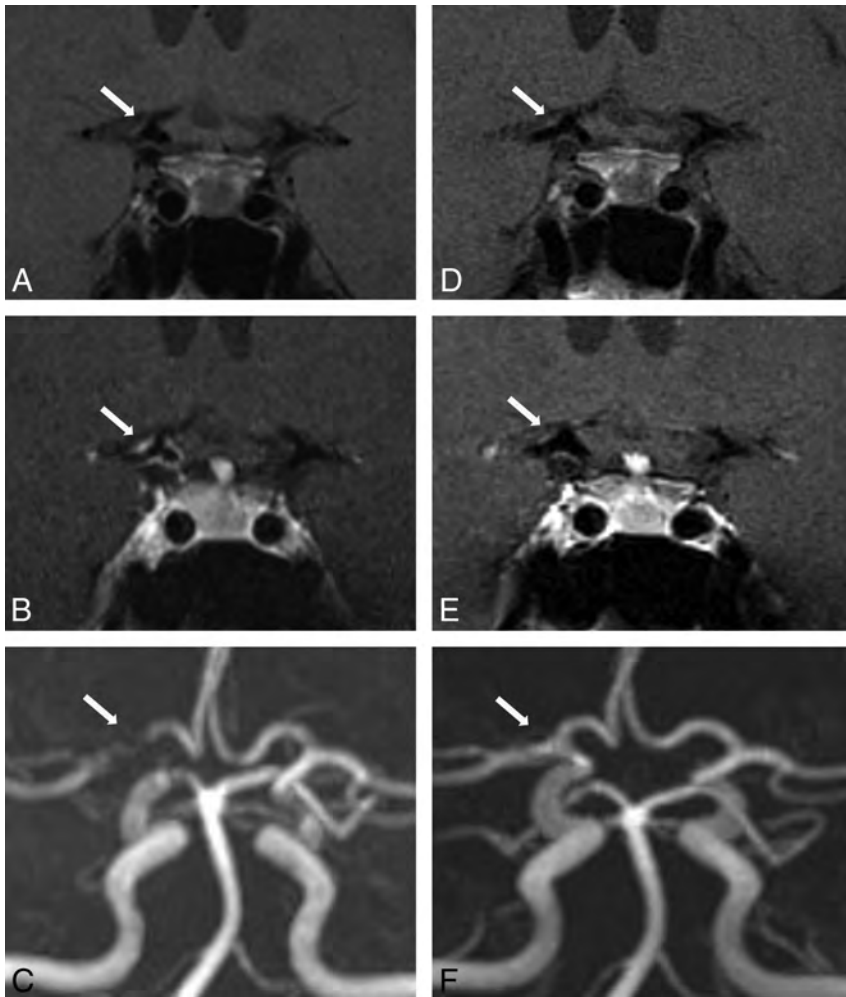
FIG 1. A 41-year-old woman with CNS vasculitis. 3T-HRMRI pre- and postgadolinium (*A* and *B*) T1-weighted arterial wall coronal images of terminal supraclinoid ICA and proximal M1 with strong smooth, concentric wall enhancement and thickening. *C*, MRA shows stenosis of the lumen and narrowing of M1 and the terminal supraclinoid ICA. Follow-up at 12 months. *D* and *E*, Pre- and post-gadolinium T1WI with near resolution of enhancement on coronal view. *F*, MRA with interval resolution of luminal narrowing and stenosis.

patient still had improved diffuse irregularity, and 1 patient had narrowing.

DISCUSSION

With the advent of higher field strength magnets and higher spatial resolution imaging, arterial wall characteristics of thickening and enhancement have been described for intracranial arterial diseases.[6-9] In this study, we describe distinct arterial wall findings for RCVS and CNS vasculitis at initial diagnostic HRMRI. In addition, we describe a long period of stable persistent arterial wall findings for CNS vasculitis compared with a shorter period of resolution of vessel wall findings for RCVS at follow-up.

There has been notable interest in understanding the clinical manifestations and underlying pathophysiology of reversible cerebral vasoconstriction syndrome since it was coined by Calabrese et al.[1] The syndrome describes a cluster of self-limiting disease entities that present with sudden recurrent thunderclap headaches, with or without additional neurologic symptoms and less commonly ischemic or hemorrhagic stroke resulting from persistent cerebral arterial vasoconstriction.[1-4] The definitive patho-

physiology of the cerebral artery vasoconstriction or the relation of symptoms to vasoconstriction is not yet clearly understood.[3,4,13] Clinically, RCVS is known to closely resemble CNS vasculitis, which also presents with headache and neurologic symptoms from cortical and/or subcortical infarctions.[14] Straightforward cases of RCVS may be distinguished from CNS vasculitis by using established RCVS criteria.[2] On the other hand, with clinically ambiguous cases, diagnosis is often further confounded by similar angiographic findings. On DSA, the nonspecific characteristic "beading" pattern of segmental dilation and narrowing of multiple cerebral arteries seen in CNS vasculitis is identical to the multifocal alternating vasoconstriction and dilation/normal caliber vessels seen in RCVS.[2,14-16] Likewise, both cerebrovascular entities share identical findings of segmental vessel stenosis on both MRA and CTA.[1,3] Reversibility of angiographic findings for RCVS known to occur after 3 months may provide some radiographic differentiation for CNS vasculitis.[2] However, delay in diagnosis may preclude immunosuppressive treatment critical for CNS vasculitis disease management to prevent the debilitating long-term sequelae of stroke; or immunosuppressive treatment, wrongly administered due to incorrect diagnosis, may worsen the prognosis for RCVS.[2,17]

On review of the literature, only 1 study to date has characterized the HRMRI vessel wall findings for RCVS and contrasted it with CNS vasculitis. Mandell et al,[7] compared HRMRI artery wall characteristics for RCVS and CNS vasculitis. Their study, with findings similar to ours, clearly differentiated distinct wall characteristics for both diseases. However, like other HRMRI studies,[6,7,18-20] it is limited in that it does not further characterize temporal wall patterns during the course of disease activity. Using HRMRI of 3 patients with RCVS and 4 patients with CNS vasculitis, the group described wall thickening and enhancement in CNS vasculitis, wall thickening with absent enhancement in RCVS, and similar findings of moderate-to-severe narrowing on TOF-MRA for both RCVS and CNS vasculitis. On follow-up TOF-MRA, their study showed persistence of the initial luminal findings for CNS vasculitis during a median of 15 months (range, 6–36 months) and resolution of RCVS after a median of 1.5 months (range, 1–3 months). This length of time for CNS vasculitis and RCVS on TOF-MRA was fairly consistent with the length of time for CNS vasculitis and RCVS on TOF-MRA in our study. However, their study did not describe follow-up HRMRI for CNS vasculitis and RCVS.
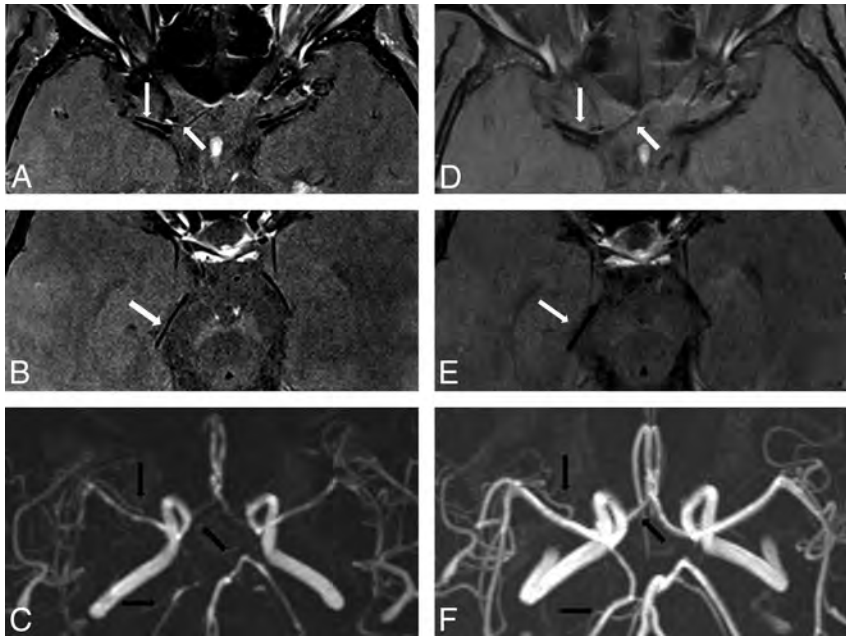
FIG 2. A 61-year-old woman with RCVS. 3T-HRMRI postgadolinium T1-weighted arterial wall with fat suppression and saturation band. *A* and *B*, Axial images in the same planes show bilateral A1, M1, and P2 with diffuse uniform wall thickening and wall narrowing with mild enhancement. *C*, MRA shows corresponding bilateral A1, M1, posterior communicating artery, and P2 narrowing. Follow-up vessel wall imaging at 3 months. *D* and *E*, Postgadolinium axial imaging with interval near resolution of uniform wall thickening and wall narrowing in the A1 and M1 segments and resolution of uniform wall thickening and wall narrowing in the P2 segment. *F*, Follow-up MRA with resolution of luminal narrowing with patent bilateral A1, M1, posterior communicating artery, and P2.

We observed, in our larger study population, that HRMRI findings were remarkably different for CNS vasculitis and RCVS at initial imaging and at follow-up. In the earlier disease course of RCVS, the pattern of diffuse uniformity with or without mild enhancement was continuous throughout the entire wall of the diseased vessel. This finding was clearly distinct in the short segments of wall thickening with concentric or eccentric enhancement in a unilateral distribution or bilateral artery distribution localized to 1 or multivessel segments seen in CNS vasculitis. The postgadolinium pattern of smooth, concentric wall enhancement and thickening was seen in 70% of patients, and eccentric wall enhancement and thickening was seen in 30% of patients.

In addition, CNS vasculitis had greater enhancement compared with mild enhancement if present in RCVS. On follow-up HRMRI for RCVS, there was early resolution of initial findings within a median of 3 months for all patients compared with CNS vasculitis, with a longer median of 7 months for resolution and 13.5 months for stable persistence of enhancement. These follow-up vessel wall and lumen findings on HRMRI appear compatible with the respective cerebrovascular disease course of RCVS and CNS vasculitis. The vessel wall findings of diffuse luminal narrowing and wall thickening with a short reversal time to normal vessel morphology appear consistent with the disease course of RCVS.[1] The HRMRI findings of short, scattered segments of vessel wall enhancement and thickening in a multivessel distribution appear compatible with the pathologic course of CNS vasculitis.[2]

To our knowledge, on review of the literature, there are no studies that describe follow-up vessel wall imaging characteristics

for RCVS, while 2 studies attempt to describe follow-up for CNS vasculitis.[21,22] Pfefferkorn et al,[22] in their HRMRI study, described moderate-to-strong enhancement in 4 patients with diagnoses of large-artery primary angiitis of the CNS. After immunosuppressive therapy, follow-up HRMRI showed that 2 patients had stable enhancement for 2 months and 2 patients had resolution of enhancement by 6 months. The second study, a case report by Saam et al,[22] reported strong vessel wall enhancement in multiple arteries of a patient with intracranial arteritis. Follow-up imaging at 3 months showed a slight decrease in enhancement, and at 6 months, there was further substantial decrease with some persistent enhancement. In our study, the wall characteristics of smooth, concentric enhancement and thickening were stable for a follow-up median of 13.5 months in 4 patients. In contrast, in 2 patients, there was complete resolution of the smooth, concentric wall enhancement and thickening after a mean of 7 months. The findings in our study compared with the other authors[21,22] demonstrate a greater period of wall thickening and enhancement for CNS vasculitis.

There were several limitations to our study. This retrospective study was conducted by using a small number of patients. However, it may represent the largest follow-up HRMRI comparison series of RCVS and CNS vasculitis to date. We are uncertain whether the mild wall enhancement seen in the 4 patients with RCVS is indeed inflammation because this has been refuted.[7] However, inflammation has been reported in persistent vasoconstriction from vasospasm in subarachnoid hemorrhage.[23] Larger prospective studies are need to further investigate and clarify these wall findings of enhancement in RCVS. We are also uncertain as to why there were variations in the length of time of enhancement, hence inflammation, in the CNS vasculitis group. These variations during follow-up may be the result of remission or flare-up of disease in response to therapy. We were unable to clearly determine the cause due to the retrospective nature of our study. However, in studies of extracranial vasculitis, wall enhancement has been shown to be strongest in the clinically acute symptomatic stage of the disease and with time with minimal or no enhancement with steroids.[24,25] We postulated that similar to extracranial vasculitis, postgadolinium wall enhancement as a marker for inflammation in vasculitis would not be indefinite; rather, there would be a gradual loss of enhancement as the inflammation subsides. However, we found there was stable enhancement for many months in some patients in the CNS vasculitis patient group while on chronic immunosuppressive therapy. We are uncertain whether this stable enhancement with treatment is indicative of continuous active inflammatory activity, poor response to treatment, inadequate immunosuppressive therapy, or persistent con-

trast leakage into the vessel wall after initial inflammatory damage of the endothelial lining. We also cannot ascertain whether response to treatment was a confounder that accounts for differences in enhancement in the CNS vasculitis group. This study also warrants a larger prospective study to answer questions as to the relationship of HRMRI findings and corresponding flare imaging or remission of disease activity with treatment.

CONCLUSIONS

Our study shows distinguishing HRMRI wall patterns for RCVS and CNS vasculitis at initial diagnostic imaging and at follow-up. It may also show that the ability of HRMRI to visualize the wall and lumen of large intracranial vessels can potentially increase the specificity of imaging to diagnose disparate vascular diseases with similar angiographic findings.

REFERENCES

1. Calabrese LH, Dodick DW, Schwedt TJ, et al. **Narrative review: reversible cerebral vasoconstriction syndromes.** *Ann Intern Med* 2007;146:34–44
2. Singhal AB, Hajj-Ali RA, Topcuoglu MA, et al. **Reversible cerebral vasoconstriction syndromes: analysis of 139 cases.** *Arch Neurol* 2011;68:1005–12
3. Ducros A, Boukobza M, Porcher R, et al. **The clinical and radiological spectrum of reversible cerebral vasoconstriction syndrome: a prospective series of 67 patients.** *Brain* 2007;130:3091–101
4. Ducros A. **Reversible cerebral vasoconstriction syndrome.** *Lancet Neurol* 2012;11:906–17
5. Chen SP, Fuh JL, Wang SJ, et al. **Magnetic resonance angiography in reversible cerebral vasoconstriction syndromes.** *Ann Neurol* 2010;67:648–56
6. Swartz RH, Bhuta SS, Farb RI, et al. **Intracranial arterial wall imaging using high-resolution 3-Tesla contrast-enhanced MRI.** *Neurology* 2009;72:627–34
7. Mandell DM, Matouk CC, Farb RI, et al. **Vessel wall MRI to differentiate between reversible cerebral vasoconstriction syndrome and central nervous system vasculitis: preliminary results.** *Stroke* 2012;43:860–62
8. Kim YS, Lim SH, Oh KW, et al. **The advantage of high-resolution MRI in evaluating basilar plaques: a comparison study with MRA.** *Atherosclerosis* 2012;224:411–16
9. Vergouwen MD, Silver FL, Mandell DM, et al. **Eccentric narrowing and enhancement of symptomatic middle cerebral artery stenoses in patients with recent ischemic stroke.** *Arch Neurol* 2011;68:338–42
10. Headache Classification Subcommittee of the International Headache Society. **The International Classification of Headache Disorders: 2nd ed.** *Cephalalgia* 2004;24:9–160
11. Calabrese LH, Mallek JA. **Primary angiitis of the central nervous system: report of 8 new cases, review of the literature, and proposal for diagnostic criteria.** *Medicine (Baltimore)* 1988;67:20–39
12. Ferguson GG, Eliasziw M, Barr HW, et al. **The North American Symptomatic Carotid Endarterectomy Trial: surgical results in 1415 patients.** *Stroke* 1999;30:1751–58
13. Ducros A, Fiedler U, Porcher R, et al. **Hemorrhagic manifestations of reversible cerebral vasoconstriction syndrome: frequency, features, and risk factors.** *Stroke* 2010;41:2505–11
14. Koopman K, Uyttenboogaart M, Luijckx GJ, et al. **Pitfalls in the diagnosis of reversible cerebral vasoconstriction syndrome and primary angiitis of the central nervous system.** *Eur J Neurol* 2007;14:1085–87
15. Gerretsen P, Kern RZ. **Reversible cerebral vasoconstriction syndrome or primary angiitis of the central nervous system?** *Can J Neurol Sci* 2007;34:467–77
16. Demaerel P, De Ruyter N, Maes F, et al. **Magnetic resonance angiography in suspected cerebral vasculitis.** *Eur Radiol* 2004;14:1005–12
17. French KF, Hoesch RE, Allred J, et al. **Repetitive use of intra-arterial verapamil in the treatment of reversible cerebral vasoconstriction syndrome.** *J Clin Neurosci* 2012;19:174–76
18. Küker W, Gaertner S, Nagele T, et al. **Vessel wall contrast enhancement: a diagnostic sign of cerebral vasculitis.** *Cerebrovasc Dis* 2008;26:23–29
19. Aoki S, Hayashi N, Abe O, et al. **Radiation-induced arteritis: thickened wall with prominent enhancement on cranial MR images report of five cases and comparison with 18 cases of Moyamoya disease.** *Radiology* 2002;223:683–88
20. Pfefferkorn T, Schuller U, Cyran C, et al. **Giant cell arteritis of the basal cerebral arteries: correlation of MRI, DSA, and histopathology.** *Neurology* 2010;74:1651–53
21. Pfefferkorn T, Linn J, Habs M, et al. **Black blood MRI in suspected large artery primary angiitis of the central nervous system.** *J Neuroimaging* 2013;23:379–83
22. Saam T, Habs M, Pollatos O, et al. **High-resolution black-blood contrast-enhanced T1 weighted images for the diagnosis and follow-up of intracranial arteritis.** *Br J Radiol* 2010;83:e182–84
23. Carr KR, Zuckerman SL, Mocco J. **Inflammation, cerebral vasospasm, and evolving theories of delayed cerebral ischemia.** *Neurol Res Int* 2013;2013:506584
24. Bley TA, Wieben O, Uhl M, et al. **High-resolution MRI in giant cell arteritis: imaging of the wall of the superficial temporal artery.** *AJR Am J Roentgenol* 2005;184:283–87
25. Bley TA, Wieben O, Leupold J, et al. **Images in cardiovascular medicine: magnetic resonance imaging findings in temporal arteritis.** *Circulation* 2005;111:e260

Brain White Matter Involvement in Hereditary Spastic Paraplegias: Analysis with Multiple Diffusion Tensor Indices

G. Aghakhanyan, A. Martinuzzi, F. Frijia, M. Vavla, H. Hlavata, A. Baratto, N. Martino, G. Paparella, and D. Montanaro

ABSTRACT

BACKGROUND AND PURPOSE: The hereditary spastic paraplegias are a group of genetically heterogeneous neurodegenerative disorders, characterized by progressive spasticity and weakness of the lower limbs. Although conventional brain MR imaging findings are normal in patients with pure hereditary spastic paraplegia, microstructural alteration in the cerebral WM can be revealed with DTI. Concomitant investigation of multiple intrinsic diffusivities may shed light on the neurobiologic substrate of the WM degeneration pattern in patients with pure hereditary spastic paraplegia across the whole brain.

MATERIALS AND METHODS: Tract-based spatial statistics analysis was performed to compare fractional anisotropy and mean, axial, and radial diffusivities of the WM skeleton in a group of 12 patients with pure hereditary spastic paraplegia and 12 healthy volunteers. Data were analyzed counting age and sex as nuisance covariates. The threshold-free cluster-enhancement option was applied, and the family-wise error rate was controlled by using permutation tests for nonparametric statistics.

RESULTS: In pure hereditary spastic paraplegia, group widespread fractional anisotropy decreases and radial diffusivity and mean diffusivity increases ($P < .05$, corrected) were found. No voxelwise difference was observed for the axial diffusivity map. Percentage of voxels within the WM skeleton that passed the significance threshold were 51%, 41.6%, and 11.9%, respectively, for radial diffusivity, fractional anisotropy, and mean diffusivity clusters. An anteroposterior pattern with preferential decrease of fractional anisotropy in the frontal circuitry was detected.

CONCLUSIONS: In patients with pure hereditary spastic paraplegia, alterations in multiple DTI indices were found. Radial diffusivity seems more sensitive to hereditary spastic paraplegia–related WM pathology and, in line with the lack of axial diffusivity changes, might indicate a widespread loss of myelin integrity. A decrease of fractional anisotropy alone in the frontal circuitry may reflect subtle disruption of the frontal connections.

ABBREVIATIONS: AD = axial diffusivity; FA = fractional anisotropy; FMRIB = Functional MRI of the Brain; FSL = Functional MRI of the Brain Software Library; HSP = hereditary spastic paraplegia; MD = mean diffusivity; pHSP = pure hereditary spastic paraplegia; RD = radial diffusivity; TBSS = tract-based spatial statistics

The hereditary spastic paraplegias (HSPs), also called familial spastic paraparesis or Strümpell-Lorrain disease, represent a genetically and clinically heterogeneous group of neurodegenerative

disorders.[1] The main clinical feature is progressive spasticity due to slowly progressing "dying back" axonal degeneration, which is maximal in the terminal portions of the longest descending and ascending tracts.[2] On the basis of clinical symptoms, HSPs are classified into pure or uncomplicated, in which the spastic paraplegia is the major clinical manifestation; and complex or complicated forms, presenting with additional neurologic signs, such as intellectual disability or cognitive decline, deafness, cerebellar ataxia, epilepsy, dysarthria, peripheral neuropathy, optic atrophy, and visual dysfunction.[3] Autosomal dominant, autosomal recessive, or X-linked inheritance is associated with multiple genes or loci and leads to genetic heterogeneity of this disorder. The HSP loci are designated as spastic paraplegia loci and are numbered 1–56 according to their discovery.[4] There is scarce evidence about the epidemiology of HSP, though its prevalence is estimated at 1.27:100,000 population in Europe.[5]

Findings of conventional MR imaging of the brain are usually normal in pure hereditary spastic paraplegia (pHSP). In contrast,

nonspecific findings such as cortical atrophy and subcortical and periventricular WM alterations are present in complicated HSP.[6] Distinct MR imaging findings may accompany complicated HSP; for instance, a common form of autosomal recessive HSP with *SPG11* mutation (linked to the 15q13-q15 chromosome) is frequently associated with a thin corpus callosum.[7] Optic nerve and cerebellar atrophy may be revealed when visual symptoms and cerebellar ataxia are present.[8]

DTI is an efficient technique used to characterize the in vivo microstructural organization of the WM.[9] The common DTI indices are fractional anisotropy (FA) (sensitive to microstructural changes and associated with the presence of oriented structures in tissue) and mean diffusivity (MD) (characterizes mean-square displacement of molecules and the overall presence of obstacles to diffusion).[10] Other indices, axial diffusivity (AD) and radial diffusivity (RD), offer suggestive elements to differentiate axonal injury and demyelination.[11] To extend our knowledge of the neurobiologic basis of WM pathology, using multiple diffusivity matrices (FA, MD, RD, and AD) is recommended.[12]

The present study was set up to investigate WM alterations across the whole brain in a group of patients with pHSP with *SPG4*, *SPG5*, *SPG3a*, and *SPG10* mutations, applying tract-based spatial statistics (TBSS) analysis with multiple DTI indices.

MATERIALS AND METHODS
Subjects
We recruited 12 adult patients with pHSP (mean age, 49.2 ± 8.1 years), from the Medea Scientific Institute in Conegliano, Treviso, Italy, and 12 healthy volunteers matched by age and sex (mean age, 48.2 ± 5.4 years). All patients with pHSP underwent molecular genetic studies that confirmed mutations in *SPG4*, *SPG5*, *SPG3a*, and *SPG10* loci. Careful visual inspection of each patient's MR images was performed by 3 experienced neuroradiologists (D.M., N.M., and A.B.), and structural MR imaging evidence of tumor, infection, infarction, or other focal lesions was excluded. All patients underwent a clinical examination with detailed neurologic evaluation, including measurements of spasticity, motoricity, and autonomy. Local ethics committee approval (n 63/09-CE) and written informed consent from all subjects were obtained before the study.

MR Imaging Acquisition and DTI Processing
All subjects underwent MR imaging brain scans (1.5T Achieva 2.5 XR; Philips Healthcare, Best, the Netherlands) at the MR imaging laboratory of Ospedale Civile ULSS7, Conegliano, Treviso, Italy. Diffusion-weighted images were acquired by using EPI sequences (TR/TE/TI, 10,000/69/2400 ms; bandwidth, 2117.4 kHz; acquisition matrix, 104 × 102; voxel size, 2 × 2 × 2.03 mm; b-value = 0 and 1.000 s/mm; 102 contiguous sections; 32 different gradient directions).

DTI processing was performed by using FSL, Version 4.1.1 (http://fsl.fmrib.ox.ac.uk/fsl).[13] First, raw diffusion data were corrected for motion artifacts and eddy current distortions; then, brain was extracted by using the Brain Extraction tool. The FMRIB Diffusion Toolbox, Version 2.0 (http://www.fmrib.ox.ac.uk/fsl/fdt/index.html), was used to fit the diffusion tensor and compute the diagonal elements ($\lambda1$, $\lambda2$, and $\lambda3$) at each brain voxel,

from which the derived metrics AD, MD, and FA were also inferred. We calculated the RD matrix for each subject, averaging $\lambda2$ and $\lambda3$ diagonal elements of the diffusion tensor [RD = 1 / 2 × ($\lambda2$ + $\lambda3$)].

Tract-Based Spatial Statistics Analysis
Voxelwise statistical analysis of the FA, MD, RD, and AD data were performed by using TBSS.[14] All subjects' FA data were aligned into a common space by using the Nonlinear Registration Tool in FMRIB. The FMRIB58-FA standard-space image was used as a target image following the recommendations of the FSL software guidelines. Next, the mean FA image was created and thinned (threshold FA value of 0.25) to create a mean FA skeleton, which represented the centers of all tracts common to the group. Finally, all subjects' spatially normalized FA, AD, RD, and MD data were projected onto the skeleton, and resulting data were fed into voxelwise cross-subject statistics.

Conjunction Map
To obtain a spatial distribution pattern of FA and RD changes, we created a conjunction map. First, resulting FA and RD maps of the voxelwise statistics were thresholded at $P = .05$, corrected for multiple comparisons and then binarized and masked. The fslmaths program (part of FSL, http://www.mit.edu/~satra/nipype-nightly/interfaces/generated/nipype.interfaces.fsl.maths.html), which allows mathematic manipulation of images, was used to subtract binarized and masked maps of significance for FA and RD matrices.

Statistical Analysis
Demographic and descriptive differences for continuous variables (eg, age) between HSP and control groups were examined with the Wilcoxon rank sum test; for categoric variables (eg, sex), group differences were evaluated by using the Pearson χ^2 test. Statistical analyses were performed by using R software, Version 2.15.1 (http://www.r-project.org/).

DTI-based voxelwise statistics were performed by using the program Randomize, part of FSL. Voxelwise differences among groups were assessed, applying 2-sample t tests. We used the thresholded mean FA skeleton (mean value of 0.25), setting the number of permutations to 5000 with the threshold-free cluster-enhancement option and the significance threshold at $P = .05$, corrected for multiple comparisons to control the family-wise error rate. Data were analyzed counting age and sex as a nuisance covariates.

RESULTS
Demographic and clinical characterizations are summarized in Table 1. The patients with pHSP and healthy controls did not differ in terms of age and sex distribution. All patients enlisted in our study showed a phenotype consistent with pHSP.

Analysis of Multiple DTI Indices
The mean diffusion metrics (FA, MD, AD, and RD) in the WM skeleton were extracted for each subject. Statistical analysis revealed significant group differences in all mean diffusivity indices (On-line Table 1). Compared with controls, patients with pHSP had significantly decreased mean FA ($P < .001$), increased mean

RD ($P < .001$), increased mean MD ($P < .005$), and a less notable increase in mean AD ($P = .01$).

Voxelwise TBSS analyses revealed widespread alterations in multiple DTI indices (Fig 1). Compared with the healthy group, patients with pHSP showed decreases of FA ($P < .05$, corrected) in multiple WM regions (Fig 1A), including the bilateral anterior thalamic radiations, corticospinal tracts, corpus callosum with forceps major and minor, and parts of the inferior and superior longitudinal fasciculi. Significant clusters for each matrix were separately masked and labeled with reference to the JHU ICBM-DTI-81 White Matter Labels, part of the FSL atlas tools (Table 2).

Table 1: Demographic and clinical characteristics for patients with HSP and the control group[a]

	Patients with HSP (n = 12)	Healthy Controls (n = 12)	P Value
Age at MRI (yr)	50 (49 ± 8)	48 (48 ± 5)	.5[b]
Sex (female)	50%	67%	.4[c]
Disease duration (yr)	23 (24 ± 16)	–	–
Disease onset (yr)	23 (25 ± 18)	–	–
Spastic gate loci			
SPG10	8% (1)		
SPG3a	8% (1)		
SPG4	58% (7)		
SPG7+SPG4	8% (1)		
SPG5	17% (2)		

[a] Values are median, mean ± SD, or No. (%). Numbers after percentages are frequencies.
[b] Wilcoxon test.
[c] Pearson test.

Most regions showing a decrease in FA showed a corresponding increase in RD ($P < .05$, corrected, Fig 1C). Changes in MD ($P < .05$, corrected, Fig 1B) were more restricted in comparison with regions of decreased FA and increased RD. No significant differences emerged after voxelwise TBSS analysis of AD.

Percentage changes of the voxels in the WM skeleton that passed the significance threshold ($P < .05$, corrected) were 51%, 41.6%, and 11.9%, respectively, for RD, FA, and MD clusters. All clusters consisted of a large number of voxels that did not split into smaller clusters even after increasing the significance threshold to $P < .01$. All cluster characteristics are detailed in the supplementary material (On-line Table 2).

The magnitude and topographic pattern of significant changes in multiple DTI indices were not equivalent. To address this issue, we created a conjunction map of FA and RD changes. Anterior frontal structures showed a reduction in FA, without significant changes in RD, while posterior supratentorial brain regions and the brain stem showed a pre-eminent increase in RD compared with FA changes (Fig 2).

DISCUSSION

We aimed to investigate cerebral WM changes in patients with HSP, applying voxelwise analysis of multiple diffusivity indices. Accounting for the huge genetic and phenotypic variability in HSPs,[15] we carefully selected patients with pHSP with confirmed SPG mutations and without structural abnormalities on MR imaging. Exploring otherwise normal-appearing cerebral WM in patients with pHSP, we found remarkable and diffuse abnormalities in WM microstructure, including a decrease in FA, an increase in MD and RD, but no changes in AD.

Currently, DTI is one of the most successful techniques among clinicians and researchers to study WM architecture. The FA index is frequently used to describe the shape of diffusion with a scalar value, while MD is used to describe the local magnitude of diffusion, regardless of direction.[9,16] Overall, breakdown of WM integrity leads to a decrease in FA and/or an increase in MD. Although the FA is quite sensitive to a broad spectrum of pathologic conditions, it has been argued that a single scalar value cannot describe the full shape, orientation, and anisotropy of the WM.[12] For instance, different combinations of diffusion tensor eigenvalues (which are the diagonal elements of the tensor and proportional to the squares of the lengths of the ellipsoid axes) can generate the same FA values.[10] Not surprising, the apparent diffusivities in the directions parallel and perpendicular to the WM tracts, designated as the axial and radial diffusivities, become more
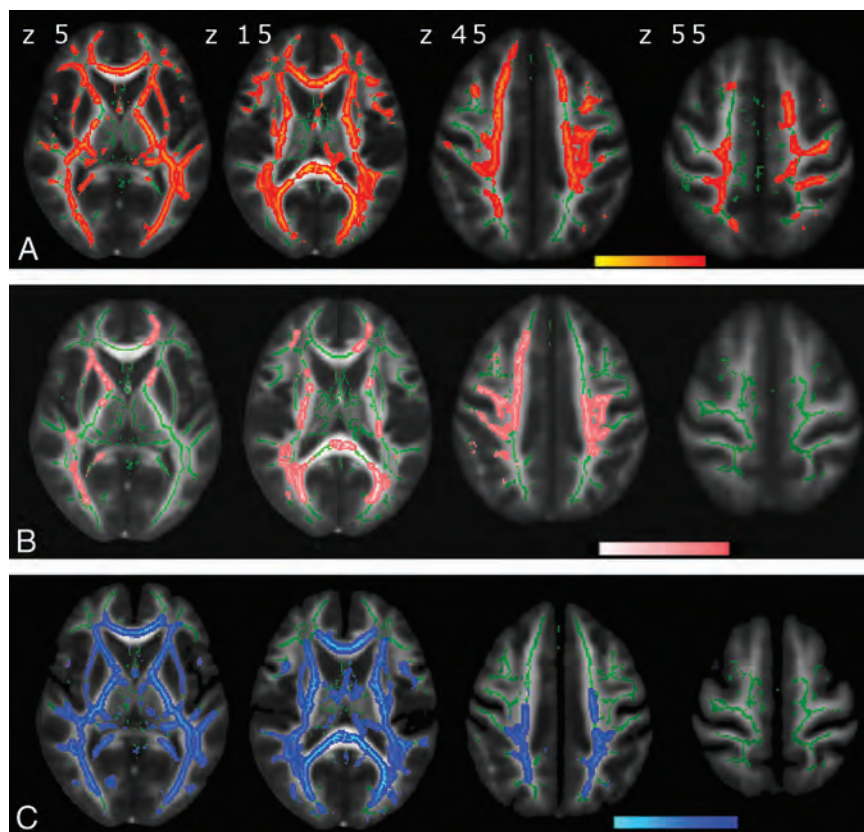
FIG 1. DTI indices maps ($P < .05$, corrected) are represented in the FMRIB58_FA template on the axial plan with z-axis coordinates (in millimeters) above the upper row images. Green corresponds to the mean white matter skeleton of all participants. A, Red-yellow represents decreased FA. B, Pink-light pink represents increased MD. C, Blue-light blue represents increased RD.

appealing.[17] Animal studies indicated that these measures may be selectively sensitive to specific neural changes, with AD reflecting axonal differences (eg, axonal damage or loss) and RD reflecting differences in the degree of myelin integrity, myelination, and demyelination.[11,18]

The major neuropathologic feature in HSPs is axonal degeneration, which is maximal in the terminal portions of the longest descending and ascending tracts due to the disruption of the axonal transport.[19] The most severely affected pathways are the corticospinal tracts and the fasciculus gracilis. Spinocerebellar tracts may also be involved in approximately 50% of cases.[20]

In HSPs, the extension of the neurodegenerative process to the cerebral WM is still less known. Only a few small cohort DTI studies have demonstrated widespread alteration of multiple indices in patients with complicated HSP with a thin corpus callosum and SPG11 mutation.[21,22] This form of complicated HSP is characterized by rapidly progressive spasticity of early onset, mental deterioration, and other neurologic manifestations such as seizures and cerebellar ataxia.[23] Furthermore, it was shown that complicated HSPs display a different pattern of topography and severity of cerebral WM volume changes in respect to pHSP.[24] This finding may suggest that pure and complicated HSPs are not uniform entities and need to be explored separately.

Table 2: Suprathreshold (P < .05, corrected) cluster distribution (%) respectively for FA, MD, and RD indices

JHU White-Matter Tractography Atlas Labels	FA	MD	RD
L anterior thalamic radiation	1.27	1.17	1.54
R anterior thalamic radiation	0.81	0.94	1.01
L corticospinal tract	0.96	0.95	0.96
R corticospinal tract	1.03	1.40	1.02
L cingulum (cingulate gyrus)	0.44	0.28	0.43
Corpus callosum with forceps major	1.26	1.94	1.17
Corpus callosum with forceps minor	3.26	2.63	2.04
L inferior fronto-occipital fasciculus	1.95	0.40	1.80
R inferior fronto-occipital fasciculus	1.47	1.85	1.79
L inferior longitudinal fasciculus	0.93	0.30	1.58
R inferior longitudinal fasciculus	2.02	0.88	1.22
L superior longitudinal fasciculus	1.10	3.13	1.98
R superior longitudinal fasciculus	0.76	3.56	1.67
L superior longitudinal fasciculus (temporal part)	0.96	1.01	0.96
R superior longitudinal fasciculus (temporal part)	0.44	1.07	0.66

Note:—L indicates left; R, right.
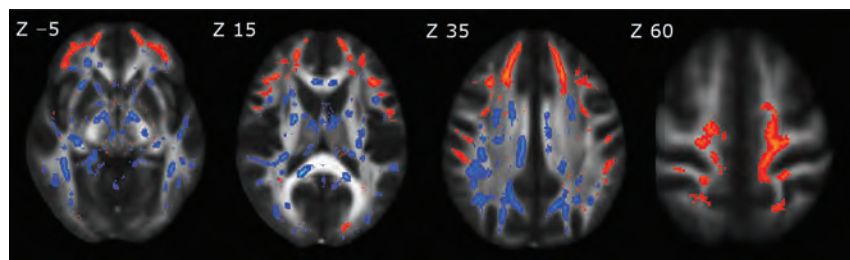
FIG 2. Conjunction map of spatial differences between reduced FA and increased RD maps, represented in the FMRIB58_FA template on the axial plane with Montreal Neurological Institute 152 coordinates (in millimeters) above each upper row image. Red-yellow represents decreased FA; blue-light blue, increased RD. A decrease in FA alone shows an anterior frontal circuitry pattern, while an increase in RD is more prominent in the posterior supratentorial brain regions and brain stem.

Meanwhile, the evidence from multiple DTI studies exploring WM alterations in different motor neuron disorders, such as amyotrophic and primary lateral sclerosis, consistently indicated a widespread decrease in FA and a variable increase in MD, AD, and RD values along motor and extramotor areas.[25-28] One recent study directly linked a WM alteration pattern in patients with HSP and a group of patients with amyotrophic and primary lateral sclerosis, demonstrating a similar pattern of FA reduction in the corticospinal tracts and corpus callosum.[29] Some phenotype variations of HSPs may mimic upper motor neuron disorders, but different neuropathologic elements characterize these 2 nosologic entities: axonopathy, thought to be the primary cause of neurodegeneration in HSPs, while cell bodies are relatively unaffected until late in the disease course[1]; and degeneration of motor neurons, on the contrary, the pathophysiologic hallmark in motor neuron disorders.[30]

In HSPs, axonopathy is mainly characterized by focal swelling of axons with marked accumulation of organelles and intermediate filaments associated with impaired retrograde transport.[31] In addition, morphologic changes (axonal attenuation loss and decreased caliber) were observed at all levels from the lumbar to the medullar portion of the axons.[19] Even though axonal damage is mainly associated with changes in diffusion properties parallel to the neuroaxis, in our patients with pHSP, we did not find changes in the AD map by using voxel-by-voxel analysis. To further address this issue, we extracted all mean diffusivities from the WM skeleton for each subject (On-line Table 1), and in contrast to other diffusivity indices (FA, RD, and MD), we observed only a slight increase in mean AD ($P = .01$).

One possible explanation for the lack of AD changes may be related to complexity and temporal dynamism that occurs with axonal breakdown and clearance: alteration of axonal transport and accumulation of organelles create barriers to the longitudinal displacement of water molecules causing a decrease in AD.[32] Subsequently, the cellular debris are cleared by microglia, resulting in re-establishment or even an increase in the diffusion in the longitudinal direction leading to an increase in AD.[33]

Myelin loss in patients with HSP is presumed to be secondary, due to axonal damage.[19] As a consequence of degraded axonal membranes and disruption of myelin sheaths, the hindrance of water moving across fibers is reduced, which leads to an increase in RD.[32] In agreement with this feature, we found a widespread increase in RD in all major WM tracts, suggesting the presence of extensive demyelination in the cerebral level of patients with pHSP.[34] It is difficult to conclude whether myelin loss is primary or secondary due to axonal damage. Neuropathology in HSPs is complex and combines elements of axonal loss, gliosis, and demyelination, which will result in competing influences on the diffusion tensor.

The next interesting finding emerging from our study is the inconsistency in spatial overlapping of FA and RD changes. Although both DTI indices were diffusely altered, in the conjunction

map of the decreased FA and increased RD, an anteroposterior pattern was detected (Fig 2): The anterior WM seemed more susceptible to FA changes; meanwhile, the posterior supratentorial brain regions and brain stem were more prone to RD changes. Because the FA metric is a function of all 3 eigenvalues of the diffusion tensor, concurrent changes in parallel and perpendicular diffusivities may reduce the sensitivity of FA in the posterior brain regions. Mild microstructural alterations of the minor fibers and subtle disruption of the frontal lobe connections solely may lead to a decrease of FA in the anterior frontal circuitry.[35] However, the neurobiologic substrate and neuropsychological correlates of these topographic discordances need to be further elucidated.

The study is not lacking limitations. First, we involved a limited number of patients with pHSP due to low prevalence of the disease and the strict inclusion criteria of the study. Second, our cohort is heterogeneous in terms of *SPG* genes and loci, but phenotype homogeneity is consistent for the group sample because we enrolled only patients with pHSP with confirmed *SPG* mutations. Next, TBSS analysis has many advantages, but it still has limitations in analyzing small fiber tracts and regions of crossing fibers or tract junctions. Nevertheless, TBSS is a revolutionary method for detecting group voxelwise changes in the whole brain. It is successfully designed to overcome problems with registration algorithms and arbitrariness of spatial smoothing presented in other voxel-by-voxel approaches, such as voxel-based analysis, which may crucially affect the results due to the highly directional and topographic nature of DTI.[36] Furthermore, the current cross-sectional design of our study cannot address longitudinal changes in correlation with disease onset, severity, and progression rate. Future longitudinal DTI studies are needed to unveil those questions.

CONCLUSIONS

We obtained a comprehensive landscape of multiple DTI matrices in patients with pHSP and demonstrated significant reductions in FA and increases in RD and MD, but no changes in AD in the areas of otherwise normal-appearing cerebral WM. This finding indicates that HSPs diffusely affect cerebral WM microstructure. A widespread increase in RD with the absence of AD changes may indicate extensive demyelination, whereas a decrease in FA alone in the frontal circuitry might reflect subtle disruption of the frontal lobe connections. Whether lack of AD changes reflects the temporal dynamism of the underlying neuropathologic process during which various neuronal components may be affected by different stages of the disease still needs to be elucidated.

ACKNOWLEDGMENTS

We thank all patients participating in this study and their families.

REFERENCES

1. Schwarz GA. **Hereditary (familial) spastic paraplegia.** *AMA Arch Neurol Psychiatry* 1952;68:655–62
2. Behan WM, Maia M. **Strümpell's familial spastic paraplegia: genetics and neuropathology.** *J Neurol Neurosurg Psychiatry* 1974;37:8–20
3. Harding AE. **Classification of the hereditary ataxias and paraplegias.** *Lancet* 1983;1:1151–55
4. Dürr A. **Genetic testing for the spastic paraplegias: drowning by numbers.** *Neurology* 2008;71:236–38
5. McMonagle P, Webb S, Hutchinson M. **The prevalence of "pure" autosomal dominant hereditary spastic paraparesis in the island of Ireland.** *J Neurol Neurosurg Psychiatry* 2002;72:43–46
6. Casali C, Valente EM, Bertini E, et al. **Clinical and genetic studies in hereditary spastic paraplegia with thin corpus callosum.** *Neurology* 2004;62:262–68
7. Paisan-Ruiz C, Dogu O, Yilmaz A, et al. **SPG11 mutations are common in familial cases of complicated hereditary spastic paraplegia.** *Neurology* 2008;70:1384–89
8. Depienne C, Stevanin G, Brice A, et al. **Hereditary spastic paraplegias: an update.** *Curr Opin Neurol* 2007;20:674–80
9. Basser PJ, Pierpaoli C. **Microstructural and physiological features of tissues elucidated by quantitative-diffusion-tensor MRI.** *J Magn Reson B* 1996;111:209–19
10. Le Bihan D, Mangin JF, Poupon C, et al. **Diffusion tensor imaging: concepts and applications.** *J Magn Reson Imaging* 2001;13:534–46
11. Song SK, Sun SW, Ramsbottom MJ, et al. **Dysmyelination revealed through MRI as increased radial (but unchanged axial) diffusion of water.** *Neuroimage* 2002;17:1429–36
12. Alexander AL, Lee JE, Lazar M, et al. **Diffusion tensor imaging of the brain.** *Neurotherapeutics* 2007;4:316–29
13. Smith SM, Jenkinson M, Woolrich MW, et al. **Advances in functional and structural MR image analysis and implementation as FSL.** *Neuroimage* 2004;23(suppl 1):S208–19
14. Smith SM, Jenkinson M, Johansen-Berg H, et al. **Tract-based spatial statistics: voxelwise analysis of multi-subject diffusion data.** *Neuroimage* 2006;31:1487–505
15. Fink JK. **Hereditary spastic paraplegia.** *Neurol Clin* 2002;20:711–26
16. Pierpaoli C, Barnett A, Pajevic S, et al. **Water diffusion changes in Wallerian degeneration and their dependence on white matter architecture.** *Neuroimage* 2001;13:1174–85
17. Wheeler-Kingshott CA, Cercignani M. **About "axial" and "radial" diffusivities.** *Magn Reson Med* 2009;61:1255–60
18. Xie M, Wang Q, Wu TH, et al. **Delayed axonal degeneration in slow Wallerian degeneration mutant mice detected using diffusion tensor imaging.** *Neuroscience* 2011;197:339–47
19. Deluca GC, Ebers GC, Esiri MM. **The extent of axonal loss in the long tracts in hereditary spastic paraplegia.** *Neuropathol Appl Neurobiol* 2004;30:576–84
20. McDermott C, White K, Bushby K, et al. **Hereditary spastic paraparesis: a review of new developments.** *J Neurol Neurosurg Psychiatry* 2000;69:150–60
21. França MC, Yasuda CL, Pereira FRS, et al. **White and grey matter abnormalities in patients with SPG11 mutations.** *J Neurol Neurosurg Psychiatry* 2012;83:828–33
22. Garaci F, Toschi N, Lanzafame S, et al. **Diffusion tensor imaging in SPG11- and SPG4-linked hereditary spastic paraplegia.** *Int J Neurosci* 2014;124:261–70
23. Lossos A, Stevanin G, Meiner V, et al. **Hereditary spastic paraplegia with thin corpus callosum: reduction of the SPG11 interval and evidence for further genetic heterogeneity.** *Arch Neurol* 2006;63:756–60
24. Kassubek J, Juengling FD, Baumgartner A, et al. **Different regional brain volume loss in pure and complicated hereditary spastic paraparesis: a voxel-based morphometric study.** *Amyotroph Lateral Scler* 2007;8:328–36
25. Kassubek J, Ludolph AC, Müller HP. **Neuroimaging of motor neuron diseases.** *Ther Adv Neurol Disord* 2012;5:119–27
26. Agosta F, Galantucci S, Riva N, et al. **Intrahemispheric and inter-**

hemispheric structural network abnormalities in PLS and ALS. *Hum Brain Mapp* 2014;35:1710−22

27. Lombardo F, Frijia F, Bongioanni P, et al. **Diffusion tensor MRI and MR spectroscopy in long lasting upper motor neuron involvement in amyotrophic lateral sclerosis.** *Arch Ital Biol* 2009;147:69−82

28. Prudlo J, Bißbort C, Glass A, et al. **White matter pathology in ALS and lower motor neuron ALS variants: a diffusion tensor imaging study using tract-based spatial statistics.** *J Neurol* 2012; 259:1848−59

29. Müller HP, Unrath A, Huppertz HJ, et al. **Neuroanatomical patterns of cerebral white matter involvement in different motor neuron diseases as studied by diffusion tensor imaging analysis.** *Amyotroph Lateral Scler* 2012;13:254−64

30. Redler RL, Dokholyan NV. **The complex molecular biology of amyotrophic lateral sclerosis (ALS).** *Prog Mol Biol Transl Sci* 2012; 107:215−62

31. Tarrade A, Fassier C, Courageot S, et al. **A mutation of spastin is responsible for swellings and impairment of transport in a region of axon characterized by changes in microtubule composition.** *Hum Mol Genet* 2006;15:3544−58

32. Sun SW, Liang HF, Cross AH, et al. **Evolving Wallerian degeneration after transient retinal ischemia in mice characterized by diffusion tensor imaging.** *Neuroimage* 2008;40:1−10

33. Concha L, Gross DW, Wheatley BM, et al. **Diffusion tensor imaging of time-dependent axonal and myelin degradation after corpus callosotomy in epilepsy patients.** *Neuroimage* 2006;32:1090−99

34. Alexander AL, Hurley SA, Samsonov AA, et al. **Characterization of cerebral white matter properties using quantitative magnetic resonance imaging stains.** *Brain Connect* 2011;1:423−46

35. Burzynska AZ, Preuschhof C, Bäckman L, et al. **Age-related differences in white matter microstructure: region-specific patterns of diffusivity.** *Neuroimage* 2010;49:2104−12

36. Soares JM, Marques P, Alves V, et al. **A hitchhiker's guide to diffusion tensor imaging.** *Front Neurosci* 2013;7:31

Diffusion and Perfusion MRI Findings of the Signal-Intensity Abnormalities of Brain Associated with Developmental Venous Anomaly

H.N. Jung, S.T. Kim, J. Cha, H.J. Kim, H.S. Byun, P. Jeon, K.H. Kim, B.-J. Kim, and H.-J. Kim

ABSTRACT

BACKGROUND AND PURPOSE: Developmental venous anomalies are the most common intracranial vascular malformation. Increased signal-intensity on T2-FLAIR images in the areas drained by developmental venous anomalies are encountered occasionally on brain imaging studies. We evaluated diffusion and perfusion MR imaging findings of the abnormally high signal intensity associated with developmental venous anomalies to describe their pathophysiologic nature.

MATERIALS AND METHODS: We retrospectively reviewed imaging findings of 34 subjects with signal-intensity abnormalities associated with developmental venous anomalies. All subjects underwent brain MR imaging with contrast and diffusion and perfusion MR imaging. Regions of interest were placed covering abnormally high signal intensity around developmental venous anomalies on fluid-attenuated inversion recovery imaging, and the same ROIs were drawn on the corresponding sections of the diffusion and perfusion MR imaging. We measured the apparent diffusion coefficient, relative cerebral blood volume, relative mean transit time, and time-to-peak of the signal-intensity abnormalities around developmental venous anomalies and compared them with the contralateral normal white matter. The Mann-Whitney U test was used for statistical analysis.

RESULTS: The means of ADC, relative cerebral blood volume, relative mean transit time, and TTP of signal-intensity abnormalities around developmental venous anomalies were calculated as follows: $0.98 \pm 0.13 \ 10^{-3} \mathrm{mm}^2/\mathrm{s}$, 195.67 ± 102.18 mL/100 g, 16.74 ± 7.38 seconds, and 11.65 ± 7.49 seconds, respectively. The values of normal WM were as follows: $0.74 \pm 0.08 \ 10^{-3} \mathrm{mm}^2/\mathrm{s}$ for ADC, 48.53 ± 22.85 mL/100 g for relative cerebral blood volume, 12.12 ± 4.27 seconds for relative mean transit time, and 8.35 ± 3.89 seconds for TTP. All values of ADC, relative cerebral blood volume, relative mean transit time, and TTP in the signal-intensity abnormalities around developmental venous anomalies were statistically higher than those of normal WM (All $P < .001$, respectively).

CONCLUSIONS: The diffusion and perfusion MR imaging findings of the signal-intensity abnormalities associated with developmental venous anomaly suggest that the nature of the lesion is vasogenic edema with congestion and delayed perfusion.

ABBREVIATIONS: DVA = developmental venous anomaly; rCBV = relative cerebral blood volume; rMTT = relative mean transit time; SI = signal intensity

Developmental venous anomalies (DVAs) are encountered frequently on brain imaging studies. DVAs are identified in up to 2% of the general population, and they are the most common intracranial vascular malformation (63% and 50% of all malformations in postmortem examinations and MR imaging series, respectively).[1,2] They are composed of dilated medullary veins that drain centripetally and radially into enlarged transcortical or subependymal collector veins.[3-5] DVAs serve as normal drainage routes of the brain tissue because the normal venous drainage pattern is underdeveloped in the area adjacent to the DVA. These venous channels have no malformed or neoplastic elements and are generally described as having normal intervening parenchyma.[6,7] However, increased signal intensity (SI) on T2 FLAIR images in the areas drained by DVAs have been reported in 7.8%–54.1% of MR imaging investigations.[8-10] Such abnormal SI related to DVAs has been explained as edema, ischemia, demyelination, gliosis, leukoaraiosis, or a combination of these conditions.[11,12] Several studies have been undertaken to understand the mechanism of SI change.[13-15] However, there has been no report of the diffusion and perfusion changes of abnormal SI in the area of DVAs by using diffusion- and perfusion-weighted MR imaging, to our knowledge. Therefore, the aim of this study was to

characterize these SIs by using DWI and PWI. DWI would discriminate between vasogenic edema and gliosis, and PWI would demonstrate signs of outflow obstruction and venous congestion.

MATERIALS AND METHODS

Patients

We searched the reports of brain MR imaging with contrast, diffusion, and perfusion studies for the terms "developmental venous anomaly" or "venous angioma" through the databank of our hospital from January 2005 to January 2013. Two hundred fifty-six consecutive patients with DVAs were found. Sixty-eight of 256 (26.6%) subjects showed SI abnormalities in the DVA drainage area. No patient had suspected or known multiple sclerosis. Within these subjects, 34 were omitted from the study group due to the following exclusion criteria: 1) area of SI abnormality <5 mm^2 ($n = 23$), 2) the lesion not distinguishable from ischemic lesions or infarction of underlying small-vessel disease ($n = 7$), and 3) DVAs accompanied by cavernous malformations ($n = 4$). Finally, 34 subjects (13.3%, 34/256) formed the study group. Our institutional review board approved this study, and informed consent was waived in this retrospective study.

MR Imaging Protocol and Postprocessing

MR imaging was performed at 3T (Achieva; Philips Healthcare, Best, the Netherlands) with an 8-channel sensitivity-encoding head coil. For all patients, we obtained the following images: axial contrast-enhanced spin-echo T1-weighted images after intravenous injection of contrast material (gadoterate meglumine, Dotarem; Guerbet, Aulnay-sous-Bois, France; 0.1 mmol/kg body weight by power injector) (TR/TE = 500/10 ms, section thickness = 5 mm, acquisition matrix = 256 × 226); axial T2-weighted fluid-attenuated inversion recovery images (TR/TE = 11000/125 ms, section thickness = 5 mm, acquisition matrix = 368 × 265); spin-echo EPI DWI (TR/TE = 3000/76 ms, section thickness = 5 mm, acquisition matrix = 128 × 128, b-value = 0, 1000 s/mm^2); and dynamic susceptibility contrast MR PWI (TR/TE = 1720/35 ms, flip angle = 40°, section thickness = 5 mm, acquisition matrix = 128 × 128, 50 volumes, acquisition time = 1 minute 30 seconds). All MR images were acquired with the same FOV (240 × 240 mm).

We processed the dynamic susceptibility-weighted contrast-enhanced perfusion MR imaging by using a dedicated software package (nordicICE; NordicNeuroLab, Bergen, Norway). Perfusion maps of relative cerebral blood volume (rCBV), relative mean transit time (rMTT), and time-to-peak were made by using an acknowledged tracer kinetic model applied to first-pass data.[16,17] We used γ-variate fit to diminish the recirculation effect. We performed deconvolution of the measured signal-time curves by using singular-value decomposition with the arterial input function of approximately 5 pixels retrieved from the middle cerebral artery branches. TTP was obtained by computing the arrival time of contrast material to maximum concentration.

MR Imaging Data Analysis and Statistics

Two neuroradiologists (S.T.K., H.N.J.) analyzed the MR images retrospectively. One had 22 years' experience with brain imaging,

The ADC, rCBV, rMTT, and TTP values of signal-intensity abnormalities associated with developmental venous anomalies and contralateral normal white matter

	DVAs	Normal WM	P Values[a]
ADC[b]	0.98 ± 0.13	0.74 ± 0.08	<.001
rCBV[c]	195.67 ± 102.18	48.53 ± 22.85	<.001
rMTT[d]	16.74 ± 7.38	12.12 ± 4.27	<.001
TTP[e]	11.65 ± 7.49	8.35 ± 3.89	<.001

[a] Mann-Whitney U test.
[b] Apparent diffusion coefficient is expressed as 10^{-3} mm^2/s.
[c] Relative cerebral blood volume is expressed as mL/100 g.
[d] Relative mean transit time is expressed as seconds.
[e] Time-to-peak is expressed as seconds.

and the other had 5 years' experience with brain imaging. DVAs were identified on contrast-enhanced T1WI. We defined the drainage territory as brain parenchyma directly adjacent to the visualized medullary and collector vein of the DVA. When increased SI was seen within the drainage territory of a DVA on a T2 FLAIR image, it was defined as an SI abnormality associated with a DVA.

Regions of interest were placed covering the abnormally high SI around DVAs on T2 FLAIR imaging, not including the collecting vein because these can confound perfusion measurements. All ROIs were copied to corresponding sections of the apparent diffusion coefficient and perfusion maps. ROIs were manually drawn on the T2 FLAIR images for normal-appearing contralateral white matter, and ROIs on the ADC and perfusion maps were obtained in the same way. We measured the values of ADC, rCBV, rMTT, and TTP, respectively, and analyzed differences in values of ADC, rCBV, rMTT, and TTP between the SI abnormalities associated with the DVA and contralateral normal WM. The Mann-Whitney U test was used for statistical analysis. Null hypotheses of no difference were rejected if P values were <.05. A commercially available software program (PASW, Version 18.0; IBM, Armonk, New York) was used for all statistical analyses.

RESULTS

The mean age of the 34 patients was 63.7 years (range, 38–81 years), and 52.9% ($n = 18$) were men. The mean area of the region of interest of SI abnormalities associated with DVAs was 64.5 mm^2 (range, 8.8–260.2 mm^2).

The values of ADC, rCBV, rMTT, and TTP of abnormal SI associated with DVAs and normal WM are summarized in the Table. The mean values of SI around DVAs were 0.98 ± 0.13 10^{-3} mm^2/s for ADC, 195.67 ± 102.18 mL/100 g for rCBV, 16.74 ± 7.38 seconds for rMTT, and 11.65 ± 7.49 seconds for TTP, respectively. The mean ADC, rCBV, rMTT, and TTP values of normal WM were as follows: 0.74 ± 0.08 10^{-3} mm^2/s, 48.53 ± 22.85 mL/100 g, 12.12 ± 4.27 seconds, and 8.35 ± 3.89 seconds. There was a significant difference between the SI abnormalities associated with DVAs and normal WM in all terms of ADC, rCBV, rMTT, and TTP (all $P < .001$, respectively) (Fig 1).

DISCUSSION

In the present study, SI abnormalities associated with DVAs were seen in 13.3% of DVAs (34/256), and this value is in the range of prevalence of 7.8%–54.1% that is reported in previous studies.[8-10] Abnormal SI associated with DVAs is not a rare finding in an imaging study, and some possibilities have been proposed as the
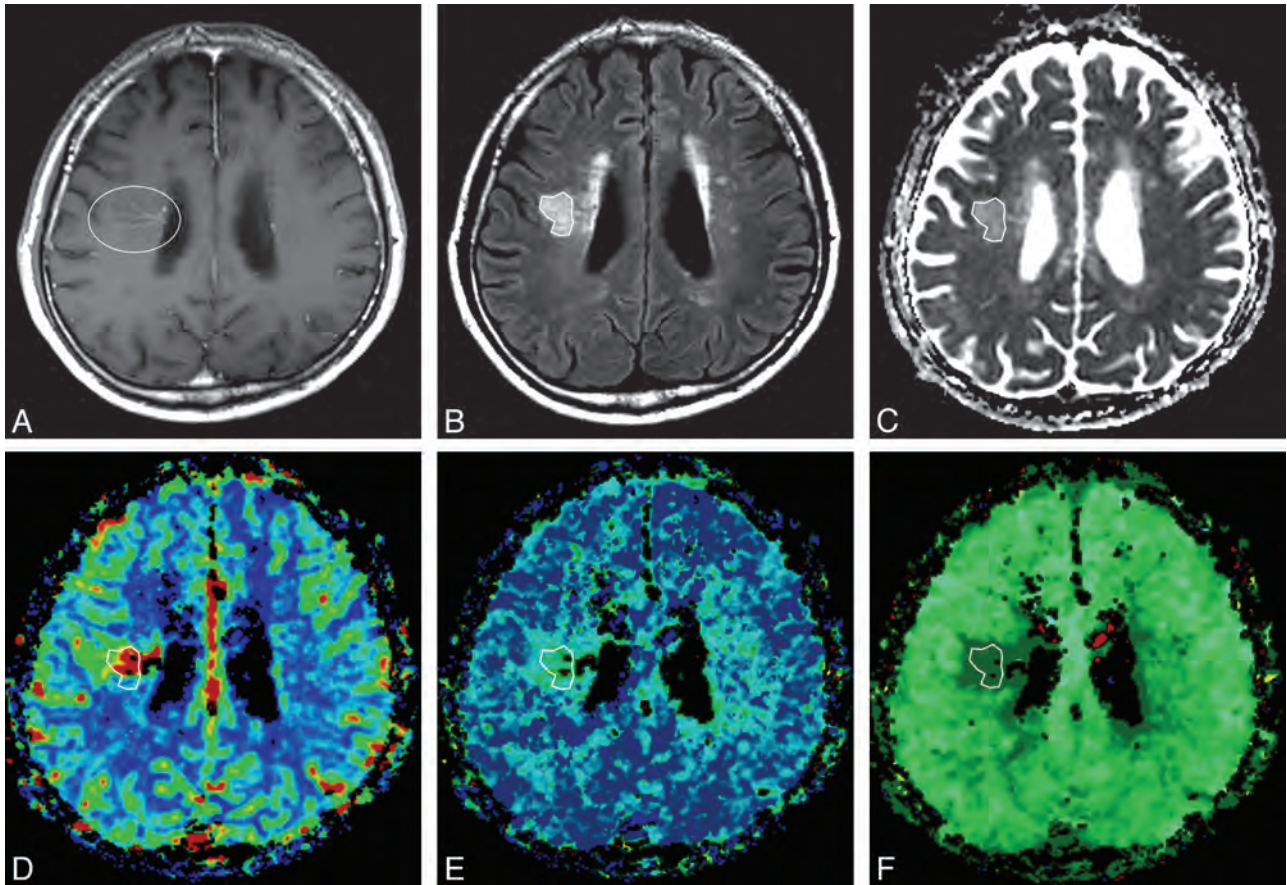
FIG 1. A 60-year-old man with blurred vision and headache. *A*, Postcontrast T1-weighted axial image shows a dilated medullary vein draining into the subependymal collecting vein in the right corona radiata (*circle*), representing a developmental venous anomaly. *B*, Abnormal signal intensity is seen in the area of the DVA (*polygon*) on the axial T2 fluid-attenuated inversion recovery imaging. *C*, Apparent diffusion coefficient. *D*, Relative cerebral blood volume. *E*, Relative mean transit time. *F*, Time-to-peak map demonstrates increased values of the corresponding area compared with contralateral normal white matter. These findings suggest that the nature of the SI abnormalities around DVAs is vasogenic edema with congestion and delayed perfusion.

etiology. Among them, considerable studies have supported venous congestion as the cause of SI change around a DVA.[3,8,10,18-25] Some studies have shown that DVAs may have thickened and hyalinized vessel walls without a smooth-muscle layer or elastic lamina.[11,18-20] Dillon[21] substantiated increased venous pressure within a DVA by measuring a 15-mm Hg pressure gradient across the stenotic collecting vein of a DVA in 1 patient. Truwit[3] reported that a focal stenosis of the draining vein may be seen at the point where it penetrates the dura to enter the dural sinus, resulting in delayed filling and emptying of the DVA. Narrowing of the veins can cause lessened compliance, increase resistance to flow, and reduce the capacity of the vessel to adjust to pressure changes.[10] Besides, a single collecting vessel in a DVA drains an abnormally large parenchymal territory, resulting in relative volume overload and chronic cerebral edema or ischemia.[10,22] Impaired cerebral blood flow attributed to venous congestion has been reported in the drainage vicinity of the DVA.[23-25] In recent CT and MR perfusion studies, increased CBV, CBF, and MTT can be observed in the region of the DVA.[26,27]

Abnormal SI lesions are understood as vascular-induced leukoaraiosis associated with chronic cerebral ischemia, resulting from venous congestion.[10] In addition, it seems reasonable that the underlying venous hypertension may be a causative factor in

hemorrhage, one of the rare complications of DVAs, as well as ischemia. A recent study revealed a significant relationship between abnormal SI in the drainage territory of DVAs and hypointense foci on phase-sensitive MR imaging, indicating microhemorrhage or cavernous malformation.[8] Venous hypertension would overload the vessel wall and cause injury, resulting in microhemorrhage from the weakest point and reactive angiogenesis.[28,29] For the angiogenesis, lack of vasoregulatory capacity of the neovasculature leads to repeated hemorrhage and formation of cavernous malformations, eventually.[30,31]

The results of the present study correspond well with the aforementioned studies. SI abnormalities in the draining area of DVAs showed higher ADC value, increased rCBV, and perfusion delay, compared with the normal white matter, representing venous congestion. The ADC value would increase in reactive gliosis—disruption of cell membranes, loss of myelin, or any process that may alter the integrity of axons that would reduce the restriction of water motion.[32] However, gliosis alone did not cause increased rCBV and perfusion delay. A previous study showed that areas of gliosis demonstrated significantly higher ADC values ($1.76 \pm 0.09 \times 10^{-3}$ mm^2/s) than areas of vasogenic edema ($1.35 \pm 0.06 \times 10^{-3}$ mm^2/s) without overlap.[32] The ADC value for SI abnormalities in the draining area of DVAs was 0.98 ± 0.13

$\times 10^{-3}$ mm^2/s, which is lower than that of gliosis. It is difficult to simply compare the ADC value in our study with that in the references because there is an absence of comparable gliosis evaluation and the area range of 34 cases in our study is quite broad. However, the alteration of perfusion parameters in SI abnormalities around DVAs compared with normal white matter could suggest that it has at least a component of vasogenic edema rather than gliosis alone.

Our study has several limitations. First, this was a retrospective study. Second, it had a small sample size. Third, the prevalence of SI abnormalities in the territory of DVAs in our study may not be entirely accurate and may potentially have selection bias because cases with DVAs were detected from reports of brain MR imaging with contrast and diffusion and perfusion studies. Fourth, we did not include the collecting vein in ROIs to avoid confusion of values of the perfusion measurements. However, the tributary veins were included in the ROIs, and this inclusion may have affected the results. Fifth, there was a lack of information about the values of DWI and PWI in the vicinity of the DVA without SI change. Further research is needed from 2 perspectives: Radiologically, diffusion tensor imaging could determine the pathophysiology of abnormally high signal intensity of white matter around DVAs in more detail. The clinical correlations, detailed follow-up, and management in clinical practice would be outside the scope of this imaging-based study.

CONCLUSIONS

The prevalence of abnormal SI associated with DVAs is not low, and vasogenic edema and venous congestion are the primary pathophysiologic characteristics of the SI abnormalities in the draining territory of DVAs.

REFERENCES

1. Garner TB, Del Curling O Jr, Kelly DL Jr, et al. **The natural history of intracranial venous angiomas.** *J Neurosurg* 1991;75:715–22
2. Sarwar M, McCormick WF. **Intracerebral venous angioma: case report and review.** *Arch Neurol* 1978;35:323–25
3. Truwit CL. **Venous angioma of the brain: history, significance, and imaging findings.** *AJR Am J Roentgenol* 1992;159:1299–307
4. Mateos JH, Dorfsman J, Lombardorivera L. **Vascular malformations of the spinal cord** [in Spanish]. *Rev Med Hosp Gen (Mex)* 1963;26:851–60
5. Calem WS, Jimenez FA. **Vascular malformations of the intestine: their role as a source of hemorrhage.** *Arch Surg* 1963;86:571–79
6. Aimes A. **Vascular malformations and lesions in pathology** [in French]. *Angeiologie* 1963;15:33–39
7. Lasjaunias P, Burrows P, Planet C. **Developmental venous anomalies (DVA): the so-called venous angioma.** *Neurosurg Rev* 1986;9:233–42
8. Takasugi M, Fujii S, Shinohara Y, et al. **Parenchymal hypointense foci associated with developmental venous anomalies: evaluation by phase-sensitive MR imaging at 3T.** *AJNR Am J Neuroradiol* 2013;34:1940–44
9. Santucci GM, Leach JL, Ying J, et al. **Brain parenchymal signal abnormalities associated with developmental venous anomalies: detailed MR imaging assessment.** *AJNR Am J Neuroradiol* 2008;29:1317–23
10. San Millán Ruíz D, Delavelle J, Yilmaz H, et al. **Parenchymal abnormalities associated with developmental venous anomalies.** *Neuroradiology* 2007;49:987–95
11. Courville CB. **Morphology of small vascular malformations of the brain: with particular reference to the mechanism of their drainage.** *J Neuropathol Exp Neurol* 1963;22:274–84
12. Djindjian R, Faure C. **Neuro-radiological investigations (arteriography and phlebography) in vascular malformations of the spinal cord** [in French]. *Rontgeneur Radiodiagn Clin Eur* 1963;158:171–95
13. Munoz DG, Hastak SM, Harper B, et al. **Pathologic correlates of increased signals of the centrum ovale on magnetic resonance imaging.** *Arch Neurol* 1993;50:492–97
14. Noran HH. **Intracranial vascular tumors and malformations.** *Arch Pathol* 1945;39:393–416
15. Moody DM, Brown WR, Challa VR, et al. **Periventricular venous collagenosis: association with leukoaraiosis.** *Radiology* 1995;194:469–76
16. Galambos C, Nodit L. **Identification of lymphatic endothelium in pediatric vascular tumors and malformations.** *Pediatr Dev Pathol* 2005;8:181–89
17. Koch G. **Hereditary of vascular tumors and malformations of the brain** [in undetermined language]. *J Med (Oporto)* 1953;21:657–70
18. McCormick WF. **The pathology of vascular ("arteriovenous") malformations.** *J Neurosurg* 1966;24:807–16
19. Koussa A, Chiras J, Poirier B, et al. **X-ray computed tomographic and angiographic aspects of venous angiomas of the brain: apropos of 15 cases** [in French]. *Neurochirurgie* 1985;31:161–68
20. Abe M, Hagihara N, Tabuchi K, et al. **Histologically classified venous angiomas of the brain: a controversy.** *Neurol Med Chir (Tokyo)* 2003;43:1–10, discussion 11
21. Dillon WP. **Cryptic vascular malformations: controversies in terminology, diagnosis, pathophysiology, and treatment.** *AJNR Am J Neuroradiol* 1997;18:1839–46
22. Pereira VM, Geibprasert S, Krings T, et al. **Pathomechanisms of symptomatic developmental venous anomalies.** *Stroke* 2008;39:3201–15
23. Matsuda H, Terada T, Katoh M, et al. **Brain perfusion SPECT in a patient with a subtle venous angioma.** *Clin Nucl Med* 1994;19:785–88
24. Uchida K, Tamura K, Takayama H, et al. **Xenon-enhanced CT CBF measurements in intracranial vascular malformations** [in Japanese]. *No Shinkei Geka* 1989;17:239–46
25. Tomura N, Inugami A, Uemura K, et al. **Multiple medullary venous malformations decreasing cerebral blood flow: case report.** *Surg Neurol* 1991;35:131–35
26. Kroll H, Soares BP, Saloner D, et al. **Perfusion-CT of developmental venous anomalies: typical and atypical hemodynamic patterns.** *J Neuroradiol* 2010;37:239–42
27. Sharma A, Zipfel GJ, Hildebolt C, et al. **Hemodynamic effects of developmental venous anomalies with and without cavernous malformations.** *AJNR Am J Neuroradiol* 2013;34:1746–51
28. Perrini P, Lanzino G. **The association of venous developmental anomalies and cavernous malformations: pathophysiological, diagnostic, and surgical considerations.** *Neurosurg Focus* 2006;21:e5
29. Awad IA, Robinson JR Jr, Mohanty S, et al. **Mixed vascular malformations of the brain: clinical and pathogenetic considerations.** *Neurosurgery* 1993;33:179–88, discussion 88
30. Rammos SK, Maina R, Lanzino G. **Developmental venous anomalies: current concepts and implications for management.** *Neurosurgery* 2009;65:20–29, discussion 29–30
31. Hong YJ, Chung TS, Suh SH, et al. **The angioarchitectural factors of the cerebral developmental venous anomaly; can they be the causes of concurrent sporadic cavernous malformation?** *Neuroradiology* 2010;52:883–91
32. Hagen T, Ahlhelm F, Reiche W. **Apparent diffusion coefficient in vasogenic edema and reactive astrogliosis.** *Neuroradiology* 2007;49:921–26

Generalized versus Patient-Specific Inflow Boundary Conditions in Computational Fluid Dynamics Simulations of Cerebral Aneurysmal Hemodynamics

I.G.H. Jansen, J.J. Schneiders, W.V. Potters, P. van Ooij, R. van den Berg, E. van Bavel, H.A. Marquering, and C.B.L.M. Majoie

ABSTRACT

BACKGROUND AND PURPOSE: Attempts have been made to associate intracranial aneurysmal hemodynamics with aneurysm growth and rupture status. Hemodynamics in aneurysms is traditionally determined with computational fluid dynamics by using generalized inflow boundary conditions in a parent artery. Recently, patient-specific inflow boundary conditions are being implemented more frequently. Our purpose was to compare intracranial aneurysm hemodynamics based on generalized versus patient-specific inflow boundary conditions.

MATERIALS AND METHODS: For 36 patients, geometric models of aneurysms were determined by using 3D rotational angiography. 2D phase-contrast MR imaging velocity measurements of the parent artery were performed. Computational fluid dynamics simulations were performed twice: once by using patient-specific phase-contrast MR imaging velocity profiles and once by using generalized Womersley profiles as inflow boundary conditions. Resulting mean and maximum wall shear stress and oscillatory shear index values were analyzed, and hemodynamic characteristics were qualitatively compared.

RESULTS: Quantitative analysis showed statistically significant differences for mean and maximum wall shear stress values between both inflow boundary conditions ($P < .001$). Qualitative assessment of hemodynamic characteristics showed differences in 21 cases: high wall shear stress location ($n = 8$), deflection location ($n = 3$), lobulation wall shear stress ($n = 12$), and/or vortex and inflow jet stability ($n = 9$). The latter showed more instability for the generalized inflow boundary conditions in 7 of 9 patients.

CONCLUSIONS: Using generalized and patient-specific inflow boundary conditions for computational fluid dynamics results in different wall shear stress magnitudes and hemodynamic characteristics. Generalized inflow boundary conditions result in more vortices and inflow jet instabilities. This study emphasizes the necessity of patient-specific inflow boundary conditions for calculation of hemodynamics in cerebral aneurysms by using computational fluid dynamics techniques.

ABBREVIATIONS: CFD = computational fluid dynamics; PC-MR imaging = 2D phase-contrast MR imaging; WSS = wall shear stress

It has been estimated that the prevalence of intracranial aneurysms in the adult population is between 1% and 5%.[1] Although most aneurysms go undetected, acute rupture resulting in subarachnoid hemorrhage is associated with high morbidity and fatality rates.[2,3] Ruptured aneurysms are treated by coiling or clipping to prevent rebleed. The indication for preventive treatment of unruptured aneurysms is, however, not straightforward.[4,5] The risk of treatment has to be carefully balanced against the risk of rupture. At present, rupture-risk assessment of unruptured intracranial aneurysms and the decision to treat or wait and scan are mainly based on size, location, and growth of the aneurysm.[6] It is, however, clear that the predictive value of these characteristics is limited.[1,6-8] It is therefore crucial to search for additional and more predictive parameters for aneurysm rupture risk assessment.

Aneurysmal hemodynamics, in particular wall shear stress (WSS) and vortex instability, have been proposed as additional risk factors for aneurysm growth and rupture.[9,10] It has been shown that the combination of vortex instability and high or low WSS within the aneurysm is more prevalent in ruptured cases.[11-13]

In many studies, computational fluid dynamics (CFD) is used to simulate aneurysmal hemodynamics. CFD is traditionally performed by using generalized inflow boundary conditions based on typical flow rates in a healthy adult.[14-27] Recently, several studies have replaced these generalized inflow boundary conditions by patient-specific velocity measurements in the vessels proximal to the aneurysm.[10,12,28-32] In these studies, either 2D phase-contrast MR imaging (PC-MR imaging) or transcranial Doppler sonography was used to measure the flow. So far, only 3 studies have compared patient-specific with generalized inflow boundary conditions in a total of 14 aneurysms.[28-30] Evidently, the necessity of using patient-specific inflow boundary conditions has not been elucidated to the full extent. In this study, we assessed the effects of patient-specific inflow boundary conditions in a group of 36 patients.

MATERIALS AND METHODS

Patient Selection
Image data of 36 aneurysms in 36 patients who presented at the Academic Medical Center, Amsterdam, The Netherlands with ruptured or unruptured aneurysms from January 2009 to October 2011 were retrospectively selected from a cohort of 164 patients in an ongoing study of aneurysm hemodynamics. This was done on the basis of the high signal quality of inflow velocity measurements. Of the selected aneurysms, 9 were located in the medial cerebral artery; 7 in the carotid artery; 6 in the anterior communicating artery; 6 in the posterior communicating artery; 3 in the basilar artery; 2 in the pericallosal artery; 1 in the anterior cerebral artery; 1 in the vertebral artery; and 1 in the ophthalmic artery. Six aneurysms were ruptured. Aneurysm size ranged from 3.2 to 12.4 mm. Dome-to-neck ratio ranged from 0.72 to 2.32. A Glasgow Outcome Score of $\geq$4 for patients with ruptured aneurysms was mandatory.[33] Exclusion criteria were contraindications for MR imaging, including treatment of the aneurysm by surgical clipping. The study was approved by the local ethics committee. Written informed consent was obtained from all patients.

Imaging
All patients underwent high-resolution 3D rotational angiography as part of the standard clinical work-up with de novo aneurysms. This was done in either the awake state (in the case of unruptured aneurysms) or during endovascular treatment with the patient under general anesthesia (in the case of ruptured aneurysms). A single-plane angiographic unit was used (Integris Allura Neuro; Philips Healthcare, Best, the Netherlands). Twenty-one milliliters of contrast agent was administered at 3 mL/s (iodixanol, Visipaque; GE Healthcare, Cork, Ireland). This resulted in a 256^3 isotropic image volume. Following this, 3D velocity measurements proximal to the aneurysm were obtained with PC-MR imaging. A single-section PC-MR imaging was performed on a 3T scanner (Intera; Philips Healthcare). Scan resolution was 0.64 $\times$ 0.65 $\times$ 3 mm. Further imaging parameters were the following: TE/TR/flip angle, 5.7 ms/8.5 ms/10°; receiver bandwidth, 172 kHz; imaging volume, 200 $\times$ 200 $\times$ 3 mm in 1 section; parallel imaging factor, 2. The velocity-encoding was 100 cm/s in all directions. The number of measured cardiac phases (ie, temporal resolution) depended on the heart rate and ranged between

23 and 36 cardiac phases, to keep the scanning time close to 3 minutes 30 seconds. The view-sharing factor for the retrospective sorting of acquired k-lines was set to 1.8.

Because patients with ruptured aneurysms were treated within 24 hours after onset, MR imaging velocity measurements to assess inflow boundary conditions could not be performed before the coiling procedure. Therefore, for this patient group, postprocedural PC-MR images were obtained at the standard follow-up 6 months after coiling. Patients with unruptured aneurysms were requested to undergo an additional preprocedural PC-MR imaging study at admission.

Geometric Vascular Models
To generate vascular models that were usable for CFD, we segmented the aneurysm and its connected arteries in 3D rotational angiography images by using a level-set algorithm by using the Vascular Modeling Toolkit, VMTK Version 0.9.0 (http://www.vmtk.org). Subsequently, the segmented volumes were converted to volumetric meshes consisting of approximately 1,000,000 tetrahedral elements.

Computational Fluid Dynamics
For each aneurysm, we performed 2 CFD simulations: one applying spatiotemporal patient-specific inflow boundary conditions, acquired by PC-MR imaging velocity measurements, and the other applying generalized inflow boundary conditions.[34] The generalized inflow velocity profile was defined by predetermined Womersley profiles for fully developed pulsatile flow.[35,36] The flow was scaled so that the total generalized inflow equaled the measured inflow rate as determined by PC-MR imaging. Zero pressure boundary conditions were prescribed at all outlets. A no-slip boundary was set, and rigid walls were assumed. Transient Navier-Stokes equations were solved by using a pressure-based, 3D double-precision solver following the Semi-Implicit Method for Pressure Linked Equations.[37] Blood was modeled with an attenuation of 1040 kg/m^3 and a dynamic viscosity of 0.004 Pa/s. CFD simulations were performed with Fluent software (ANSYS, Canonsburg, Pennsylvania). Three cardiac cycles were simulated to account for the transient character. Only the third complete cycle was used for analysis.[36]

Quantitative Assessment of Hemodynamic Features
The mean WSS, maximum WSS, mean oscillatory shear index, and maximum oscillatory shear index values were calculated. Paired differences between the generalized and patient-specific inflow boundary conditions were analyzed by using paired t test statistics. Results with P values of <.05 were considered statistically significant.

Qualitative Assessment of Hemodynamic Features
Velocity-based streamlines and WSS patterns within the aneurysm during 1 cardiac cycle were visualized as movie clips with ParaView software (Kitware; Los Alamos National Laboratory, Los Alamos, New Mexico). On the basis of these movie clips, hemodynamic characteristics were scored in consensus by 2 neuroradiologists with >10 years of experience. The cases were randomly presented to the observers, who were blinded to the method of inflow boundary conditions used.
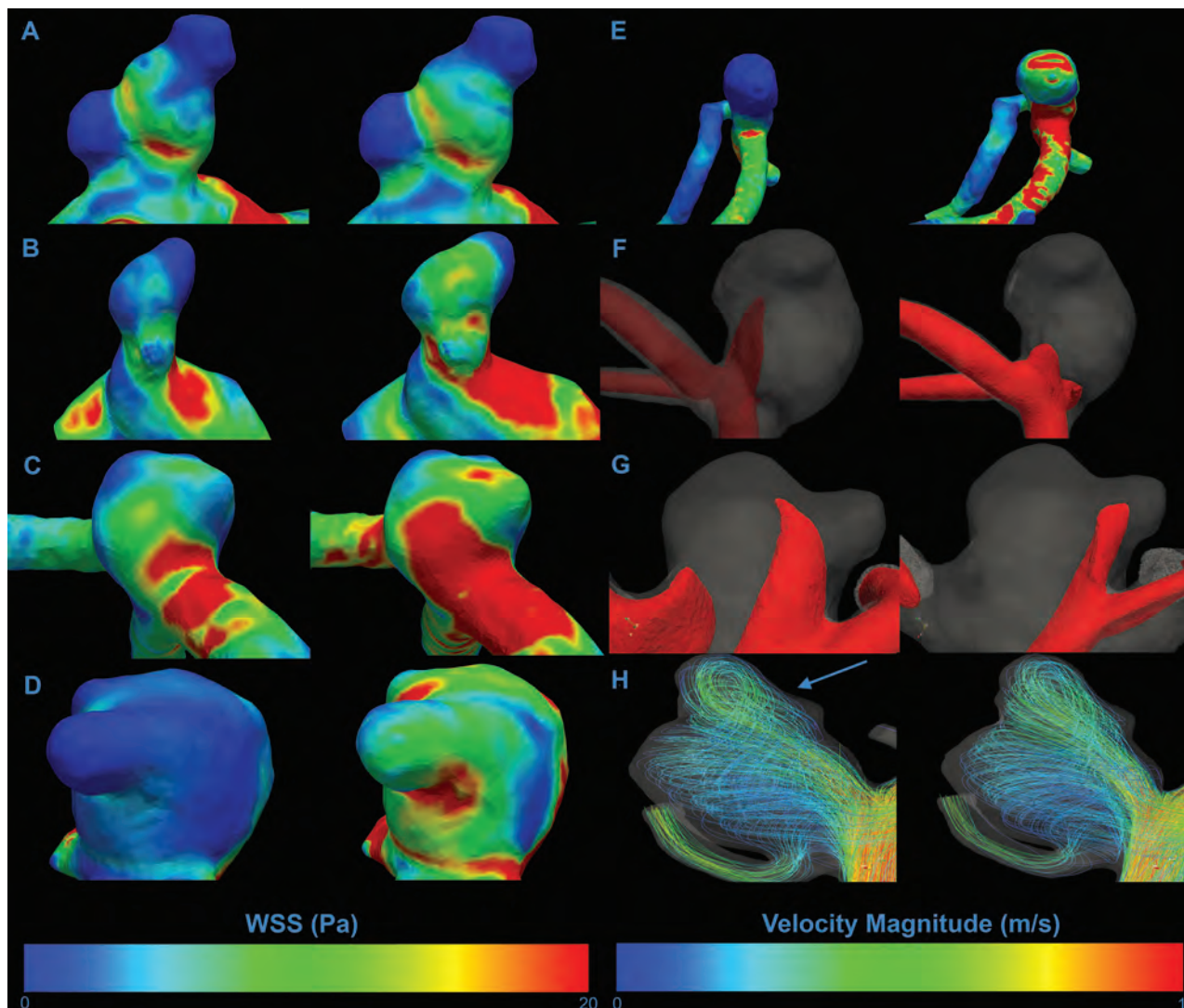
FIG 1. Examples of visualized differences in hemodynamic characteristics. The left column shows patient-specific inflow boundary conditions; the right column shows generalized boundary conditions. *A–H*, Differences in distribution for all assessed WSS characteristics. *A*, No difference in any characteristic. *B*, High WSS area on the ostium of lobulation. *C*, High WSS location on the primary aneurysm. *D*, High WSS on the lobulation sac. *E*, Deflection zone. *F* and *G*, Isosurface projections of inflow jet characteristics. *F*, Inflow jet concentration. *G*, Inflow jet aim in the lobulation. *H*, Visualization of intra-aneurysmal flow structures represented by velocity magnitude streamlines. On this figure, a difference in the number of vortices can be appreciated, with an additional vortex for the patient-specific inflow boundary conditions (*blue arrow*).

We assessed the following hemodynamic characteristics: inflow jet concentration, inflow jet stability, number of vortices, vortex stability, location of the highest WSS, and location of the deflection zone. If the aneurysm contained a lobulation, WSS on the lobulation sac and on the ostium of the lobulation were also assessed, as well as the direction of the main inflow jet toward the lobulation.

The inflow jet was defined as an isosurface of 25% of the maximum velocity magnitude within the aneurysm. It was considered "concentrated" when interpreted as smaller than half the size of the aneurysm neck, and "diffuse" if larger. In the event of the flow pattern deteriorating or changing considerably during the cardiac cycle, it was labeled as "unstable." The number of vortices was defined as the number of flow structures within the aneurysm and, if present, in the lobulation. The location of the highest WSS and deflection zone were classified according to their position as dome, body, or neck.[36] The "deflection zone" was defined as the area of divergence of the inflow jet on the aneurysm wall. For each

hemodynamic parameter, differences between the 2 inflow boundary conditions were assessed and the amount of difference was rated between 1 and 5, with 5 representing a large difference. Differences between the scores of the observers were discussed in an additional meeting to reach a consensus.

RESULTS

Figure 1 presents differences in hemodynamic characteristics between generalized or patient-specific inflow boundary conditions in the same aneurysm. For each scored hemodynamic characteristic, 1 example is given. An example of the flow rate curve for both methods is displayed in Fig 2.

Quantitative Assessment of Hemodynamic Features

Table 1 displays the mean and maximum WSS and oscillatory shear index values per method, including their relative differences. Mean WSS was larger for the generalized inflow boundary

conditions, with an average of 3.5 Pa ($P < .001$). The maximum WSS was also larger for the generalized approach with an average of 65 Pa ($P = .0013$). The differences for mean or maximum oscillatory shear index values were not statistically significant ($P = .42$ and $P = .65$, respectively). In On-line Table 1, all measured values per case used in the quantitative assessment, including their relative differences, are displayed.

Qualitative Assessment of Hemodynamic Features

Table 2 displays the number of differences in hemodynamic characteristics as scored during the qualitative assessment. In 21 of 36 aneurysms, at least 1 of the characteristics was scored differently for the 2 inflow boundary conditions. Seven aneurysms with differences in WSS characteristics showed no differences in vortex and inflow jet characteristics (eg, patient 16). Six patients with no differences in WSS characteristics showed distinct differences in vortex and inflow jet characteristics (eg, patient 27). Furthermore, aneurysms showing differences in vortex and inflow jet characteristics were more often assessed as unstable for the generalized inflow boundary conditions. This was seen in 7 of 9 aneurysms with differences in vortex characteristics and all aneurysms with differences in inflow jet characteristics. In On-line Table 2, a detailed overview of the qualitative assessment is given, in which
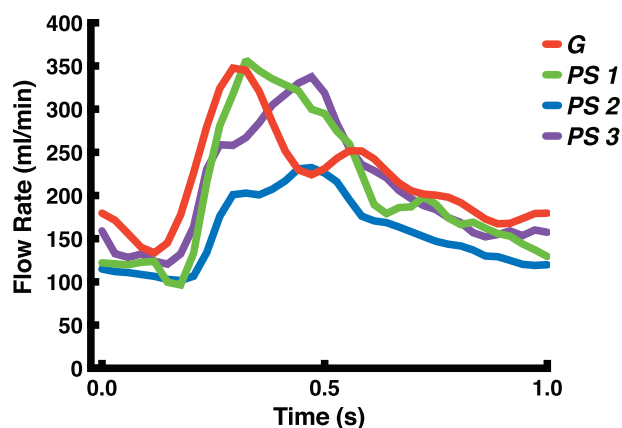
FIG 2. Examples of the applied flow-rate pattern during 1 heart cycle for both methods. PS indicates patient-specific flow rate curves of 3 separate cases (blue, purple, and green); G, generalized flow-rate curve (red).

each case can be appreciated for which hemodynamic characteristic differences between the 2 methods were scored.

DISCUSSION

We showed that the choice of general or patient-specific inflow boundary conditions results in large differences in WSS magnitude and distribution. Differences in vortex and inflow jet characteristics occurred less frequently. The approach by using generalized inflow boundary conditions led to considerably more unstable vortices and inflow jets, suggesting that inflow jet and vortex instability are sensitive to inflow boundary conditions. These data indicate that previous findings on vortex instability by using generalized inflow boundary conditions should be considered with caution.[38]

Both patient-specific and generalized inflow boundary conditions are traditionally used for CFD analysis of cerebral aneurysm hemodynamics. However, only 2 authors have so far compared both approaches.[28-30] The large differences in WSS magnitude and WSS distribution found in our study are in line with findings of a smaller study in 6 patients by Karmonik et al,[28] who pointed out differences in both WSS values and in WSS distribution between the 2 inflow boundary conditions. In addition, Venugopal et al[39] showed that WSS distributions are sensitive to changes in flow-rate distribution in the proximal artery. Marzo et al[30] also reported differences in WSS magnitude but did not report changes in WSS distribution outside the order of physiologic variations.

Twenty-one of 36 aneurysms showed at least 1 difference in a hemodynamic characteristic for the 2 inflow boundary conditions. Most of these were WSS-related, such as high WSS location and level of WSS on the lobulation sac. Fewer differences were found in vortex- or inflow jet–related characteristics. This discrepancy could be explained by findings of Cebral et al,[36] who have shown that variations of up to 25% in blood flow rate do not affect the flow patterns inside the aneurysm.

There are several limitations related to the design of this study. It did not address the role of outflow boundary conditions and flow divisions distal to the aneurysm, which could influence the accuracy of the results. In addition, for patients with a ruptured aneurysm, postprocedural PC-MR imaging velocity measurements were used for the inflow boundary conditions to simulate preprocedural hemodynamics. The embolization itself may alter the local hemodynamics, resulting in an inadequate representa-

Table 1: Quantitative values for mean and maximum WSS and OSI[a]

Method	Mean WSS (Pa)			Max WSS (Pa)			Mean OSI (Pa)			Max OSI (Pa)		
	PS	G	Δ	PS	G	Δ	PS	G	Δ	PS	G	Δ
Median	2.1	2.9	−28%	38	54	−11%	0.013	0.011	18%	0.40	0.36	11%
Average	2.5	3.5	−29%	43	64	−33%	0.020	0.017	18%	0.36	0.35	0.3%
SD	1.7	2.7	−29%	27	44	−39%	0.024	0.021	14%	0.11	0.10	1%

Note:—PS indicates patient-specific inflow boundary conditions; G, generalized inflow boundary conditions; Δ, (PS−G)/G × 100%; Max, maximum; OSI, oscillatory shear index.
[a] Relative differences are presented as percentages.

Table 2: Qualitative assessment: number of cases for each scored hemodynamic characteristic showing a difference between the patient-specific inflow boundary conditions and the generalized inflow boundary conditions

	Inflow Jet		Vortex		WSS Location		Lobulation		
	Concentration	Stability	No.	Stability	High WSS	Deflection	WSS	Jet Aim	Ostium WSS
No.	1	7	5	6	9	3	9	2	8

tion of pre-embolization hemodynamics. However, we have compared pre- and postprocedural PC-MR imaging measurements of the parent artery in a small number of patients (with unruptured aneurysms) and did not detect notable differences. Finally, vascular compliance and fluid-wall interaction were not incorporated in this model. Disregarding these effects may have influenced the resulting hemodynamic characteristics and may have led to an overestimation of mean and maximum WSS values.[10]

The findings of this study emphasize that running simulations with generalized boundary conditions may result in variations in WSS magnitude and distribution and may overestimate vortex instability. These variations could greatly influence the association of hemodynamics with the rupture of cerebral aneurysms. Therefore, interpretation of WSS profiles should be applied with great caution when generalized inflow boundary conditions are used for this purpose. More research is also needed to further investigate the influence of other boundary conditions on CFD in aneurysms, ideally incorporating the effect of wall and outflow boundary conditions.

CONCLUSIONS

Patient-specific and generalized inflow boundary conditions in CFD-based simulations of aneurysmal hemodynamics resulted in large differences in WSS magnitudes. In addition, 21 of 36 aneurysms showed differences in hemodynamics characteristics. Aneurysms showing differences in vortex and inflow jet characteristics were more often assessed as unstable when generalized inflow boundary conditions were applied. This study emphasizes the necessity of the use of patient-specific inflow boundary conditions for the calculation of hemodynamics in cerebral aneurysms by using CFD techniques.

REFERENCES

1. Brisman JL, Song JK, Newell DW. **Cerebral aneurysms.** *N Engl J Med* 2006;355:928–39
2. Taylor TN. **The medical economics of stroke.** *Drugs* 1997;54(suppl 3): 51–57
3. Taylor TN, Davis PH, Torner JC, et al. **Lifetime cost of stroke in the United States.** *Stroke* 1996;27:1459–66
4. Raymond J, Guilbert F, Weill A, et al. **Long-term angiographic recurrences after selective endovascular treatment of aneurysms with detachable coils.** *Stroke* 2003;34:1398–403
5. Murayama Y, Nien YL, Duckwiler G, et al. **Guglielmi detachable coil embolization of cerebral aneurysms: 11 years' experience.** *J Neurosurg* 2003;98:959–66
6. The International Study of Unruptured Intracranial Aneurysms Investigators. **Unruptured intracranial aneurysms: risk of rupture and risks of surgical interventions.** *N Engl J Med* 1998;339:1725–33
7. Tsutsumi K, Ueki K, Morita A, et al. **Risk of rupture from incidental cerebral aneurysms.** *J Neurosurg* 2000;93:550–53

8. Juvela S, Porras M, Poussa K. **Natural history of unruptured intracranial aneurysms: probability of and risk factors for aneurysm rupture.** *J Neurosurg* 2000;93:379–87
9. Metaxa E, Tremmel M, Natarajan SK, et al. **Characterization of critical hemodynamics contributing to aneurysmal remodeling at the basilar terminus in a rabbit model.** *Stroke* 2010;41:1774–82
10. Jou LD, Quick CM, Young WL, et al. **Computational approach to quantifying hemodynamic forces in giant cerebral aneurysms.** *AJNR Am J Neuroradiol* 2003;24:1804–10
11. Meng H, Tutino VM, Xiang J, et al. **High WSS or low WSS? Complex interactions of hemodynamics with intracranial aneurysm initiation, growth, and rupture: toward a unifying hypothesis.** *AJNR Am J Neuroradiol* 2014;35:1254–62
12. Boussel L, Rayz V, Mcculloch C, et al. **Aneurysm growth occurs at region of low wall shear stress: patient-specific correlation of hemodynamics and growth in a longitudinal study.** *Stroke* 2008;39:2997–3002
13. Xiang J, Natarajan SK, Tremmel M, et al. **Hemodynamic-morphologic discriminants for intracranial aneurysm rupture.** *Stroke* 2011;42:144–52
14. Ford MD, Alperin N. **Characterization of volumetric flow rate waveforms in the normal internal carotid and vertebral arteries.** *Physiol Meas* 2005;26:477–88
15. Castro MA, Putman CM, Cebral JR. **Computational fluid dynamics modeling of intracranial aneurysms: effects of parent artery segmentation on intra-aneurysmal hemodynamics.** *AJNR Am J Neuroradiol* 2006;27:1703–09
16. Castro MA, Putman CM, Cebral JR. **Patient-specific computational fluid dynamics modelling of anterior communicating artery aneurysms: a study of sensitivity of intra-aneurysmal flow patterns to flow conditions in the carotid arteries.** *AJNR Am J Neuroradiol* 2006;27:2061–68
17. Cebral J, Sheridan M, Putman CM. **Hemodynamics and bleb formation in intracranial aneurysms.** *AJNR Am J Neuroradiol* 2010;31:304–10
18. Cebral JR, Castro MA, Burgess JE, et al. **Characterization of cerebral aneurysms for assessing risk of rupture by using patient-specific computational hemodynamics models.** *AJNR Am J Neuroradiol* 2005;26:2550–59
19. Cebral JR, Löhner R. **Efficient simulation of blood flow past complex endovascular devices using an adaptive embedding technique.** *IEEE Trans Med Imaging* 2005;24:468–76
20. Cebral JR, Pergolizzi RS, Putman CM. **Computational fluid dynamics modeling of intracranial aneurysms: qualitative comparison with cerebral angiography.** *Acad Radiol* 2007;14:804–13
21. Dempere-Marco L, Oubel E, Castro M, et al. **CFD analysis incorporating the influence of wall motion: application to intracranial aneurysms.** *Med Image Comput Comput Assist Interv* 2006;9(pt 2): 438–45
22. Ford MD, Stuhne GR, Nikolov HN, et al. **Virtual angiography for visualization and validation of computational models of aneurysm hemodynamics.** *IEEE Trans Med Imaging* 2005;24:1586–92
23. Hoi Y, Woodward SH, Kim M, et al. **Validation of CFD simulations of cerebral aneurysms with implication of geometric variations.** *J Biomech Eng* 2006;128:844–51
24. Imai Y, Sato K, Ishikawa T, et al. **Inflow into saccular cerebral aneurysms at arterial bends.** *Ann Biomed Eng* 2008;36:1489–95
25. Mantha A, Karmonik C, Benndorf G, et al. **Hemodynamics in a cerebral artery before and after the formation of an aneurysm.** *AJNR Am J Neuroradiol* 2006;27:1113–18
26. Shojima M, Nemoto S, Morita A, et al. **Role of shear stress in the blister formation of cerebral aneurysms.** *Neurosurgery* 2010;67: 1268–74
27. Shojima M, Oshima M, Takagi K, et al. **Magnitude and role of wall shear stress on cerebral aneurysm: computational fluid dynamic study of 20 middle cerebral artery aneurysms.** *Stroke* 2004;35: 2500–05
28. Karmonik C, Yen C, Diaz O, et al. **Temporal variations of wall shear**

stress parameters in intracranial aneurysms: importance of patient-specific inflow waveforms for CFD calculations. *Acta Neurochir (Wien)* 2010;152:1391–98, discussion 1398

29. Karmonik C, Yen C, Grossman RG, et al. **Intra-aneurysmal flow patterns and wall shear stresses calculated with computational flow dynamics in an anterior communicating artery aneurysm depend on knowledge of patient-specific inflow rates.** *Acta Neurochir (Wien)* 2009;151:479–85, discussion 485

30. Marzo A, Singh P, Larrabide I, et al. **Computational hemodynamics in cerebral aneurysms: the effects of modeled versus measured boundary conditions.** *Ann Biomed Eng* 2011;39:884–96

31. Omodaka S, Sugiyama S, Inoue T, et al. **Local hemodynamics at the rupture point of cerebral aneurysms determined by computational fluid dynamics analysis.** *Cerebrovasc Dis* 2012;34:121–29

32. Hassan T, Ezura M, Timofeev EV, et al. **Computational simulation of therapeutic parent artery occlusion to treat giant vertebrobasilar aneurysm.** *AJNR Am J Neuroradiol* 2004;25:63–68

33. Mitchell P, Kerr R, Mendelow AD, et al. **Could late rebleeding overturn the superiority of cranial aneurysm coil embolization over clip ligation seen in the International Subarachnoid Aneurysm Trial?** *J Neurosurg* 2008;108:437–42

34. van Ooij P, Schneiders JJ, Marquering HA, et al. **3D cine phase-contrast MRI at 3T in intracranial aneurysms compared with patient-specific computational fluid dynamics.** *AJNR Am J Neuroradiol* 2013;34:1785–91

35. Steinman DA, Hoi Y, Fahy P, et al. **Variability of computational fluid dynamics solutions for pressure and flow in a giant aneurysm: the ASME 2012 Summer Bioengineering Conference CFD Challenge.** *J Biomech Eng* 2013;135:021016

36. Cebral JR, Castro MA, Appanaboyina S, et al. **Efficient pipeline for image-based patient-specific analysis of cerebral aneurysm hemodynamics: technique and sensitivity.** *IEEE Trans Med Imaging* 2005;24:457–67

37. Patankar SV, Spalding DB. **A calculation procedure for heat, mass and momentum transfer in three-dimensional parabolic flows.** *Int J Heat Mass Transf* 1972;15:1787–806

38. Byrne G, Mut F, Cebral JR. **Quantifying the large-scale hemodynamics of intracranial aneurysms.** *AJNR Am J Neuroradiol* 2014;35:333–38

39. Venugopal P, Valentino D, Schmitt H, et al. **Sensitivity of patient-specific numerical simulation of cerebral aneurysm hemodynamics to inflow boundary conditions.** *J Neurosurg* 2007;106:1051–60

40. González-Alonso J, Dalsgaard MK, Osada T, et al. **Brain and central haemodynamics and oxygenation during maximal exercise in humans.** *J Physiol* 2004;557(pt 1):331–42

Toward Improving Fidelity of Computational Fluid Dynamics Simulations: Boundary Conditions Matter

In their paper entitled "Generalized versus Patient-Specific Inflow Boundary Conditions in Computational Fluid Dynamics Simulations of Cerebral Aneurysmal Hemodynamics," Jansen et al[1] compare results from computational fluid dynamics (CFD) simulations performed with 2 different kinds of boundary conditions: a spatiotemporal inflow waveform measured with 2D phase-contrast MR imaging in the individual patient and a generalized inflow velocity profile previously described in the literature. In their comparison, Jansen et al focus on wall shear stress (WSS) and, derived from it, the oscillatory shear index as well as intra-aneurysmal flow patterns. In agreement with previously published results,[2-5] they report statistically significant differences for the 2 approaches.

Simulating hemodynamics in cerebral aneurysms with CFD techniques is a relatively new approach translating a well-established engineering technology into clinical research. Essentially, a computational model as an approximation of the real world is created and the governing equations for blood flow (Navier Stokes equations) are numerically solved based on this mathematic construct. The output of these simulations includes the velocity fields and the values of other hemodynamic parameters such as WSS or pressure.

The fidelity of the results depends on the kinds of approximations or simplifications made when creating the computational model. For instance, early simulations using 2D models with simple geometric approximations were able to demonstrate low WSS at the aneurysm dome[6]; however, because of inherent limitations, these models could not provide any information about the 3D distribution of the flow or WSS. In many studies to date, 3D volumetric information derived from medical image data specific to the individual patient is used, often from 3D digital subtraction angiography but also from CT angiography or MR angiography. Boundary conditions are approximated by generalized waveforms. These simulations succeed in providing a true 3D description of the spatial and temporal distributions of hemodynamic parameters. As there are no variations in the inflow boundary condition, differences in the simulation results between individual aneurysms originate from the aneurysm geometries alone. With this approach it was demonstrated that CFD can visualize and quantify hemodynamic differences between ruptured and unruptured aneurysms.[7-9]

As Jansen et al[1] demonstrate, simulations may be further refined by incorporating patient-derived flow information into the model as the exact shape of the inflow waveform may exert significant effects on at least some of the calculated hemodynamic parameters. However, physiologic waveforms may also vary. For instance, intense physical efforts or emotional excitement typically result in a sudden change in heart rate and blood pressure. A CFD study investigating the effects of increase in cardiac frequency found significant changes in the overall intra-aneurysmal flow patterns (eg, vortex formation and translation) and an increase in WSS.[10] These effects may also need to be considered for an accurate assessment of hemodynamics in cerebral aneurysms with CFD techniques.

CFD simulations are the results of mathematic constructs and validation of their results is necessary. Validation studies comparing virtual angiograms (derived from CFD) with acquired angiograms[11-14] and comparing simulated intra-aneurysmal flow patterns with those measured with 2D phase-contrast MR imaging[15-18] or 4D phase-contrast MR imaging[19,20] reported generally good agreement and thereby encourage the continued advancement of CFD. Still, a better understanding of the limitations of CFD simulations is warranted.[21-23]

Computational simulations will play an increased role in the future for enhancing and complementing the information in medical images. Furthermore, such simulations will not be limited to studies of hemodynamics in cerebral aneurysms. As an indicative example, CFD studies have been recently performed for investigating CSF flow in Chiari malformations.[24,25] Further validation and optimization of CFD techniques as well as streamlining the simulation process itself, eg, by using dedicated CFD simulation and visualization systems,[26] may foster further integration of this exciting technology into clinical research.

REFERENCES
1. Jansen IG, Schneiders JJ, Potters WV, et al. **Generalized versus patient-specific inflow boundary conditions in computational fluid**

dynamics simulations of cerebral aneurysmal hemodynamics. *AJNR Am J Neuroradiol* 2014;35:1543–48

2. Karmonik C, Yen C, Diaz O, et al. **Temporal variations of wall shear stress parameters in intracranial aneurysms–importance of patient-specific inflow waveforms for CFD calculations.** *Acta Neurochir (Wien)* 2010;152:1391–98; discussion 1398

3. Karmonik C, Yen C, Grossman RG, et al. **Intra-aneurysmal flow patterns and wall shear stresses calculated with computational flow dynamics in an anterior communicating artery aneurysm depend on knowledge of patient-specific inflow rates.** *Acta Neurochir (Wien)* 2009;151:479–85; discussion 485

4. Venugopal P, Valentino D, Schmitt H, et al. **Sensitivity of patient-specific numerical simulation of cerebal aneurysm hemodynamics to inflow boundary conditions.** *J Neurosurg* 2007;106:1051–60

5. Marzo A, Singh P, Larrabide I, et al. **Computational hemodynamics in cerebral aneurysms: the effects of modeled versus measured boundary conditions.** *Ann Biomed Eng* 2011;39:884–96

6. Burleson AC, Strother CM, Turitto VT. **Computer modeling of intracranial saccular and lateral aneurysms for the study of their hemodynamics.** *Neurosurgery* 1995;37:774–82; discussion 782–84

7. Byrne G, Mut F, Cebral J. **Quantifying the large-scale hemodynamics of intracranial aneurysms.** *AJNR Am J Neuroradiol* 2014; 35:333–38

8. Cebral JR, Mut F, Weir J, et al. **Association of hemodynamic characteristics and cerebral aneurysm rupture.** *AJNR Am J Neuroradiol* 2011;32:264–70

9. Jou LD, Lee DH, Morsi H, et al. **Wall shear stress on ruptured and unruptured intracranial aneurysms at the internal carotid artery.** *AJNR Am J Neuroradiol* 2008;29:1761–67

10. Jiang J, Strother C. **Computational fluid dynamics simulations of intracranial aneurysms at varying heart rates: a "patient-specific" study.** *J Biomech Eng* 2009;131:091001

11. Ford MD, Stuhne GR, Nikolov HN, et al. **Virtual angiography for visualization and validation of computational models of aneurysm hemodynamics.** *IEEE Trans Med Imag* 2005;24:1586–92

12. Endres J, Kowarschik M, Redel T, et al. **A workflow for patient-individualized virtual angiogram generation based on CFD simulation.** *Comput Math Methods Med* 2012;2012:306765

13. Sun Q, Groth A, Bertram M, et al. **Phantom-based experimental validation of computational fluid dynamics simulations on cerebral aneurysms.** *Med Phys* 2010;37:5054–65

14. Sun Q, Groth A, Aach T. **Comprehensive validation of computational fluid dynamics simulations of in-vivo blood flow in patient-specific cerebral aneurysms.** *Med Phys* 2012;39:742–54

15. Karmonik C, Klucznik R, Benndorf G. **Blood flow in cerebral aneurysms: comparison of phase contrast magnetic resonance and computational fluid dynamics–preliminary experience.** *Rofo* 2008; 180:209–15

16. Karmonik C, Klucznik R, Benndorf G. **Comparison of velocity patterns in an AComA aneurysm measured with 2D phase contrast MRI and simulated with CFD.** *Technol Health Care* 2008;16:119–28

17. Boussel L, Rayz V, Martin A, et al. **Phase-contrast magnetic resonance imaging measurements in intracranial aneurysms in vivo of flow patterns, velocity fields, and wall shear stress: comparison with computational fluid dynamics.** *Magn Reson Med* 2009; 61:409–17

18. Rayz VL, Boussel L, Acevedo-Bolton G, et al. **Numerical simulations of flow in cerebral aneurysms: comparison of CFD results and in vivo MRI measurements.** *J Biomed Eng* 2008;130:051011

19. Berg P, Stucht D, Janiga G, et al. **Cerebral blood flow in a healthy circle of Willis and two intracranial aneurysms: computational fluid dynamics versus 4D phase-contrast magnetic resonance imaging.** *J Biomed Eng* 2014;136:041003

20. Jiang J, Johnson K, Valen-Sendstad K, et al. **Flow characteristics in a canine aneurysm model: a comparison of 4D accelerated phase-contrast MR measurements and computational fluid dynamics simulations.** *Med Phys* 2011;38:6300–12

21. Cebral JR, Meng H. **Counterpoint: realizing the clinical utility of computational fluid dynamics– closing the gap.** *AJNR Am J Neuroradiol* 2012;33:396–98

22. Kallmes DF. **Point: CFD–computational fluid dynamics or confounding factor dissemination.** *AJNR Am J Neuroradiol* 2012; 33:395–96

23. Strother CM, Jiang J. **Intracranial aneurysms, cancer, x-rays, and computational fluid dynamics.** *AJNR Am J Neuroradiol* 2012; 33:991–92

24. Hentschel S, Mardal KA, Lovgren AE, et al. **Characterization of cyclic CSF flow in the foramen magnum and upper cervical spinal canal with MR flow imaging and computational fluid dynamics.** *AJNR Am J Neuroradiol* 2010;31:997–1002

25. Linge SO, Mardal KA, Haughton V, et al. **Simulating CSF flow dynamics in the normal and the Chiari I subarachnoid space during rest and exertion.** *AJNR Am J Neuroradiol* 2013;34:41–45

26. Karmonik C, Chintalapani G, Redel T, et al. **Hemodynamics at the ostium of cerebral aneurysms with relation to post-treatment changes by a virtual flow diverter: a computational fluid dynamics study.** *Conf Proc IEEE Eng Med Biol Soc* 2013;2013:1895–98

Christof Karmonik
Departments of Neurosurgery and Translational Imaging
Houston Methodist Hospital Research Institute
Houston, Texas
Weill Medical College of Cornell University
New York, New York

Effects of Circle of Willis Anatomic Variations on Angiographic and Clinical Outcomes of Coiled Anterior Communicating Artery Aneurysms

E. Tarulli, M. Sneade, A. Clarke, A.J. Molyneux, and A.J. Fox

ABSTRACT

BACKGROUND AND PURPOSE: Anterior communicating artery aneurysms account for one-fourth of all intracranial aneurysms and frequently occur in the context of A1 vessel asymmetry. The purpose of this study was to correlate circle of Willis anatomic variation association to angiographic and clinical outcomes of anterior communicating aneurysm coiling.

MATERIALS AND METHODS: The Cerecyte Coil Trial provides a subgroup of 124 cases with anterior communicating artery aneurysms after endovascular coiling. One hundred seventeen of 124 anterior communicating artery aneurysms had complete imaging and follow-up for clinical outcome analysis, stability of aneurysm coil packing, and follow-up imaging between 5 and 7 months after treatment. Clinical outcomes were assessed by the mRS at 6 months.

RESULTS: Anterior cerebral artery trunk-dominance was seen in 91 of 124 (73%) anterior communicating artery aneurysms and codominance in 33 of 124 (27%) anterior communicating artery aneurysms. There was no significant difference ($P > .5$) in treatment success at 5–7 months for anterior communicating artery aneurysms between the anterior cerebral artery trunk-dominant (49 of 86, 57%) and anterior cerebral artery trunk-codominant (19 of 31) groups. Angiographic follow-up demonstrates a statistically significant increase in neck remnants and progressive aneurysm sac filling with the A1 dominant configuration ($n = 21$, 24% at follow-up versus $n = 11$, 12% at immediate posttreatment, $P = .035$). There was no statistically significant difference in clinical outcomes between types of anterior cerebral artery trunk configuration ($P > .5$).

CONCLUSIONS: Anterior communicating artery aneurysms with anterior cerebral artery trunk-dominant circle of Willis configurations show less angiographic stability at follow-up than those with anterior cerebral artery trunk-codominance similar to other "termination" type aneurysms. This supports the hypothesis that anterior cerebral artery trunk-dominant flow contributes to aneurysm formation, growth, and instability after coiling treatment.

ABBREVIATIONS: AcomA = anterior communicating artery; A1 = anterior cerebral artery trunk; A2 = pericallosal artery; CCT = Cerecyte Coil Trial

The most common site of intracranial aneurysms is the anterior communicating artery (AcomA). AcomA aneurysms account for approximately one-fourth of all intracranial aneurysms.[1] Also very common in the setting of AcomA aneurysms is unilateral anterior cerebral artery trunk (A1) dominance where 1 side supplies both pericallosal artery (A2) arteries, a well-known phenom-

enon previously shown to be a potent risk factor for AcomA aneurysm formation and rupture.[1-3]

To what extent vessel dominance influences the long-term result of endovascular packing of these aneurysms with detachable platinum coils and the patients' clinical outcome is less well known.[4-6] One previous study indicates that vessel dominance is not a major factor in predicting short-term treatment outcome; however, the methodology and definition of vessel dominance as used in this instance was not stated.[7] Yet, anterior communicating aneurysms are commonly "termination type" with the aneurysm forming with a relatively wide neck at the site of the inferred jet of flowing blood dynamics, with main branches nearly perpendicular to the parent vessel, also commonly seen for basilar tip, internal carotid tip, and middle cerebral bifurcations.[8]

The Cerecyte Coil Trial (CCT) was a prospective, randomized, controlled study that entered 500 cases comparing endovascular coiling of ruptured and unruptured cerebral aneurysms with

FIG 1. DSA studies showing examples of A1 segment categories with white and black arrows indicating right and left A1, respectively, for codominant (*A*) and dominant (*B* and *C*) configurations. Panels *B* and *C* demonstrate A1 dominant cases with diminutive and absent contralateral A1 segments, respectively.

either Cerecyte or bare platinum coils that showed no difference between groups.[9,10] There was an expected large subset of AcomA aneurysms within the CCT cohort ($n = 124$).[9] Therefore, data from this trial provided a unique opportunity to obtain a large number of AcomA aneurysm cases for determination of A1 dominance in relation to coiling treatment and angiographic outcomes immediately posttreatment and at follow-up. Our goal was to determine the impact of A1 dominance on treatment success, stability, and clinical outcomes of endovascularly coiled AcomA aneurysms.

MATERIALS AND METHODS
The methodology of the CCT core laboratory analysis of angiographic outcomes has been previously published with 249 and 251 aneurysm cases randomized and treated by bare platinum and Cerecyte coils.[9] The CCT data base was made available for this analysis. All CCT cases were studied by selective DSA at the completion of coiling treatments and most follow-up imaging data were from selective catheter DSA and a few from CTA and MRA.

The CCT core laboratory data base has $n = 124$ cases of AcomA aneurysms with copies of baseline imaging data pre- and postendovascular coiling available for determination of A1 dominance. Of these 124 AcomA cases, $n = 117$ had complete follow-up imaging data at 5–7 months (7 cases with incomplete available data were omitted from assessment) and $n = 86$ had follow-up data at 12–14 months.[3] A subgroup of "termination type" aneurysms (basilar tip and MCA) was used for comparison with $n = 89$ cases at baseline and $n = 78$ at 5–7 month follow-up.

A1 vessel dominance of either anterior cerebral artery trunk supplying both pericallosal arteries was determined by the combined anatomic and flow dilution method illustrated in Fig 1 as previously shown.[3] This allowed division of the AcomA aneurysm group into 2 groups: A1 codominant and A1 dominant. In the A1 codominant group, there was no clear dominance of the inflow contribution of one A1 segment over the other. If flow data were not available, the A1 codominance was determined if diameter of A1 (large) $\leq 2 \times$ A1 (small). In the A1 dominant group, there was clearly more contribution of flow from one A1 segment to the distal A2 segments than the contralateral A1 segment, or no detectable inflow contribution from the contralateral A1 segment. If flow data were not available, A1 dominance was classified when A1 (large) $\geq 2 \times$ A1 (small) or A1 (small) was not apparent or detectable on the available imaging.

Angiographic appearance at the end of endovascular procedure was considered as baseline for this analysis and the degree of aneurysm occlusion was categorized as complete, neck remnant, sac filling/incomplete, and overlapping coils/neck as determined by the CCT core laboratory.[9,11]

To be consistent with prior publications that did not recognize the difference between presumed complete occlusion and overlapping coils/neck, and to facilitate comparison between baseline and follow-up angiographic appearance, overlapping coils/neck was combined with complete occlusion, and no change at follow-up was assigned to the postembolization category.[8,11] Cases with incomplete angiographic data or no follow-up data were excluded from this analysis.

The follow-up images between 5 and 7 months were analyzed with reference to the initial posttreatment angiogram. The CCT core laboratory determined angiographic treatment success at 5–7 months by comparison with the initial degree of occlusion on the posttreatment angiogram as complete, improved, or not changed (for example: stable neck remnant) in appearance from baseline. Clinical outcomes were assessed by the mRS at 6 months as collected by the CCT Coordinating Centre through Web-based forms and previously published.[10]

Statistical comparisons were made both within and between groups using the Fisher exact test or χ^2 test with a 2-sided P value of .05, as appropriate. McNemar and Stuart-Maxwell tests for marginal homogeneity were applied to baseline and 5–7 month follow-up to determine the proportion of change in angiographic case classification over time.[12]

RESULTS
Table 1 summarizes angiographic outcomes at the end of the coiling procedures and at 5–7 month follow-up for the A1 subgroups and "termination" aneurysms. A1 dominance was seen in 73% ($n = 91$) of AcomA aneurysms and 27% ($n = 33$) of A1 codominant. Postcoiling sac filling was seen in similar proportions in both groups at baseline and at 5–7 month follow-up. There were 7 patients who had required retreatment (1 A1-codominant, 6 A1-dominant), and 1 of the patients who was A1-dominant had retreatment after re-bleed. At 12–14 month follow-up, 86 of 117 cases from the 5–7 month follow-up had complete follow-up data. The proportion of A1 codominant aneurysms with sac filling remained stable at 23% ($n = 7$) while the A1 dominant group increased to 30% ($n = 18$). The "termination" aneurysm group had a significant increase in neck remnants from 29 to 41 (33% to 53%).

Table 2 presents the CCT definition of success for A1 dominant and codominant AcomA aneurysms; 57% ($n = 49$ of 86) of A1-dominant AcomA aneurysms and 61% ($n = 19$ of 31) of A1-codominant AcomA aneurysms were deemed successfully treated. The Fisher exact test showed no statistical significance in

Table 1: Angiographic classification data

	Baseline Post-Coiling			5–7 Month Follow-Up		
Angiographic Occlusion	AcomA Aneurysm A1 Codominant (n = 33), No. (%)	AcomA Aneurysm A1 Dominant (n = 91), No. (%)	Basilar/MCA Termination Aneurysms (n = 89), No. (%)	AcomA Aneurysm A1 Codominant (n = 31), No. (%)	AcomA Aneurysm A1 Dominant (n = 86), No. (%)	Basilar/MCA Termination Aneurysms (n = 78), No. (%)
Complete	12 (36%)	48 (53%)	45 (50%)	13 (42%)	34 (40%)	22 (28%)
Neck remnant	16 (49%)	32 (35%)	29 (33%)	11 (35%)	31 (36%)	41 (53%)
Sac filling	5 (15%)	11 (12%)	15 (17%)	7 (23%)	21 (24%)	15 (19%)

Table 2: CCT definition of success at 5–7 months

Angiographic Occlusion at First Follow-Up	AcomA Aneurysm A1 Co-Dominant (n = 31), No. (%)	AcomA Aneurysm A1 Dominant (n = 86), No. (%)
Complete	13 (42%)	29 (34%)
Stable	0 (0%)	3 (3%)
Improved	6 (19%)	17 (20%)
Total[a]	19 (61%)	49 (57%)

[a] There were 12 (39%) and 37 (43%) from each group that did not meet the CCT definition of success at 5–7 month follow-up.

Table 3: Change in angiographic appearance from baseline to first follow-up

	Baseline (n = 31[a])		
	Complete (n = 12)	Neck Remnant (n = 15)	Sac Filling (n = 4)
A1 Codominant First follow-up (n = 31)			
Complete (n = 13)	9	4	0
Neck remnant (n = 11)	1	9	1
Sac filling (n = 7)	2	2	3

	Baseline (n = 86[a])		
	Complete (n = 47)	Neck Remnant (n = 30)	Sac Filling (n = 9)
A1 Dominant First follow-up (n = 86)			
Complete (n = 34)	26	7	1
Neck remnant (n = 31)	8	18	5
Sac filling (n = 21)	13	5	3

[a] Only baseline cases with follow-up data were included (31 of 33 and 86 of 91).

treatment success as defined between A1-dominant and codominant AcomA aneurysms (P = .8).

Angiographic follow-up demonstrates a statistically significant increase in progressive aneurysm sac filling of initially incompletely coiled AcomA aneurysms with A1 dominant configuration (n = 21, 24% at follow-up versus n = 11, 12% at immediate posttreatment, P = .035) and similarly a significant increase in neck remnants in the "termination" aneurysms group (P = .01).

McNemar and Stuart-Maxwell tests were applied to paired baseline and 5–7 month follow-up angiographic classification (Table 3). The A1-dominant AcomA aneurysm group showed significant change in angiographic classification (P = .03) and an increase in the proportion of cases with aneurysm sac filling (P = .01). The same tests applied to the A1 codominant group were not significant.

There was no difference found in clinical outcomes between cases of AcomA aneurysms with A1 dominant and codominant

configurations as quantified by the mRS applying the Fisher exact test consistent with the CCT trial as published previously.[9,10]

DISCUSSION

A1 dominance of one or another of the anterior cerebral artery trunks supplying both pericallosal arteries has previously been shown to be a significant risk factor for AcomA aneurysm incidence.[1-3] There have been several hypotheses posed to explain the role of this observation in the formation of aneurysms of the AcomA artery region. Factors such as vessel wall shear stress, A1–A2 bifurcation angles, and flow patterns all depend intimately on the vessel geometry[1,4,13] and likely contribute to aneurysm formation. However, the influence of A1 dominance on the angiographic and clinical outcomes of endovascularly coiled AcomA aneurysms has not been extensively studied.[4-6] A previous study concluded that vessel dominance is not a major factor in predicting immediate postcoiling success; however, no long-term outcome assessments were available and both methodology and consistent definition of vessel dominance were not stated.[7] Another study on the impact of morphologic features on 32 cases of endovascularly coiled AcomA aneurysms did not include A1 dominance as a factor but did conclude superiorly oriented aneurysm domes are more likely to be incompletely occluded postcoiling.[14] More recently, a single-center multivariate retrospective analysis of the impact of morphologic factors on initial occlusion and long-term follow-up of 96 cases of AcomA aneurysms demonstrated A1 dominance and dome orientation as being most contributory to predicting the endovascular coiling outcome.[15] Aneurysm orientation was not studied for this analysis given most of the data came from orthogonal DSA images that precluded measurement of true 3D orientation angles.

A recent meta-analysis of endovascular coiling outcomes of AcomA aneurysms reported overall immediate posttreatment rates of "complete and near complete occlusions" at 88% and long-term follow-up (at least 6 months) at 85%.[16] If the same definition were applied to our study, combining complete and neck remnants to be equivalent to "complete and near complete occlusions," the immediate postcoiling success rates are comparable at 85% and 88% for the A1 codominant and A1 dominant AcomA aneurysms, respectively. At the follow-up, however, this drops to 77% and 76%, and applying the CCT trial definition of success at follow-up, the rate further reduces to 57% and 61%. These discrepancies can be interpreted in several ways; however, the most important factor clearly lies in the angiographic interpretation. An independent study on the differences between the angiographic classifications reported by the operators versus the independent core laboratory reader found a 2-fold difference in
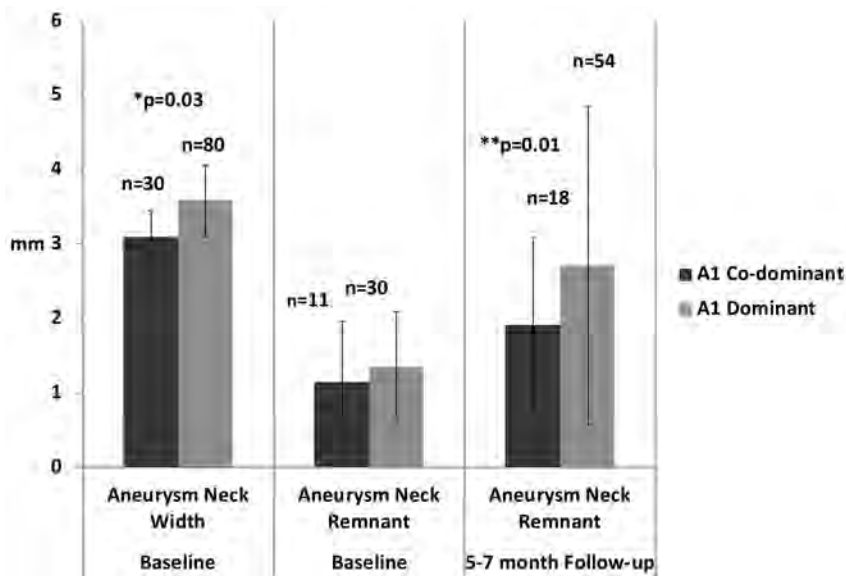
FIG 2. Anatomic dimensions of aneurysm neck width and remnants taken at baseline and follow-up imaging. All cases with available measurements in each group were included regardless of angiographic classification as listed in Table 1. The A1-dominant AcomA aneurysm group had a larger mean neck width at baseline and more variance in neck remnant at follow-up, $P = .03$ and .01 by *t test and **F test, respectively.

the rate of reporting an unfavorable angiographic outcome.[11] This factor alone could explain the differences between our study and the recent meta-analysis by Fang et al.[16] Interestingly, the largest sources of data heterogeneity cited in the meta-analysis were angiographic outcomes immediately after coiling and in long-term follow-up.

Inherent to any subanalysis are the limitations of smaller numbers of cases within the subgroups. With 91 and 33 cases of AcomA aneurysms with A1 dominant and codominant configurations, respectively, the ability to detect small differences in outcomes comparing the groups directly is statistically underpowered. However, the significant results we present are highlighting the temporal changes of angiographic appearance as a marker of treatment stability within the same group.

Specifically, the A1 dominant group of coiled AcomA aneurysms showed angiographic instability over time with significant increase in cases with sac filling between baseline and follow-up time points (12 to 24%–30%).

This suggests that endovascularly coiled A1 dominant AcomA aneurysms may be less stable. The A1 codominant group provides an important comparison: It has significant flow from both A1 vessels into the AcomA aneurysm and beyond to the A2 vessels. Therefore, one can postulate that in this situation there may not be a single jet of blood flowing directly into the aneurysm or neck remnant, pushing down on the coils and expanding the aneurysm over time. This phenomenon has been studied more extensively with computational flow dynamics of MCA "termination" type aneurysms, and similar concepts may apply here as well.[17]

Most the flow originates from a single vessel in the A1-dominant group, and compared with A1 codominant aneurysms, the aneurysm neck widths are significantly larger and both the size and variation of neck remnants on follow-up imaging are larger (Fig 2). This further supports the hypothesis that large jets of

blood directed to 1 spot at a bifurcation leads to formation of a termination aneurysm predisposed to stretching, and, after coiling, to molding and flattening of coil masses. This would result in more remnants and sac filling.

The recently introduced of flow diverters and woven intrasaccular devices are interesting endovascular solutions that aim to prevent blood flow from entering the aneurysm thereby removing the source of the problem.[18-21] Perhaps patients with A1-dominant AcomA aneurysms are a subgroup that might particularly benefit from treatment with such novel devices if they could be developed to maneuver through the sharp angles and small A1 artery.

CONCLUSIONS

AcomA aneurysms with A1-dominant circle of Willis configurations (one A1 supplying both A2 arteries) with incomplete occlusion at baseline may be less stable at follow-up than A1 codominant AcomA aneurysms, similar to other "termination" type aneurysms such as basilar tip and MCA bifurcation. This supports the hypothesis that A1-dominant flow contributes to AcomA aneurysm formation, growth, and instability of treatment by coiling.

REFERENCES

1. Castro MA, Putman CM, Sheridan MJ, et al. **Hemodynamic patterns of anterior communicating artery aneurysms: a possible association with rupture.** *AJNR Am J Neuroradiol* 2009;30:297–302
2. De Rooij NK, Velthuis BK, Algra A, et al. **Configuration of the circle of Willis, direction of flow, and shape of the aneurysm as risk factors for rupture of intracranial aneurysms.** *J Neurol* 2009;256:45–50
3. Tarulli E, Fox AJ. **Potent risk factor for aneurysm formation: termination aneurysms of the anterior communicating artery and detection of A1 vessel asymmetry by flow dilution.** *AJNR Am J Neuroradiol* 2010;31:1186–91
4. Alnaes MS, Isaksen J, Mardal KA, et al. **Computation of hemodynamics in the circle of Willis.** *Stroke* 2007;38:2500–05
5. Wiebers DO, Whisnant JP, Huston J III, et al. **Unruptured intracranial aneurysms: natural history, clinical outcome, and risks of surgical and endovascular treatment.** *Lancet* 2003;362:103–10

6. van der Schaaf I, Algra A, Wermer M, et al. **Endovascular coiling versus neurosurgical clipping for patients with aneurysmal subarachnoid haemorrhage.** *Cochrane Database Syst Rev* 2005;4:CD003085

7. Gonzalez N, Sedrak M, Martin N, et al. **Impact of anatomic features in the endovascular embolization of 181 anterior communicating artery aneurysms.** *Stroke* 2008;39:2776–82

8. Osborn AG. *Diagnostic Cerebral Angiography.* Philadelphia: Lippincott Williams & Wilkins; 1999:241–55

9. Molyneux AJ, Clarke A, Sneade M, et al. **Cerecyte coil trial: angiographic outcomes of a prospective randomized trial comparing endovascular coiling of cerebral aneurysms with either Cerecyte or bare platinum coils.** *Stroke* 2012;43:2544–50

10. Coley S, Sneade M, Clarke A, et al. **Cerecyte coil trial: procedural safety and clinical outcomes in patients with ruptured and unruptured intracranial aneurysms.** *AJNR Am J Neuroradiol* 2012;33:474–80

11. Rezek I, Lingineni R, Sneade M, et al. **Differences in the angiographic evaluation of coiled cerebral aneurysms between a core laboratory reader and operators: results of the Cerecyte coil trial.** *AJNR Am J Neuroradiol* 2014;35:124–27

12. Twisk JWR. **Categorical and "count" outcome variables.** *Applied Longitudinal Data Analysis for Epidemiology.* Cambridge, UK: Cambridge University Press; 2013:141–62

13. Kasuya H, Shimizu T, Nakaya K, et al. **Angles between A1 and A2 segments of the anterior cerebral artery visualized by three-dimensional computed tomographic angiography and association of anterior communicating artery aneurysms.** *Neurosurgery* 1999;45:89–93; discussion 93–94

14. Uemura A, Kamo M, Matsukawa H. **Angiographic outcome after endovascular therapy for anterior communicating artery aneurysms: correlation with vascular morphological features.** *Jpn J Radiol* 2012;30:624–27

15. Songsaeng D, Geibprasert S, ter Brugge KG, et al. **Impact of individual intracranial arterial aneurysm morphology on initial obliteration and recurrence rates of endovascular treatments: a multivariate analysis.** *J Neurosurg* 2011;114:994–1002

16. Fang S, Brinjikji W, Murad MH, et al. **Endovascular treatment of anterior communicating artery aneurysms: a systematic review and meta-analysis.** *AJNR Am J Neuroradiol* 2014;35:943–47

17. Valen-Sendstad K, Steinman DA. **Mind the gap: impact of computational fluid dynamics solution strategy on prediction of intracranial aneurysm hemodynamics and rupture status indicators.** *AJNR Am J Neuroradiol* 2014;35:536–43

18. Pierot L, Liebig T, Sychra V, et al. **Intrasaccular flow-disruption treatment of intracranial aneurysms: preliminary results of a multicenter clinical study.** *AJNR Am J Neuroradiol* 2012;33:1232–38

19. Pierot L, Klisch J, Cognard C, et al. **Endovascular WEB flow disruption in middle cerebral artery aneurysms: preliminary feasibility, clinical, and anatomical results in a multicenter study.** *Neurosurgery* 2013;73:27–34; discussion 34–35

20. Gross BA, Frerichs KU. **Stent usage in the treatment of intracranial aneurysms: past, present and future.** *J Neurol Neurosurg Psychiatry* 2013;84:244–53

21. Piano M, Valvassori L, Quilici L, et al. **Midterm and long-term follow-up of cerebral aneurysms treated with flow diverter devices: a single-center experience.** *J Neurosurg* 2013;118:408–16

Building Multidevice Pipeline Constructs of Favorable Metal Coverage: A Practical Guide

M. Shapiro, E. Raz, T. Becske, and P.K. Nelson

ABSTRACT

BACKGROUND AND PURPOSE: The advent of low-porosity endoluminal devices, also known as flow diverters, exemplified by the Pipeline in the United States, produced the greatest paradigm shift in cerebral aneurysm treatment since the introduction of detachable coils. Despite robust evidence of efficacy and safety, key questions regarding the manner of their use remain unanswered. Recent studies demonstrated that the Pipeline device geometry can dramatically affect its metal coverage, emphasizing the negative effects of oversizing the device relative to its target vessels. This follow-up investigation focuses on the geometry and coverage of multidevice constructs.

MATERIALS AND METHODS: A number of Pipeline devices were deployed in tubes of known diameters and photographed, and the resultant coverage was determined by image segmentation. Multidevice segmentation images were created to study the effects of telescoped devices and provide an estimate of coverages resulting from device overlap.

RESULTS: Double overlap yields a range of metal coverage, rather than a single value, determined by the diameters of both devices, the size of the recipient artery, and the degree to which strands of the overlapped devices are coregistered with each other. The potential variation in coverage is greatest during overlap of identical-diameter devices, for example, ranging from 24% to 41% for two 3.75-mm devices deployed in a 3.5-mm vessel. Overlapping devices of progressively different diameters produce correspondingly more uniform ranges of coverage, though reducing the maximum achievable value, for example, yielding a 33%–34% range for 3.75- and 4.75-mm devices deployed in the same 3.5-mm vessel.

CONCLUSIONS: Rational strategies for building multidevice constructs can achieve favorable geometric outcomes.

ABBREVIATIONS: PED = Pipeline Embolization Device; PUFS = Pipeline for Uncoilable or Failed Aneurysms

U se of endoluminal constructs such as the Pipeline Embolization Device (PED; Covidien, Irvine, California) remains characterized by heterogeneity in the selection of device size, number, and deployment technique. The average number of devices used in a particular case is, in part, determined by the size, shape, and location of the aneurysm and whether adjunctive endosaccular coiling is concomitantly performed. The average number of devices used in the Pipeline Embolization Device for the Intracranial Treatment of Aneurysms[1] and the Pipeline for

Uncoilable or Failed Aneurysms (PUFS)[2] trials was 1.52 and 3.1, respectively, a notable difference notwithstanding the larger dimensions of PUFS aneurysms. The UK National Prospective Flow-Diverter Registry averages 1.7 devices per case, with 67% of aneurysms reported as large or giant.[3] In the IntrePED data base, as of 2013, fifty-eight percent of aneurysms were treated with a single device.[4] Neither approach has so far been subjected to rigorous targeted investigation with respect to outcome. One may, therefore, argue that results of the best-controlled study to date— PUFS[2]—set the metrics of efficacy on the basis of using multiple-coverage constructs, thereby placing the burden of proof on the minimalist approach to demonstrate superiority or equipoise.

The deleterious geometric consequences of oversizing, a situation in which a device of a given nominal diameter is purposefully implanted in a vessel of smaller caliber, have been demonstrated in several publications.[5,6] This issue frequently arises when a single device is used to cover an aneurysm with varied proximal and distal landing zone artery diameters. For the purpose of the subsequent discussion, the term "coverage" will be used inter-

Please address correspondence to Maksim Shapiro, MD, Departments of Radiology and Neurology, Bernard and Irene Schwartz Neurointerventional Radiology Section, NYU Langone Medical Center, 660 First Ave, 7th Fl, New York, NY 10016; e-mail: maksim.shapiro@nyumc.org, neuroangio@neuroangio.org

changeably with "metal coverage," defined as the percentage of artery surface area covered with the metal strands of the device. This is the inverse of the term "porosity," which refers to the percentage of uncovered artery area. The percentage of metal coverage of all Pipeline devices decreases quickly and substantially under conditions of oversizing, also resulting in undesirable geometric effects at the transition zone between the recipient artery and the fusiform aneurysmal segment. The only effective strategy for minimizing these untoward effects relies on building multidevice constructs, with each device appropriately sized to its landing zone. To our knowledge, there is as yet no literature on the geometry or quantitative metal coverage of multidevice constructs. Existing animal data suggest the apparent feasibility of multidevice perforator coverage,[7] though this information is not directly applicable to issues of treatment efficacy.

The PED is a self-expanding, cylindrical, braided device consisting of 48 strands of cobalt-chromium and platinum-tungsten wire, in a 3:1 respective ratio, braided to produce devices ranging from 2.5- to 5.0-mm nominal diameters, with lengths varying from 10 to 35 mm. The device is mounted within the delivery sheath by stretching, and its leading edge is packaged beneath a capture coil to protect the lead edges of the device filaments from damage during advancement within the microcatheter. During delivery, the device may expand to its maximum size, which is ~0.25 mm larger than the nominal diameter if unconstrained in its deployment across a large or fusiform aneurysm neck, or it will conform to the diameter of the vessel in which it is implanted.

On close inspection, the ultrastructure of the device consists of a series of curved rhomboid cells (Fig 1A). The angle θ, or pitch, of the strands at nominal size is set during manufacture and, along with the diameter of the strand (mean diameter, 30 μm per manufacturer specifications) and the number of strands, determines the metal coverage and pore (cell) size of the device. However, when a device is placed into vessels of progressively smaller sizes relative to its nominal diameter, the pitch angle of the cells changes proportional to the degree of device constraint, resulting in lower coverage until a minimum value is reached. With even more oversizing, the cells again assume a diamond shape, now oriented along the long axis of the device, thus again increasing metal coverage (Fig 1A) and completing the parabolic relationship of coverage versus vessel diameter for each device (Fig 1B). In practice, metal coverage falls quickly with oversizing, reaching near-minimum values at recipient artery diameters approximately 1 mm smaller than the nominal device diameter. While coverage values at nominal expansion may be in the range of 30%–35%, with even minor degrees of oversizing, these values fall to 20%–25% and as low as 18% for larger nominal diameter devices (Fig 1B). Oversizing also creates geometric disturbances at the "transition zone" of lower metal coverage between the undersized recipient artery and the dysplastic aneurysmal segment that the device is intended to treat (Fig 2A). This low coverage zone cannot be compressed or otherwise changed by "loading" or pushing the device and may have negative consequences on the inflow and outflow dynamics of the aneurysm.[6,8,9]

To minimize these untoward geometric effects, one may use multidevice constructs, with overlapping devices intended for the proximal and distal landing zones, both appropriately sized to
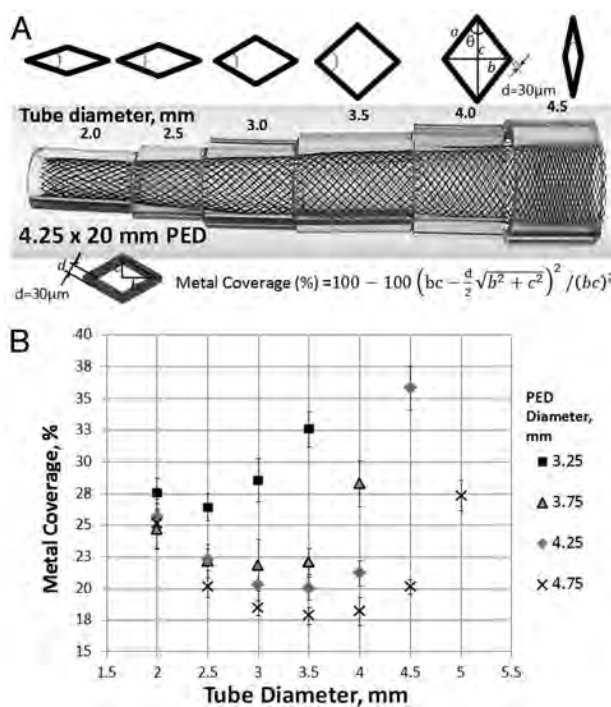
FIG 1. *A*, Representative image of a 4.25 × 20 mm Pipeline device inserted into plastic tubes of 0.5-mm incremental diameters. Variation in the degree of metal coverage is apparent. The configuration of cells is schematically depicted above the construct. Metal coverage can be calculated directly on the basis of measurements of the long and short diagonals of the rhombus and the diameter of each strand (30-μm), according to the formula above. Minimum coverage is seen when $\theta = 90°$, corresponding to a square cell configuration. *B*, Scatterplot of tube diameter versus metal coverage for various device and "artery" combinations. All functions have a parabolic configuration. Note that absolute coverage values are higher for smaller diameter devices at each given tube diameter. The overall single-device coverage is, therefore, likely to be somewhat smaller for appropriately sized devices deployed in larger vessels.

their target artery diameters (Fig 2B). Multiple devices are also often needed to bridge large or giant aneurysms to build a construct of sufficient structural integrity and produce adequate intra-aneurysmal stasis in the judgment of the operator.

This study was performed to investigate how metal coverage is affected by overlapping devices. For example, one may conceive of how 2 devices of identical diameter may be telescoped in a way that results in a near-perfect overlap of one device's braids with another, so that the actual metal coverage will only be minimally increased. On the other hand, a fortuitous phase shift of the braids by 50% would nearly double the percentage of coverage expected from each device alone. More complex results may be expected from using devices of different diameters, as seen below.

MATERIALS AND METHODS

A number of various-diameter Pipeline Embolization Devices were deployed in clear plastic tubes of known inner diameters, with a representative sample shown in Fig 1A. In a previous study, metal coverage for each device/tube configuration was determined by direct measurement of the long and short axes of device cells and by calculating coverage on the basis of the 30-μm braid diameter specified by the manufacturer, according to the formula listed in Fig 1A.[5] In the current study, a calibration ruler was
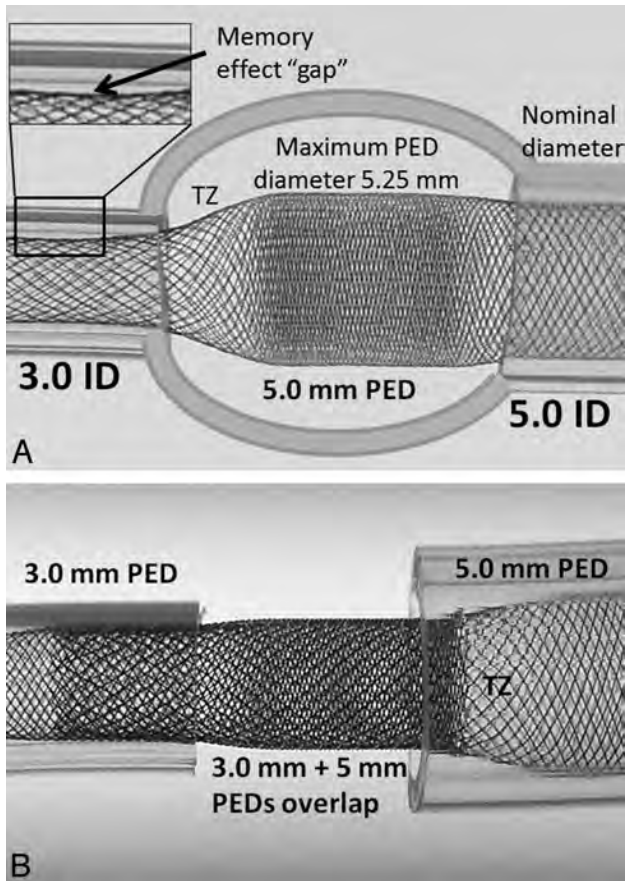
FIG 2. Consequences of device oversizing and the proposed solution. *A*, A model of a fusiform aneurysm with 3.0- and 5.0-mm landing zones, bridged by a single 5 × 20 mm device. A transition zone (TZ) of minimum coverage is created as the device is constrained from its fully opened state into the 3-mm landing zone. Despite adequate length of the "landing zone" at the 3.0-mm end, the "shape memory" of the transition zone, TZ, nevertheless produces a "gap" where the device remains unapposed to the inner wall of the tube. *B*, To address these issues, 2 devices are required, each of which is appropriately sized for its recipient artery. The first 3.0-mm device is deployed from the 3.0-mm-diameter vessel into the 5-mm recipient vessel, following which a second 5.0-mm diameter device is telescoped into the first, with the 5.0-mm device anchored into its 5.0-mm vessel. Thus, the transition zone, TZ, is shifted outside the aneurysm, while the aneurysmal segment receives the benefit of double-coverage.

placed alongside the deployed device and a photograph of the construct was uploaded into a PowerPoint (Microsoft, Redmond, Washington) slide. A curved black line was then traced over each device braid, with the line thickness calibrated to 30 μm by using the ruler as an internal reference standard. The resulting manually segmented image was then saved as a Portable Network Graphics image file and opened by using ImageJ freeware (National Institutes of Health, Bethesda, Maryland). Multiple rectangular regions of interest over the construct were drawn, and the "mean gray value" within each region, normalized to a standard "white" pixel value of 255 at 8 bits per pixel and corresponding to the percentage of metal coverage, was calculated for each area by using the "Measure" plug-in of the ImageJ tool (Fig 3): Metal Coverage (%) = 100 − 100 × (Mean Gray Value) / 255. Five random-area measurements were made for each segmented image and were averaged to produce a range of metal coverage values and SDs.
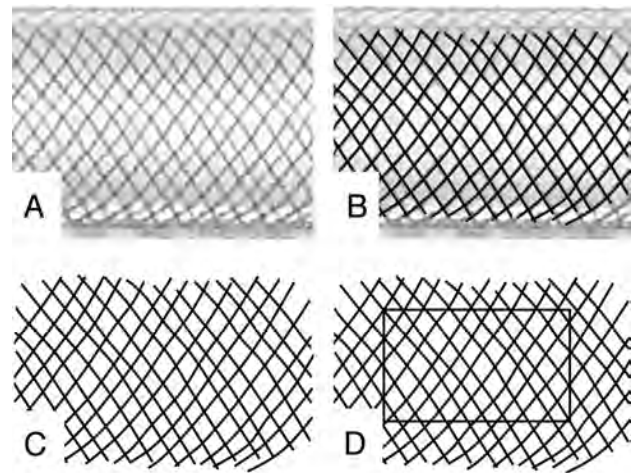
FIG 3. Manual segmentation method of determining metal coverage. *A*, Photographic image of a 3.75-mm device deployed within a 3.5-mm plastic tube. A translucent fiberoptic rod is placed inside the construct to eliminate visualization of the "back" portion of the braids. *B*, Curved lines, with thickness corresponding to 30 μm (calibrated to a ruler placed alongside the construct) are traced along each braid. *C*, The underlying image is removed, leaving a black and white segmentation image. *D*, With the ImageJ measurement tool, the proportion of black pixels within a given rectangular area corresponds to the percentage of metal coverage, according to the formula listed in the "Materials and Methods" section.

To determine combined-coverage values for overlapped devices, we "grouped" segmented curved lines derived for individual devices in PowerPoint and overlaid them on each other (Fig 4). For example, the segmented image of a 3.75-mm-diameter device placed into a 3.5-mm tube was overlaid on a segmented image of a 4.25-mm device deployed into the same-diameter 3.5-mm tube. The resulting overlapped image, representing an estimate of "double coverage" as might be achieved by actual deployment of one device inside another, was saved and uploaded into ImageJ, and the combined coverage was calculated by the method above. Because coverage varies with the degree of strand misregistration, especially when overlapping devices of identical diameter (in which perfect overlap of the braids might produce no change in surface metallic coverage, whereas a phase shift of 50% might almost double it), 3 separate patterns, in different phases of strand overlap, were created and analyzed to yield a range of coverage values and corresponding SDs for each device pairing (Fig 4).

The minimum and maximum coverage values for each configuration are listed in the "Results" section, as representative of the range that might be expected from overlapping these particular devices in an artery of given size. The "overlap" segmentation method was validated by analysis of an actual in situ double-coverage construct created by sequential deployment of 3.75- and 4.25-mm devices into a 3.5-mm-diameter tube. Manual segmentation of the construct was performed, and its coverage values were compared with estimated values based on the overlap of separate segmented images of individual devices (Fig 5).

RESULTS
Images of coverage patterns resulting from the overlap of two 3.75-mm PEDs versus 3.75- and 4.25-mm-diameter PEDs, all de-
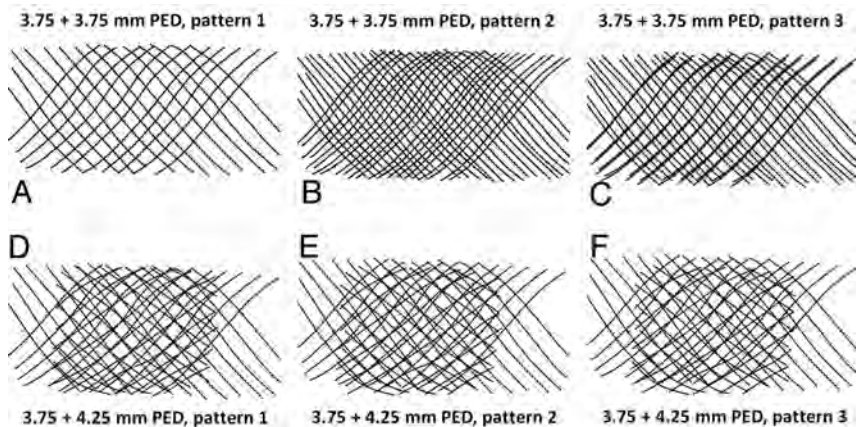
FIG 4. Overlapping segmentation images illustrating patterns of double coverage with identical-diameter (*A–C*) and different-diameter devices (*D–F*). It can be readily seen from Figs *A–C* that 2 overlapping 3.75-mm devices can result in a wide range of coverage, depending on the exact alignment of device braids of identical pitch relative to each other. In contrast, an overlap of 3.75- and 4.25-mm devices (Figs *D–F*), because of the different braid pitch for each device, produces a more consistent overall coverage pattern, regardless of the particular phase of overlap.
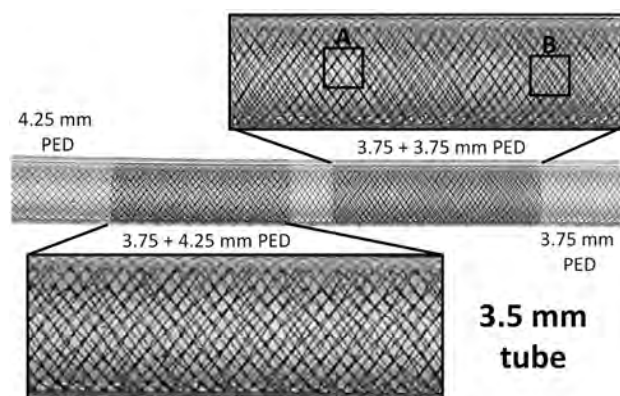
FIG 5. Photographs of overlapping 3.75- and 4.25-mm-diameter devices deployed in a 3.5-mm tube. Visual appreciation of nonuniform coverage for two 3.75-mm devices: Area A shows near-perfect overlap of both device braids, with no practical increase in coverage for this segment, whereas the braid phase shift in area B produces significantly higher coverage. In contrast, overlap of 3.75- and 4.25-mm devices yields a more consistent pattern, with less potential variation in coverage values. The absolute value of such coverage is between the minimal and maximal potential values expected from overlapping two 3.75-mm devices.

Table 1: Correlation between manual and estimated coverage values for the construct pictured in Fig 5[a]

3.5-mm-Vessel Manual Segmentation	Manual	Estimated
3.75 PED	22%	
3.75 + 4.25 PED	36%–37%	36%–37%
4.25 PED	18%–19%	

[a] Manual segmentation was done by tracing curved lines over each braid in the double-coverage area and comparing the result with values estimated by overlapping segmented images from separate 3.75- and 4.25-mm devices individually deployed within a 3.5-mm artificial vessel. The 2 methods are in excellent agreement.

ployed within the same 3.5-mm tube, are shown in Fig 5. It can be visually appreciated that the construct made with two 3.75-mm devices results in a wide range of local coverage, depending on the exact pattern of braid overlap. Because devices of identical diameter will have nearly identical braid pitch (allowing negligible dif-

ferences in deployed diameters of inner and outer devices), near-exact overlap of the filaments may be possible, producing essentially no increase in surface metallic coverage (area A, Fig 5), whereas fortuitous alignment of device cells with a half-phase shift can substantially increase coverage (area B, Fig 5). In contrast, the overlap of 4.25- and 3.75-mm-diameter devices will produce a construct in which the filaments composing each device have different pitches, yielding a narrower (more consistent) range of coverage variation. The resulting coverage will be lower than the potentially achievable maximum when overlapping devices of identical diameter; however, it will be more consistent. The manually determined range of metal coverage for this construct is in excellent agreement with estimated values produced by overlapping individual segmented maps for each device (Table 1).

In this fashion, a range of metal-coverage values for devices placed in tubes of 3, 3.5, 4, and 4.5-mm diameters was calculated, as shown in Table 2. Again, for each vessel size, the widest range of potential combined coverage values is seen with overlapping devices of identical diameter. For example, telescoping two 3.75-mm devices in a 3.5-mm vessel leads to a range of metal coverage from 24% to 41%, as seen in Table 2. If instead of overlapping two 3.75-mm devices, a combination of 3.75- and 4.75-mm devices is used, the result is a much more consistent range of 33% to 34%—values that lie between the 24% and 41% extremes of identical device use. Thus, use of progressively different-diameter PEDs yields a correspondingly tighter range of coverage, as seen in Table 2.

From these Tables, it can be appreciated that most coverage values obtained by using different-diameter devices are at least in the 30% range, whereas telescoping identical devices could lead to values as low as 20%. Thus, when the first device is appropriately sized to the parent artery, adding a second device of slightly larger diameter is expected to more consistently produce coverage in mid-to-high 30% values, which may be predictive of clinical success.[10,11]

DISCUSSION

The substantial decrease in coverage resulting from even modest oversizing of a single device relative to the diameter of its recipient artery[5] and the frequent need to use multiple devices in bridging and securing complex aneurysm constructs are 2 factors that prompted this study of multidevice geometry. We see our results as arguing against telescoping identical-diameter devices because metal coverage along the length of overlap in this scenario is likely to be highly variable. This variability will be manifested on a pore-to-pore basis, with areas of low coverage, as seen in Fig 4, underscoring the distinction between coverage and individual pore size, as illustrated by Lieber and Sadasivan.[12] These relatively bare patches may fail to undergo endothelialization, resulting in per-

Table 2: The range of coverage values expected from overlap of various size devices in tubes of 3, 3.5, 4, and 4.5-mm diameters[a]

	3-mm Vessel			
	3.25	**3.75**	**4.25**	**4.75**
3.25	30%–47%	30%–40%	31%–37%	34%–37%
3.75		20%–37%	30%–37%	30%–35%
4.25			21%–35%	31%–34%
4.75				20%–36%

	3.5-mm Vessel		
	3.75	**4.25**	**4.75**
3.75	24%–41%	36%–37%	33%–34%
4.25		22%–36%	31%–32%
4.75			18%–31%

	4-mm Vessel		
	3.75	**4.25**	**4.75**
3.75	38%–46%	37%–39%	36%–37%
4.25		21%–35%	29%–33%
4.75			22%–32%

	4.5-mm Vessel	
	4.25	**4.75**
4.25	36%–57%	40%–44%
4.75		25%–34%

[a] Note that the broadest range of coverage for each device/artery combination is always observed during overlap of identical-diameter devices. Use of devices with progressively different diameters produces correspondingly narrower ranges of coverage (due to the more consistent misregistration of strands arising from the differing pitches imposed on devices of different diameters constrained within a given diameter vessel), with absolute coverage values falling in-between the potential minima and maxima expected from overlap of identical devices.

FIG 6. Example of triple coverage with 3 different-diameter stents. Note that despite overall relatively high coverage, areas of lower coverage and significantly larger pore size remain (*white rectangle*).

sistent communication between the aneurysm and new vessel lumen and perhaps contributing to unexpected treatment failures, notwithstanding apparently complete or near-complete angiographic occlusion.

Despite the plausibility of this hypothesis, the clinical significance of our observations, as they relate to the degree of flow diversion, thrombus formation, endothelialization scaffolding, and ultimate cure, is as yet largely undetermined in human subjects. There is some evidence in animal models supporting a 35% neck-coverage benchmark as highly predictive of treatment success.[10] Values in this range are practically impossible to achieve with single PED use, especially because this strategy frequently necessitates oversizing the device at 1 (usually distal) landing zone. The behavior of multidevice constructs is expected to be even more complex at sites of curvature, where conditions are substantially more varied. It is critical to note that results of our study are only applicable to the Pipeline device. Other flow diverters have substantially different geometries and will not behave in the same manner under conditions of single-device oversizing[13]—and by extension during overlap.

The presently used methodology of overlapping individually segmented images to produce a robust estimate of double coverage can be easily and quickly extended to study triple and higher coverage conditions (Fig 6), keeping in mind that aggregate PED wall thickness may eventually play a role in reducing the diameter of the construct and impacting flow across the overall mesh. One intriguing property of these triple-coverage constructs is that despite shifting segmented device images relative to each other, there will nearly always remain several pores where no substantial overlap will take place, so that coverage will be nearly as low and pore size as large as would be expected from a single device (Fig 6, white rectangle). It is perhaps this mechanism that is responsible for some treatment failures, especially when characterized by the presence of focal residual inflow into the aneurysm. Nevertheless, it is difficult to estimate the applicability of these in vitro observations to in vivo scenarios. Effort is ongoing by several groups to study in vivo device coverage by using cross-sectional methods derived from CT and rotational angiography methods. These cross-sectional approaches have the potential to become clinically practical methods for evaluating the functional degree of coverage and may be used in combination with presently shown in vitro high-resolution studies to help devise optimal treatment strategies.
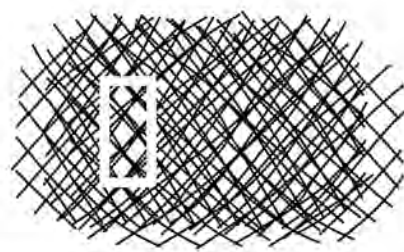
CONCLUSIONS

We present bench top observations on the geometric properties of the Pipeline Embolization Device under conditions of multidevice coverage. Our findings quantitatively illustrate that building multistent constructs by using devices of different diameters can create a more uniform pattern of metal coverage than would be expected from use of identical- or near-identical-diameter devices, thus achieving a more consistent coverage outcome. In extrapolated clinical scenarios, overlapping 2 appropriately sized devices appears to reliably provide coverage of 30% and higher—values that are rarely attainable with single-device use. These results support the need to consider vessel size and the strategic selection of overlapping devices to achieve the desired degree and pattern of coverage necessary to maximize the overall efficacy of treatment.

REFERENCES

1. Nelson PK, Lylyk P, Szikora I, et al. **The Pipeline embolization device for the intracranial treatment of aneurysms trial.** *AJNR Am J Neuroradiol* 2011;32:34–40

2. Becske T, Kallmes DF, Saatci I, et al. **Pipeline for uncoilable or failed aneurysms: results from a multicenter clinical trial.** *Radiology* 2013;267:858–68

3. Molyneux A, White PM. **Update on the UK Flow Diverter Registry.** In: *Proceedings of the 51st Annual Meeting of the American Society of Neuroradiology,* San Diego, California; May 18–23, 2013:570

4. Kallmes D. **Safety of flow diversion: results from a multicentre registry.** In: *Proceedings of the 10th Annual Meeting of the Society of Neurointerventional Surgery,* Miami, Florida; July 29-August 1, 2013

5. Shapiro M, Raz E, Becske T, et al. **Variable porosity of the Pipeline embolization device in straight and curved vessels: a guide for optimal deployment strategy.** *AJNR Am J Neuroradiol* 2014;35:727–33

6. Mut F, Cebral JR. **Effects of flow-diverting device oversizing on hemodynamics alteration in cerebral aneurysms.** *AJNR Am J Neuroradiol* 2012;33:2010–16

7. Dai D, Ding YH, Kadirvel R, et al. **Patency of branches after coverage with multiple telescoping flow-diverter devices: an in vivo study in rabbits.** *AJNR Am J Neuroradiol* 2012;33:171–74

8. Makoyeva A, Bing F, Darsaut TE, et al. **The varying porosity of braided self-expanding stents and flow diverters: an experimental study.** *AJNR Am J Neuroradiol* 2013;34:596–602

9. Bing F, Darsaut TE, Salazkin I, et al. **Stents and flow diverters in the treatment of aneurysms: device deformation in vivo may alter porosity and impact efficacy.** *Neuroradiology* 2013;55:85–92

10. Wang K, Huang Q, Hong B, et al. **Correlation of aneurysm occlusion with actual metal coverage at neck after implantation of flow-diverting stent in rabbit models.** *Neuroradiology* 2012;54:607–13

11. Wang K, Yuan S. **Actual metal coverage at the neck is critical for flow-diverting stents in treating intracranial aneurysms.** *AJNR Am J Neuroradiol* 2013;34:E31–32

12. Lieber BB, Sadasivan C. **Endoluminal scaffolds for vascular reconstruction and exclusion of aneurysms from the cerebral circulation.** *Stroke* 2010;41:S21–25

13. Aurboonyawat T, Blanc R, Schmidt P, et al. **An in vitro study of Silk stent morphology.** *Neuroradiology* 2011;53:659–67

A Single Pipeline Embolization Device is Sufficient for Treatment of Intracranial Aneurysms

N. Chalouhi, S. Tjoumakaris, J.L.H. Phillips, R.M. Starke, D. Hasan, C. Wu, M. Zanaty, D. Kung, L.F. Gonzalez, R. Rosenwasser, and P. Jabbour

ABSTRACT

BACKGROUND AND PURPOSE: The Pipeline Embolization Device has emerged as an important treatment option for intracranial aneurysms. The number of devices needed to treat an aneurysm is uncertain and is the subject of vigorous debate. The purpose of this study was to compare rates of complications, aneurysm occlusion, and outcome in patients treated with a single-versus-multiple Pipeline Embolization Devices.

MATERIAL AND METHODS: One hundred seventy-eight patients were treated with the Pipeline Embolization Device at our institution. Patients were divided into 2 groups: a single-device group ($n = 126$) and a multiple-device group ($n = 52$).

RESULTS: There was no statistically significant difference between the 2 groups with respect to baseline characteristics except for age and aneurysm size (higher with multiple Pipeline Embolization Devices). Complications occurred more frequently with multiple (15%) versus a single device (5%, $P = .03$). In multivariate analysis, the use of multiple devices independently predicted complications. A similar proportion of patients achieved adequate aneurysm obliteration at follow-up in the single-device (84%) and the multiple-device groups (87%, $P = .8$). In multivariate analysis, age and follow-up time predicted obliteration. At follow-up, a significantly higher proportion of patients treated with a single device (97%) achieved a favorable outcome compared with those treated with multiple devices (89%, $P = .03$). In multivariate analysis, there was a strong trend for the use of a single device to predict favorable outcomes ($P = .06$).

CONCLUSIONS: Treatment with a single Pipeline Embolization Device provides similar occlusion rates with less complications and better overall outcomes. These findings suggest that a single Pipeline Embolization Device is sufficient for treatment of most intracranial aneurysms.

ABBREVIATIONS: ICH = intracerebral hemorrhage; PED = Pipeline Embolization Device

The Pipeline Embolization Device (PED; Covidien, Irvine, California) is a dedicated flow diverter, which received US Food and Drug Administration approval in 2011 for the treatment of large and giant wide-neck aneurysms of the internal carotid artery. The device appears to be highly efficient in promoting durable aneurysm occlusion, and its safety profile has been shown to be favorable in several well-designed studies.[1-3] In an increasing number of cerebrovascular centers, the PED has become a routine first-line option for unruptured intracranial aneurysms.

The number of PEDs needed to treat an aneurysm is uncertain and is the subject of vigorous debate at present.[4] The question is a crucial one and has potential implications for procedural cost, safety, and efficacy. To our knowledge, this is the first study to compare rates of complications, aneurysm occlusion, and outcome in patients treated with single-versus-multiple PEDs.

MATERIALS AND METHODS

Patient Population

The study protocol was approved by the Thomas Jefferson University Institutional Review Board. All patients with intracranial aneurysms treated with the PED at our institution between May 2011 and May 2013 were identified from a prospectively maintained data base. One hundred seventy-eight patients were treated during this period and constituted our study population.

The patient population was divided into 2 groups based on the number of PEDs deployed during initial aneurysm embolization. There were 126 (70.8%) patients treated with a single device and 52 (29.2%) patients treated with >1 device. The rates of compli-

cations, aneurysm obliteration, retreatment, and clinical outcome were compared between the 2 groups. All symptomatic procedural complications were included. Delayed complications were also recorded through follow-up. Angiographic follow-up was scheduled at 3–6 months, 1 year, 2 years, and 5 years after treatment. Aneurysm occlusion at follow-up was categorized as complete/near-complete ($\geq$90%) or incomplete (<90%). Clinical follow-up was performed at 1, 3, and 6 months. Outcome was reported according to the modified Rankin Scale.

Technique

All patients received 75 mg/day of clopidogrel (Plavix) and 81 mg/day of aspirin for 10 days before the procedure. Platelet function tests were performed on all patients by using aspirin and P2Y12 assays (VerifyNow; Accumetrics, San Diego, California). The procedure was performed only if the platelet inhibition level was >30% but less <90%. Patients with inhibition <30% were reloaded, and the assay was rechecked. Patients found to be poor responders to clopidogrel were then switched to prasugrel (40-mg loading dose followed by a 5-mg daily maintenance dose). Patients with inhibition above 90% were admitted to the hospital, their procedure was canceled, and clopidogrel was held until the platelet inhibition level fell below 90%. An initial heparin bolus was administered, and activated clotting time was maintained at 2–3 times the patient's baseline intraoperatively. Heparin was discontinued at the end of the procedure. Patients were maintained on dual antiplatelet therapy for at least 6 months after the procedure followed by aspirin indefinitely.

PEDs were generally deployed through a Marksman microcatheter (Covidien) by using a triaxial guide-catheter system to maximize support during forward loading of the system and to optimize stent opening and apposition. Inadequate vessel wall apposition was remedied with balloon angioplasty when needed. The number of devices deployed was dependent on the operator's preference and experience but was also based on subjective assessment of intra-aneurysmal stasis. When the landing zone was missed, further devices were placed to cover the aneurysm neck. In addition, we may tend to use >1 device specifically for fusiform aneurysms. In the basilar artery, whenever possible, we try to avoid using >1 device to preserve the patency of side branches. Placement of additional PEDs was considered at follow-up if the aneurysm remained unchanged or did not sufficiently decrease in size despite treatment.

Statistical Analysis

Data are presented as mean and range for continuous variables and as frequency for categoric variables. Analysis was performed by using an unpaired t test, Wilcoxon rank sum test, χ^2 test, and Fisher exact test as appropriate. Univariate analysis was used to test covariates predictive of the following dependent variables, each independently: complications, aneurysm obliteration at follow up, retreatment, and unfavorable outcome (mRS 3–6). Interaction and confounding were assessed through stratification and relevant expansion covariates. Factors predictive in univariate analysis ($P <$ .20)[5] were entered into a multivariate logistic regression analysis. P values $\leq$.05 were considered statistically signifi-

Table 1: Aneurysm locations

Aneurysm Location	1 PED (%)	Multiple PEDs (%)
Carotid cavernous artery	17 (13.5)	13 (25)
Carotid ophthalmic artery	53 (42)	19 (36.5)
Paraclinoid artery	36 (28.6)	7 (13.5)
Middle cerebral artery	4 (3.1)	5 (9.6)
Basilar trunk	3 (2.4)	2 (3.8)
Posterior circulation (other than basilar trunk)	8 (6.4)	4 (7.7)
Other	5 (4.0)	2 (3.9)
Total	126	52

cant. Statistical analysis performed with STATA 10.0 (StataCorp, College Station, Texas).

RESULTS

Baseline Characteristics

The proportion of female patients was 86% (108/126) in the single-PED group and 81% (42/52) in the multiple-PED group ($P =$ .4). Patients in the multiple-PED group were significantly older than those in the single-PED group (mean age, 61.1 years versus 54.2 years; $P =$ .002). Mean aneurysm size was also higher in the multiple-PED group (11.8 mm versus 9.2 mm, $P =$ .02), but the proportion of patients with large aneurysms did not differ significantly between the 2 groups (39%, 49/126, with a single PED versus 52%, 27/52, with multiple PEDs; $P =$ .2). The proportion of aneurysms arising from the posterior circulation did not differ between the 2 groups (8.7%, 11/126, with a single PED versus 11.5%, 6/52, with multiple PEDs; $P =$ .6). Likewise, the proportion of aneurysms arising from the basilar trunk did not differ between the 2 groups (2.4%, 3/126, with a single PED versus 3.8%, 2/52, with multiple PEDs; $P =$ .8). The distribution of aneurysm locations is detailed in Table 1. Fusiform or dissecting aneurysms accounted for 12.7% (16/126) and 23% (12/52) of aneurysms treated with a single and multiple PEDs, respectively ($P =$ .09). The proportion of previously treated aneurysms was comparable in those treated with single (20.6%, 26/126) versus multiple devices (19.2%, 10/52; $P =$ .8).

Adjunctive coiling was undertaken in 11% (14/126) of aneurysms treated with a single PED versus 5.8% (3/52) of those treated with multiple PEDs ($P =$ .3). Balloon angioplasty was necessary in $\approx$9.5% (12/126, 5/52) of patients in either group ($P =$ .9). A single PED was used in 126 (70.8%) patients; 2 PEDs, in 40 (22.5%); 3 PEDs, in 7 (3.9%); 4 PEDs, in 4 (2.3%); and 5 PEDs, in 1 (0.7%).

Outcomes

Complications occurred more frequently in those treated with multiple (15%, 8/52) versus a single device (5%, 7/126, $P =$ .03). In the single-device group, there were 3 hemorrhagic complications (1 distal parenchymal hemorrhage, 1 spontaneous delayed aneurysm rupture after 4 months, and 1 aneurysm rupture due to proximal device migration causing a direct jet of blood against the dome) and 4 ischemic complications (1 associated with distal device migration in a patient with schizophrenia who was not compliant with his antiplatelet regimen). In the multiple-PED group, there were 4 hemorrhagic complications (all distal parenchymal

Table 2: Aneurysm obliteration

Latest Occlusion	Single PED (%)	Multiple PED (%)	Total (%)
Complete (100%)	58 (68.2)	28 (70)	86 (68.8)
Near-complete (90%–99%)	13 (15.3)	7 (17.5)	20 (16)
Incomplete (<90%)	15 (16.5)	5 (12.5)	19 (15.2)
Total	85	40	125

hemorrhages) and 4 ischemic complications. None of the hemorrhagic complications occurred in patients with middle cerebral artery aneurysms. The following factors were tested as predictors of complications: age, sex, aneurysm location, aneurysm size, aneurysm morphology, previous aneurysm treatment, number of PEDs used per aneurysm, adjunctive use of coils, and balloon angioplasty. In univariate analysis, predictors of complications were the following: 1) increasing age ($P = .04$); 2) increasing aneurysm size ($P = .004$); and 3) the use of >1 device ($P = .04$). These factors were subsequently entered into a multivariate analysis. In multivariate analysis, the use of >1 device was the only statistically significant predictor of complications (OR = 3.0; 95% CI, 1.1–8.8; $P = .04$).

Angiographic follow-up was available for 85 patients in the single-PED group and 40 patients in the multiple-PED group. Mean follow-up time was longer in the multiple- (8.9 months) than in the single-PED group (7.0 months, $P = .01$). A similar proportion of patients achieved complete or near-complete aneurysm obliteration at follow-up in the single-device (71/85, 84%) and multiple-device (35/40, 87%, $P = .8$) groups (Table 2). The following factors were tested as predictors of aneurysm obliteration: age, sex, aneurysm location, aneurysm size, aneurysm morphology, previous aneurysm treatment, number of PEDs used per aneurysm, adjunctive use of coils, balloon angioplasty, procedural complications, and angiographic follow-up time. In univariate analysis, the following factors were negative predictors of aneurysm obliteration (<90%): 1) increasing age ($P = .1$), and 2) decreasing angiographic follow-up duration ($P = .09$). In multivariate analysis, increasing age (OR = 0.4; 95% CI, 0.16–0.91; $P = .03$) and decreasing angiographic follow-up duration (OR = 0.9; 95% CI, 0.8–0.99; $P = .04$) were independent negative predictors of aneurysm obliteration. The number of devices was not a predictive factor, even after controlling for these variables.

Retreatment was necessary in a similar proportion of patients after embolization with single (6%, 5/85) or multiple devices (7.5%, 3/40, $P = .8$). In-stent stenosis was noted in ≈5% (4/85, 2/40) of patients in each group ($P = .95$).

Clinical follow-up was available for 125 patients in the single-PED group and 52 patients in the multiple-PED group. At the latest follow-up, a significantly higher proportion of patients treated with a single device (97%, 121/125) achieved a favorable outcome (mRS 0–2) compared with those treated with >1 device (89%, 46/52, $P = .03$). In the single-PED group, 3 of the 4 patients with an unfavorable outcome sustained a procedural complication and 1 was disabled at baseline. In the multiple-PED group, 4 of the 6 patients with an unfavorable outcome sustained a complication and 1 was severely disabled before PED treatment. The same factors as those used for occlusion were tested as predictors of clinical outcome. In univariate analysis, the following factors

were predictors of unfavorable outcome (mRS > 2): 1) increasing aneurysm size ($P > .001$), and 2) the use >1 device ($P = .03$). In multivariate analysis, increasing aneurysm size (OR = 1.1; 95% CI, 1.06–1.6; $P = .001$) was an independent predictive factor, and there was a strong trend toward the use of >1 device to predict unfavorable outcome (OR = 3.5; 95% CI, 0.9–13; $P = .06$).

DISCUSSION

Flow diversion is now a well-established treatment for intracranial aneurysms.[2,6-10] Flow diverters, most typically the PED, have proved to be more efficient than and at least as safe as traditional embolization strategies.[6,11,12] Lanzino et al[13] reported a significantly higher rate of complete occlusion in patients with the PED (76%) than in patients (21%) treated with coils with a similar rate of morbidity. Likewise, Chalouhi et al[2] compared the safety and efficacy of the 2 techniques in unruptured, large, and giant (≥10 mm) aneurysms, reporting a similar complication rate (7.5%) and a higher aneurysm occlusion rate (86% versus 41%) with flow diversion. They concluded that the PED is a preferred treatment option for large unruptured saccular aneurysms. The Pipeline for Uncoilable or Failed Aneurysms study is a recently published prospective, international multicenter series that included large and giant, wide-neck aneurysms arising from the internal carotid artery.[1] The results of this study confirmed the safety (5.6% rate of major ipsilateral stroke or neurologic death) and high efficacy of the PED (73.6% rate of complete occlusion at day 180 without major stenosis of the parent vessel) in the most complex aneurysms.

Aside from thromboembolic complications, which may occur in any neuroendovascular procedure, treatment with flow diverters carries the risk of specific complications not encountered with standard embolization techniques. Distal intracerebral hemorrhage (ICH) is a dreaded complication of flow diversion, and its incidence is reported to be approximately 1%–2%.[14,15] The mechanism of ICH after flow diversion may involve hemorrhagic conversion of ischemic infarcts in the setting of dual antiplatelet therapy, modification of intracranial blood pressure in the distal territories, and intraprocedural embolization of foreign material.[2,16,17] Delayed aneurysm rupture after flow diversion occurs in approximately 1.0% of patients, and its mechanism may involve sudden hemodynamic changes in intra-aneurysmal flow patterns or aneurysm wall weakening due to inflammation and proteolytic enzymes within the developing red thrombus.[17] Some have suggested using intraluminal coils or steroids to attenuate the effects of intra-aneurysmal thrombosis, but whether this strategy can reduce the risk of aneurysm rupture remains to be seen. Last, device migration has recently been recognized as a potential, severe complication of flow diversion that can be associated with hemorrhagic or thromboembolic events.[18] Migration may occur proximally or distally and is related to the mismatch in arterial diameter between inflow and outflow vessels and to stretching of the device.[19]

The present study was undertaken to address a pressing and crucial question that has been recently debated in the neurointerventional community. Specifically, we aimed to determine whether treatment with a single PED is sufficient for treatment of intracranial aneurysms. Although there might not be a categoric

answer to this question, this study provides strong evidence supporting the use of only a single PED in the initial treatment of aneurysms. As such, the complication rate was thrice as high in the multiple-device group (15%) compared with the single-device group (5%). Moreover, the use of >1 device was a strong independent predictor of complications with an odds ratio as high as 3. We believe that this is explained by a higher propensity for thromboembolic complications with the use of multiple PEDs, which are highly thrombogenic constructs with high metal surface area coverage. Because ICH may be secondary to ischemic lesions, hemorrhagic events are more likely to occur when multiple devices are used as well. In addition, it is well known that placement of the second and third PED is usually more technically complex, given the presence of the previously deployed device. The difficulty of deploying PEDs over previous stents has been highlighted in a recent article.[10] Although one may naturally tend to think that placing additional devices provides further flow diversion and better angiographic results, the present study demonstrates similar occlusion rates at follow-up with the use of a single (84%) versus multiple devices (87%). This crucial finding suggests that a single device provides enough flow diversion for occlusion of most aneurysms and that placement of additional devices will only add morbidity, cost, and radiation exposure. Accordingly, we believe that complete intra-aneurysmal stasis during initial embolization is not required for ultimate aneurysm thrombosis and should not be considered the end point of the procedure. Using multiple devices did not decrease the rate of retreatment; this result may suggest that aneurysms that fail flow diversion have an inherent tendency to do so regardless of the number of devices used. The senior author's strategy entails treating most aneurysms with a single PED initially and reserving further device deployment only for those aneurysms that remain unchanged or do not sufficiently decrease in size at the 3- to 6-month follow-up. This strategy avoids the unnecessary use of additional devices and is undoubtedly an important factor in procedural safety. The trend toward better clinical outcomes in the single-device group further supports this strategy. Potential exceptions include fusiform aneurysms, ruptured aneurysms in which immediate occlusion is warranted, and cases in which the initial device has not provided adequate neck coverage or vessel reconstruction. Using multiple PEDs may increase the stability of the construct and prevent device migration.[20] Also, there were no aneurysm ruptures in the multiple-device group. The 2 aneurysm ruptures that occurred in the single-device group may suggest that both could have been prevented with a multiple-device construct from the outset.

Although the studied question has not been previously addressed, the literature may suggest a similar trend. In the German study by Fischer et al,[21] in which multiple devices were used in as many as 66% of cases (median, 3), major complications occurred in 6% of patients. Likewise, the major complication rate was 8.5% in the US multicenter series in which 2.12 PEDs were used on average per aneurysm.[22] In the Canadian experience, O'Kelly et al[23] used >1 device in almost half of the patients and experienced a combined morbidity and mortality rate of 10.7% (6.3% mortality, 4.4% morbidity). In contrast, Lylyk et al[24] used a single PED in 70% of aneurysms and reported a 0% rate of morbidity and mor-

tality. Likewise, Saatci et al[14] used only 1.3 PEDs on average per aneurysm (1 device in ≈70%) and noted a combined morbidity-mortality rate as low as 1.5%. Thus, the use of multiple devices may be associated with higher complication rates and worse clinical outcomes, as corroborated in the present report.

This study is limited by its overall retrospective design, though the safety data on the PED are prospectively recorded at our institution. This study reports the experience of a single cerebrovascular center; thus, results may not be entirely generalizable. Although the 2 groups were well-matched with regard to most baseline characteristics, the older age, larger aneurysm size, and higher proportion of fusiform aneurysms (though not significantly) in the multiple-PED group may have favored the single-device group. Fusiform aneurysms are higher risk lesions with poorer outcomes across all treatment methods. Some may argue that the higher occurrence of intraparenchymal hemorrhages in the multiple-device group may be related to more challenging cases with a higher risk of wire perforations and more manipulation, causing more vessel stretching and tearing. However, in contrast to coiling, complication and recurrence rates with the PED are not affected by aneurysm size.[19,25] This outcome limits the effect of this factor on the comparative analysis. In addition, the shorter follow-up time in the single-PED group has favored the multiple-PED group because the occlusion rate of aneurysms treated with flow diverters increases with time.[3,14] A multivariate analysis was performed to control for those differences, and it identified treatment with multiple devices as an independent predictor of complications and poor outcome (strong trend).

CONCLUSIONS

The results of this study show that treatment with a single PED is associated with fewer complications, better functional outcomes, and similar occlusion rates compared with multiple PEDs. These results suggest that a single PED is sufficient for treatment of most intracranial aneurysms. Placement of additional devices may only add morbidity, cost, and radiation exposure.

In the era of flow diverters, ongoing trials should not only confirm the noninferiority of flow diversion to traditional embolization techniques (which is already known from several well-designed studies) but should also investigate ways to further improve the procedural safety and efficacy of flow diverters.

REFERENCES

1. Becske T, Kallmes DF, Saatci I, et al. **Pipeline for Uncoilable or Failed Aneurysms: results from a multicenter clinical trial.** *Radiology* 2013;267:858–68

2. Chalouhi N, Tjoumakaris S, Starke RM, et al. **Comparison of flow diversion and coiling in large unruptured intracranial saccular aneurysms.** *Stroke* 2013;44:2150–54

3. Yu SC, Kwok CK, Cheng PW, et al. **Intracranial aneurysms: mid-term outcome of Pipeline embolization device: a prospective study in 143 patients with 178 aneurysms.** *Radiology* 2012;265:893–901

4. Tse MM, Yan B, Dowling RJ, et al. **Current status of Pipeline embolization device in the treatment of intracranial aneurysms: a review.** *World Neurosurg* 2013;80:829–35

5. Altman DG. *Practical Statistics for Medical Research.* Boca Raton, Florida: Chapman & Hall/CRC; 1999

6. Yavuz K, Geyik S, Saatci I, et al. **Endovascular treatment of middle cerebral artery aneurysms with flow modification with the use of the Pipeline embolization device.** *AJNR Am J Neuroradiol* 2014;35:529–35

7. McAuliffe W, Wycoco V, Rice H, et al. **Immediate and midterm results following treatment of unruptured intracranial aneurysms with the Pipeline embolization device.** *AJNR Am J Neuroradiol* 2012;33:164–70

8. Chalouhi N, Chitale R, Starke RM, et al. **Treatment of recurrent intracranial aneurysms with the Pipeline embolization device.** *J Neurointerv Surg* 2014;6:19–23

9. Chalouhi N, Starke RM, Yang S, et al. **Extending the indications of flow diversion to small, unruptured, saccular aneurysms of the anterior circulation.** *Stroke* 2014;45:54–58

10. Chalouhi N, Tjoumakaris S, Dumont AS, et al. **Treatment of posterior circulation aneurysms with the Pipeline embolization device.** *Neurosurgery* 2013;72:883–89

11. Crobeddu E, Lanzino G, Kallmes DF, et al. **Marked decrease in coil and stent utilization following introduction of flow diversion technology.** *J Neurointerv Surg* 2013;5:351–53

12. Brinjikji W, Murad MH, Lanzino G, et al. **Endovascular treatment of intracranial aneurysms with flow diverters: a meta-analysis.** *Stroke* 2013;44:442–47

13. Lanzino G, Crobeddu E, Cloft HJ, et al. **Efficacy and safety of flow diversion for paraclinoid aneurysms: a matched-pair analysis compared with standard endovascular approaches.** *AJNR Am J Neuroradiol* 2012;33:2158–61

14. Saatci I, Yavuz K, Ozer C, et al. **Treatment of intracranial aneurysms using the Pipeline flow-diverter embolization device: a single-center experience with long-term follow-up results.** *AJNR Am J Neuroradiol* 2012;33:1436–46

15. Leung GK, Tsang AC, Lui WM. **Pipeline embolization device for intracranial aneurysm: a systematic review.** *Clin Neuroradiol* 2012;22:295–303

16. Deshmukh V, Hu YC, McDougall CG, et al. **Histopathological assessment of delayed ipsilateral parenchymal hemorrhages after the treatment of paraclinoid aneurysms with the Pipeline embolization device.** *Neurosurgery* 2012;71:E551–52

17. Pierot L, Wakhloo AK. **Endovascular treatment of intracranial aneurysms: current status.** *Stroke* 2013;44:2046–54

18. Chalouhi N, Satti SR, Tjoumakaris S, et al. **Delayed migration of a Pipeline embolization device.** *Neurosurgery* 2013;72(2 suppl operative):ons229–34, discussion ons234

19. Jabbour P, Chalouhi N, Tjoumakaris S, et al. **The Pipeline embolization device: learning curve and predictors of complications and aneurysm obliteration.** *Neurosurgery* 2013;73:113–20, discussion 120

20. Chalouhi N, Tjoumakaris SI, Gonzalez LF, et al. **Spontaneous delayed migration/shortening of the Pipeline embolization device: report of 5 cases.** *AJNR Am J Neuroradiol* 2013;34:2326–30

21. Fischer S, Vajda Z, Aguilar Perez M, et al. **Pipeline embolization device (PED) for neurovascular reconstruction: initial experience in the treatment of 101 intracranial aneurysms and dissections.** *Neuroradiology* 2012;54:369–82

22. Kan P, Siddiqui AH, Veznedaroglu E, et al. **Early postmarket results after treatment of intercrainal aneurysms with the Pipeline embolization device: a US multicenter experience.** *Neurosurgery* 2012; 71:1080–87

23. O'Kelly CJ, Spears J, Chow M, et al. **Canadian experience with the Pipeline embolization device for repair of unruptured intracranial aneurysms.** *AJNR Am J Neuroradiol* 2013;34:381–87

24. Lylyk P, Miranda C, Ceratto R, et al. **Curative endovascular reconstruction of cerebral aneurysms with the Pipeline embolization device: the Buenos Aires experience.** *Neurosurgery* 2009;64:632–42, discussion 642–43, quiz N6

25. Chalouhi N, Tjoumakaris S, Gonzalez LF, et al. **Coiling of large and giant aneurysms: complications and long-term results of 334 cases.** *AJNR Am J Neuroradiol* 2014;35:546–52

Analysis of Hemodynamics and Aneurysm Occlusion after Flow-Diverting Treatment in Rabbit Models

J.R. Cebral, F. Mut, M. Raschi, S. Hodis, Y.-H. Ding, B.J. Erickson, R. Kadirvel, and D.F. Kallmes

ABSTRACT

BACKGROUND AND PURPOSE: Predicting the outcome of flow diversion treatment of cerebral aneurysms remains challenging. Our aim was to investigate the relationship between hemodynamic conditions created immediately after flow diversion and subsequent occlusion of experimental aneurysms in rabbits.

MATERIALS AND METHODS: The hemodynamic environment before and after flow-diversion treatment of elastase-induced aneurysms in 20 rabbits was modeled by using image-based computational fluid dynamics. Local aneurysm occlusion was quantified by using a voxelization technique on 3D images acquired 8 weeks after treatment. Global and local voxel-by-voxel hemodynamic variables were used to statistically compare aneurysm regions that later thrombosed to regions that remained patent.

RESULTS: Six aneurysms remained patent at 8 weeks, while 14 were completely or nearly completely occluded. Patent aneurysms had statistically larger neck sizes ($P = .0015$) and smaller mean transit times ($P = .02$). The velocity, vorticity, and shear rate were approximately 2.8 times ($P < .0001$) larger in patent regions—that is, they had larger "flow activity" than regions that progressed to occlusion. Statistical models based on local hemodynamic variables were capable of predicting local occlusion with good precision (84% accuracy), especially away from the neck (92%–94%). Predictions near the neck were poorer (73% accuracy).

CONCLUSIONS: These results suggests that the dominant healing mechanism of occlusion within the aneurysm dome is related to slow-flow-induced thrombosis, while near the neck, other processes could be at play simultaneously.

ABBREVIATIONS: CFD = computational fluid dynamics; FD = flow-diverting; 3DRA = 3D rotational angiography

D espite the increased use of flow-diverting (FD) devices for treating intracranial aneurysms, the exact effects and processes responsible for the evolution of the aneurysm, and the ultimate outcome of these procedures are poorly understood.[1-4] Intrasaccular thrombosis and endothelial cell growth across the aneurysm neck have been observed after flow diversion and have been proposed as the main mechanisms driving the healing process.[5-7] However, the interaction, dominance, relative importance, and time precedence of these processes are not well-understood. Knowledge of these mechanisms is important to facilitate the development of future devices and therapies.

The purpose of this study was to investigate the relationship between the hemodynamic conditions created immediately after deployment of FD devices and the subsequent aneurysm occlusion in a rabbit model of saccular aneurysms.

MATERIALS AND METHODS
Animal Models and Imaging
Twenty-three elastase-induced aneurysms were created in New Zealand white rabbits, following the approach described in Altes et al.[8] Four weeks after their creation, the aneurysms were treated with a FD device (Pipeline Embolization Device; Covidien, Irvine, California). Two days before treatment, the subjects were premedicated with aspirin (10 mg/kg by mouth) and clopidogrel (10 mg/kg by mouth) and were continued on these for 1 month after treatment. Immediately before treatment, 3D rotational angiography (3DRA) images were acquired, and velocities in the surrounding vessels were measured with Doppler sonography. Six animals were sacrificed before 1 week after treatment; all others, after 8 weeks. Immediately before sacrifice, 3DRA imaging was

repeated. Some of the rabbits used in this study were part of another investigation in which we analyzed the mechanism of the endothelialization after flow diverter implantation. This article is entirely unrelated to the previous study.

Hemodynamics Modeling

Subject-specific computational fluid dynamics (CFD) models were constructed from pretreatment 3DRA images.[9] Unstructured grids were generated with a resolution of 0.2 mm. Models of the FD devices used to treat the aneurysms were created and virtually deployed within the reconstructed vascular models.[10] Blood flows were modeled by solving the unsteady 3D incompressible Navier-Stokes equations.[11] Physiologic flow conditions were derived from the Doppler sonography velocity measurements and imposed as boundary conditions in the computational models. Wall compliance was not included in the model. Blood attenuation was set to $\rho = 1.0$ g/cm^3, and blood viscosity, to $\mu = 0.04$ poise. The governing equations were numerically solved by using an efficient finite-element solver with a time-step of 0.01 seconds.[12] After deployment of the FD device, the mesh was adaptively refined to resolve the stent wires and a new CFD simulation was performed by using immersed grids.[13,14]

Occlusion Modeling

Regions of the aneurysm that remained open or patent and regions that were occluded at the time of sacrifice were identified by constructing a second vascular model from the 3DRA image acquired before sacrifice. The pretreatment model and this premortem or follow-up model were manually aligned by using rigid registration. A new grid was generated filling the volume of the follow-up model. The aneurysm neck was interactively delineated on the pretreatment model by connecting selected points along the path of minimum geodesic distance.[15] The aneurysm orifice defined by the delineated neck was triangulated, and grid points on each side of this surface were labeled as belonging to the aneurysm or the vessel.[15] The bounding box of the aneurysm was found and voxelized with isotropic voxels of the same resolution as the 3DRA images. Mesh points in the aneurysm region were then labeled as "open" or "occluded," depending on whether they were inside or outside the aligned follow-up model. The methodology is illustrated in Fig 1.

Global (per Aneurysm) Data Analysis

The degree of aneurysm occlusion at the time of sacrifice was quantified by the percentage of occluded voxels identified as described above. Aneurysms were then classified into 2 groups: 1) patent group: <80% of the voxels occluded at follow-up; 2) occluded group: >80% of the voxels occluded at follow-up. This 80% threshold was chosen because aneurysms with >80% occlusion of their volume looked almost completely closed on DSA images with perhaps a small "bump" in the parent artery—that is, they did not exhibit remnant necks of persistent filling of the sac.

Using the 3D meshes, we calculated geometric variables, including volume, maximum size, neck area, and maximum neck size for each aneurysm. Similarly, the following hemodynamic quantities were calculated over the aneurysm region and averaged over the cardiac cycle: mean aneurysm inflow rate <Q>, mean
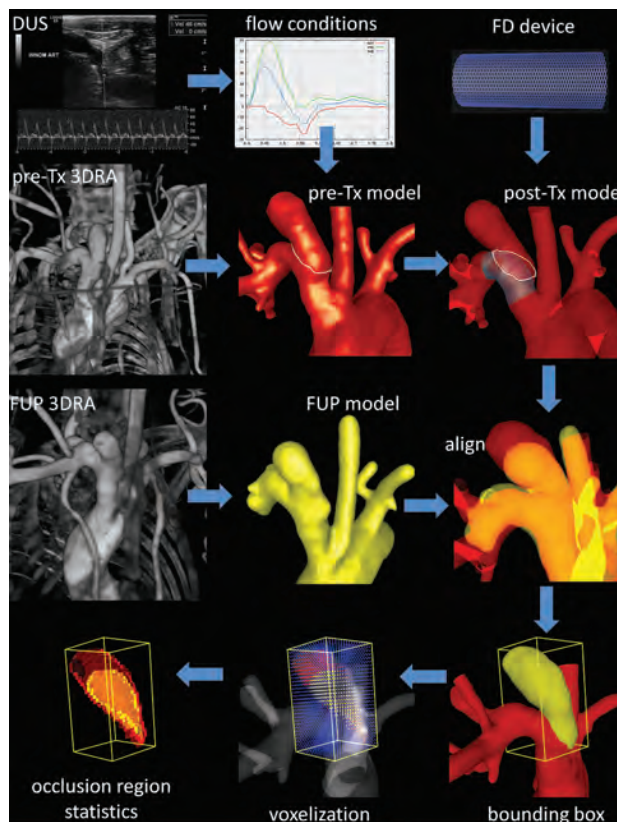
FIG 1. Imaging, modeling, and data analysis.

aneurysm velocity <v>, mean aneurysm wall shear stress <τ>, and mean aneurysm shear rate <γ̇>. These quantities were computed before and after treatment. Additionally, a new variable denoted "mean aneurysm transit time" (MATT) was defined as

$$MATT = \frac{(V/A)}{<v>}$$

where V is the aneurysm volume, A is the neck area, and <v> is the mean aneurysm velocity. The rationale is that this variable, which has units of time, should do the following:

1) Increase with the aneurysm volume (ie, it takes longer to traverse a large aneurysm)
2) Decrease with the neck area (ie, a larger neck implies more chances of getting out of the aneurysm, while a smaller neck implies more chances of staying within the aneurysm and recirculating)
3) Decrease with the blood velocity (ie, slower velocities imply longer transit times).

The values of geometric and hemodynamic variables were then averaged over the patent and occluded groups. Cases belonging to the incompletely occluded group sacrificed before 1 week after treatment (between brackets in the Tables) were excluded from the statistical analysis. The Wilcoxon nonparametric test was used to test whether the means were statistically different between the occluded and patent groups.

Local (Voxel-by-Voxel) Data Analysis

Velocity (v), vorticity (ω), and shear rate ($\dot{\gamma}$) were calculated on the CFD mesh and interpolated and averaged over each aneurysm voxel. The mean values of these quantities over open or occluded voxels of each aneurysm were calculated and compared.

Predictive statistical models of regional occlusion were then constructed. We defined 2 classes or outcomes: 1) occluded voxels ($+1$), and 2) open voxels (-1). Seven attributes or features were considered: 1) $\langle v \rangle_{pre}$, 2) $\langle \omega \rangle_{pre}$, 3) $\langle \dot{\gamma} \rangle_{pre}$, 4) $\langle v \rangle_{post}$, 5) $\langle \omega \rangle_{post}$, 6) $\langle \dot{\gamma} \rangle_{post}$, and 7) d = path distance to the neck. These values were calculated for each voxel from the pretreatment and posttreatment CFD simulations. A logistic regression model[16] was trained by using a "leave-one-out" methodology. Specifically, it was trained with all open and occluded voxels from all aneurysms except 1. The aneurysm left out was then used to test the accuracy of the model. The probabilities of each voxel of this aneurysm belonging to each class were calculated, and the voxel was "predicted" to belong to the class of the highest probability. The accuracy of the prediction was calculated by counting the number of correctly and incorrectly classified voxels. The process was repeated by leaving each aneurysm out one at a time, and the total predictive accuracy of the model was computed.

Next, the voxels of each aneurysm were divided into 3 groups according to their distance to the aneurysm neck. Denoting by d the distance from a voxel to the neck and d_{max} the maximum distance from any voxel to the neck, we assigned voxels to the following 3 groups: a) dome if $d/d_{max} > 2/3$, b) body if $1/3 \leq d/d_{max} \leq 2/3$, and c) neck if $d/d_{max} < 1/3$. The predictive statistical analysis described above by using the logistic regression model was repeated for voxels in each of these 3 regions. The corresponding predictive accuracies were calculated and compared.

Finally, we computed and compared the predictive power of the following statistical models typically used in machine-learning studies [17]: 1) logistic regression, 2) neural network, and 3) support vector machine. Each of these models was trained with data from all aneurysms except 1 and was tested on the one left out. The process was repeated by leaving each aneurysm out in turn. The total predictive accuracy of each model was computed and compared.

RESULTS

Hemodynamics

Flow visualizations revealed that velocities within the aneurysm are substantially reduced after treatment, that flow structures may change and, in particular, become smoother and simpler (ie, less swirling), and that the location of the inflow stream may shift from the distal part of the neck to the proximal part. To illustrate these observations, we present 2 examples in Fig 2, corresponding to incomplete and complete occlusions. The placement of FD devices thus causes both quantitative and qualitative changes in the hemodynamic environment within the aneurysm.

Global (per Aneurysm) Characteristics

Geometric characteristics of the aneurysms, the parent arteries, and the FD devices are presented in Tables 1 and 2. Aneurysms have been ordered by percentage occlusion. The aneurysm vol-
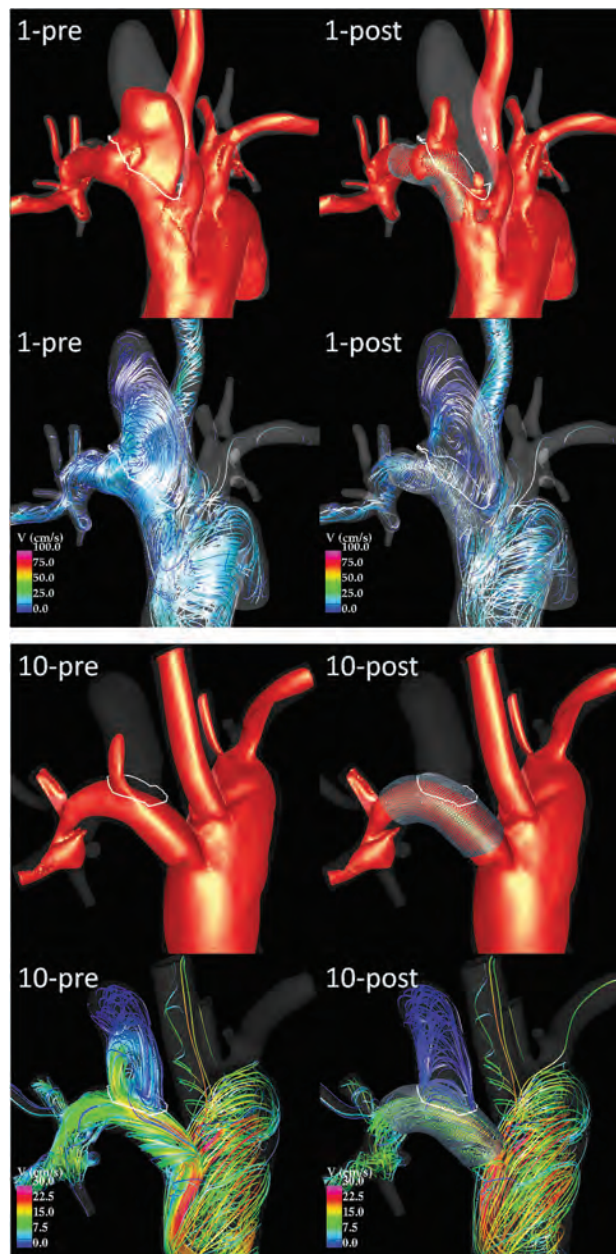
FIG 2. Visualization of peak systole flow structures pre- and posttreatment in an incompletely occluded aneurysm (case 1, top) and in a completely occluded aneurysm (case 10, bottom). Each panel shows 20 cm/s velocity isosurfaces (top) and flow streamlines (bottom) before (left) and after (right) treatment.

ume was not statistically different between the open and occluded aneurysm groups. The neck area ($P = .0006$), maximum neck size ($P = .0015$), and maximum aneurysm size ($P = .02$) were significantly larger in the patent than in the occluded groups.

Results from the global hemodynamics analysis are presented in the On-line Table. Only the mean inflow rate and mean aneurysm transit time were significantly different between the patent and occluded groups. The inflow rates before ($P = .0015$) and after treatment ($P = .0305$) were approximately 2.8 times larger in the patent group. The mean aneurysm transit time after treatment ($P = .02$) was approximately 3 times larger in occluded aneurysms than in patent aneurysms. The mean posttreatment shear rate

Table 1: Aneurysm occlusion, geometry, and device data[a]

Case	Aneurysm Occlusion (%)	PPA Diameter (mm)	DPA Diameter (mm)	Device Size (mm)	Aneurysm Volume (cm³)	Aneurysm Size (cm)	Neck Size (Cm)	Neck Area (Cm²)
1	7%	3.23	3.18	3.75 × 10	0.36	1.90	0.93	0.45
2	19%	3.28	2.66	4.5 × 12	0.17	1.13	0.86	0.48
3	31%	2.96	3.94	3.75 × 10	0.13	1.20	0.79	0.34
4	41%	3.72	3.54	3.75 × 12	0.06	1.17	0.65	0.27
[5]	46%	3.47	3.11	3.50 × 12	0.12	1.31	0.60	0.22
[6]	73%	3.19	3.40	3.25 × 10	0.08	0.74	0.53	0.14
7	75%	3.41	3.89	4.75 × 10	0.19	1.43	0.61	0.30
[8]	76%	3.11	3.34	3.50 × 12	0.13	1.20	0.57	0.22
9	77%	2.86	3.79	4.75 × 10	0.03	1.49	0.64	0.31
[10]	82%	3.26	3.02	3.50 × 10	0.08	0.94	0.47	0.14
11	84%	3.97	4.18	4.00 × 10	0.20	1.33	0.61	0.25
[12]	90%	3.44	3.11	3.50 × 10	0.12	1.20	0.42	0.12
13	91%	3.07	3.58	3.50 × 12	0.32	1.42	0.70	0.34
14	91%	3.95	4.24	4.00 × 10	0.08	1.01	0.53	0.09
15	94%	3.10	3.03	4.75 × 12	0.25	1.42	0.65	0.28
16	98%	3.57	3.57	4.25 × 10	0.06	0.91	0.34	0.07
[17]	100%	3.25	3.48	4.75 × 10	0.15	1.17	0.60	0.25
18	100%	3.82	3.25	3.50 × 10	0.01	0.39	0.24	0.04
19	100%	3.70	2.50	4.25 × 10	0.03	0.62	0.30	0.07
20	100%	4.24	3.96	4.75 × 10	0.03	0.59	0.41	0.12
21	100%	3.79	3.43	4.75 × 12	0.12	1.09	0.56	0.19
22	100%	3.65	2.89	4.00 × 10	0.02	0.53	0.31	0.05
23	100%	3.53	3.79	3.50 × 12	0.07	0.74	0.63	0.17

Note:—PPA indicates proximal parent artery; DPA, distal parent artery.
[a] Cases between brackets were sacrificed before 1 week and were not included in the analysis.

Table 2: Statistics of aneurysm geometrical data

Value	Aneurysm Volume (cm³)	Aneurysm Size (cm)	Neck Size (cm)	Neck Area (cm²)
Average over patent group	0.16	1.39	0.75	0.36
Average over occluded group	0.11	0.96	0.49	0.16
Ratio (patent/occluded)	1.41	1.44	1.54	2.25
P value		.2655	.0200[a]	.0015[a]	.0006[a]
AUC	0.51	0.67	0.70	0.73

Note:—AUC indicates area under the curve.
[a] Statistically significant differences ($P < .05$).

achieved marginal significance ($P = .0757$) and was approximately 1.6 times larger in the patent group. All other quantities were not statistically different between the open and occluded groups.

To assess the possibility of predicting whether the aneurysm will be completely occluded at follow-up, we performed a receiving operating curve analysis. The area under the curve was calculated for each geometric and hemodynamic variable (listed in Tables 1 and 2 and the On-line Table). The best predictor was neck area and size, with an accuracy of approximately 70%–73%. However, our sample included a small number of aneurysms. and it is likely that this accuracy could be improved with larger samples.

Regional (Voxel-by-Voxel) Characteristics
Results from the local hemodynamics analysis are presented in Fig 3. This figure shows the mean value of posttreatment hemodynamics variables (velocity, vorticity, and shear rate) averaged over the open (red) and occluded (green) voxels of each aneurysm. Aneurysms in the x-axis are ordered by percentage occlusion. Open voxels have larger posttreatment velocity, vorticity, and

shear rates than occluded voxels. These differences are less pronounced in aneurysms that had large patent regions (toward the left of Fig 3). The differences seem to increase with the percentage of occluded voxels (to the right of Fig 3). Ratios of posttreatment hemodynamic variables in open voxels over occluded voxels are presented in Table 3 for aneurysms that were not completely occluded. These results indicate that velocity, vorticity, and shear rate are on average larger by a factor of approximately 2.6 in open regions than in occluded regions. The ratios, however, are larger in aneurysms that were nearly completely occluded than in incompletely occluded ones. The P values indicate that these differences are statistically significant.

Predictive Models
Table 4 presents the accuracy and number of correctly predicted voxels over the total number of voxels for logistic regression models created for the entire aneurysm (sac), the dome, the body, and the neck regions. In addition, a range of accuracy values is provided for each region. These ranges were computed by calculating the accuracy of all possible combinations of the 7 features used to build the models (255 models for each region). Overall, the logistic regression model is capable of predicting which voxels will be occluded with very good accuracy and that voxels near the dome are more easily predicted than voxels near the neck.

A comparison of different statistical classifiers typically used in machine learning is presented in Table 5. Overall, all statistical models had similar accuracies. The best performance was obtained with the neural network. The cases that were most difficult to predict were the ones with patent regions that were approximately 60%–70% of the aneurysm volume. The predictive accuracy for aneurysms that were approximately 30%–46% occluded ranged from approximately 40% to 50% (data not shown).

FIG 3. Posttreatment hemodynamic variables averaged over open and occluded regions.

Table 3: Ratio of mean posttreatment hemodynamic variables in open-over-occluded regions[a]

Case	Ratio (v)	Ratio (ω)	Ratio <γ̇>
1	1.88	1.40	1.43
2	1.87	1.22	1.40
3	0.64	0.45	0.63
4	0.92	0.62	0.89
[5]	2.03	1.04	1.29
[6]	0.95	1.22	1.07
7	2.05	2.15	2.05
[8]	2.38	2.31	2.11
9	1.66	0.96	1.35
[10]	4.42	4.38	4.04
11	3.90	5.06	4.16
[12]	4.96	3.56	3.83
13	1.61	1.27	1.63
14	3.38	3.58	3.72
15	3.46	5.87	4.24
16	6.06	7.15	5.86
Mean	2.64	2.64	2.48
Mean open	1.60	1.26	1.36
Mean occluded	3.97	4.41	3.93
P value	.0139[b]	.0046[b]	.0023[b]

[a] Cases between brackets were sacrificed before 1 week and were not included in the analysis.
[b] Statistically significant differences ($P < .05$).

Table 4: Accuracy of logistic regression models of local occlusion

Region	Accuracy	Correct/Total	Range (%)
Sac	84%	28,054/33,254	(82.6,84.5)
Dome	94%	9649/10,299	(92.7,94.0)
Body	92%	12,232/13,274	(91.5,92.4)
Neck	73%	11,060/15,050	(71.8,73.9)

Table 5: Accuracy of different statistical models of local occlusion

Model	Accuracy	RMS Error
Logistic regression	86%	0.32
Neural network	90%	0.27
Support vector machine	85%	0.38

Note:—RMS indicates root mean square.

DISCUSSION

Flow diverters cause a significant disruption of the aneurysm inflow stream, which induces both qualitative and quantitative changes in the hemodynamic environment within the aneurysm. Aneurysms completely or almost completely occluded after treatment had statistically smaller necks than aneurysms that re-

mained patent. They also had larger mean aneurysm transit times (related to the aneurysm residence time). Immediately after flow diverter implantation, the local velocity, vorticity (speed of rotation or swirling of fluid elements), and shear rate (rate of deformation of fluid elements) were all statistically smaller in regions later observed to occlude than in regions that remained patent. Statistical models based on local hemodynamic conditions were able to predict local occlusion with a very good accuracy. For a given aneurysm, regions close to the neck were more difficult to predict than regions that were close to the aneurysm dome.

The mechanism of intrasaccular thrombosis and subsequent aneurysm occlusion is intimately related to the hemodynamic environment created after treatment. This environment depends mainly on the geometry of the aneurysm and parent artery and on the hemodynamic effects of the FD device. Aneurysm morphol-

ogy, in particular the location of the orifice on the parent artery and the neck size, determines the inflow stream into the aneurysm. The characteristics of the FD device, in turn, determine the disruption of this inflow stream and subsequent recirculation within the aneurysm sac. Thus, associations between both geometric and hemodynamic variables with outcome are expected. However, in this series, all aneurysms were created at the same location and were treated with similar FD devices. Thus, it is not surprising that the best predictor of complete occlusion was the neck size. Further studies with larger samples are needed to better understand the relationships among geometry, hemodynamics, and outcomes.

Previous studies have largely focused on the changes of hemodynamic quantities from pre- to posttreatment. Pereira et al[18] used dynamic DSA images to estimate the mean aneurysm velocity (mean aneurysm flow amplitude) before and after FD treatment in a pilot clinical study ($n = 21$), and found that at a later follow-up examination, aneurysms that were completely occluded ($n = 18$) had larger reductions of the mean aneurysm flow amplitude than aneurysms still patent ($n = 3$). Zhang et al[19] used CFD porous media to model the flow in 2 stented aneurysms, one remaining patent and the other completely occluded. They reported a larger reduction of aneurysm inflow velocity in the occluded than in the patent aneurysm. Huang et al[20] analyzed the flow dynamics in 14 rabbit aneurysm models treated with flow diverters. They used micro-CT images of harvested arteries with the flow diverter to create a model of the stent and place it in CFD models and found larger reductions in aneurysm inflow and larger increases of relative residence time in occluded aneurysms ($n = 10$) than in patent aneurysms ($n = 4$), though these differences did not reach statistical significance. They also observed changes in the location of the inflow stream, from the distal part of the neck to a more central/proximal position. In our study, we used CFD models with subject-specific flow conditions and FD models that reproduced the geometric characteristics of the implanted devices and compared global and local hemodynamic quantities in both occluded and patent aneurysms as well as between occluded and patent regions of each aneurysm. Our study focused on hemodynamic conditions created immediately after treatment rather than on changes from pre- to posttreatment.

The results of our study suggest that global hemodynamic conditions may not be sufficient to understand or predict aneurysm occlusion following flow-diversion treatment. They also suggest that thrombosis induced by the local hemodynamic conditions seems to be the main driver of aneurysm occlusion at the dome and body of the aneurysm, while other mechanisms such as endothelial tissue growth may be important near the neck. It is also possible that the thrombosis starts at the dome and progresses toward the neck, altering the intra-aneurysmal hemodynamic environment and inducing thrombus formation near the neck later followed by endothelialization. The regional analysis described in this work provides local information that could potentially be used to establish thresholds for thrombosis initiation and develop quantitative predictive models of local aneurysm occlusion.

The current study has a number of limitations that should be considered when interpreting the results. Unlike human cerebral arteries, flow reversals were observed in the parent arteries of our animal models. This could affect the values of the time-averaged hemodynamic quantities investigated. Alignment of follow-up and pretreatment vascular models was performed manually. This could result in inaccuracies of the quantification of the patent and occluded regions of the aneurysm. Our analysis did not distinguish between voxels that were close to the wall or near the middle of the aneurysm, which may have different hemodynamic environments. Likewise, the changes in the hemodynamic environment as the aneurysm progressively thromboses were not taken into account, only the hemodynamic conditions immediately posttreatment were studied. More refined models incorporating thrombus formation and proximity to the wall should be considered in future studies. The virtual deployment, the estimation of flow conditions from Doppler sonography images, as well as the many assumptions and approximations made during the CFD modeling process may affect the hemodynamic results. However, previous studies have indicated that these models could reproduce in vivo velocity measurements and observed flow characteristics.[21]

Finally, the number of animal models included in the study is limited. Studies with a larger number of subjects are needed to confirm the trends observed in this work and to achieve stronger statistical significance.

Despite these limitations, this study confirms that local hemodynamic conditions created immediately after flow diverter implantation play an important role in determining whether different regions of the aneurysm will thrombose and occlude or remain patent. The next set of studies should focus on the connection between hemodynamic conditions and biologic processes responsible for not only thrombosis and aneurysm occlusion but also endothelial tissue growth and parent artery reconstruction.

CONCLUSIONS

Aneurysms completely occluded at follow-up had statistically smaller necks and longer mean transit times than aneurysms that remained patent. Posttreatment velocity, vorticity, and shear rate were significantly larger in regions that remained patent (ie, had larger "flow activity") than in regions that occluded. Machine-learning models based on local hemodynamic variables were capable of predicting local occlusion with good precision, especially away from the neck. This suggests that the dominant healing mechanism at the dome and body of the aneurysm is related to flow-induced thrombosis, while near the neck, other processes such as flow-modulated endothelialization may also play a fundamental role.

REFERENCES

1. Lylyk P, Miranda C, Ceratto R, et al **Curative endovascular reconstruction of cerebral aneurysms with the Pipeline embolization device: the Buenos Aires experience.** *Neurosurgery* 2009;64:632–642

2. Nelson PK, Lylyk P, Szikora I, et al. **The Pipeline embolization device for the intracranial treatment of aneurysms trial. AJNR.** *AJNR Am J Neuroradiol* 2011;32:34–40

3. Seong J, Wakhloo AK, Lieber BB. **In vitro evaluation of flow divertors in an elastase-induced saccular aneurysm model in rabbit.** *J Biomech Eng* 2007;129:863–72

4. Kulcsár Z, Houdart E, Bonafe A, et al. **Intra-aneurysmal thrombosis as a possible cause of delayed aneurysm rupture after flow-diversion treatment.** *AJNR Am J Neuroradiol* 2011;32:20–25

5. Kallmes D, Ding YH, Dai D, et al. **A new endoluminal, flow disrupting device for treatment of saccular aneurysms.** *Stroke* 2007;38:2346–52

6. Kallmes D, Ding YH, Dai D, et al. **Low-disrupting device for treatment of saccular aneurysms.** *AJNR Am J Neuroradiol* 2009;30:1153–58

7. Szikora I, Berentei Z, Kulcsar Z, et al. **Treatment of intracranial aneurysms by functional reconstruction of the parent artery: the Budapest experience with the Pipeline embolization device.** *AJNR Am J Neuroradiol* 2010;31:1139–47

8. Altes TA, Cloft HJ, Short JG, et al. **1999 ARRS Executive Council Award: creation of saccular aneurysms in the rabbit—a model suitable for testing endovascular devices.** *AJR Am J Roentgenol* 2000;174:349–54

9. Cebral JR, Castro MA, Appanaboyina S, et al. **Efficient pipeline for image-based patient-specific analysis of cerebral aneurysm hemodynamics: technique and sensitivity.** *IEEE Trans Med Imaging* 2005;24:457–67

10. Mut F, Cebral JR. **Effects of flow-diverting device oversizing on hemodynamics alteration in cerebral aneurysms.** *AJNR Am J Neuroradiol* 2012;33:2010–16

11. Kundu PK, Cohen LM, Dowling DL. *Fluid Mechanics.* 5th ed. New York: Academic Press (Elsevier); 2011

12. Mut F. Aubry R, Löhner R, et al. **Fast numerical solutions in patient-specific blood flows in 3D arterial systems.** *Int J Num Method Biomed Eng* 2010;26:73–85

13. Appanaboyina S, Mut F, Löhne R, et al. **Computational fluid dynamics of stented intracranial aneurysms using adaptive embedded unstructured grids.** *Int J Numer Methods Fluids* 2008;57:457–93

14. Appanaboyina S, Mut F, Löhne R, et al. **Simulation of intracranial aneurysm stenting: techniques and challenges.** *Comput Methods Appl Mech Eng* 2009;198:3567–82

15. Mut F, Löhner R, Chien A, et al. **Computational hemodynamics framework for the analysis of cerebral aneurysms.** *Int J Numer Meth Biomed Eng* 2011;27:822–39

16. Fab RE, Chang KW, Hsieh CJ, et al. **LIBLINEAR: a library for large linear classification.** *J Machine Learning Res* 2008;9:1871–74

17. Hall M, Frank E, Holmes G, et al. **The WEKA data mining software: an update.** *SIGKDD Explorations* 2009;11:10–18

18. Pereira VM, Bonnefous O, Ouared R, et al. **A DSA-based method using contrast-motion estimation for the assessment of the intra-aneurysmal flow changes induced by flow-diverter stents.** *AJNR Am J Neuroradiol* 2013;34:805–15

19. Zhang Y, Chong W, Qian Y. **Investigation of intracranial aneurysm hemodynamics following flow diverter stent treatment.** *Med Eng Phys* 2013;35:608–15

20. Huang Q, Xu J, Cheng J, et al. **Hemodynamic changes by flow diverters in rabbit aneurysm models: a computational fluid dynamic study based on micro-computed tomography reconstruction.** *Stroke* 2013;44:1936–41

21. Cebral, JR, Mut F, Raschi M, et al. Flow diversion in rabbit aneurysm models. In: *Proceedings of the American Society of Mechanical Engineering Summer Bioengineering Conference,* Sunriver, Oregon; June 26–29, 2013

Elevated Cerebral Blood Volume Contributes to Increased FLAIR Signal in the Cerebral Sulci of Propofol-Sedated Children

J.H. Harreld, N.D. Sabin, M.G. Rossi, R. Awwad, W.E. Reddick, Y. Yuan, J.O. Glass, Q. Ji, A. Gajjar, and Z. Patay

ABSTRACT

BACKGROUND AND PURPOSE: Hyperintense FLAIR signal in the cerebral sulci of anesthetized children is attributed to supplemental oxygen (fraction of inspired oxygen) but resembles FLAIR hypersignal associated with perfusion abnormalities in Moyamoya disease and carotid stenosis. We investigated whether cerebral perfusion, known to be altered by anesthesia, contributes to diffuse signal intensity in sulci in children and explored the relative contributions of supplemental oxygen, cerebral perfusion, and anesthesia to signal intensity in sulci.

MATERIALS AND METHODS: Supraventricular signal intensity in sulci on pre- and postcontrast T2 FLAIR images of 24 propofol-sedated children (6.20 ± 3.28 years) breathing supplemental oxygen and 18 nonsedated children (14.28 ± 2.08 years) breathing room air was graded from 0 to 3. The Spearman correlation of signal intensity in sulci with the fraction of inspired oxygen and age in 42 subjects, and with dynamic susceptibility contrast measures of cortical CBF, CBV, and MTT available in 25 subjects, were evaluated overall and compared between subgroups. Factors most influential on signal intensity in sulci were identified by stepwise logistic regression.

RESULTS: CBV was more influential on noncontrast FLAIR signal intensity in sulci than the fraction of inspired oxygen or age in propofol-sedated children (CBV: $r = 0.612$, $P = .026$; fraction of inspired oxygen: $r = -0.418$, $P = .042$; age: $r = 0.523$, $P = .009$) and overall (CBV: $r = 0.671$, $P = .0002$; fraction of inspired oxygen: $r = 0.442$, $P = .003$; age: $r = -0.374$, $P = .015$). MTT (CBV/CBF) was influential in the overall cohort ($r = 0.461$, $P = .020$). Signal intensity in sulci increased with contrast in 45% of subjects, decreased in none, and was greater ($P < .0001$) in younger propofol-sedated subjects, in whom the signal intensity in sulci increased with age postcontrast ($r = 0.600$, $P = .002$).

CONCLUSIONS: Elevated cortical CBV appears to contribute to increased signal intensity in sulci on noncontrast FLAIR in propofol-sedated children. The effects of propofol on age-related cerebral perfusion and vascular permeability may play a role.

ABBREVIATIONS: FiO_2 = fraction of inspired oxygen; SSI = signal intensity in sulci

Accurate detection of leptomeningeal metastatic disease is critical for appropriate risk stratification and treatment of patients with CNS malignancies, particularly childhood posterior fossa tumors such as ependymoma and medulloblastoma, for which the diagnosis of metastasis is critical to staging and treatment.[1] T2-weighted FLAIR imaging is particularly sensitive for detection of intracranial leptomeningeal metastasis due to intrinsic sensitivity to the T1 effects of gadolinium at low concentrations, nonvisualization of intravascular blood, and CSF suppression,[2-4] but it is subject to artifactual increases in CSF signal in sulci, most commonly at the cerebral convexities, which could obscure or mimic leptomeningeal disease.[5]

In 2001, it was reported that children receiving propofol, but not chloral hydrate, showed CSF hyperintensity on FLAIR imaging.[5] Early theories that this artifactual signal might be due to intrinsic T1 hyperintensity of anesthetics crossing the blood-pial barrier were laid to rest by phantom studies.[5-7] Subsequent studies found that patients receiving high concentrations of supplemental oxygen were more likely than those receiving lower concentrations to have increased CSF signal intensity, even without anesthesia.[7,8] However, in the largest such study in anesthetized children, there was considerable overlap between groups, with 67%

of patients with low fraction of inspired oxygen (FiO_2) having hyperintense CSF compared with 84% in the high-FiO_2 group.[9] A later finding that sulcal signal intensity (SSI) decreased when FiO_2 was reduced from 100% to 30% in intubated children under propofol anesthesia[10] confirmed an influence of hyperoxygenation on SSI, but SSI persisted in 35% of children with FiO_2 of 30%, contrary to a previously established threshold of 50% below which no abnormal SSI was seen.[8] No studies to date have documented a linear relationship between FiO_2 and SSI, to our knowledge.

Physiologic factors may account for a nonlinear relationship of SSI and FiO_2, apparent differences in SSI between anesthesia protocols, and the overlap in SSI with low-versus-high FiO_2. It has been our observation that the diffuse, symmetric FLAIR SSI in anesthetized children resembles the asymmetric FLAIR signal seen in the sulci of patients with intracranial vascular stenosis, found to correlate with angiographically evident pial collaterals.[11] The appearance is also similar to the leptomeningeal "ivy sign" in patients with Moyamoya disease, found to correlate with cerebral perfusion, dilated pial vessels, and decreased cerebrovascular reserve.[12-14] We hypothesized that cerebral perfusion, known to be altered by anesthesia,[15] may contribute to diffuse FLAIR SSI. The purpose of this study was to investigate whether cerebral perfusion and enhancing pial vessels contribute to diffuse SSI in a relatively homogeneous pediatric neuro-oncology cohort and, if contributory, to explore the relative contributions of supplemental oxygen, cerebral perfusion, and anesthesia to SSI on T2-weighted FLAIR imaging.

MATERIALS AND METHODS
Subjects
A retrospective search of our institutional data base, conducted with institutional review board approval and waiver of consent, yielded 198 children with brain tumors without leptomeningeal metastasis who had pre- and postcontrast FLAIR MR imaging with supratentorial dynamic susceptibility contrast perfusion imaging at our institution between April 2008 and March 2011. MR imaging and anesthesia chart review were conducted in tandem until 50 complete MR imaging examinations without evidence of intracranial tumor or supratentorial resection, ischemia, metallic artifacts, or vascular or other supratentorial brain abnormality, performed with propofol-only anesthesia or no anesthesia, were identified. Patients receiving other anesthetic agents or opioids were ineligible due to potential confounding effects on cerebral perfusion.[15] Two subjects who had intravenous contrast within 48 hours before the graded scan[16] and 6 subjects with remote documented or suspected leptomeningeal disease not captured in our data base search were subsequently excluded. This process yielded 42 total subjects ranging in age from 1.2 to 18 years (mean, 9.66 ± 4.92 years; 48% male). Of these, 25 subjects (1.2–18 years; mean, 10.3 ± 4.60 years; 36% male) had technically adequate supraventricular PWI. To increase statistical power to detect associations between age, FiO_2, and SSI, we included the 17 subjects without perfusion imaging (1.3–16 years; mean, 8.75 ± 5.36 years; 65% male) for those analyses.

Anesthesia
Twenty-four subjects received propofol anesthesia (6.20 ± 3.28 years; range, 1.2–13 years). One hundred percent oxygen was administered by simple face mask, the flow rate in liters per minute (LPM) was recorded, and the FiO_2 was calculated by:

$$FiO_2 = LPM \times 4 + 20.$$

Eighteen subjects received no anesthesia (14.28 ± 2.08 years; range, 12–18 years) and breathed room air ($FiO_2 = 21\%$).

MR Imaging
Dynamic susceptibility contrast PWI was performed at 1.5T (Magnetom Avanto; Siemens, Erlangen, Germany) during injection of 0.1-mmol/kg gadopentetate dimeglumine (Magnevist; Bayer HealthCare Pharmaceuticals, Wayne, New Jersey) at 0.8–1 mL/s (standardized to be tolerated by all vascular access devices), with TR, 1910 ms; TE, 50 ms; flip angle, 90°; 15 sections; 4- to 5-mm section thickness (0 gap); 128 × 128 matrix; 1.6 × 1.6 mm in-plane voxel size; and bandwidth of 1346 Hz/pixel (86.144 kHz). T2-weighted fast FLAIR imaging was performed before and ~21 minutes after (mean, 20.90 ± 2.25 minutes) contrast injection, with TR = 7000–9140 ms; $TE_{effective} = 106–115$ ms; TI = 2500 ms; 4- to 5-mm section thickness (0 gap).

Image Analysis
Supraventricular SSI was rated from 0 to 3 (Fig 1) on pre- and postcontrast T2-weighted FLAIR images by 2 independent board-certified neuroradiologists with Certificates of Added Qualification (N.D.S. and J.H.H., with 9 and 5 years' experience) blinded to anesthesia and contrast status. Differences were resolved in consensus. Signal intensity was not graded in the basilar cisterns or ventricles due to potentially confounding CSF flow-related artifacts, lack of evidence for significant oxygen effects on ventricular CSF FLAIR signal, and our primary interest in evaluating sulci for factors affecting leptomeningeal metastasis detection.[7-9,17]

Twenty-five subjects (12 awake, 13 propofol-sedated) had technically adequate supraventricular PWI. Time-dependent contrast concentration, C(t), was calculated from T2* signal intensity as described by Østergaard.[18] Following automated arterial input function determination via iterative Kohonen self-organizing map-based pattern recognition,[19] the global arterial input function was used for nonparametric deconvolution by standard-form Tikhonov regularization by using minimized generalized cross-validation for pixel-by-pixel truncation threshold selection.[20]

CBF, CBV, and MTT were calculated relative to the arterial input function as

$$CBF = \frac{k_H}{\rho} \times \frac{C(t)}{\int_0^t C_a(\tau)R(t-\tau)d\tau}$$

$$CBV = \frac{k_H}{\rho} \times \frac{\int C_t(t)dt}{\int C_a(t)dt}$$

$$MTT = \frac{CBV}{CBF}$$

where $C_a(t)$ is the arterial input function, $R(t-\tau)$ is the tissue residual function, $C_a(\tau)R(t-\tau)$ represents the fraction of contrast in

the difference in the proportion of subjects with changes from pre- to postcontrast SSI between propofol-sedated and awake groups. Statistical analyses were performed by using SAS 9.2 software (SAS Institute, Cary, North Carolina). Values of $P < .05$ were statistically significant.

RESULTS
FiO$_2$ and Age
There was a moderate positive correlation of SSI and FiO$_2$ before and after contrast in the overall cohort, and SSI appeared to decrease with age (Table 1). However, subgroup analysis demonstrated these correlations to be driven by differences between propofol-sedated and nonsedated children.

Patients under propofol anesthesia were younger, had higher FiO$_2$, and had significantly greater SSI before and after contrast than awake subjects (Table 2). Contrary to the overall trend, SSI increased with age before and after contrast in anesthetized subjects, and SSI decreased with increasing FiO$_2$ before, but not after, contrast (Table 1). In awake subjects, FiO$_2$ was constant at 21%, and there was no correlation of SSI with age.

Age was not a significant influence once the other factors, including CBV, were accounted for in multivariate analysis by stepwise ordinal logistic regression (Table 1).

CBV, CBF, and MTT
Like SSI, cortical CBV and MTT were significantly greater in anesthetized than in awake subjects, though CBF did not differ between groups (Tables 2 and 3). There was a strong positive correlation of SSI with CBV in anesthetized subjects before, but not after, contrast (Table 1). On multivariate analysis, only CBV significantly influenced precontrast SSI in propofol-sedated children once the other factors, including age, were accounted for (Table 1 and Fig 2). CBF, CBV, and MTT had no significant correlation with SSI before or after contrast in awake subjects.

Overall, SSI increased with CBV before and after contrast. These relationships and a positive relationship of MTT with precontrast SSI remained significant by multivariate analysis (Table 1).

Contrast
SSI increased with contrast in 45% (19/42) of all subjects. In propofol-sedated subjects, SSI grade ranged from 0 to 3 before contrast and increased in 9/24 (37%) after contrast. In awake subjects, SSI was nonexistent-to-minimal (grades 0–1) before and after contrast, and it increased with contrast in 10/18 (56%) subjects. The increase in SSI did not exceed 1 grade in any subject.

FIG 1. Visual scale for grading SSI in supraventricular sulci: 0 = complete nulling, 1 = stippled hyperintensity, 2 = stippled with areas of confluent hyperintensity, 3 = confluent hyperintensity in sulci. The same grading scale was applied to precontrast and postcontrast FLAIR images.

the tissue at time t after contrast injection at time τ, $C_t(t)$ is the total concentration, and k_H/ρ corrects for the attenuation of brain tissue and the difference between large- and small-vessel hematocrit.[21] GM, WM, and CSF were segmented by an automated hybrid neural network method by using axial T1WI, T2WI, proton density, and FLAIR images.[22,23] CBV, CBF, and MTT were evaluated for cortical GM volumes.

Statistical Analysis
Descriptive statistics include mean and SD (unless otherwise noted) for continuous variables and frequencies and proportions for categoric variables. Wilcoxon rank sum tests were used to examine differences for continuous and ordinal variables between propofol-sedated and awake groups. Univariate analysis based on Spearman rank correlation coefficients was performed to assess the relationships among age, FiO$_2$, CBF, CBV, MTT, and pre-/postcontrast SSI. Multivariate analysis was performed by backward stepwise ordinal logistic regression modeling to identify the most significant variables influencing SSI from the above potential covariates. The Mantel-Haenszel χ^2 test was used to examine

Table 1: Univariate and multivariate analyses for the effects of selected factors on pre-/postcontrast SSI, overall and for propofol subjects

	Overall				Propofol			
	Univariate		Multivariate[a]		Univariate		Multivariate[a]	
	R^b	P	OR (95% CI)	P	R^b	P	OR (95% CI)	P
Precontrast SSI								
FiO$_2$	0.442	.003			−0.418	.042		
Age	−0.372	.015			0.523	.009	1.661 (0.954–2.893)	.073
GM CBF	0.036	.864			0.274	.364		
GM CBV	0.671	.0002	4.127 (1.688–10.089)	.002	0.612	.026	3.964 (1.118–14.054)	.033
GM MTT	0.461	.020	3.769 (1.231–11.537)	.020	0.331	.269		
Postcontrast SSI								
FiO$_2$	0.453	.003	−	.022	−0.357	.087		
Age	−0.374	.015			0.600	.002	1.658 (0.982–2.8)	.058
GM CBF	0.062	.770			0.180	.557		
GM CBV	0.625	.0008	2.613 (1.225–5.575)	.013	0.376	.205		
GM MTT	0.368	.071			0.199	.516		

[a] Multivariate analysis by stepwise ordinal logistic regression.
[b] Spearman correlation coefficient.

Table 2: SSI, Age, and FiO$_2$ overall and by anesthesia status[a]

	Overall (n = 42)	Propofol (n = 24)	Awake (n = 18)	P^b
Pre-SSI				
0	21 (50%)	6 (25%)	15 (83%)	.0001
1	12 (29%)	9 (38%)	3 (17%)	
2	8 (19%)	8 (33%)	0 (0%)	
3	1 (2%)	1 (4%)	0 (0%)	
Post-SSI				
0	5 (12%)	0 (0%)	5 (28%)	.0001
1	26 (62%)	13 (54%)	13 (72%)	
2	9 (21%)	9 (38%)	0 (0%)	
3	2 (5%)	2 (8%)	0 (0%)	
Age (yr)	9.66 (4.92)	6.2 (3.3)	14.3 (2.1)	<.0001
FiO$_2$	0.35 (0.14)	0.5 (0.1)	0.2 (0)	<.0001

[a] Age, FiO$_2$, given as means (SDs).
[b] P value for testing differences between propofol vs awake groups.

Table 3: Perfusion measures overall and by anesthesia status[a]

	Overall (n = 25)	Propofol (n = 13)	Awake (n = 12)	P^b
CBF (mL/min/100 g)	66.86 (15.45)	67.2 (17.7)	66.5 (13.4)	.765
CBV (mL/100 g)	7.45 (1.46)	8.2 (1.5)	6.6 (0.8)	.008
MTT (s^{-1})	6.69 (1.12)	7.2 (1)	6.2 (1)	.013

[a] CBF, CBV, and MTT given as means (SDs).
[b] P value for testing differences between propofol vs awake groups.

DISCUSSION

Hyperintense FLAIR signal in the cerebral sulci of anesthetized children has been attributed to T1 shortening effects of supplemental oxygen but resembles the leptomeningeal FLAIR hyperintensity associated with dilated pial vessels in Moyamoya disease and carotid stenosis.[11,12,14,24] In our study, diffuse SSI on noncontrast T2 FLAIR was more strongly correlated with CBV than FiO$_2$, both in propofol-sedated children and overall, with MTT (CBV/CBF) significantly influential in the overall cohort.

These findings are consistent with studies demonstrating a positive correlation of CBV and a negative correlation of cerebrovascular reserve (an index of cerebral perfusion pressure represented by CBF/CBV, the inverse of MTT[25]) with the severity of the leptomeningeal ivy sign on noncontrast T2-FLAIR in Moyamoya disease.[12-14,24] Asymmetric FLAIR SSI has also been associated with altered cerebral hemodynamics in patients undergoing internal carotid artery balloon occlusion testing.[26] In such cases,

autoregulatory mechanisms triggered by decreased CBF lead to compensatory precapillary vasodilation, increased CBV, prolonged MTT, and decreased cerebrovascular reserve.[27] Indeed, in Moyamoya disease, the ivy sign has been associated with ischemic symptoms and dilated pial vessels at surgery[14] and resolves after revascularization.[24]

We found moderate positive correlations of FiO$_2$ with SSI before and after contrast in the overall cohort, in keeping with prior studies reporting increased CSF signal intensity with high FiO$_2$,[5,7-10] but these were driven by significantly higher FiO$_2$ and SSI in propofol subjects, in whom SSI actually decreased with increasing FiO$_2$. To our knowledge, no prior study has demonstrated a direct correlation of SSI with FiO$_2$ under anesthesia-specific conditions, which could account for this apparent discordance. Although no subjects received more than the 60% FiO$_2$ threshold for increased CSF signal described by Frigon et al[9] and most received less than the "all or none" threshold of 50% FiO$_2$ described by Braga et al,[8] SSI was sometimes significant. Because nonsedated children did not receive supplemental oxygen, this study does not exclude a direct influence of FiO$_2$ on SSI. However, we found no FiO$_2$ threshold below which SSI was nonexistent because even some subjects breathing room air had increased SSI.

Typical of clinical practice, propofol-sedated children were younger and had greater SSI than nonsedated children in this study, raising the question of whether younger children are more likely to have increased SSI due to age alone. If this were the case, one would expect SSI to decrease with age, even in propofol-sedated children. We found the opposite (Table 1), consistent with prior reports,[9] though CBV had a stronger influence. Age-related changes in SSI were not detected in older nonsedated children but cannot be excluded in young nonsedated children because young children generally require anesthesia for MR imaging.

On the other hand, the overall trend of increasing SSI with CBV is consistent with, and apparently driven by, CBV-related increases in SSI in the propofol group before contrast. SSI was uniformly low in nonsedated subjects, even in the range of CBV overlapping that of sedated children.

Differences between propofol-sedated and nonsedated children unexplained by age, FiO$_2$, or perfusion alone, suggest propofol as a common thread. Indeed, age-related increases in CBV in propofol-sedated children have been previously described[28] and could account for the positive associations of SSI with both age and CBV in our propofol-sedated subjects.

Like SSI, CBV was greater in the younger, propofol-sedated subjects, as previously described (Tables 2 and 3).[28] Although CBF is expected to be greater in younger children,[29,30] there was no significant difference in CBF between (younger) sedated and (older) awake subjects, likely because propofol reduces CBF.[15,31] As a result, MTT (CBV/CBF) was also greater in younger sedated subjects, though MTT is expected to be greater in older children.[32] We speculate that
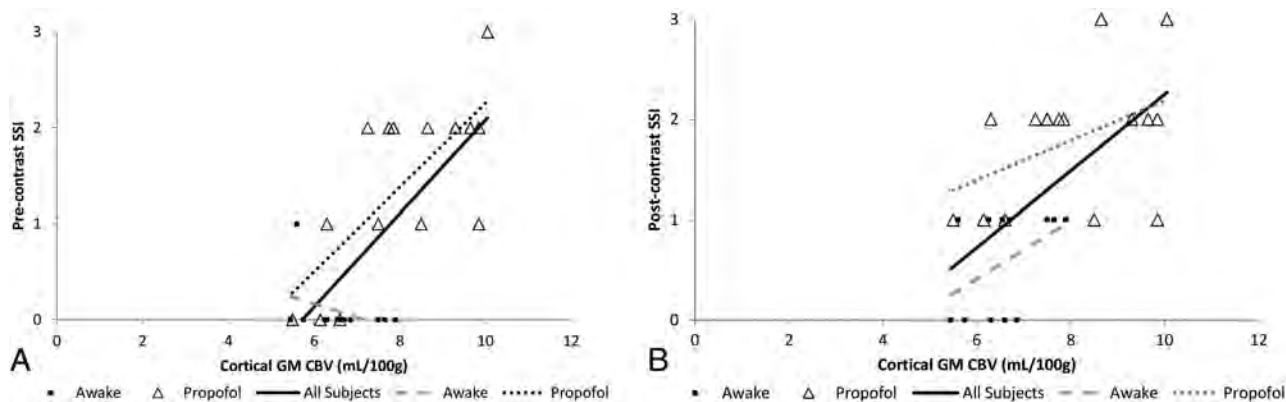
FIG 2. Relationship of CBV with pre-contrast (*A*) and post-contrast (*B*) FLAIR SSI. Significant correlations (*P* < .05) are in black.

propofol-induced decreases in CBF could lead to compensatory dilation of precapillary pial vessels, increasing CBV and prolonging MTT and resulting in diffusely increased SSI, as occurs asymmetrically in patients with Moyamoya disease and temporary ICA balloon occlusion.[24,26] Diffuse SSI may thereby serve as a visual "marker" for general cerebral hemodynamic status in propofol-sedated children without cerebrovascular disease.

SSI increased with intravascular contrast, supporting a vascular contribution to SSI. Greater "stasis" of blood as evidenced by prolonged MTT in sedated children may promote increased diffusion of oxygen to CSF.[33] Additionally, propofol has been found to facilitate disruption of the BBB.[34] Propofol-related increases in vascular permeability to proteins or oxygen,[34] with resultant T1 shortening of CSF,[35] may account for the finding of Filippi et al[5] that children sedated with propofol, but not chloral hydrate, exhibited SSI. Differences in perfusion effects may also contribute; unlike propofol, chloral hydrate increases CBF, potentially precluding a compensatory CBV response.[31,36] Vascular enhancement and leakage of gadolinium across vessel walls rendered more permeable by propofol could obscure more subtle changes related to perfusion or FiO$_2$, accounting for the loss of a significant relationship of SSI with CBV after contrast in propofol-sedated children. Age-related changes in vessel wall permeability to gadolinium may also influence postcontrast FLAIR SSI.[28,37] Thus, as with CBV,[28] there may be an interactive effect of propofol and age on vascular permeability and SSI.

This study has limitations. The small sample size may have contributed to the lack of a significant association of age with SSI on logistic ordinal regression, for which we could not include subjects without perfusion imaging. However, univariate correlations of age with SSI (by using all subjects) were lower than those for CBV for all but propofol postcontrast, consistent with the multivariate results (Table 1). Dynamic susceptibility contrast measures of CBV are less quantitative than PET, and our low contrast injection rate may have increased variability via a decreased contrast-to-noise ratio,[20] potentially decreasing the strength of linear relationships of CBF, CBV, and MTT with SSI. Future study with PET-MR imaging may better evaluate these relationships. We calculated FiO$_2$ from the administration rate of oxygen via face mask, an imprecise relationship. Our findings suggest that decreasing the oxygen-administration rate in nonintubated children under propofol anesthesia will not reliably ame-

liorate artifactual SSI, perhaps due to this imprecision. Similar to authors of other studies, we did not perform concurrent CSF analysis and did not address the potential contribution of CSF protein levels to SSI, which could contribute to variability not captured by our models. We did exclude patients with known, suspected, or remote CSF abnormalities to minimize potential disruption of relationships of SSI with perfusion and FiO$_2$. Because the threshold for CSF protein detection at our TE$_{effective}$ of 106−110 ms is ~250 mg/dL,[35] far greater than the upper range of normal (60 mg/dL at our institution) and indicative of significant leptomeningeal CNS disease, the contribution of CSF protein to SSI would not be expected to be significant in this study.

CONCLUSIONS
Elevated cortical CBV appears to contribute to increased SSI on noncontrast T2 FLAIR brain images in propofol-sedated children. SSI increased with intravascular contrast regardless of anesthesia, supporting a vascular contribution to SSI. Further investigations into the potential of increased FLAIR SSI as a marker for elevated CBV in propofol-sedated children should consider the potentially interactive effects of age and propofol on cerebral perfusion and vascular permeability.

REFERENCES

1. Engelhard HH, Corsten LA. **Leptomeningeal metastasis of primary central nervous system (CNS) neoplasms.** *Cancer Treat Res* 2005;125:71–85

2. Griffiths PD, Coley SC, Romanowski CA, et al. **Contrast-enhanced fluid-attenuated inversion recovery imaging for leptomeningeal disease in children.** *AJNR Am J Neuroradiol* 2003;24:719–23

3. Kremer S, Abu Eid M, Bierry G, et al. **Accuracy of delayed post-contrast FLAIR MR imaging for the diagnosis of leptomeningeal infectious or tumoral diseases.** *J Neuroradiol* 2006;33:285–91

4. Mathews VP, Caldemeyer KS, Lowe MJ, et al. **Brain: gadolinium-enhanced fast fluid-attenuated inversion-recovery MR imaging.** *Radiology* 1999;211:257–63

5. Filippi CG, Ulug AM, Lin D, et al. **Hyperintense signal abnormality in subarachnoid spaces and basal cisterns on MR images of children anesthetized with propofol: new fluid-attenuated inversion recovery finding.** *AJNR Am J Neuroradiol* 2001;22:394–99

6. Anzai Y, Ishikawa M, Shaw DW, et al. **Paramagnetic effect of supplemental oxygen on CSF hyperintensity on fluid-attenuated inversion recovery MR images.** *AJNR Am J Neuroradiol* 2004;25:274–79

7. Deliganis AV, Fisher DJ, Lam AM, et al. **Cerebrospinal fluid signal intensity increase on FLAIR MR images in patients under general anesthesia: the role of supplemental O2.** *Radiology* 2001;218:152–56

8. Braga FT, da Rocha AJ, Hernandez Filho G, et al. **Relationship between the concentration of supplemental oxygen and signal intensity of CSF depicted by fluid-attenuated inversion recovery imaging.** *AJNR Am J Neuroradiol* 2003;24:1863–68

9. Frigon C, Jardine DS, Weinberger E, et al. **Fraction of inspired oxygen in relation to cerebrospinal fluid hyperintensity on FLAIR MR imaging of the brain in children and young adults undergoing anesthesia.** *AJR Am J Roentgenol* 2002;179:791–96

10. Frigon C, Shaw DW, Heckbert SR, et al. **Supplemental oxygen causes increased signal intensity in subarachnoid cerebrospinal fluid on brain FLAIR MR images obtained in children during general anesthesia.** *Radiology* 2004;233:51–55

11. Sanossian N, Saver JL, Alger JR, et al. **Angiography reveals that fluid-attenuated inversion recovery vascular hyperintensities are due to slow flow, not thrombus.** *AJNR Am J Neuroradiol* 2009;30:564–68

12. Kaku Y, Iihara K, Nakajima N, et al. **The leptomeningeal ivy sign on fluid-attenuated inversion recovery images in Moyamoya disease: positron emission tomography study.** *Cerebrovasc Dis* 2013;36:19–25

13. Kawashima M, Noguchi T, Takase Y, et al. **Unilateral hemispheric proliferation of ivy sign on fluid-attenuated inversion recovery images in Moyamoya disease correlates highly with ipsilateral hemispheric decrease of cerebrovascular reserve.** *AJNR Am J Neuroradiol* 2009;30:1709–16

14. Mori N, Mugikura S, Higano S, et al. **The leptomeningeal "ivy sign" on fluid-attenuated inversion recovery MR imaging in Moyamoya disease: a sign of decreased cerebral vascular reserve?** *AJNR Am J Neuroradiol* 2009;30:930–35

15. Szabó EZ, Luginbuehl I, Bissonnette B. **Impact of anesthetic agents on cerebrovascular physiology in children.** *Paediatr Anaesth* 2009;19:108–18

16. Morris JM, Miller GM. **Increased signal in the subarachnoid space on fluid-attenuated inversion recovery imaging associated with the clearance dynamics of gadolinium chelate: a potential diagnostic pitfall.** *AJNR Am J Neuroradiol* 2007;28:1964–67

17. Tha KK, Terae S, Kudo K, et al. **Differential diagnosis of hyperintense cerebrospinal fluid on fluid-attenuated inversion recovery images of the brain. Part II. Non-pathological conditions.** *Br J Radiol* 2009;82:610–14

18. Østergaard L. **Principles of cerebral perfusion imaging by bolus tracking.** *J Magn Reson Imaging* 2005;22:710–17

19. Jain JJ, Glass JO, Reddick WE. **Automated arterial input function identification using self organizing maps.** In: *Proceedings of SPIE International Symposium on Medical Imaging, Image Processing Conference*, San Diego, California; February 17–22, 2007

20. Sourbron S, Luypaert R, Van Schuerbeek P, et al. **Choice of the regularization parameter for perfusion quantification with MRI.** *Phys Med Biol* 2004;49:3307–24

21. Calamante F, Thomas DL, Pell GS, et al. **Measuring cerebral blood flow using magnetic resonance imaging techniques.** *J Cereb Blood Flow Metab* 1999;19:701–35

22. Reddick WE, Glass JO, Cook EN, et al. **Automated segmentation and classification of multispectral magnetic resonance images of brain using artificial neural networks.** *IEEE Trans Med Imaging* 1997;16:911–18

23. Glass JO, Reddick WE, Reeves C, et al. **Improving the segmentation of therapy-induced leukoencephalopathy in children with acute lymphoblastic leukemia using a priori information and a gradient magnitude threshold.** *Magn Reson Med* 2004;52:1336–41

24. Kawashima M, Noguchi T, Takase Y, et al. **Decrease in leptomeningeal ivy sign on fluid-attenuated inversion recovery images after cerebral revascularization in patients with Moyamoya disease.** *AJNR Am J Neuroradiol* 2010;31:1713–18

25. Schumann P, Touzani O, Young AR, et al. **Evaluation of the ratio of cerebral blood flow to cerebral blood volume as an index of local cerebral perfusion pressure.** *Brain* 1998;121(pt 7):1369–79

26. Michel E, Liu H, Remley KB, et al. **Perfusion MR neuroimaging in patients undergoing balloon test occlusion of the internal carotid artery.** *AJNR Am J Neuroradiol* 2001;22:1590–96

27. Kikuchi K, Murase K, Miki H, et al. **Measurement of cerebral hemodynamics with perfusion-weighted MR imaging: comparison with pre- and post-acetazolamide 133Xe-SPECT in occlusive carotid disease.** *AJNR Am J Neuroradiol* 2001;22:248–54

28. Harreld JH, Helton KJ, Kaddoum RN, et al. **The effects of propofol on cerebral perfusion MRI in children.** *Neuroradiology* 2013;55:1049–56

29. Biagi L, Abbruzzese A, Bianchi MC, et al. **Age dependence of cerebral perfusion assessed by magnetic resonance continuous arterial spin labeling.** *J Magn Reson Imaging* 2007;25:696–702

30. Ogawa A, Sakurai Y, Kayama T, et al. **Regional cerebral blood flow with age: changes in rCBF in childhood.** *Neurol Res* 1989;11:173–76

31. Schlünzen L, Juul N, Hansen KV, et al. **Regional cerebral blood flow and glucose metabolism during propofol anaesthesia in healthy subjects studied with positron emission tomography.** *Acta Anaesthesiol Scand* 2012;56:248–55

32. Jain V, Duda J, Avants B, et al. **Longitudinal reproducibility and accuracy of pseudo-continuous arterial spin-labeled perfusion MR imaging in typically developing children.** *Radiology* 2012;263:527–36

33. Maas AI, Fleckenstein W, de Jong DA, et al. **Monitoring cerebral oxygenation: experimental studies and preliminary clinical results of continuous monitoring of cerebrospinal fluid and brain tissue oxygen tension.** *Acta Neurochir Suppl (Wien)* 1993;59:50–57

34. Remsen LG, Pagel MA, McCormick CI, et al. **The influence of anesthetic choice, PaCO2, and other factors on osmotic blood-brain barrier disruption in rats with brain tumor xenografts.** *Anesth Analg* 1999;88:559–67

35. Melhem ER, Jara H, Eustace S. **Fluid-attenuated inversion recovery MR imaging: identification of protein concentration thresholds for CSF hyperintensity.** *AJR Am J Roentgenol* 1997;169:859–62

36. Uematsu M, Takasawa M, Hosoi R, et al. **Uncoupling of flow and metabolism by chloral hydrate: a rat in-vivo autoradiographic study.** *Neuroreport* 2009;20:219–22

37. Kratzer I, Vasiljevic A, Rey C, et al. **Complexity and developmental changes in the expression pattern of claudins at the blood-CSF barrier.** *Histochem Cell Biol* 2012;138:861–79

PET in Infancy Predicts Long-Term Outcome during Adolescence in Cryptogenic West Syndrome

J. Natsume, N. Maeda, K. Itomi, H. Kidokoro, N. Ishihara, H. Takada, A. Okumura, T. Kubota, K. Miura, K. Aso, T. Morikawa, K. Kato, T. Negoro, and K. Watanabe

ABSTRACT

BACKGROUND AND PURPOSE: Developmental and seizure outcomes in patients with cryptogenic West syndrome are variable. Our aim was to clarify the relationship between FDG-PET findings in infancy and long-term seizure and developmental outcome in cryptogenic West syndrome.

MATERIALS AND METHODS: From 1991 to 1999, we prospectively performed FDG-PET from the onset of cryptogenic West syndrome in 27 patients. PET was performed at onset and at 10 months of age. In 2012, we evaluated the educational status, psychomotor development, and seizure outcome in 23 of the 27 patients (13–22 years of age). The correlation between PET findings and outcome was evaluated.

RESULTS: At onset, PET showed hypometabolism in 13 patients (57%). The second PET after the initial treatment revealed cortical hypometabolism in 7 patients (30%). While hypometabolism at onset disappeared on the second PET in 9 patients, it was newly revealed in 3 patients on the second PET. In 2012, seven patients had persistent or recurrent seizures. Eight patients had intellectual impairment. The first PET did not correlate with seizure or developmental outcome. Five of 7 patients (71%) with hypometabolism seen on the second PET had persistent or recurrent seizures, while 14 of 16 (88%) patients with normal findings on the second PET were free of seizures. Five of 7 patients (71%) showing hypometabolism on the second PET had intellectual impairment. Thirteen of 16 (81%) patients with normal findings on the second PET showed normal intelligence. A significant correlation was found between the second PET and long-term seizure ($P = .01$) or developmental outcome ($P = .03$).

CONCLUSIONS: Cortical hypometabolism is not permanent; it changes with clinical symptoms. Hypometabolism after initial treatment predicts long-term seizures and poor developmental outcome.

ABBREVIATIONS: ACTH = adrenocorticotropic hormone; DQ = developmental quotient; EEG = electroencephalography; IQ = intelligence quotient

West syndrome is an age-dependent epileptic encephalopathy characterized by epileptic spasms and the specific interictal electroencephalography (EEG) abnormality of hypsarrhythmia. Patients with West syndrome often show deterioration of psychomotor development after the onset. Although the long-term outcome is better in patients with cryptogenic etiology, the developmental and seizure outcomes in cryptogenic patients are variable.[1-3]

Since the description by Chugani et al,[4,5] the use of PET to detect hypometabolism in cryptogenic West syndrome has come into the spotlight. We and others have reported PET hypometabolism or SPECT hypoperfusion during the early stage of cryptogenic West syndrome.[6-11] We also have reported evolutional changes in cortical hypometabolism on PET and have suggested the usefulness of PET for predicting the prognosis.[6-9] The results of our studies and others revealed that persistent hypometabolism or hypoperfusion after initial pharmacologic treatment suggests poor developmental outcome.[6-9,11,12] However, the follow-up period of these studies was limited to a minimum of 2 or 3 years. Developmental statuses and seizures in school age or adulthood should be investigated to reveal long-term outcome.

In the present study, we investigated the educational and occupational statuses, psychomotor development, and seizure

outcome in patients with cryptogenic West syndrome who underwent prospective serial PET scans from the onset in our previous studies and were now 13 years of age or older.

MATERIALS AND METHODS

Between April 1991 and December 1999, we prospectively registered all 27 children (16 boys) with new-onset cryptogenic West syndrome who were admitted to Nagoya University Hospital and performed PET studies. The criteria for diagnosing cryptogenic West syndrome were as follows: 1) normal birth and absence of any etiologic factors related to West syndrome, 2) normal development before the onset and absence of neurologic abnormalities at the onset, 3) the occurrence of clusters of spasms without any other types of seizures before the onset of spasms, and 4) normal laboratory and MR imaging findings at onset. We excluded patients who had epilepsy surgery in infancy. The term "cryptogenic" was replaced by "unknown" by the International League Against Epilepsy Commission on Classification and Terminology in 2010.[13] However, the definition of cryptogenic here includes seizure types and development and unknown etiology. Therefore, we decided to use the term "cryptogenic" in this study.

FDG-PET was performed twice. The first scans were obtained at the onset of spasms before adrenocorticotropic hormone (ACTH) therapy, and the second scans were obtained at 10 months of age. The first scans were obtained at 4–8 months of age except in 2 patients who were diagnosed and scanned at 13 and 28 months of age. The second scans were obtained >1 month after the administration of ACTH therapy to avoid the effect of brain shrinkage by ACTH. In the 2 patients who were diagnosed after 12 months of age, the second scans were obtained 3 months after the initial treatment, at 16 months of age in one patient and at 31 months of age in the other. The scans were obtained as part of the clinical routine to search for underlying pathology. Before the PET scan, we explained to the parents that the results would be used for research, and informed consent was obtained from the parents.

All patients were sedated by chloral hydrate suppository (30–50 mg/kg) during the PET examination. Fifty minutes after intravenous administration of FDG (36–111 MBq), 14 axial images (11-mm thick) were obtained with a Headtome IV scanner (Shimadzu, Kyoto, Japan) with spatial resolution at 6.51-mm intervals parallel to the orbitomeatal line, starting from the orbitomeatal line +0 mm. PET images were analyzed with visual inspection by 3 pediatric neurologists (J.N., N.M., and K.I). All 3 pediatric neurologists were regularly involved in neuroimaging studies and had experience in the interpretation of pediatric PET images. We referred to the PET study in infants by Chugani et al[14] to evaluate the PET findings correctly.

"Regional hypometabolism" was defined as a regional decrease in FDG accumulation in ≥2 gyri on ≥2 sections. Diffuse hypometabolism was considered present when there was a decrease in the entire cerebral cortex compared with accumulation in the basal ganglia. We did not use quantitative methods because measuring absolute glucose metabolic rates with arterial blood sampling during the scan is difficult in infants who are kept still. We also did not use a coregistration method of PET and MR imaging because myelination is not complete in the early infantile

period and we could not apply coregistration programs that use T1-weighted images with completed myelination.

Patients were initially treated by the following protocol: Sodium valproate, clonazepam, or pyridoxine was administered for 1 week. If these agents failed to control the spasms, thyrotropin-releasing hormone was administered intramuscularly for 2 weeks. If thyrotropin-releasing hormone could not control the spasms, ACTH therapy was started. Since 1998, we have excluded thyrotropin-releasing hormone therapy from our protocol because it was found to be less effective than ACTH therapy. In the present study, 5 patients (patients 19–23) did not receive thyrotropin-releasing hormone therapy. In the present study, synthesized ACTH was injected intramuscularly at 0.015 mg/kg/day for 2–4 weeks followed by alternate-day administration for 1 week. The effectiveness of each drug was evaluated on the basis of the frequency and intensity of spasms and the interictal EEG findings.

MRIs were repeated at 10 months of age in all patients and at 2–16 years of age in 17 patients to reveal structural lesions that had not been detected at the onset. We rereviewed the MRIs for subtle structural abnormality if the MRIs were available in 2012.

Evaluation of developmental and seizure outcome was performed between August and December 2012. The age at the evaluation ranged from 13 to 22 years (median, 17 years). The information was obtained from the medical charts at Nagoya University or affiliated hospitals. In cases in which the follow-up was terminated, we interviewed the parents by questionnaire after informed consent was obtained. We determined educational status and intelligence quotient (IQ) or developmental quotient (DQ). The IQ was measured by the Wisconsin Intelligence Scale for Children or the Tanaka-Binet Intelligence Scale, and DQ was measured by the Tsumori-Image Developmental Questionnaire. Developmental status was considered as follows: 1) normal, when patients attended regular classes at a regular school or had an IQ of 70 or greater; 2) mild intellectual disability, when patients attended a special needs class at a regular primary school or had an IQ between 50 to 69; and 3) severe intellectual disability, when patients attended a school for handicapped children during primary school or had an IQ of <50. We also determined from the medical chart whether the patients were diagnosed with autism. Seizure outcome was categorized as follows: 1) free of seizures, when patients had no seizures since 2 years of age, except for simple febrile seizures, and were off antiepileptic medications in 2012; and 2) persistent or recurrent seizures, when patients continued to have epileptic seizures after 2 years of age and were on antiepileptic medications.

The present study was performed continuously from our previous studies.[6-9] We added 9 patients to the previous report by Itomi et al[9] and excluded 3 patients who were out of contact in 2012.

The Fisher exact test was used for statistical analysis of the correlation between hypometabolism at onset or second scans and seizure or developmental outcome. Significance was established at $P < .05$. We calculated positive and negative predictive values of the PET studies.

This study was approved by the research ethics committee of Nagoya University Graduate School of Medicine.
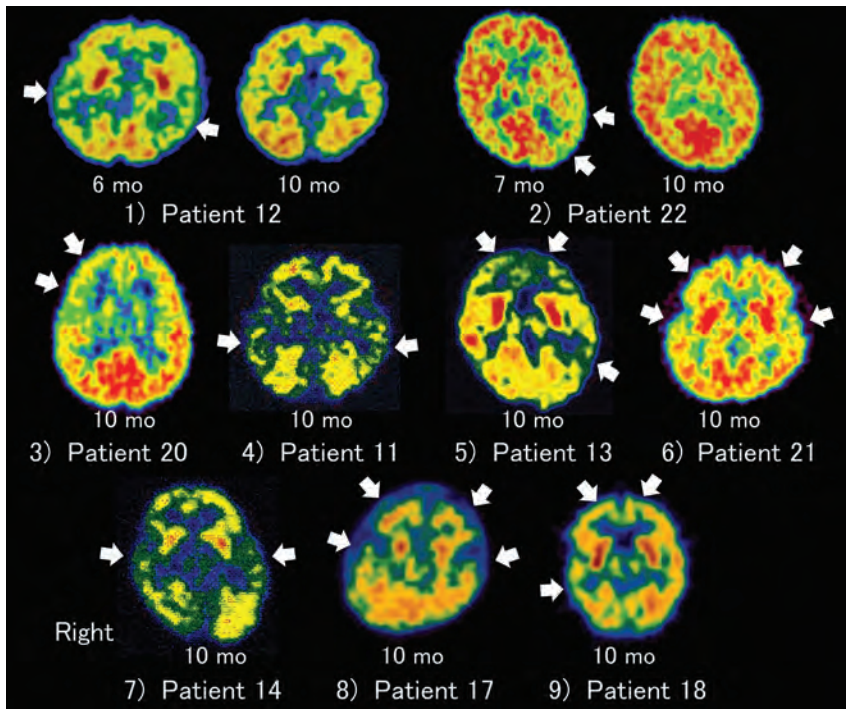
FIG 1. Hypometabolism as seen on the first and second PET scans. 1) Patient 12: PET at 6 months of age reveals bilateral temporal hypometabolism. Hypometabolism is resolved at 10 months of age. The patient is free of seizures without medication and in normal high school at 17 years of age. 2) Patient 22: PET at 7 months of age shows left temporal hypometabolism that is resolved at 10 months of age. The patient is free of seizures without medication and in a normal high school at 13 years of age, though he is diagnosed with Asperger syndrome. 3) Patient 20: PET at 10 months of age shows right frontal hypometabolism. The patient is free of seizures without medication and in a normal high school at 14 years of age. 4) Patient 11: PET at 10 months of age reveals bitemporal hypometabolism. The patient experienced a relapse of spasms at 16 months of age and continues to have partial seizures since 4 years of age and mild intellectual disability. 5) Patient 13: PET at 10 months of age reveals multifocal hypometabolism in the bilateral frontal lobes and right temporal lobe. The patient has severe intellectual impairment. 6) Patient 21: PET at 10 months of age shows bifrontotemporal hypometabolism. The patient has persistent seizures and severe intellectual impairment. 7) Patient 14: PET at 10 months of age reveals bitemporal hypometabolism. The patient is free of seizures except for febrile seizures at 3 years of age and attends normal high school. 8) Patient 17: PET at 10 months of age shows bifrontotemporal hypometabolism. The patient has experienced partial seizures since 10 years of age and has severe intellectual impairment. 9) Patient 18: PET at 10 months of age shows bifrontal and right temporal hypometabolism. The patient has spasms, tonic seizures, atypical absence seizures, and severe intellectual impairment.

RESULTS

Twenty-seven patients with cryptogenic West syndrome underwent serial PET during the study period. In 2012, information could not be obtained from 3 patients who were out of contact. We also excluded 1 patient because MR imaging at 2 years of age revealed focal cortical dysplasia. Therefore, we analyzed 23 patients (11 boys) in whom enough clinical information was available. We rereviewed MRIs of patients for subtle structural abnormalities if the MRIs were available in 2012. In 10 patients, the MRIs were not available in 2012; therefore, prior readings were used. In the other 13 patients, we re-evaluated the MR imaging findings and interpreted them as normal except for diffuse mild atrophy in 1 patient. Our MR imaging protocol in 1991–1999 did not include modern 3D high-resolution images, and there is a possibility that subtle focal cortical dysplasia may have been missed. The results are summarized in the On-line Table. The ages at onset ranged from 3 to 26 months (median, 5 months). ACTH therapy was administered as initial treatment in 21 patients. In the other 2 patients, spasms and hypsarrhythmia disappeared with administration of thyrotropin-releasing hormone or valproate. The time interval from the onset of spasms to initial treatment ranged from 1 to 7 months.

PET Hypometabolism

The initial PET scans demonstrated cortical hypometabolism in 13 of 23 patients. Hypometabolism was bilateral, symmetric, and regional in 7 patients; unilateral regional in 4; and diffuse in 2. The regions of hypometabolism were occipitotemporal or occipital parietal temporal in 3 patients, temporal or temporoparietal in 4 patients (Fig 1), parietal in 2 patients, frontotemporal in 2 patients, and diffuse in 2 patients.

The second PET showed regional hypometabolism in 7 patients. Bilateral temporal or bilateral temporofrontal hypometabolism was seen in 4 patients; unilateral frontal hypometabolism, in 1 patient; and bilateral multifocal hypometabolism, in 2 patients (Fig 1). In 9 of 13 patients with hypometabolism on the first PET, hypometabolism was normalized on the second PET. On the other hand, 3 patients with normal findings on the first scan had hypometabolism on the second PET. Three patients with hypometabolism on the second PET underwent a third PET at 1 year of age, and they still showed cortical hypometabolism. Interictal EEG at the time of the second PET showed epileptiform discharges in 9 patients. All 7 patients with hypometabolism on the second PET had EEG abnormality at the second PET. Two patients with normal second PET findings had EEG abnormalities at the second PET. In 4 of 6 patients with bilateral hypometabolism on the second PET, EEG at 10 months of age showed bilateral abnormality, including hypsarrhythmia or diffuse spike-waves. The other 2 patients (patients 11 and 14) with bitemporal hypometabolism had unilateral temporal spikes at 10 months of age. One patient with right frontal hypometabolism at 10 months of age had bilateral centro-parieto-temporal spikes. The localization of PET hypometabolism and EEG abnormality correlated anatomically, though the distribution of hypometabolism was more widespread in 2 patients and more focal in 1 patient than that of EEG abnormality. Ictal recordings of partial seizures during the follow-up period were not made because the seizures were not frequent. In 4 of 7 patients with hypometabolism on the second PET, MRIs were repeated at 24–36 months of age, and corresponding lesions were not revealed.

Seizure and Developmental Outcome

No patient had any special comorbidity except for epileptic seizures or delayed psychomotor development. After initial treat-

Table 1: Correlations between PET hypometabolism and seizure outcome[a]

	Hypometabolism	Patients with Persistent or Recurrent Seizures	Patients Free of Seizures
1st PET	Normal	4	9
		3	7
2nd PET	Normal	5	2
		2	14

[a] Positive predictive value of second PET was 71%; negative predictive value of second PET, 88%; $P = .01$.

Table 2: Correlations between PET hypometabolism and developmental outcome[a]

	Hypometabolism	Patients with Special Education	Patients in Regular High School
1st PET	Normal	4	9
		4	6
2nd PET	Normal	5	2
		3	13

[a] Positive predictive value of second PET was 71%; negative predictive value of second PET, 81%; $P = .03$.

ment, spasms disappeared in 19 patients, but 4 of the 19 patients had relapse of seizures. One patient with relapse of spasms at 9 months of age received a second round of ACTH therapy and has become free of seizures. At the final follow-up period in 2012, sixteen patients had no seizures since 2 years of age, without antiepileptic medication. The other 7 patients still had spasms, tonic seizures, atypical absences, or partial seizures and were receiving antiepileptic medication. Four of these 7 patients continued to have seizures from infancy. The other 3 patients did not have seizures from infancy, but partial seizures had occurred since 4 or 13 years of age. Regarding education, 16 patients completed their education at a normal primary school. Three patients attended special needs classes in regular primary schools, and 4 patients attended schools for handicapped children. During high school, 15 patients entered regular high schools, and 8 patients entered high schools for handicapped children. In 6 patients who completed their education at regular high schools, 4 attended college and 2 began working in an occupation after high school graduation. Two patients with intellectual disability were diagnosed with autism, and 1 patient with normal intelligence was diagnosed with Asperger syndrome.

In 16 patients, MR images were obtained between 2 and 16 years of age to see if any lesions had been overlooked, but they did not reveal any abnormality except mild atrophy in one patient. MRIs were not re-performed at 2 years of age or later in 7 patients, including 2 patients with severe intellectual disability and persistent seizures in whom sedation was difficult during scans.

Correlation of PET Hypometabolism and Long-Term Outcome

Tables 1 and 2 show correlations between hypometabolism on the first or second PET scans and long-term outcome. In 13 patients with hypometabolism on the initial PET, 4 (31%) had persistent or recurrent seizures during the follow-up period. In 10 patients with normal initial PET findings, 3 (30%) had persistent or relapsing seizures. No correlation was observed between the initial PET results and seizure outcome. Regarding the second PET, 5 of

7 patients with hypometabolism had persistent or recurrent seizures (positive predictive value, 71%). In 16 patients without hypometabolism on the second PET, 14 were free of seizures without medication (negative predictive value, 88%). A significant correlation was seen between the second PET findings and seizure outcome ($P = .01$).

Concerning development and educational statuses, special education in high school was needed for 4 of 13 patients with hypometabolism on the initial PET and 4 of 10 patients with normal findings on the initial PET. No significant correlation was observed between initial PET results and educational status. Regarding the second PET, 5 of 7 patients with hypometabolism had intellectual impairment and required special needs education. All 4 patients who had bilateral frontal hypometabolism with or without temporal hypometabolism on the second PET had the most severe intellectual disability, with an IQ of <20. On the other hand, only 3 of 16 patients with normal second PET findings required special needs education. A significant correlation was seen between the second PET results and educational status ($P = .01$). The positive predictive value of second-PET hypometabolism for poor developmental outcome was 71%, and the negative predictive value was 81%. In 9 patients with EEG abnormality at the time of the second PET, only 2 of 7 patients with a second PET abnormality entered regular high schools, while both of the patients with normal second PET findings entered regular high schools. In patient 22, who had Asperger syndrome, PET showed left temporal hypometabolism at onset (Fig 1). However, the hypometabolism was resolved on the second PET. At 6 years of age, EEG still showed left frontal spikes, but 3T MR imaging and PET did not show any abnormality.

DISCUSSION

We performed serial PET studies from the onset of cryptogenic West syndrome in infancy and studied the correlation between PET findings and long-term outcome in adolescence. The second PET finding after initial treatment was correlated with poor seizure and developmental outcome. On the other hand, long-term outcome was not correlated with the initial PET findings before effective treatment. This is the first report revealing the usefulness of PET performed in infancy to predict long-term outcome during adolescence in patients with cryptogenic West syndrome.

We previously reported serial PET studies in cryptogenic and symptomatic West syndrome.[6-9] In our studies, PET at the onset of spasms showed cortical hypometabolism in two-thirds of patients. However, the hypometabolism was not persistent but resolved in many patients after initial treatment. Persistent cortical hypometabolism after initial treatment was correlated with poor developmental outcome in infancy and early childhood. Other investigators have confirmed these results by using SPECT or PET.[10,11] In all of the previous studies, the follow-up period was limited to a minimum of 2 or 3 years, and educational outcome was not reported. Although gross motor development or simple language development can be evaluated by 2 or 3 years of age, evaluation at this age is not sufficient for higher cognitive functioning or socioeducational status. Dilber et al[12] revealed a correlation between PET findings and autism in patients with West syndrome. However, the age of the study subjects varied from 3 to 16 years; therefore, the investigators could not determine whether

PET in the infantile period is useful for predicting autism or poor psychomotor development. In the evaluation of seizures, though the cessation of spasms can be confirmed by 2 or 3 years of age, focal epilepsy often develops after cessation of spasms; a longer follow-up period is therefore needed to conclusively learn the outcome. The present study has confirmed the usefulness of PET after initial treatment to predict long-term outcome in patients with cryptogenic West syndrome.

A correlation was observed between second PET studies in the infantile period after initial treatment and long-term developmental outcome. Latent cortical dysplasia may cause persistent regional hypometabolism and may result in poor developmental outcome. The second PET showed bitemporal hypometabolism in 4 patients. Three of these patients had autism or severe intellectual impairment. This finding had been earlier reported by Chugani et al[15] as a distinct phenotype characterized by developmental delay and autism. Another 2 patients had multifocal or bilateral hypometabolism, which has also been reported as a major type of PET abnormality in patients with poor outcome.[16] The seventh patient had unifocal frontal hypometabolism, but her seizure and developmental outcome was favorable. Although rare, there may be some patients with focal cortical dysplasia and West syndrome in whom seizures disappear and cognitive function is preserved. The sensitivity of PET in the second scans in our series was much lower than that in the study by Chugani and Conti.[16] Their study focused on patients with intractable spasms, but our study patients were enrolled prospectively from the onset and may have had characteristics similar to those of patients in the general population with cryptogenic West syndrome. On the other hand, the initial PET revealed cortical hypometabolism in more than half of the patients in our study. Most of these findings have resolved, especially in the patients with favorable seizure and developmental outcome. Reversible functional abnormalities caused by abnormal epileptic activities may cause transient cortical hypometabolism in some of these patients. From our observations, PET at the onset is not necessary for all patients, though it is useful for early surgery in patients with poor seizure control.[4] Yet, as in the patient with Asperger syndrome, transient hypometabolism might be related to high-functioning developmental disorders, but the correlation with them remains to be clarified.

Indeed, the correlation between PET findings and seizure outcome was not conclusive in previous studies. While our previous report on patients with cryptogenic and symptomatic West syndrome in 1994 showed a significant correlation between the results of the second scan and seizure outcome,[7] another of our reports in 2002, which focused on cryptogenic patients, did not show any correlation between PET and seizure outcome.[9] The ages of the study patients in the follow-up period of our 1994 report ranged from 19 to 47 months, and the ages of the study patients in the follow-up period in our 2002 report ranged from 3 to 8 years. The difference in the follow-up periods may have been responsible for the dissimilar results. Another possible reason for the varying results among the different studies is whether symptomatic patients were included. Metsähonkala et al[10] studied PET hypometabolism in cryptogenic or symptomatic patients and concluded that PET did not have prognostic value for seizure outcome. In the present study with a longer follow-up in crypto-genic patients, we found a significant correlation between PET findings in infancy and seizure outcome. However, seizure outcomes were not predicted from the second PET findings in some patients. One patient with normal findings on the first and second PET scans developed partial seizures at 13 years of age after a seizure-free period of >10 years. The condition of epileptic networks could change variably with maturation, and the onset of partial seizures at older ages cannot be ruled out from the PET findings in the infantile period.

Factors associated with good prognosis in West syndrome have been determined in many studies.[1-3,17,18] Reported favorable factors are cryptogenic etiology, age at onset older than 4 months, no or mild mental deterioration at presentation, short treatment lag, good response to ACTH therapy, no reappearance of paroxysmal discharges on EEG, and no other types of seizures. Treatment lag has been especially emphasized because prognosis is possibly improved by prompt diagnosis and early treatment. In view of our previous study about hypometabolism and delayed myelination on MR imaging, persistent cortical hypometabolism may result in the delay of cerebral maturation and impaired cognitive function.[8] Early treatment of functional abnormalities may improve the long-term developmental outcome. In the present study, 4 patients had a treatment lag of 3 months or longer, and the developmental outcome was poor in all 4 of these patients. A patient with a treatment lag of 7 months had diffuse hypometabolism at the first PET scan. Long-lasting electrographic abnormalities of hypsarrhythmia may cause widespread cerebral glucose hypometabolism and developmental delay, even with normalized metabolism, as seen at the second scan in this patient. PET at the time of initial treatment might add information about the adverse effects of a long treatment lag.

Although the response of seizures and EEG findings to initial treatments are also good markers for predicting outcome, patients 22 and 23, who had persistent EEG abnormalities after treatment, showed good seizure responses and outcomes. PET findings at 10 months were normal in these patients, and this outcome may give additional useful information for predicting long-term prognosis. Response to ACTH therapy is also a factor for favorable outcome. However, 3 patients in our study initially responded to ACTH but had a relapse of seizures and intellectual disability. One of the 3 patients with a relapse of seizures had bitemporal hypometabolism at 10 and 20 months of age, and the PET finding may suggest poor long-term outcome.

Other factors may affect educational and developmental outcomes. Concerning the duration of the follow-up period, educational and developmental outcomes did not have significant correlation with the duration of the follow-up period, though 8 patients with developmental delay tended to have a shorter follow-up period (mean, 16.6 ± 2.1 years) than patients with normal development (mean, 17.5 ± 3.0 years). Treatment protocol had not changed largely except for the exclusion of thyrotropin-releasing hormone therapy from 1998, and the change of the treatment protocol did not seem to affect the long-term outcome.

CONCLUSIONS

The evaluation of hypometabolism as seen on PET during the infantile period is useful for predicting long-term seizure and de-

velopmental outcome in patients with cryptogenic West syndrome. We suggest that PET should be performed at 10–12 months of age for early detection of underlying abnormality and prediction of long-term outcome. The hypometabolism seen at the onset often resolves; persistent hypometabolism after initial treatment is related to poor long-term outcome.

REFERENCES
1. Riikonen R. **Long-term outcome of patients with West syndrome.** *Brain Dev* 2001;23:683–87
2. Kivity S, Lerman P, Ariel R, et al. **Long-term cognitive outcomes of a cohort of children with cryptogenic infantile spasms treated with high-dose adrenocorticotropic hormone.** *Epilepsia* 2004;45:255–62
3. Hamano S, Yoshinari S, Higurashi N, et al. **Developmental outcomes of cryptogenic West syndrome.** *J Pediatr* 2007;150:295–99
4. Chugani HT, Shields WD, Shewmon DA, et al. **Infantile spasms: I. PET identifies focal cortical dysgenesis in cryptogenic cases for surgical treatment.** *Ann Neurol* 1990;27:406–13
5. Chugani HT, Shewmon DA, Sankar R, et al. **Infantile spasms: II. Lenticular nuclei and brain stem activation on positron emission tomography.** *Ann Neurol* 1992;31:212–19
6. Maeda N, Watanabe K, Negoro T, et al. **Transient focal cortical hypometabolism in idiopathic West syndrome.** *Pediatr Neurol* 1993;9:430–34
7. Maeda N, Watanabe K, Negoro T, et al. **Evolutional changes of cortical hypometabolism in West's syndrome.** *Lancet* 1994;343:1620–23
8. Natsume J, Watanabe K, Maeda N, et al. **Cortical hypometabolism and delayed myelination in West syndrome.** *Epilepsia* 1996;37:1180–84
9. Itomi K, Okumura A, Negoro T, et al. **Prognostic value of positron emission tomography in cryptogenic West syndrome.** *Dev Med Child Neurol* 2002;44:107–11
10. Metsähonkala L, Gaily E, Rantala H, et al. **Focal and global cortical hypometabolism in patients with newly diagnosed infantile spasms.** *Neurology* 2002;58:1646–51
11. Hamano S, Yoshinari S, Higurashi N, et al. **Regional cerebral blood flow and developmental outcome in cryptogenic West syndrome.** *Epilepsia* 2007;48:114–19
12. Dilber C, Calişkan M, Sönmezoğlu K, et al. **Positron emission tomography findings in children with infantile spasms and autism.** *J Clin Neurosci* 2013;20:373–76
13. Berg AT, Berkovic SF, Brodie MJ, et al. **Revised terminology and concepts for organization of seizures and epilepsies: report of the ILAE Commission on Classification and Terminology, 2005–2009.** *Epilepsia* 2010;51:676–85
14. Chugani HT, Phelps ME, Mazziotta JC. **Positron emission tomography study of human brain functional development.** *Ann Neurol* 1987;22:487–97
15. Chugani HT, Da Silva E, Chugani DC. **Infantile spasms: III. Prognostic implications of bitemporal hypometabolism on positron emission tomography.** *Ann Neurol* 1996;39:643–49
16. Chugani HT, Conti JR. **Etiologic classification of infantile spasms in 140 cases: role of positron emission tomography.** *J Child Neurol* 1996;11:44–48
17. Riikonen RS. **Favourable prognostic factors with infantile spasms.** *Eur J Paediatr Neurol* 2010;14:13–18
18. O'Callaghan FJ, Lux AL, Darke K, et al. **The effect of lead time to treatment and of age of onset on developmental outcome at 4 years in infantile spasms: evidence from the United Kingdom Infantile Spasms Study.** *Epilepsia* 2011;52:1359–64

Midbrain-Hindbrain Involvement in Septo-Optic Dysplasia

M. Severino, A.E.M. Allegri, A. Pistorio, B. Roviglione, N. Di Iorgi, M. Maghnie, and A. Rossi

ABSTRACT

BACKGROUND AND PURPOSE: Midbrain-hindbrain involvement in septo-optic dysplasia has not been well described, despite reported mutations of genes regulating brain stem patterning. We aimed to describe midbrain-hindbrain involvement in patients with septo-optic dysplasia and to identify possible clinical-neuroimaging correlations.

MATERIALS AND METHODS: Using MR imaging, we categorized 38 patients (21 males) based on the presence (group A, 21 patients) or absence (group B, 17 patients) of visible brain stem anomalies. We measured height and anteroposterior diameter of midbrain, pons, and medulla, anteroposterior midbrain/pons diameter (M/P ratio), vermian height, and tegmento-vermian angle, and compared the results with 114 healthy age-matched controls. Furthermore, patients were subdivided based on the type of midline anomalies. The associations between clinical and neuroradiological features were investigated. Post hoc tests were corrected according to Bonferroni adjustment (p_B).

RESULTS: Patients with brain stem abnormalities had smaller anteroposterior pons diameter than controls ($p_B < .0001$) and group B ($p_B = .012$), higher M/P ratio than controls ($p_B < .0001$) and group B ($p_B < .0001$), and smaller anteroposterior medulla diameter ($p_B = .001$), pontine height ($p_B = .00072$), and vermian height ($p_B = .0009$) than controls. Six of 21 patients in group A had thickened quadrigeminal plate, aqueductal stenosis, and hydrocephalus; 3 also had agenesis of the epithalamus. One patient had a short midbrain with long pons and large superior vermis. There was a statistically significant association between brain stem abnormalities and callosal dysgenesis ($P = .011$) and developmental delay ($P = .035$), respectively.

CONCLUSION: Midbrain-hindbrain abnormalities are a significant, albeit underrecognized, component of the septo-optic dysplasia spectrum, and are significantly associated with developmental delay in affected patients.

ABBREVIATIONS: AP = anteroposterior; MH = midbrain-hindbrain; SOD = septo-optic dysplasia

Septo-optic dysplasia (SOD) is a highly heterogeneous, usually sporadic condition with a multifactorial etiology. Currently, genetic abnormalities are identified only in 1% of patients, whereas the etiology remains unclear in most.[1] However, an increasing number of early developmental transcription factors and associated pathway genes have been implicated in the etiology of SOD, ie, *HESX1, SOX2, SOX3, OTX2, PROKR2, FGF1*, and

FGF8.[2-4] These genes are expressed in regions that determine the formation of forebrain and related midline structures, such as the hypothalamus and pituitary gland, and mutations in these genes are therefore associated with marked phenotypic heterogeneity. Classically, the diagnosis of SOD is made when 2 or more features of the classic triad of optic nerve hypoplasia, pituitary hormone abnormalities, and midline brain defects are present.[1] However, only one-third of patients present with all cardinal features of SOD.[3] Visual deficits due to optic nerve hypoplasia and ocular malformations are usually the first presenting sign, whereas endocrine dysfunction may become apparent later on.[1] The severity of pituitary-hypothalamic dysfunction is highly variable, ranging from isolated deficit of pituitary hormones to panhypopituitarism.[3] Neurologic deficits are common, and range from global retardation to focal deficits such as epilepsy or hemiparesis.[5]

Interestingly, *OTX2* and *FGF8* are also pivotal genes regulating brain stem patterning during early embryologic development.[6-9] In recent years, there has been a growing interest in the descrip-
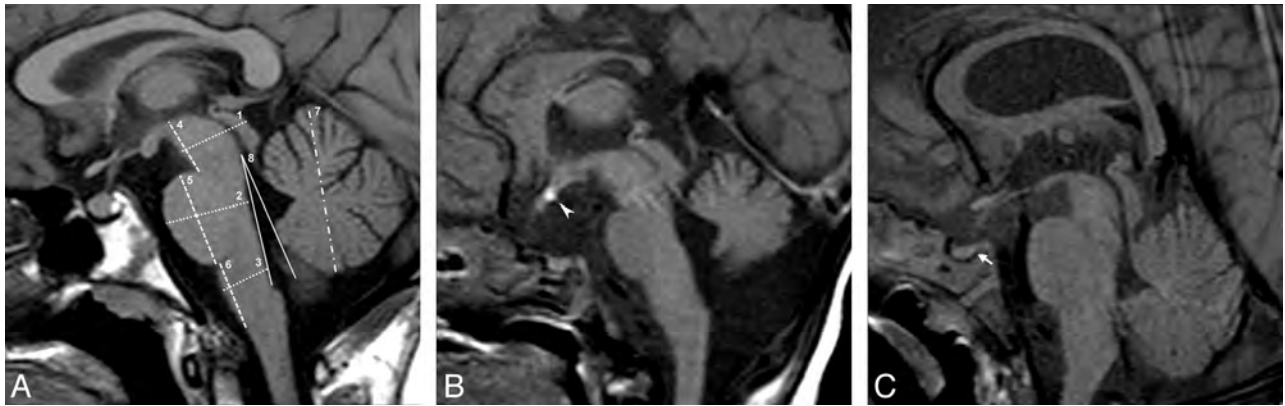
FIG 1. *A*, Midsagittal T1-weighted image in a healthy child demonstrates how the measurements were performed: dotted lines indicate the AP diameter of the midbrain (1), pons (2), and medulla (3), dashed lines indicate the height of the midbrain (4), pons (5), and medulla (6), dash-dot line indicates the height of the vermis (7), and solid lines indicates the tegmento-vermian angle (8). *B*, Midsagittal T1-weighted image in a patient with SOD with visible brain stem abnormalities (group A) reveals hypoplasia of the pons and cerebellar vermis. Note the hypoplasia of the pituitary gland with ectopic posterior lobe (*arrowhead*) and associated small corpus callosum. *C*, Midsagittal T1-weighted image in a patient with SOD without visible brain stem abnormalities (group B) reveals grossly normal brain stem and vermis. Note the absence of the normal posterior pituitary bright spot (*arrow*).

tion of congenital brain stem abnormalities. However, midbrain-hindbrain (MH) involvement in SOD has not been described so far. Here, we aimed to describe midbrain abnormalities and to identify possible correlations with clinical features in a relatively large group of patients with SOD.

METHODS
Subjects
This was a single-center retrospective case-control study. We reviewed the MR studies of 38 children who were diagnosed with SOD between 2006 and 2012 (21 males, mean age 61.8 ± 60.7 months, and age range from 2 days to 18.3 years at the time of scan). The study received institutional review board approval. Exclusion criteria were uncertain SOD diagnosis and poor-quality or incomplete images. Complete neurologic evaluation was available in 32 of 38 patients. Griffiths Mental Development and Binet-Simon scales were used to define the developmental delay. Karyotype was performed in all patients. One patient harbored a mosaicism of trisomy chromosome 8 in skin fibroblast karyotypes, whereas the remainder presented normal karyotype. Comparative genomic hybridization by microarray was performed in 12 out of 38 patients, revealing de novo chromosomal aberrations in 2 cases: 1 duplication at 16p13.3p13.13 and 1 deletion at 14q22.1q23.1.

We selected 114 age-and sex-matched healthy children as a control group, ie, 3 controls for every patient with SOD. Controls underwent brain MR imaging for transient febrile convulsion or headaches. All were diagnosed as neurologically and developmentally normal by pediatric neurologists and had normal MR imaging findings.

Imaging Analysis
All MR imaging examinations were performed on a 1.5 T magnet (Intera Achieva 2.6; Philips, Best, the Netherlands). Children under 6 years of age or uncooperative patients were sedated during examinations. All MR imaging studies included 3-mm-thick sagittal spin-echo T1-weighted images, axial and coronal FSE T2-weighted images, axial FLAIR images, and axial DWI. Additional sequences performed in patients with SOD included axial and

sagittal 0.6-mm-thick 3D driven equilibrium sequences, sagittal FSE T2-weighted images, and 3D turbo-field-echo T1-weighted images.

Patients with SOD were subjectively categorized based on the presence (group A, 21 patients) or absence (group B, 17 patients) of visible brain stem anomalies. Systematic visual analysis included midbrain dorsoventral and rostrocaudal size, tectal thickness, and collicular morphology, as well as dorsoventral and rostrocaudal size of the pons and medulla oblongata, and vermian size. We then measured the height and anteroposterior (AP) diameter of midbrain, pons, and medulla, the vermian height, and the tegmento-vermian angle (Fig 1*A*). All measurements were performed by one pediatric neuroradiologist (M.S.) on midline sagittal T1-weighted images. We calculated the ratio of AP midbrain diameter to AP pons diameter (M/P ratio). We then compared the measurements and the M/P ratios of patients with SOD versus the controls.

Patients with SOD were also subdivided based on the presence and type of midline anomalies into 3 subtypes: group I (septal agenesis, 23 patients; complete in 13 cases and partial in 10 cases); group II (abnormal corpus callosum, 7 patients); and group III (no midline brain defects, 8 patients). Then, we investigated the association between brain stem and midline abnormalities.

Images were also analyzed for abnormalities involving the eyes, optic nerves, pituitary gland, olfactory bulbs, hypothalamus and hippocampi, as well as for cortical malformations including polymicrogyria, periventricular nodular heterotopia, and schizencephaly. Optic nerve hypoplasia was evaluated on coronal T2-weighted images at the level of the intraorbital segment, and was defined as an optic nerve caliber below 2 mm. Finally, we studied the association between brain stem abnormalities and the presence or absence of pituitary gland abnormalities, hippocampal malrotation, cortical malformations, developmental delay (irrespective of the degree of cognitive impairment), and epilepsy.

Statistics
Descriptive statistics were firstly performed: categoric variables were reported in terms of absolute frequencies and percentages;
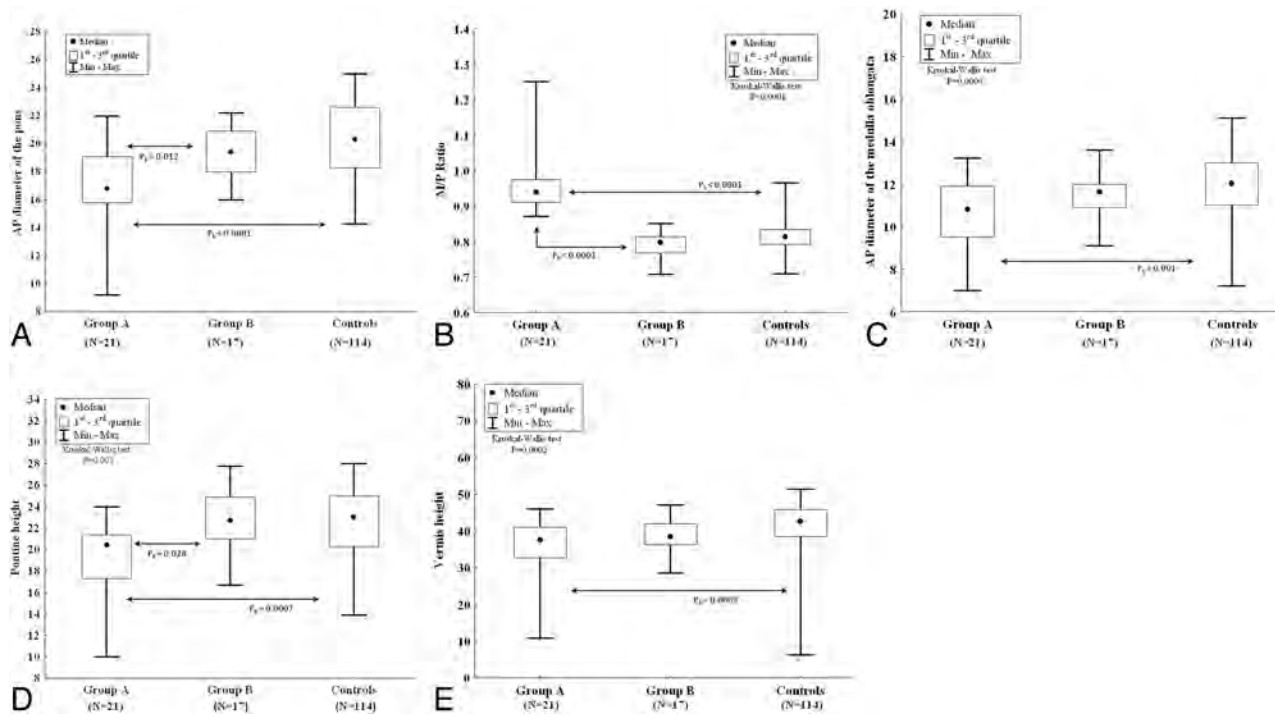
FIG 2. Boxplots of MH measurements in patients with SOD (group A and B) and healthy controls. AP diameter of the pons (*A*) and medulla (*B*), midbrain to pons ratio (*C*), height of the pons (*D*), and vermis (*E*) are shown.

quantitative variables were reported in terms of median values with 1st–3rd quartiles. Differences between groups were evaluated by means of the nonparametric ANOVA (Kruskal-Wallis test) and post hoc tests were corrected according to Bonferroni adjustment (p_B). The association between categoric variables was evaluated by χ^2 test, or by the Fisher exact test in case of expected frequencies $<$ 5. All tests were 2-sided and a *P* value less than .05 was considered as statistically significant. Data were analyzed by means of the statistical software Statistica 9 (StatSoft Corporation, Tulsa, Oklahoma) and STATA 7 (StataCorp, College Station, Texas).

RESULTS
Clinical and neuroradiologic characteristics of patients with SOD are described in On-line Table 1. The AP pontine diameter in patients with SOD with brain stem abnormalities (group A, Fig. 1*B*) was significantly smaller (median: 16.8 mm; 1st–3rd quartiles: 15.8–19.1) than in the control group (median: 19.4 mm; 1st–3rd quartiles: 17.8–22.2, $p_B <$ .0001) and in patients with SOD with normal-appearing brain stem (group B, Fig 1*C*) (median: 19.4 mm; 1st–3rd quartiles: 18.0–20.9, $p_B =$ .012) (Fig 2A). No significant statistical difference was found in the AP diameter of midbrain between patients with SOD (both group A and B) and healthy controls. As a consequence, the M/P ratio was higher in patients with SOD with visible brain stem abnormalities (group A, median: 0.94; 1st–3rd quartiles: 0.91–0.97) compared with controls (median: 0.81; 1st–3rd quartiles: 0.79–0.84, $p_B <$ .0001) and to group B (median: 0.80; 1st–3rd quartiles: 0.77–0.81, $p_B <$ .0001) (Fig 2*B*).

The AP diameter of the medulla in patients with SOD with brain stem abnormalities (group A) was significantly smaller (median: 10.8 mm; 1st–3rd quartiles: 9.5–11.9) (Fig. 1*B*) than in the

control group (median 11.8 mm; 1st–3rd quartiles: 10.6–13, $p_B =$ .001) (Fig 2*C*).

The height of the pons (median: 20.4 mm; 1st–3rd quartiles: 17.3–21.4) and of the vermis (median: 37.4 mm; 1st–3rd quartiles: 32.7–41.0) was significantly shorter in patients with SOD with visible brain stem abnormalities (group A) than in controls (median: 22.0 mm; 1st–3rd quartiles: 19.3–25.0, $p_B =$ .0007 and median: 41.4 mm; 1st–3rd quartiles: 36.3–45.0, $p_B =$ .0009, respectively) (Fig 2*D*, -*E*).

In patients of group A, the AP diameter of the pons and medulla and the pontine and vermian height were lower compared with the values observed in control subjects of the same age category (Fig 3); in patients of group B, pontine and vermis height values tended to be lower compared with the values of control subjects of the same age category but these differences did not reach statistical significance.

No significant statistical difference was found regarding the tegmento-vermian angle and height of midbrain and medulla between patients with SOD (both group A and B) and controls. There were no patients with isolated vermis anomalies.

Six of 21 patients (28.6%) with brain stem abnormalities (group A) showed thickening of the quadrigeminal plate with aqueductal stenosis and triventricular hydrocephalus (Fig 4*A*); 3 also had agenesis of the epithalamus (Fig 4*B*, -*C*).

Callosal dysgenesis was present in 7 patients with SOD (group II) with complete agenesis in 3 cases and partial agenesis in 4 cases. Brain stem abnormalities were more frequent in patients with callosal dysgenesis (7/21, 33.3%) compared with those without visible brain stem abnormalities (0/17, 0%) (*P* = .011, On-line Table 2).

Finally, in 1 patient harboring 14q22.1-q23.1 deletion the
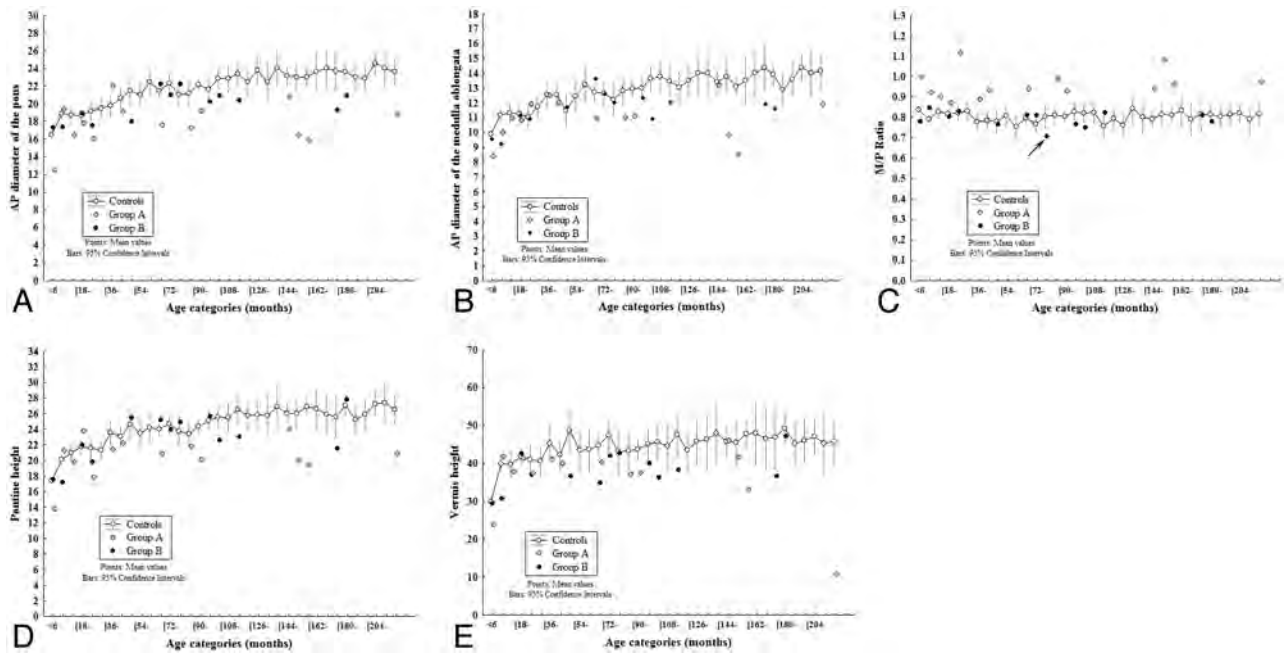
FIG 3. Scatterplots of MH measurements for age categories in patients with SOD and healthy controls. AP diameter of the pons (*A*) and medulla (*B*), midbrain to pons ratio (*C*), height of the pons (*D*), and vermis (*E*) are shown. In healthy controls, the AP diameters and height of brain stem structures and vermis showed an exponential growth curve. The growth spurt was steep until 16 months of age. Thereafter, it became less steep, reaching the adult level at about 8 years of age. On the other hand, the M/P ratios remained stable in controls over time, with a mean value of 0.82. In patients of group A, the AP diameter of the pons and medulla and the pontine and vermian height were lower compared with the values observed in control subjects of the same age category; in patients of group B, pontine and vermis height values tended to be lower compared with the values of control subjects of the same age category but these differences did not reach statistical significance. *C*, Note the lower M/P ratio in the patient harboring the 14q22.1-q23.1 deletion (*arrow*) compared with the corresponding values in age-matched controls.
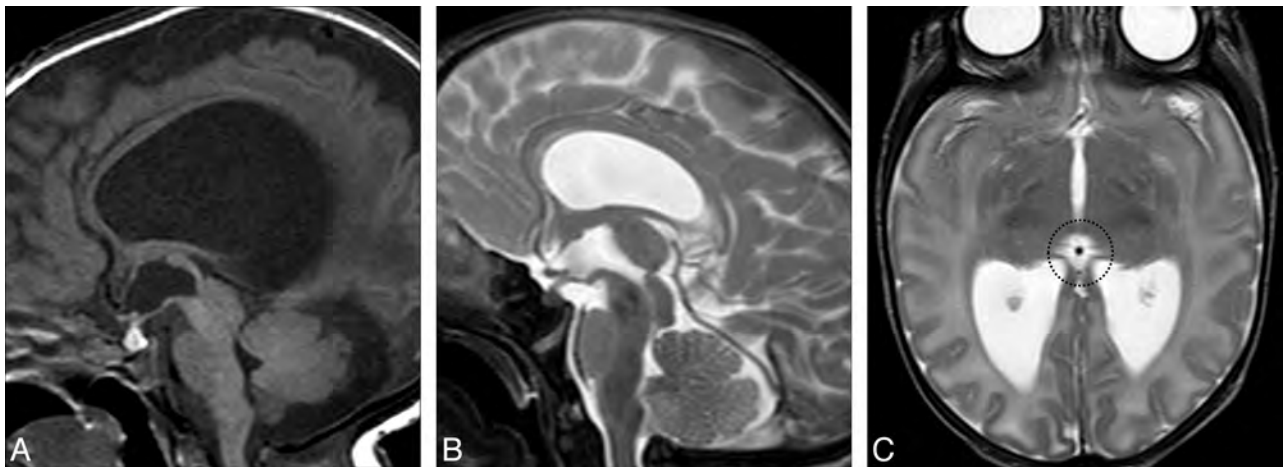
FIG 4. *A*, Midline sagittal T1-weighted image demonstrates hypoplasia of the pons and small vermis, and enlarged quadrigeminal plate with secondary aqueductal stenosis and triventricular hydrocephalus. Midline sagittal (*B*) and axial (*C*) T2-weighted images in another patient reveal agenesis of the epithalamus including agenesis of the pineal gland (dotted circle), stria medullaris, and posterior commissure.

midbrain was smaller (height 11 mm and AP diameter 13.8 mm versus 13.5–16.2 mm and 16.6–17.2 mm minimal-maximal values of age-matched controls, respectively) compared with the pons, which appeared slightly elongated (pons height 25.4 mm versus 23.2–25.3 mm minimal-maximal values of age-matched controls) (Fig 5). The M/P ratio in this patient was lower (0.76) compared with the corresponding minimal-maximal values in age-matched controls (0.78–0.81) (Fig 3*C*).

Twenty-six of 38 patients presented with pituitary hypoplasia (68.4%) with additional ectopic posterior pituitary lobe in 7 cases and absent posterior bright spot in 2 cases. Hypothalamic hamar-

tomas were additionally present in 2 cases, whereas hypothalamic dysgenesis was evident in 3 other patients. Twenty-seven of 38 patients presented with optic nerve hypoplasia (71%) with microphthalmia in 3 cases and colobomas in 4 cases. Septal agenesis and optic nerve hypoplasia without any pituitary abnormality were present in 10 patients. Seventeen patients presented with hippocampal malrotation (44.7%) whereas 14 patients presented with a cortical malformation (36.8%). In particular, unilateral or bilateral polymicrogyria was present in 8 patients whereas 2 patients presented with an abnormal cortical gyration pattern. Periventricular nodular heterotopias were evident in 6 patients. Only 1 patient

FIG 5. Midsagittal T1-weighted image of the patient harboring the 14q22.1-q23.1 deletion shows a small and short midbrain with elongated pons and relatively larger superior portion of the cerebellar vermis. Note the small anterior pituitary gland with ectopic posterior lobe along the pituitary stalk (*arrowhead*).

had a unilateral schizencephaly. The association between these neuroradiologic abnormalities and brain stem malformation are summarized in On-line Table 3. We found a statistically significant association between pituitary and brain stem anomalies ($P = .002$, χ^2). Seventeen of 32 patients (53.1%) were developmentally delayed; 5 of 32 patients (15.6%) had epilepsy. We found a statistically significant association between brain stem abnormalities and developmental delay ($P = .035$; χ^2).

DISCUSSION

The wide spectrum of imaging findings in SOD includes variable combinations of abnormalities of midline brain structures, the pituitary gland, optic nerves and eyes, olfactory bulbs, and other brain structures.[10] Midline brain defects classically consist of complete or partial absence of the septum pellucidum with fused midline fornices (60% of cases) and/or corpus callosum abnormalities, such as agenesis, dysplasia, or hypoplasia.[1,10,11] Pituitary gland malformations include anterior pituitary hypoplasia, ectopic posterior lobe, and/or thin or interrupted pituitary stalk.[3] Optic nerve hypoplasia is frequently associated with ocular anomalies such as coloboma, anophthalmia, and microphthalmia.[12] The olfactory bulbs may be absent or hypoplastic.[13] Other common associations include schizencephaly (so-called SOD-plus), gray matter heterotopia, polymicrogyria, and hippocampal malformations.[14-16]

MH abnormalities have not been described in patients with SOD to the best of our knowledge. Qualitative assessment of MH structures in the present study revealed abnormalities in 55% of patients, especially in the corpus callosum agenesis subgroup and in patients with pituitary gland abnormalities. Careful measurement and comparison of the height and AP diameter of midbrain, pons, medulla, and vermian height in patients with SOD versus healthy controls confirmed the visual analysis. Hypoplasia of the

pons was the major finding, leading to a significantly higher midbrain to pons ratio compared with controls. Moreover, hypoplasia of the vermis and medulla was also associated, resulting in a globally small hindbrain. The term "hypoplasia" refers to a condition of incomplete or arrested development in which an organ or part of it remains below the normal size. Generalized or segmental brain stem hypoplasia may be an isolated malformative feature or part of a more complex MH malformation, such as pontocerebellar hypoplasia,[17] horizontal gaze palsy with progressive scoliosis,[18] pontine tegmental cap dysplasia,[19] and anteroposterior or dorsoventral MH patterning defects.[20,21] More frequently, brain stem hypoplasia is identified in patients with cerebral malformations such as congenital muscular dystrophies,[22] lissencephalies,[23] or cerebral commissural anomalies.[20] As previously described in other MH malformations,[24] we found that cognitive impairment or developmental delay was more frequent in patients with SOD with small hindbrain, worsening the prognosis and impairing rehabilitative strategies.

Recently, mutations in *OTX2* and *FGF8* genes have been described in patients with SOD.[2-4] Interestingly, *OTX2* and *FGF8* play an important role both in the development of the anterior forebrain[25] and in the differentiation along the anteroposterior axis of the neural tube, with formation of the primary and secondary brain vesicles.[26] The latter process determines the correct regionalization of the forebrain (which rapidly divides into telencephalon and diencephalon), mesencephalon (midbrain), and hindbrain (which further divides into the rostral metencephalon, ie, pons and cerebellum, and caudal myelencephalon, ie, medulla oblongata). This delicate embryologic process requires the orderly expression and interaction of several signaling molecules and the formation of patterning centers such as the isthmus organizer at the MH junction.[27] In particular, Otx2 is expressed in the midbrain both in mice[28] and humans,[29] whereas Gbx2 is expressed in the anterior hindbrain, with a shared border at the level of IsO.[30] In rodent fetuses, the formation and normal location of IsO depends on a delicate interplay between the expression of Otx2, Gbx2,[6,7] and Fgf8.[30] Animal models have shown that repression of Otx2 expression induces Gbx2 formation to establish the location of the MH junction rostrally, resulting in a short midbrain and long pons. On the other hand, overexpression of Otx2 shifts the MH junction caudally, resulting in an elongated midbrain with a small pons and vermis.[27] Similarly, alterations of Pax6 or En1/Pax2 will change the location of the diencephalic-mesencephalic junction.[27]

Remarkably, 6 patients with SOD spectrum and hypoplasia of hindbrain structures also showed hypertrophy of the mesencephalic tectum with consequent aqueductal stenosis and triventricular hydrocephalus. Broccoli et al[6] assessed the effect of ectopic expression of Otx2 on MH development in mutant mice, and noticed that the superior and inferior colliculi appeared enlarged and were shifted posteriorly in all analyzed mutants. Furthermore, 3 patients also showed evidence of agenesis of the epithalamus (ie, stria medullaris, habenular trigone, pineal gland, and posterior commissure). Larsen et al[29] recently demonstrated that Otx2 is expressed in the pineal gland at later stages in human fetuses. Gene ablation experiments in mice revealed that Otx2 is a key regulatory gene for the development of the pineal gland.[31]

Furthermore, agenesis of the pineal gland has been described in patients with mutations of *PAX6* gene and congenital aniridia.[32,33] Intriguingly, *PAX6* is another important gene involved in the AP patterning of the brain. In particular, in murine and chick models, the correct formation of the diencephalic-mesencephalic junction depends on the interaction of Pax6 from the diencephalon and En1/Pax2 from the rostral mesencephalon, with the contributing role of FGf8 that induces forebrain cells to secrete Pax6.[27] Webb et al[34] recently studied the 24-hour melatonin profiles in 6 patients with SOD and sleep disorders. Interestingly, 2 children appeared to produce virtually no melatonin throughout the 24-hour period of measurement. These findings raise the suspicion of a possible correlation between pineal gland agenesis and abnormally reduced melanin production in patients with SOD, which awaits confirmation in prospective studies.

Finally, 1 patient in this study harboring a de novo deletion at 14q22.1–23.1 presented with a short, small midbrain with elongated pons and enlarged superior cerebellar vermis, suggesting an abnormality of MH anteroposterior patterning due to rostral misplacement of the IsO.[20-21] This patient also had right anophthalmia and left colobomatous microphthalmia, small corpus callosum, bilateral hippocampal malformation, and hypoplasia of the anterior pituitary lobe with an ectopic posterior lobe. Interestingly, the 14q22.1–23.1 deletion includes the Otx2 gene, supporting the hypothesis that loss of Otx2 expression may determine rostral misplacement of the IsO also in humans. *OTX2* heterozygous mutations or deletions in humans have been linked to severe ocular malformations associated with forebrain abnormalities such as hippocampal and callosal malformations, and combined or multiple pituitary hormone deficiencies.[12] However, no careful description of MH structures has been provided so far in these patients. We reviewed the available brain MR midline sagittal images including the posterior cranial fossa of previously reported patients with Otx2 mutations[35-38] or chromosome 14 deletions including Otx2,[39-43] and we recognized a similar midbrain hypoplasia with a long pons and large superior vermis in 5 patients.[35,36,40,41,43] We therefore suggest that MH abnormalities may have been underestimated in patients with Otx2 mutations or deletion; further studies on larger series are awaited to address this hypothesis.

This study has several limitations, mainly including its retrospective design, the relatively small sample size, and the incomplete genetic assessment. Furthermore, the functional role and clinical implications of MH abnormalities in patients with SOD remain uncertain, and require further prospective studies.

CONCLUSION

MH abnormalities are a significant, albeit under-recognized, component of the SOD spectrum. We demonstrated that the pons, medulla, and vermis were significantly hypoplastic in more than 50% of patients with SOD. Additional features included midbrain tectum enlargement and agenesis of the epithalamus. Patients with these abnormalities were more likely to present with developmental delay. Interestingly, these anomalies are similar to those reported in mutant mice with caudal shift of the MH junction due to ectopic Otx2 expression

or Fgf8 mutations. Conversely, a short midbrain with an elongated pons and large superior vermis was observed in one SOD patient with 14q22.1–23.1 deletion, supporting the hypothesis that deletion of the Otx2 gene may determine a rostral shift of the MH also in humans.

REFERENCES

1. Webb EA, Dattani MT. **Septo-optic dysplasia.** *Eur J Hum Genet* 2010;18:393–97
2. McCabe MJ, Gaston-Massuet C, Tziaferi V, et al. **Novel FGF8 mutations associated with recessive holoprosencephaly, craniofacial defects, and hypothalamo-pituitary dysfunction.** *J Clin Endocrinol Metab* 2011;96:1709–18
3. McCabe MJ, Alatzoglou KS, Dattani MT. **Septo-optic dysplasia and other midline defects: the role of transcription factors: HESX1 and beyond.** *Best Pract Res Clin Endocrinol Metab* 2011;25:115–24
4. Raivio T, Avbelj M, McCabe MJ, et al. **Genetic overlap in Kallmann syndrome, combined pituitary hormone deficiency, and septo-optic dysplasia.** *J Clin Endocrinol Metab* 2012;97:694–99
5. Signorini SG, Decio A, Fedeli C, et al. **Septo-optic dysplasia in childhood: the neurological, cognitive and neuro-ophthalmological perspective.** *Dev Med Child Neurol* 2012;54:1018–24
6. Broccoli V, Boncinelli E, Wurst W. **The caudal limit of Otx2 expression positions the isthmic organizer.** *Nature* 1999;401:164–68
7. Millet S, Campbell K, Epstein DJ, et al. **A role for Gbx2 in repression of Otx2 and positioning the mid/hindbrain organizer.** *Nature* 1999;401:161–64
8. Sato T, Joyner AL. **The duration of Fgf8 isthmic organizer expression is key to patterning different tectal-isthmo-cerebellum structures.** *Development* 2009;136:3617–26
9. Beby F, Lamonerie T. **The homeobox gene Otx2 in development and disease.** *Exp Eye Res* 2013;111:9–16
10. Severino M. **Septo-optic dysplasia.** In: Rumboldt Z, Castillo M, Huang B, Rossi A, eds. *Brain Imaging With MRI and CT: An Image Pattern Approach.* New York: Cambridge University Press; 2012:146–47
11. Belhocine O, André C, Kalifa G, et al. **Does asymptomatic septal agenesis exist? A review of 34 cases.** *Pediatr Radiol* 2005;35:410–18
12. Ragge NK, Brown AG, Poloschek CM, et al. **Heterozygous mutations of OTX2 cause severe ocular malformations.** *Am J Hum Genet* 2005;76:1008–22
13. Levine LM, Bhatti MT, Mancuso AA. **Septo-optic dysplasia with olfactory tract and bulb hypoplasia.** *Journal of AAPOS* 2001;5:398–99
14. Barkovich AJ, Fram EK, Norman D. **Septo-optic dysplasia: MR imaging.** *Radiology* 1989;171:189–92
15. Miller SP, Shevell MI, Patenaude Y, et al. **Septo-optic dysplasia plus: a spectrum of malformations of cortical development.** *Neurology* 2000;54:1701–03
16. Riedl S, Vosahlo J, Battelino T, et al. **Refining clinical phenotypes in septo-optic dysplasia based on MRI findings.** *Eur J Pediatr* 2008;167:1269–76
17. Namavar Y, Barth PG, Poll-The BT, et al. **Classification, diagnosis and potential mechanisms in pontocerebellar hypoplasia.** *Orphanet J Rare Dis* 2011;12:6:50
18. Rossi A, Catala M, Biancheri R, et al. **MR imaging of brain-stem**

hypoplasia in horizontal gaze palsy with progressive scoliosis. *AJNR Am J Neuroradiol* 2004;25:1046–48

19. Briguglio M, Pinelli L, Giordano L, et al. **Pontine tegmental cap dysplasia: developmental and cognitive outcome in three adolescent patients.** *Orphanet J Rare Dis* 2011;6:36

20. Barkovich AJ, Millen KJ, Dobyns WB. **A developmental classification of malformations of the brainstem.** *Ann Neurol* 2007;62:625–39

21. Barkovich AJ, Millen KJ, Dobyns WB. **A developmental and genetic classification for midbrain-hindbrain malformations.** *Brain* 2009; 132:3199–230

22. Clement E, Mercuri E, Godfrey C, et al. **Brain involvement in muscular dystrophies with defective dystroglycan glycosylation.** *Ann Neurol* 2008;64:573–82

23. Jissendi-Tchofo P, Kara S, Barkovich AJ. **Midbrain-hindbrain involvement in lissencephalies.** *Neurology* 2009;72:410–18

24. Soto-Ares G, Joyes B, Lemaître MP, et al. **MRI in children with mental retardation.** *Pediatr Radiol* 2003;33:334–45

25. Matsuo I, Kuratani S, Kimura C, et al. **Mouse Otx2 functions in the formation and patterning of rostral head.** *Genes Dev* 1995;9: 2646–58

26. Acampora D, Gulisano M, Broccoli V, et al. **Otx genes in brain morphogenesis.** *Prog Neurobiol* 2001;64:69–95

27. Nakamura H, Watanabe Y. **Isthmus organizer and regionalization of the mesencephalon and metencephalon.** *Int J Dev Biol* 2005;49: 231–35

28. Simeone A, Acampora D, Gulisano M, et al. **Nested expression domains of four homeobox genes in developing rostral brain.** *Nature* 1992;358:687–90

29. Larsen KB, Lutterodt MC, Møllgård K, et al. **Expression of the homeobox genes OTX2 and OTX1 in the early developing human brain.** *J Histochem Cytochem* 2010;58:669–78

30. Liu A, Joyner AL. **EN and GBX2 play essential roles downstream of FGF8 in patterning the mouse mid/hindbrain region.** *Development* 2001;128:181–91

31. Nishida A, Furukawa A, Koike C, et al. **Otx2 homeobox gene controls retinal photoreceptor cell fate and pineal gland development.** *Nat Neurosci* 2003;6:1255–63

32. Abouzeid H, Youssef MA, ElShakankiri N, et al. **PAX6 aniridia and interhemispheric brain anomalies.** *Mol Vis* 2009;15:2074–83

33. Bamiou DE, Free SL, Sisodiya SM, et al. **Auditory interhemispheric transfer deficits, hearing difficulties, and brain magnetic resonance imaging abnormalities in children with congenital aniridia due to PAX6 mutations.** *Arch Pediatr Adolesc Med* 2007;161:463–69

34. Webb EA, O'Reilly MA, Orgill J, et al. **Rest-activity disturbances in children with septo-optic dysplasia characterized by actigraphy and 24-hour plasma melatonin profiles.** *J Clin Endocrinol Metab* 2010;95:198–203

35. Ashkenazi-Hoffnung L, Lebenthal Y, Wyatt AW, et al. **A novel loss-of-function mutation in OTX2 in a patient with anophthalmia and isolated growth hormone deficiency.** *Hum Genet* 2010;127:721–29

36. Tajima T, Ohtake A, Hoshino M, et al. **OTX2 loss of function mutation causes anophthalmia and combined pituitary hormone deficiency with a small anterior and ectopic posterior pituitary.** *J Clin Endocrinol Metab* 2009;94:314–19

37. Wyatt A, Bakrania P, Bunyan DJ, et al. **Novel heterozygous OTX2 mutations and whole gene deletions in anophthalmia, microphthalmia and coloboma.** *Hum Mutat* 2008;29:278–83

38. Schilter KF, Schneider A, Bardakjian T, et al. **OTX2 microphthalmia syndrome: four novel mutations and delineation of a phenotype.** *Clin Genet* 2011;79:158–68

39. Elliott J, Maltby EL, Reynolds B. **A case of deletion 14(q22.1->q22.3) associated with anophthalmia and pituitary abnormalities.** *J Med Genet* 1993;30:251–52

40. Lemyre E, Lemieux N, Decarie JC, et al. **Del(14)(q22.1q23.2) in a patient with anophthalmia and pituitary hypoplasia.** *Am J Med Genet* 1998;77:162–65

41. Nolen LD, Amor D, Haywood A, et al. **Deletion at 14q22–23 indicates a contiguous gene syndrome comprising anophthalmia, pituitary hypoplasia, and ear anomalies.** *Am J Med Genet A* 2006; 140:1711–18

42. Hayashi S, Okamoto N, Makita Y, et al. **Heterozygous deletion at 14q22.1-q22.3 including the BMP4 gene in a patient with psychomotor retardation, congenital corneal opacity and feet polysyndactyly.** *Am J Med Genet A* 2008;146:2905–10

43. Bakrania P, Efthymiou M, Klein JC, et al. **Mutations in BMP4 cause eye, brain, and digit developmental anomalies: overlap between the BMP4 and hedgehog signaling pathways.** *Am J Hum Genet* 2008;82: 304–19

Prevalence and Spectrum of In Utero Structural Brain Abnormalities in Fetuses with Complex Congenital Heart Disease

M. Brossard-Racine, A.J. du Plessis, G. Vezina, R. Robertson, D. Bulas, I.E. Evangelou, M. Donofrio, D. Freeman, and C. Limperopoulos

ABSTRACT

BACKGROUND AND PURPOSE: Brain injury is a major complication in neonates with complex congenital heart disease. Preliminary evidence suggests that fetuses with congenital heart disease are at greater risk for brain abnormalities. However, the nature and frequency of these brain abnormalities detected by conventional fetal MR imaging has not been examined prospectively. Our primary objective was to determine the prevalence and spectrum of brain abnormalities detected on conventional clinical MR imaging in fetuses with complex congenital heart disease and, second, to compare the congenital heart disease cohort with a control group of fetuses from healthy pregnancies.

MATERIALS AND METHODS: We prospectively recruited pregnant women with a confirmed fetal congenital heart disease diagnosis and healthy volunteers with normal fetal echocardiogram findings who underwent a fetal MR imaging between 18 and 39 weeks gestational age.

RESULTS: A total of 338 fetuses (194 controls; 144 with congenital heart disease) were studied at a mean gestational age of 30.61 ± 4.67 weeks. Brain abnormalities were present in 23% of the congenital heart disease group compared with 1.5% in the control group ($P < .001$). The most common abnormalities in the congenital heart disease group were mild unilateral ventriculomegaly in 12/33 (36.4%) and increased extra-axial spaces in 10/33 (30.3%). Subgroup analyses comparing the type and frequency of brain abnormalities based on cardiac physiology did not reveal significant associations, suggesting that the brain abnormalities were not limited to those with the most severe congenital heart disease.

CONCLUSIONS: This is the first large prospective study reporting conventional MR imaging findings in fetuses with congenital heart disease. Our results suggest that brain abnormalities are prevalent but relatively mild antenatally in fetuses with congenital heart disease. The long-term predictive value of these findings awaits further study.

ABBREVIATIONS: CHD = congenital heart disease; GA = gestational age; HLHS = hypoplastic left-heart syndrome

B rain injury is a major complication in neonates with complex congenital heart disease (CHD).[1,2] During the past decade, a growing body of evidence has demonstrated the high prevalence

of preoperative brain imaging abnormalities in neonates with CHD, suggesting an antenatal origin in many cases.[3-6] More recently, our group has used quantitative MR imaging to demonstrate a progressive third-trimester deceleration in volumetric brain growth and metabolism in fetuses with CHD,[7] reduced volumes of gray (cortical and subcortical) and white matter, and significant delays in cortical gyrification and surface area in fetuses with hypoplastic left-heart syndrome (HLHS).[8] To date, there is only 1 published report of brain findings in fetuses with CHD by using conventional MR imaging.[9] This retrospective chart review of 53 cases reported a 39% incidence of brain anomalies in fetuses with CHD. Taken together, preliminary evidence suggests that fetuses with CHD are at risk of brain abnormalities, including delayed maturation and brain injury. However, to date, no study has prospectively ascertained the frequency and nature of brain abnormalities by conventional MR imaging in fetuses with CHD. The primary objective of this study was to determine

the prevalence and spectrum of brain abnormalities detected on conventional clinical MR imaging in fetuses with complex CHD and, second, to compare the CHD cohort with a control group of fetuses from healthy pregnancies.

MATERIALS AND METHODS

Subjects

As part of an ongoing prospective observational study that started in September 2007, pregnant women with a fetal CHD diagnosis confirmed by echocardiography at Boston Children's Hospital[7] and Children's National Medical Center were recruited as patients. A fetal echocardiography was performed by one of the center's experienced fetal echocardiographers on the day of the mother's appointment. Fetal CHD diagnoses were subsequently categorized as cyanotic-versus-acyanotic and single- versus 2-ventricle physiology as determined by oxygen saturation and anatomic classification. During the same study timeframe, healthy controls were also recruited from healthy volunteers with normal fetal echocardiography findings or pregnant women for whom an echocardiography was performed for a previous family history of CHD. Patients and controls with multiple pregnancies, abnormalities on fetal sonography, congenital infection, documented chromosomal abnormalities, and/or multiorgan dysmorphic conditions were excluded from the study.[7] Thereafter, enrolled pregnant women completed a fetal MR imaging during the second or third trimester of pregnancy. Additionally, we amended our original protocol in 2013 to include serial fetal MR imaging studies (ie, 2 fetal MR imaging studies) as part of this prospective study, to examine fetal brain development during the second and third trimesters. For the subset of fetuses that underwent 2 fetal MR imaging scans, both studies were included in our analyses. Clinical and demographic information for each subject was collected through medical record reviews or questionnaires. Written informed consent was obtained for every participant, and the study was approved by the institutional review boards of Boston Children's Hospital and Children's National Medical Center.

MR Imaging Data Acquisition

Each fetal MR imaging study was performed on a 1.5T scanner either on an Achieva (Philips Healthcare, Best, Netherlands) device by using a 5-channel phased-array coil (Boston Children's cohort) or on a Discovery MR450 scanner (GE Healthcare, Milwaukee, Wisconsin) by using an 8-channel phased-array coil (Children's National Medical Center cohort). Multiplanar single-shot fast spin-echo imaging sequences were performed as follows: on the Philips scanner, single-shot fast spin-echo TE = 120 ms, TR = 971 ms/section, 330-mm FOV, 256 × 204 acquisition matrix; for the GE scans, TE = 160 ms, TR = 1110 ms/section, 320-mm FOV, 256 × 192 acquisition matrix. Diffusion tensor imaging was acquired in 12 directions with the following parameters: TE = minimum, TR = 8000 ms, and 4-mm section thickness. The FOV was 330 mm on the GE scanner versus 280 mm on the Philips scanner. Finally, a T1 spoiled gradient-recalled acquisition was performed with TE = minimum, TR = 100 ms/section, 360-mm FOV, 256 × 160 acquisition matrix on the GE scanner. No contrast or sedation was used for any of the MR imaging studies.

All MR imaging studies were reviewed for clinical findings by one of the center's expert pediatric neuroradiologists, both of whom had >15 years of experience with fetal brain MR imaging (R.R. at Boston Children's Hospital and G.V. at Children's National Medical Center). The neuroradiologists were blinded to patient-versus-control status, the subject's medical history, and type of CHD. All studies were reviewed for the presence of developmental malformations, acquired abnormalities, and brain maturation following the clinical guidelines in place at the time of the study. Mild ventriculomegaly was diagnosed when the maximum width of the lateral ventricles at the level of the atrium measured between 10 and 15 mm.[10] Increased extra-axial space was diagnosed when the distance between the inner margin of the cranium and the outer margin of the frontal, temporal, parietal, and/or occipital regions was considered enlarged for gestational age (GA).[11,12] Finally, images were also examined for signal abnormality on T2/T1 images and the presence of restricted diffusion on diffusion imaging acquisitions.

Statistical Analysis

Descriptive statistics by using means, SDs, and frequencies were used to characterize the sample and the nature of the brain abnormalities described on conventional MR imaging. Independent sample t tests and χ^2 analyses were used to explore differences and associations between groups, CHD diagnoses, cyanotic CHD versus acyanotic, single- versus 2-ventricle physiology, sex, GA, and MR imaging abnormalities. All analyses were performed by using the Statistical Package for the Social Sciences, Version 20 (IBM, Armonk, New York).

RESULTS

Group Characteristics

A total of 338 pregnant women (144 with fetuses with CHD, 194 controls) successfully completed second- or third-trimester MR imaging. Of these fetuses, 182 (53.8%) were male (82 with CHD, 100 controls). As described in our "Materials and Methods" section, in 2013, a second fetal MR imaging was added to our MR imaging protocol (ie, 2 fetal MR imaging studies) to examine fetal brain development serially. Consequently, 28 women (10 fetuses with CHD, 28 controls) completed 2 fetal MR imaging studies, the first during the second trimester and the second during the third trimester, resulting in 376 MR imaging studies. The mean GA of these 376 studies was 30.61 ± 4.67 weeks (range, 18.29–39.29 weeks), of which 273 (72.6%) were performed during the third trimester. Although a significantly smaller proportion of studies was performed during the second trimester in the control group compared with the CHD group ($\chi^2 = 12.75$, $P < .001$), the mean GA at MR imaging for the control group (29.94 ± 5.14 weeks) was significantly lower compared with that in the CHD group (31.57 ± 3.71 weeks; $t = 3.57$; $P < .001$).

The most common CHD diagnostic categories in our sample were the following: HLHS (32/144, 22.2%), transposition of the great arteries (24/144, 18.8%), pulmonary atresia (12/144, 8.3%), tetralogy of Fallot (17/144, 11.8%), and double-outlet right ventricle (16/144, 11.1%). The complete distribution of fetal CHD diagnoses is presented in Table 1.

Abnormal Conventional MR Imaging Findings

Brain abnormalities detected on MR imaging were significantly more frequent among patients with CHD ($\chi^2 = 36.87$, $P < .001$) and were detected in approximately one-quarter (33/144, 22.9%) of the fetuses with CHD compared with only 1.5% (3/194) in the controls. The type and distribution of brain abnormalities on fetal MR imaging in the CHD group are summarized in Table 2. Mild unilateral ventriculomegaly (Fig 1) was the most common abnormality reported in 8.3% (12/144). Of these cases, left-sided ventriculomegaly was twice as common ($n = 8$) as right-sided ($n = 4$). Ventriculomegaly was isolated in all cases, with the exception of 2 fetuses, one of which also presented with increased extra-axial CSF spaces and the second with a frontal subependymal cyst. Only 1 fetus presented with mild symmetric ventriculomegaly. The presence of increased extra-axial CSF spaces (Fig 2) was the second most common MR imaging abnormality in our cohort, reported in 6.9% (10/144) of CHD subjects. Three fetuses (2.1%) with CHD were diagnosed with isolated inferior vermian hypoplasia on MR imaging (ie, no other associated cerebral malformations were identified). Three other fetuses (2.1%) presented with immature brain appearance defined as an underdevelopment of the anatomic structures, such as fissures and sulci being less developed than expected for the estimated GA. Finally 4 patients presented with white matter abnormalities, which included cysts in 2 fetuses (1.4%) and signal hyperintensity on T2-weighted imaging in 2 others (1.4%), one of which also demonstrated globally decreased diffusion in the white matter.

The 3 brain abnormalities detected in the control group included the following: right-sided mild unilateral ventriculomegaly (0.5%), left germinal matrix hemorrhage (0.5%), and mild cerebral underdevelopment (0.5%). A fourth fetus had 2D brain biometrics that were slightly less than expected for GA on a second-trimester MR imaging; however, these normalized on a third-trimester MR imaging, and the brain was considered normal. As indicated in our inclusion criteria, no brain abnormalities were previously reported on fetal sonography in our cohort.

Fetal Brain Anomalies and Type of CHD

There was no significant association between type of brain abnormality and CHD diagnosis, GA at MR imaging, or sex. Unilateral ventriculomegaly was more frequent in the fetuses with HLHS (5/12, 41.7%), while increased extra-axial CSF spaces were more common in fetuses with a double-outlet right ventricle (3/10, 30.0%). Of the 3 fetuses with isolated inferior vermian hypoplasia, the first had HLHS, the second was diagnosed with tetralogy of Fallot, and the third had truncus arteriosus. One fetus with tetralogy of Fallot presented with cysts in the periventricular white matter, and another fetus with transposition of the great arteries demonstrated isolated left-frontal subependymal cysts. Immature brain appearance was reported in 3 fetuses, one with tetralogy of Fallot, the second with double-outlet right ventricle, and the third with transposition of the great arteries. Finally, in 2 fetuses with transposition of the great arteries, there was evidence of diffuse white matter hyperintensity in the first and a focal hyperintense signal in the deep frontal white matter in the second.

Subgroup analyses based on cardiac physiology (ie, single-versus-2-ventricle physiology and cyanotic-versus-acyanotic lesions) were performed, but no significant association was found ($\chi^2 = 1.91$, $P = .662$). However, increased extra-axial CSF spaces were primarily diagnosed in fetuses with acyanotic heart disease (7/10), while unilateral ventriculomegaly was 3 times more frequent in fetuses with cyanotic CHD. White matter signal abnormalities, cysts, and vermian hypoplasia were exclusively described in the subgroup with cyanotic lesions. The distribution of brain abnormalities between fetuses with cyanotic-versus-acyanotic CHD is reported in Table 3.

Table 1: CHD diagnoses distribution ($n = 144$)

Diagnosis	Counts (%)	Abnormal MRI Findings (%)
Hypoplastic left-heart syndrome	32 (22.2)	7 (21.21)
Transposition of the great artery	27 (18.8)	5 (15.2)
Double-outlet right ventricle	16 (11.1)	5 (15.2)
Tetralogy of Fallot	17 (11.8)	5 (15.2)
Pulmonary atresia	12 (8.3)	1 (3.0)
Atrioventricular septal defect	7 (5.9)	4 (12.1)
Aortic stenosis	6 (4.2)	2 (6.1)
Tricuspid atresia	6 (4.2)	0 (0.0)
Ventricular septal defect	4 (2.8)	0 (0.0)
Hypoplastic right-heart syndrome	4 (2.8)	1 (3.0)
Pulmonary stenosis	2 (1.4)	1 (3.0)
Truncus arteriosus	2 (1.4)	2 (6.1)
Ebstein anomaly	1 (0.7)	0 (0.0)
Severe coarctation of the aorta	1 (0.7)	0 (0.0)
Total	144 (100)	33 (100)

Table 2: Abnormal brain MRI findings per congenital heart disease diagnoses ($n = 33$)

CHD Diagnosis	Ventriculomegaly	Increased Extra-Axial Spaces	Vermis Hypoplasia	Cysts	WM Signal Hyperintensity	Immature Appearance	Total
HLHS	5	1	1	–	–	–	7
TGA	1	–	–	1	2	1	5
TOF	2	–	1	1	–	1	5
DORV	1	3	–	–	–	1	5
AS	1	1	–	–	–	–	2
AV canal SD	2	2	–	–	–	–	4
PA	–	1	–	–	–	–	1
PS	1	–	–	–	–	–	1
HRH	–	1	–	–	–	–	1
Truncus arteriosus	–	1	1	–	–	–	1
Total	13	10	3	2	2	3	33

Note:—TGA indicates transposition of the great arteries; TOF, tetralogy of Fallot; DORV, double-outlet right ventricle; AS, aortic stenosis; AV canal SD, atrioventricular septal defect; PA, pulmonary atresia; PS, pulmonary stenosis; HRH, hypoplastic right-heart syndrome.
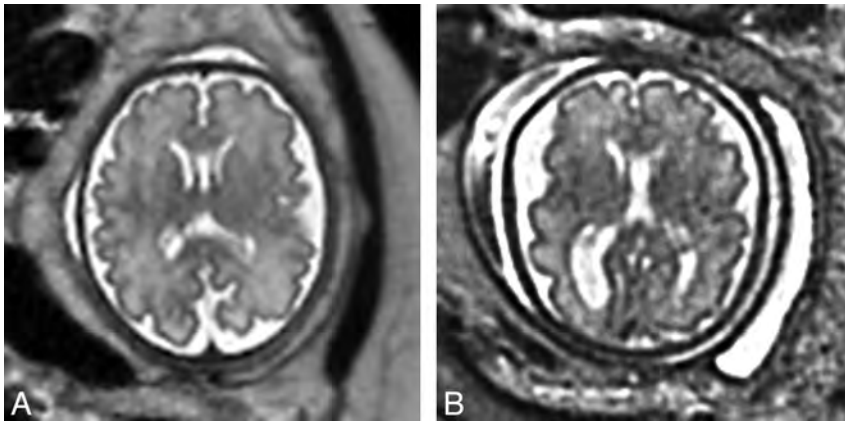
FIG 1. *A*, T2-weighted axial view of the brain of a healthy control at 32.55 weeks' GA. *B*, T2-weighted axial view of the brain of a patient with unilateral left ventriculomegaly at 32.00 weeks' GA.
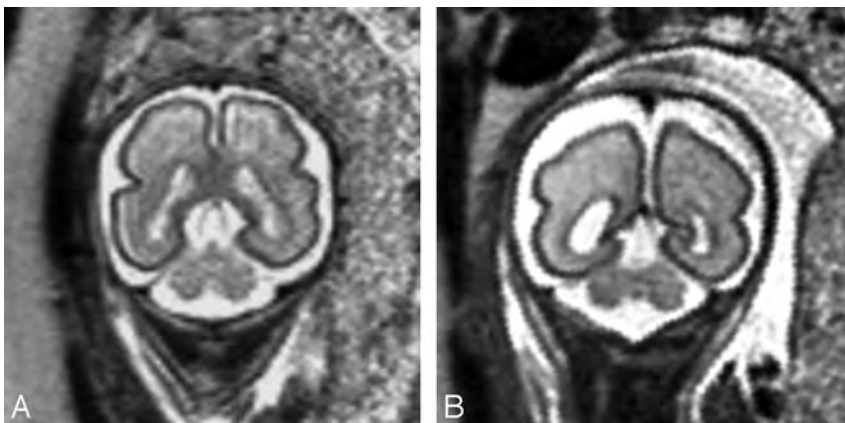

FIG 2. *A*, T2-weighted axial view of the brain of a healthy control at 26.56 weeks' GA. *B*, T2-weighted axial view of the brain of a patient with extra-axial spaces at 27.28 weeks' GA.

Table 3: Distribution of abnormal brain MRI findings in cyanotic-versus-acyanotic fetuses with CHD (*n* = 33)

Brain Abnormalities	Acyanotic	Cyanotic	Total
Increased extra-axial spaces	7	3	10
Ventriculomegaly	4	9	13
Vermis hypoplasia	0	3	3
Immature appearance	1	2	3
White matter signal hyperintensity	0	2	2
Cysts	0	2	2
Total	12	21	33

Fetal Brain Abnormalities and Gestational Age

The mean GA of fetuses with CHD with brain abnormalities was 31.15 ± 3.46 weeks and was not significantly different compared with fetuses with CHD with normal findings on brain MR imaging studies (mean GA = 31.78 ± 3.78 weeks; $t = 0.748$, $P = .44$). Abnormalities were not found to be significantly more frequent during the second or third trimester ($\chi^2 = 1.91$, $P = .662$), and their distribution is reported in Table 4. Among the 35 MR imaging studies with abnormal findings in the CHD group, 2 fetuses were scanned twice (ie, in the second and third trimesters). One fetus presented with mild bilateral ventriculomegaly, while the second presented with immature brain appearance. For both fetuses, findings remained consistent at both MR imaging time points.

In the control group, the 3 brain abnormalities were noted on second-trimester MR imaging studies. The fetus with a germinal matrix hemorrhage in the left ventricle underwent a second MR imaging during the third trimester, and mild enlargement of the lateral ventricle secondary to the hemorrhage was reported.

DISCUSSION

This is the first prospective study to describe the prevalence of brain abnormalities by conventional clinical MR imaging in a large, consecutive cohort of fetuses with CHD and to compare them with a control group of fetuses from healthy pregnancies. We found that structural brain abnormalities were significantly more frequent in fetuses with CHD, with approximately one-quarter (23%) demonstrating in utero structural brain abnormalities compared with <2% in the control group. Mild unilateral ventriculomegaly and increased extra-axial CSF spaces were most commonly reported, together representing almost 70% (22/33) of all antenatal brain abnormalities in fetuses with CHD. Other findings among fetuses with CHD included vermian hypoplasia (*n* = 3), cerebral cortical immaturity (*n* = 3), periventricular cysts (*n* = 2), white matter signal hyperintensity (*n* = 2), and mild bilateral ventriculomegaly (*n* = 1). Finally, we found no significant difference in the prevalence of brain abnormalities in fetuses with single- versus 2-ventricle physiology or in cyanotic-versus-acyanotic lesions.

Unilateral ventriculomegaly was found in 12 (8%) of the fetuses with CHD. Our findings corroborate the retrospective findings reported by Mlczoch et al,[9] who described mild asymmetric dilation of the lateral ventricles as the most common brain anomaly in this population. Unilateral mild ventriculomegaly is, in fact, one of the most common brain abnormalities referred for fetal MR imaging and counseling in clinical fetal centers[11,13] and is estimated to affect 0.07% of all pregnancies.[10] Only 1 fetus in our control group (0.05%) presented with mild unilateral ventriculomegaly.

Increased extra-axial CSF spaces were uniquely reported in fetuses with CHD and were present in 10 cases (9 reported in the third trimester), making this the second most common abnormality in this group. Enlarged extra-axial CSF spaces were mild and isolated in all cases, except in 1 fetus that also had mild unilateral ventriculomegaly. The finding of increased extra-axial CSF spaces could be due to delayed parenchymal brain development or disturbed CSF dynamics (possibly due to the fetal cardiac anomaly) or both. Additionally, immature cerebral cortical development was detected in 2 fetuses with CHD (2%) compared with

Table 4: Distribution of abnormal brain MRI findings among fetuses with CHD per trimester of pregnancy (n = 35)[a]

Brain Abnormalities	Second Trimester	Third Trimester	Total
Increased extra-axial spaces	1	9	10
Ventriculomegaly	4	10	14
Vermian hypoplasia	0	3	3
Immature appearance	2	2	4
White matter signal hyperintensity	0	2	2
Cysts	0	2	2
Total	7	28	35

[a] Two fetuses were scanned twice, once at each trimester. One had immature brain appearance, and the other had bilateral ventriculomegaly. Both anomalies were detected at the second-trimester MRI and persisted at the third-trimester MRI.

only 1 (0.5%) in the control group. Together, these findings support the notion that delayed brain maturation is likely a direct consequence of the cardiac defect. In our previous studies of fetuses with CHD by using quantitative brain MR imaging techniques, we described a progressive third-trimester deceleration in cerebral growth[7] and delayed cortical maturation (in fetuses with HLHS)[8] compared with healthy fetuses. In the current study, 3 of these cases of suspected delay in brain maturation were detected by clinical MR imaging readings before the third trimester. Ten women in our CHD sample underwent repeated fetal MR imaging studies in the second and third trimesters, and in all cases, the findings were enduring within cases. Nevertheless, a larger sample with serial fetal MR imaging studies is needed to better delineate the onset and progression of delayed brain development in fetuses with CHD.

Disturbances in oxygen/substrate supply present a major threat to brain development in fetuses with CHD.[14,15] Using Doppler sonography, Donofrio et al[15] compared the cerebral-placental ratio between fetuses with CHD and healthy controls and showed that the normal intrinsic cerebral compensatory response to insufficient oxygen-substrate delivery (ie, cerebral vasodilation) was activated in fetuses with CHD. The cerebral-placental ratio was significantly lower overall in fetuses with CHD, with values <1.0 most prevalent in fetuses with a single-ventricle physiology. Reduced cerebral-placental ratio was significantly associated with decreased head circumference, supporting the notion that the "brain-sparing" response was insufficient to sustain brain growth. In addition, we have previously reported a significant association between smaller total brain volume and lower combined ventricular output from the aorta in fetuses with CHD.[7] In the current study, evidence of brain abnormalities, including delayed brain development, was present among fetuses with various CHD diagnoses, suggesting that the risk of disturbed brain maturation in fetuses with CHD is not restricted to those with the most complex cardiac lesions, such as HLHS. This is also consistent with Mlczoch et al,[9] who found no association between brain abnormalities and the type of CHD diagnosis. Future studies that relate brain abnormalities to specific Doppler ultrasound measures are needed to address this important question.

One fetus in the control group had a germinal matrix hemorrhage detected on MR imaging at 23 weeks' GA. Germinal matrix hemorrhage is a common complication of premature birth but has been rarely described in the fetus in utero. The history of the pregnancy was unremarkable. Secondary enlargement of the af-

fected ventricle was reported on the follow-up MR imaging at 32 weeks and was consistent with the few in vivo cases reported in the literature.[16] The patient was referred for clinical neurologic consultation and follow-up.

Three fetuses in our CHD cohort were diagnosed with inferior vermian hypoplasia, an anomaly that may represent delayed or arrested development of the cerebellar vermis. In previous studies, we have described an overall favorable prognosis for infants and school-aged children with a fetal MR imaging diagnosis of isolated vermian hypoplasia.[17] However, the impact of inferior vermian development on subsequent neuropsychologic development in fetuses with CHD is unknown and awaits further investigation.

White matter abnormalities were detected in 4 fetuses with CHD and in none of the control fetuses. These abnormalities included T2-weighted signal abnormality and cysts in the white matter. Acquired white matter signal hyperintensity was exclusively found in 2 fetuses with transposition of the great arteries. Subependymal cysts (possibly the residua of ischemic-hemorrhagic injury) were present in 2 fetuses, one with transposition of the great arteries and another with tetralogy of Fallot. Although the available literature is limited, the prognosis of isolated subependymal cysts diagnosed in utero has been good.[18,19] White matter abnormalities, thought to be a form of periventricular leukomalacia, have been reported in fetuses with HLHS[20] on postmortem examination and in a number of postnatal studies of infants with CHD.[5,21,22] The relation between the fetal WM abnormalities seen in our population and the periventricular leukomalacia described after birth in infants with CHD is not clear but could support an antenatal onset in some cases. The prognostic significance of fetal white matter signal intensity in this population remains to be determined. The current limitations of conventional fetal MR imaging may have hindered our ability to detect other cases of white matter abnormalities in utero. Although diffusion-weighted imaging is increasingly used in fetal MR imaging, this acquisition is particularly sensitive to fetal motion that results in image degradation.[23] A recent case report suggested that differences in the white matter microstructural organization could also be detected in utero during the third trimester of 3 fetuses with CHD compared with healthy fetuses.[24] However, further studies that assess white matter integrity in fetuses with CHD are needed to better understand the relationship between these macro- and microstructural preliminary findings and their long-term consequences.

In postnatal preoperative studies of infants with CHD, the most prevalent brain lesions included ischemic lesions[21] and diffuse and focal white matter injury,[6,25,26] including periventricular leukomalacia.[5,27] The brain MR imaging findings in our fetal cohort with CHD differed in both type and severity from these postnatal studies of infants with CHD. In fact, with the exception of 1 fetus with diffuse white matter injury, the brain anomalies described in our sample were all mild in severity. This difference in lesion severity could be explained, in part, by hemodynamic insults occurring during the complex transition from a fetal to postnatal circulation, a potentially hazardous period for infants with CHD.[28] Moreover, recent evidence suggests that brain injuries found in neonates with CHD preoperatively are associated with

microstructural and metabolic markers of brain immaturity.[29] Follow-up postnatal MR imaging studies and neurodevelopmental outcome assessments are needed to determine whether the prenatal findings described herein are transient or persistent in nature and their impact on long-term outcome. These studies are currently underway.

To our knowledge, this study is the first prospective study to describe conventional clinical MR imaging findings in a large sample of fetuses with CHD during the second and third trimesters of pregnancy and to compare them with a large control group of fetuses from healthy pregnancies. Moreover, our CHD sample included a representative range of cardiac diagnostic categories and was not limited to those with the most severe forms of CHD (eg, HLHS). However, given that we carefully excluded cases with multiorgan dysmorphic conditions, as well as chromosomal or genetic conditions, we may have underestimated the true prevalence of brain abnormalities in the overall fetal CHD population. Structural abnormalities of the brain may result as part of a spectrum of other congenital malformations including CHD. Finally, our overall goal was to describe the prevalence and spectrum of brain abnormalities detected on conventional MR imaging in fetuses with complex CHD. This objective was carried out by determining the frequency with which neuroradiologists made the clinical diagnosis of brain abnormality in fetuses with CHD compared with healthy control fetuses. Therefore, we did not perform repeat blinded MR imaging interpretations to assess intra- and inter-reader reliability. Nevertheless, our study was conducted in 2 major referral centers for congenital heart disease, and all MR imaging studies were reviewed by an experienced fetal neuroradiologist following clinical best practice standards. Consequently, we are confident that the findings reported in this study are representative of the current findings in clinical settings.

CONCLUSIONS

During the past decade, in vivo fetal MR imaging has contributed enormously to our understanding of fetal brain abnormalities in the living fetus. Our findings demonstrate that structural brain abnormalities are much more prevalent in fetuses with complex CHD than in controls and are not confined to those with the most critical forms of CHD.

However, although prevalent, the findings in our study were relatively mild in extent and were often suggestive of delayed or arrested brain maturation. These data contribute to a growing body of evidence suggesting that an important component of neurologic dysfunction in survivors of CHD is prenatal in origin.

REFERENCES

1. Owen M, Shevell M, Majnemer A, et al. **Abnormal brain structure and function in newborns with complex congenital heart defects before open heart surgery: a review of the evidence.** *J Child Neurol* 2011;26:743–55

2. Donofrio MT, Massaro AN. **Impact of congenital heart disease on brain development and neurodevelopmental outcome.** *Int J Pediatr* 2010;2010. pii:359390

3. Block AJ, McQuillen PS, Chau V, et al. **Clinically silent preoperative brain injuries do not worsen with surgery in neonates with congenital heart disease.** *J Thorac Cardiovasc Surg* 2010;140:550–57

4. Licht DJ, Shera DM, Clancy RR, et al. **Brain maturation is delayed in infants with complex congenital heart defects.** *J Thorac Cardiovasc Surg* 2009;137:529–36, discussion 536–37

5. Licht DJ, Wang J, Silvestre DW, et al. **Preoperative cerebral blood flow is diminished in neonates with severe congenital heart defects.** *J Thorac Cardiovasc Surg* 2004;128:841–49

6. Miller SP, McQuillen PS, Hamrick S, et al. **Abnormal brain development in newborns with congenital heart disease.** *N Engl J Med* 2007;357:1928–38

7. Limperopoulos C, Tworetzky W, McElhinney DB, et al. **Brain volume and metabolism in fetuses with congenital heart disease: evaluation with quantitative magnetic resonance imaging and spectroscopy.** *Circulation* 2010;121:26–33

8. Clouchoux C, du Plessis AJ, Bouyssi-Kobar M, et al. **Delayed cortical development in fetuses with complex congenital heart disease.** *Cereb Cortex* 2013;23:2932–43

9. Mlczoch E, Brugger P, Ulm B, et al. **Structural congenital brain disease in congenital heart disease: results from a fetal MRI program.** *Eur J Paediatr Neurol* 2013;17:153–60

10. Wax JR, Bookman L, Cartin A, et al. **Mild fetal cerebral ventriculomegaly: diagnosis, clinical associations, and outcomes.** *Obstet Gynecol Surv* 2003;58:407–14

11. Girard NJ, Raybaud CA. **Ventriculomegaly and pericerebral CSF collection in the fetus: early stage of benign external hydrocephalus?** *Childs Nerv Syst* 2001;17:239–45

12. Watanabe Y, Abe S, Takagi K, et al. **Evolution of subarachnoid space in normal fetuses using magnetic resonance imaging.** *Prenat Diagn* 2005;25:1217–22

13. Glenn OA, Barkovich AJ. **Magnetic resonance imaging of the fetal brain and spine: an increasingly important tool in prenatal diagnosis, part 1.** *AJNR Am J Neuroradiol* 2006;27:1604–11

14. Donofrio MT. **The heart–brain interaction in the fetus: cerebrovascular blood flow in the developing human.** *Prog Pediatr Cardiol* 2006;22:41–51

15. Donofrio MT, Bremer YA, Schieken RM, et al. **Autoregulation of cerebral blood flow in fetuses with congenital heart disease: the brain sparing effect.** *Pediatr Cardiol* 2003;24:436–43

16. Fukui K, Morioka T, Nishio S, et al. **Fetal germinal matrix and intraventricular haemorrhage diagnosed by MRI.** *Neuroradiology* 2001;43:68–72

17. Tarui T, Limperopoulos C, Sullivan NR, et al. **Long-term developmental outcome of children with a fetal diagnosis of isolated inferior vermian hypoplasia.** *Arch Dis Child Fetal Neonatal Ed* 2014;99:F54–58

18. Bats AS, Molho M, Senat MV, et al. **Subependymal pseudocysts in the fetal brain: prenatal diagnosis of two cases and review of the literature.** *Ultrasound Obstet Gynecol* 2002;20:502–05

19. D'Addario V, Selvaggio S, Pinto V, et al. **Fetal subependymal cysts with normal neonatal outcome: a case report.** *Fetal Diagn Ther* 2003;18:170–73

20. Hinton RB, Andelfinger G, Sekar P, et al. **Prenatal head growth and white matter injury in hypoplastic left heart syndrome.** *Pediatr Res* 2008;64:364–69

21. Mahle WT, Tavani F, Zimmerman RA, et al. **An MRI study of neurological injury before and after congenital heart surgery.** *Circulation* 2002;106(12 suppl 1):I109–14

22. Andropoulos DB, Hunter JV, Nelson DP, et al. **Brain immaturity is associated with brain injury before and after neonatal cardiac surgery with high-flow bypass and cerebral oxygenation monitoring.** *J Thorac Cardiovasc Surg* 2010;139:543–56

23. Clouchoux C, Limperopoulos C. **Novel applications of quantitative MRI for the fetal brain.** *Pediatr Radiol* 2012;42(suppl 1):S24–32

24. Berman JI, Hamrick SEG, McQuillen PS, et al. **Diffusion-weighted imaging in fetuses with severe congenital heart defects.** *AJNR Am J Neuroradiol* 2011;32:E21–22

25. McQuillen PS, Hamrick SE, Perez MJ, et al. **Balloon atrial septostomy is associated with preoperative stroke in neonates with transposition of the great arteries.** *Circulation* 2006;113:280–85

26. Partridge SC, Vigneron DB, Charlton NN, et al. **Pyramidal tract maturation after brain injury in newborns with heart disease.** *Ann Neurol* 2006;59:640–51

27. Petit CJ, Rome JJ, Wernovsky G, et al. **Preoperative brain injury in transposition of the great arteries is associated with oxygenation and time to surgery, not balloon atrial septostomy.** *Circulation* 2009;119:709–16

28. Friedman AH, Fahey JT. **The transition from fetal to neonatal circulation: normal responses and implications for infants with heart disease.** *Semin Perinatol* 1993;17:106–21

29. Dimitropoulos A, McQuillen PS, Sethi V, et al. **Brain injury and development in newborns with critical congenital heart disease.** *Neurology* 2013;81:241–48

Brain Parenchymal Signal Abnormalities Associated with Developmental Venous Anomalies in Children and Young Adults

L.L. Linscott, J.L. Leach, B. Zhang, and B.V. Jones

ABSTRACT

BACKGROUND AND PURPOSE: Abnormal signal in the drainage territory of developmental venous anomalies has been well described in adults but has been incompletely investigated in children. This study was performed to evaluate the prevalence of brain parenchymal abnormalities subjacent to developmental venous anomalies in children and young adults, correlating with subject age and developmental venous anomaly morphology and location.

MATERIALS AND METHODS: Two hundred eighty-five patients with developmental venous anomalies identified on brain MR imaging with contrast, performed from November 2008 through November 2012, composed the study group. Data were collected for the following explanatory variables: subject demographics, developmental venous anomaly location, morphology, and associated parenchymal abnormalities. Associations between these variables and the presence of parenchymal signal abnormalities (response variable) were then determined.

RESULTS: Of the 285 subjects identified, 172 met inclusion criteria, and among these subjects, 193 developmental venous anomalies were identified. Twenty-six (13.5%) of the 193 developmental venous anomalies had associated signal-intensity abnormalities in their drainage territory. After excluding developmental venous anomalies with coexisting cavernous malformations, we obtained an adjusted prevalence of 21/181 (11.6%) for associated signal-intensity abnormalities in developmental venous anomalies. Signal-intensity abnormalities were independently associated with younger subject age, cavernous malformations, parenchymal atrophy, and deep venous drainage of developmental venous anomalies.

CONCLUSIONS: Signal-intensity abnormalities detectable by standard clinical MR images were identified in 11.6% of consecutively identified developmental venous anomalies. Signal abnormalities are more common in developmental venous anomalies with deep venous drainage, associated cavernous malformation and parenchymal atrophy, and younger subject age. The pathophysiology of these signal-intensity abnormalities remains unclear but may represent effects of delayed myelination and/or alterations in venous flow within the developmental venous anomaly drainage territory.

ABBREVIATIONS: CM = cavernous malformation; DVA = developmental venous anomaly; P' = a χ^2 test or Fisher exact test for categoric variables and the t test or the Wilcoxon rank sum test for continuous variables; P'' = multivariate logistic regression models

Developmental venous anomalies (DVAs) are frequently identified on routine MR imaging of the brain with contrast. DVAs are typically considered normal variants of venous development and usually have no associated imaging findings.

However, a subset of DVAs has been associated with findings such as cavernous malformations (CMs),[1-3] thrombosis with subsequent venous infarction,[4-8] lobar atrophy,[9] T2 and FLAIR signal-intensity abnormalities,[9,10] and SWI hypointensities.[11] Signal abnormalities can occur in the drainage territory of DVAs and may produce diagnostic uncertainty with regard to the significance and relationship to presenting symptoms. Signal abnormalities on MR imaging have been described in 12.5%[10] to 28.3%[9] of DVAs in adults, with an increasing prevalence with older age. While well described in adults, this relationship has not been investigated in children, to our knowledge. The MR imaging appearance of the brain in children is quite different from that in adults during myelination, and the effect of DVAs on regional brain maturation has not been studied.

The most commonly proposed etiologies for parenchymal abnormalities associated with DVAs are chronic venous hypertension/insufficiency leading to ischemia or microhemorrhage.[9-12] Although the effect of brain maturation is unknown, on the basis of these pathophysiologic mechanisms, we hypothesized that parenchymal abnormalities would be less common in children compared with adults. This study was performed to test this hypothesis and to investigate clinical factors and DVA characteristics associated with parenchymal signal abnormalities in children and young adults.

MATERIALS AND METHODS
Cohort Identification
This retrospective study was approved by our institutional review board. The study was performed at a tertiary care children's hospital. A cutoff age of 35 years was chosen to ensure some age overlap with a similar study performed in adults.[10] Using a radiology data base search engine (Softek Illuminate; Softek Solutions, Prairie Village, Kansas), we searched brain MR imaging with contrast reports for the term "developmental venous anomaly" from November 2008 to November 2012. This search resulted in the identification of 285 consecutive patients with developmental venous anomalies identified on brain MR imaging with contrast. The examinations were reviewed by a neuroradiologist (J.L.L.) and pediatric neuroradiology fellow (L.L.L.).

Criteria for inclusion in the study were the following: 1) subjects were younger than 35 years in age, 2) subjects had undergone MR imaging of the brain with contrast, and 3) the term "developmental venous anomaly" was used by the interpreting radiologist in the subject's final diagnostic radiology report. Exclusion criteria based on imaging included the following: incomplete/nondiagnostic examinations (defined as those examinations that did not include FLAIR or T2-weighted imaging or examinations limited by motion or other artifacts, 5 subjects), examinations in which the presence of a DVA was questionable on imaging review (23 subjects), and examinations in which the DVA was too small to characterize its morphology (35 subjects). Also excluded were subjects with underlying diagnoses that alone could explain the presence of parenchymal signal abnormalities, including tuberous sclerosis, neurofibromatosis type 1, intracranial vascular malformations (eg, Sturge-Weber Syndrome, dural arteriovenous fistulas, and so forth), and subjects who had undergone surgery involving brain parenchyma in the drainage territory of the DVA (50 subjects).

Imaging
One hundred thirty-six DVAs were scanned at 1.5T, and 57 DVAs were scanned at 3T. Typical 3T protocol included the following: a 3D volumetric T1-weighted gradient-echo sequence (TR, 10 ms; TE, 4.6 ms), an axial T2-weighted sequence (TR, 3000 ms; TE, 100 ms), and an axial T2-weighted FLAIR sequence (TR, 11,000 ms; TE, 125 ms; TI, 2800 ms). The 1.5T protocol included the following: a sagittal T1-weighted FLAIR sequence (TR, 2200 ms; TE, 26 ms), an axial T2-weighted sequence (TR, 5000 ms; TE, 85 ms), and a T2 FLAIR sequence (TR, 10,000 ms; TE, 120 ms; TI, 2200 ms). Section thickness was 3–5 mm with a 0- to 1-mm intervening gap. Postcontrast imaging included a 3D volumetric T1 gradient-

echo sequence for 3T examinations and a T1-weighted FLAIR sequence in 3 planes for 1.5T examinations. Gadolinium was administered at a dose of 0.2 mmol/kg intravenously.

Image Analysis
The examinations were reviewed in detail by 2 experienced radiologists. The first radiologist (J.L.L.) has 20 years of experience in interpreting MR imaging examinations and holds a Certificate of Added Qualification in neuroradiology. The second radiologist (L.L.L.) has 6 years of experience in interpreting MR imaging examinations and is currently a clinical fellow in pediatric neuroradiology.

DVA location was divided into 3 groups: 1) lobar, 2) basal ganglia/thalamus, and 3) brain stem/cerebellum. DVA morphology was described by using a previously published system devised by Lee et al.[13] The DVAs were classified by depth as juxtacortical, subcortical, or periventricular. "Juxtacortical" depth was defined as within the gray matter or at the gray-white junction. "Subcortical" depth was defined as below the juxtacortical region but not adjacent to the ventricular wall. "Periventricular" depth was defined as adjacent to the lateral, third, or fourth ventricle or within the center of the structure, such as the pons. The drainage direction of the terminal or draining vein to which the venous radicles join was classified as either a deep (toward the ventricle) draining vein, superficial (toward the brain surface) draining vein, or both deep and superficial draining veins.

Images were specifically reviewed for the following: parenchymal atrophy, increased signal intensity on both FLAIR and T2-weighted images, and cavernous malformations within the drainage territory of the DVA. "Cavernous malformations" were defined as focal lesions with T2 hypointense borders and associated exaggerated signal hypointensity on gradient recalled-echo or SWI sequences. Signal-intensity abnormalities associated with the DVA were defined as increased extravascular signal intensity on both FLAIR and T2-weighted images within the drainage territory of the DVA.[9,10] The drainage territory was defined as the brain parenchyma directly adjacent to the visualized radicles of the DVA. Special care was taken to exclude increased signal intensity often seen within the venous radicles or draining vein, as described previously.[10] In infants and young children, signal abnormality was defined as signal intensity qualitatively greater than that of surrounding white matter and white matter in the corresponding gyrus of the contralateral cerebral hemisphere.

The prevalence of signal-intensity abnormalities within the DVA drainage territory was correlated with the presence or absence of CM and parenchymal atrophy, as well as DVA location, depth of the draining vein, direction of the draining vein, age, and sex. For those patients with associated signal abnormality, follow-up duration and number of follow-up examinations were tabulated. Follow-up examinations were reviewed to determine whether the extent or character of parenchymal signal abnormality changed with time.

Clinical and Imaging Findings Correlation
Clinical indications and dominant imaging findings (other than the presence of a DVA) were identified from the radiology report (or electronic medical record, when necessary) for all DVAs with
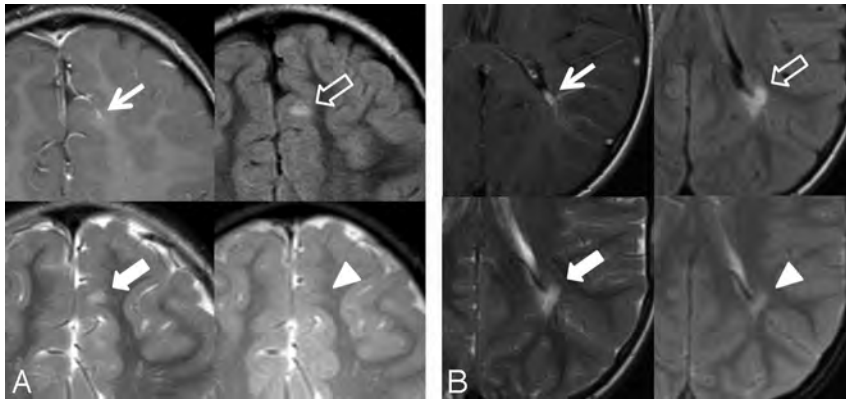
FIG 1. Two DVAs with associated signal abnormality in a 5-year-old boy (*A*) and a 7-year-old boy (*B*). T1WI with contrast (*arrow*), FLAIR (*outlined arrow*), T2WI (*block arrow*), and gradient recalled-echo (*arrowhead*). *A*, Left frontal lobe DVA with juxtacortical depth, superficial venous drainage, and associated increased FLAIR and T2 signal abnormality. Note the lack of gradient recalled-echo hypointensity in the same region. *B*, Left parietal lobe DVA with periventricular depth, deep venous drainage, and associated signal abnormality.

and without associated signal abnormality. They were then correlated with the presence or absence of DVA-associated signal intensity in the DVA drainage territory.

Statistical Analysis

A χ^2 test or Fisher exact test for categoric variables and the *t* test or the Wilcoxon rank sum test for continuous variables (P') were used to assess the relationship between signal change within the DVA drainage region (response variable) and DVA location, DVA depth, DVA drainage direction, age, sex, presence of atrophy or CM, clinical indication, and additional MR imaging findings (explanatory variables). Values for the 2-sample *t* test are expressed as mean ± SD (95% CI) unless stated otherwise. OR for age was calculated as the likelihood of signal abnormality with each additional year. OR for sex was calculated as the likelihood of signal abnormality if the subject was female. ORs for focal atrophy and CM were calculated as the likelihood of signal abnormality in the presence of either associated abnormality. ORs for location, depth, and direction of the draining vein were calculated as the likelihood of signal abnormality compared with the first DVA morphologic descriptor (ie, lobar, periventricular, superficial), which was given an OR of 1.0. Multivariate logistic regression models (P'') were used to evaluate the independent effects of age, sex, CM, parenchymal atrophy, location, depth, and direction of draining vein on signal change. Model selection under a stepwise criterion was performed to avoid multicollinearity. $P < .05$ was considered statistically significant. All analyses were performed by using SAS statistical software, Version 9.3 (SAS Institute, Cary, North Carolina.)

RESULTS

Of the 285 subjects initially identified in our data base search, 172 met the inclusion criteria. The mean age of the cohort was 10.8 years (14 months to 34 years) with an SD of 6.6 years and a 95% CI of 9.9–11.8 years. The cohort consisted of 91 males and 81 females. In these 172 subjects, 193 DVAs were identified. Thirteen patients had >1 DVA (11 subjects had 2 DVAs identified and 2 subjects had >2 DVAs identified). Five of the 26 DVAs with

associated signal abnormalities were found in 2 patients with multiple DVAs. Cavernous malformations were identified in the drainage territory of 12 of the 193 (6.2%) DVAs. Parenchymal atrophy was identified in 8 of the 193 (4.1%) DVAs.

Twenty-six (13.5%) of the 193 DVAs had associated signal-intensity abnormalities in their drainage territory. Five of the 26 DVAs with signal-intensity abnormalities were associated with cavernous malformations. After excluding the DVAs with associated CMs, an adjusted prevalence of 21/181 (11.6%) for associated signal-intensity abnormalities in DVAs was obtained. No diffusion restriction was identified in the brain parenchyma adjacent to the signal abnormalities. Examples of DVA-associated signal abnormalities are shown in Fig 1.

The Table outlines the association of signal abnormalities with other factors by using 193 DVAs from 172 subjects. The presence of increased FLAIR and T2 signal abnormality was associated with the presence of both CMs and parenchymal atrophy. Specifically, 5/26 (19.2%) DVAs with signal abnormality were associated with CMs versus only 7/167 (4.2%) DVAs without signal abnormality ($P' = .003$, $P'' = .002$). Five of 26 (19.2%) DVAs with signal abnormality were associated with parenchymal atrophy versus 3/167 (1.8%) DVAs without signal abnormality ($P' < .001$, $P'' = .004$). Examples of CMs and parenchymal atrophy associated with signal-positive DVAs are shown in Figs 2 and 3, respectively.

There was a trend toward lobar location being associated with signal abnormality, but this did not reach statistical significance ($P' = 0.26$, $P'' = 0.589$). The depth of the DVA was found to be associated with signal abnormality by using χ^2 analysis, but it did not reach statistical significance by using a multivariate logistic regression analysis. Specifically, periventricular depth was more likely to be associated with signal abnormality than juxtacortical or subcortical depth. Eight of 27 (29.6%) periventricular DVAs had associated signal abnormalities versus 8/96 (8.3%) juxtacortical and 10/70 (14.3%) subcortical DVAs ($P' = .016$, $P'' = .909$). The direction of venous drainage was independently associated with signal abnormality. Specifically, deep or bidirectional venous drainage was more likely to be associated with signal abnormality than superficial venous drainage. Fourteen of 66 (21.2%) deep and 3/6 (50%) bidirectional draining DVAs had associated signal abnormalities versus 9/121 (7.4%) superficial draining DVAs ($P' = .001$, $P'' = .047$).

A lower subject age was associated with signal abnormality. Specifically, the median age of those subjects with signal abnormality was 7.3 ± 5.5 years (95% CI, 5.1–9.5) compared with 11.4 ± 6.6 years (95% CI, 10.4–12.4) for those subjects without signal abnormalities ($P' = .003$, $P'' = .001$). When subsets of age groups were further investigated, the prevalence of signal abnormalities was 5/19 (26%) in subjects 12–36 months, 12/68 (17.6%) in subjects 3–10 years, 4/75 (5.6%) in subjects 11–20 years, and 1/11 (9.1%) in subjects older than 20 years of age (Fig 4). An

Signal abnormalities related to subject age, sex, CM, and parenchymal atrophy

	Signal Abnormality	No Signal Abnormality	Total	P'	OR (95% CI)[a]	P''
Total No.	26[b]	167[c]	193[d]			
Demographics						
Age	7.3 ± 5.5 [5.1–9.5]	11.4 ± 6.6 [10.4–12.4]	10.8 ± 6.6 [9.9–11.8]	.003	0.84 (0.76–0.94)	.001
Female	10 (38.5%)	75 (44.9%)	85 (44%)	.538	0.94 (0.32–2.83)	.918
Associated abnormalities						
Focal atrophy	5 (17.8%)	3 (1.8%)	8 (4.1%)	<.001	17.1 (2.52–117)	.004
CM	5 (19.2%)	7 (4.2%)	12 (6.2%)	.003	19.3 (2.95–126)	.002
Location				.260		.589
Lobar	24 (92.3%)	129 (77.2%)	153 (79.3%)		1.0	
Thalamus/BG	0 (0%)	6 (3.6%)	6 (3.1%)		0 (0–∞)	
Cerebellum/BS	2 (7.7%)	32 (19.2%)	34 (17.6%)		0.37 (0.05–2.49)	
Depth of draining vein				.016		.909
Periventricular	8 (30.8%)	19 (11.4%)	27 (14%)		1.0	
Subcortical	10 (38.5%)	60 (35.9%)	70 (36.3%)		0.73 (0.18–3.01)	
Juxtacortical	8 (30.8%)	88 (52.7%)	96 (49.7%)		0.81 (0.16–4.09)	
Direction of draining vein				.001		.047
Superficial	9 (34.6%)	112 (67.1%)	121 (62.7%)		1.0	
Deep	14 (53.8%)	52 (31.1%)	66 (34.2%)		5.21 (1.22–22.2)	
Both	3 (11.6%)	3 (1.8%)	6 (3.1%)		6.85 (0.84–56.0)	

Note:—BS indicates brain stem; BG, basal ganglia; P', univariate analysis (t test or χ² test); P'', multivariate logistic regression; brackets, 95% confidence interval for age.
[a] OR for age is expressed as the likelihood of signal abnormality with each additional year. OR for sex is expressed as the likelihood of signal abnormality for a female subject. ORs for focal atrophy and CM are expressed as the likelihood of signal abnormality in the presence of either associated abnormality. ORs for location, depth, and direction of draining vein are expressed as the likelihood of signal abnormality compared with the first DVA morphologic descriptor (eg, lobar, periventricular, superficial), defined as a baseline OR of 1.0.
[b] % is the percentage of DVAs with a certain characteristic or associated finding divided by the total number of DVAs with signal abnormality.
[c] % is the percentage of DVAs with a certain characteristic or associated finding divided by the total number of DVAs without signal abnormality.
[d] % is the percentage of DVAs with a certain characteristic or associated finding divided by the total number of DVAs.
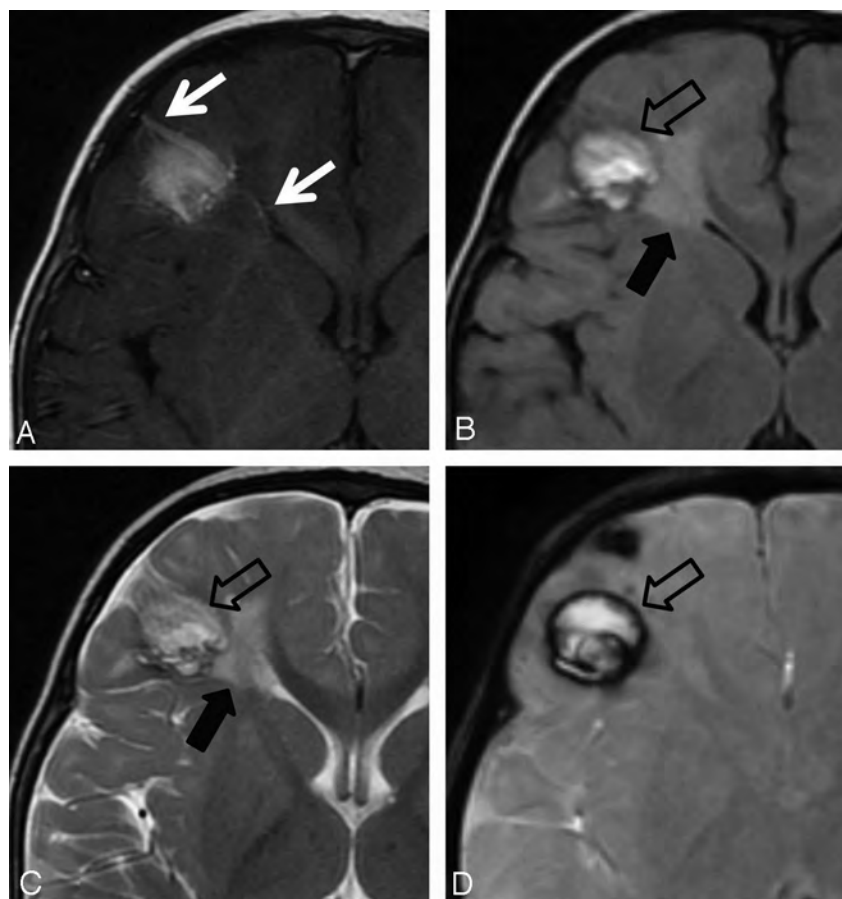
FIG 2. DVA with associated signal abnormality (*black arrows*) and CM (*open black arrows*) in a 13-month-old boy. *A*, T1WI with contrast. *B*, FLAIR. *C*, T2WI. *D*, SWI. Right frontal lobe DVA with subcortical depth and bidirectional venous drainage (*white arrows*).

example of signal abnormality in the very young age group (12–36 months) is given in Fig 5. There was a trend toward more males with signal abnormalities than females, but this was not statistically significant (P' = .538, P'' = .918). We found no association between clinical indication and signal abnormalities. Secondary imaging findings of CMs and atrophy remote from the DVA were associated with signal abnormalities (On-line Table 1). Secondary imaging findings of remote intracranial mass were associated with the absence of signal abnormality (On-line Table 2).

Twenty-one of 26 (80.1%) DVAs with associated signal abnormality had follow-up examinations with a median follow-up of 26 months (1–42 months). The median number of follow-up MR imaging examinations for these 21 DVAs was 2 (1–7 examinations). There was no change in the extent or character of signal abnormalities on follow-up in 19 of 21 DVAs with associated signal abnormality alone. Two DVAs with signal abnormality alone showed a subtle decrease in signal abnormality on follow-up examinations. These patients were 2 years and 17 months of age at the time of initial study with a follow-up of 3 and 4 years, respectively (Fig 6). Two of
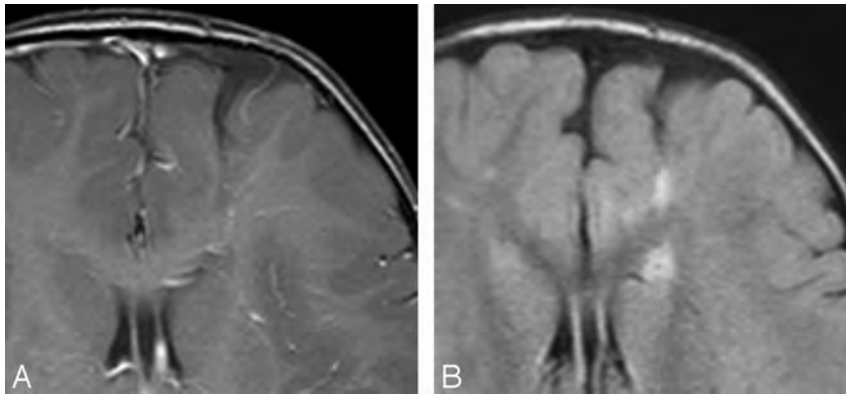
FIG 3. DVA in a 23-month-old boy with associated signal abnormality and parenchymal atrophy. *A*, T1WI with contrast. *B*, FLAIR. Left frontal lobe DVA with periventricular depth and deep venous drainage. Note the increased FLAIR and T2 signal abnormality with associated parenchymal atrophy.
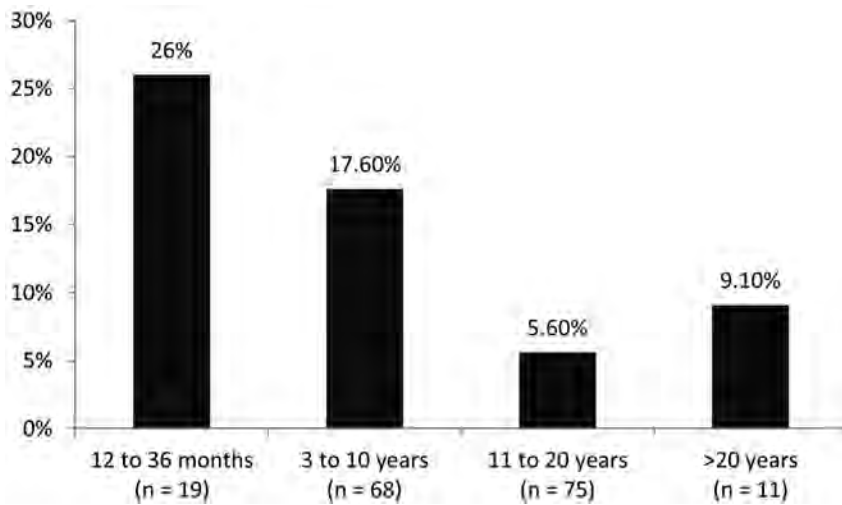
FIG 4. Percentage signal abnormalities associated with DVAs by age group. *n* indicates the number of subjects in each age group.

the 5 DVAs with signal abnormality and associated CMs showed a decrease in signal hyperintensity on follow-up examinations.

DISCUSSION

The major finding of this study is that in children and young adults, signal-intensity abnormalities detectable by MR imaging were identified in 11.6% of consecutively identified DVAs. This is similar to the prevalence identified in prior investigations of adult patients.[10] Although not proved, our results suggest that these signal abnormalities occur with a higher prevalence in younger patients and may decrease with brain maturation. To our knowledge, this is a novel finding because change in signal with time has not been identified in any of the similar studies performed in adults.[9-11] Additional parenchymal abnormalities such as CMs and parenchymal atrophy were strongly associated with signal abnormalities. Finally, we identified deep venous drainage as the only morphologic characteristic of DVAs that is independently predictive of associated signal abnormality.

The etiology of parenchymal signal abnormalities associated with DVAs in adults and children is incompletely understood. Prior investigators have suggested that abnormal FLAIR signal intensity may represent edema or gliosis secondary to chronic venous insufficiency/hypertension related to anomalous venous drainage.[9,10] Altered hemodynamics in the drainage territory of DVAs has been established with case reports that described increased perfusion parameters in "atypical" DVAs.[14,15] More recently, a larger study of DVAs found increased relative CBV, relative CBF, and MTT in most DVA studies.[12] Additionally, they found that those DVAs with associated CMs had higher MTT values than those DVAs without CMs, suggesting that hemodynamic factors may influence parenchymal manifestations of DVAs. A similar study of perfusion parameters in the setting of white matter signal abnormalities would be informative. Perfusion was performed in too few of our cases to evaluate its possible contribution to signal abnormalities. Other studies have suggested that stenosis of the draining vein may cause venous hypertension/insufficiency.[16,17] A recent investigation of morphologic factors associated with CMs and DVAs found tortuosity of the medullary veins and angulation of the draining vein to be associated with the presence of a CM in the DVA territory.[18] This finding also supports the hypothesis that hemodynamic variables may impact the presence of parenchymal abnormalities. Given the small size of most DVAs in our study, resolution was not adequate to assess draining vein stenosis and medullary vein tortuosity.

Based on these prior investigations of parenchymal abnormalities associated with DVAs, our hypothesis was that the prevalence of white matter signal abnormalities would be less common in children than in adults. Contrary to our hypothesis, we found a nearly equal prevalence of brain parenchymal signal abnormalities in children and young adults (median age, 10 years) (11.6%) compared with older adults (median age, 47 years) (12.5%).[10] Most interesting, when we performed a subset analysis by age group, we identified an unexpected inverse relationship between subject age and signal abnormality, with the highest prevalence being found in the youngest subjects and the lowest prevalence in teenagers. When we compared our findings with those of Santucci et al,[10] which found a higher prevalence of signal abnormalities in older patients, a bimodal age distribution of signal abnormalities is suggested. The highest prevalence of signal abnormalities occurs in the very young, steadily decreases to a nadir in the teenage and early adult years, and then increases with age. One possible explanation for this finding is delayed myelination in the drainage territory of the DVA in young children. Perhaps alterations in the venous pressure within the DVA cause delayed egress of inter-
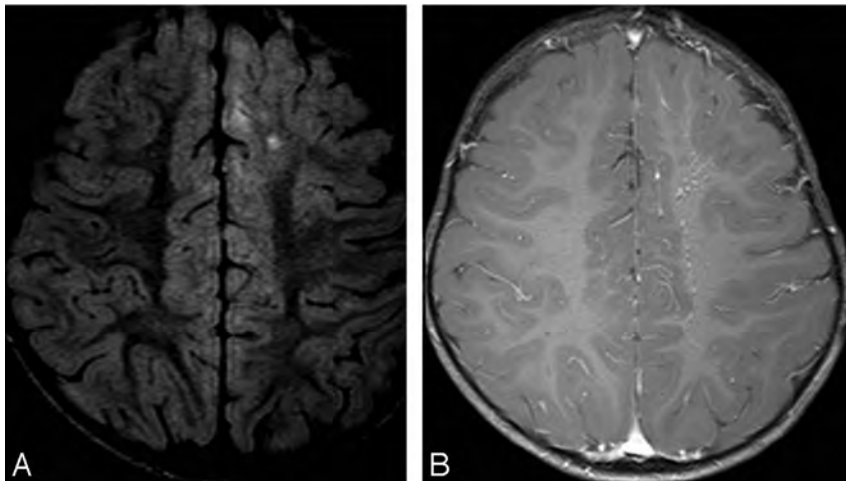
FIG 5. FLAIR (*A*) and T1WI with contrast (*B*) show signal abnormality in the images of a 23-month-old boy, showing relative increased signal within the drainage territory of the DVA compared with normal contralateral myelinating white matter. Left frontal lobe DVA with periventricular depth and deep venous drainage.
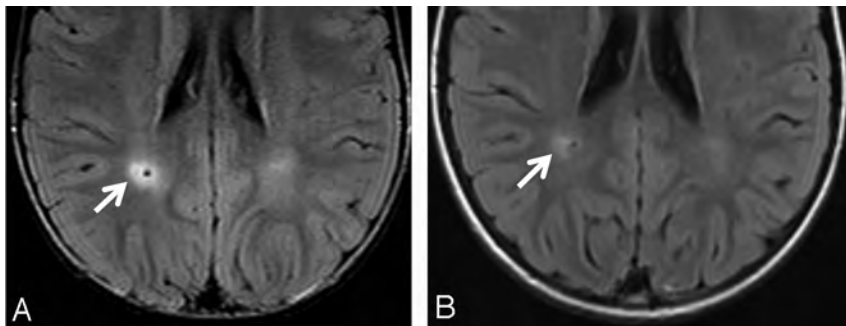

FIG 6. DVA with a subtle decreased extent of signal abnormality on follow-up examination. Axial FLAIR images at 2 years (*A*) and 5 years (*B*) of age. Note subtle decreased signal intensity in the drainage territory of the DVA along the lateral aspect of the DVA draining vein.

stitial water as myelination progresses in infancy and early childhood, leading to relatively increased signal intensity in the brain parenchyma drained by the DVA.[19]

If the higher prevalence of signal abnormalities in a younger population is to be explained by delayed myelination, we would expect some percentage of these signal abnormalities to decrease or resolve with time with progressive myelination. In fact, this was our observation, because 2 of the 21 DVAs with signal abnormality alone did demonstrate subtle decreased signal abnormality on follow-up examinations. On the basis of our study and the existing adult literature, it is interesting to speculate that myelination changes may be primarily responsible for signal abnormalities in the DVA drainage territory in infants and young children, resolving or becoming less apparent in older children and adolescents. With aging, gliosis may become a more dominant process, becoming nonreversible on imaging evaluation. Additional investigations with larger populations of young children, expanded mixed-age populations, and more subjects with long-term follow-up will be needed to confirm these age associations.

As we investigated the possible association of DVA morphology and location with the presence of signal abnormality, we identified deep venous drainage as the only independently predictive variable. The physiologic basis for this association is uncertain, but perhaps cerebral deep venous drainage has less venous flow capacity and may be more likely to cause venous insufficiency/hypertension. Deep venous drainage has been identified as a significant predictor of hemorrhage in arteriovenous malformations.[20-22] We found no significant association between the location of the DVA and signal abnormality. This finding is supported by a similar study in adults, which found no association with DVA location.[10] The DVA depth was associated with signal abnormality when using univariate analysis, but not when using a multivariate analysis, suggesting that the influence of depth on signal is related, in some fashion, to the direction of drainage.

In the course of our investigation of white matter signal abnormalities, we were interested in identifying the prevalence of other well-documented parenchymal abnormalities associated with DVAs, namely CMs[1-3] and parenchymal atrophy.[9] The prevalence of CMs (6.2%) in our study population is similar to that of 2 previously reported studies investigating the association of DVAs and CMs in adults, which found CMs in 3.4%[10] and 13.3% of DVAs.[9] This outcome was contrary to our expectations because many have suggested that the development of CMs in the DVA drainage territory is a dynamic process that evolves with time, beginning with small microhemorrhages within the drainage territory of DVAs.[23-27] Under such a scenario, one would expect the prevalence of CMs associated with DVAs to increase with time and be more common in adults than in children. We also found that those DVAs with CMs were more likely to have associated signal abnormality. Despite the small number of cavernous malformations, this association reached statistical significance. The association between signal abnormality and CMs is problematic because the etiology of the signal abnormality may not be confidently attributed to the presence of the DVA alone. One could argue that the signal abnormality is secondary to hemorrhage of the CM; however, this association between signal abnormality and cavernous malformations is supported by a recent investigation of DVAs in adults by using susceptibility-weighted imaging to identify the prevalence of hypointense foci on SWI within the drainage territory of DVAs.[11] The study found that white matter hyperintense lesions were more frequently observed in patients with hypointense SWI foci versus those without hypointense SWI foci. Additionally, the study found a 62% prevalence of SWI hypointense foci in the study population, which is much higher than that in our study. This discrepancy may, in part, be explained by the relatively small number of examinations that included SWI in our study. Alternatively, SWI hypointense foci may be less com-

monly encountered in the pediatric population. A dedicated examination of hypointense foci in children by using SWI is warranted.

In regard to parenchymal atrophy and associated signal abnormalities, we found a low prevalence of parenchymal atrophy (4.1%), significantly less than that in a study of adults (29.7%).[9] This may be related to the development of localized atrophy with increasing age but could also be related to selection bias used in some prior investigations (ie, potentially selecting only larger DVAs for evaluation). Atrophy was more commonly encountered in those DVAs with associated signal abnormality, suggesting that these 2 parenchymal abnormalities may share common etiologic factors such as venous hypertension/insufficiency.

We found no association between clinical indication and signal abnormalities, suggesting that these signal abnormalities are predominantly asymptomatic or have no typical presenting symptoms associated with them. When we evaluated possible associations with secondary imaging findings and signal abnormalities, we found an association between CMs and atrophy remote from the DVA. The association of atrophy remote from the DVA is noteworthy. It may be that factors contributing to remote atrophy (eg, radiation, ischemia, systemic venous hypertension, and so forth) make the development of signal abnormality in the DVA territory more likely, especially if the altered hemodynamics within the DVA territory predispose this brain parenchyma to such injury. Finally, a peculiar association identified in our study was that DVAs without signal abnormality were associated with a secondary imaging finding of a remote intracranial mass. We have no explanation for this association, and it may represent a statistical anomaly.

Our study does have some limitations. Case selection was based initially on imaging reports. Some small DVAs may have been missed and therefore not selected for our study cohort. Clinical indications were often obtained from the study indication and may not fully represent the patient's clinical presentation. The relatively small number of subjects limits our ability to compare DVA characteristics and signal change between age subgroups. The differentiation between DVA-related parenchymal signal changes and intrinsic DVA-related signal can be problematic; however, it has been applied successfully in prior studies by our group.[10]

CONCLUSIONS

Signal-intensity abnormalities detectable by standard clinical MR images were identified in 13.5% of consecutively identified DVAs in children and young adults (11.6% adjusted prevalence when CMs were excluded). Signal abnormalities were more common in DVAs with associated CM and parenchymal atrophy, with deep venous drainage, and in younger subjects in our cohort. The pathophysiology of these signal-intensity abnormalities remains unclear but may represent effects of delayed myelination and/or alterations in venous flow within the DVA drainage territory. More work in this area is warranted.

REFERENCES

1. Abe T, Singer RJ, Marks MP, et al. **Coexistence of occult vascular malformations and developmental venous anomalies in the central nervous system: MR evaluation.** *AJNR Am J Neuroradiol* 1998; 19:51–57
2. Beall DP, Bell JP, Webb JR, et al. **Developmental venous anomalies and cavernous angiomas: a review of the concurrence, imaging, and treatment of these vascular malformations.** *J Okla State Med Assoc* 2005;98:535–38
3. Perrini P, Lanzino G. **The association of venous developmental anomalies and cavernous malformations: pathophysiological, diagnostic, and surgical considerations.** *Neurosurg Focus* 2006; 21:e5
4. Ballarin R, Di Benedetto F, De Ruvo N, et al. **Thrombosis of developmental venous anomalies of the brain after liver transplantation.** *Transplantation* 2009;87:615–16
5. Dorn F, Brinker G, Blau T, et al. **Spontaneous thrombosis of a DVA with subsequent intracranial hemorrhage.** *Clin Neuroradiol* 2013;23:315–57
6. Kiroglu Y, Oran I, Dalbasti T, et al. **Thrombosis of a drainage vein in developmental venous anomaly (DVA) leading venous infarction: a case report and review of the literature.** *J Neuroimaging* 2011;21:197–201
7. Lai PH, Chen PC, Pan HB, et al. **Venous infarction from a venous angioma occurring after thrombosis of a drainage vein.** *AJR Am J Roentgenol* 1999;172:1698–99
8. Teo M, St George J, Jenkins S, et al. **Developmental venous anomalies: two cases with venous thrombosis.** *Br J Neurosurg* 2012;26:886–87
9. San Millán Ruíz D, Delavelle J, Yilmaz H, et al. **Parenchymal abnormalities associated with developmental venous anomalies.** *Neuroradiology* 2007;49:987–95
10. Santucci GM, Leach JL, Ying J, et al. **Brain parenchymal signal abnormalities associated with developmental venous anomalies: detailed MR imaging assessment.** *AJNR Am J Neuroradiol* 2008;29:1317–23
11. Takasugi M, Fujii S, Shinohara Y, et al. **Parenchymal hypointense foci associated with developmental venous anomalies: evaluation by phase-sensitive MR imaging at 3T.** *AJNR Am J Neuroradiol* 2013;34:1940–44
12. Sharma A, Zipfel GJ, Hildebolt C, et al. **Hemodynamic effects of developmental venous anomalies with and without cavernous malformations.** *AJNR Am J Neuroradiol* 2013;34:1746–51
13. Lee C, Pennington MA, Kenney CM, 3rd. **MR evaluation of developmental venous anomalies: medullary venous anatomy of venous angiomas.** *AJNR Am J Neuroradiol* 1996;17:61–70
14. Kroll H, Soares BP, Saloner D, et al. **Perfusion-CT of developmental venous anomalies: typical and atypical hemodynamic patterns.** *J Neuroradiol* 2010;37:239–42
15. Camacho DL, Smith JK, Grimme JD, et al. **Atypical MR imaging perfusion in developmental venous anomalies.** *AJNR Am J Neuroradiol* 2004;25:1549–52
16. Truwit CL. **Venous angioma of the brain: history, significance, and imaging findings.** *AJR Am J Roentgenology* 1992;159:1299–307
17. Dillon WP. **Cryptic vascular malformations: controversies in terminology, diagnosis, pathophysiology, and treatment.** *AJNR Am J Neuroradiol* 1997;18:1839–46
18. Hong YJ, Chung TS, Suh SH, et al. **The angioarchitectural factors of the cerebral developmental venous anomaly: can they be the causes of concurrent sporadic cavernous malformation?** *Neuroradiology* 2010;52:883–91
19. Branson HM. **Normal myelination: a practical pictorial review.** *Neuroimaging Clin N Am* 2013;23:183–95
20. Kader A, Young WL, Pile-Spellman J, et al. **The influence of hemodynamic and anatomic factors on hemorrhage from cerebral arteriovenous malformations.** *Neurosurgery* 1994;34:801–07, discussion 807–08

21. Langer DJ, Lasner TM, Hurst RW, et al. **Hypertension, small size, and deep venous drainage are associated with risk of hemorrhagic presentation of cerebral arteriovenous malformations.** *Neurosurgery* 1998;42:481–86, discussion 487–89

22. Turjman F, Massoud TF, Vinuela F, et al. **Correlation of the angio-architectural features of cerebral arteriovenous malformations with clinical presentation of hemorrhage.** *Neurosurgery* 1995;37:856–60, discussion 860–62

23. Maeder P, Gudinchet F, Meuli R, et al. **Development of a cavernous malformation of the brain.** *AJNR Am J Neuroradiol* 1998;19:1141–43

24. Cakirer S. **De novo formation of a cavernous malformation of the brain in the presence of a developmental venous anomaly.** *Clin Radiol* 2003;58:251–56

25. Campeau NG, Lane JI. **De novo development of a lesion with the appearance of a cavernous malformation adjacent to an existing developmental venous anomaly.** *AJNR Am J Neuroradiol* 2005;26:156–59

26. Awad IA, Robinson JR, Jr, Mohanty S, et al. **Mixed vascular malformations of the brain: clinical and pathogenetic considerations.** *Neurosurgery* 1993;33:179–88, discussion 188

27. Rigamonti D, Spetzler RF, Medina M, et al. **Cerebral venous malformations.** *J Neurosurg* 1990;73:560–64

Enhanced Repair Effect of Toll-Like Receptor 4 Activation on Neurotmesis: Assessment Using MR Neurography

H.J. Li, X. Zhang, F. Zhang, X.H. Wen, L.J. Lu, and J. Shen

ABSTRACT

BACKGROUND AND PURPOSE: Alternative use of molecular approaches is promising for improving nerve regeneration in surgical repair of neurotmesis. The purpose of this study was to determine the role of MR imaging in assessment of the enhanced nerve regeneration with toll-like receptor 4 signaling activation in surgical repair of neurotmesis.

MATERIALS AND METHODS: Forty-eight healthy rats in which the sciatic nerve was surgically transected followed by immediate surgical coaptation received intraperitoneal injection of toll-like receptor 4 agonist lipopolysaccharide ($n = 24$, study group) or phosphate buffered saline ($n = 24$, control group) until postoperative day 7. Sequential T2 measurements and gadofluorine M-enhanced MR imaging and sciatic functional index were obtained over an 8-week follow-up period, with histologic assessments performed at regular intervals. T2 relaxation times and gadofluorine enhancement of the distal nerve stumps were measured and compared between nerves treated with lipopolysaccharide and those treated with phosphate buffered saline.

RESULTS: Nerves treated with lipopolysaccharide injection achieved better functional recovery and showed more prominent gadofluorine enhancement and prolonged T2 values during the degenerative phase compared with nerves treated with phosphate buffered saline. T2 values in nerves treated with lipopolysaccharide showed a more rapid return to baseline level than did gadofluorine enhancement. Histology exhibited more macrophage recruitment, faster myelin debris clearance, and more pronounced nerve regeneration in nerves treated with toll-like receptor 4 activation.

CONCLUSIONS: The enhanced nerve repair with toll-like receptor 4 activation in surgical repair of neurotmesis can be monitored by using gadofluorine M-enhanced MR imaging and T2 relaxation time measurements. T2 relaxation time seems more sensitive than gadofluorine M-enhanced MR imaging for detecting such improved nerve regeneration.

ABBREVIATIONS: LFB = Luxol fast blue; LPS = lipopolysaccharide; PBS = phosphate buffered saline; SFI = sciatic functional index; SI = signal intensity; TLR = toll-like receptor

Neurotmesis is the most common type of traumatic peripheral nerve injury and could result in complete paralysis of an affected limb or development of intractable neuropathic pain.[1] Peripheral nerve repair, either by direct suturing of the nerve ends or by nerve grafting, remains the standard treatment of choice. However, despite advancements of microsurgical techniques and

different repair methods, full functional outcome, especially of motor function, is rarely achievable.[2] Alternative use of Schwann cell or stem cell–based tissue-engineered conduits has been shown to exert a beneficial effect on peripheral nerve repair. However, the number of regenerating neurons following injury and repair is still suboptimal.[3] Other strategies, particularly the use of molecular approaches, are promising for improving nerve regeneration in surgical repair of neurotmesis.[4]

The success of nerve regeneration depends largely on the severity of the initial injury and resultant degenerative changes.[5] A variety of cellular and molecular mechanisms are found to regulate Wallerian degeneration and axonal regeneration in the injured peripheral nerve.[6] Recent studies demonstrated that toll-like receptor (TLR) signaling is critical for Wallerian degeneration and functional recovery in peripheral nerve injury[7] and spinal cord injury.[8] The use of TLR4 agonist lipopolysaccharide (LPS) was able to accelerate myelin phagocytosis during Wallerian de-

generation in the crushed sciatic nerve and injured spinal cord, thereby promoting recovery of nerve functions.[7,8]

MR neurography, including quantitative T2 measurements, has been widely used to evaluate traumatic injuries of peripheral nerves,[9,10] to monitor native process of nerve recovery,[11] and to reveal enhanced nerve regeneration by stem cell transplantation in peripheral nerve injuries.[12] Taking advantage of a strong affinity for degenerating nerve tissues, gadofluorine M-enhanced MR imaging has been successfully applied to monitor nerve regeneration in transected nerve repaired with tissue-engineered nerve conduits.[13] However, little is known about the use of MR neurography to evaluate nerve repair with surgical coaptation in presence of simultaneous TLR4 pathway activation.

The purpose of this study was to observe the longitudinal changes of nerve repair on MR imaging and then to determine whether the enhanced nerve regeneration with use of TLR4 activation in surgical repair of neurotmesis could be assessed by gadofluorine M-enhanced MR imaging or nerve T2 relaxation time measurement.

MATERIALS AND METHODS
Animals and Surgery
All interventions and animal care procedures were performed in accordance with the Guidelines and Policies for Animal Surgery provided by our university and were approved by the Institutional Animal Use and Care Committee. All animals were obtained from the Animal Experiment Center of our university and were housed in a standard animal facility with 12-hour on/off light conditions, and allowed free access to standard food and water. Forty-eight adult Sprague-Dawley rats weighing 250 $\pm$ 20 g were used to establish peripheral nerve transection injury models. Animals were anesthetized with an intraperitoneal injection of sodium pentobarbital at a dosage of 30 mg per kilogram of body weight (Sigma-Aldrich, St Louis, Missouri). After anesthesia, the left hind limb of each animal was selected to establish sciatic nerve transection injury. In brief, the sciatic nerve was exposed and transected at the midportion of the nerve trunk. Immediately after transection, the nerve was repaired in an end-to-end coaptation with the manner of epineural suturing. The wound was then closed and the animal was returned and housed separately. The right hind limb served as the control, on which sham operations (incision and exploration of the nerve only) were performed.

After surgery, animals were randomly assigned to 2 groups by means of a random number table. The first group was subdivided into groups A ($n = 6$) and B ($n = 6$), and the second group was subdivided into groups C ($n = 18$) and D ($n = 18$). Groups A and C received daily intraperitoneal injection of LPS (Sigma-Aldrich) at a dosage of 0.32 mg per kilogram of body weight for 7 days postoperatively, as previously reported,[8] whereas groups B and D received intraperitoneal injection of the same volume of phosphate buffered saline (PBS) as controls. Animals of the first group (subgroups A and B) underwent serial MR imaging before surgery (baseline), at 3 days, and 1, 2, 3, 4, 6, and 8 weeks after the surgery. In the second group (subgroups C and D), 6 animals each were randomly selected and sacrificed for histologic evaluation at 1, 3, and 6 weeks after MR imaging.

MR Imaging
MR imaging was performed on a 1.5T scanner (Intera; Philips Medical Systems, Best, the Netherlands) with use of a 5-cm linearly polarized birdcage radiofrequency mouse coil (Chenguang Medical Technologies, Shanghai, China). After anesthesia, animals were placed in the prone position. Coronal images including T2WI and T2 measurements and gadofluorine-enhanced T1WI were obtained in a longitudinal plane parallel to the course of the sciatic nerve. T2WI was acquired by using a 3D FSE sequence (TR/TE = 2500/138 ms, flip angle = 90°, echo-train length = 25, section thickness = 1 mm, section gap = 0 mm); T2 relaxation data were obtained by using a single-section multi-spin-echo (TR/TE = 2000/20–160 ms; echo spacing, 20 ms) sequence as previously described.[11] Gadofluorine M (250 mmol Gd/L; Bayer Schering Pharma, Berlin, Germany) enhanced imaging was acquired by using fat-suppressed 2D FSE T1WI (TR/TE = 300/17 ms, flip angle = 120°, section thickness = 1 mm, section gap = 0 mm) 24 hours after intravenous injection of gadofluorine M at a dose of 0.1 mmol/L/kg body as previously described.[13] Other parameters of all sequences were: FOV = 60 $\times$ 60 mm, matrix size = 512 $\times$ 512, and NEX = 2.

The nerve signal abnormalities were observed in a blinded manner by 2 authors in consensus (J.S., with more than 10 years of experience with musculoskeletal MR imaging, and F.Z., with 5 years of experience with musculoskeletal MR imaging). Nerve signal intensities (SIs) and T2 relaxation times were measured by these 2 authors independently and in a blinded manner. The average values from the 2 datasets were used for analysis. SIs of the distal stumps of the injured nerves and the sham-operated nerves were measured on gadofluorine M–enhanced T1WI. Nerve enhancement rate was calculated as the ratio of SI of the injured nerve to SI of contralateral sham-operated nerves. T2 relaxation times of the distal stumps were measured by using the region of interest technique. For each measurement, a rectangular region of interest with a minimal size of 85 pixels covering a 10-mm proximal segment of the distal stump was placed within the nerve and along the course of the nerve. The average value generated from all analyzed pixels of each region of interest was adopted and an effort was made to avoid including fatty tissue, edema, and muscle in the measured volume, as previously described.[13]

Functional Assessment
Sciatic nerve functional recovery was assessed in subgroups A and B by using walking track analysis, which was performed at each time point before MR imaging by 2 authors (X.Z. and X.H.W., both with 3 years of experience with sciatic nerve functional assessment) in a blinded manner by consensus. The sciatic functional index (SFI) was calculated by the formula of Bain et al[14] as an indicator of nerve locomotor dysfunction.

Histologic Examination
Animals in the second group (subgroups C and D) were sacrificed after MR imaging at specific time points by transcardial perfusion with PBS followed by 4% paraformaldehyde in 0.1 mol/L PBS (pH = 7.4). The distal stumps of the injury nerves were harvested and postfixed in 4% paraformaldehyde for 1 hour and then cryoprotected in 20% sucrose solution until examination. In addition,
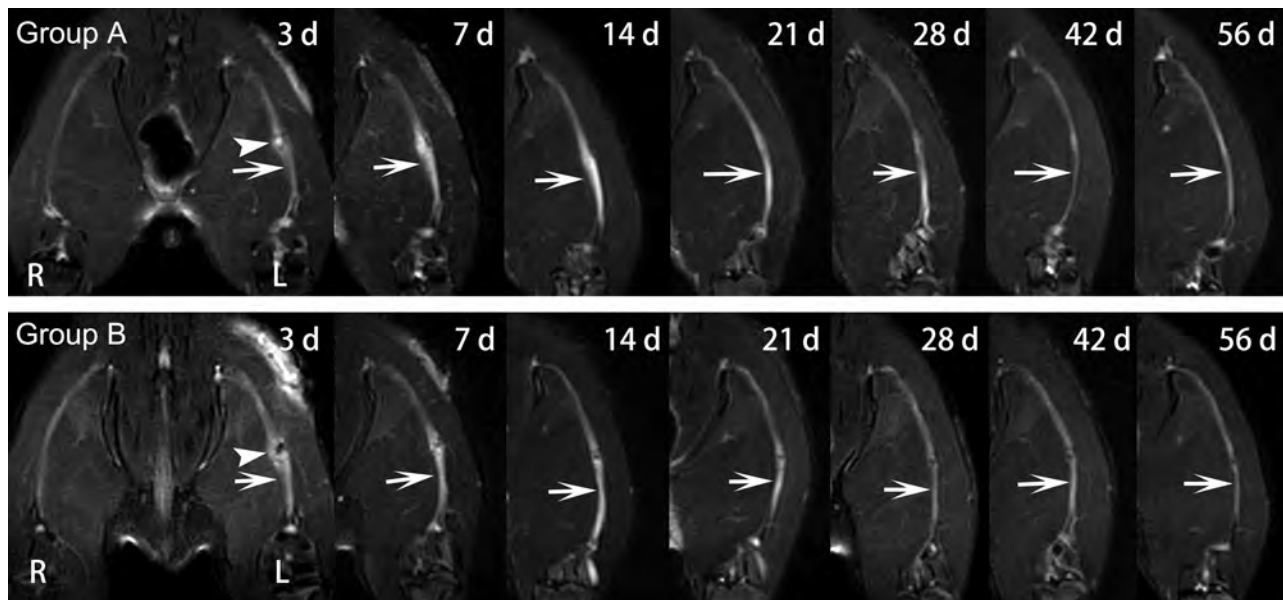
FIG 1. Sequential fat-suppressed T2-weighted images of injured nerves repaired with epineural coaptation. Nerves in group A (LPS treatment) and group B (PBS treatment) show obvious signal abnormalities in the lesion site (*arrowhead*) and distal stumps (*arrows*), which gradually declined over time. R = right hind limb; L = left hind limb.

a 5-mm segment distal to the injured site was prepared from each distal nerve stump. Contiguous 6-μm cross-sections were obtained from the distal end of the tissue specimens and processed for Luxol fast blue (LFB) (Sigma-Aldrich) and oil red (Sigma-Aldrich) staining as described[7] to detect myelin load and myelin debris. Contiguous 15-μm thickness longitudinal sections were obtained in the proximal end of the tissue specimens and processed for multiple immunohistochemical staining to assess macrophage infiltration, TLR4 expression, Schwann cell proliferation, and axonal regeneration. Briefly, sections were blocked with donkey serum (10:100 vol/vol) for 30 minutes, followed by incubation overnight at 4°C with primary antibodies against cluster of differentiation 68 (CD68) (1:200 vol/vol; Abcam, Cambridge, United Kingdom) to detect activated macrophages, S-100 (1:200 vol/vol; Abcam) to detect Schwann cells, TLR4 (1:200 vol/vol; Abcam) to detect TLR4 expression, or small proline-rich protein 1A (SPRR1A) to detect regenerating axons (1:200 vol/vol; Abcam). After being rinsed 3 times with PBS, sections were allowed to incubate with the corresponding Alexa Fluor 594- or 488-conjugated secondary antibody (1:200 vol/vol; Invotrogen, Carlsbad, California) at room temperature for 30 minutes and subsequently with 4′,6-diamidino-2-phenylindole (DAPI) for nuclear staining. The immunoreactive signals were then observed by a confocal laser scanning microscope (LSM710; Carl Zeiss, Jena, Germany).

The quantification of LFB myelin staining, the number of activated macrophages, and the number of regenerating axons were measured per nerve segment. For the quantification of LFB myelin staining, the proportional area of tissue occupied by labeling within the entire cross-sectional area was measured by using a microscope (Axio Observer; Carl Zeiss) equipped with a digital imaging analysis system, as described previously.[7] For the quantification of activated macrophages and regenerating axons, the number of labeled cells on CD68-stained longitudinal sections or axons on SPRR1A-stained longitudinal sections per nerve seg-

ment was estimated by the optical fractionator method[7] using the digital image analysis system equipped with a confocal laser scanning microscope (LSM710).

Statistical Analysis

All data are presented as mean ± standard deviation. In groups A and B, gadofluorine enhancement rates, T2 values, and SFIs obtained at specific acquisition points were compared by using a repeated-measures 1-way analysis of variance, followed by the Student-Neuman-Keuls post hoc test for multiple pair-wise comparisons among different times. In groups C and D, the quantification of myelin LFB staining, the number of activated macrophages, and regenerating axons were compared using an independent *t* test. A 2-sided *P* value less than .05 was considered to indicate a significant difference. All statistical tests were performed by using SPSS 13.0 software (IBM, Armonk, New York).

RESULTS
Signal Abnormalities

In groups A and B, obvious nerve enlargement, and substantial gadofluorine enhancement and signal abnormality were observed in the distal stumps 3 days after surgery, followed by gradual decrease during the 8-week follow-up. T2 signal abnormality and nerve enlargement returned to almost normal at 6 weeks after surgery in group A, whereas it was at 8 weeks after surgery in group B (Fig 1). Gadofluorine enhancement in groups A and B slowly declined but persisted until 8 weeks after surgery in the distal stumps of nerve. Gadofluorine enhancement was more prominent in the distal stumps of nerves in group A than in group B during the entire study period (Fig 2).

T2 Values

T2 values are shown in the Table and their time courses are shown in Fig 3. In groups A and B, T2 values in both groups showed a rapid
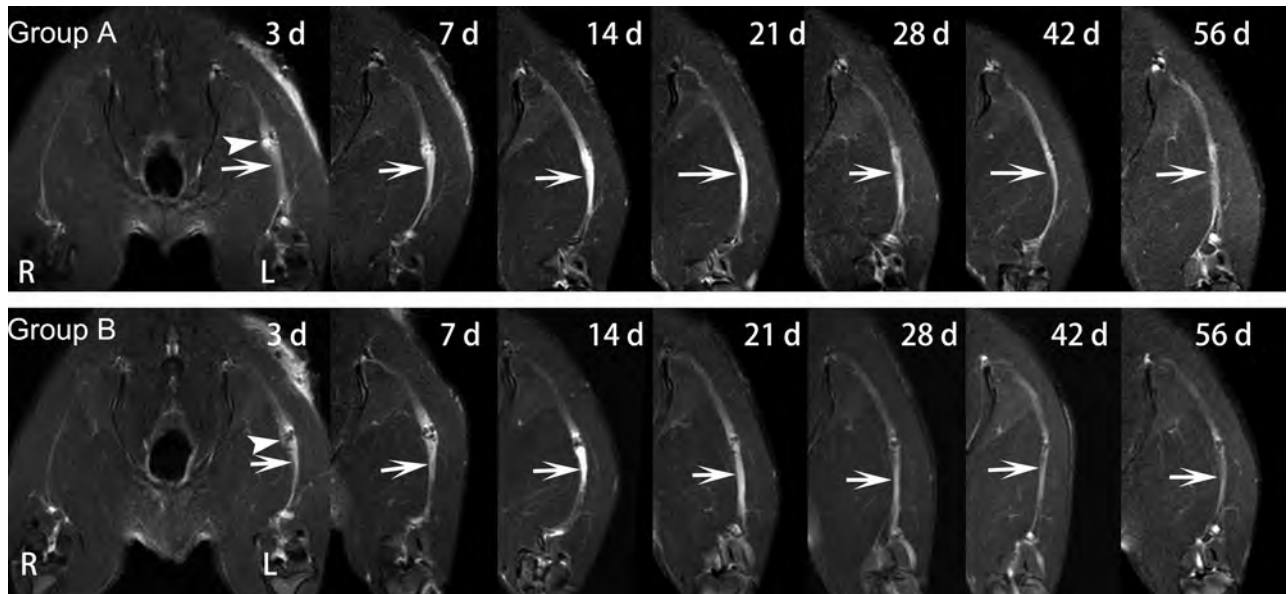
FIG 2. Sequential gadofluorine-enhanced fat-suppressed T1-weighted images of injured nerve repaired with epineural coaptation. Persistent enhancement appears in the lesion site (*arrowhead*) and distal stumps (*arrows*) in group A (LPS treatment) and group B (PBS treatment). R = right hind limb; L = left hind limb.

T2 values and gadofluorine enhancement rates of the distal stumps in the injured nerves after surgical repair

Follow-Up Interval	T2 Values (msec)		Gadofluorine Enhancement Rates (%)	
	Group A	Group B	Group A	Group B
0 Days	44.6 ± 3.0	44.6 ± 2.8	100.4 ± 5.4	101.4 ± 6.0
3 Days	84.5 ± 6.3	73.5 ± 5.5	259.6 ± 12.4	235 ± 10.9
1 Week	80.3 ± 5.2	65.9 ± 8.0	245.9 ± 16.4	220.8 ± 7.3
2 Weeks	68.4 ± 6	59.6 ± 3.7	230.7 ± 16.7	207.5 ± 13.3
3 Weeks	61.1 ± 4.5	56.4 ± 2.5	210 ± 16.5	191 ± 10.2
4 Weeks	49.1 ± 3.4	48.3 ± 6.2	150.3 ± 9.7	138.3 ± 10.9
6 Weeks	47 ± 2.7	45.1 ± 4.8	141.3 ± 4.9	133.4 ± 12.0
8 Weeks	43.8 ± 1.5	43.8 ± 3.1	125.5 ± 11.5	130 ± 4.9
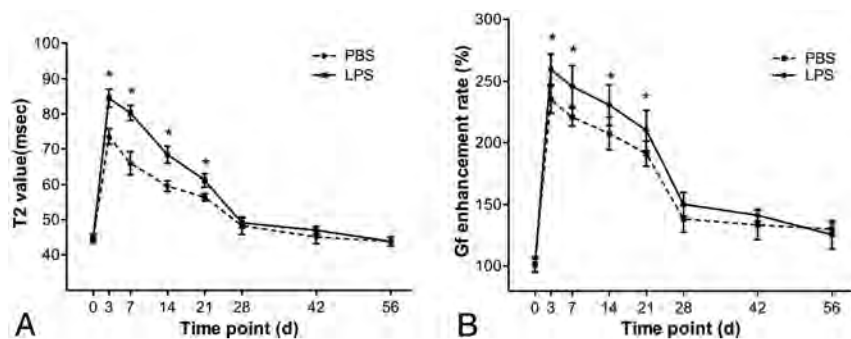
FIG 3. Graphs show the time courses of T2 values (*A*) and gadofluorine enhancement rates for distal stump of injured nerves (*B*) in group A (LPS treatment) and group B (PBS treatment). * = $P < .05$. Vertical bars represent the standard deviation.

increase, then slowly decreased and returned to almost baseline level at 6-week follow-up. Comparatively, the distal stumps in group A had significantly higher T2 values than in group B during the period from 3 days to 3 weeks after surgery ($P = .009 – .048$).

Gadofluorine Enhancement Rates
Gadofluorine enhancement rates are shown in the Table and their time courses are shown in Fig 3. In groups A and B, gadofluorine

enhancement rates of the distal stumps of injured nerves showed a similar time course to T2 values. Gadofluorine enhancement rates in both groups showed a rapid increase, then slowly decreased but remained elevated until 8-week follow-up. The distal stumps in group A had significantly higher gadofluorine enhancement rates than in group B during the period from 3 days to 3 weeks after surgery ($P = .004 – .037$).

Functional Recovery
The SFI values are showed in Fig 4. Nerves in groups A and B both demonstrated maximal functional impairment until 2 weeks after surgery, followed by gradual recovery, and reached preinjury levels by 8 weeks after surgery. The SFIs in group A were significantly higher than those in group B during the period from 3 weeks to 8 weeks after surgery ($P = .003 – .015$).

Histology
Myelin LFB and oil red staining showed that groups C and D had similar myelin swelling at 1 week after surgery. At 3 weeks after surgery, group C had less prominent myelin breakdown or myelin debris than group D. By 6 weeks after surgery, there was more prominent remyelination in group C than in group D (On-line Fig 1). Immunofluorescence staining showed that group C had higher SPPR1A expression at 3 weeks and 6 weeks after surgery (On-line Fig 2), more CD68^{+} macrophages as well as more prominent co-expression of TLR4 in macrophages at 1 week and 3 weeks after surgery (On-line Fig 3), more pronounced Schwann

cell proliferation from 1 week to 6 weeks after surgery, and more prominent co-expression of TLR4 in Schwann cells at 1 week after surgery in comparison with group D (On-line Fig 4).

Quantification of myelin stained with LFB, the number of CD68^{+} macrophages, and the number of regenerating axons are shown in Fig 5. The load of myelin debris was higher in group D compared with group C at 3 weeks after surgery ($P < .001$). The number of CD68^{+} macrophages was significantly higher in group C at 1 week and 3 weeks after surgery ($P = .0007–.0001$), and the number of regenerating axons was higher in group C beginning at 3 weeks after surgery ($P = .0003–.0008$).

DISCUSSION

In our study, systemic injection of LPS was applied to active TLR4 pathways to promote nerve regeneration after surgical repair of the transected nerves. Animals that received LPS injection had more pronounced gadofluorine enhancement and more prolonged T2 values of nerves on MR neurography during the degenerative phase, and achieved slightly higher SFIs and had faster myelin debris clearance and subsequently more pronounced axonal regeneration than those treated with PBS injection.

In Wallerian degeneration following acute nerve injury, axonal degeneration products activate TLR pathway in Schwann cells,[15] then TLR signaling activation initiates the innate immune response and aids in subsequent macrophage recruitment, whereas acute neurodegeneration without any intervention would induce a shift in the TLR expression pattern of Schwann cells from normally high expression of TLR3 and TLR4 to strong expression of TLR1.[16] Further study also suggests that Wallerian degeneration in animals deficient in TLR2 or TLR4 showed impaired macrophage-mediated debris clearance and axon regeneration. When treated with intraneural delivery of TLR2 or TLR4 ligands into the sciatic nerve crush lesion, the recruitment and myelin phagocytic activity of macrophages could be enhanced, myelin debris clearance could be accelerated, and eventually the locomotor recovery was improved as measured by SFI.[7]

MR T2 signal intensities can be used to monitor nerve regeneration after the nerve is transected and then repaired with epineural coaptation.[17] Furthermore, quantitative T2 relaxation time measurement and gadofluorine enhancement on MR imaging are shown to be able to assess the enhanced nerve regeneration associated with stem cell transplantation[12] or stem cell–based tissue-engineered conduit treatment of injured nerves.[13] In this study, besides SFI, nerve regeneration after surgical repair was assessed with T2 relaxation time measurements and gadofluorine-enhanced MR imaging. The result of this study showed that T2 values and gadofluorine enhancement in the distal stumps of surgically repaired nerves with or without TLR4 activation had a similar time course with the functional recovery pattern. A return to baseline T2 values or decline in gadofluorine enhancement is correlated well with locomotor recovery. Because T2 values of the distal stumps of injured nerves returned to baseline level at 6 weeks after surgery while gadofluorine enhancement persisted at 8-week follow-up, T2 values are likely a better predictor for assessment of the nerve repair process.

Our study showed that nerves treated with surgical repair in combination with TLR4 activation achieved better functional recovery. Histology revealed that more macrophage recruitment, higher TLR4 expression in macrophages and Schwann cells, and faster myelin debris clearance were present in the degenerative stage, with a subsequent more prominent axon regeneration and Schwann cell proliferation in the regenerative stage. This confirmed the previous beneficial effect of LPS on nerve regeneration after peripheral nerve injury.[7] Interestingly, these nerves showed a more prolonged T2 value and more pronounced gadofluorine enhancement during the degenerative phase. In normal nerve tissues, T2 relaxation time has been assigned to 3 components in

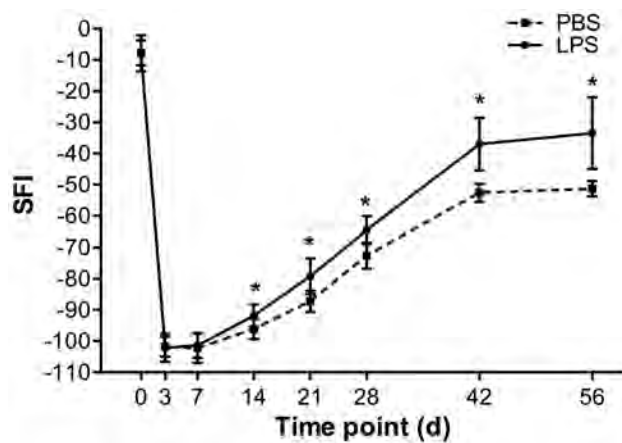**FIG 4.** Graphs show time courses of functional recovery in group A (LPS treatment) and group B (PBS treatment). * = $P < .05$. Vertical bars represent the standard deviation.
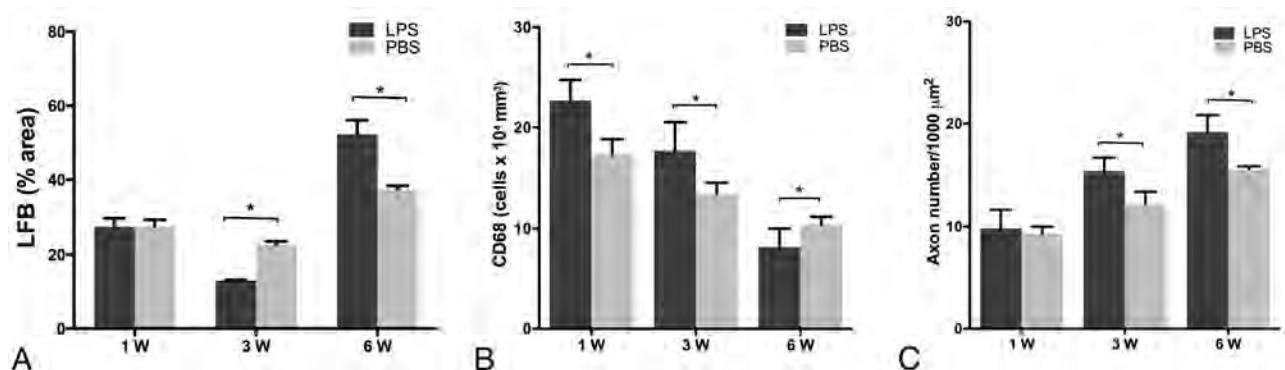

FIG 5. Graphs show the quantification of myelin stained with LFB (A), the number of CD68^{+} macrophages (B), and the number of regenerating axons (C) in group C (LPS treatment) and group D (PBS treatment). * = $P < .05$.

order of increasing T2 value: myelinic, axonal, and extra-axonal water protons.[18] At clinical field strength of MR imaging, intact and disintegrated myelin may not have a crucial effect on the nerve signal on T2-weighted images, whereas axonal disintegration and in particular nerve edema are main determinants for a T2-signal increase.[19] As histology revealed that there was less myelin debris load in the distal nerve treated with TLR4 activation at the degenerative phase, the sustained increase of T2 values in nerves treated with TLR4 activation was likely caused by increased extracellular water content that was associated with relatively larger extracellular space left by the preceding enhanced myelin debris clearance. Gadofluorine M could enter nerves through a disturbed blood-nerve barrier and interacts with local extracellular matrix proteins such as collagens I and IV, proteoglycan, decorin, and tenascin, thereby being locally trapped in the degenerating nerve fibers.[20,21] Histology confirmed that gadofluorine could bind to fibrillary structures of the extracellular space and less frequently, to intracellular myelin debris.[22] The pronounced gadofluorine enhancement in the degenerating nerves treated with TLR4 activation is probably caused by increased extracellular volume in degenerating nerve tissues where more gadofluorine bound to extracellular matrix after their passive diffusion through the disturbed blood-nerve barrier. Therefore, a sustained increase in T2 values or pronounced gadofluorine enhancement in degenerating nerve might indicate a better myelin debris clearance effect relevant to the use of TLR4 activation.

Notably, nerves treated with TLR4 activation showed slightly higher T2 value and prominent gadofluorine enhancement during the regenerative phase. However, no significant difference was determined. This suggested that a major difference in T2 value or gadofluorine enhancement between nerves treated with and without TLR4 activation occurred during the degenerative phase rather than the regenerative phase. As histology revealed that there were more regenerating axons and Schwann cells at the degenerative phase, the marginal increase of T2 values might indicate more prominent nerve regeneration resulted from TLR4 activation treatment. It has been shown that complete clearance of myelin debris usually takes 4 weeks in degenerated nerves,[23] and the nerve degeneration and regeneration process with the blood-nerve barrier broken can last much longer, such as over 15 weeks.[24] Gadofluorine enhancement can persist until there is complete remyelination and regeneration of the injured nerve.[25] Thus, the higher gadofluorine enhancement in nerves treated with TLR4 activation could be assumed in the enhanced nerve fiber regeneration and the ongoing disturbed blood-nerve barrier in the regenerative phase of a severed nerve.

Our study had several limitations. First, nerve repair process was assessed by using conventional T2 values. Diffusion-weighted imaging or diffusion tensor tractography are believed to have great potential as sensitive and noninvasive techniques to detect axonal injury and are objective and reproducible techniques to measure nerve fiber degeneration and regeneration in peripheral nerves.[26,27] DTI has been successfully applied to human peripheral nerves by using a 3T scanner, whereas DTI of smaller nerve structures such as rat sciatic nerves in this study need a high performing MR scanner and a dedicated coil technology. On the other hand, DWI is more susceptible to the magnetic susceptibility effect caused by postoperative subtle hemorrhage or micro air bubble, which are most likely introduced during microsurgical manipulation of nerve transection and nerve coaptation. Direct end-to-end repair is technically challenging to perform and usually not feasible in many clinical cases.[28,29] Nerve grafts and conduits are becoming increasingly utilized,[30] and, in the future, the same methodology as in this study can be applied to regeneration of nerves with grafts and conduits.[31] Second, nerve regeneration was only followed for 8 weeks after surgery when gadofluorine enhancement of the injured nerve was still present. Because histology showed that myelin debris clearance had almost completed and nerves showed no significant changes over time since 6 weeks after surgery, increasing observation time probably does not provide additional information to determine the role of T2 value and gadofluorine M– enhanced imaging in monitoring the enhanced nerve repair process mediated by TLR4 activation.

CONCLUSIONS

Our study demonstrated that the combined use of TLR4 activation with surgical repair may be associated with a better functional recovery and nerve regeneration. The resultant improved functional recovery and nerve regeneration can be predicted by the sustained increase patterns of nerve gadofluorine enhancement and T2 relaxation times in the degenerative phase. Gadofluorine-enhanced MR imaging as well as nerve T2 values can be used to monitor the enhanced nerve repair process in neurotmesis when treated with the TLR4 activation after surgical coaptation.

REFERENCES

1. Robinson LR. **Traumatic injury to peripheral nerves.** *Muscle Nerve* 2000;23:863–73
2. Siemionow M, Brzezicki G. **Chapter 8: current techniques and concepts in peripheral nerve repair.** *Int Rev Neurobiol* 2009;87:141–72
3. Terenghi G, Wiberg M, Kingham PJ. **Chapter 21: use of stem cells for improving nerve regeneration.** *Int Rev Neurobiol* 2009;87:393–403
4. Scheib J, Höke A. **Advances in peripheral nerve regeneration.** *Nat Rev Neurol* 2013;9:668–76
5. Burnett MG, Zager EL. **Pathophysiology of peripheral nerve injury: a brief review.** *Neurosurg Focus* 2004;16:E1
6. Snider WD, Zhou FQ, Zhong J, et al. **Signaling the pathway to regeneration.** *Neuron* 2002;35:13–16
7. Boivin A, Pineau I, Barrette B, et al. **Toll-like receptor signaling is critical for Wallerian degeneration and functional recovery after peripheral nerve injury.** *J Neurosci* 2007;27:12565–76
8. Vallières N, Berard JL, David S, et al. **Systemic injections of lipopolysaccharide accelerates myelin phagocytosis during Wallerian degeneration in the injured mouse spinal cord.** *Glia* 2006;53:103–13
9. Bendszus M, Stoll G. **Technology insight: visualizing peripheral nerve injury using MRI.** *Nat Clin Pract Neurol* 2005;1:45–53
10. Zhang H, Xiao B, Zou T. **Clinical application of magnetic resonance neurography in peripheral nerve disorders.** *Neurosci Bull* 2006; 22:361–67
11. Shen J, Zhou CP, Zhong XM, et al. **MR neurography: T1 and T2 measurements in acute peripheral nerve traction injury in rabbits.** *Radiology* 2010;254:729–38
12. Cheng LN, Duan XH, Zhong XM, et al. **Transplanted neural stem cells promote nerve regeneration in acute peripheral nerve traction injury: assessment using MRI.** *AJNR Am J Neuroradiol* 2011; 196:1381–87
13. Liao CD, Zhang F, Guo RM, et al. **Peripheral nerve repair: monitoring by using gadofluorine M– enhanced MR imaging with chitosan**

nerve conduits with cultured mesenchymal stem cells in rat model of neurotmesis. *Radiology* 2012;262:161–71

14. Bain JR, Mackinnon SE, Hunter DA. **Functional evaluation of complete sciatic, peroneal, and posterior tibial nerve lesions in the rat.** *Plast Reconstr Surg* 1989;83:129–38

15. Karanth S, Yang G, Yeh J, et al. **Nature of signals that initiate the immune response during Wallerian degeneration of peripheral nerves.** *Exp Neurol* 2006;202:161–66

16. Goethals S, Ydens E, Timmerman V, et al. **Toll-like receptor expression in the peripheral nerve.** *Glia* 2010;58:1701–09

17. Behr B, Schnabel R, Mirastschijski U, et al. **Magnetic resonance imaging monitoring of peripheral nerve regeneration following neurotmesis at 4.7 Tesla.** *Plast Reconstr Surg* 2009;123:1778–88

18. Peled S, Cory DG, Raymond SA, et al. **Water diffusion, T(2), and compartmentation in frog sciatic nerve.** *Magn Reson Med* 1999; 42:911–18

19. Webb S, Munro CA, Midha R, et al. **Is multicomponent T2 a good measure of myelin content in peripheral nerve?** *Magn Reson Med* 2003;49:638–45

20. Meding J, Urich M, Licha K, et al. **Magnetic resonance imaging of atherosclerosis by targeting extracellular matrix deposition with gadofluorine M.** *Contrast Media Mol Imaging* 2007;2:120–29

21. Wessig C, Jestaedt L, Sereda MW, et al. **Gadofluorine M-enhanced magnetic resonance nerve imaging: comparison between acute inflammatory and chronic degenerative demyelination in rats.** *Exp Neurol* 2008;210:137–43

22. Bendszus M, Wessig C, Schütz A, et al. **Assessment of nerve degeneration by gadofluorine M-enhanced magnetic resonance imaging.** *Ann Neurol* 2005;57:388–95

23. Colavincenzo J, Levine RL. **Myelin debris clearance during Wallerian degeneration in the goldfish visual system.** *J Neurosci Res* 2000;59:47–62

24. Guilbaud G, Gautron M, Jazat F, et al. **Time course of degeneration and regeneration of myelinated nerve fibres following chronic loose ligatures of the rat sciatic nerve: can nerve lesions be linked to the abnormal pain-related behaviours?** *Pain* 1993;53:147–58

25. Wessig C, Bendszus M, Stoll G. **In vivo visualization of focal demyelination in peripheral nerves by gadofluorine M-enhanced magnetic resonance imaging.** *Exp Neurol* 2007;204:14–19

26. Lehmann HC, Zhang J, Mori S, et al. **Diffusion tensor imaging to assess axonal regeneration in peripheral nerves.** *Exp Neurol* 2010;223:238–44

27. Takagi T, Nakamura M, Yamada M, et al. **Visualization of peripheral nerve degeneration and regeneration: monitoring with diffusion tensor tractography.** *Neuroimage* 2009;44:884–92

28. Diao E, Vannuyen T. **Techniques for primary nerve repair.** *Hand Clin* 2000;16:53–66

29. Maggi SP, Lowe JB, III, Mackinnon SE. **Pathophysiology of nerve injury.** *Clin Plast Surg* 2003;30:109–26

30. Dvali L, Mackinnon S. **Nerve repair, grafting, and nerve transfers.** *Clin Plast Surg* 2003;30:203–21

31. Thawait SK, Wang K, Subhawong TK, et al. **Peripheral nerve surgery: the role of high-resolution MR neurography.** *AJNR Am J Neuroradiol* 2012;33:203–10

Conventional and Functional MR Imaging of Peripheral Nerve Sheath Tumors: Initial Experience

S. Demehri, A. Belzberg, J. Blakeley, and L.M. Fayad

ABSTRACT

BACKGROUND AND PURPOSE: Differentiating benign from malignant peripheral nerve sheath tumors can be very challenging using conventional MR imaging. Our aim was to test the hypothesis that conventional and functional MR imaging can accurately diagnose malignancy in patients with indeterminate peripheral nerve sheath tumors.

MATERIALS AND METHODS: This institutional review board–approved, Health Insurance Portability and Accountability Act–compliant study retrospectively reviewed 61 consecutive patients with 80 indeterminate peripheral nerve sheath tumors. Of these, 31 histologically proved peripheral nerve sheath tumors imaged with conventional (unenhanced T1, fluid-sensitive, contrast-enhanced T1-weighted sequences) and functional MR imaging (DWI/apparent diffusion coefficient mapping, dynamic contrast-enhanced MR imaging) were included. Two observers independently assessed anatomic (size, morphology, signal) and functional (ADC values, early arterial enhancement by dynamic contrast-enhanced MR) features to determine interobserver agreement. The accuracy of MR imaging for differentiating malignant from benign was also determined by receiver operating characteristic analysis.

RESULTS: Of 31 peripheral nerve sheath tumors, there were 9 malignant (9%) and 22 benign ones (81%). With anatomic sequences, average tumor diameter (6.3 ± 1.8 versus 3.9 ± 2.3 mm, $P = .009$), ill-defined/infiltrative margins (77% versus 32%; $P = .04$), and the presence of peritumoral edema (66% versus 23%, $P = .01$) were different for malignant peripheral nerve sheath tumors and benign peripheral nerve sheath tumors. With functional sequences, minimum ADC ($0.47 \pm 0.32 \times 10^{-3}$ mm^2/s versus $1.08 \pm 0.26 \times 10^{-3}$ mm^2/s; $P < .0001$) and the presence of early arterial enhancement (50% versus 11%; $P = .03$) were different for malignant peripheral nerve sheath tumors and benign peripheral nerve sheath tumors. The minimum ADC (area under receiver operating characteristic curve was 0.89; 95% confidence interval, 0.73–0.97) and the average tumor diameter (area under the curve = 0.8; 95% CI, 0.66–0.94) were accurate in differentiating malignant peripheral nerve sheath tumors from benign peripheral nerve sheath tumors. With threshold values for minimum ADC $\leq 1.0 \times 10^{-3}$ mm^2/s and an average diameter of $\geq$4.2 cm, malignancy could be diagnosed with 100% sensitivity (95% CI, 66.4%–100%).

CONCLUSIONS: Average tumor diameter and minimum ADC values are potentially important parameters that may be used to distinguish malignant peripheral nerve sheath tumors from benign peripheral nerve sheath tumors.

ABBREVIATIONS: AUC = area under the curve; BPNST = benign peripheral nerve sheath tumor; DCE = dynamic contrast-enhanced; MPNST = malignant peripheral nerve sheath tumor; NF-1 = neurofibromatosis type 1; PNST = peripheral nerve sheath tumor; ROC = receiver operating characteristic analysis

Malignant peripheral nerve sheath tumors (MPNSTs) have a much smaller prevalence compared with benign peripheral nerve sheath tumors (BPNSTs) in the general population,[1] though a higher prevalence of MPNSTs occurs in the setting of neurofibromatosis type 1 (NF-1),[2] where patients have a 10% lifetime risk of developing MPNST.[3] Distinguishing BPNSTs from MPNSTs is important, because most sporadic tumors are BPNSTs, and unnecessary biopsies of benign tumors can be obviated if the accurate characterization of peripheral nerve sheath tumors (PNSTs) by noninvasive imaging techniques is available. Differentiating BPNSTs from MPNSTs can be very challenging because not only do their clinical features overlap but character-

istics by conventional MR imaging sequences are also shared.[4-6] In patients with NF-1, benign neurofibromas with small <5-cm[7] well-defined margins, a target sign, homogeneous signal intensity, and the absence of necrosis are considered as benign "determinate" tumors[8]; but without such characteristics, with large or increasing size of a lesion with time or significant uptake by positron-emission tomography, PNSTs in patients with NF-1 are defined as "indeterminate" and potentially malignant.[9-11] Additionally, sporadic PNSTs are also deemed "indeterminate",[12] especially if they are large, contain heterogeneous signal or internal necrosis, or exhibit ill-defined or infiltrative margins.[7] Patients with indeterminate PNSTs, which may be benign or malignant, are typically referred for an image-guided percutaneous biopsy or surgical removal for definitive histologic diagnosis, while patients with determinate BPNSTs do not necessarily require a biopsy and may be referred for follow-up.[8,12]

The addition of functional MR imaging sequences with DWI and dynamic contrast-enhanced (DCE) MR imaging to conventional MR imaging has been suggested as a useful approach to the assessment of soft-tissue tumors.[13] In particular, quantitative DWI with apparent diffusion coefficient mapping has been investigated for the characterization of musculoskeletal lesions, by demonstrating differences in cellularity between benign and malignant tumors.[14] With DCE-MR imaging, specific patterns of enhancement have been associated with benign and malignant soft-tissue lesions.[15,16] Hence, the purpose of this study was to test the hypothesis that conventional and functional MR imaging can accurately diagnose malignancy in patients with indeterminate peripheral nerve sheath tumors.

MATERIALS AND METHODS

Subject Population
This retrospective study was approved by the institutional review board, and informed consent was waived. A study population of consecutive soft-tissue tumors with features suggestive of "indeterminate" PNSTs was created by reviewing consecutive MR imaging studies obtained in our institution or outside MR imaging reviewed in our multidisciplinary nerve tumor clinics from May 2008 and January 2013. "Determinate" PNSTs were excluded (PNSTs in patients with NF-1 of a small size of <5 cm, a target sign, homogeneous signal, and absence of peritumoral edema or necrosis). Of the remaining 80 "indeterminate" PNSTs, we excluded the following: Sixteen (20%) tumors had no available functional imaging; 18 (22.5%) had no available contrast-enhanced imaging ($n = 12$) and/or DWI/ADC mapping ($n = 8$). In 3 patients (3.8%), the DWI sequences were nondiagnostic due to susceptibility or motion artifacts; and 12 presumed benign PNSTs had no histologic proof. The remaining 31 PNSTs were included in the study.

MR Imaging Acquisition Protocols
Conventional MR Imaging. MR imaging was performed at 3T (Siemens, Erlangen, Germany) by using a flexible phased array body-matrix coil and included the following sequences: T1-weighted (TR/TE, 790/15 ms; section thickness, 5 mm), fat-suppressed T2-weighted (TR/TE, 3600/70 ms; section thickness, 5 mm), and short tau inversion recovery (TR/TE, 3600/70 ms; sec-

tion thickness, 5 mm; axial plane), followed by unenhanced and gadolinium-based contrast agent–enhanced 3D fat-suppressed T1-weighted imaging (volumetric interpolated breath-hold examination, isotropic resolution; TR/TE, 4.6/1.4 ms; flip angle, 9.5°; section thickness, 1 mm; coronal plane with axial and sagittal reconstructions; 0.1-mmol/kg gadolinium-based contrast agent; Siemens Medical Solutions, Malvern, Pennsylvania).

Functional MR Imaging. Diffusion weighted-imaging with ADC mapping (TR/TE, 760/80 ms; section thickness, 5 mm; b-values = 50, 400, and 800 ss/mm^2) of the entire tumor was performed in the axial plane in all cases. Dynamic contrast-enhanced MR imaging was also performed in 26 of 31 tumors, immediately before and after the administration of the gadolinium-based contrast agent (time-resolved angiography with interleaved stochastic trajectories; TR/TE 2.5/0.9 ms; injection rate, 2–5 mL/s; flip angle, 20°; FOV, 45 × 45 cm; acquisition plane, usually coronal; temporal resolution, 10 seconds for total of 5 minutes).

Image Interpretation
Two independent observers interpreted MR imaging features independently to determine interobserver agreement. Discrepancies were subsequently resolved by consensus to determine the accuracy of specific MR imaging features in differentiating benign and malignant PNSTS. During interpretation, the observers were blinded and had no knowledge of the patients' clinical information, the histologic results of the PNSTs, and the follow-up status of each tumor.

Conventional MR Imaging
The following lesion features were categorized by anatomic sequences: Maximum tumor diameter measurements were performed in 3 planes (craniocaudal, anteroposterior, transverse), and an "average diameter" of each tumor was determined. Next, signal intensity (hypointense, isointense, or hyperintense to muscle) and heterogeneity (<25%, 25%–50%, >50%) on T1- and T2-weighted sequences were assessed. The shape (round/ovoid, irregular) and margin type (well-defined; partially defined, >50% of lesion margin defined; ill-defined, <50% of its margin defined; infiltrative) were identified. The presence or absence of the split fat sign, target sign, peritumoral edema, encasement or invasion into the adjacent vessels, periosteal/cortical involvement, bone marrow involvement, and joint extension were recorded. The presence or absence of enhancement following contrast administration on static postcontrast images and the percentage of tumor enhancement (<25%, 25%–50%, 50%–75%, and >75%) were detailed.

Functional MR Imaging
Using DWI/ADC mapping, each observer placed the largest oval or round region of interest entirely within each tumor on 3 axial sections, at the cranial, caudal, and central portions of the tumor. The minimum and mean ADC values for each axial section were reported, and the minimum and average mean ADC values for the 3 sections were determined. Using DCE-MR imaging, we recorded the presence or absence of early arterial enhancement.

Statistical Analysis

A Pearson correlation t test and Spearman rank order correlation test were performed to evaluate interobsever agreement for continuous and categoric data, respectively. To compare continuous and categoric MR imaging measurements for features of BPNSTs and MPNSTs, we used a 2-tailed Student t test and Fisher exact test, respectively. Receiver operating characteristic analysis (ROC) was performed to determine the accuracy of each measurement by using consensus measurements.

Using the ROC curve, we obtained optimal threshold values for continuous measurements, as the maximum Youden index, defined as threshold value = sensitivity − (1-specificity) of each measurement.[17] Statistical analysis of the data was performed with a statistical software program MedCalc for Windows (MedCalc Software, Mariakerke, Belgium). A P value ≤ .05 was considered significant.

Table 1: Demographic characteristics of patients with biopsy-proved benign and malignant nerve sheath tumors[a]

	MPNST (n = 9)	BPNST (n = 22)
No. of patients	8	21[a]
Sex		
Male	4	13
Female	4	8
Age (median) (range) (yr)	38, 18–54	52, 13–78
NF-1	9	4
Benign pathologies	–	Schwannoma (n = 14)
		Neurofibroma (n = 6)
		Perineuroma (n = 1)
		Ganglioneuroma (n = 1)

Note:—— indicates not applicable.
[a] One patient with NF-1 had 2 MPNSTs and 1 patient with NF-1 had 1 MPNST and 2 BPNSTs.

Table 2: Comparison between benign and malignant peripheral nerve sheath tumors using conventional and functional MRI and determination of interobserver agreement

	MPNST (n = 9)	BPNST (n = 22)	P Value	Interobserver Agreement[a]
Diameter (cm)				
Maximum (mean)	8 ± 2.4	5.6 ± 3.8	.17	0.89
Average (mean)	6.3 ± 1.8	3.9 ± 2.3	.009	0.82
Conventional MRI				
T1 (Hyponintense to muscle)	0% (0/9)	14% (3/22)	.22	0.90
T2 (Hyperintense to the muscle)	100% (9/9)	100% (21/22)	.99	0.98
Following features present:				
Ill-defined or infiltrative margins	77% (7/9)	32% (7/22)	.04	0.66
Irregular shape	0% (0/9)	12.5% (3/22)	.528	0.80
Split fat sign	10% (1/9)	33% (8/22)	.11	0.21
Target sign	10% (1/9)	21% (5/22)	.51	0.92
T1 heterogeneity (<50%)	0% (0/9)	4% (1/22)	.49	0.76
T2 heterogeneity (<50%)	55% (5/9)	29% (7/22)	.31	0.71
Peritumoral edema	66% (6/9)	23% (5/22)	.01	0.71
Eccentric to the nerve	55% (5/9)	42% (10/22)	.18	0.53
Vascular encasement	11% (1/9)	0% (0/22)	.65	0.95
Periosteal/cortical invasion	11% (1/9)	0% (0/22)	.65	1
Bone marrow invasion	0% (0/9)	0% (0/22)	.99	1
Joint extension	0% (0/9)	0% (0/22)	.99	1
Delayed contrast enhancement	100% (9/9)	92% (22/22)	.39	0.70
Functional MRI				
ADC values ($\times 10^{-3}$ mm^2/s)				
Average (mean)	1.57 ± 0.27	1.7 ± 0.28	.22	0.90
Minimum (mean)	0.47 ± 0.32	1.08 ± 0.26	<.0001	0.89
DCE-MRI				
Early arterial enhancement	50% (4/8)	11% (2/18)	.03	0.81

[a] Spearman rank-order correlation coefficient.

RESULTS

Subject Characteristics

Of 31 biopsy-proved PNSTs, 22 were benign and 9 were MPNSTs. The patients with MPNSTs (mean age, 38 years; range, 18–54 years) were younger than patients with BPNSTs (mean age, 52 years of age; range, 13–78 years) (P = .02). All MPNSTs (9/9) and only 22% of BPNSTs (5/22) occurred in patients with NF-1 (P = .0001) (Table 1).

MR Imaging Features

There was moderate-to-high interobserver agreement for MR imaging measurements and determinations by using both anatomic and functional sequences (Table 2). Among the measurements obtained by using conventional MR imaging (Table 2), the average tumor diameter (6.3 ± 1.8 versus 3.9 ± 2.3 cm, P = .009), the presence of peritumoral edema (6/9, 66% versus 5/22, 23%; P = .01), and the presence of ill-defined/infiltrative margins (7/9, 77% versus 7/22, 32%; P = .04) were significantly different in MPNSTs than in BPNSTs, respectively.

With functional MR imaging sequences, the minimum ADC values were significantly lower in MPNSTs than in BPNSTs (0.47 ± 0.32 × 10^{-3} mm^2/s versus 1.08 ± 0.26 × 10^{-3} mm^2/s, respectively; P < .0001), while average ADC values were not significantly different. With DCE-MR imaging, 50% of MPNSTs (4/8, DCE-MR was not performed for 1 MPNST) demonstrated early arterial enhancement compared with only 11% of BPNSTs (n = 2/18, P = .03).

Diagnostic Performance with ROC

With conventional MR imaging, the average tumor diameter showed the highest accuracy for differentiating MPNSTs and BPNSTs (area under the curve; AUC = 0.83; 95% CI, 0.66–0.94). Other important diagnostic features included maximum lesion diameter, peritumoral edema, and tumor margin, which offered AUCs of 0.77 (95% CI, 0.59–0.90), 0.68 (95% CI, 0.49–0.84), and 0.68 (95% CI, 0.49–0.84), respectively (On-line Table).

With functional MR imaging, the minimum ADC value (AUC = 0.89; 95% CI, 0.73–0.97, P = .02) was a more accurate parameter in differentiating BPNSTs and MPNSTs than the average ADC value (AUC = 0.63; 95% CI, 0.43–0.76) (Fig 1). The AUC for the presence of early arterial enhancement by using DCE-MR was 0.69 (95% CI, 0.46–0.86).

With the Youden index, the threshold values for the features with the highest diagnostic performance (minimum ADC of 1.0 × 10^{-3} mm^2/s and an average diameter of 4.2 cm) were combined to stratify (Fig. 2) the "indeterminate" PNSTs, and ROC was further used to determine the accuracy of this combination of an-

atomic and functional MR imaging data. For PNSTs with both minimum ADC value $\geq 1.0 \times 10^{-3}$ mm^2/s and an average diameter of <4.2 cm, the sensitivity and negative predictive value for diagnosing malignancy were 100% (95% CI, 66%–100%) and 100%, respec-

tively. Conversely, for PNSTs with both minimum ADC values <1.0×10^{-3} mm^2/s and average diameter of ≥ 4.2 cm, the specificity and positive predictive value for malignancy were 77% (95% CI, 54%–92%) and 64%, respectively (Figs 3 and 4).

DISCUSSION

Any improvement in the diagnostic accuracy of noninvasive imaging for characterizing the population of "indeterminate" PNSTs is valuable, given the high prevalence of benign PNSTs (22/31, 71%) that may be unnecessarily referred for biopsy rather than follow-up. In this study, we showed that the combined anatomic and functional MR imaging features of "indeterminate" PNSTs may be helpful to rule out malignancy.

With anatomic MR imaging features, results of the current study are in agreement with prior investigations, in that a large tumor diameter is a useful feature for differentiating BPNSTs and MPNSTs. Our study also showed that within "indeterminate" PNSTs, the average diameter ($P = .009$) and not the maximum diameter ($P = .17$) is significantly larger in MPNSTs in comparison with BPNSTs. This result may be due to the fact that typical fusiform BPNSTs usually grow along the nerve and, therefore, may have a large maximum diameter along the nerve of origin, but average measurements that incorporate length in the other 2 planes may be smaller than the maximum diameter alone. Using ROC, in our study, we observed a threshold value of 4.2 cm, a value that is close to the commonly used metric of 5 cm for differentiating benign and malignant soft-tissue tumors.[7,18]
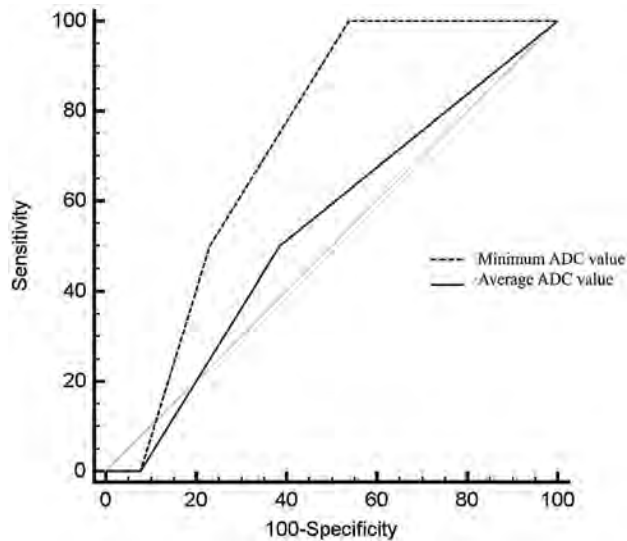

FIG 1. ROC for ADC values by using DWI in differentiation of BPNSTs and MPNSTs. The minimum ADC value (AUC = 0.89; 95% CI, 0.73–0.97; $P = .02$) was a more accurate parameter in differentiating BPNSTs and MPNSTs than the average ADC value (AUC = 0.63; 95% CI, 0.43–0.76). (The ADC values plotted here are consensus values determined from a mean of the measurements made by each reader.)
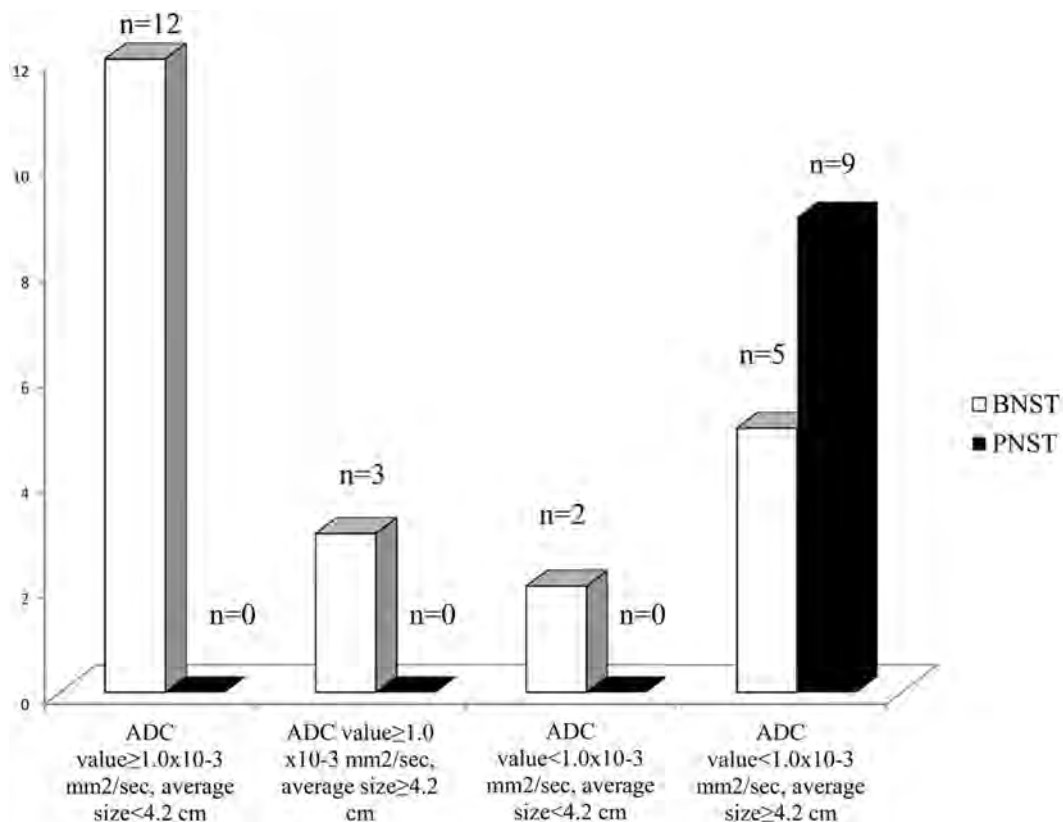

FIG 2. Distribution bar plots for BPNSTs and MPNSTs stratified on the basis of threshold values obtained from ROC of anatomic (average diameter = 4.2 cm) and functional (minimum ADC = 1.0×10^{-3} mm^2/s) MR imaging sequences.
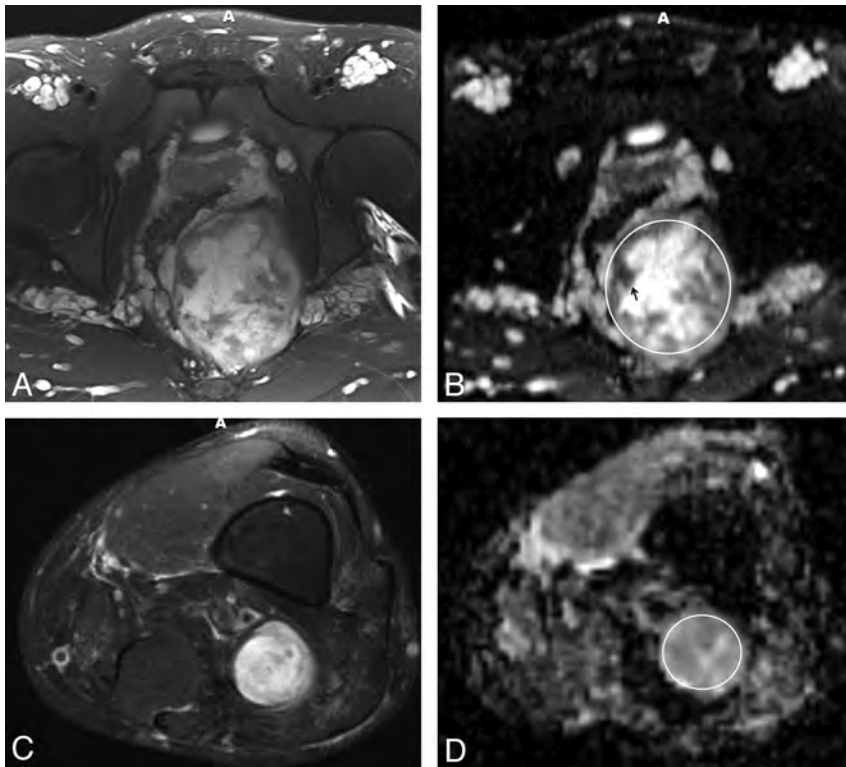
FIG 3. A 21-year-old man with a history of NF-1 and an "indeterminate" PNST. Axial T2-weighted image (A) and ADC map (B) both show heterogeneous signal with a large pelvic mass with an average diameter of 8.7 cm and a minimum ADC value of 0.4×10^{-3} mm^2/s within this mass (arrow), subsequently diagnosed as MPNST. For comparison, a benign neurofibroma in 54-year-old man with a history of NF-1 is shown in the distal thigh, with an average diameter of 3.4 cm (C) and a minimum ADC value of 1.0×10^{-3} mm^2/s (D). The circle indicates the region of interest for ADC measurements.
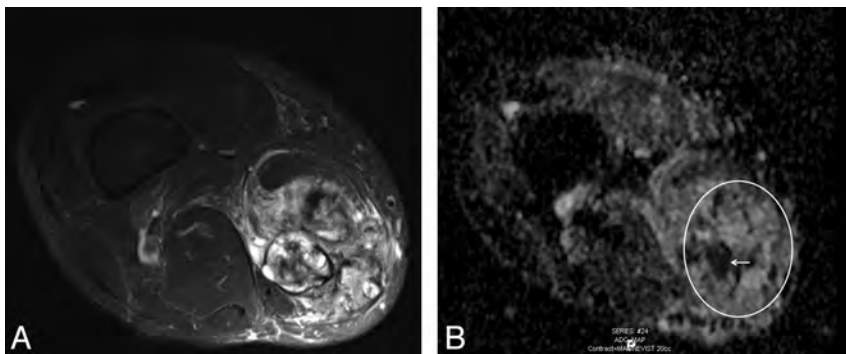

FIG 4. "Indeterminate" PNST in the distal right thigh of a 65-year-old man with an average size of 9.0 cm shown on an axial T2-weighted image (A) and a minimum ADC value of 0.1×10^{-3} mm^2/s (B, arrow). Although PNSTs with a minimum ADC value $\leq 1.0 \times 10^{-3}$ mm^2/s and/or an average diameter of >4.2 cm can still be benign, these tumors must proceed to histologic diagnosis to rule out malignancy. In this case, a benign schwannoma was found. The circle indicates the region of interest for ADC measurements.

Other anatomic features that have been explored in the literature include the presence of peritumoral edema and heterogeneous enhancement following contrast administration, both of which were shown to be supporting features for MPNST in our study. However, signal heterogeneity on noncontrast sequences and cystic changes on contrast-enhanced sequences have also been described as important differentiating features between neurofibromas and MPNSTs, but our study did not support this observation. A large number of schwannomas (14/22, 63%) were

included in our study, and such tumors are more likely to be "indeterminate," because they can be very heterogeneous and contain cystic regions (so-called ancient schwannomas), unlike the more uniform signal characteristics in typical neurofibromas.[19] Similarly, there was no significant difference in the presence of a target sign in MPNSTs (10%) and BPNSTs (21%), though the lack of a target sign has been reported as a useful diagnostic sign of MPNST in a population comparing neurofibromas and MPNSTs.[4]

Because the histologic evaluation of PNSTs commonly shows increased cellularity in MPNSTs, it follows that DWI is helpful in differentiating BPNSTs and MPNSTs. In particular, the results of our study show that the minimum ADC value is a better predictor of malignancy than the average ADC value in PNSTs, in sporadic cases and in patients with NF-1. This observation can be explained by the heterogeneity in cellularity present within both benign and malignant PNSTs, which can result in a large range of intralesional ADC values, making the minimum value more valuable than the diluted average ADC value. In addition, in patients with NF-1, MPNSTs typically arise within neurofibromas[2] and are associated with foci of highest cellularity. Minimum ADC values may also be helpful for image-guided biopsy planning because targeting areas with the lowest ADC values can improve the diagnostic yield.[20] In our study, a threshold minimum ADC value of 1.0×10^{-3} mm^2/s was determined as an accurate quantitative measure of malignancy, as has been suggested anecdotally in soft-tissue tumors in general.[14] Similar to MPNSTs, BPNSTs with high cellularity, such as schwannomas,[19] can also demonstrate low minimum ADC values, as found in 4 schwannomas and 1 ganglioneuroma with minimum ADC values $<1.0 \times 10^{-3}$ mm^2/s.

Another functional technique explored in this study was DCE-MR imaging. Although nonspecific,[19] malignant tumors more often demonstrate early arterial enhancement than benign tumors.[13] In our study, early arterial enhancement was detected in MPNSTs (50%) more commonly than in BPNSTs (11%, $P = .03$), suggesting that the presence of early arterial enhancement may also be a useful sign for distinguishing MPNSTs from BPNSTs, when present.

To combine the information obtained from conventional and functional MR imaging, by using ROC and the Youden index, we

stratified PNSTs on the basis of the threshold values for average lesion diameters ($\geq$4.2 cm) and minimum ADC values ($\leq$1.0 $\times 10^{-3}$ mm^2/s). With these thresholds, for PNSTs with an average diameter <4.2 cm and a minimum ADC value of $\geq$1.0 $\times$ 10^{-3} mm^2/s, the possibility of an MPNST is unlikely. Hence, the impact of these results on clinical care, while yet to be definitively determined, may be anticipated. In our retrospective study, 38% of the indeterminate tumors met these threshold criteria; therefore, conservative management and continued surveillance of these tumors may have been sufficient (because these tumors were histologically proved benign). However, these imaging features are by no means diagnostic for malignancy, and in our cohort, 36% of "indeterminate" tumors in this subgroup were diagnosed as BPNSTs (Fig 4). There was also high interobserver agreement for minimum ADC values ($r = 0.89$) and average-diameter ($r = 0.82$) measurements.

This study had limitations. First, our retrospective study had a nonrandomized design; therefore, the presence of selection bias was unavoidable. Second, in our study, MPNSTs composed 29% (9/31) of the "indeterminate" PNSTs, a much higher incidence than in the general population. This is likely due to our inclusion criteria, because MPNSTs are more likely than BPNSTs to undergo a histologic evaluation. Third, a limited analysis of DCE-MR imaging data was performed, because we only investigated the presence of early arterial enhancement for distinguishing MPNSTs from BPNSTs; the latter technique, though not quantitative, has recently been shown to be adequate for assessing soft-tissue sarcomas.[21] Further quantitative analysis of tumor perfusion can also be performed, which may enhance the differentiation of benign and malignant tumors, but it is a cumbersome analysis that is not as easily performed clinically as the quantification of ADC maps. Finally, 1 observer (Laura M. Fayad) was directly involved in the diagnosis and management of some tumors included in this study. Therefore, it is possible that this observer remembered at least some of the cases during interpretation. However, we determined the accuracy of MR imaging features in the differentiation of BPNSTs and MPNSTs by using a consensus interpretation of 2 observers.

CONCLUSIONS

This study provides initial evidence that the addition of functional imaging with DWI and ADC mapping to a conventional MR imaging examination has a potential role for distinguishing benign and malignant PNSTs and may impact the clinical care of patients with these common tumors.

REFERENCES

1. Kransdorf MJ. **Benign soft-tissue tumors in a large referral population: distribution of specific diagnoses by age, sex, and location.** *AJR Am J Roentgenol* 1995;164:395–402
2. Ducatman BS, Scheithauer BW, Piepgras DG, et al. **Malignant peripheral nerve sheath tumors: a clinicopathologic study of 120 cases.** *Cancer* 1986;57:2006–21
3. Evans DG, Baser ME, McGaughran J, et al. **Malignant peripheral nerve sheath tumors in neurofibromatosis 1.** *J Med Genet* 2002;39: 311–14
4. Bhargava R, Parham DM, Lasater OE, et al. **MR imaging differentiation of benign and malignant peripheral nerve sheath tumors: use of the target sign.** *Pediatr Radiol* 1997;27:124–29
5. Kehrer-Sawatzki H, Kluwe L, Fünsterer C, et al. **Extensively high load of internal tumors determined by whole body MRI scanning in a patient with neurofibromatosis type 1 and a non-LCR-mediated 2-Mb deletion in 17q11.2.** *Hum Genet* 2005;116:466–75
6. Koşucu P, Ahmetoğlu A, Cobanoğlu U, et al. **Mesenteric involvement in neurofibromatosis type 1: CT and MRI findings in two cases.** *Abdom Imaging* 2003;28:822–26
7. Wasa J, Nishida Y, Tsukushi S, et al. **MRI features in the differentiation of malignant peripheral nerve sheath tumors and neurofibromas.** *AJR Am J Roentgenol* 2010;194:1568–74
8. Frassica FJ, Khanna JA, McCarthy EF. **The role of MR imaging in soft tissue tumor evaluation: perspective of the orthopedic oncologist and musculoskeletal pathologist.** *Magn Reson Imaging Clin N Am* 2000;8:915–27
9. Beert E, Brems H, Daniëls B, et al. **Atypical neurofibromas in neurofibromatosis type 1 are premalignant tumors.** *Genes Chromosomes Cancer* 2011;50:1021–32
10. Friedrich RE, Gawad K, Derlin T, et al. **Surgery for atypical plexiform neurofibromas of the trunk in NF1 with high standardised uptake value (SUV) in positron-emission tomography (PET) expressing podoplanin: a long-term follow-up.** *Anticancer Res* 2012;32:4547–51
11. Meany H, Dombi E, Reynolds J, et al. **18-fluorodeoxyglucose-positron emission tomography (FDG-PET) evaluation of nodular lesions in patients with neurofibromatosis type 1 and plexiform neurofibromas (PN) or malignant peripheral nerve sheath tumors (MPNST).** *Pediatr Blood Cancer* 2013;60:59–64
12. Papp DF, Khanna AJ, McCarthy EF, et al. **Magnetic resonance imaging of soft-tissue tumors: determinate and indeterminate lesions.** *J Bone Joint Surg Am* 2007;89(suppl 3):103–15
13. Fayad LM, Jacobs MA, Wang X, et al. **Musculoskeletal tumors: how to use anatomic, functional, and metabolic MR techniques.** *Radiology* 2012;265:340–56
14. Maeda M, Matsumine A, Kato H, et al. **Soft-tissue tumors evaluated by line-scan diffusion-weighted imaging: influence of myxoid matrix on the apparent diffusion coefficient.** *J Magn Reson Imaging* 2007;25:1199–204
15. Van Rijswijk CS, Geirnaerdt MJ, Hogendoorn PC, et al. **Soft-tissue tumors: value of static and dynamic gadopentetate dimeglumine-enhanced MR imaging in prediction of malignancy.** *Radiology* 2004;233:493–502
16. Hawighorst H, Libicher M, Knopp MV, et al. **Evaluation of angiogenesis and perfusion of bone marrow lesions: role of semiquantitative and quantitative dynamic MRI.** *J Magn Reson Imaging* 1999; 10:286–94
17. Perkins NJ, Schisterman EF. **The inconsistency of "optimal" cut-points obtained using two criteria based on the receiver operating characteristic curve.** *Am J Epidemiol* 2006;163:670–75
18. Rydholm A, Berg N. **Size, site and clinical incidence of lipoma: factors in the differential diagnosis of lipoma and sarcoma.** *Acta Orthop Scand* 1983;54:929–34
19. Ahlawat S, Blakeley J, Montgomery E, et al. **Schwannoma in neurofibromatosis type 1: a pitfall for detecting malignancy by metabolic imaging.** *Skeletal Radiol* 2013;42:1317–22
20. Rosenkrantz AB, Kim S, Lim RP, et al. **Prostate cancer localization using multiparametric MR imaging: comparison of Prostate Imaging Reporting and Data System (PI-RADS) and Likert scales.** *Radiology* 2013;269:482–92
21. Fayad LM, Mugera C, Soldatos T, et al. **Technical innovation in dynamic contrast-enhanced magnetic resonance imaging of musculoskeletal tumors: an MR angiographic sequence using a sparse k-space sampling strategy.** *Skeletal Radiol* 2013;42:993–1000

Variation in Anisotropy and Diffusivity along the Medulla Oblongata and the Whole Spinal Cord in Adolescent Idiopathic Scoliosis: A Pilot Study Using Diffusion Tensor Imaging

Y. Kong, L. Shi, S.C.N. Hui, D. Wang, M. Deng, W.C.W. Chu, and J.C.Y. Cheng

ABSTRACT

BACKGROUND AND PURPOSE: Disturbed somatosensory evoked potentials have been demonstrated in patients with adolescent idiopathic scoliosis (but this functional delay was found to originate above the C5–6 level, while the lower cord level was unaffected). Together with MR imaging observation of tonsillar ectopia and a relatively tethered cord, we hypothesized that there is disturbed mean diffusivity integrity along the spinal cord. In this study, advanced DTI was used to evaluate whether there was underlying decreased WM integrity within the brain stem and spinal cord in adolescent idiopathic scoliosis and any relationship to cerebellar tonsillar ectopia. Clinical impact on balance testing was also correlated.

MATERIALS AND METHODS: Thirteen girls with adolescent idiopathic scoliosis with right thoracic curves were compared with 13 age-matched healthy girls. DTI of the brain and whole spinal cord was performed. ROIs were manually defined for the medulla oblongata and along each intervertebral segment of the cord. Mean values of fractional anisotropy and mean diffusivity were computed at the defined regions. Between-group comparisons were performed by 1-way ANOVA.

RESULTS: Significantly decreased fractional anisotropy values and increased mean diffusivity values were found at the medulla oblongata and C1–2, C2–3, C3–4, and C4–5 segments in patients with adolescent idiopathic scoliosis compared with healthy subjects. No significant difference was found in the lower cord levels. Significant correlation was found between the tonsillar level and fractional anisotropy value at the C4–5 level in patients with adolescent idiopathic scoliosis only.

CONCLUSIONS: The findings from this study are in agreement with previous findings showing abnormal somatosensory evoked potential readings occurring only above the C5–6 level in patients with adolescent idiopathic scoliosis; these findings might partially explain the pathophysiology of the neural pathway involved.

ABBREVIATIONS: AIS = adolescent idiopathic scoliosis; FA = fractional anisotropy; MD = mean diffusivity; SEP = somatosensory evoked potential; SOT = sensory organization test

Adolescent idiopathic scoliosis (AIS) is a complex 3D deformity of the spine that affects approximately 4% of school children worldwide.[1] Despite intensive research in the past decades, the pathophysiology of AIS remains uncertain.[2] There is, however, growing evidence suggesting that an underlying neurologic disorder may be a causative factor of AIS.[3] Previous studies have reported changes in central nervous system structures in patients with AIS based on advanced medical imaging modalities.[4-6] Furthermore in a number of MR imaging studies, the observable changes in morphologic shape and position of the cord,[7] mismatch in lengthening between the cord and vertebral column,[8] and increased incidence of low-lying cerebellar tonsils[9] have led to the postulation of the presence of subclinical tethering of the spinal cord in AIS.[10]
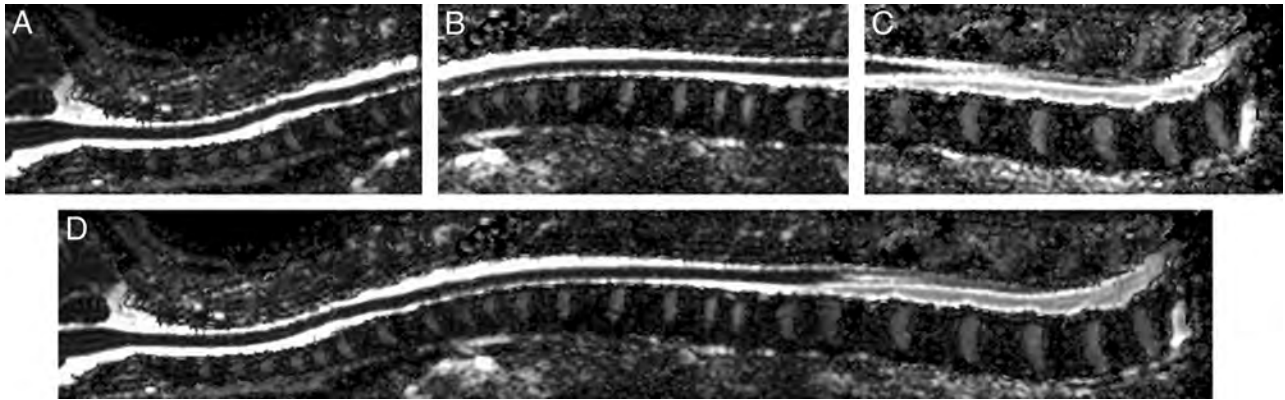
FIG 1. Sagittal mean diffusivity images show an example of spinal cord DTI stitching. Upper part (*A*), middle part (*B*), lower part (*C*), and stitched (*D*) spinal cord DTI of the whole spinal cord.

The proposed disturbed spinal cord function in AIS was further supported by the clinical observation of abnormal somatosensory function, which has been widely reported in this group. Prolonged latency or absent waveforms in posterior tibial nerve somatosensory evoked potentials (SEPs) were reported in 12%–61% of patients with scoliosis in different series.[8,11-13] A previous study also suggested that balance control was affected by somatosensory input.[14] In the study by Cheng et al,[15] 14.6% of patients with AIS had abnormal SEPs with either prolonged latency or decreased amplitude, while tonsillar ectopia was found in 33.3% of those with abnormal SEPs. A subsequent study with detailed analysis of SEPs recorded at 3 different levels (popliteal fossa, cervical level C4–6, and the scalp) showed that in patients with AIS with abnormal SEPs, the readings were only abnormal at the scalp level, while the readings at the popliteal and cervical regions were normal, indicating that the level of abnormality along the somatosensory pathway was superior to that at the cervical C5–6 level.[16]

DTI is a recent advanced imaging technique to evaluate WM architecture within the brain and spinal cord in vivo.[17] This technique can detect the microstructural changes of the WM and is presently a promising tool to study WM fiber bundles in vivo. In recent years, the advanced technique has been increasingly used to examine the spinal cord parenchyma for multiple diseases, including myelitis, spinal cord injury,[18] multiple sclerosis,[19] and intramedullary spinal cord neoplasms.[20] On the basis of the observation of tonsillar ectopia, relatively tethered cord, and abnormal SEP, we hypothesized that there is disturbed WM integrity within the brain stem and the spinal cord, most likely at the more cranial level as indicated by the level of SEP abnormality in the previous study.[16] The disturbed WM integrity is likely reflecting underlying cord abnormality in patients with AIS in addition to their skeletal abnormality. We sought to prove the above hypothesis by evaluating the fractional anisotropy (FA) and mean diffusivity (MD) values of the spinal cord and correlating them with the position of cerebellar tonsils and balance testing.

MATERIALS AND METHODS
Subjects
Thirteen girls with AIS and 13 age-matched healthy girls were recruited. The AIS group consisted of patients with a dominant right thoracic curve (the most common curve type in AIS) from 11 to 16 years of age (mean, 13.6 years of age). The Cobbs angle ranged from 16° to 37°(mean, 24.67°). They were consecutively recruited from our outpatient clinic. The healthy controls were recruited from local schools and were from 12 to 15 years of age (mean, 13.9 years of age). Inclusion criteria of AIS were the following: 1) age between 12 and 18 years, 2) right thoracic curves, 3) availability of medical history from the parents or legal guardians. Inclusion criteria of healthy controls were the following: 1) age between 12 and 18 years, and 2) no signs of scoliosis from the annual assessment by the Student Health Service. Exclusion criteria for both patients with AIS and healthy controls included any history of head or back injury; neurologic symptoms such as headache, weakness, or numbness in any limbs; urinary incontinence; nocturnal enuresis; or any space-occupying lesion found on screening MR imaging. All participants were right-handed Chinese adolescents with normal neurologic examination findings. Approval was obtained from the ethics committee of the hospital and university.

MR Imaging Data Acquisition
All MR imaging examinations were performed on the brain and spinal cord for each subject by using a 3T scanner (Achieva TX series; Philips Healthcare, Best, the Netherlands). An 8-channel sensitivity encoding head coil was used to acquire T1-weighted images and DTI covering the whole brain. Brain T1-weighted images were obtained by using a 3D fast-field echo imaging sequence with the following parameters: TR = 18 ms, TE = 2.4 ms, FOV = 210 × 210 mm^2, flip angle = 30°, NEX = 1, matrix = 232 × 232, section = 200. Brain DTI was performed by using the single-shot EPI sequence with the following parameters: TR = 8667 ms, TE = 60 ms, FOV = 224 × 224 mm^2, flip angle = 90°, NEX = 1, matrix = 112 × 109, section = 70, section thickness = 2 mm, gap = 2 mm. After reconstruction, images were zero-padded and interpolated to 224 × 224 with a voxel size of 1 × 1 × 2 mm^3. Thirty-two directions of diffusion gradients with b-value of 1000 s/mm^2 and 1 B0 volume were collected.

A 15-channel sensitivity encoding spine coil was used to scan the spinal cord for each subject. Conventional T2-weighted images were acquired with a turbo spin-echo sequence with the following parameters: TR = 4048 ms, TE =

FIG 2. Regions of interest of the spinal cord at different intervertebral disk levels.

FIG 3. The basion and opisthion line and the measurement of the cerebellar tonsil level.

120 ms, flip angle = 90°, NEX = 2. Spinal cord DTI was acquired at the upper, middle, and lower parts with sufficient overlapping areas. Figures 1*A–C* show an example of these 3 parts. In each part, sagittal sections parallel to the long axis of the subject's body were acquired to cover the whole spinal cord. Thirty sagittal sections were collected for the healthy girls in each part. Due to the curves of spinal cord in AIS, an equal or larger number of sagittal sections, ranging from 30 to 40, were required to capture the entire spinal cord. Spinal cord DTI was performed by using the single-shot EPI sequence with the following parameters: TR = 8180 ms, TE = 63 ms, FOV = 130 × 219 mm^2, flip angle = 90°, NEX = 6, matrix = 64 × 110, section thickness = 2 mm, gap = 2 mm. After reconstruction, images were zero-padded and interpolated to 224 × 224 with voxel size of 0.98 × 0.98 × 2 mm^3. Six directions of diffusion gradients with a b-value of 500 s/mm^2 and 1 B0 volume were collected. The number of gradients was reduced compared with the brain DTI because of time constrains because DTI acquisition of the whole spinal cord required 3 separate sessions. Together with the morphologic T2-weighted sequences, the total scanning time of the spinal cord was 30 minutes or longer if the scoliosis curve was severe. The scanning time was, therefore, kept to a minimum to avoid motion artifacts and discomfort of the subject while image quality was acceptable for analysis.

MR Image Preprocessing
The FMRIB Diffusion Toolbox (http://www.fmrib.ox.ac.uk/fsl/fdt/index.html)[21] was used to perform preprocessing of brain and spinal cord DTI datasets. Distortion correction was first performed to remove eddy currents and motion artifacts. Diffusion tensors and parameters, including FA, colored FA, and MD, were then computed in the Diffusion Toolbox by using the robust weighted least-squares fitting method.

Quantification of Fiber Integrity of the Spinal Cord
For each subject, diffusion tensor images of the spinal cord were adjacently stitched together to produce the DTI of the entire spinal cord.[22] In brief, the adjacent diffusion tensor images were first aligned by using a feature-based registration algorithm. All the images were then warped to the same space and were stitched together by using an effective feathering approach with the Log-Euclidean metrics. The FA and MD scalar maps were visualized to evaluate the effectiveness of the stitching results. Figure 1 shows an MD map of the stitched spinal cord DTI from 1 healthy subject.

Region-of-Interest Definition of FA and MD for the Medulla Oblongata and Spinal Cord
A commonly used method was adopted to evaluate the mean value of the DTI metrics on the whole medulla oblongata.[23] The medulla oblongata was first manually defined on the high-resolution T1-weighted image. The inferior margin was defined at the level of the foramen magnum, while the superior margin was defined at the level of the bulbopontine sulcus. The defined region was mapped to DTI space by affine-registering the T1 image to the B0 image by using a linear image registration approach[24]

A segmental approach was used to obtain different ROIs throughout the spinal cord because it was not feasible to adopt a voxel-by-voxel approach in view of the anatomy of the cord and the intrinsic limitation that the high-dimensional tensor structure of DTI could not be directly used for analysis. The spinal cord was segmented and numbered according to its corresponding vertebral levels from C2 to L1. The FA and MD values were then measured at different intervertebral disk levels (ranging from C1/2 to T12/L1, shown in Fig 2). Eighteen ROIs were obtained in each subject. ROIs were manually drawn on FA maps at every axial section at designated levels along the whole spinal cord. To ensure the proper anatomic localization, an experienced research associate with neuroradiology training was responsible for identifying and drawing the ROIs. Besides, special attention was paid to avoid CSF and the gradient inhomogeneity effects in the region-of-interest selections.[19] Each region of interest included approximately 50 voxels at each level. With the resolution of 0.98 × 0.98 ×2 mm^3, the volumes were approximately 100 mm^3. Special attention was made to avoid partial volume effects from the CSF during the selection of ROIs.

Measurement of Cerebellar Tonsil Level
Because low-lying tonsils have been commonly reported in AIS and this finding might be related to the severity of cord tethering and might exert some compressive effect on the brain stem/cervical cord, the position of the cerebellar tonsil was assessed on the midsagittal image according to the method described in previous studies.[8,15,25] The level of the cerebellar tonsil relative to a reference line connecting the basion and opisthion line was measured according to the method described by Aboulezz et al (Fig 3).[26] The distance measured from above the basion and opisthion line was conventionally assigned as a positive value, while the distance
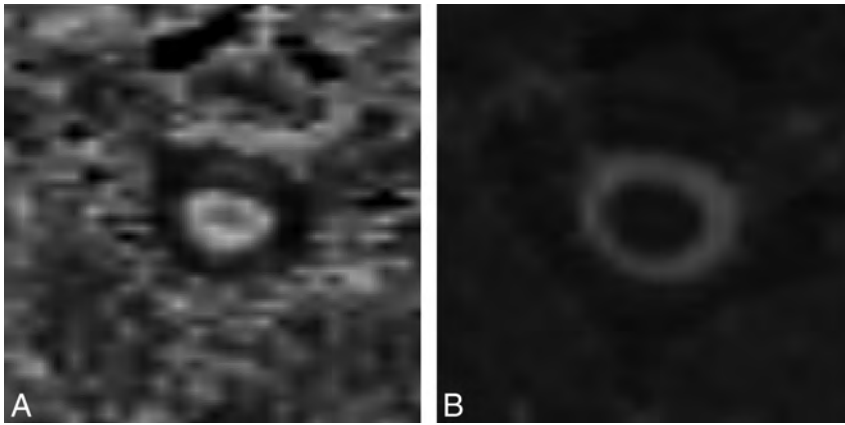
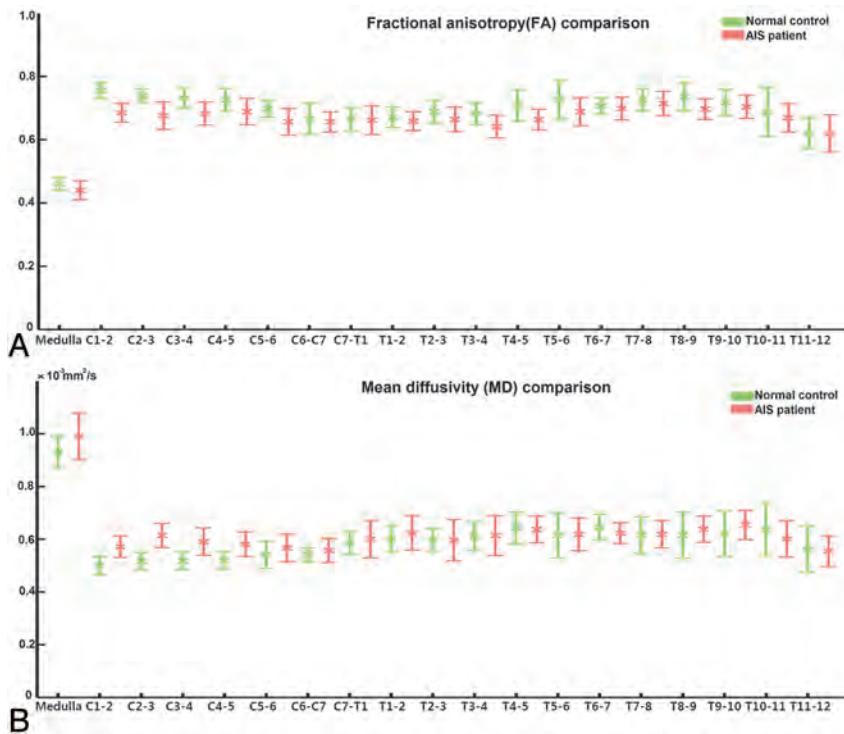**FIG 4.** Fractional anisotropy and mean diffusivity maps of 1 axial section at C2–3 from 1 healthy control.

FIG 5. Fractional anisotropy (*A*) and mean diffusivity (*B*) values for regions of interest at different levels of the medulla oblongata and spinal cord for healthy controls and patients with adolescent idiopathic scoliosis.

(ranging from 0.86 to 0.99). The MD mean value was 0.85 (ranging from 0.79 to 0.96).

The level of the cerebellar tonsils was independently measured by 2 observers (1 radiologist and 1 research associate who had 3 years of experience in MR imaging measurement). The intraclass correlation coefficient was 0.89.

Postural Balance Study
Smart Equitest-Computerized Dynamic Posturography (NeuroCom International, Clackamas, Oregon) was used for the study. A standardized sensory organization test (SOT)[27] protocol was used to identify objectively any abnormalities in the postural control. The SOT measured how well a patient could maintain their postural stability under 6 sensory conditions: 1) normal vision, firm surface; 2) eyes closed, firm surface; 3) sway-referenced visual surroundings, firm surface; 4) normal vision, sway-referenced surface; 5) eyes closed, sway-referenced surface; and 6) sway-referenced visual surroundings, sway-referenced surface. The equilibrium score quantified the center of gravity sway or postural stability under each of the 3 trials of the 6 sensory conditions.[14]

Statistical Analysis
Between-group comparisons of FA and MD values were performed at the medulla oblongata and all the segments by using the 1-way ANOVA test and the false discovery rate, with $P = .05$ used to correct the multiple comparisons. Due to a small sample size, a Spearman correlation was performed to look for relationships among FA/MD values, tonsillar level, and the SOT score.

measured below the basion and opisthion line was assigned as a negative value.

Measurement Reproducibility
For FA and MD assessment of the medulla oblongata and spinal cord at different levels, we strictly obeyed the precise anatomic definition for the ROIs. Figure 4 shows the FA and MD maps of 1 axial section at the C2–3 level from 1 healthy control. The boundary can be manually recognized without difficulty. The intraclass correlation coefficients of intraobserver variation for the medulla oblongata and different segments of the spinal cord were measured for FA and MD to test the reproducibility of the measurements. The mean intraclass correlation coefficient for FA was 0.91

RESULTS
FA and MD Values in the Medulla Oblongata and Spinal Cord

The mean values of FA and MD obtained from ROIs at different levels of the medulla oblongata and spinal cord were compared between the AIS and healthy control groups. The summary of FA and MD values (mean ± SE) at different levels is shown in Fig 5. The FA and MD values had similar ranges between the 2 groups. The FA values ranged from 0.4 to 0.8, while the MD values were in the range of 0.4–1 ($\times 10^{-3}$mm^2/s). The data above were in agreement with measurements from a previous study.[28] The patterns of variation of FA and MD along the spinal cord were similar in the AIS and healthy groups.

Table 1: Descriptive statistics of the FA comparison between AIS and controls

	AIS	Control	P Value
Medulla	0.44 (0.03)	0.46 (0.02)	<.01
C1–2	0.68 (0.03)	0.75 (0.02)	<.01
C2–3	0.68 (0.04)	0.74 (0.02)	<.01
C3–4	0.68 (0.04)	0.73 (0.03)	<.01
C4–5	0.69 (0.04)	0.72 (0.04)	.03

Table 2: Descriptive statistics of the MD comparison between AIS and controls

	AIS ($\times10^{-3}$ mm^2/s)	Control ($\times10^{-3}$ mm^2/s)	P Value
Medulla	0.99 (0.05)	0.93 (0.05)	<.01
C1–2	0.57 (0.05)	0.50 (0.03)	<.01
C2–3	0.60 (0.06)	0.52 (0.03)	<.01
C3–4	0.58 (0.05)	0.52 (0.03)	<.01
C4–5	0.57 (0.04)	0.52 (0.03)	.01

Statistical analysis revealed significant difference in FA values between the AIS and control groups ($P < .05$). The FA values in the AIS group were significantly lower at the medulla oblongata and along the cervical cord at C1–2, C2–3, C3–4, and C4–5 levels. Significantly higher MD values were observed in all the corresponding levels when comparing the AIS group with normal controls ($P < .05$). The results are summarized in Tables 1 and 2. There was, however, no significant difference in FA or MD values in the cord between the 2 groups from C5–6 downward, including the entire thoracic cord. In the AIS group, a significant correlation was found between the Cobbs angle and FA at the T8–9 level ($P = .002$), which corresponded to the level of the scoliotic apex in most of the subjects in this cohort; the FA values, however, showed no significant difference between patients with AIS and controls.

Cerebellar Tonsil Level and Correlations

The tonsil level between patients with AIS and healthy controls was analyzed. The average tonsil level was −0.28 mm (range, −9.07–5.11 mm) in AIS, while it was 1.32 mm (range, −5.47–5.43 mm) in healthy controls. A positive value indicated the tip of the tonsil above the basion and opisthion line and vice versa. Although the level of the cerebellar tonsils was lower than that in controls, this did not reach statistical significance ($P = .165$), likely, in part, due to the small sample size.

In general when taking into account all subjects (both patients with AIS and healthy controls), there was no significant correlation between the FA values in the medulla oblongata/spinal cord and the tonsillar level. However, if only the AIS group was considered, a significant correlation was noted between the tonsillar level and FA values at C4–5 ($P = .007$ and correlation coefficient $= 0.707$), while a trend toward significance was at C7–T1 ($P = .059$, correlation coefficient $= -0.536$). No such correlation was observed in the healthy control group.

SOT Findings

For the SOT, a lower score was observed in AIS only at condition 6 (ie, sway-referenced visual surroundings, sway-referenced surface). A borderline significance was found in the correlation between the SOT core and FA values at the medulla ($P = .05$).

DISCUSSION

A number of studies have analyzed the morphologic changes within the central nervous system in AIS.[29,30] MR imaging has long been used for assessment of the brain and spinal cord in AIS in view of its high resolution and excellent soft-tissue contrast.[10] Geissele et al[31] found asymmetry in the ventral medulla relating to the location of the corticospinal tracts in some patients with AIS. Dohn et al[32] reported a significant rotation of the spinal cord in patients with AIS. Smorgick et al[29] reported the spinal cord in AIS following the curve of scoliosis on T2-weighted MR imaging. In previous works,[7,8,30] significantly reduced ratios of spinal cord to vertebral column were found in patients with AIS by using multiplanar reformatted MR imaging. All the above observations were based on conventional MR imaging, which only revealed macroscopic information of the brain stem and spinal cord. DTI provides information about the anisotropy and diffusivity of WM fibers within the central nervous system and, hence, is more sensitive to pathologic changes compared with conventional MR imaging. In this pilot study, we used the DTI technique to evaluate the medulla oblongata and spinal cord of the patients with AIS at the microstructural level, which might help to understand the pathophysiology accounting for the abnormal SEP, which was commonly observed in this group.

In this study, we applied the DTI technique to examine the entire spinal cord in AIS. In previous studies, only part of the cord was examined because this was the intrinsic limitation of DTI by its relatively small FOV.[33,34] In this study, we have used an effective validated in-house method,[22] which enabled analysis of the entire spinal cord by stitching DTI acquired at different levels. As the diffusion tensor images of the entire spinal cord were stitched and connected together, ROIs could then be correctly positioned with reference to the vertebral and intervertebral levels.

However, there were still technical difficulties that we tried to overcome as illustrated below: First, compared with brain DTI, the small structure of spinal cord was more sensitive to distortion derived from eddy currents and physiologic artifacts. The distortion can potentially occur on DTI of both healthy controls and patients with AIS. It may lead to inaccurate calculation of diffusion tensors and scalar maps. Of note, it was even more challenging for patients with AIS compared with healthy controls. The stretching of the cord in AIS made it lie closer to the thecal sac and spinal canal over the curved segments,[8,33] leading to gradient inhomogeneities in these areas. Furthermore, the ROIs were defined in an oblique manner in the coronal view at the curved segments. The powerful Diffusion Toolbox was used to correct the distortion. To minimize measurement errors due to the intrinsic limitations of DTI in the spinal cord, we did not include the voxels influenced by gradient inhomogeneities in the region-of-interest definition. A relatively large number of voxels were selected to reduce the influence of the oblique manner of region-of-interest selection in patients with AIS. The curves of the patients with AIS in our study began at a vertebral level lower than T6; hence, when we compared FA and MD values between patients with AIS and controls, measurements were only affected by the above factor in segments below T6, while measurements at the cervical segments were not affected.

Last, in our study, different numbers of noncollinear gradients

were used for the brain and spinal cord DTI. A relatively small number of gradients were acquired for the spinal cord DTI compared with the brain DTI. This may affect the accuracy of the tensor estimation. To maximally reduce the influence, we applied the robust weighted least-squares fitting approach to guarantee the high image quality in the spinal cord DTI.

Significant differences in FA and MD values were found along the medulla oblongata and the cervical spinal cord in AIS. These changes were correlated with the SEP dysfunction that was reported in AIS as discussed in the introduction. Recent studies demonstrated a correlation between DTI and SEP,[35-37] in which a decrease of FA values was found to be associated with abnormal SEPs.[35,36] Petersen et al[35] proposed that both DTI metrics and neuronal excitability were affected by morphometry and permeability of the axonal membrane to water. In our study, a decrease in FA values within the medulla oblongata and from C1–2 to C4–5 cervical cord levels in AIS was in agreement with previously observed high percentage of disturbed somatosensory function in this group. Most interesting, a correlative relationship was also found between the tonsillar level and abnormal FA values in AIS. Our proposed explanation for the above changes was that there was an anatomic compression of the relatively low-set cerebellar tonsil[9] onto the craniocervical junction. This subclinical type of cord compression might affect the neural pathway above and below the maximal area of compression (ie, the lower part of the brain stem [the medulla oblongata] and the upper cervical cord region). Another consideration was that the cord compression caused by the low-set tonsils could be dynamic and might not be readily reflected by the static MR images of the subjects with AIS who were scanned in a supine position. However, the tonsil might descend further and the cord compression might be more significant when the patients with AIS resume an upright position, hence causing chronic insult to the brain stem and cervical cord during the daytime. The DTI findings support our proposed hypothesis of disturbed WM integrity within the brain stem and spinal cord, which, together with low-lying cerebellar tonsils, is an associated feature of a tethered cord in AIS. The changes in FA and MD are in line with abnormal SEPs observed clinically.

One of the main limitations of our study is that we did not have SEP correlations due to equipment malfunction. However, SEPs have been well-documented and reproduced in other studies.[8,11-15] We are confident that a consistent observation will be found in the current cohort if SEP testing has been performed. However, in future research, the SEP abnormalities should be further quantified and correlated with the FA/MD values to enhance a better understanding of the relationships between anatomic and electrophysiologic derangement within the cord in AIS with different curve severity and resulting cord tethering.

In this study, we tried to look at other available clinical tests for correlation. The SOT test was, therefore, chosen. A lower score at SOT condition 6 (ie, sway-referenced visual surroundings, sway-referenced surface) with borderline correlation with FA values at the medulla might not be just a causal relationship because part of the function of the medulla is body balance. The disturbed WM integrity at the medulla level might, therefore, affect the balance control, which was reflected by a lower SOT score in this particular condition 6 when the body relied heavily on brain stem input

to maintain body posture; however, this observation needs to be substantiated by future large-scale studies.

Another limitation is the relatively small number of subjects in this cohort. However, our preliminary findings are encouraging, and we hope to undergo a larger-scale study if we have enough funding to pursue both SEP and DTI assessment in more subjects. Because the medulla oblongata/brain stem is the cross-road for nerve fibers involved in other higher cerebral functions, the changes on DTI may also correlate with other known neurologic abnormalities in AIS, such as abnormal postural balance or impaired vestibular function, which may be partially related to somatosensory function. Further investigations correlating DTI and other neurologic functions should be addressed in future research. The information obtained may provide a new insight to the pathophysiology of the neural pathway in AIS and may potentially affect treatment of AIS in the future.

CONCLUSIONS

We applied the DTI technique to evaluate the function of WM fibers along the medulla oblongata and spinal cord in patients with AIS. This study has demonstrated that there is altered DTI metrics in the medulla oblongata and the cervical spinal cord in patients with AIS compared with age-matched healthy subjects. Significant correlation is presented between FA values at the C4–5 and low-set tonsillar level. The findings from this study are in agreement with those in previous studies showing that abnormal SEP readings only occurred above the C5–6 level in patients with AIS and might partially explain the pathophysiology of the neural pathway involved. If substantiated, this hypothesis may potentially affect treatment of AIS in the future.

REFERENCES

1. Shi L, Wang D, Chu WC, et al. **Automatic MRI segmentation and morphoanatomy analysis of the vestibular system in adolescent idiopathic scoliosis,** *Neuroimage* 2011;54(suppl 1):S180–88
2. Burwell RG, Dangerfield PH, Freeman BJC. **Concepts on the pathogenesis of adolescent idiopathic scoliosis, bone growth and mass, vertebral column, spinal cord, brain, skull, extra-spinal left-right skeletal length asymmetries, disproportions and molecular pathogenesis.** In: Grivas TB, ed. *Conservative Scoliosis Treatment: 1st Sosort Instructional Course Lectures Book.* Amsterdam: IOS Press; 2009;135:3–52
3. Domenech J, Garcia-Marti G, Marti-Bonmati L, et al. **Abnormal activation of the motor cortical network in idiopathic scoliosis demonstrated by functional MRI.** *Eur Spine J* 2011;20:1069–78
4. Shi L, Wang D, Chu WCW, et al. **Volume-based morphometry of brain MR images in adolescent idiopathic scoliosis and healthy control subjects.** *AJNR Am J Neuroradiol* 2009;30:1302–07
5. Wang DF, Shi L, Chu WCW, et al. **Abnormal cerebral cortical thinning pattern in adolescent girls with idiopathic scoliosis.** *Neuroimage* 2012;59:935–42
6. Liu TM, Chu WC, Young G, et al. **MR analysis of regional brain**

volume in adolescent idiopathic scoliosis: neurological manifestation of a systemic disease. *J Magn Reson Imaging* 2008;27:732–36

7. Chu WC, Man GC, Lam WW, et al. **Morphological and functional electrophysiological evidence of relative spinal cord tethering in adolescent idiopathic scoliosis.** *Spine (Phila Pa 1976)* 2008; 33:673–80

8. Chu WC, Lam WW, Chan YI, et al. **Relative shortening and functional tethering of spinal cord in adolescent idiopathic scoliosis? Study with multiplanar reformat magnetic resonance imaging and somatosensory evoked potential.** *Spine (Phila Pa 1976)* 2006;31: E19–25

9. Chu WC, Man GC, Lam WW, et al. **A detailed morphologic and functional magnetic resonance imaging study of the craniocervical junction in adolescent idiopathic scoliosis.** *Spine* 2007;32:1667–74

10. Chu WC, Rasalkar DD, Cheng JC. **Asynchronous neuro-osseous growth in adolescent idiopathic scoliosis–MRI-based research.** *Pediatr Radiol* 2011;41:1100–11

11. Cheng JC, Guo X, Sher AH. **Posterior tibial nerve somatosensory cortical evoked potentials in adolescent idiopathic scoliosis.** *Spine* 1998;23:332–37

12. Hausmann ON, Boni T, Pfirrmann CWA, et al. **Preoperative radiological and electrophysiological evaluation in 100 adolescent idiopathic scoliosis patients.** *Eur Spine J* 2003;12:501–06

13. Lao ML, Chow DH, Guo X, et al. **Impaired dynamic balance control in adolescents with idiopathic scoliosis and abnormal somatosensory evoked potentials.** *J Pediatr Orthop* 2008;28:846–49

14. Guo X, Chau WW, Hui-Chan CW, et al. **Balance control in adolescents with idiopathic scoliosis and disturbed somatosensory function.** *Spine* 2006;31:E437–40

15. Cheng JC, Guo X, Sher AH, et al. **Correlation between curve severity, somatosensory evoked potentials, and magnetic resonance imaging in adolescent idiopathic scoliosis.** *Spine* 1999;24:1679–84

16. Chau WW, Guo X, Fu LLK, et al. **Abnormal somatosensory evoked potential (SSEP) in adolescent with idiopathic scoliosis—the site of abnormality.** In: *International Research Society of Spinal Deformities Symposium*. Vancouver, Canada. 2004:279–81

17. Kong Y, Wang D, Wang T, et al. **3D diffusion tensor magnetic resonance images denoising based on sparse representation.** In: *International Conference on Machine Learning and Cybernetics*. Guilin, China. 2011:1602–06

18. Konomi T, Fujiyoshi K, Hikishima K, et al. **Conditions for quantitative evaluation of injured spinal cord by in vivo diffusion tensor imaging and tractography: preclinical longitudinal study in common marmosets.** *Neuroimage* 2012;63:1841–53

19. Théaudin M, Saliou G, Ducot B, et al. **Short-term evolution of spinal cord damage in multiple sclerosis: a diffusion tensor MRI study.** *Neuroradiology* 2012;54:1171–78

20. Setzer M, Murtagh RD, Murtagh FR, et al. **Diffusion tensor imaging tractography in patients with intramedullary tumors: comparison with intraoperative findings and value for prediction of tumor resectability.** *J Neurosurg Spine* 2010;13:371–80

21. Jbabdi S, Sotiropoulos SN, Savio AM, et al. **Model-based analysis of multishell diffusion MR data for tractography: how to get over fitting problems.** *Magn Reson Med* 2012;68:1846–55

22. Wang D, Kong Y, Shi L, et al. **Fully automatic stitching of diffusion tensor images in spinal cord.** *J Neurosci Methods* 2012;209:371–78

23. Zhao DD, Zhou HY, Wu QZ, et al. **Diffusion tensor imaging characterization of occult brain damage in relapsing neuromyelitis optica using 3.0T magnetic resonance imaging techniques.** *Neuroimage* 2012;59:3173–77

24. Jenkinson M, Smith S. **A global optimisation method for robust affine registration of brain images.** *Medical Image Anal* 2001; 5:143–56

25. Cheng JCY, Chau WW, Guo X, et al. **Redefining the magnetic resonance imaging reference level for the cerebellar tonsil: a study of 170 adolescents with normal versus idiopathic scoliosis.** *Spine* 2003;28:815–18

26. Aboulezz AO, Sartor K, Geyer CA, et al. **Position of cerebellar tonsils in the normal population and in patients with Chiari malformation: a quantitative approach with MR imaging.** *J Comput Assist Tomogr* 1985;9:1033–36

27. Brouwer B, Culham EG, Liston RA, et al. **Normal variability of postural measures: implications for the reliability of relative balance performance outcomes.** *Scand J Rehabil Med* 1998;30:131–37

28. Cui J, Wen CY, Hu Y, et al. **Orientation entropy analysis of diffusion tensor in healthy and myelopathic spinal cord.** *Neuroimage* 2011;58:1028–33

29. Smorgick Y, Settecerri JJ, Baker KC, et al. **Spinal cord position in adolescent idiopathic scoliosis.** *J Pediatr Orthop* 2012;32:500–03

30. Chu WC, Lam WM, Ng BK, et al. **Relative shortening and functional tethering of spinal cord in adolescent scoliosis: result of asynchronous neuro-osseous growth, summary of an electronic focus group debate of the IBSE.** *Scoliosis* 2008;3:8

31. Geissele AE, Kransdorf MJ, Geyer CA, et al. **Magnetic resonance imaging of the brain stem in adolescent idiopathic scoliosis.** *Spine (Phila Pa 1976)* 1991;16:761–63

32. Dohn P, Vialle R, Thevenin-Lemoine C, et al. **Assessing the rotation of the spinal cord in idiopathic scoliosis: a preliminary report of MRI feasibility.** *Childs Nerv System* 2009;25:479–83

33. Porter RW. **Can a short spinal cord produce scoliosis?** *Eur Spine J* 2001;10:2–9

34. Mohammadi S, Freund P, Feiweier T, et al. **The impact of post-processing on spinal cord diffusion tensor imaging.** *Neuroimage* 2013;70:377–85

35. Petersen JA, Wilm BJ, von Meyenburg J, et al. **Chronic cervical spinal cord injury: DTI correlates with clinical and electrophysiological measures.** *J Neurotrauma* 2012;29:1556–66

36. Ellingson BM, Kurpad SN, Schmit BD. **Functional correlates of diffusion tensor imaging in spinal cord injury.** *Biomed Sci Instrum* 2008;44:28–33

37. Ellingson BM, Kurpad SN, Schmit BD. **Characteristics of mid- to long-latency spinal somatosensory evoked potentials following spinal trauma in the rat.** *J Neurotrauma* 2008;25:1323–34

Bone Mineral Density Values Derived from Routine Lumbar Spine Multidetector Row CT Predict Osteoporotic Vertebral Fractures and Screw Loosening

B.J. Schwaiger, A.S. Gersing, T. Baum, P.B. Noël, C. Zimmer, and J.S. Bauer

ABSTRACT

BACKGROUND AND PURPOSE: Established methods of assessing bone mineral density are associated with additional radiation exposure to the patient. In this study, we aimed to validate a method of assessing bone mineral density in routine multidetector row CT of the lumbar spine.

MATERIALS AND METHODS: In 38 patients, bone mineral density was assessed in quantitative CT as a standard of reference and in sagittal reformations derived from standard multidetector row CT studies without IV contrast. MDCT-to-quantitative CT conversion equations were calculated and then applied to baseline multidetector row scans of another 62 patients. After a mean follow-up of 15 ± 6 months, patients were re-assessed for incidental fractures and screw loosening after spondylodesis ($n = 49$).

RESULTS: We observed conversion equations bone mineral density$_{MDCT}$ = 0.78 × Hounsfield unit$_{MDCT}$ mg/mL (correlation with bone mineral density$_{quantitative\ CT}$, $R^2 = 0.92$, $P < .001$) for 120 kV(peak) tube voltage and bone mineral density$_{MDCT}$ = 0.86 × Hounsfield unit$_{MDCT}$ mg/mL ($R^2 = 0.81$, $P < .001$) for 140 kVp, respectively. Seven patients (11.3%) had existing osteoporotic vertebral fractures at baseline, while 8 patients (12.9%) showed incidental osteoporotic vertebral fractures. Screw loosening was detected in 28 patients (57.1% of patients with spondylodesis). Patients with existing vertebral fractures showed significantly lower bone mineral density$_{MDCT}$ than patients without fractures ($P < .01$). At follow-up, patients with incidental fractures and screw loosening after spondylodesis, respectively, showed significantly lower baseline bone mineral density$_{MDCT}$ ($P < .001$ each).

CONCLUSIONS: This longitudinal study demonstrated that converted bone mineral density values derived from routine lumbar spine multidetector row CT adequately differentiated patients with and without osteoporotic fractures and could predict incidental fractures and screw loosening after spondylodesis.

ABBREVIATIONS: BMD = bone mineral density; CV = coefficient of variation; qCT = quantitative CT; RMSE = root-mean-square error; HU = Hounsfield unit

O steoporosis is defined as a skeletal disorder characterized by compromised bone strength predisposing a person to an increased risk of fracture.[1] Osteoporotic fractures are associated with increased mortality.[2] Because osteoporosis is a disease of the elderly, prevalence of osteoporosis and thus financial costs in-duced by this disease are increasing with the aging population.[3] Therefore, osteoporosis is classified as a public health problem.[4]

Bone strength consists of 2 main parameters, bone quality and bone mineral density (BMD). Bone quality refers to architecture, turnover, damage accumulation, and mineralization.[1,5] Although BMD is only 1 component in bone strength, mineral density values have been adapted to define osteoporosis.[5,6] There are several diagnostic techniques available for measuring BMD, such as dual-energy x-ray absorptiometry or quantitative CT (qCT).[5,7-11] All established methods are associated with additional radiation exposure to the patient (eg, up to 360 μSv in qCT)[12] and additional expenses. Therefore, the purpose of this study was to establish a method to assess BMD in routine lumbar multidetector row CT data without additional radiation exposure and examination time.

Recent studies have not only demonstrated that BMD values of the lumbar spine derived from sagittal reformations of routine abdominal contrast-enhanced MDCT scans are able to differen-tiate postmenopausal women with osteoporotic vertebral frac-
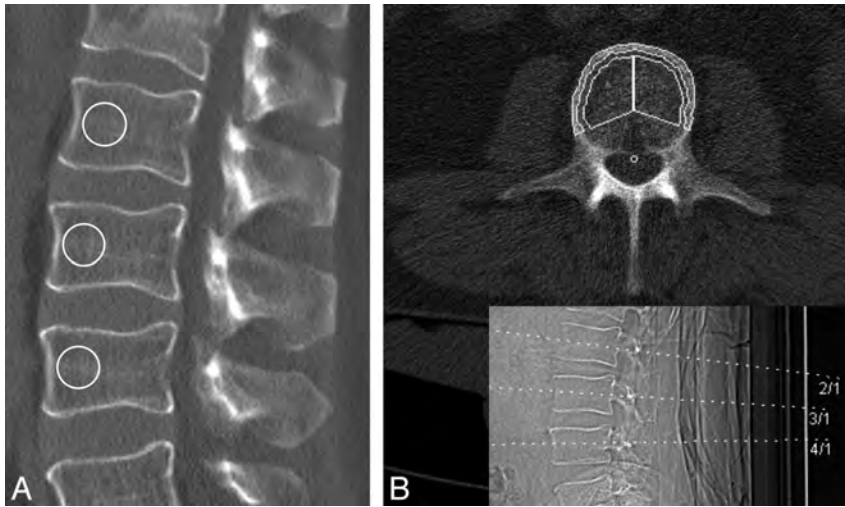
FIG 1. *A*, Reformatted sagittal 15-mm section (increment, 5 mm) located in the vertebral midline obtained by MDCT. Circular ROIs half the vertebral height are placed in the ventral halves of the trabecular compartment of the vertebrae and show mean attenuation values of the trabecular bone (Hounsfield units). *B*, Sagittal topogram showing qCT section positioning in the very same vertebrae.

tures,[13] they may also be able to predict incidental fractures.[14] However, from a neuroradiologist's perspective, there are further questions unanswered. First, it would be beneficial to understand whether BMD assessed by this method can predict screw loosening after spondylodesis, because planning of the procedure depends on bone strength.[15] Second, most of the lumbar spine MDCT scans in patients with spine disease are performed without prior application of IV contrast medium. Therefore, the method should be analyzed without the influence of IV contrast medium. Third, male patients should be included in the analysis of BMD values obtained from MDCT scans as well. With a special emphasis on these 3 aspects presented, the first aim of this study was to calculate equations to convert BMD values derived from routine lumbar spine MDCT scans to qCT-equivalent values. The second aim of this study was to analyze differences in patients with and without baseline fractures, by using converted BMD_{MDCT} values and to determine whether these baseline values predict incidental fractures and screw loosening in patients with spondylodesis.

MATERIALS AND METHODS
Patients
Patients were retrospectively identified in the PACS data base of our institution. Patients with pathologic bone changes like bone metastases and hematologic or metabolic bone disorders aside from osteoporosis were excluded from the study. Therefore, clinically available data and previous imaging studies were thoroughly analyzed.

For the development of MDCT-to-qCT conversion equations as outlined below, 38 consecutive patients (mean age, 74 ± 6.5 years; 25 women) were included, in whom both a standard lumbar MDCT without prior application of IV contrast medium and a qCT scan were performed within 90 days. Patients were categorized in 2 subgroups considering applied tube voltage: 120 kVp for standard lumbar spine studies (*n* = 24) and 140 kVp for postmyelography studies (*n* = 14), respectively. Imaging data of the subgroups were used separately to develop 2 MDCT-to-qCT conversion equations.

Next, 62 consecutive patients (mean age, 71 ± 5.8 years; 29 women) were identified in whom follow-up imaging was performed for the evaluation of incidental fractures and screw fit within 6 to 36 months. Forty-nine of those patients had spondylodesis at follow-up. The mean follow-up time was 15 ± 6 months.

The study was performed in accordance to the Declaration of Helsinki[16] and our institutional guidelines on human research. The patients gave written consent for scientific evaluation of material at the time of admission.

Imaging and Imaging Analysis
Lumbar qCT examinations were performed with two 64-row MDCT scanners (either Sensation Cardiac 64 or Somatom Definition AS; Siemens Healthcare, Erlangen, Germany) following a standard protocol according to the manufacturer's instructions. Reference phantoms with a bonelike and a waterlike phase (Osteo Phantom; Siemens) were used for calibration. Tube voltage was 80 kVp; tube load, 140 mAs; and axial section thickness, 10 mm.

The implemented automated analysis software (syngo Osteo CT, Siemens) was used to select midvertebral sections of L1, L2, and L3 based on lateral topograms of the lumbar spine. Vertebrae with fractures were excluded from analysis, and other lumbar or thoracic vertebrae were selected instead.

Afterward, axial sections were positioned in the midvertebral sections while tilting the gantry before each vertebra scan to ensure that sections were parallel to the upper and lower endplate of each vertebra. A region of interest was automatically placed by the software in the trabecular region of each vertebra, and trabecular BMD values were measured (Fig 1). Experienced radiology technologists performed the qCT studies while being supervised by experienced radiologists. For this study, the plausibility of readings was re-evaluated by 1 author (B.J.S.).

All noncalibrated lumbar spine studies were obtained with the same 64-row MDCT scanner (Brilliance 64; Philips Healthcare, Best, the Netherlands). Scanning parameters were 120 kVp tube voltage for standard lumbar spine studies and 140 kVp for postmyelography spine studies, respectively; the adapted tube load was averaged at 200 mAs and minimum collimation (0.6 mm). To ensure continuous imaging quality, the CT scanner was calibrated weekly by air calibration and on the basis of phantom scans (CT calibration phantom; Mindways Software, Austin, Texas). Sagittal reformations of the spine were reconstructed with a section thickness of 2 mm. For analysis of attenuation values (Hounsfield units [HU]) in MDCT scans (HU_{MDCT}), the sagittal reformations were loaded into the institutional PACS (EasyVision R11.4.1, Philips Healthcare).

The built-in multiplanar reconstruction tool of the PACS software was used to create a sagittal 15-mm section (increment, 5 mm) located in the vertebral midline. Thereafter, by using the attenuation measurement tool of the PACS viewer, circular ROIs

with a diameter of half the vertebral height in the ventral halves of the trabecular compartment of the vertebrae (Fig 1). In the 38 patients included in the calculation of the conversion equations, the same vertebral bodies as in the corresponding qCT scan analysis were measured. In the 62 patients in whom follow-up scans were performed, the vertebral bodies L1–L3 were analyzed. If vertebral fractures were diagnosed, other thoracic or lumbar bodies (maximum, T11–L5) were selected. The placement of all ROIs was performed by 1 author (B.J.S.). The time for region-of-interest placement and BMD calculation was <1 minute for 1 patient.

All follow-up scans were obtained with one of the previously mentioned 64-row MDCT scanners at our institution. Existing and incidental osteoporotic vertebral fractures from T12–L5 were diagnosed by 2 radiologists in consensus according to Genant et al[17] in baseline and follow-up MDCT images, respectively. They were rated according to the following scale: grade 0, normal; grade 1, mildly deformed (approximately 20%–25% reduction in anterior, middle, and/or posterior height and a reduction of area of 10%–20%); grade 2, moderately deformed (approximately 25%–40% reduction in any height and a reduction in area of 20%–40%); and grade 3, severely deformed (approximately 40% reduction in any height and area). Screw loosening was diagnosed on the follow-up MDCT images by 2 radiologists in consensus reading.

Statistical Analysis

Mean BMD_{qCT} and mean HU_{MDCT} values were calculated for vertebrae scanned in qCT and MDCT, respectively. Two separate MDCT-to-qCT conversion equations were calculated for patients scanned with 120 kVp and 140 kVp tube voltage, respectively, by using a linear regression model. The calculated prediction errors were summarized as the root-mean-square error (RMSE, in milligrams per milliliter) and the RMSE coefficient of variation (CV, percentage).[18] For further evaluation of the agreement between BMD_{qCT} and converted BMD_{MDCT}, a Bland-Altman plot was used.[19]

Patients included for follow-up analysis were split into different groups depending on their baseline fracture status, follow-up fracture status, and screw fit after spondylodesis. Mean attenuation values (HU_{MDCT}) obtained from baseline examinations were converted to BMD_{MDCT} values by applying the conversion equations for 120 kVp and 140 kVp, respectively.

General linear models were used to compare BMD_{MDCT} values between patients with versus those without existing fractures, incidental fractures at follow-up, and new signs of screw loosening at follow-up, respectively. The independent variable was the patient group, while the dependent variable was BMD_{MDCT}. Age, sex, follow-up time, and kilovolt(peak) were included as covariates in the models to obtain adjusted effects.

Receiver operator characteristic analyses were performed, and the areas under the receiver operating characteristic analysis curves were used to evaluate the overall diagnostic performance of the converted BMD_{MDCT} values to differentiate patients with and without fractures at baseline and follow-up and patients with screw loosening versus patients with proper spondylodesis status. The Youden J statistic was used to identify the optimal cutoff values for differentiation of groups.[20]

Statistical analysis was performed with the Statistical Package for the Social Sciences (IBM, Armonk, New York) and was super-
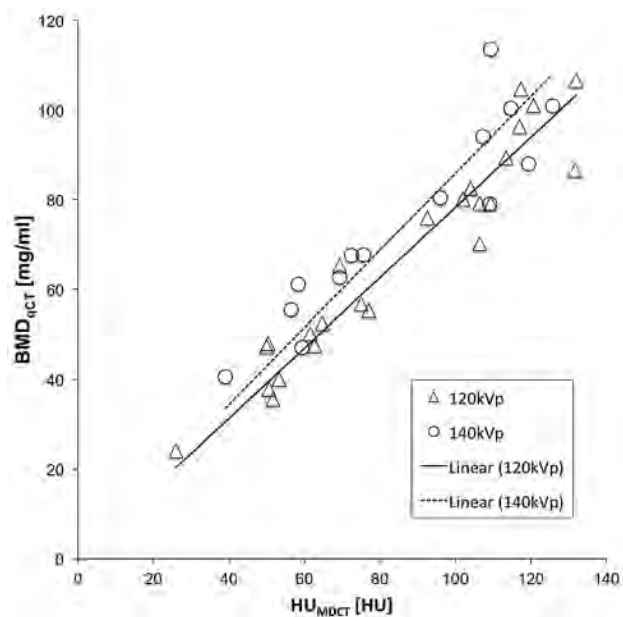
FIG 2. Linear regression of mean attenuation (Hounsfield units) and BMD of lumbar vertebrae obtained by MDCT and qCT, respectively ($R^2 = 0.92$ in 120 kVp scans and $R^2 = 0.81$ in 140 kVp scans, respectively).

vised by a statistician. All tests were performed by using a 2-sided .05 level of significance.

Reproducibility

Intrareader reproducibility was analyzed by redefining ROIs and remeasuring HU_{MDCT} values in 11 patients at least 1 week later than the first reading, and it was specified by using the root-mean-square error. Interreader reproducibility was analyzed the same way between 2 authors (A.S.G. and B.J.S) in 14 patients.

RESULTS

For calculation of the MDCT-to-BMD conversion equations, 106 vertebral bodies were selected in 38 patients. Two separate conversion equations were calculated on the basis of 24 patients for 120 kVp and 14 patients for 140 kVp, respectively.

In patients scanned with 120 kVp, linear regression analysis produced the equation $BMD_{MDCT} = 0.78 \times HU_{MDCT(120 \text{ kVp})}$ mg/mL (Fig 2), while the correlation coefficient was $R^2 = 0.92$ ($P < .001$). In 140 kVp scans, the equation $BMD_{MDCT} = 0.86 \times HU_{MDCT(140 \text{ kVp})}$ mg/mL was calculated (Fig 2) with a correlation coefficient of $R^2 = 0.81$ ($P < .001$). Calculation of prediction errors showed an overall RMSE of 13.5 mg/mL and an RMSE CV of 15.9%.

The Bland-Altman plot showed good agreement between BMD values obtained from qCT and MDCT (Fig 3).

Intrareader reproducibility analysis showed an RMSE of 2.2 mg/mL and an RMSE CV of 2.5%, while interreader reproducibility analysis showed an RMSE of 2.0 mg/mL and an RMSE CV of 2.7%.

Among the 62 patients with follow-up scans, 7 had an osteoporotic fracture at baseline (11.3%), while in 8 patients, incidental osteoporotic fractures were found at follow-up (12.9%). Twenty-eight of 49 patients with spondylodesis showed signs of screw loosening on follow-up imaging (57.1%).

After adjustment for age, sex, follow-up time, and tube voltage,

FIG 3. Bland-Altman plot showing the means versus the difference of the converted BMD values and BMD values obtained by MDCT and qCT, respectively. The solid line indicates the mean BMD difference of MDCT and qCT (-0.75 mg/mL). The dotted lines indicate mean difference $\pm 1.96 \times$ SD.

FIG 4. This plot shows mean $\pm$ SD converted BMD_{MDCT} values for patients with/without baseline fractures, with/without incidental fractures at follow-up, and with/without screw loosening during follow-up. The asterisk indicates $P < .01$; the degree sign, $P < .001$.

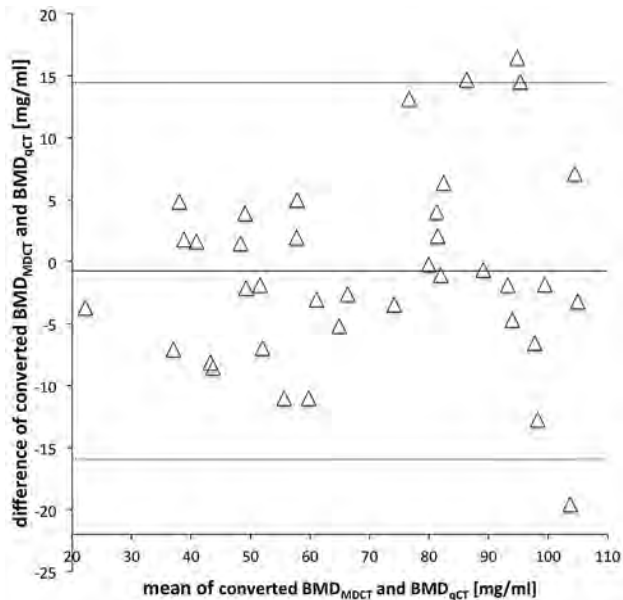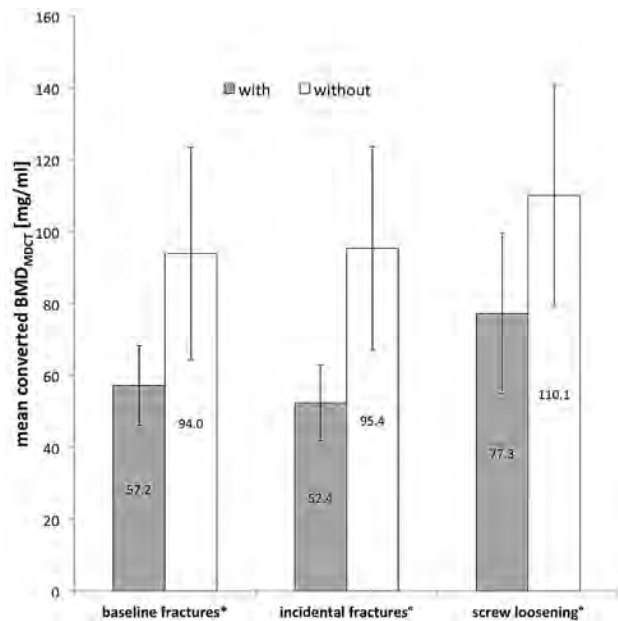patients with osteoporotic fractures at baseline had significantly lower BMD_{MDCT} values than patients without fractures (57.2 $\pm$ 11.2 versus 94.0 $\pm$ 29.5 mg/mL; $P < .01$; Fig 4). For differentiating these patients, an area under the ROC curve of 0.912 ($P < .001$) was computed in the receiver operating characteristic analysis. The Youden index showed an optimal cutoff at 68.9 mg/mL (sensitivity, 0.78; specificity, 1.00; $J = 0.78$; Table).

Patients who developed incidental fractures during follow-up showed significantly lower baseline BMD_{MDCT} values than pa-

tients without incidental fractures (52.4 $\pm$ 10.5 versus 95.4 $\pm$ 28.4 mg/mL; $P < .001$; adjusted for age, sex, follow-up time, and tube voltage; Fig 4). In the receiver operating characteristic analysis of these groups, the area under the ROC curve was 0.972 ($P < .001$). Optimal cutoff for the prediction of incidental fractures was 66.8 mg/mL (sensitivity, 0.87; specificity, 1.00; $J = 0.87$; Table).

Patients with spondylodesis and signs of screw loosening at follow-up (Fig 5) had significantly lower BMD_{MDCT} values than patients without screw loosening (77.3 $\pm$ 22.3 versus 110.1 $\pm$ 30.7 mg/mL; $P < .001$; adjusted for age, sex, follow-up time, and tube voltage; Fig 4). An area under the ROC curve value of 0.827 ($P < .001$) was computed in the receiver operating characteristic analysis to differentiate these groups. The Youden index showed an optimal cutoff at 92.0 mg/mL (sensitivity, 0.81; specificity, 0.79; $J = 0.60$; Table).

A significant ($P < .05$) influence of age and follow-up time on BMD_{MDCT} values was found in general linear models for all analyses: A lower BMD_{MDCT} was associated with higher age and shorter follow-up time. While we compared groups with versus without fractures at baseline and follow-up and with versus without screw loosening, there was no significant sex-related influence in linear models ($P = .52$ at baseline and $P = .10$ at follow-up, respectively; screw loosening, $P = .94$).

DISCUSSION

In this study, we have shown that converted BMD values obtained from noncalibrated, lumbar spine MDCT studies (BMD_{MDCT}) cannot only differentiate patients with and without existing osteoporotic fractures at baseline and incidental fractures during follow-up, but also may be used as prognostic markers for screw loosening in patients with spondylodesis. For clinical routine, we have calculated an easy-to-use MDCT-to-qCT conversion equation.

Existing methods for assessment of BMD such as dual-energy x-ray absorptiometry and qCT are well-established and, in most cases, provide reliable information.[7,9,10] However, while acquiring data for this study, we have seen that qCT validity highly depends on the technician performing the analysis. In qCT, there is only basic morphologic information provided by the sagittal topogram; therefore, pathologies such as fractures or hemangiomas may not be detected. By contrast, studies have shown that detection of osteoporotic fractures is reliable in sagittal reformations of MDCT scans.[21,22] Similar to previous studies, we were able to avoid incorrect measurements by using the sagittal reformations to perform BMD measurements.[13,14]

In previous studies, it has been demonstrated that routine contrast-enhanced and non-contrast-enhanced abdominal CT as well as cardiac CT scans may be used to determine BMD of the spine.[13,14,23-26] We have developed 2 MDCT-to-qCT conversion equations for 120 kVp and 140 kVp tube voltage, respectively, which both show a high correlation coefficient and are comparable with previous studies.[13,14]

To our knowledge, there were 3 aspects that have been analyzed in this study for the first time: First, we were able to confirm converted BMD values obtained from MDCT scans as prognostic markers for screw loosening in patients with spondylodesis. Second, this study presented conversion equations for 2 different tube voltages, both based on standard lumbar scans without prior application of IV contrast medium. Third, men were included in

Mean Hounsfield unit and BMD$_{MDCT}$ values of patients with/without osteoporotic fractures at baseline and follow-up and with/without screw loosening[a]

	Group Size	Baseline HU	Baseline BMD$_{MDCT}$ Values	Pathology vs No Pathology (HU and BMD$_{MDCT}$)	ROC AUC (BMD$_{MDCT}$)	Cutoff and Youden Index
With baseline fractures	7	70.1 ± 13.2	57.2 ± 11.2			
Without baseline fractures	55	114.4 ± 37.4	94.0 ± 29.5	$P < .01$[b]	0.912[c]	68.9 ($J = 0.78$)
With incidental fractures	8	63.8 ± 12.7	52.4 ± 10.5			
Without incidental fractures	54	116.1 ± 36.0	95.4 ± 28.4	$P < .001$[b]	0.972[c]	66.8 ($J = 0.87$)
Screw loosening	28	93.4 ± 26.5	77.3 ± 22.3			
Without screw loosening	21	132.9 ± 40.5	110.1 ± 30.7	$P < .001$[b]	0.827[c]	92.0 ($J = 0.60$)

Note:—ROC indicates receiver operating characteristic analysis; AUC, area under the ROC curve.

[a] Hounsfield units and BMD$_{MDCT}$ values are given as mean ± SD in milligrams per milliliter. Cutoff values are given in milligrams per milliliter.

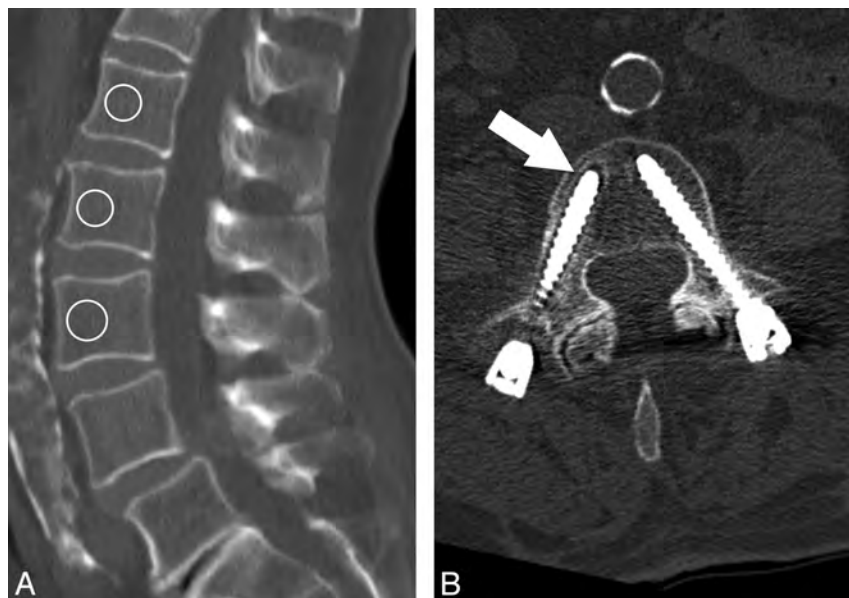[b] Adjusted for age, sex, follow-up time, and tube voltage.

[c] $P < .001$.

FIG 5. A 70-year-old female patient with chronic back pain due to instability in the L4/L5 segment. *A*, Vertebrae showing a mean converted BMD$_{MDCT}$ of 66.8 mg/mL, diagnosed as osteoporosis according to Felsenberg and Gowin.[28] *B*, Follow-up MDCT of the same patient 9 months later showing signs of screw loosening after spondylodesis in L3 (*arrow*).

this study, whereas similar studies were based only on postmenopausal women.[13,14] From a neuroradiologist's perspective, these aspects are particularly noteworthy because all patients included in this study were primarily referred by the department of neurosurgery. Those patients routinely undergo MDCT without application of IV contrast medium before surgery. Because operation planning (eg, planning of spondylodesis material) depends on bone structure and condition,[15] additional information provided by the method presented may be highly beneficial for patients.

Meredith et al[27] recently described preoperative Hounsfield units to be lower in patients with adjacent segment fractures after spinal fusion than in controls without fractures. These findings agree with our results, because we found both original Hounsfield units as well as converted BMD$_{MDCT}$ values able to predict osteoporotic fractures.

In previous studies, Baum et al[13,14] described the difficulties of estimating the influence of IV contrast medium on the reproducibility of the method as the major limitation. Because no IV contrast medium was applied to the patients in this study, this limitation is removed. All patients scanned with 140 kVp had received intrathecal contrast medium for myelography. General linear models have shown that there was no significant influence of the contrast medium on the prediction of fractures or screw loosening.

Of note, the presented BMD$_{MDCT}$ cutoff values corresponded well to the standard values described in the literature.[28] The cutoff value for prediction of incidental fractures (66.8 mg/mL) was just within the range of BMD values considered as osteoporosis (<80 mg/mL). The cutoff value for the prediction of screw loosening (92.02 mg/mL) was in the lower range of osteopenia (120–80 mg/mL), which is consistent with the finding that in patients with healthy bone, screw loosening very rarely occurs.

The method presented is not associated with additional radiation exposure to patients. Therefore, additional information beneficial for patients may be gathered by using already available data obtained from the examinations performed in daily clinical routine.

As in previous studies,[13,14] conversation equations are limited to the CT scanner and the scan protocols used. However, given an adequate comparison group, this method can be transferred to any clinical MDCT scanner. Recently, Budoff et al[29] analyzed phantomless BMD measurements performed with 14 different scanner models. The quoted study reported calibration factors comparable with the conversion equation presented in this study to vary significantly across scanner models.

Compared with the short-term reproducibility of qCT (CV, 1.0%–1.5%[7]), this method had slightly higher intrareader and interreader reproducibility errors (CVs of 2.5% and 2.7%, respectively). However, the reproducibility error was lower than the BMD differences between the investigated groups. Thus, BMD$_{MDCT}$ measurements represent a reliable prognostic marker for incidental osteoporotic vertebral fractures and screw loosening after spondylodesis which, may help for surgical decision-making of whether to extend a spondylodesis or use cement fixation of the screws.

A significant correlation between follow-up time and BMD values obtained from MDCT scans has been found. Our hypoth-

esis is that patients with lower BMD values are at a higher risk for spine diseases in general and therefore are more often examined by radiologists. It is congruent with qCT findings of other investigators that age has a significant influence on BMD values obtained from MDCT scans.[30,31]

CONCLUSIONS

This study presented a reproducible and valid method for obtaining converted BMD values from standard lumbar spine MDCT scans. This method may easily be integrated into clinical routine by using already available standard PACS tools. Converted BMD values cannot only differentiate patients with and without baseline fractures but also predict incidental fractures and screw loosening in patients with spondylodesis. These findings suggest that additional analysis of data obtained from noncalibrated MDCT scans may replace dedicated densitometry measurements in certain settings.

REFERENCES

1. NIH Consensus Development Panel on Osteoporosis Prevention, Diagnosis, and Therapy. **Osteoporosis prevention, diagnosis, and therapy.** *JAMA* 2001;285:785–95
2. Ioannidis G, Papaioannou A, Hopman WM, et al. **Relation between fractures and mortality: results from the Canadian Multicentre Osteoporosis Study.** *CMAJ* 2009;181:265–71
3. Cole ZA, Dennison EM, Cooper C. **Osteoporosis epidemiology update.** *Current Rheumatology Reports* 2008;10:92–96
4. Holroyd C, Cooper C, Dennison E. **Epidemiology of osteoporosis.** *Best Pract Res Clin Endocrinol Metab* 2008;22:671–85
5. Link TM. **Osteoporosis imaging: state of the art and advanced imaging.** *Radiology* 2012;263:3–17
6. Kanis JA, Kanis JA. **Assessment of fracture risk and its application to screening for postmenopausal osteoporosis: synopsis of a WHO report.** *Osteoporosis Int* 1994;4:368–81
7. Adams JE. **Quantitative computed tomography.** *Eur J Radiol* 2009;71:415–24
8. Bauer JS, Link TM. **Advances in osteoporosis imaging.** *Eur J Radiol* 2009;71:440–49
9. Bergot C, Laval-Jeantet AM, Hutchinson K, et al. **A comparison of spinal quantitative computed tomography with dual energy X-ray absorptiometry in European women with vertebral and nonvertebral fractures.** *Calcif Tissue Int* 2001;68:74–82
10. Blake GM, Fogelman I. **An update on dual-energy x-ray absorptiometry.** *Semin Nucl Med* 2010;40:62–73
11. Damilakis J, Maris TG, Karantanas AH. **An update on the assessment of osteoporosis using radiologic techniques.** *Eur Radiol* 2007;17:1591–602
12. Njeh CF, Fuerst T, Hans D, et al. **Radiation exposure in bone mineral density assessment.** *Appl Radiat Isot* 1999;50:215–36
13. Baum T, Muller D, Dobritz M, et al. **BMD measurements of the spine derived from sagittal reformations of contrast-enhanced MDCT without dedicated software.** *Eur J Radiol* 2011;80:e140–145
14. Baum T, Muller D, Dobritz M, et al. **Converted lumbar BMD values derived from sagittal reformations of contrast-enhanced MDCT predict incidental osteoporotic vertebral fractures.** *Calcif Tissue Int* 2012;90:481–87
15. Ponnusamy KE, Iyer S, Gupta G, et al. **Instrumentation of the osteoporotic spine: biomechanical and clinical considerations.** *Spine J* 2011;11:54–63
16. World Medical Association General Assembly. *Declaration of Helsinki: Ethical Principles for Medical Research Involving Human Subjects.* Helsinki: World Medical Association: 1964
17. Genant HK, Wu CY, van Kuijk C, et al. **Vertebral fracture assessment using a semiquantitative technique.** *J Bone Miner Res* 1993;8:1137–48
18. Glüer CC, Blake G, Lu Y, et al. **Accurate assessment of precision errors: how to measure the reproducibility of bone densitometry techniques.** *Osteoporos Int* 1995;5:262–70
19. Bland JM, Altman DG. **Statistical methods for assessing agreement between two methods of clinical measurement.** *Lancet* 1986;1:307–10
20. Youden WJ. **Index for rating diagnostic tests.** *Cancer* 1950;3:32–35
21. Bauer JS, Muller D, Ambekar A, et al. **Detection of osteoporotic vertebral fractures using multidetector CT.** *Osteoporos Int* 2006;17:608–15
22. Müller D, Bauer JS, Zeile M, et al. **Significance of sagittal reformations in routine thoracic and abdominal multislice CT studies for detecting osteoporotic fractures and other spine abnormalities.** *Eur Radiol* 2008;18:1696–702
23. Bauer JS, Henning TD, Mueller D, et al. **Volumetric quantitative CT of the spine and hip derived from contrast-enhanced MDCT: conversion factors.** *AJR Am J Roentgenol* 2007;188:1294–301
24. Lenchik L, Shi R, Register TC, et al. **Measurement of trabecular bone mineral density in the thoracic spine using cardiac gated quantitative computed tomography.** *J Comput Assis Tomogr* 2004;28:134–39
25. Link TM, Koppers BB, Licht T, et al. **In vitro and in vivo spiral CT to determine bone mineral density: initial experience in patients at risk for osteoporosis.** *Radiology* 2004;231:805–11
26. Papadakis AE, Karantanas AH, Papadokostakis G, et al. **Can abdominal multi-detector CT diagnose spinal osteoporosis?** *Eur Radiol* 2009;19:172–76
27. Meredith DS, Schreiber JJ, Taher F, et al. **Lower preoperative Hounsfield unit measurements are associated with adjacent segment fracture after spinal fusion.** *Spine* 2013;38:415–18
28. Felsenberg D, Gowin W. **Bone densitometry by dual energy methods** [in German]. *Radiologe* 1999;39:186–93
29. Budoff MJ, Malpeso JM, Zeb I, et al. **Measurement of phantomless thoracic bone mineral density on coronary artery calcium CT scans acquired with various CT scanner models.** *Radiology* 2013;267:830–36
30. Bouxsein ML, Melton LJ, 3rd, Riggs BL, et al. **Age- and sex-specific differences in the factor of risk for vertebral fracture: a population-based study using QCT.** *J Bone Miner Res* 2006;21:1475–82
31. Riggs BL, Melton LJ, 3rd, Robb RA, et al. **Population-based study of age and sex differences in bone volumetric density, size, geometry, and structure at different skeletal sites.** *J Bone Miner Res* 2004;19:1945–54

Acute Myelopathy or Cauda Equina Syndrome in HIV-Positive Adults in a Tuberculosis Endemic Setting: MRI, Clinical, and Pathologic Findings

S. Candy, G. Chang, and S. Andronikou

ABSTRACT

BACKGROUND AND PURPOSE: Cape Town is the center of an HIV-tuberculosis coepidemic. This study's aim was to highlight the importance and to describe the MR imaging features of tuberculosis in acute myelopathy and cauda equina syndrome in HIV-positive adults. To accomplish this we retrospectively reviewed the MR imaging and clinico-pathologic findings of HIV-positive patients presenting to our hospital with recent onset paraplegia and sphincter dysfunction over a 4-year period, 2008–2011.

MATERIALS & METHODS: MR imaging, CD4 count, and CSF analysis and pathology were correlated in 216 cases.

RESULTS: Fifty-eight percent (127) of subjects were female. The mean age was 37 years. The median CD4 count was 185 cells/μL. Twenty-five percent (54) of patients were on antiretroviral therapy. MR imaging showed spondylitis in 30% (65). The median CD4 count in these patients was significantly higher than in the remainder. Disk destruction was common and 10% had synchronous spondylitis elsewhere in the spinal column. Thirty percent (64) had features of myelitis/arachnoiditis. Twenty-five percent (55) had no MR imaging abnormality. In 123 (57%) of cases with a definitive etiology on CSF culture or biopsy, 84 (68%) were attributable to tuberculosis including all spondylitis cases and 40% of nonspondylitis cases. Twelve (10%) were due to nontuberculous infection and 12 (10%) had HIV-associated tumors including 2 rare Epstein-Barr–related tumors.

CONCLUSIONS: In our setting, acute onset myelopathy/cauda equina syndrome in HIV-positive patients is largely attributable to tuberculosis with nonspondylitic forms being more common than spondylitis and associated with a lower CD4 count.

ABBREVIATIONS: TB = tuberculosis; ARV = antiretroviral; EB = Epstein-Barr virus

Cape Town, South Africa is presently experiencing a coepidemic of HIV and tuberculosis (TB). South Africa currently ranks fourth in the world for tuberculosis disease with an annual incidence rate in the Western Cape of 935/100,000.[1] The HIV epidemic has greatly increased the prevalence of both drug sensitive and resistant forms of tuberculosis and extrapulmonary forms of the disease.[2] Spinal tuberculosis particularly is reported to be more common in persons infected with HIV.[3]

Over the past decade, increasing numbers of young HIV-positive adults have been referred to our institution for spinal MR imaging after the onset of myelopathy or cauda equina syndrome. Although many of these patients have the typical MR findings of TB spondylitis, many do not. Nonspondylitic spinal tuberculosis has not received wide attention in the literature and in particular has not been widely reported in association with HIV.

Aim

This study's aim was to highlight the importance of tuberculosis and document the MR imaging findings in relation to other causes in the setting of acute myelopathy and cauda equina syndrome in HIV-positive adults.

METHOD
Study Design

The design was a retrospective descriptive study of MR imaging scans and clinical/laboratory data in HIV-positive patients presenting with paraplegia and sphincter dysfunction to 1 tertiary referral center in the Western Cape of South Africa.

Defining the Study Population

The study population included patients who had received MR imaging scans for recent onset myelopathic or cauda equina symptoms at our institution, which provides MR imaging, specialist neurologic, neurosurgical, and orthopaedic care to the population of Greater Cape Town (population 3 million).

MR Imaging Scanning

All imaging was performed on the same 1.5T MR scanner (Symphony; Siemens, Erlangen, Germany). A routine protocol was observed: T2 sagittal whole spine and T2 axial (through any area of pathology) with T1 sagittal and axial images in selected cases. FISP imaging of the chest and abdomen was used to determine the presence of lymphadenopathy, solid organ lesions, and marrow edema. In accordance with hospital protocol in a resource constrained environment, gadolinium was administered only when an intramedullary lesion, epidural abscess, or arachnoiditis was suspected (42% of those without spondylitis received gadolinium). Diffusion-weighted spinal imaging was not successfully implemented at the time of the study.

Source of Data, Inclusion, and Exclusion Criteria

A manual search of the MR imaging archive was conducted for referrals of recent onset myelopathic or cauda equina symptoms (lower limb weakness with loss of sphincter control with or without a sensory level), in HIV-positive adults over a 42-month period (2008–2011). The hospital records and National Health Laboratory Service data base were reviewed to confirm HIV and antiretroviral (ARV) status, a diagnosis of pre-existing tuberculosis and antituberculous treatment, age, sex, CD4 count, CSF microscopy, biochemistry, and culture yield from any site. Patients were excluded when HIV status was not confirmed.

Determining the Diagnosis

For the purpose of the study, etiology was confirmed by using laboratory information. The diagnosis of tuberculosis was made definitively when culture was positive or when acid fast bacilli were identified on a Ziell Nielsen stain from any tissue sample (including samples from sites outside the CNS).

An alternative diagnosis was made where an organism other than *Mycobacterium tuberculosis* was observed directly or on CSF culture. Neoplasms were diagnosed on fine-needle aspiration or tissue biopsy.

MR Imaging Diagnoses

The MR imaging scans were evaluated by 1 senior neuroradiologist for the presence of pathologic features in the spinal column, spinal cord, thecal sac, and outside of the CNS. These findings were used to define the following diagnostic imaging categories: spondylitis, myelitis/arachnoiditis, bone neoplasm, nonbone neoplasm, isolated syrinx, and other (Appendix 1).

Assessment and Analysis

1. The causes of acute paraplegia and the extent of spondylitis and nonspondylitic lesions were determined.
2. The CD4 count was compared in those with and without spondylitis on MR imaging.
3. The CD4 counts were compared for those on ARVs with those who were not.
4. The MR imaging appearance, CSF, and biopsy findings in all patients are described with particular reference to the imaging findings in those patients with a definitive diagnosis of tuberculosis.
5. The subgroup of patients with a definitive etiologic diagnosis (TB or alternative causation) was analyzed to determine the causal relationship of TB with myelopathy/cauda equina.
6. Statistical analysis was done by using the Mann Whitney U test to assess differences between groups.

Limitations

The retrospective nature of the study meant that no control was possible on standardizing laboratory tests to confirm an etiologic diagnosis. MR imaging scanning techniques were limited to standard hospital protocol and gadolinium was not routinely used.

RESULTS

Demographics

From a group of 227 patients, 11 were excluded because HIV was not confirmed or the clinical criteria of paraplegia and loss of sphincter function were not met. The study group (216 cases) comprised 127 women (58%) and 89 men (42%). The mean age was 36.7 years (range 19–64 years; men 39 years, women 35 years). The median CD4 count was 185 cells/μL. Fifty-four (25%) patients were on ARVs, though the duration of their treatment and their pretreatment CD4 count were not available. Fifty-five patients were being treated for documented tuberculosis, though only 9 had documented tuberculous meningitis at the time of onset of myelopathic/cauda equina symptoms.

Overall Analysis of MR Imaging Findings for the Total Group (n = 216)

Fifty-five (25%) of the patients had no abnormality on MR imaging, 65 (30%) had spondylitis, 64 (30%) had myelitis/arachnoiditis/intramedullary lesions. The remaining 15% comprised 10 cases of lymphoma, 2 Epstein-Barr (EB)–related tumors, 7 bone tumors, 8 disk herniations, 2 cases of syrinx, and 3 cases in which the findings could not be categorized (Table 1 and Appendix 2).

CD4 Counts and MR Imaging Findings

CD4 Counts in Patients on ARVs (54) versus Those Not on ARVs (162). There was no difference in the mean CD4 count between those on ARVs and those who were not (185 cells/μL in each group).

No significant differences were found in either the CSF or on MRI between those on ARVs versus those not on ARVs: Spondylitis in 35% on ARVs versus 28% in those not; myelitis (33% versus 28%); no MR abnormality (20% versus 27%); lymphoma (6% in each group); incidental findings (6% versus 10%).

CD4 Counts in Patients with Spondylitis (65) versus Those without Spondylitis (161). The median CD4 count for the entire group was 185 cells/μL. We found a significant difference in the median CD4 counts of patients with spondylitis (225 cells/μL) and those without spondylitis (147 cells/μL) by using the Mann-Whitney U test ($P = .0017$).

Table 1: MRI-based pathologic categories in 216 patients with HIV and acute onset myelopathy/cauda equina

MRI Normal	MRI Abnormal									
Normal Group	Spondylitis Group	Nonspondylitis Groups								
		Arachnoiditis-Myelitis Intramedullary Tuberculomas	Neoplasm Nonbone		Neoplasm Bone			Other		
	Spondylitis		HIV Associated	Lymphoma	Lymphoma	Plasmacytoma	Mets	Disk	Syrinx	?
55	65	64	2	10		3	4	8	2	3

Note:—? indicates no final diagnosis.
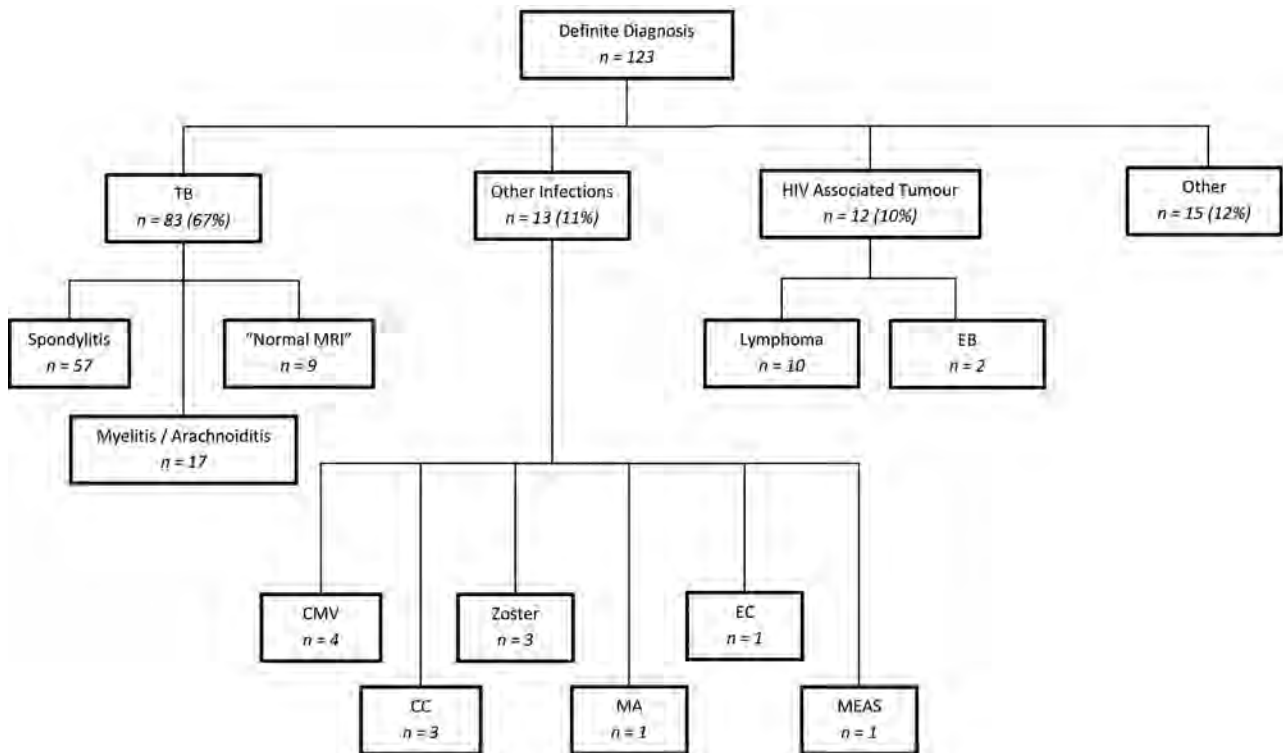
FIG 1. Summary of causation of myelopathy. Abbreviations: CC indicates *cryptococcus*; Zoster, Varicella zoster; MA, *Mycobacterium avium*; EC, *enterococcus;* and MEAS, measles; CMV, cytomegalovirus.

Clinical and Laboratory Diagnosis

Patients with a Definitive Etiologic Diagnosis (*n* = 123). A definitive etiologic diagnosis was made in 123 of 216 (57%) (Fig 1). Most of these cases (84) (68%) were attributable to TB, including 1 case of *Mycobacterium avium.* Multidrug resistance was found in only 1 of the 84 tuberculosis cases. Thirteen (10%) patients had nontuberculous infections. Twelve (10%) had HIV-associated tumors, of which 10 were lymphoma (6 Burkitt, 2 large B-cell, and 2 plasmablastic variant), and 2 were EB-related tumors (1 angiomyofibroma and 1 myopericytoma). Fifteen patients (12%) had non-HIV–related conditions (3 plasmacytoma, 4 metastases, and 8 disk herniations). There were no documented cases of bacterial or fungal infection.

Of the 84 cases of culture-proved *Mycobacterium tuberculosis,* 57 (68%) presented with MR imaging features of spondylitis, 17 (20%) with myelitis, and 10 (12%) had no discernible MR imaging abnormality. The case of *Mycobacterium avium* had normal MR imaging. Of the 12 with nontuberculous infection, 4 had cytomegalovirus (2 with MR imaging–diagnosed myelitis and 2 with no MR imaging abnormality).

Table 2: *Mycobacterium tuberculosis* as a cause of myelopathy/cauda equina syndrome in subset of patients with a confirmed aetiology on laboratory testing

	MRI Spondylitis	MRI Nonspondylitis	Total
TB			
Yes	57	26	83
No	0	40	40
Total	57	66	123

There was 1 case with both TB and *Cryptococcus* that had florid arachnoiditis and myelitis. There were 2 with *Cryptococcus* that had normal MR imaging. There were 3 cases of Varicella zoster, 1 of *Enterococcus*, and 1 of measles that presented with myelitis.

Causal Relationship of TB with Myelopathy/Cauda Equina

Of the total number of spondylytic cases seen on MR imaging, 88% (57/65) had a confirmed laboratory diagnosis and all of these were attributable to TB (Table 2). In addition, of all cases with a confirmed laboratory diagnosis that did not have spondylitits, 40% (26/65) were attributable to TB.

Comparison of Patients with Myelitis/Arachnoiditis with Those with a Normal MR Imaging with Regard to CSF Parameters

Using the Mann-Whitney statistical test, there was a significant difference between the median CSF lymphocyte count ($P = .0053$) and protein levels ($P = .0017$) in those patients with myelitis/arachnoiditis on MR imaging compared with those with no abnormality on MR imaging. The median polymorphonuclear count was not significantly different ($P = .2082$) (Table 3).

Pathologic Features on MR Imaging

MR Imaging Features in the Spondylitis Group: ($n = 65$). The average number of contiguous affected bodies was 3 (range 1–9). The spinal location was cervical in 20% (13/65), thoracic in 62% (40/65), and lumbar/sacral 18% (12/65).

Disk abnormality (destruction) was present in 40/65 cases (62%). Epidural cord or thecal sac compression was present in all but 1 patient (98%). Discontinuous synchronous osteitic lesions were found in 7/65 (10%). Psoas and/or paravertebral abscess collections accompanied spondylitis in 48/65 (76%) (Fig 2).

MR Imaging Features in the Myelitis/Arachnoiditis Group ($n = 64$)

Cord Edema. Fifty-three of the 64 patients (83%) had high signal in the cord on T2WI. Involvement of the entire cord from craniocervical junction to conus was documented in 8/53 (15%). In addition, 26/53(49%) had cervico-thoracic involvement, 5/53 (9%) had signal abnormality only in the cervical region, and 22

(42%) in the thoracic cord. Seven patients, 4 of whom were on ARVs, had discretely enhancing intramedullary lesions.

Arachnoiditis. In 25/64 cases (39%), there was thickening, nodularity, and/or enhancement of the cauda equina. Discrete leguminous nodules with low signal on T2WI and solid enhancement postgadolinium were present in the CSF in 3 patients. Four had subtle enhancement of the pial surface of the cord or cauda equina roots. These findings were often in association with cord edema; however, in 8 patients, thickened cauda equina roots and increased signal in the CSF on precontrast T1-weighted imaging were isolated findings. Four patients in whom tuberculous meningitis had been diagnosed prior to their developing spinal symptoms had basal meningeal, intracerebral, and intramedullary ring enhancing lesions on MR imaging of the brain.

Epidural Abscess. In 13/64 patients (20%), loculated and/or enhancing epidural/subarachnoid collections were associated with extensive cord signal abnormality (Fig 3).

DISCUSSION

Globally, TB is the most common cause of death among patients with AIDS, killing 1 in 3 patients.[4]

In South Africa, an estimated 5.7 million people are infected with HIV (11% of the population), making it the country with the highest prevalence of HIV in the world.[5] A recent audit has shown a new TB index case load in excess of 1600 per 100,000 in the greater Cape Town area.[2]

The background high rate of TB, together with the delay in the provision of antiretrovirals until late in the HIV epidemic, plausibly explains the large number of tuberculosis-related neurologic complications seen in the Western Cape. This study serves as the largest reported collection of HIV-positive patients presenting with myelopathy and is the first to categorize the MR imaging findings in a TB endemic area.

Determining the Range of Causes of Myelopathy in Patients with HIV

This study showed that two-thirds of HIV-positive patients presenting with myelopathy to our institution with a determined diagnosis have an infectious etiology. *Mycobacterium tuberculosis* is the most common infective agent in both spondylitic and non-spondylitic presentation, even in the setting of a normal MR imaging and often despite ARVs. Fifty-eight percent of the total group are women reflecting the heterosexual nature of transmission and sex pattern of HIV in South Africa.

Other South African Experience

In a study in 2001, of 33 HIV-positive South African patients presenting with myelopathy, Bhigjee et al[6] found tuberculosis to be the most common etiologic agent and predicted that opportunistic infections would persist until routine antiretrovirals became widely available in South Africa.

Table 3: Comparison of myelitis group and normal MRI groups with regard to CSF parameters using Mann-Whitney U test

MRI Group	Lymphocyte Count Median (per mm³) and Range	Polymorphonuclear Median (per mm³) and Range	Protein Median (g/l) Normal 0.15–0.45 and Range
Myelitis	38.5 (0–265)	0 (0–300)	2 (0.14–2)
Normal	1 (0–160)	0 (0–5)	0.49 (0.11–2.6)
P value	.0053[a]	.2082	.0017[a]

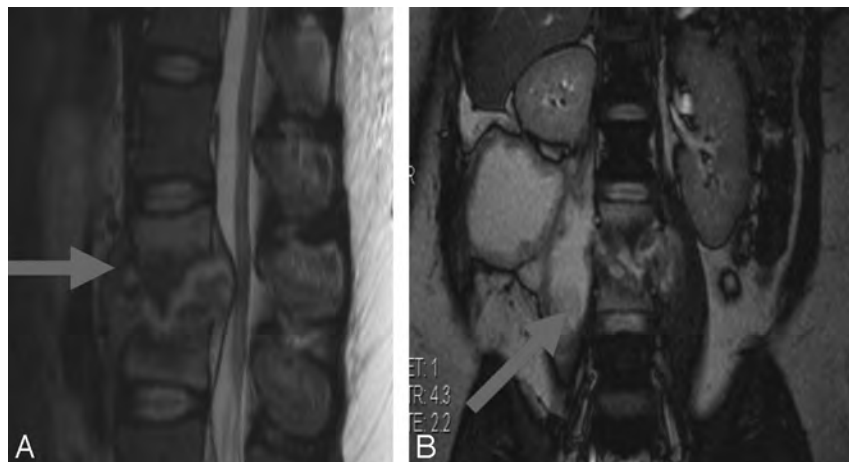[a] Indicates significance.

FIG 2. Tuberculous spondylo-diskitis. *A*, Sagittal T2-weighted MR imaging demonstrates caseous destruction of the L2–3 disk with epidural collection causing compression of the conus. *B*, Coronal FISP demonstrates large psoas abscesses communicating with the L2–3 disk. A thick walled collection displaces the right kidney superiorly.

FIG 3. Nonspondylitic spinal tuberculosis. *A*, T1 sagittal pregadolinium image with increased signal of the CSF. *B*, T2 sagittal shows root thickening. *C* and *D*, T1 sagittal postgadolinium demonstrates circumferential cord and root enhancement. *E*, T2 sagittal shows loculated CSF with extensive cord signal abnormality.

Despite a nationwide roll-out of antiretroviral therapy, Modi et al[7] found in a more recent study of 100 South African patients with nontraumatic myelopathy that infections were again largely responsible for myelopathy in the HIV-positive patients, with *Mycobacterium tuberculosis* being causative in 50%. Varicella zoster, human T-lymphotropic virus 1, and cytomegalovirus were implicated only rarely and incidental neoplastic and degenerative causes made up the remainder.

The Developing World

Studies of myelopathy in sub-Saharan Africa, India, Zimbabwe, Nigeria, and Ethiopia emphasize the role of infection as a cause of myelopathy in developing countries. Although none of these reports specifically examined an HIV cohort, HIV and TB were the most common infections described in patients presenting with myelopathy.[8-10]

MR Imaging in HIV-Associated Myelopathy

In a collaborative retrospective study published in 2000, Thurnher et al[11] reviewed the MRI of 55 HIV-positive European and North American patients presenting with spine-related neurology. The study was limited by nonuniformity of clinical presentation and by the absence of a single imaging protocol (only 2 had the entire spine imaged). In 23 cases with osseous and epidural involvement, 4 were attributable to TB spondylodiskitis, 2 to pyogenic spondylodiskitis, and 7 to lymphoma.

In our study, TB spondylitis was diagnosed on MR imaging with a high degree of certainty with 57 of 65 MR imaging–positive cases (88%) being confirmed on open biopsy or by CSF. Localized epidural collection and kyphosis resulted in focal cord compression. None of these cases had diffuse cord swelling, signal abnormality, or arachnoiditis beyond the spondylitic segment.

Even in those in whom the disk appeared to be preferentially involved, pyogenic diskitis was not identified. Jung et al[12]

reported tuberculous spondylitis as having thin smooth enhancement of the abscess wall and a well-defined paraspinal abscess, whereas pyogenic spondylitis demonstrates a thick-walled, irregular collection centered on the disk. Given that the diagnosis in our institution is founded on biopsy, gadolinium is not administered routinely in this context.

Nonspondylitic tuberculous myelitis is less widely reported. Gupta et al[13] described the MR imaging findings in a series of 20 patients with nonspondylitic intraspinal tuberculosis.

Our study suggests that in HIV, this "atypical" or nonosseous form of spinal tuberculosis is more common than previously described in TB endemic areas.[14-17] The high prevalence of coexisting extra-spinal tuberculosis in our myelitis group argues strongly for a tuberculous etiology. The myelitis in these cases may be explained by granulomatous or caseous arachnoiditis with secondary vascular (arterial or venous) cord ischemia. The preponderance of thoracic cord signal abnormality in our patients would support this. In addition, our study demonstrates good correlation between inflammatory/infective MR imaging features and inflammatory activity in CSF.

Other proposed mechanisms include edema surrounding hematogenous spread of tuberculomas directly to cord tissue[18] or from the subarachnoid space[19] and postinfectious or postinflammatory demyelination. Enhancing intramedullary lesions with surrounding edema are described in many conditions including tuberculosis, cryptococcosis, neurocysticercosis, toxoplasmosis, and schistosomiasis. Because cord biopsy is seldom an option, empiric treatment relies on knowledge of clinical status and CSF findings. HIV itself often results in mild CSF abnormalities.[20] Our low CSF culture yield may reflect antituberculous treatment or the difficulty of culturing *Mycobacterium tuberculosis* from the CSF especially with HIV co-infection.[21-24]

Direct contiguous spread from infected cervical, mediastinal, or retroperitoneal lymph nodes may provide another route for spinal infection in the absence of bony involvement. This was convincingly demonstrated in only 2 of our cases.

Nontuberculous Myelitis/Arachnoiditis

Cytomegalovirus is usually characterized by painless radiculomyelitis and less commonly by necrotizing myelopathy.[25] Commonly described with enhancement of the conus and thickened clumped roots, the diagnosis may be presumptive in the presence of enhancing roots on MR imaging and the presence of cytomegalovirus retinitis.[11] This organism was found in the CSF of only 3 of our patients (2%). One had coexisting disseminated tuberculous meningitis with floridly enhancing arachnoiditis, and 1 had only subtle CSF signal abnormality on T1WI but no root clumping. All 3 patients had profoundly reduced CD4 counts (less than 5 cells/μL). The absence of retinitis and the low prevalence on CSF
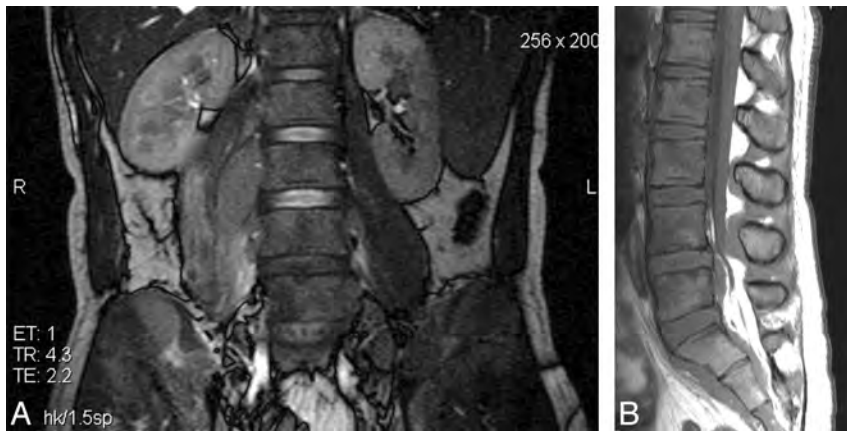
FIG 4. Burkitt lymphoma. *A*, Coronal FISP showing nonfluid-containing right L2/3 paraspinal and right pelvic masses infiltrating the right iliac bone and multiple low-signal lesions in both renal cortices. *B*, Sagittal T1 shows diffusely low marrow signal with isointense epidural masses posterior to the bodies of L5, S1, and S2.

specimens in both Bhigjee et al[6] and our study suggests that cytomegalovirus may be a less common opportunistic infection in South African patients with AIDS than elsewhere.

Arterial and/or venous infarction may complicate meningovascular infection in CNS syphilis[26]; however, no cases of *Treponema pallidum* were documented in our study. Similar long segment cord involvement is seen on MR imaging in neuromyelitis optica. Explained by molecular mimicry, inflammation and damage to the spinal cord occur secondary to a shared antigenic profile between an invading virus, bacterium or plant protein, and spinal cord tissue.[27] Aquaporin 4 antibody levels were not done routinely at the time of our study. Long segment cord signal abnormality is also described with B_{12} deficiency, though no documented cases of pernicious anemia were encountered in our group.

Fungal causes of myelitis are extremely rare. Cryptococcal CNS involvement typically manifests as meningitis or parenchymal brain lesions. Spinal cord disease, when it occurs, may take the form of epidural abscess, chronic arachnoiditis, intramedullary granuloma, myelitis, or vasculitis with cord infarction. Although most cases are secondary to vertebral osteomyelitis,[28] none of our spondylitis cases were attributable to *Cryptococcus*. Two had a normal MR imaging and a third with associated disseminated tuberculosis had florid arachnoiditis, cord edema, and splenic microabscesses. All 3 cases had very low CD4 counts.

Herpes zoster myelopathy is rare. This organism was isolated from the CSF of 3 patients, all of whom demonstrated long segment cord signal abnormality. Two had associated zoster skin rash at the time of presentation.

Direct HIV Infection Resulting in Myelopathy

HIV infection may cause an acute transverse myelitis on the basis of immune dysregulation even before the development of full-blown AIDS. During this early stage of infection, the myelopathy may be responsive to steroids and combination antiretroviral therapy.[29]

Vacuolar myelopathy frequently co-occurs with HIV-related encephalopathy and polyneuropathy and is a pathologic and postmortem diagnosis.[25] The MR imaging findings include cord atrophy with or without signal abnormality and lack of enhancement.[30] It is possible that vacuolar myelopathy explained some of

our cases with bland CSF and negative MR imaging; however, postmortem results were available on only 1 of our patients whose death was attributed to subacute measles encephalopathy.

Diffuse infiltrative lymphocytosis syndrome warrants mention in the context of antigen-driven HIV manifestation. This condition represents a peripheral neuropathy rather than a myelopathy, may be symmetrical, acute, or subacute, but is always painful.

On MR imaging, there is typically leptomeningeal and cauda equina enhancement. Nerve biopsy is confirmatory with angiocentric CD8 infiltrates, prominent expression of HIV p24 protein in macrophages, and detection of the HIV genome by polymerase chain reaction in nerve homogenates.[31] This diagnosis may have been overlooked in some of our patients.

CONCLUSIONS

Despite the limitations of a retrospective study and the lack of MR imaging contrast administration in all cases, our study re-emphasizes the importance of tuberculous infection in the development of acute myelopathy/cauda equina syndrome in the setting of HIV/AIDS. In the Western Cape, tuberculosis in its various forms accounts for at least 68% of cases with a documented etiology, often complicating tuberculosis at another site. Both spondylitis and myelitis/arachnoiditis may be diagnosed on MR imaging and may develop or progress on established anti-TB and ARV treatment.

MR imaging, in addition, allows for triage to medical or surgical treatment, though nonspondylitic infection lacks specificity on MR imaging even with the administration of gadolinium. Future research by using advanced physiologic MR imaging sequences (DWI and MR spectroscopy) and more accurate confirmatory testing with molecular-based assays of CSF may expand the role for MR imaging, both in diagnosis and management of this devastating disease presentation.

APPENDIX 1
Definition of MR Imaging Classification

- Spondylitis. Vertebral collapse; kyphosis; disk signal alteration/destruction/height loss; endplate destruction; paraspinal/epidural mass. A confident diagnosis was reached when the paraspinal mass returned fluid signal and demonstrated subligamentous extension, or when there was endplate and disk involvement. Cord or thecal sac compression was considered present when there was loss of the anterior CSF signal at the level of kyphosis, indentation of the cord, or focal cord signal abnormality.
- Myelitis. Cord expansion/cord signal abnormality/enhancement within the thecal sac in the absence of spondylitic bone change.
- Arachnoiditis. Thickening/nodularity/or clumping of the cauda roots.
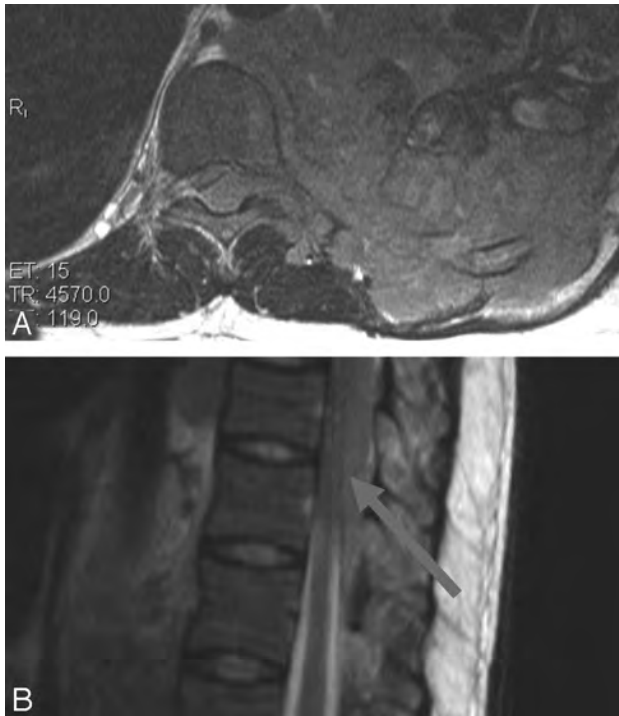- Bone neoplasm. Expansion/collapse with epidural cord or

FIG 5. Plasmablastic lymphoma. *A*, Axial T2-weighted MR imaging shows a large destructive lobulated mass in the left hemithorax infiltrating the thoracic spinal canal via the neural foramen. *B*, T2-weighted sagittal MR imaging showing posterior epidural cord compression.

FIG 6. EB-associated myopericytoma. *A*, Sagittal T2-weighted MR imaging shows predominantly low-signal epidural mass causing significant cord compression at T6/7 with abnormal marrow in the adjacent vertebral body. *B*, Coronal FISP demonstrates improved conspicuity of marrow signal abnormality. *C*, Axial T2-weighted image shows tumor displacing and compressing the cord.

cauda compression/associated epidural thecal sac compression /"curtain" sign.
- Nonbone neoplasm. Intramedullary/extramedullary intrathecal/epidural soft tissue/contiguous spread from an adjacent chest wall or lung parenchymal, abdominal or pelvic mass, or lymphadenopathy suggesting lymphoma.
- Isolated syrinx. Cord expansion with nonenhancing intramedullary fluid signal (isointense to CSF on both T1 and T2WI) with or without loculations.
- Other. Disk herniation/degenerative spondolytic change.

APPENDIX 2

Descriptions of MR Imaging Findings in Documented Nontuberculous Infection

Varicella zoster was isolated from the CSF of 3 patients with features of myelitis on MR imaging, none of whom were on ARVs. A 31-year-old man with a relatively preserved CD4 (346 cells/μL) had been hospitalized for sepsis and a dermatomal skin rash typical for zoster 2 weeks before developing paraplegia and loss of sphincter control. His MR imaging demonstrated mild cord swelling and patchy leptomeningeal enhancement between T6 and T9. A second patient, a 49-year-old man with a CD4 of 158 cells/μL presented with meningitis and myelopathy and had only patchy signal abnormality without cord expansion at T8/9. The third patient, a 28-year-old man (CD4 127cells/μL) presented with a right T6 distribution zoster rash. His MR imaging demonstrated extensive cord swelling and signal abnormality between the midcervical level and the conus.

Cytomegalovirus was isolated from the CSF in 4 cases. The MR imaging was abnormal in only 2: one of these (CD4 3 cells/μL) demonstrated nonenhancing cord edema between C1 and C7. The other had focal dural enhancement at T7/8 but no cord signal abnormality and no evidence of root enhancement.

Lymphoma was diagnosed histologically in 10 cases. Burkitts lymphoma was proved in 6 patients (Fig 4). Two patients had large B-cell and 2 had plasmablastic variant (Fig 5). Radiologically, there was no consistency in MR imaging appearance within histologic subtypes of lymphoma. These tumors were, however, distinct from the TB spondylitis group in that there was no endplate involvement, vertebral body height loss, or kyphosis. In 2 cases, the marrow signal was diffusely reduced throughout the spinal axis on T1 imaging. In several cases the cord or thecal sac was compressed by contiguous spread of paraspinal or mediastinal soft tissue into the epidural compartment via the neural foramina. Retroperitoneal and mediastinal lymphadenopathy was commonly identified on FISP imaging.

EB/HIV Associated Tumors

A 37-year-old man (CD4 47 cells/μL) presented with a T6 sensory level and

motor fallout. MR imaging revealed an enhancing dumbbell-shaped mass expanding the right T4/5 neural foramen and causing epidural compression of the cord. The mass had low signal on T2WI, and histology revealed a spindle cell lesion with interlacing fascicles of smooth muscle fibers surrounding thick-walled vessels, consistent with an angioleiomyoma. The diagnosis was confirmed by a diffusely positive muscle-specific actin in the absence of positive staining for other immune-histochemical markers (EMA, S-100, Desmin, and CD34).

A 35-year-old woman (CD4 45cells/μL), presenting with motor weakness and a T6 sensory level, had an extradural soft tissue mass with low signal on T2WI and bony infiltration causing cord compression at T6/7. Histology revealed hypocellular and cellular areas. These were composed of relatively monomorphic oval to spindle-shaped myoid appearing cells with multilayered concentric growth around vessels. The cells had eosinophilic and amphophilic (staining with both acid and basic dyes) cytoplasm. Cells were arranged in a storiform (cartwheel) pattern with scanty eosinophilic cytoplasm. Interspersed among the tumor cells were numerous small lymphocytes as well as more primitive cells with darker nuclei. Mitotic index and Ki67 were low and the tumor stained moderately positive for EB. IS100, epithelial membrane antigen (EMA), cytokeratin stains (AE1/3), B cell lymphoma 2 stain (BCL2), and haemopoetic progenitor cell stain (CD34) were negative. These findings favored an EB-associated smooth muscle tumor: myopericytoma (Fig 6).

Non-HIV–Associated Cases

Metastases and Primary Bone Tumors. Four patients had bony metastases. The MR imaging findings included posterior element/pedicular infiltration, osseous destruction, and solid rather than fluid-containing paraspinal mass. Another feature favoring bone tumor over tuberculous spondylitis was the "curtain sign," referring to tumorous tissue bulging out laterally into the spinal canal on either side of the firmly attached midline posterior longitudinal ligament. In addition, 2 solitary plasmacytomas and a case of multiple myeloma were found.

Disk Herniations

Eight patients had large disk herniations causing cord or thecal sac compression: 3 cervical, 4 lumbar, and 1 at T10/11.

REFERENCES

1. **World TB Day, 24 March 2012.** http://www.westerncape.gov.za/news/world-tb-day-24-march-2012. Accessed April 18, 2014
2. Marais S, Pepper DJ, Schutz C, et al. **Presentation and outcome of tuberculous meningitis in a high HIV prevalence setting.** *PloS One* 2011;6:e20077
3. Jain AK. **Tuberculosis of the spine: a fresh look at an old disease.** *J Bone Joint Surg Br* 2010;92:905–13
4. World Health Organization. **WHO report 2011. Global tuberculosis control**. 2011. Available at: http://www.tbvi.eu/news-agenda/news/news-message/who-2011-global-tuberculosis-control-report.html. Accessed August 20, 2013
5. Statistical release P0302. **Mid-year population estimates 2013.** http://beta2.statssa.gov.za/publications/P0302/P03022013.pdf. Accessed July 11, 2013
6. Bhigjee AI, Madurai S, Bill PL, et al. **Spectrum of myelopathies in HIV seropositive South African patients.** *Neurology* 2001;57:348–51
7. Modi G, Ranchhod J, Hari K, et al. **Non-traumatic myelopathy at the Chris Hani Baragwanath Hospital. South Africa—the influence of HIV.** *QJM* 2011;104:697–703
8. Zenebe G. **Myelopathies in Ethiopia.** *East Afr Med J* 1995;72:42–45
9. Owolabi LF, Ibrahim A, Samalia AA. **Profile and outcome of non-traumatic paraplegia in Kano, northwestern Nigeria.** *Ann Afr Med* 2011;10:86–90
10. Lekoubou Looti AZ, Kengne AP, Djientcheu Vde P, et al. **Patterns of non-traumatic myelopathies in Yaounde (Cameroon): a hospital based study.** *J Neurol Neurosurg Psychiatry* 2010;81:768–70
11. Thurnher MM, Post MJ, Jinkins JR. **MRI of infections and neoplasms of the spine and spinal cord in 55 patients with AIDS.** *Neuroradiology* 2000;42:551–63
12. Jung NY, Jee WH, Ha KY, et al. **Discrimination of tuberculous spondylitis from pyogenic spondylitis on MRI.** *AJR* 2004;182:1405–10
13. Gupta RK, Gupta S, Kumar S, et al. **MRI in intraspinal tuberculosis.** *Neuroradiology* 1994;36:39–43
14. Babhulkar SS, Tayade WB, Babhulkar SK. **Atypical spinal tuberculosis.** *J Bone Joint Surg Br* 1984;66:239–42
15. Pande KC, Babhulkar SS. **Atypical spinal tuberculosis**. *Clin Orthop Relat Res* 2002;May(398):67–74
16. Jena A, Banerji AK, Tripathi RP, et al. **Demonstration of intramedullary tuberculomas by magnetic resonance imaging: a report of two cases.** *Br J Radiol* 1991;64:555–57
17. Parmar H, Shah J, Patkar D, et al. **Intramedullary tuberculomas. MR findings in seven patients.** *Acta Radiol* 2000;41:572–77
18. Trivedi R, Saksena S, Gupta RK. **Magnetic resonance imaging in central nervous system tuberculosis.** *Indian J Radiol Imag* 2009;19:256–65
19. Janse van Rensburg P, Andronikou S, van Toorn R, et al. **Magnetic resonance imaging of miliary tuberculosis of the central nervous system in children with tuberculous meningitis.** *Pediat Radiol* 2008;38:1306–13
20. Price RW, Spudich S. **Antiretroviral therapy and central nervous system HIV type 1 infection.** *J Infect Dis* 2008;197(Suppl 3):S294–306
21. Croda MG, Vidal JE, Hernandez AV, et al. **Tuberculous meningitis in HIV-infected patients in Brazil: clinical and laboratory characteristics and factors associated with mortality.** *Int J Infect Dis* 2010;14:e586–91
22. Puccioni-Sohler M, Brandao CO. **Factors associated to the positive cerebrospinal fluid culture in the tuberculous meningitis.** *Arq Neuropsiquiatr* 2007;65:48–53
23. Berenguer J, Moreno S, Laguna F, et al. **Tuberculous meningitis in patients infected with the human immunodeficiency virus.** *N Engl J Med* 1992;326:668–72
24. Marais S, Pepper DJ, Marais BJ, et al. **V-associated tuberculous meningitis– diagnostic and therapeutic challenges.** *Tuberculosis (Edinb)* 2010;90:367–74
25. Cho TA, Vaitkevicius H. **Infectious myelopathies.** *Continuum (Minneap Minn)* 2012;18:1351–73
26. Tsui EY, Ng SH, Chow L, et al. **Syphilitic myelitis with diffuse spinal cord abnormality on MR imaging.** *Eur Radiol* 2002;12:2973–76
27. Vaishnav RA, Liu R, Chapman J, et al. **Aquaporin 4 molecular mimicry and implications for neuromyelitis optica.** *J Neuroimmunol* 2013;260:92–98
28. Murthy JM. **Fungal infections of the central nervous system: the clinical syndromes.** *Neurol India* 2007;55:221–25
29. Hamada Y, Watanabe K, Aoki T, et al. **Primary HIV infection with acute transverse myelitis.** *Intern Med* 2011;50:1615–17
30. Chong J, Di Rocco A, Tagliati M, et al. **MR findings in AIDS-associated myelopathy.** *AJNR Am J Neuroradiol* 1999;20:1412–16
31. Moulignier A, Authier FJ, Baudrimont M, et al. **Peripheral neuropathy in human immunodeficiency virus-infected patients with the diffuse infiltrative lymphocytosis syndrome.** *Ann Neurol* 1997;41:438–45

Reliability of the STIR Sequence for Acute Type II Odontoid Fractures

F.D. Lensing, E.F. Bisson, R.H. Wiggins III, and L.M. Shah

ABSTRACT

BACKGROUND AND PURPOSE: The STIR sequence is routinely used to assess acute traumatic osseous injury. Because the composition of the odontoid in older individuals may be altered with osteopenia and decreased vascularity, the STIR sequence may not accurately depict the acuity of an odontoid fracture. The purpose of this study was to evaluate the reliability of the STIR sequence to differentiate acute-versus-chronic type II odontoid fractures in older patients, particularly those with osteopenia.

MATERIALS AND METHODS: A retrospective review was performed for patients with type II odontoid fractures during a 10-year period with both CT and MR imaging performed within 24 hours of injury. Patients were paired with controls of similar ages and were grouped by age. The STIR images were evaluated in a blinded fashion for the presence of hyperintensity in the odontoid. Demographic and clinical characteristics were also recorded.

RESULTS: Seventy-five patients with type II odontoid fracture and 75 healthy controls (mean and median age of 57 years) were identified. The sensitivity of STIR to detect fracture in the age group 57 years and older was significantly worse than that in the age group younger than 57 years (54% and 82%, respectively; $P = .018$).

CONCLUSIONS: Older patients, particularly those with osteopenia, may have acute odontoid injuries without corresponding STIR hyperintensity. Additionally, interobserver agreement in STIR interpretation decreases with increasing patient age. As such, in this patient population, in which the presence of bone marrow edema as an indicator of fracture acuity may impact therapeutic decisions, correlation with CT findings and clinical history is crucial.

Spine fractures in older patients following ground-level falls are common, with type II odontoid fractures occurring most frequently.[1-3] Prompt and accurate diagnosis of these fractures is critical in patient management because they are associated with a high rate of nonunion in some patient populations, particularly if acuity is unrecognized.[4]

Treatment of type II odontoid fractures remains controversial. Some series have reported successful fracture healing with external mobilization alone in 37%–75% of patients.[5,6] However, specific factors that have been shown to contribute to nonunion with orthosis alone include advanced patient age, increased degree and angulation of odontoid displacement (4–6 mm and >10° angu-

lation), and delayed treatment.[4,7-9] While operative intervention may result in high rates of fracture healing, surgery may involve excess morbidity and mortality in elderly patients.[10,11] Because fracture acuity is a critical factor in healing, both for nonoperative and surgical interventions, it is important to identify the odontoid fracture when advising patients on treatment recommendations.[12]

Currently, cervical spine trauma is most commonly evaluated with multidetector CT with sagittal and coronal reconstructions, which have improved delineation of fractures compared with plain radiographs.[13,14] There is an increasing role for MR imaging, with its superior soft-tissue resolution, in the acute setting in patients with neurologic injury not only to evaluate the spinal cord but also to define areas of ligamentous injury that may relate to clinical instability. Although the routine evaluation of MR imaging of the cervical spine involves careful review of all sequences, the STIR sequence is relied on to reveal marrow edema related to an acute fracture. In addition to the increased detection of soft-tissue injury, the STIR sequence is exquisitely sensitive to bone marrow pathology.[15-17] This feature may be useful in identifying the acuity of a fracture. With acute fractures in young healthy patients, there is increased bone marrow edema resulting in in-

FIG 1. Sagittal CT reconstruction (*A*) and sagittal STIR (*B*) images from a 65-year-old man after a ground-level fall demonstrate a minimally displaced fracture at the odontoid base (*white arrow*) with minimal hyperintensity on the STIR sequence (*white arrow*).

FIG 2. Sagittal CT reconstruction (*A*) and sagittal STIR (*B*) images from a 37-year-old man after a motor vehicle collision show a minimally displaced fracture at the odontoid base (*white arrow*) with robust STIR hyperintensity in the bone marrow (*white arrow*).

traosseous STIR hyperintensity,[15,18] which is often used in clinical decision-making as a marker of acuity. In contradistinction, in older patients with osteopenia, vertebral body fractures have been characterized by focal areas of enchondral bone formation adjacent to avascular necrotic bone and unreactive marrow.[19] Because older patients, particularly those with osteopenia, have a more heterogeneous composition of the odontoid process with known decreased vascularity, we hypothesized that STIR hyperintensity would be less reliable as an indicator of the acuity of these fractures in this population.

MATERIALS AND METHODS

After approval by the institutional review board, a retrospective query of the radiology information system at a level 1 trauma center for the terms "odontoid fracture," "dens fracture," and/or "C2 fracture" during a 10-year period from 2002 to 2012 was performed. We identified patients presenting to the emergency department with a history of acute trauma and documented acute type II odontoid fracture on the basis of clinical history and CT evaluation who subsequently had MR imaging of the cervical spine. The same number of control patients with similar ages, also presenting with a history of acute trauma but without docu-

mented C2 fracture by both CT and MR imaging, was also identified. Although these patients may have presented with trauma at other locations, this study focused solely on the C2 trauma. CT of the cervical spine was performed per trauma protocol when the patient was initially brought to the hospital. MR imaging of the cervical spine was performed within 12 hours of CT. All patients with C2 fractures were included in the analysis. Because patients' complex histories are often not known at the time of trauma, patients and controls were not excluded on the basis of comorbidities. In the retrospective review of these cases, all C2 fractures were considered secondary to trauma, not secondary to other unrelated pathologies.

Imaging and Evaluation

All MR imaging was performed on a 1.5T scanner (either Avanto or Aera; Siemens, Erlangen, Germany). The STIR sequence was performed by using TI = 180, TE = 55 ms, TR = 4000 ms, matrix = 256 × 192 mm, FOV = 220 × 220 mm, and voxel size = 0.9 × 0.9 × 3 mm. Two senior neuroradiologists with Certificates of Added Qualification, each with >10 years of experience, independently evaluated the midline sagittal STIR sequences of all patients for the presence or absence of STIR hyperintensity, defined as nonlinear signal elevation within the odontoid (compared with the C3 vertebral body) (Figs 1 and 2).The images were presented to each reader in random order with the readers blinded to patient age and clinical history. If there was disagreement, a third reader, a spine-specialized neurosurgeon, made an independent assessment to break the tie; then, those images were reviewed with the neuroradiologists for a true consensus determination of STIR hyperintensity. Spine surgeons routinely use CT and MR imaging findings to make treatment decisions and often discuss their interpretation with the neuroradiologist, as was discussed in this study.

All CT was performed on a 64-section scanner (Somatom Definition AS Siemens, Erlangen, Germany) with 0.6-mm collimation and a helical acquisition. Sagittal and coronal 2.0-mm-thick images with 2.0-mm skip intervals were reconstructed from the axial data. All CT scans were evaluated for the presence or absence of acute fracture in the odontoid, by using features such as cortical disruption and irregular linear lucency without corticated margins. The readers were blinded to the CT results during their interpretation of the STIR images.

Statistical Analysis

The accuracy of using STIR hyperintensity to diagnose a fracture was measured by using a diagnostic test statistical approach. The

Table 1: Presence of odontoid STIR hyperintensity in patients with acute fractures younger than 57 years of age

Acute Fracture	STIR Present	STIR Absent	Total
Present	22	5	27
Absent	4	39	43
Total	26	44	70

Table 2: Presence of odontoid STIR hyperintensity in patients with acute fractures 57 years of age and older

Acute Fracture	STIR Present	STIR Absent	Total
Present	26	22	48
Absent	2	30	32
Total	28	52	80

reference standard was fracture (either present or absent) as determined by CT and clinical history. The diagnostic test was STIR hyperintensity (either present or absent). The sensitivity and specificity were reported, along with 95% confidence intervals. To determine whether the diagnostic accuracy varied by age, we first dichotomized the patient age at the total sample median age of 57 years (into 2 groups: younger than 57 years and 57 years and older). Then a 2 × 2 cross-tabulation of fracture and STIR hyperintensity was formulated for each age subgroup. Next, in order to compare the sensitivity measured separately for the 2 age subgroups, the sensitivity row (fracture present cases) was taken from each table and combined them into a new 2 × 2 table, which was then tested for statistical significance by using a χ^2 test, or Fisher exact test if any expected cell frequency was <5.[20] A similar approach was used for the specificity comparison, by combining the specificity row of each age subgroup into a 2 × 2 table. All reported P values are for a 2-sided comparison. Interrater reliability was measured with a κ coefficient and was reported with an accompanying 95% confidence interval. Statistical analysis was performed by using STATA (Version 12; StataCorp, College Station, Texas).

RESULTS

There were 75 patients (40 men and 35 women, median age of 67 years) with acute type II odontoid fractures found by clinical history and CT evaluation. These patients were then combined with 75 control patients of similar ages (41 men and 34 women, median age of 55 years) presenting with a history of acute trauma without documented C2 fracture. Dividing the subjects into 2 groups based on the overall mean and median age of 57 years, with 70 subjects in group 1 (younger than 57 years of age) and 80 in group 2 (57 years of age or older), with mean ± SD age of 37.29 ± 12.98 years and 73.05 (SD ± 10.55) in the groups, respectively.

For both readers, odontoid bone marrow STIR hyperintensity was more frequently observed in patients with acute fractures than in the nonfractured control subjects across all ages. The sensitivity of the STIR sequence for acute fracture was 88.9% (95% CI, 77.4–95.8) and the specificity was 71.9% (95% CI, 61.8–80.6). The sensitivity of STIR to detect fracture in the age group 57 years and older was significantly worse than that in the age group younger than 57 years (sensitivity 54% and 82%, respectively; $P =$ .018). The specificity of negative STIR in the age group 57 years and older without fracture was similar to that in the age group younger than 57 years without fracture (specificity 94% and 91%, respectively; $P = 0.63$) (Tables 1 and 2).

There was substantial interobserver agreement between readers in the detection of STIR signal in patients younger than 57 years of age with type II odontoid fracture ($\kappa = 0.79$; 95% CI, 0.64–0.94). In subjects 57 years of age and older with odontoid fracture, there was moderate interobserver agreement in the evaluation of STIR signal intensity ($\kappa = 0.50$; 95% CI, 0.30–0.69).[21]

DISCUSSION

Elderly patients are vulnerable to cervical spine injuries with the upper cervical spine (C0–C2) being involved in >50% of cases.[22-25] These injuries have an associated increased morbidity and mortality related to fracture nonunion and high comorbidity rates in this particular patient population.[2,26,27] Therefore, it is important to identify parameters that may play a role in fracture healing, including treatment recommendations, which are often based on the acuity of the fracture.

As MR imaging becomes more readily available and acquisition times become more rapid with newer scanners, MR imaging is being more frequently used in the acute trauma setting. The STIR sequence is very sensitive for the detection of osseous and soft-tissue edema as a result of fractures or microfractures[28] and is routinely used to identify such edema in the cervical spine and other skeletal sites.[15] One study showed STIR to be superior to CT in detecting subtle fractures, such as insufficiency fractures.[29]

Our data suggest that the STIR sequence, while sensitive for the detection of acute type II odontoid fracture in patients younger than 57 years, is significantly less sensitive in older patients, particularly those with osteopenia. Additionally, as patient ages increase, the agreement between observers evaluating STIR hyperintensity in acute type II odontoid fractures decreases from substantial to only moderate agreement.

We speculate that the decrease in sensitivity of STIR to detect osseous edema in the presence of acute type II odontoid fracture in older and osteopenic patients may relate to the unique anatomic and histologic changes that occur in the odontoid with senescence and with osteopenia. Angiographic studies in cadavers have suggested a watershed zone at the odontoid base between the anterior ascending and posterior ascending arteries.[30] This area of decreased vascularity may account, in part, for the increased frequency of type II odontoid fractures in this population.[31,32] In addition, the odontoid is located intrasynovially and, as such, does not receive periosteal blood supply.[33] The combination of the vascular watershed and the lack of a periosteal blood supply contributes to overall poor vascularity in the odontoid, which contributes to the absence of bone marrow edema and, subsequently, the absence of STIR hyperintensity in the setting of acute fracture in the older population.

Osteopenia, characterized by decreased bone mineral attenuation with microarchitectural deterioration, is also a contributory factor in the occurrence of odontoid fractures.[4] In addition to its tenuous blood supply, the odontoid base has a zone of decreased trabecular volume, decreased trabecular interconnection, and decreased cortical thickness.[34,35] The zone of decreased trabeculation at the odontoid base undergoes substantial changes in the setting of osteoporosis, losing 64% of its bone mass compared with the adjacent C2 vertebral body and the tip of the odontoid.[35] Therefore, osteopenia decreases the likelihood of bone marrow

edema and consequent paucity of STIR hyperintensity in the setting of acute type II odontoid fracture in this patient population.

Although bone mineral densitometry was not available to categorize our subjects as osteoporotic, the literature has shown a significant correlation between a decreased bone mineral attenuation and advanced patient age.[36,37] Gradual loss of skeletal mass begins in women in the fourth decade and accelerates following menopause. In men, bone loss begins in the fifth and sixth decades. There is no exact age that osteoporosis begins because there are multiple cofactors that can bring on an early onset of osteoporosis. Fifty-four percent of postmenopausal white women are estimated to have osteopenia, and 30% have osteoporosis in at least 1 skeletal site.[38] The general prevalence of osteoporosis rises from 5% among women 50 years of age to 50% at 85 years of age; among men, the comparable figures are 2.4% and 20%, respectively.[39]

Despite the relative frequency of odontoid fractures in the elderly, there has been a lack of consensus regarding the optimal management of these fractures. Recent data, however, show level 2 evidence for the recommendation of surgical stabilization of acute type II odontoid fractures in patients 50 years of age or older,[40] with higher union rates described with operative management in elderly patients.[37,41-43] A recent multicenter study showed high rates of mortality and nonunion in nonoperatively treated type II odontoid fractures in the elderly.[12] As such, there is an increasing tendency toward the surgical treatment in the literature.[11,44] Because MR imaging and the STIR sequence, in particular, are used to determine fracture acuity and, therefore, treatment recommendations, it is important that we understand the limitations of this sequence. On the basis of our results, we speculate that STIR signal hyperintensity in the odontoid process may reflect a surrogate marker of vascularity and the presence of normal bone marrow composition.

This study has some limitations. First, the retrospective design may have introduced bias in suspecting fracture, despite the randomization with controls of similar ages. This may have contributed to the variability in the detection of STIR signal between readers. The focus of this article is the detection of STIR hyperintensity in odontoid fractures, particularly type II given the common occurrence of this type of injury. We did not assess the presence of additional fractures, which can occur with odontoid fractures. Although the readers were limited to the sagittal midline STIR image for the evaluation of signal intensity, it is conceivable that edema in the C1 body and/or the adjacent soft tissues may have influenced the interpretation.

Second, there were false-positive results (ie, STIR hyperintensity without fracture) in both age groups, but they were higher in the younger group. These are likely due to the subtly increased STIR signal intensity around the hypointense dentocentral synchondrosis (simulating a fracture cleft) at the odontoid base, due to a persistent cartilaginous matrix (Fig 3).[45]

Third, our MR imaging scans were obtained on a 1.5T Siemens system, and because imaging parameters may vary depending on the field strength, our results may not be generalizable across different manufacturers and different imaging protocols. Increased magnetic susceptibility from bony trabeculae has been described
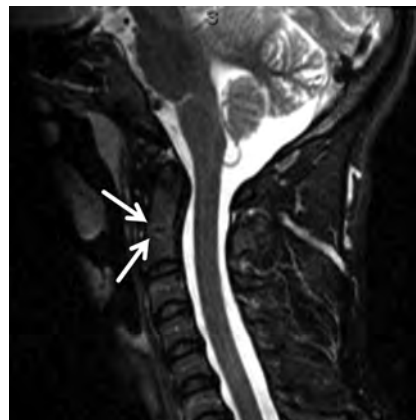

FIG 3. Sagittal STIR image of a 32-year-old female trauma patient shows slight STIR hyperintensity around the hypointense dentocentral synchondrosis (simulating a fracture cleft) at the odontoid base, due to persistent cartilaginous matrix (*white arrows*).

at 3T, possibly resulting in lower signal intensity on T2-weighted and STIR imaging.[15]

Last, we did not exclude studies on the basis of motion artifacts. Motion artifacts may limit the diagnostic utility of MR imaging, and the STIR sequence has been shown to be particularly sensitive to patient motion.[17,46] While our readers did not comment on the quality of the images, it is possible that relatively minor patient motion could have masked subtle STIR signal elevation in the bone marrow.

CONCLUSIONS

The STIR signal elevation is relatively insensitive for the presence of an acute type II odontoid fracture in patients 57 years of age and older, particularly in those patients with osteopenia. Furthermore, interobserver agreement for the detection of the STIR signal abnormality declined in older patients compared with younger patients. These findings suggest that in older patients, possibly with osteopenia, with an acute odontoid fracture, the STIR sequence is limited in its detection of bone marrow edema and, therefore, should be interpreted with caution.

REFERENCES
1. Lomoschitz FM, Blackmore CC, Mirza SK, et al. **Cervical spine injuries in patients 65 years old and older: epidemiologic analysis regarding the effects of age and injury mechanism on distribution, type, and stability of injuries.** *AJR American J Roentgenol* 2002;178:573–77
2. Malik SA, Murphy M, Connolly P, et al. **Evaluation of morbidity, mortality and outcome following cervical spine injuries in elderly patients.** *Eur Spine J* 2008;17:585–91
3. Chutkan NB, King AG, Harris MB. **Odontoid fractures: evaluation and management.** *J Am Acad Orthop Surg* 1997;5:199–204
4. Ryan MD, Taylor TK. **Odontoid fractures in the elderly.** *J Spinal Disord* 1993;6:397–401
5. Polin RS, Szabo T, Bogaev CA, et al. **Nonoperative management of Types II and III odontoid fractures: the Philadelphia collar versus the halo vest.** *Neurosurgery* 1996;38:450–56, discussion 456–57
6. Wang GJ, Mabie KN, Whitehill R, et al. **The nonsurgical management of odontoid fractures in adults.** *Spine (Phila Pa 1976)* 1984;9:229–30

7. Greene KA, Dickman CA, Marciano FF, et al. **Transverse atlantal ligament disruption associated with odontoid fractures.** *Spine* 1994;19:2307–14

8. Lennarson PJ, Mostafavi H, Traynelis VC, et al. **Management of type II dens fractures: a case-control study.** *Spine (Phila Pa 1976)* 2000;25:1234–37

9. Lind B, Nordwall A, Sihlbom H. **Odontoid fractures treated with halo-vest.** *Spine* 1987;12:173–77

10. Geisler FH, Cheng C, Poka A, et al. **Anterior screw fixation of posteriorly displaced type II odontoid fractures.** *Neurosurgery* 1989;25:30–37, discussion 37–38

11. Campanelli M, Kattner KA, Stroink A, et al. **Posterior C1–C2 transarticular screw fixation in the treatment of displaced type II odontoid fractures in the geriatric population: review of seven cases.** *Surg Neurol* 1999;51:596–600, discussion 600–01

12. Smith JS, Kepler CK, Kopjar B, et al. **The effect of type II odontoid fracture nonunion on outcome among elderly patients treated without surgery: based on the AOSpine North America Geriatric Odontoid Fracture study.** *Spine (Phila Pa 1976)* 2013;38:2240–46

13. Sheikh K, Belfi LM, Sharma R, et al. **Evaluation of acute cervical spine imaging based on ACR Appropriateness Criteria(R).** *Emerg Radiol* 2012;19:11–17

14. Gale SC, Gracias VH, Reilly PM, et al. **The inefficiency of plain radiography to evaluate the cervical spine after blunt trauma.** *J Trauma* 2005;59:1121–25

15. Shah LM, Hanrahan CJ. **MRI of spinal bone marrow. Part I. Techniques and normal age-related appearances.** *AJR Am J Roentgenol* 2011;197:1309–21

16. Alyas F, Saifuddin A, Connell D. **MR imaging evaluation of the bone marrow and marrow infiltrative disorders of the lumbar spine.** *Magn Reson Imaging Clin N Am* 2007;15:199–219, vi

17. Mirowitz SA, Apicella P, Reinus WR, et al. **MR imaging of bone marrow lesions: relative conspicuousness on T1-weighted, fat-suppressed T2-weighted, and STIR images.** *AJR American J Roentgenol* 1994;162:215–21

18. Long SS, Yablon CM, Eisenberg RL. **Bone marrow signal alteration in the spine and sacrum.** *AJR American J Roentgenol* 2010;195:W178–200

19. Antonacci MD, Mody DR, Rutz K, et al. **A histologic study of fractured human vertebral bodies.** *J Spinal Disord Tech* 2002;15:118–26

20. Pepe MS. *The Statistical Evaluation of Medical Tests for Classification and Prediction.* Oxford, UK: Oxford University Press; 2003

21. Landis JR, Koch GG. **The measurement of observer agreement for categorical data.** *Biometrics* 1977;33:159–74

22. Lieberman IH, Webb JK. **Cervical spine injuries in the elderly.** *J Bone Joint Surg Br* 1994;76:877–81

23. Müller EJ, Wick M, Russe O, et al. **Management of odontoid fractures in the elderly.** *Eur Spine J* 1999;8:360–65

24. Weller SJ, Malek AM, Rossitch E Jr. **Cervical spine fractures in the elderly.** *Surg Neurol* 1997;47:274–80, discussion 280–81

25. Ryan MD, Henderson JJ. **The epidemiology of fractures and fracture-dislocations of the cervical spine.** *Injury* 1992;23:38–40

26. Irwin ZN, Arthur M, Mullins RJ, et al. **Variations in injury patterns, treatment, and outcome for spinal fracture and paralysis in adult versus geriatric patients.** *Spine* 2004;29:796–802

27. Jackson AP, Haak MH, Khan N, et al. **Cervical spine injuries in the elderly: acute postoperative mortality.** *Spine* 2005;30:1524–27

28. Spiegl UJ, Beisse R, Hauck S, et al. **Value of MRI imaging prior to a kyphoplasty for osteoporotic insufficiency fractures.** *Eur Spine J* 2009;18:1287–92

29. Cabarrus MC, Ambekar A, Lu Y, et al. **MRI and CT of insufficiency fractures of the pelvis and the proximal femur.** *AJR American J Roentgenol* 2008;191:995–1001

30. Schiff DC, Parke WW. **The arterial supply of the odontoid process.** *J Bone Joint Surg Am* 1973;55:1450–56

31. Maiman DJ, Larson SJ. **Management of odontoid fractures.** *Neurosurgery* 1982;11:820

32. Elgafy H, Dvorak MF, Vaccaro AR, et al. **Treatment of displaced type II odontoid fractures in elderly patients.** *Am J Orthop* 2009;38:410–16

33. Southwick WO. **Management of fractures of the dens (odontoid process).** *J Bone Joint Surg Br* 1980;62:482–86

34. Amling M, Hahn M, Wening VJ, et al. **The microarchitecture of the axis as the predisposing factor for fracture of the base of the odontoid process: a histomorphometric analysis of twenty-two autopsy specimens.** *J Bone Joint Surg Br* 1994;76:1840–46

35. Amling M, Posl M, Wening VJ, et al. **Structural heterogeneity within the axis: the main cause in the etiology of dens fractures: a histomorphometric analysis of 37 normal and osteoporotic autopsy cases.** *J Neurosurg* 1995;83:330–35

36. Lilley J, Eyre S, Walters B, et al. **An investigation of spinal bone mineral density measured laterally: a normal range for UK women.** *Br J Radiol* 1994;67:157–61

37. Reinhold M, Bellabarba C, Bransford R, et al. **Radiographic analysis of type II odontoid fractures in a geriatric patient population: description and pathomechanism of the "Geier"-deformity.** *Eur Spine J* 2011;20:1928–39

38. Woolf AD, Pfleger B. **Burden of major musculoskeletal conditions.** *Bull World Health Organ* 2003;81:646–56

39. Kanis JA, Johnell O, Oden A, et al. **Risk of hip fracture according to the World Health Organization criteria for osteopenia and osteoporosis.** *Bone* 2000;27:585–90

40. Ryken TC, Hadley MN, Aarabi B, et al. **Management of isolated fractures of the axis in adults.** *Neurosurgery* 2013;72(suppl 2):132–50

41. Frangen TM, Zilkens C, Muhr G, et al. **Odontoid fractures in the elderly: dorsal C1/C2 fusion is superior to halo-vest immobilization.** *J Trauma* 2007;63:83–89

42. Collins I, Min WK. **Anterior screw fixation of type II odontoid fractures in the elderly.** *J Trauma* 2008;65:1083–87

43. Dailey AT, Hart D, Finn MA, et al. **Anterior fixation of odontoid fractures in an elderly population.** *J Neurosurg Spine* 2010;12:1–8

44. Börm W, Kast E, Richter HP, et al. **Anterior screw fixation in type II odontoid fractures: is there a difference in outcome between age groups?** *Neurosurgery* 2003;52:1089–92, discussion 1092–94

45. Gebauer M, Lohse C, Barvencik F, et al. **Subdental synchondrosis and anatomy of the axis in aging: a histomorphometric study on 30 autopsy cases.** *Eur Spine J* 2006;15:292–98

46. Mirowitz SA. **Fast scanning and fat-suppression MR imaging of musculoskeletal disorders.** *AJR American J Roentgenol* 1993;161:1147–57

Diffusion-Weighted MRI "Claw Sign" Improves Differentiation of Infectious from Degenerative Modic Type 1 Signal Changes of the Spine

K.B. Patel, M.M. Poplawski, P.S. Pawha, T.P. Naidich, and L.N. Tanenbaum

ABSTRACT

BACKGROUND AND PURPOSE: Modic type 1 degenerative signal changes can mimic/suggest infection, leading to additional costly and sometimes invasive investigations. This retrospective study analyzes the utility and accuracy of a novel, diffusion-weighted "claw sign" for distinguishing symptomatic type 1 degeneration from vertebral diskitis/osteomyelitis.

MATERIALS AND METHODS: Seventy-three patients with imaging features resembling type 1 degeneration were classified clinically into 3 groups: true degenerative type 1 changes ($n = 33$), confirmed diskitis/osteomyelitis ($n = 20$), and radiologically suspected infection later disproved clinically ($n = 20$). A claw sign was defined on DWI as well-marginated, linear, regions of high signal situated within the adjacent vertebral bodies at the interface of normal with abnormal marrow. Two blinded neuroradiologists independently rated the presence of the claw sign, along with T2 disk signal and disk and endplate enhancement to determine the utility of each for identifying degeneration versus infection.

RESULTS: When the 2 neuroradiologists identified a definite claw, 38 of 39 patients (97%) and 29 of 29 patients (100%) proved to be infection-free. When the readers identified a probable claw, 14 of 14 patients (100%) and 16 of 19 patients (84%) proved to be infection-free. Conversely, when the readers identified the absence of claw sign (diffuse DWI pattern), there was proved infection in 17 of 17 cases (100%) and 13 of 14 cases (93%).

CONCLUSIONS: In patients with type 1 signal changes of the vertebral disk space, a claw sign is highly suggestive of degeneration and its absence strongly suggests diskitis/osteomyelitis.

D iffusion-weighted imaging is a critical tool for the evaluation of brain diseases, including ischemia, infection, and inflammation. Recently DWI has gained increasing use in diagnosing pathology in the spine, despite cited limitations,[1,2] and is becoming valuable in the assessment of a variety of disease processes, including tumor and infection.[3-13] Modic type 1 degenerative signal changes on conventional MR imaging sequences can mimic or suggest infection, leading to additional costly and sometimes invasive investigations.[14-17] This study assesses the utility of a specific pattern of diffusion abnormality, the "claw sign," for confirming the presence of true degenerative endplate changes and reducing concern for possible vertebral diskitis/osteomyelitis.

MATERIALS AND METHODS

With prior approval by the institutional review board, the imaging studies and clinical data of patients referred for spinal MR imaging were retrospectively reviewed to select 73 patients with MR imaging features resembling Modic type 1 degeneration at a specific disk level. These patients fell into 3 groups: those with type 1 changes and 1) degeneration with no clinical or imaging suspicion of infection ($n = 33$); 2) clinically confirmed diskitis/osteomyelitis ($n = 20$); and 3) radiologically suspected infection, later disproved clinically ($n = 20$).

In group 2, work-up and clinical evidence of infection included bacteremia, confirmatory biopsy, and/or follow-up imaging. There were 3 biopsy-positive cases of infection with tuberculosis, oxacillin-sensitive *Staphylococcus aureus*, and *Propionibacteria* species. Positive blood cultures were used as sup-
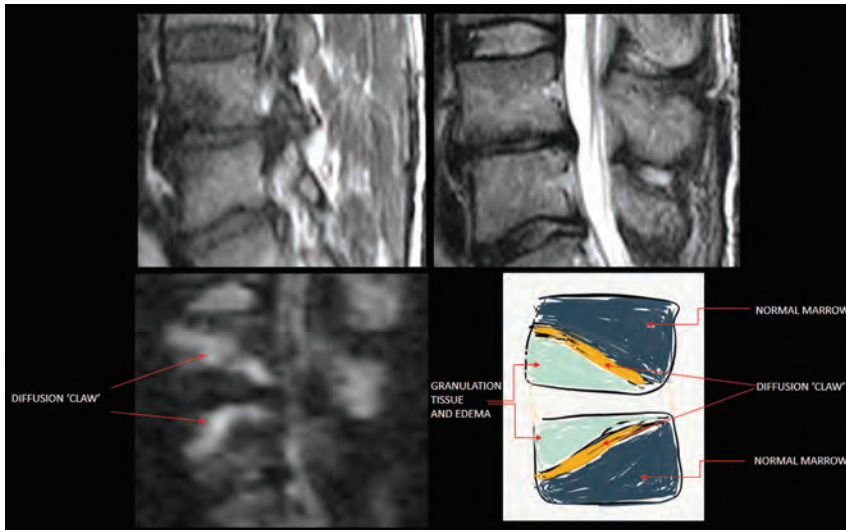
FIG 1. The claw sign is identified on trace/combined DWI as well-marginated, linear, typically paired, regions of high signal situated within adjoined vertebral bodies at the boundaries between the normal bone marrow and vascularized bone marrow.
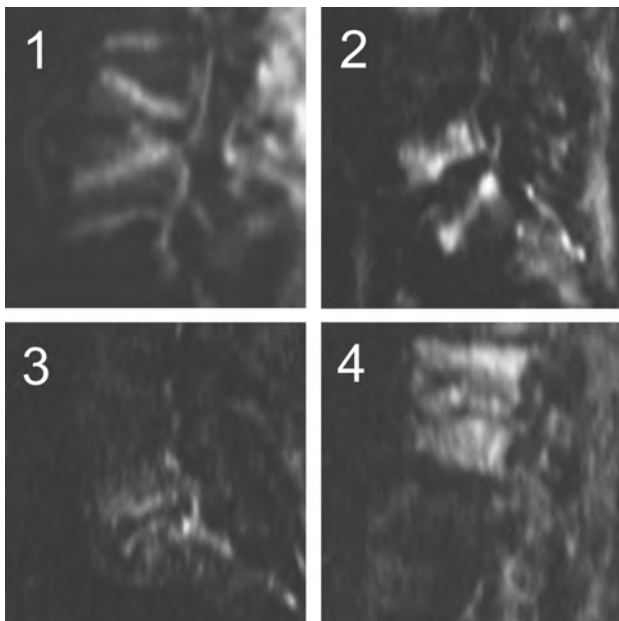

FIG 2. Characterization of the diffusion claw sign. Exemplars of the 4 categories: 1 = definite, 2 = probable, 3 = questionable, 4 = negative (diffuse signal).

of MR imaging signal changes beyond just type 1 changes (predominantly high T2 disk signal and sometimes endplate or disk enhancement). The interpreting radiologists either "could not exclude" or outright suspected infection. Note that in these patients, there was typically no clinical suspicion of infection, including absent symptoms, and lack of any laboratory data to support infection, including negative findings on blood cultures. In certain patients, results of additional work-up were also negative (one, nuclear imaging; another, surgical exploration yielding granulation tissue only). In several patients, while infection could not be definitively excluded on a clinical basis, there was no treatment, and follow-up imaging revealed minimal change, resolution, or evolution to Modic type 2 changes. In some cases, there was no follow-up imaging and no treatment, with presumed resolution of clinical symptoms making infection unlikely.

Modic et al[15] described type 1 degenerative signal changes by using conventional MR imaging techniques, attributed to vascularized bone marrow and edema. The claw sign is identified on trace/combined diffusion-weighted images as well-marginated, linear, typically paired regions of high signal situated within the adjoining vertebral bodies at the boundaries between the normal bone marrow and vascularized bone marrow that lies close to the affected disk, presumed to represent a form of physiologic reactive response or induration (Figs 1–3). The claw sign was deemed absent if the diffusion findings were diffuse and not well-marginated. It seems logical that a gradual, progressive process such as degenerative disk disease would produce a well-defined border response. A destructive process such as infection might progress too quickly and diffusely infiltrate with pathogens or edema and fail to produce a defined border zone response.

The 73 patients were scanned on 3 MR imaging scanner platforms: 1.5T Avanto (Siemens, Erlangen, Germany) and 1.5T Signa HDxt, and 3T Discovery MR750 (GE Healthcare, Milwaukee, Wisconsin). Diffusion-weighted echo-planar imaging was performed in the sagittal plane, with single-shot echo-planar imaging at TR/TE, minimum; FOV, 26 cm; section thickness, 4 mm; intersection gap, 1 mm; and 2–3 excitations (averages). Conventional 6-direction, 3-direction, or tetrahedral diffusion encoding was obtained for a total sequence time of 60–90 seconds. Sagittal T2 and sagittal T1 FLAIR images were obtained in all cases. Sagittal contrast-enhanced, fat-suppressed T1WI was obtained in 49 of the 73 patients. No particular advantage of 3T over 1.5T was noted. This is largely because the diagnosis is primarily based on contrast resolution and coarse morphology of abnormality and not spatial resolution. The additional distortion-based challenges of 3T mitigate any potential SNR advantage.

At each level evaluated with type 1-like conventional signal changes, the images were scored as 1 = definite, 2 = probable, 3 = questionable, or 4 = negative or absent claw sign (Fig 2). Each

porting evidence in 12 patients, including 7 patients with *S aureus* (methicillin-resistant *S aureus, n* = 5; oxacillin-sensitive *S aureus, n* = 2), 1 with *Escherichia coli*, 1 with *Enterococcus faecalis*, 1 with *Streptococcus sanguinis*, and 2 with *Staphylococcus epidermidis*. The patient with *E faecalis* bacteremia was also noted to be immunocompromised. One of the patients with methicillin-resistant *S aureus* bacteremia had positive findings on a nuclear medicine indium-111 white blood cell scan. Progression of disease was noted on follow-up imaging of 4 patients, and 1 patient showed treatment response on subsequent imaging. Also of note, 18 of 20 patients in this group showed epidural, paraspinal, or psoas involvement, which strongly supported the diagnosis of infection.

In group 3, the cases were suspicious for infection on the basis

FIG 3. Both cases show high T2 signal in the affected disk. The claw sign successfully distinguishes disk degeneration from disk infection.

neuroradiologist first assessed and scored the claw sign at a single level on each of the 73 sagittal DWIs. Then each neuroradiologist evaluated the signal intensity of the affected disk on the concurrent sagittal T2 and, when available, STIR series (*n* = 73) and scored the disk signal as high, normal, or low. In the 49 of 73 cases with concurrent, contrast-enhanced fat-suppressed sagittal T1 FLAIR series, the 2 neuroradiologists also noted any enhancement of the disk and any enhancement of the adjacent bone marrow. The 2 readers scored the series separately as no enhancement, mild, moderate, or marked enhancement of the disk and the endplates.

RESULTS

The patients fell into 3 groups: 33 with degenerative Modic type 1 changes and no clinical or imaging suspicion of infection, 20 with clinically confirmed diskitis/osteomyelitis, and 20 with radiologically suspected infection later disproved clinically. For the 2 readers, the diffusion claw sign was identified as present in 26 of 33 and 19 of 33 levels with simple type 1 degenerative endplate changes; 0 of 20 and 1 of 20 patients with proved diskitis/osteomyelitis; and 12 of 20 and 10 of 20 patients with ultimately disproven radiolog-

ically suspected infection. Because the neuroradiologists had different levels of experience using the subjective claw sign in the clinical setting, scoring differed. The scoring data are thus provided for each reader separately in Tables 1–3 and Fig 4*A*, -*B* and are then summarized below.

Diffusion Claw Sign

When a definite claw sign was identified, 38 of 39 patients (97%) and 29 of 29 patients (100%), respectively, were infection-free. When a probable claw was deemed present, 14 of 14 patients (100%) and 16 of 19 patients (84%), respectively, were infection-free. Conversely, when the 2 neuroradiologists identified diffuse signal changes within the adjoining vertebral bodies (negative or absent claw), the patient proved to have infection in 17 of 17 cases (100%) and 13 of 14 cases (93%), respectively. In the specific subgroup of 20 patients with radiologically suspected infection later disproved clinically, the diffusion claw sign was scored definite or probable in 19 of 20 (95%) and 16 of 20 (80%) of cases, respectively.

Disk Signal

High T2 signal within the disk was common in both infected and degenerated disks, reported in 39 of the 73 cases (53%) by reader 1 and in 33 of the 73 cases (45%) by reader 2 (Fig 3 and Tables 2 and 3). However, high T2 disk signal was more common at infected interspaces, 19 of 20

(95%) and 17 of 20 (85%), than in degenerative disks, 20 of 53 (38%) and 16 of 53 (30%). In the specific subgroup of 20 patients with radiologically suspected infection later disproved clinically, the T2 disk signal was scored high in 15 of 20 (75%) and 11 of 20 (55%). Low or normal signal within the disk was more common in patients without infection, 33 of 53 (62%) and 37 of 53 (70%), than in patients with infection, 1 of 20 (3%) and 3 of 20 (15%).

Contrast Enhancement

Contrast enhancement was assessed within a subgroup of 49 of the 73 patients, 17 (35%) with infection and 32 (65%) without infection. Both readers identified at least some enhancement in the endplates in all 49 patients, infected or not. Enhancement of the disk itself was identified slightly more frequently in infected disks: 5 of 20 (25%) and 6 of 20 (30%) than in degenerative disks: 6 of 53 (11%) and 9 of 53 (17%).

DISCUSSION

In this study, infected and degenerative disks could manifest high, normal, or low T2 signal intensity. However, high T2 signal within the affected disk strongly favored a diagnosis of infection over

Table 1: Scoring of the claw sign by 2 readers

	Neuroradiologist 1				Neuroradiologist 2		
Claw Score	Group 1 (n = 33)	Group 2 (n = 20)	Group 3 (n = 20)	Claw Score	Group 1 (n = 33)	Group 2 (n = 20)	Group 3 (n = 20)
1	26	1	12	1	19	0	10
2	7	0	7	2	10	3	6
3	0	2	1	3	3	4	4
4	0	17	0	4	1	13	0

Table 2: Scoring of high T2 signal disk by 2 readers

	Neuroradiologist 1			Neuroradiologist 2	
Claw Score	Groups 1 and 3 (n = 20)	Group 2 (n = 19)	Claw Score	Groups 1 and 3 (n = 16)	Group 2 (n = 17)
1	15	1	1	10	0
2	4	0	2	3	3
3	1	2	3	3	4
4	0	16	4	0	10

Table 3: Scoring of low/normal T2 signal disk by 2 readers

	Neuroradiologist 1			Neuroradiologist 2	
Claw Score	Groups 1 and 3 (n = 33)	Group 2 (n = 1)	Claw Score	Groups 1 and 3 (n = 37)	Group 2 (n = 3)
1	23	0	1	19	0
2	10	0	2	13	0
3	0	0	3	4	0
4	0	1	4	1	3

degeneration when Modic type 1 endplate changes were present. Specifically, high T2 disk signal was seen in 85%–95% of infected disks but in only 30%–35% of degenerative disks with type 1 endplate changes. Low-to-normal T2 signal within the disk strongly favored a diagnosis of degeneration. Specifically, low-normal T2 disk signal was seen in 62%–70% of degenerative disks but only 3%–15% of infected disks.

Contrast enhancement of the disks and endplates proved to be indeterminate findings, as reported in prior studies.[14] At least some contrast enhancement of the vertebral endplates was seen in all cases but did not help to differentiate infection from degeneration. Contrast enhancement of the disk itself was seen slightly more frequently in infected disks (25%–30%) than in degenerative disks (11%–17%), but it was not a distinguishing feature. Return examinations for the sole purpose of postcontrast characterization of type 1 disk levels are advised against because of low efficacy and incremental cost. This policy does not diminish the value of contrast in delineating and characterizing epidural and paraspinal disease in cases in which these conditions are present or strongly suspected.

Of all parameters tested, the diffusion-weighted claw sign proved to be the most successful for predicting the final clinical diagnosis of degeneration versus infection. A definite claw sign accurately identified degenerative spondylosis in 97%–100% of cases. A probable claw sign identified degenerative spondylosis in 84%–100% of cases. Diffusion signal that was increased diffusely throughout the adjoining vertebral bodies (ie, a negative or absent claw sign) indicated the presence of diskitis/osteomyelitis in 93%–100% of cases with that MR imaging feature. No significant difference in diffusion abnormality between organisms was observed, including diffuse restricted diffusion in the tuberculosis, *E coli*, or *Escherichia faecium*, and *S aureus*.

In the specific subgroup of 20 patients with radiologically suspected infection who ultimately proved infection-free, the diffusion claw sign was scored definite or probable in 19 of 20 (95%) and 16 of 20 (80%) cases, strongly indicating degeneration. The T2 disk signal in this subgroup was scored high in 15 of 20 (75%) and 11 of 20 (55%) cases, a finding that would have favored an incorrect diagnosis of infection.

On the basis of these data, we propose an efficient algorithm for the work-up of patients with endplate changes suggestive of Modic type 1 change with degeneration versus infection (Fig 5).

Earlier Work
Eguchi et al[18] evaluated diffusion-weighted imaging in 15 healthy volunteers and 16 patients with vertebral abnormalities. In 11 patients with 20 levels of disk degeneration (7 Modic 1, 7 Modic 2, and 6 Modic 3), the authors reported no high-diffusion signal "at the site of endplate abnormalities in any patients with degenerative changes." In 5 other patients with 9 levels of spinal infection, high diffusion signal was seen at all infected levels.

The apparent discordance of their results versus ours most likely stems from the following factors:

1) We studied only Modic type 1 endplate degeneration, whereas most of the endplate changes included in study of Eguchi et al were types 2 and 3: The degenerative disk illustrated in that study (their Fig 2) was specifically stated to be Modic type 3.
2) We characterized a specific form of diffusion abnormality (the diffusion claw sign), whereas Eguchi et al appear to have taken any form of increased diffusion as positive.
3) We focused on the changes at the interface between the normal marrow and vascularized bone marrow close to the affected disk, whereas Eguchi et al appear to have focused on the disks and the endplates themselves.

Limitations
The present study has a number of limitations. First, the sample size was small. Second, most patients were categorized by their final clinical diagnoses, not tissue diagnosis. Because of the difficulty of ruling out infection, this necessarily raises concern for the group classified as radiologically suspected infection later disproved clinically. Misclassification of such patients could influence the perceived accuracy of the signs described. Nonetheless, the results reported indicate a real utility of applying the diffusion claw sign in assessing patients with possible infection versus degenerative disk disease with Modic type 1 endplate changes.

ADC values have been cited as useful in quantitative assessment of bone marrow lesions.[19] ADC values were not included in our evaluation because the main focus was evaluating the morphology of the detected diffusion trace signal. ADC values ranged from slightly low to high, but image quality and SNR on these
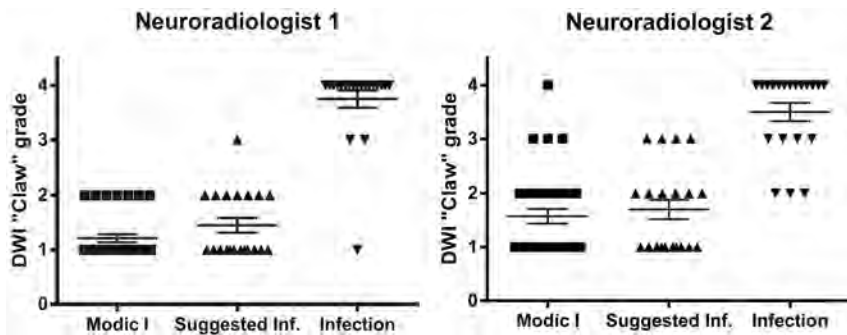
FIG 4. *A*, Modic type 1 = 1.21 ± 0.07; suggested infection = 1.45 ± 0.13; proved infection = 3.75 ± 0.16. *B*, Modic type 1 = 1.58 ± 0.14; suggested infection = 1.70 ± 0.18; proved infection = 3.50 ± 0.17.
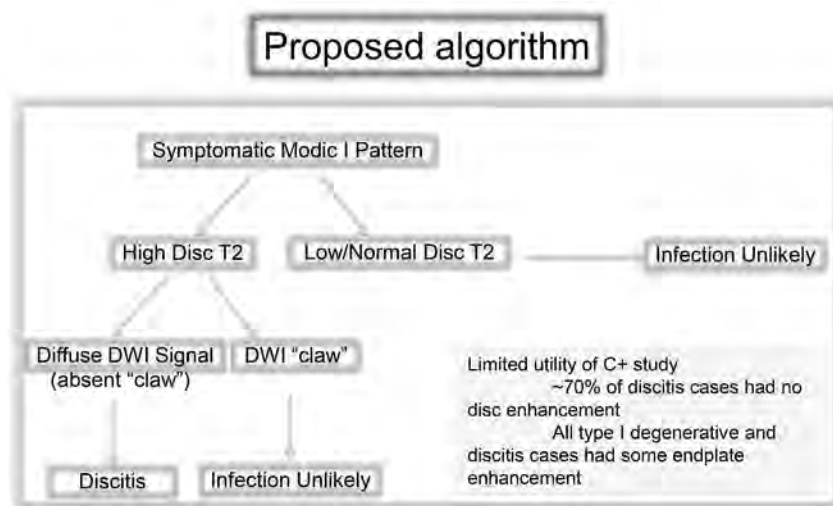

FIG 5. Proposed algorithm for the approach to symptomatic Modic type 1 pattern on spine MR imaging.

studies were poor. With the legacy diffusion techniques used in this study, noise and distortion challenges rendered ADC images unreliable. As multishot and restricted FOV EPI techniques gain widespread use and availability, resolution, SNR, and overall quality will improve, making ADC assessment more practical in day-to-day practice.

The claw pattern on diffusion is a qualitative and morphologic finding. Experience with teaching this subjective sign to clinical readers shows that there is a learning curve. Readers with greater experience apply the sign with greater ease and accuracy. In most cases, it is clear-cut and easy to recognize, even for the recently instructed, and perhaps it is no greater challenge than confirming or excluding the diagnosis of infection with traditional MR imaging indicators. With any subjective signal-based changes based on a physiologic abnormality, equivocal cases can occur. The reader is then left using the preponderance of conventional MR imaging evidence to make the definitive diagnosis. In this trial, a recently initiated reader performed nearly as well as the more experienced reader who had been considering the sign in practice for some time.

This study has defined and validated the diffusion claw sign in symptomatic patients with type 1 endplate changes and degenerative disk disease or infection. The claw sign has not been evalu-

ated at disk levels that manifest type 2 or type 3 endplate changes, but experience suggests it will have limited utility.

CONCLUSIONS

The present study introduces and illustrates a distinct pattern of diffusion abnormality, the claw sign, that is useful and accurate for distinguishing degenerative spondylosis from diskitis/osteomyelitis in patients with Modic type 1 endplate changes. At any suspicious level, a definite diffusion claw sign signifies very high likelihood of degenerative disease (97%–100%) rather than infection. A probable claw sign is highly suggestive of degenerative disk disease (85%–100%) rather than infection. Conversely, a pattern of diffusely increased diffusion signal (negative claw sign) signifies infection in 93%–100% of patients, rather than disk degeneration with Modic type 1 endplate changes. The data additionally suggest that routine use of contrast may not be cost-effective in assisting in the primary diagnosis of infection of the spine.

The diffusion claw sign supplements classic imaging features such as disk signal and can increase accuracy and confidence in the differential diagnosis of degenerative spondylosis versus diskitis/osteomyelitis. The use of the claw sign in day-to-day practice may reduce cost by eliminating or reducing concern for infection in symptomatic patients manifesting type 1 changes, which might otherwise provoke invasive testing and contrast-enhanced and follow-up examinations. With variable experience, there will be variable certainty in the confidence of the presence of the "sign" to mitigate infection. Absent a confident determination, typical decision factors and investigations will apply.

REFERENCES

1. Castillo M, Arbelaez A, Smith JK, et al. **Diffusion-weighted MR imaging offers no advantage over routine noncontrast MR imaging in the detection of vertebral metastases.** *AJNR Am J Neuroradiol* 2000;21:948–53
2. Castillo M. **Diffusion-weighted imaging of the spine: is it reliable?** *AJNR Am J Neuroradiol* 2003;24:1251–53
3. Dietrich O, Biffar A, Reiser MF, et al. **Diffusion-weighted imaging of bone marrow.** *Semin Musculoskeletal Radiol* 2009;13:134–44
4. Baur A, Dietrich O, Reiser M. **Diffusion-weighted imaging of the spinal column.** *Neuroimaging Clin N Am* 2002;12:147–60
5. Byun WM, Shin SO, Chang Y, et al. **Diffusion-weighted MR imaging of metastatic disease to the spine: assessment of response to therapy.** *AJNR Am J Neuroradiol* 2002;23:906–12
6. Koh DM, Collins DJ. **Diffusion-weighted MRI in the body: applica-**

tions and challenges in oncology. *AJR Am J Roentgenol* 2007;
188:162–63

7. Park MJ, Cha ES, Kang BJ, et al. **The role of diffusion-weighted imaging and the apparent diffusion coefficient (ADC) values for breast tumors.** *Korean J Radiol* 2007;8:390–96

8. Shimofusa R, Fujimoto H, Akamata H, et al. **Diffusion-weighted imaging of prostate cancer.** *J Comput Assist Tomogr* 2005;29:149–53

9. Park SW, Lee JH, Ehara S, et al. **Single shot fast spin echo diffusion-weighted MR imaging of the spine: is it useful in differentiating malignant metastatic tumor infiltration from benign fracture edema?** *Clin Imaging* 2004;28:102–08

10. Baur A, Stabler A, Brunning R, et al. **Diffusion-weighted MR imaging of bone marrow: differentiation of benign versus pathologic compression fractures.** *Radiology* 1998;207:349–56

11. Finelli DA. **Diffusion-weighted imaging of acute vertebral compressions: specific diagnosis of benign versus malignant pathologic fractures.** *AJNR Am J Neuroradiol* 2001;22:241–42

12. Karchevsky M, Babb JS, Schweitzer ME. **Can diffusion-weighted imaging be used to differentiate benign from pathologic fractures? A meta-analysis.** *Skeletal Radiol* 2008;37:791–95

13. Eastwood JD, Vollmer RT, Provenzale JM. **Diffusion-weighted imaging in a patient with vertebral and epidural abscesses.** *AJNR Am J Neuroradiol* 2002;23:496–98

14. Oztekin O, Calli C, Kitis O, et al. **Reliability of diffusion weighted MR imaging in differentiating degenerative and infectious end plate changes.** *Radiol Oncol* 2010;44:97–102

15. Modic MT, Steinberg PM, Ross JS, et al. **Degenerative disk disease: assessment of changes in vertebral body marrow with MR imaging.** *Radiology* 1988;166:193–99

16. Dunbar JA, Sandoe JA, Rao AS, et al. **The MRI appearances of early vertebral osteomyelitis and discitis.** *Clin Radiol* 2010;65:974–81

17. Dihlmann W. **Hemispherical spondylosclerosis: a polyetiologic syndrome.** *Skeletal Radiol* 1981;7:99–106

18. Eguchi Y, Ohtori S, Yamashita M, et al. **Diffusion magnetic resonance imaging to differentiate degenerative from infectious end-plate abnormalities in the lumbar spine.** *Spine (Phila Pa 1976)* 2011; 36:E198–202

19. Balliu E, Vilanova JC, Pelaez I, et al. **Diagnostic value of apparent diffusion coefficients to differentiate benign from malignant vertebral bone marrow lesions.** *Eur J Radiol* 2009;69:560–66

Target® Detachable Coil

See package insert for complete indications, contraindications, warnings and instructions for use.

INTENDED USE / INDICATIONS FOR USE
Target Detachable Coils are intended to endovascularly obstruct or occlude blood flow in vascular abnormalities of the neurovascular and peripheral vessels.

Target Detachable Coils are indicated for endovascular embolization of:
- Intracranial aneurysms
- Other neurovascular abnormalities such as arteriovenous malformations and arteriovenous fistulae
- Arterial and venous embolizations in the peripheral vasculature

CONTRAINDICATIONS
None known.

POTENTIAL ADVERSE EVENTS
Potential complications include, but are not limited to: allergic reaction, aneurysm perforation and rupture, arrhythmia, death, edema, embolus, headache, hemorrhage, infection, ischemia, neurological/intracranial sequelae, post-embolization syndrome (fever, increased white blood cell count, discomfort), TIA/stroke, vasospasm, vessel occlusion or closure, vessel perforation, dissection, trauma or damage, vessel rupture, vessel thrombosis. Other procedural complications including but not limited to: anesthetic and contrast media risks, hypotension, hypertension, access site complications.

WARNINGS
- Contents supplied STERILE using an ethylene oxide (EO) process. Do not use if sterile barrier is damaged. If damage is found, call your Stryker Neurovascular representative.
- For single use only. Do not reuse, reprocess or resterilize. Reuse, reprocessing or resterilization may compromise the structural integrity of the device and/or lead to device failure which, in turn, may result in patient injury, illness or death. Reuse, reprocessing or resterilization may also create a risk of contamination of the device and/or cause patient infection or cross-infection, including, but not limited to, the transmission of infectious disease(s) from one patient to another. Contamination of the device may lead to injury, illness or death of the patient.
- After use, dispose of product and packaging in accordance with hospital, administrative and/or local government policy.
- **This device should only be used by physicians who have received appropriate training in interventional neuroradiology or interventional radiology and preclinical training on the use of this device as established by Stryker Neurovascular.**
- Patients with hypersensitivity to 316LVM stainless steel may suffer an allergic reaction to this implant.
- MR temperature testing was not conducted in peripheral vasculature, arteriovenous malformations or fistulae models.
- The safety and performance characteristics of the Target Detachable Coil System (Target Detachable Coils, InZone Detachment Systems, delivery systems and accessories) have not been demonstrated with other manufacturer's devices (whether coils, coil delivery devices, coil detachment systems, catheters, guidewires, and/or other accessories). Due to the potential incompatibility of non Stryker Neurovascular devices with the Target Detachable Coil System, the use of other manufacturer's device(s) with the Target Detachable Coil System is not recommended.
- To reduce risk of coil migration, the diameter of the first and second coil should never be less than the width of the ostium.
- In order to achieve optimal performance of the Target Detachable Coil System and to reduce the risk of thromboembolic complications, it is critical that a continuous infusion of appropriate flush solution be maintained between a) the femoral sheath and guiding catheter, b) the 2-tip microcatheter and guiding catheters, and c) the 2-tip microcatheter and Stryker Neurovascular guidewire and delivery wire. Continuous flush also reduces the potential for thrombus formation on, and crystallization of infusate around, the detachment zone of the Target Detachable Coil.
- Do not use the product after the "Use By" date specified on the package.
- Reuse of the flush port/dispenser coil or use with any coil other than the original coil may result in contamination of, or damage to, the coil.
- Utilization of damaged coils may affect coil delivery to, and stability inside, the vessel or aneurysm, possibly resulting in coil migration and/or stretching.
- The fluoro-saver marker is designed for use with a Rotating Hemostatic Valve (RHV). If used without an RHV, the distal end of the coil may be beyond the alignment marker when the fluoro-saver marker reaches the microcatheter hub.
- If the fluoro-saver marker is not visible, do not advance the coil without fluoroscopy.
- Do not rotate delivery wire during or after delivery of the coil. Rotating the Target Detachable Coil delivery wire may result in a stretched coil or premature detachment of the coil from the delivery wire, which could result in coil migration.
- Verify there is no coil loop protrusion into the parent vessel after coil placement and prior to coil detachment. Coil loop protrusion after coil placement may result in thromboembolic events if the coil is detached.
- Verify there is no movement of the coil after coil placement and prior to coil detachment. Movement of the coil after coil placement may indicate that the coil could migrate once it is detached.
- Failure to properly close the RHV compression fitting over the delivery wire before attaching the InZone® Detachment System could result in coil movement, aneurysm rupture or vessel perforation.
- Verify repeatedly that the distal shaft of the catheter is not under stress before detaching the Target Detachable Coil. Axial compression or tension forces could be stored in the 2-tip microcatheter causing the tip to move during coil delivery. Microcatheter tip movement could cause the aneurysm or vessel to rupture.
- Advancing the delivery wire beyond the microcatheter tip once the coil has been detached involves risk of aneurysm or vessel perforation.
- The long term effect of this product on extravascular tissues has not been established so care should be taken to retain this device in the intravascular space.

Damaged delivery wires may cause detachment failures, vessel injury or unpredictable distal tip response during coil deployment. If a delivery wire is damaged at any point during the procedure, do not attempt to straighten or otherwise repair it. Do not proceed with deployment or detachment. Remove the entire coil and replace with undamaged product.

- After use, dispose of product and packaging in accordance with hospital, administrative and/or local government policy.

CAUTIONS / PRECAUTIONS
- Federal Law (USA) restricts this device to sale by or on the order of a physician.
- Besides the number of InZone Detachment System units needed to complete the case, there must be an extra InZone Detachment System unit as back up.
- Removing the delivery wire without grasping the introducer sheath and delivery wire together may result in the detachable coil sliding out of the introducer sheath.
- Failure to remove the introducer sheath after inserting the delivery wire into the RHV of the microcatheter will interrupt normal infusion of flush solution and allow back flow of blood into the microcatheter.
- Some low level overhead light near or adjacent to the patient is required to visualize the fluoro-saver marker; monitor light alone will not allow sufficient visualization of the fluoro-saver marker.
- Advance and retract the Target Detachable Coil carefully and smoothly without excessive force. If unusual friction is noticed, slowly withdraw the Target Detachable Coil and examine for damage. If damage is present, remove and use a new Target Detachable Coil. If friction or resistance is still noted, carefully remove the Target Detachable Coil and microcatheter and examine the microcatheter for damage.
- If it is necessary to reposition the Target Detachable Coil, verify under fluoroscopy that the coil moves with a one-to-one motion. If the coil does not move with a one-to-one motion or movement is difficult, the coil may have stretched and could possibly migrate or break. Gently remove both the coil and microcatheter and replace with new devices.
- Increased detachment times may occur when:
  – Other embolic agents are present.
  – Delivery wire and microcatheter markers are not properly aligned.
  – Thrombus is present on the coil detachment zone.
- Do not use detachment systems other than the InZone Detachment System.
- Increased detachment times may occur when delivery wire and microcatheter markers are not properly aligned.
- Do not use detachment systems other than the InZone Detachment System.

Stryker Neurovascular
47900 Bayside Parkway
Fremont, CA 94538-6515

stryker.com/neurovascular

Date of Release: JUN/2014

EX_EN_US

Trevo® XP ProVue Retrievers

See package insert for complete indications, complications, warnings, and instructions for use.

INDICATIONS FOR USE
The Trevo Retriever is intended to restore blood flow in the neurovasculature by removing thrombus in patients experiencing ischemic stroke within 8 hours of symptom onset. Patients who are ineligible for intravenous tissue plasminogen activator (IV t-PA) or who fail IV t-PA therapy are candidates for treatment.

COMPLICATIONS
Procedures requiring percutaneous catheter introduction should not be attempted by physicians unfamiliar with possible complications which may occur during or after the procedure. Possible complications include, but are not limited to, the following: air embolism; hematoma or hemorrhage at puncture site; infection; distal embolization; pain/headache; vessel spasm, thrombosis, dissection, or perforation; emboli; acute occlusion; ischemia; intracranial hemorrhage; false aneurysm formation; neurological deficits including stroke; and death.

COMPATIBILITY
3x20 mm retrievers are compatible with Trevo® Pro 14 Microcatheters (REF 90231) and Trevo® Pro 18 Microcatheters (REF 90238). 4x20 mm retrievers are compatible with Trevo® Pro 18 Microcatheters (REF 90238). Compatibility of the Retriever with other microcatheters has not been established. Performance of the Retriever device may be impacted if a different microcatheter is used. The Merci® Balloon Guide Catheters are recommended for use during thrombus removal procedures. Retrievers are compatible with the Abbott Vascular DOC® Guide Wire Extension (REF 22260).

WARNINGS
- Contents supplied STERILE, using an ethylene oxide (EO) process. Nonpyrogenic.
- To reduce risk of vessel damage, adhere to the following recommendations:
  – Take care to appropriately size Retriever to vessel diameter at intended site of deployment.
  – Do not perform more than six (6) retrieval attempts in same vessel using Retriever devices.
  – Maintain Retriever position in vessel when removing or exchanging Microcatheter.
- To reduce risk of kinking/fracture, adhere to the following recommendations:
  – Immediately after unsheathing Retriever, position Microcatheter tip marker just proximal to shaped section. Maintain Microcatheter tip marker just proximal to shaped section of Retriever during manipulation and withdrawal.
  – Do not rotate or torque Retriever.
  – Use caution when passing Retriever through stented arteries.
- Do not resterilize and reuse. Structural integrity and/or function may be impaired by reuse or cleaning.
- The Retriever is a delicate instrument and should be handled carefully. Before use and when possible during procedure, inspect device carefully for damage. Do not use a device that shows signs of damage. Damage may prevent device from functioning and may cause complications.
- Do not advance or withdraw Retriever against resistance or significant vasospasm. Moving or torquing device against resistance or significant vasospasm may result in damage to vessel or device. Assess cause of resistance using fluoroscopy and if needed resheath the device to withdraw.
- If Retriever is difficult to withdraw from the vessel, do not torque Retriever. Advance Microcatheter distally, gently pull Retriever back into Microcatheter, and remove Retriever and Microcatheter as a unit. If undue resistance is met when withdrawing the Retriever into the Microcatheter, consider extending the Retriever using the Abbott Vascular DOC guidewire extension (REF 22260) so that the Microcatheter can be exchanged for a larger diameter catheter such as a DAC® catheter. Gently withdraw the Retriever into the larger diameter catheter.
- Administer anti-coagulation and anti-platelet medications per standard institutional guidelines.

PRECAUTIONS
- Prescription only – device restricted to use by or on order of a physician.
- Store in cool, dry, dark place.
- Do not use open or damaged packages.
- Use by "Use By" date.
- Exposure to temperatures above 54°C (130°F) may damage device and accessories. Do not autoclave.
- Do not expose Retriever to solvents.
- Use Retriever in conjunction with fluoroscopic visualization and proper anti-coagulation agents.
- To prevent thrombus formation and contrast media crystal formation, maintain a constant infusion of appropriate flush solution between guide catheter and Microcatheter and between Microcatheter and Retriever or guidewire.
- Do not attach a torque device to the shaped proximal end of DOC® Compatible Retriever. Damage may occur, preventing ability to attach DOC® Guide Wire Extension.

Concentric Medical
301 East Evelyn
Mountain View, CA 94041

EC | REP

EMERGO Europe
Molenstraat 15
2513 BH, The Hague
The Netherlands

CE 0459

Stryker Neurovascular
47900 Bayside Parkway
Fremont, CA 94538-6515

stryker.com/neurovascular
stryker.com/emea/neurovascular

Date of Release: JUN/2014

EX_EN_GL

Target® Nano™

DETACHABLE COILS

Beyond Soft

The softest coil technology* available, combined with Target Coil's consistently smooth deployment and exceptional microcatheter stability, results in an experience that is beyond soft. Designed to treat small spaces, the Target Nano Coil's incredible softness delivers increased conformability and shape adjustment.

Target Nano Coils–**Smooth and Stable** has never been so soft.

For more information, please visit www.strykerneurovascular.com/Target

stryker
Neurovascular

Stroke: *Our Only Focus. Our Ongoing Promise.*